UNIVERSITY OF CALIFORNIA, SAN DIEGO

Investigations Supporting the Development of a Downhole Energy Harvesting System

A dissertation submitted in partial satisfaction of the
requirements for the degree Doctor of Philosophy

in

Structural Engineering

by

Eric John Kjolsing

Committee in charge:

Professor Michael Todd, Chair
Professor Yuri Bazilevs
Professor Chuck Farrar
Professor William Hodgkiss
Professor Chia-Ming Uang

2016

The Dissertation of Eric John Kjolsing is approved, and it is acceptable in quality and form for publication on microfilm and electronically:

_____

_____

_____

_____

_____

Chair

University of California, San Diego

2016

DEDICATION

To my wife, Taryn Kjolsing, whose patience, support, and love made this work possible.

EPIGRAPH

"We thought of life by analogy with a journey, a pilgrimage,
which had a serious purpose at the end, and the thing was to get to that end,
success or whatever it is, maybe heaven after you're dead. But we missed the point the whole way along.
It was a musical thing and you were supposed to sing or to dance while the music was being played".

Alan Watts

TABLE OF CONTENTS

LIST OF ABBREVIATIONS

AISC	American Institute of Steel Construction
AP	Acceleration Profile
API	American Petroleum Institute
CFD	Computational Fluid Dynamics
DC	Direct Current
DF	Design Factor
FE	Finite Element
FRF	Frequency Response Function
FS	First Script
KE	Kinetic Energy
LANL	Los Alamos National Laboratory
LD	Logarithmic Decrement
LTH	Longitudinal Tube Housing
MRTD	Maximum Relative Tip Displacement
OD	Outer Diameter
PE	Piezoelectric Element
PV	Photovoltaic
RF	Radio Frequency
SDOF	Single Degree of Freedom
SE	Bending Strain Energy
SL	Stroke Length
SPM	Strokes Per Minute
SS	Second Script

TEG	Thermoelectric Energy Generator

LIST OF SYMBOLS

CHAPTER 2

c	Viscous Damping Coefficient
d	Beam Outer Radius
f_d	External Driving Force per Unit Length
f_{hydro}	Hydrodynamic Force per Unit Length
i	Imaginary Unit
k	Frequency Parameter
m	Mass of Pipe per Unit Length
p	Annulus Fluid Pressure
p_0	Undisturbed Fluid Pressure
r	Radial Distance
v_r	Radial Velocity
v_θ	Tangential Velocity
s	Curvilinear Coordinate (Equation of Motion)
s	Normalized Spatial Dimension (Green's Function)
$\hat{s}$	Normalized External Forcing in Frequency Domain Equation of Motion
t	Time
w	Transverse Pipe Displacement
x	Spatial Location
A, B, C, E	Coefficients
B	Normalized Coefficient in Frequency Domain Equation of Motion
$C_{11} - C_{14}$	Green's Function Unknowns
D	Confining Shell Inner Radius
E	Young's Modulus
$\hat{F}_d$	Fourier Transform of the Driving Force
$\hat{F}_h$	Fourier Transform of the Hydrodynamic Force
$F_1(r), F_2(r)$	Stream Function Coefficients
G	Green's Function
I	Pipe Inertia
I_0, I_1, K_0, K_1	Modified Bessel Functions
L	Pipe Length
M	Bending Moment
M_i	Mass of Conveyed Fluid per Unit Length
Q	Shear Force
$U_0 e^{i\omega t}$	Pipe Velocity
$\boldsymbol{V}$	Fluid Velocity Vector
$\widehat{W}$	Fourier Transform of the Beam Displacement
δs	Differential Element Length
η	Annulus Dynamic Fluid Viscosity
ν	Annulus Kinematic Fluid Viscosity
ρ	Annulus Fluid Density
σ_{rr}	Normal Fluid Stress in the Radial Direction
$\sigma_{\theta\theta}$	Normal Fluid Stress in the Tangential Direction
$\tau_{r\theta}$	Shearing Fluid Stress

ψ	Stream Function
ω	Radial Frequency
ω_s	Sampling Frequency
Γ	Hydrodynamic Function
Γ_i	Imaginary Part of the Hydrodynamic Function
Γ_r	Real Part of the Hydrodynamic Function
$\boldsymbol{\nabla}$	Gradient Operator
Ω_s	Range of Frequencies Sampled

CHAPTER 3

$\boldsymbol{a_f}$	Acceleration of Differential Fluid Element
$\boldsymbol{a_p}$	Acceleration of Differential Pipe Element
c	Viscous Damping Coefficient
c_{cr}	Critical Damping Coefficient
c_v	Damping Coefficient
d	Pipe Outer Radius
$\boldsymbol{d}$	Element Nodal Degrees of Freedom Vector
d'	Pipe Inner Radius
$\boldsymbol{d_g}$	Global Spectral Nodal Degrees of Freedom Vector
$\boldsymbol{e}$	Exponential Vector
$\boldsymbol{f}$	Element Nodal Forces Vector
$\boldsymbol{f_g}$	Global Spectral Nodal Forces Vector
f_{hydro}	Hydrodynamic Force per Unit Length
g	Coefficient of Gravity
i	Imaginary Unit
k	Wavenumber
m	Mass of Piper per Unit Length
p	Fluid Pressure
$\overline{p}$	Mean Pressure Differential
q	Wall Shear Stress
$\boldsymbol{r}$	Pipe Position Vector
s	Curvilinear Coordinate (Equation of Motion)
t	Time
u	Axial Displacement of the Pipe (Equation of Motion)
u	Nondimensional Conveyed Fluid Velocity (Parametric Study)
u_{cr}	Normalized Critical Fluid Velocity
w	Lateral Displacement of the Pipe
w_t	Pipe Wall Thickness
x	Spatial Location
$\boldsymbol{A}$	Assembly Matrix
A_i	Conveyed Fluid Flow Area
A_p	Pipe Cross Sectional Area
$\boldsymbol{C}$	Constants Vector
D	Confining Shell Inner Radius
E	Young's Modulus
F	Fluid-Pipe Normal Reaction Force per Unit Length
I	Pipe Inertia
$Im[\,]$	Imaginary Part
K	System Stiffness
K_r	Rotational Boundary Spring Stiffness

K_t	Translational Boundary Spring Stiffness
L	Pipe Length
L^e	Spectral Element Length
M	Bending Moment (Equation of Motion)
M	Nodal Moment (Spectral Element Method)
M_i	Mass of Conveyed Fluid per Unit Length
P	Applied Load
P_{Euler}	Euler Buckling Load
Q	Shear Force (Equation of Motion)
Q	Nodal Shear (Spectral Element Method)
$Re[\,]$	Real Part
S	Pipe Internal Perimeter
$\boldsymbol{S}$	Spectral Element Matrix
$\boldsymbol{S_g}$	Global Dynamic Stiffness Matrix
T	Axial Tension
$\overline{T}$	Externally Applied Tension
T'	Axial Tension Due to Hoop Stress
U	Conveyed Fluid Velocity
U_{cr}	Critical Fluid Velocity
$U_0 e^{i\omega t}$	Pipe Velocity
$\boldsymbol{V_f}$	Velocity of Differential Fluid Element
$\boldsymbol{V_p}$	Velocity of Differential Pipe Element
$\widehat{W}$	Fourier Transform of the Pipe Displacement
δ	Delta Function
δs	Differential Element Length
ε_l	Longitudinal Strain
ζ	Damping Ratio
ν	Poisson's Ratio
ρ_e	Annulus Fluid Density
ρ_i	Conveyed Fluid Density
ρ_p	Pipe Density
σ_a	Axial Stress
σ_h	Hoop Stress
$\boldsymbol{\tau}$	Unit Vector Tangential to the Displaced Pipe
υ	Annulus Kinematic Fluid Viscosity
ω	Radial Frequency
ω_d	Damped Frequency
ω_i	Imaginary Part of Natural Frequency
ω_n	Natural Frequency
$\omega_{n,a}$	Approximation of the Natural Frequency
ω_s	Sampling Frequency
Γ	Hydrodynamic Function
Γ_i	Imaginary Part of the Hydrodynamic Function
Γ_r	Real Part of the Hydrodynamic Function
Ω	Nondimensional Radial Frequency
Ω_c	Normalized Natural Frequency Under a Compressive Load
Ω_s	Range of Frequencies Sampled

CHAPTER 4

a, b	Geometric Terms (Von Mises Criteria)
d	Pipe Outer Radius

p_i	Internal Design Pressure
p_o	External Design Pressure
r	Radial Distance
w_t	Wall Thickness
A, B	Lame Coefficients (Von Mises Criteria)
A, B, C, F, G	Collapse Coefficients
A_{gross}	Pipe Gross Cross Sectional Area
E	Young's Modulus
F	Geometric Ratio (Von Mises Criteria)
P_B	Burst Pressure
$P_{collapse}$	Collapse Pressure
P_E	Elastic Collapse Pressure
P_p	Plastic Collapse Pressure
P_T	Transition Collapse Pressure
P_{Y_p}	Yield Strength Collapse Pressure
Y_p	Yield Strength
Y_{pa}	Yield Strength of Axial Stress Equivalent Grade
σ_r	Radial Stress
σ_t	Tangential Stress
σ_{VM}	Von Mises Stress
σ_z	Axial Stress
ΔT	Temperature Differential
$\Delta\sigma_z$	Excess Axial Stress Above Neutral Value

CHAPTER 5 (FS)

a_n, a_t	Ground Acceleration Time Histories in the Global Normal and Tangential Directions
a_x, a_y, a_z	Ground Acceleration Time Histories in the Global x-, y-, and z-Directions
c_a	Fluid Viscous Damping
c_e	Electric Viscous Damping
c_{eq}	Equivalent Viscous Damping
c_m	Mechanical Viscous Damping
d_m	Maximum Uni-Directional Displacement of the Piezoelectric
f_n	Baseline Natural Frequencies
i	Imaginary Unit
k_{eq}	Equivalent Stiffness
m_{eq}	Equivalent Mass
r	Frequency Ratio
s	Laplace Transform Variable
t	Time
x	Absolute Displacement of SDOF Oscillator
y	Support Displacement
y_s	Single Term Fourier Series Support Displacement
z	Relative Displacement of SDOF Oscillator
z_{max}	Maximum Relative Displacement
z_s	Single Term Fourier Series Relative Displacement
A	Amplitude of Single Term Fourier Series Support Acceleration
A_n	Amplitude of Single Term Fourier Series Support Acceleration Driven at the Natural Frequency
B	Amplitude of Single Term Fourier Series Relative Displacement
$F_{damping}$	Damping Force
H	Transfer Function

M_b	Beam Mass
M_t	Tip Mass
P_{avg}	Average Power
$P_{avg,e}$	Average Power Attributed to the Electric Damper
$P_{avg,m}$	Average Power Attributed to the Mechanical Damper
P_{inst}	Instantaneous Power
$P_{inst,e}$	Instantaneous Power Attributed to the Electric Damper
P_{signal}	Power of the Signal
T	Time Period
$Y(s)$	Laplace Transform of Support Displacement
$Y(\omega)$	Fourier Transform of Support Displacement
$Z(s)$	Laplace Transform of Relative Displacement
$Z(\omega)$	Fourier Transform of Relative Displacement
α	Global Rotation Angle
ϕ	Phase Shift
ζ_e	Electric Viscous Damping Ratio
ζ_{eq}	Equivalent Viscous Damping Ratio
ζ_m	Mechanical Viscous Damping Ratio
θ	Angle from the Global x-Axis
ω	Radial Frequency
ω_n	Natural Frequency

CHAPTER 5 (SS)

a_n, b_n	Fourier Series Coefficients
b	Beam Width
c_a	Fluid Viscous Damping
c_s	Kelvin-Voigt Damping
c_{11}^E	Elastic Modulus of the Piezoelectric at Constant Electric Field
d_{31}	Piezoelectric Strain Constant
$\bar{e}_{31}$	Effective Piezoelectric Stress Constant
f_r	Modal Forcing Term
$h_{\tilde{p}}$	Height of the Piezoelectric Layer
$h_{\tilde{s}}$	Height of the Substrate Layer
i	Imaginary Unit
$i_{\tilde{p}}$	Current Source Stemming from Piezoelectric Layer
m	Beam Mass per Unit Length
r	Mode Number
s_{11}^E	Elastic Compliance of the Piezoelectric at Constant Electric Field
t	Time
w	Total Displacement
w_B	Displacement of the Base
w_R	Relative Displacement
x	Spatial Location Along the Length of the Beam
z	Spatial Location Along the Height of the Beam
A_k	Imposed Displacement Amplitude of the k^{th} Bimorph Tested
C	Mode Shape Coefficients (Eigenvalue Analysis)
C	Percent Accumulated Damage (Damage Accumulation)
$C_{\tilde{p}}$	Capacitance of Piezoelectric Layer
$C_{\tilde{p}}^{eq}$	Equivalent Capacitance for a Piezoelectric Bimorph
D	Electric Displacement
E_3^L	Electric Field component in the z-Direction for the Lower Piezoelectric Layer

E_3^U	Electric Field component in the z-Direction for the Upper Piezoelectric Layer
F_r	Maximum Amplitude of Forcing Function
H	Heaviside Function
H_r	Maximum Amplitude of Steady State Mechanical Response
I	Beam Inertia
I_t	Mass Moment of Inertia of the Tip Mass About $x = L$
L	Beam Length
$\overline{\overline{L}}$	Lagrangian
M	Internal Bending Moment
M_t	Tip Mass
N_k	Number of Cycles Until Failure of the k^{th} Bimorph Tested
P_{avg}	Average Power
P_{inst}	Instantaneous Power
Q	Number of Piezoelectric Bimorphs Tested to Failure
R	Resistive Load
S_1	Axial Strain
$S_1^{\tilde{p}-L}$	Axial Strain in the Lower Piezoelectric Layer
$S_1^{\tilde{p}-U}$	Axial Strain in the Upper Piezoelectric Layer
$S_1^{\tilde{s}}$	Axial Strain in the Substrate
T	Signal Length
T_1	Axial Stress
$T_1^{\tilde{p}-L}$	Axial Stress in the Lower Piezoelectric Layer
$T_1^{\tilde{p}-U}$	Axial Stress in the Upper Piezoelectric Layer
$T_1^{\tilde{s}}$	Axial Stress in the Substrate Layer
V	Property of Interest
$\bar{V}$	Maximum Amplitude of Steady State Voltage Response
V_i	Initial Value of a Property of Interest
$\bar{W}_B$	Maximum Translation Amplitude of the Base Motion
$\bar{Y}$	Circuit Admittance
YI	Weighted Flexural Rigidity
$Y_{\tilde{s}}$	Young's Modulus of the Substrate
α	Voltage Frequency Response Function
β	Relative Displacement Frequency Response Function
δ	Dirac Delta Function
$\underline{\delta}$	Variation Term
$\bar{\varepsilon}_{33}^S$	Permittivity Component at Constant Strain
$\bar{\varepsilon}_{33}^T$	Permittivity Component at Constant Stress
ζ_r	Modal Damping Ratio
η	Generalized Coordinate
ϑ_p	Coefficient of the Backward Coupling Term for Parallel Connection
ϑ_s	Coefficient of the Backward Coupling Term for Series Connection
κ_r	Modal Coupling Coefficient
λ	Eigenvalue
λ_r	Eigenvalue of the r^{th} Mode
ρ_t	Density of the Tip Mass
σ_r	Forcing Function Coefficient
υ	Voltage Across the Resistive Load
υ_p	Voltage Across the Electrodes in a Parallel Configuration
υ_s	Voltage Across the Electrodes in a Series Configuration
ϕ	Eigenfunction
ϕ_r	Eigenfunction of the r^{th} Mode

ω	Radial Frequency
ω_r	Undamped Natural Frequency for the r^{th} Mode
Θ_r	Modal Electromechanical Coupling Term
Φ	Phase Angle of the Voltage Frequency Response Function
Ψ	Phase Angle of the Relative Displacement Frequency Response Function

LIST OF FIGURES

LIST OF TABLES

ACKNOWLEDGEMENTS

I would like to acknowledge my advisor, Professor Michael Todd; I will miss our weekly meetings.

I would also like to acknowledge Chuck Farrar who provided support through the Engineering Institute; the research presented in this dissertation was funded by the Los Alamos National Laboratory.

A majority of the abstract, as well as portions of Chapters 3, 4, and 5 have been published in SPIE Smart Structures and Materials+ Nondestructive Evaluation and Health Monitoring, Eric Kjolsing and Michael Todd, 2016. The title of this paper is "Gauging the Feasibility of a Downhole Energy Harvesting System Through a Proof-of-Concept Study". The dissertation author was the primary investigator and author of this paper.

Chapter 3 also includes content from four other publications, co-authored by Eric Kjolsing and Michael Todd. In each case the dissertation author was the primary investigator and author:

1. "Shifts in the Fundamental Frequency of a Fluid Conveying Pipe Immersed in a Viscous Fluid for use in the Optimization of an Energy Harvesting System to be Deployed in a Producing Hydrocarbon Well", Society of Petroleum Engineers Western Regional Meeting, 2015.
2. "A Frequency Study of a Clamped-Clamped Pipe Immersed in a Viscous Fluid Conveying Internal Steady Flow for use in Energy Harvester Development as Applied to Hydrocarbon Production Wells", SPIE Smart Structures and Materials+ Nondestructive Evaluation and Health Monitoring, 2015.

3. “Frequency Response of a Fixed-Fixed Pipe Immersed in Viscous Fluids, Conveying Internal Steady Flow”, Journal of Petroleum Science and Engineering, 2015.
4. “The Impact of Boundary Conditions and Fluid Velocity on Damping for a Fluid Conveying Pipe in a Viscous Fluid”, SPIE Smart Structures and Materials+ Nondestructive Evaluation and Health Monitoring, 2016.

A portion of Chapter 3 has been submitted for publication in the Journal of Sound and Vibration, Eric Kjolsing and Michael Todd, 2016. The title of this paper is “Damping of a Fluid-Conveying Pipe Surrounded by a Viscous Annulus Fluid”. The dissertation author was the primary investigator and author of this paper.

VITA

2007	B.S. in Structural Engineering	University of California, San Diego
2008	M.S. in Structural Engineering	University of California, San Diego
2011	M.B.A in Finance	San Diego State University
2016	Ph.D. in Structural Engineering	University of California, San Diego

FIELDS OF STUDY

Major Field: Structural Engineering

Studies in Structural Analysis
Professor Michael Todd

Studies in Signal Processing
Professor William Hodgkiss

Studies in Computational Mechanics
Professor Yuri Bazilevs

ABSTRACT OF THE DISSERTATION

Investigations Supporting the Development of a Downhole Energy Harvesting System

by

Eric John Kjolsing

Doctor of Philosophy in Structural Engineering

University of California, San Diego, 2016

Professor Michael Todd, Chair

Hydrocarbon well operators deploy downhole reservoir monitoring equipment in order to optimize the rate at which hydrocarbons are extracted. Alternative power sources are sought that could be deployed in these harsh environments to replace or supplement standard power sources currently in use. To this end, four investigations were performed to support the design of such a device. In the first investigation base assumptions used in the preliminary design of an electromagnetic energy harvester were shown to be in doubt, implying that the expected power output would not meet initial projections. In the second investigation a parametric study was performed to understand how high uncertainty variables affect the natural frequency and damping ratio of a producing hydrocarbon well. In the third investigation a structural housing

was designed to satisfy American Petroleum Institute load cases. Using finite element models and standard tube/casing geometries, design pressures were iterated until a permissible housing design was achieved. This preliminary design provided estimates of the radial width and volume in which energy harvesting and storage elements may be situated. In the last investigation two software programs were developed to estimate the energy that might be harvested from user specified harvester configurations. The programs are dependent on user input production tube accelerations; this permits well operators to use well-specific vibrational data as inputs to generate well-specific energy output estimates. Results indicate that a downhole energy harvesting tool is structurally feasible under reasonable operating conditions but conclusions regarding power output may only be made if actual downhole accelerations are known.

Chapter 1
Introduction

The field of energy harvesting is expansive. Due to the numerous harvesting strategies, transducer designs (which range from the micro to the macro scale), circuitry design, power storage systems, and a variety of applications, the field of energy harvesting has seen significant interest from both researchers and practicing engineers. The underlying objective of energy harvesting systems is to replace or supplement standard power sources, such as batteries or generators, from wasted or unused sources. Fundamentally, this is done by converting non-electric energy into useful electrical energy [1]. The type of non-electrical energy that is converted is dependent on both the operating environment (i.e. what type of non-electrical energy is available to harvest?) and the efficiency of the selected harvesting system (i.e. how much of the available non-electrical energy can a harvesting system actually convert?). As such, the energy harvesting system must be selected based on the environment in, and the structure on which, the harvesting system will be deployed. Typical deployments might involve bridges [2]-[4], marine infrastructure [5]-[6], rail and train [7]-[9], unmanned aerial vehicles [10]-[13], or helicopters [14]-[16]. Of particular interest is the use of energy

harvesting systems to power devices where (1) there is insufficient access to standard power sources, (2) where there is a practical limitation to providing power (e.g. the size, cost, or service life of the power source; the cost and feasibility to replace a standard power source; etc.), or (3) there is an abundance of "wasted" power.

1.1. Energy Sources and Transduction Mechanisms

Non-electrical energy sources are converted into electrical energy by means of a transducer specifically designed or selected for the given application. For example, common energy sources such as solar and vibrational energy may be converted to electrical energy by means of photovoltaic cells and piezoelectric elements, respectively. The appropriate method of transduction is dependent on the available energy sources in a given environment. To select a proper harvesting system, the designer must be aware of what type of energy sources can be harvested and the corresponding transduction mechanism(s) available. The literature provides several review articles and reports discussing various transduction mechanisms as they relate to: structural health monitoring [17], remote sensors [18], microelectronics [19]-[20], embedded systems [21], autonomous systems [22]-[25], and portable electronics [26]-[27]. Comprehensive discussions are provided in the well-recognized texts Energy Harvesting Technologies [28] and Advances in Energy Harvesting Methods [29].

The following sections identify common non-electrical energy sources and briefly discuss the mechanism(s) that may be utilized to convert them to electrical energy. Mechanism-specific references are provided in each section. Considerations for selecting a transduction mechanism are briefly discussed.

1.1.1. Kinetic Energy

The following sections identify common non-electrical energy sources and briefly discuss the mechanism(s) that may be utilized to convert them to electrical energy. Mechanism-specific references are provided in each section. Considerations for selecting a transduction mechanism are briefly discussed.

1.1.1.1. Mechanical Vibration

Transduction mechanisms based on mechanical vibration typically utilize piezoelectric, electromagnetic, electrostatic, or magnetostrictive elements [30]-[31].

Piezoelectric transducers rely on the direct piezoelectric effect, found in certain crystalline materials, which converts mechanical strain into electrical energy [32]. Typical configurations include stacked piezoelectric elements which harvest axial strain energy directly or cantilever piezoelectric elements which harvest axial strain energy indirectly through flexural bending. Cantilever piezoelectrics can be oriented with one or two piezoceramic layers (i.e. a unimorph or bimorph configuration) and are often directly attached to the vibrating host structure [28]. Significant investigation into piezoelectric transducers has been performed with notable reviews by Sodano et al. (2004) [33], Priya (2007) [34], and Anton and Sodano (2007) [35]. A seminal text by Erturk and Inman (2011) [36] provides additional background.

Electromagnetic transducers are based on Farady's law of electromagnetic induction whereby voltage is generated in a conductor (e.g. coil) by varying the magnetic field around the conductor [21]; the mechanical vibration of the supporting structure displaces either the magnet or coil, resulting in the variation to the magnetic field. Popular architectures include a cylindrical magnet oscillating within a coil (either linear or rotational motion) or a planar magnet oscillating adjacent to a coil without immersion [1]. Arnold (2007) [37] provides a review of microscale magnetic power generation while Beeby et al. (2007) [38] compares micro

and macro scale generators. The text by Spreemann and Manoli (2012) [1] provides an in-depth investigation into the transduction mechanism.

Electrostatic energy harvesting is based on the changing capacitance of vibration-dependent capacitors [21]. In this mechanism, a charged capacitor carries equal and opposite charges on two plates. By maintaining the charge on the capacitor while moving the capacitor plates apart, the voltage will increase [19]. Although the development of electrostatic energy harvesters has not progressed to the same degree as piezoelectric or electromagnetic transducers, design concepts have been introduced [39]. In addition, tools to facilitate the analysis, design, and fabrication of harvesters have been developed [40]; prototypes have been designed and tested [41]-[43].

Magnetostrictive transducers utilize the Villari effect to generate a magnetic field when strained [30]. When paired with a conductor (e.g. coil), the time varying magnetic field will generate a voltage based on Faraday's law [44]. An in-depth study of magnetostriction effects is given by Lee (1955) [45]; the importance of nonlinear behavior is emphasized by others [46]-[47]. While stand-alone harvesters have been designed and tested [48]-[49], composites pairing magnetostrictive and piezoelectric elements are not uncommon [50]-[51].

1.1.1.2. Flowing Medium

The kinetic energy of wind or fluid can be harvested through wind or tidal turbines, wave energy converters, hydroelectric dams, or harvesting transducers directly immersed in the fluid flow.

Wind or tidal turbines, wave energy converters, and hydroelectric dams are typically engineered at the mega-scale. In each case, the flowing medium drives a generator resulting in the conversion of the kinetic energy of the flowing medium into electrical energy: wind or tidal flow drives a rotor, causing a torque on the rotors shaft, driving an electric generator; waves

induce motion in buoys which directly or indirectly drive electric generators; flowing or falling water from a dam reservoir drive turbines which generate electricity. Current reviews are available on the more modern technologies (wind energy [52]-[55], tidal turbines [56]-[58], and ocean wave energy converters [59]-[64]). Turbines and harvesters for each technology are either commercially available or in development by firms including: Vestas and Gamesa (wind); Atlantis Resources, Magallanes Renovables, and Tocardo (tidal); Laminaria, Seatricity, and Wello Oy (wave); General Electric and Gilkes (hydroelectric).

Smaller-scale transducer designs place the energy harvesting element directly in the path of the flowing fluid [29]. Realizations often include placing flexible piezoelectric elements, paired with a bluff body, in the fluid flow so that the resulting turbulent flow induces strain in the piezoelectric [65]-[68]. A similar concept utilizing electromagnetic induction has recently been developed [69].

1.1.2. Thermal Energy

Thermoelectric energy generators (TEGs) rely on the Seebeck effect to convert a temperature difference between two dissimilar metals into electrical energy [17]. When a thermal gradient is applied to a TEG, a negative charge builds on the "cold" end of the harvester creating a voltage while the heat flow drives the electric current [28]. The produced electric current is proportional to the applied temperature gradient [19]. TEGs are a mature technology and require no moving parts [22]. Rowe (1999) [70] and Riffat and Ma (2003) [71] provide assessments of the technology while Sootsman et al. (2009) [72] provides a more current review. Applications include geothermal harvesting [73], harvesting heat from automobile exhaust [74], and powering medical equipment using human warmth [75]; experimental investigations are also widely available [76]-[78].

1.1.3. Electromagnetic Radiation

Electromagnetic radiation refers to both solar energy and radio frequency (RF) radiation [19]. Solar energy can be harvested through the use of photovoltaic cells, photosynthesis in plants, and thermal harvesting [26].

Photovoltaic (PV) cells are typically made with semiconductor material (primarily silicon) [19] and rely on the photovoltaic effect to harvest solar energy. As light energy hits the PV cell the semiconducting material absorbs photons and releases electrons [22]. The material junction between two different semiconducting materials within the solar cell drives the free electrons, resulting in an electric current [52]. Solar cells function well in direct sunlight but see a significant reduction in power on overcast days [24]. Being a mature technology [17] there is significant literature covering the development, optimization, and deployment of photovoltaic cells. Review articles are widely available [79]-[82], as are introductory texts [52], [83]-[84]. Specific applications include use in homes, solar powered cars, unmanned aerial vehicles [85], space [86], and wireless embedded systems [87].

RF energy harvesting describes the conversion of electromagnetic radiation into DC power. The harvested energy can originate from directed or non-dedicated sources. The intent of a directed source is to generate and transmit power through electromagnetic waves in a narrow frequency band to a specific receiver which then converts the transmitted power into electric power [88]. Alternatively, RF energy harvesting strategies can utilize ambient RF energy sources whereby harvesters scavenge ambient RF energy from the environment [89]-[91]. Environmental RF energy sources may cover a wide frequency band [92] and include radio and television broadcast antennas, base stations for mobile telephone service, and wireless local area networks [19]. The harvester uses a rectifying antenna to receive and convert the RF

energy into DC power [17]. One current application thrust is in structural health monitoring where RF energy harvesting is being used to power sensor networks [93]-[97].

1.1.4. Other Mechanisms and Novel Applications

Other transduction mechanisms are also being researched. Ouellette and Todd (2014) [5] investigated a corrosion based energy harvester that took advantage of the electrochemical reactions that occur during the corrosion of a cement-seawater battery. Lal and Li (2005) [98] investigated a radioisotope-powered piezoelectric generator. Other researchers have attempted to develop an artificial photosynthetic fuel production system, mimicking the natural process of photosynthesis found in plants [99]-[100].

Hybrid energy harvesters that combine multiple transduction mechanisms or energy sources have also been developed. Combinations include piezoelectrics and electromagnetic induction [101]-[102]; mechanical and solar energy [103]-[104]; and thermal, mechanical, and solar energy [105].

Recently, novel applications in the field of biology have been explored. Starner (1996) [106] explored harnessing human energy in the form of breath, blood pressure, and body heat. Karami and Inman (2012) [107] designed piezoelectric energy harvesters to power pacemakers. Several researchers have harvested energy from implanted biofuel cells operating within living animals [108]-[110]. Others have developed skin-worn tattoo-based electrochemical devices [111].

1.1.5. Considerations for Selection

Multiple transduction mechanisms may be feasibly deployed in certain operating environments. For instance, an unmanned aerial vehicle is capable of harvesting both solar energy with photovoltaic cells and mechanical energy with piezoelectrics. In these instances, a

common comparison metric is the power density which provides a power estimate per unit volume of energy harvester. Typical power densities for commonly utilized energy sources are provided in Table 1. Note that depending on the amplitude and frequency of excitation, the power density for vibration based harvesters may be significantly less or greater than the stated value.

Table 1. Power Densities for Common Energy Sources [24]-[25], [28]

	Power Density ($\mu W/cm^3$)
Solar	15000 – direct sun 150 – cloudy day
Mechanical Vibrations	300
Thermal Gradients	15 @ 10℃
Ambient Radio Frequency	3

Beyond power density, other factors that need to be considered when selecting an energy harvesting system include: the cost of the system; physical restrictions of the size, shape, or weight of the harvester; the required maintenance of and accessibility to the harvester; and the harvesters' ability to survive the structural, moisture, and temperature loading that may be imposed by the operating environment.

1.2. Project Overview

In the current application, an energy harvester is envisioned to power commercially-available monitoring systems in a producing hydrocarbon well. These monitoring systems (e.g. pressure and temperature gauges) are typically located near the hydrocarbon reservoir, are used to optimize hydrocarbon extraction, and are powered by either battery systems or with a power cable (which runs from the ground surface to the monitoring equipment). These conventional power sources are less than optimal as batteries have a finite life span and power cables cause congestion in the well annulus. Ceasing hydrocarbon production to replace or repair these power sources is costly, and as such, alternative power sources are sought.

1.2.1. A Brief Introduction to Hydrocarbon Wells

Like most engineered designs, hydrocarbon wells are individually designed based on economic, geographic, and production limitations. One general configuration is shown in Figure 1 with one possible installation sequence described below.

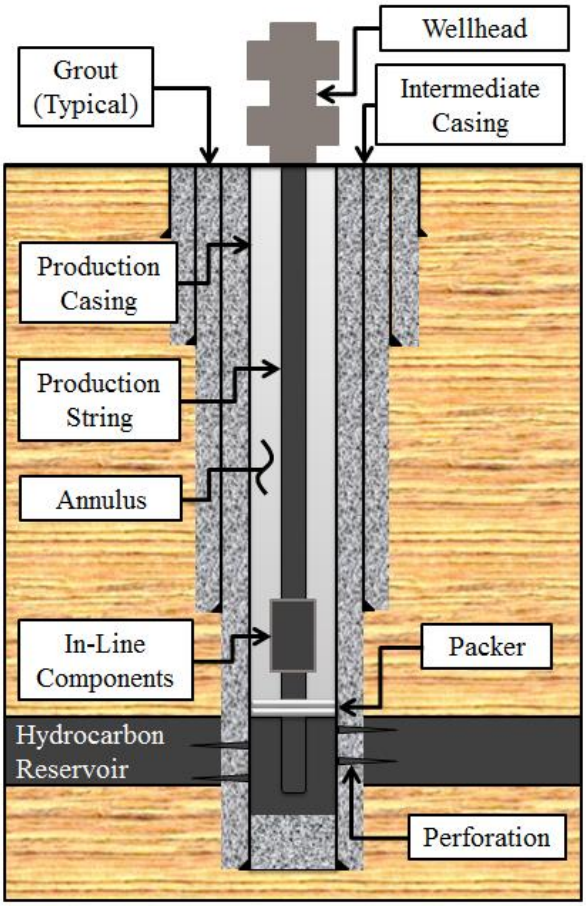

Figure 1. Typical Well Configuration [112]

The well installation begins by removing soil through a drilling process during which the well is filled with a fluid to prevent the surrounding soil from collapsing the well. Periodically, lengths of steel tubing, known as casing, are installed and grouted in place to provide a permanent structure to prevent the well's collapse. After the final length of casing (i.e. the production casing) is installed the well extends into, if not beyond, the hydrocarbon reservoir layer. A small explosive device is lowered into the well to an elevation bounded by

the hydrocarbon reservoir and detonated. This causes perforations through the production casing and grout, allowing the hydrocarbons within the hydrocarbon reservoir to flow into the annulus. Prior to detonation, the annulus fluid density is modified so that the pressure from the hydrocarbon reservoir (post-detonation) is balanced by the static fluid pressure of the annulus fluid; in this way flow of the hydrocarbons is controlled. A small diameter piping system, known as the production string, is lowered through the annulus fluid to the hydrocarbon reservoir layer. A mechanical device, known as a packer, is set in place and provides a boundary between the annulus and hydrocarbon fluids. The hydrocarbons are then extracted from the reservoir layer, through the production string, by controlling the wellhead at the ground surface. Adjacent to the packer are in-line components such as pressure and temperature gauges.

The geometries, material, and other requirements for the production string and production casing are specified by American Petroleum Institute (API) standards [113]-[114]. The lengths of piping making up these strings can be assembled using a variety of connections including integral connections or standard couplings utilizing a variety of thread types.

The reservoir fluid is a mixture of oil, gas, water, and soil particles and is produced using primary, secondary, or tertiary recovery techniques. Primary recovery uses the reservoirs natural energy for production and includes natural drive mechanisms or artificial lift. Secondary recovery relies on external energy to produce hydrocarbons. This energy can be supplied by injecting gas or fluids into the hydrocarbon reservoir using adjacent (non-producing) wells. Lastly, tertiary recovery relies on altering the reservoir fluid properties to improve the flow. This may be accomplished by thermal or chemical injection into the hydrocarbon reservoir.

1.2.2. Related Downhole Energy Harvesting Patents

Numerous patents exist covering various downhole energy harvesting strategies: harvesting elements may include magnetic induction [115], magnetostrictive [116], or piezoelectric elements [117]; the harvesting system may be external to the flow [118], require modification of the flow [119], or be placed within the flow [120]; the systems may utilize membranes [121], vibrating sleeves [122], or rely on modulated fluid flow to help in power generation [123]. One Schlumberger patent attempts to cover a broad range of downhole energy harvesting strategies and configurations [124]. One realization of the Schlumberger patent calls for a bluff body to be included within the conveyed fluid flow to enhance the downhole vibration energy. This mechanical energy can then be harvested using piezoelectric, magnetic induction, or other harvesting strategy.

1.2.3. Existing Hydrocarbon-Specific Systems

While there are many patents covering this design space, few downhole energy harvesting systems have been developed. In most cases, the specific details are unavailable and are protected as intellectual property intended for commercialization.

- *TEG Power Strap*. Developed by Marlow Industries, the TEG power strap is an energy harvesting system for use in the industrial, chemical, oil, and gas sectors. Capable of being fitted to any diameter pipe, the strap uses the thermal gradient existing between the pipe wall and ambient temperature. Its intended use is on above ground piping. The system consists of an aluminum strap, bismuth telluride (Bi_2Te_3) modules and heat sinks [125].

- *iMEC Enabled Vibration Harvester*. Capable of being deployed on drilling or completion equipment, the harvester converts drillstring vibration or hydrocarbon flow

into electric power. The device, developed by Oscilla Power, is based on the Villari effect: changes in material strain are converted to changes in the materials magnetic field [126]-[127].

- *NETL/Tubel Generator and Communications Unit*. Developed in 2005 by Tubel Technologies and funded through the U.S. Department of Energy, this unit utilizes piezoelectric wafers to generate electricity from the flow of hydrocarbons through a production tube. The energy harvesting system is paired with an acoustic telemetry system to transmit the downhole pressure and temperature data to the surface. It is intended for intelligent completions of natural gas wells [128]-[129].

1.2.4. Considered Transduction Mechanisms

Several transduction mechanisms are infeasible based on the operating environment: wind/tidal turbines, wave energy converters, hydroelectric dams, and electromagnetic radiation are inapplicable. Three general strategies remain: harvesting thermal gradients, mechanical vibrations, and the kinetic energy of the flow via an immersed harvester.

A thermal energy harvesting strategy would rely on the thermal gradient that exists between the hydrocarbon reservoir fluid and the annulus fluid/casing. However, since the energy harvesting system would be placed next to the well monitoring equipment (which the harvester is to power), and the well monitoring equipment is typically located near the hydrocarbon reservoir, the change in temperature is expected to be small. As an example, consider an energy harvester located $0.3km$ $(1000ft)$ above the hydrocarbon reservoir. Based on an average geothermal gradient of $30℃/km$ of depth, the temperature differential between the reservoir fluid and the ambient environment would be $9℃$, implying a power density on the

order of $13.5\,\mu W/cm^3$. This is much smaller than the potential power density offered by vibration based harvesters (see Table 1).

The use of an immersed harvester is questionable strictly from a durability point of view. The reservoir fluid is a mixture of oil, gas, water, and soil particles. As the conveyed fluid interacts with the immersed harvester soil particles could damage a flexible piezoelectric harvester which, over time, would become inoperable.

Within the realm of mechanical vibration harvesters, electrostatic and magnetostrictive transducers are not widely available while piezoelectric and electromagnetic harvesters are commercially available from a variety of manufacturers. Should an energy harvesting system be fabricated at any scale, this would have an economic impact on its widespread use.

Based on the above, the envisioned energy harvesting system is based on a piezoelectric or electromagnetic transducer harvesting the mechanical vibrations of the production string.

1.2.5. The Modified Well Configuration

For this project, the typical well configuration from Figure 1 is modified to include a vibration-based energy harvesting system. The envisioned system is to be located adjacent to the in-line components it will power. The energy harvesting system will be stored in a structural housing situated in the annulus and will be fixed to the production tube (i.e. the vibrating production tube will drive the energy harvesting elements). The modified well configuration is shown in Figure 2. It is assumed that a mechanical amplifier may be employed to increase the vibration amplitude of the production string. This amplifier may take the form of a bluff body generating harmonic pressure oscillations (see Figure 3) or may simply be thought of as a yet-to-be-designed amplifier (see Figure 4). Bracing elements have been

included to prevent amplified production tube vibrations from damaging adjacent lengths of tubing or equipment.

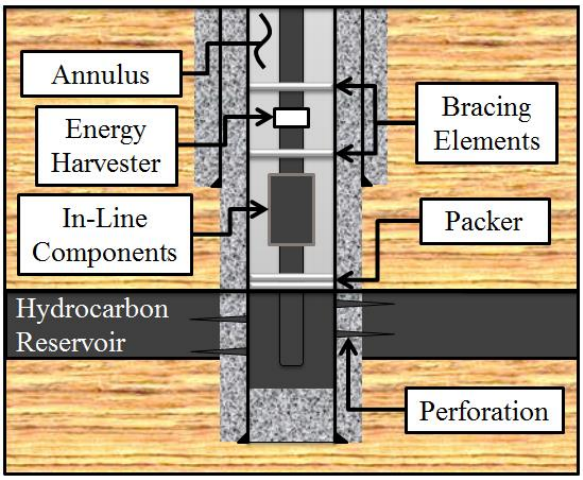

Figure 2. Modified Well Configuration [112]

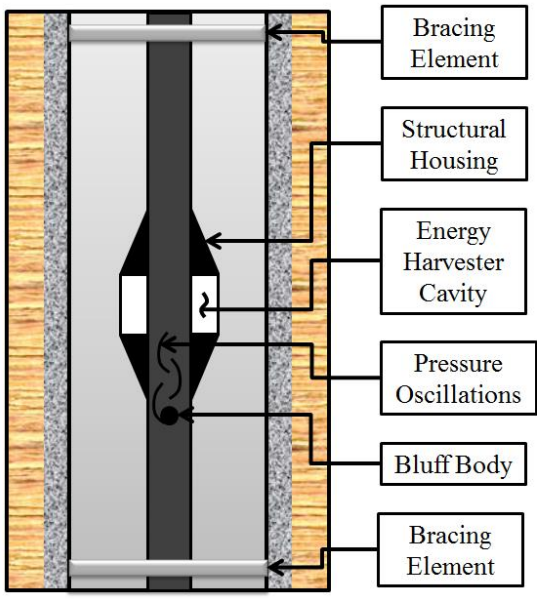

Figure 3. Bluff Body Configuration

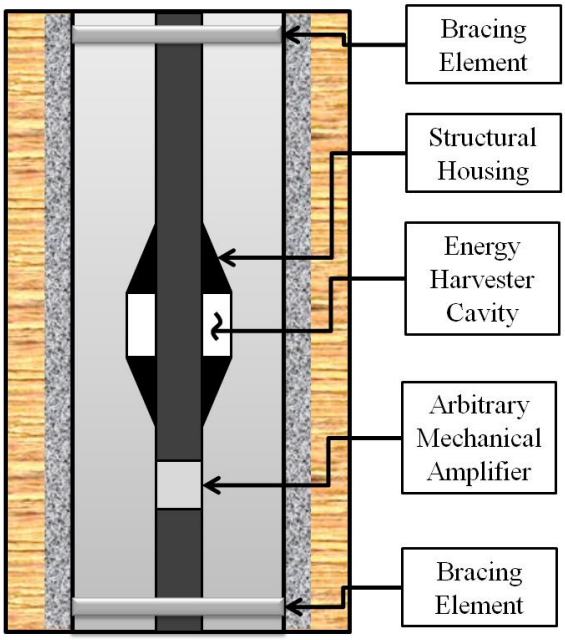

Figure 4. Generic Mechanical Amplifier Configuration

1.2.6. Project Scope and Research Contributions

The initial intent of this project, which originated at Los Alamos National Laboratory (LANL), was to design and fabricate a vibration energy harvesting system that could be used to replace or supplement conventional power sources. An energy harvesting system, in combination with commercially available acoustic telemetry systems, may reduce or eliminate the need for running conductor cable within the annulus from surface to reservoir. By including a bluff body in the conveyed fluid flow, it was believed that the ensuing harmonic pressure oscillations would result in periodic motion of the production tube, permitting the economical deployment of an energy harvesting system. Unfortunately, a numerical investigation showed that the production tube's displacement response assumed in preliminary calculations would not be achievable, implying that the expected power output would not meet initial projections. After failing to obtain intellectual support from industry practitioners, the project was forced to change directions: rather than develop and fabricate a specific energy

harvesting unit, various investigations were performed to support the future design of downhole energy harvesting systems.

This dissertation is divided into four main parts. In Chapter 2, an analytical model is developed which shows the displacement response assumed in preliminary calculations may not be achievable. The model is solved using Green's functions with the applied forcing found from separate finite element computational fluid dynamics models. In Chapter 3, parametric studies are performed to characterize the dynamic behavior of the production tube. The spectral element method is used to determine how the natural frequency and damping ratio of the production tube change as high-uncertainty inputs are varied. In Chapter 4, a preliminary structural housing is designed in which the yet-to-be-designed energy harvesting system will be placed. The preliminary housing design geometrically constrains the size of the energy harvesting system. Lastly, in Chapter 5, two MATLAB programs are introduced which provide power estimates for a user-defined well configuration and acceleration time-histories. Based on the programs outputs, well owners can make informed decisions as to the economic viability of developing and fabricating a vibration-based energy harvesting system for a specific well. These investigations lay an intellectual groundwork that facilitates the future design of a downhole energy harvesting system.

The primary theoretical contributions of this dissertation can be found in Chapter 3 and the latter half of Chapter 5. The parametric study found in Chapter 3 describes the dynamic behavior of a braced production string and identifies how certain variables affect the natural frequency and damping ratio of the system. The latter half of Chapter 5 (that corresponding to the second MATLAB program) includes demonstration cases that illustrate how cyclic damage and temperature changes might effect the power output and displacement response of a vibrating piezoelectric elemenet.

Chapter 2
Preliminary Analytical Model

2.1. Background

Initial proof of concept calculations made by Los Alamos engineers, based on an electromagnetic transducer design, assumed a $\pm 5mm$ harmonic displacement response of the production tube with frequencies generally less than $25Hz$. The initial calculations are provided in Appendix A. The harmonic response would be driven by pressure oscillations within the conveyed fluid, stemming from the inclusion of a bluff body within the production tube (i.e. a Kármán vortex street). The basis for the assumed displacement response is unknown and, as such, needs to be validated or disproved. To this end, a simple beam model is used to calculate the displacement response of the modeled system. The annulus fluid is accounted for through a hydrodynamic forcing function. The pressure oscillations are found from a separate computational fluid dynamics model and, through integration, are represented as a harmonic point load at the midspan of the beam. The effects of the conveyed fluid velocity are assumed negligible (i.e. the conveyed fluid velocity is taken to be zero). While there is an apparent contradiction (including the pressure oscillations stemming from the conveyed fluid while

assuming the conveyed fluid has zero velocity), the model is accurate for conveyed fluid velocities much lower than the divergent velocity of the system.

2.2. The Equation of Motion

The following derivation of the governing equation of motion follows the work of Rao (2007) [130]. Consider the thin beam element shown in Figure 5 with differential element length δs. Forces on the beam include moment (M), shear (Q), viscous damping ($c\ \partial w/\partial t\ \delta s$), an externally applied driving force ($f_d \delta s$), and a hydrodynamic force ($f_{hydro}\delta s$) which accounts for the effects of an external fluid surrounding the pipe. Note that gravity has been neglected.

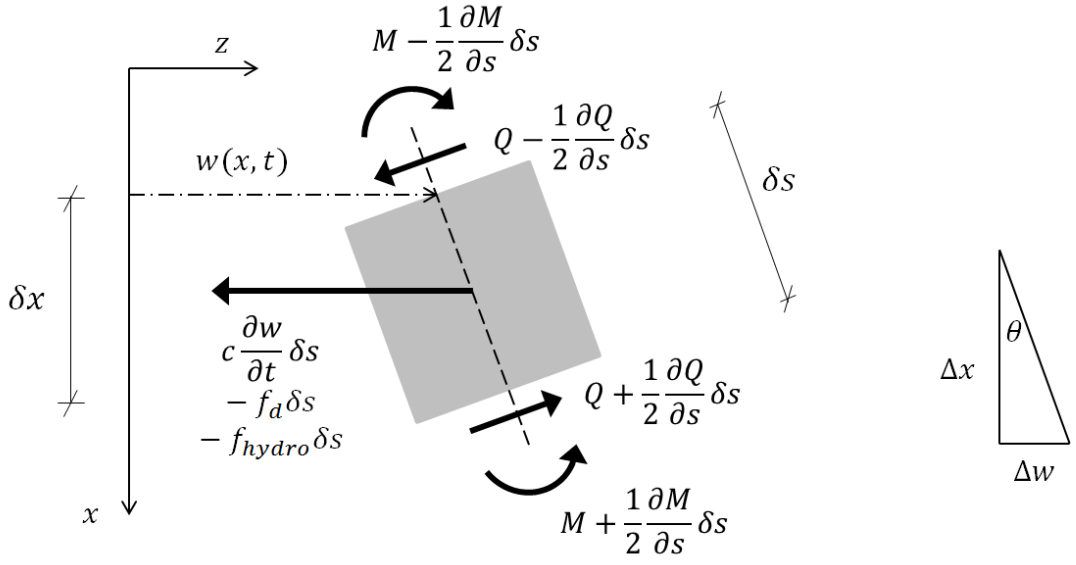

Figure 5. Transverse Vibration of Euler-Bernoulli Beam Element

Applying moment equilibrium leads to

$$\left(M + \tfrac{1}{2}\tfrac{\partial M}{\partial s}\delta s\right) - \left(M - \tfrac{1}{2}\tfrac{\partial M}{\partial s}\delta s\right) + \left(Q - \tfrac{1}{2}\tfrac{\partial Q}{\partial s}\delta s\right)\left(\tfrac{1}{2}\delta s\right) + \left(Q + \tfrac{1}{2}\tfrac{\partial Q}{\partial s}\delta s\right)\left(\tfrac{1}{2}\delta s\right) = 0, \qquad (1)$$

where rotary inertia has been neglected. Assuming that $s \approx x$ under small transverse vibration and simplifying leads to

$$Q = -\frac{\partial M}{\partial s} = -\frac{\partial M}{\partial x} = -EI\frac{\partial^3 w}{\partial x^3}, \tag{2}$$

where the Young's modulus and inertia are treated as constant over the length of interest. Applying horizontal equilibrium leads to

$$-\left[(Qcos\theta) - \frac{1}{2}\frac{\partial}{\partial s}(Qcos\theta)\delta s\right] + \left[(Qcos\theta) + \frac{1}{2}\frac{\partial}{\partial s}(Qcos\theta)\delta s\right] - c\frac{\partial w}{\partial t}\delta s + f_d\delta s + f_{hydro}\delta s = (m + M_i)\frac{\partial^2 w}{\partial t^2}\delta s, \tag{3}$$

where for a small angle approximation

$$cos\theta \approx 1, \tag{4}$$

leading to

$$\frac{\partial Q}{\partial x}\delta s - c\frac{\partial w}{\partial t}\delta s + f_d\delta s + f_{hydro}\delta s = (m + M_i)\frac{\partial^2 w}{\partial t^2}\delta s, \tag{5}$$

where again, $s \approx x$. Dividing by the differential element length and incorporating Eq. (2), the equation of motion is written as

$$EI\frac{\partial^4 w}{\partial x^4} + c\frac{\partial w}{\partial t} + (m + M_i)\frac{\partial^2 w}{\partial t^2} = f_d + f_{hydro}. \tag{6}$$

The result can be spatially normalized as $\overline{x} = x/L$. For simplicity, the following equations continue to use x with the understanding that the equations have been spatially normalized by the beam length, i.e. $x \in [0,1]$ instead of $x \in [0, L]$.

2.3. Hydrodynamic Forcing Function

A hydrodynamic forcing function is needed to represent the effects of the viscous annulus fluid. The following derivation of the hydrodynamic forcing follows the work of Wambsagnss et al. (1974) [131]. The hydrodynamic function was originally introduced by Stokes [132] and later investigated by others [133]-[135]. Its effects have been extensively discussed and validated with experimentation [136] and finite element modeling for small amplitude vibrations [137]. It has been used by a number of researchers investigating: fixed-

free beams [138]-[139], fixed-pinned beams [140], and fixed-fixed beams [141]. Recently, the hydrodynamic function has been extensively used in investigations relating to the atomic force microscope and microcantilevers [142]-[146]. The assumptions used in the derivation of the hydrodynamic forcing are summarized in Table 2.

Table 2. Assumptions Used in the Derivation of the Hydrodynamic Forcing

	Assumptions	Notes
1	The beam is vibrating in a viscous fluid enclosed by a rigid, concentric cylindrical shell.	This assumes that the production casing acts as a rigid, concentric cylindrical shell.
2	The beam is cylindrical with a uniform cross section over its entire length.	This assumes that there is no change in mass/stiffness at the harvester, storage element, or tubing coupling.
3	The fluid boundary conditions are zero velocity at the outer shell and that the fluid velocity matches the beam velocity on the beam surface.	
4	The length of the beam greatly exceeds its nominal diameter.	This assumes the fluid flow is limited to two dimensions.
5	The beam is an isotropic linearly elastic solid.	
6	The amplitude of vibration of the beam is far smaller than any length scale in the beam geometry.	This assumption will allow for the nonlinear convective inertial terms in the fluid equations of motion to be neglected.
7	The annulus fluid is assumed homogeneous, Newtonian, and incompressible.	This allows for simplification of the fluid equations of motion.

Consider a cylindrical beam with radius d vibrating in a viscous fluid, located concentrically to a rigid casing with radius D (see Figure 6).

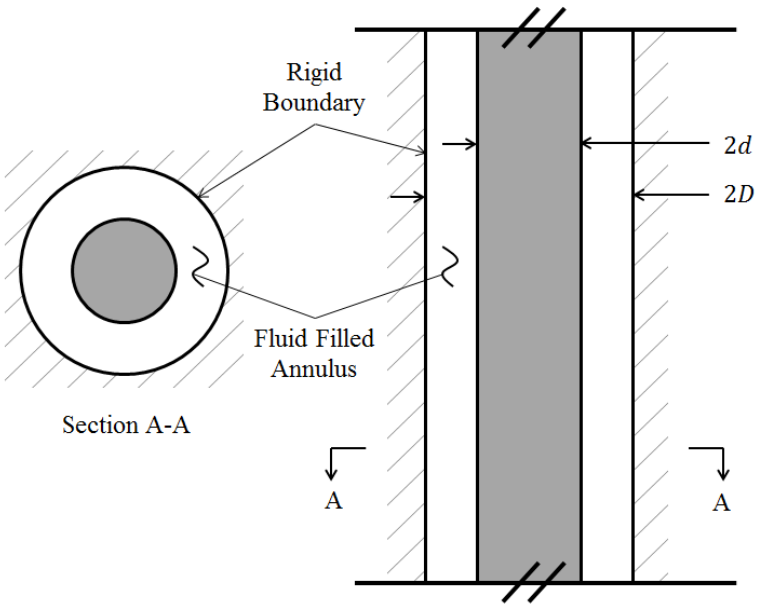

Figure 6. Configuration of Interest

Assuming small amplitude vibrations and incompressibility, the fluid equations of motion are

$$\begin{aligned} \boldsymbol{\nabla}\cdot\boldsymbol{V} &= 0, \\ \rho\left(\frac{\partial \boldsymbol{V}}{\partial t}\right) &= -\boldsymbol{\nabla}\mathrm{p} + \eta\nabla^2\boldsymbol{V}, \end{aligned} \tag{7}$$

where the first equation is the continuity equation and the second equation is the Navier-Stokes equation. As the derivation for the fluid equations are available in most fluids text (e.g. Munson et al. (2006) [147]), they are not reproduced here. Assume the length of the beam is much greater than the beams radius (i.e. L/d is large) such that the fluid motion is restricted to a plane orthogonal to the axis of the beam (i.e. two dimensional flow). Expanding Eq. (7) in cylindrical notation leads to [147]

$$\begin{aligned} \frac{1}{r}\frac{\partial(r\mathrm{v}_r)}{\partial r} + \frac{1}{r}\frac{\partial \mathrm{v}_\theta}{\partial \theta} &= 0, \\ \rho\frac{\partial \mathrm{v}_r}{\partial t} &= -\frac{\partial \mathrm{p}}{\partial r} + \eta\left[\frac{\partial^2 \mathrm{v}_r}{\partial r^2} + \frac{1}{r}\frac{\partial \mathrm{v}_r}{\partial r} - \frac{\mathrm{v}_r}{r^2} + \frac{1}{r^2}\frac{\partial^2 \mathrm{v}_r}{\partial \theta^2} - \frac{2}{r^2}\frac{\partial \mathrm{v}_\theta}{\partial \theta}\right], \\ \rho\frac{\partial \mathrm{v}_\theta}{\partial t} &= -\frac{1}{r}\frac{\partial \mathrm{p}}{\partial \theta} + \eta\left[\frac{\partial^2 \mathrm{v}_\theta}{\partial r^2} + \frac{1}{r}\frac{\partial \mathrm{v}_\theta}{\partial r} - \frac{\mathrm{v}_\theta}{r^2} + \frac{1}{r^2}\frac{\partial^2 \mathrm{v}_\theta}{\partial \theta^2} + \frac{2}{r^2}\frac{\partial \mathrm{v}_r}{\partial \theta}\right]. \end{aligned} \tag{8}$$

The relevant shear stresses can be written as [147]

$$\begin{aligned} \sigma_{rr} &= -\mathrm{p} + 2\eta\frac{\partial \mathrm{v}_r}{\partial r}, \\ \sigma_{\theta\theta} &= -\mathrm{p} + 2\eta\left(\frac{1}{r}\frac{\partial \mathrm{v}_\theta}{\partial \theta} + \frac{\partial \mathrm{v}_r}{\partial r}\right), \\ \tau_{r\theta} &= \tau_{\theta r} = \eta\left[r\frac{\partial}{\partial r}\left(\frac{\mathrm{v}_\theta}{r}\right) + \frac{1}{r}\frac{\partial \mathrm{v}_r}{\partial \theta}\right]. \end{aligned} \tag{9}$$

The velocity of the oscillating cylindrical beam can be written as $U_0 e^{i\omega t}$. At the surface of the beam (i.e. at $r = d$), the annulus fluid velocity must match the beam velocity while at the face of the encapsulating shell (i.e. at $r = D$) the velocity is zero. That is,

$$\begin{aligned} \mathrm{v}_r|_{r=d} &= U_0 e^{i\omega t}\cos\theta, \\ \mathrm{v}_r|_{r=D} &= 0, \\ \mathrm{v}_\theta|_{r=d} &= -U_0 e^{i\omega t}\sin\theta, \\ \mathrm{v}_\theta|_{r=D} &= 0, \end{aligned} \tag{10}$$

where the coordinate system is shown in Figure 7.

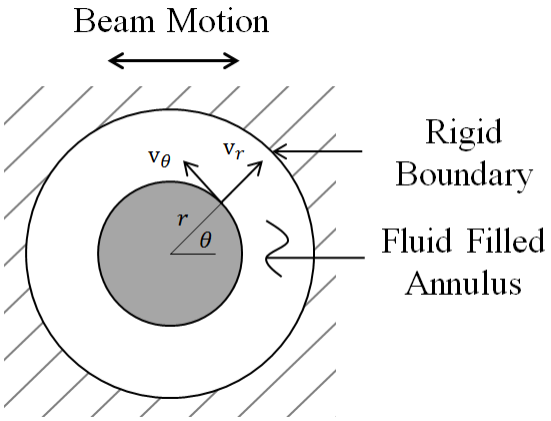

Figure 7. Two Dimensional Cross Section of Beam System

A scalar stream function can be introduced as

$$\begin{aligned} v_r &= -\frac{1}{r}\frac{\partial \psi}{\partial \theta}, \\ v_\theta &= \frac{\partial \psi}{\partial r}. \end{aligned} \tag{11}$$

Note that Wambsganss et al. (1975) [131] used the given sign convention while Stokes (1851) [132] and Rosenhead (1963) [133] used a slightly different form (that is, the negative signs were switched). Using Eq. (11), the first Navier-Stokes equation given in Eq. (8) is rewritten as

$$-\frac{\rho}{r}\frac{\partial^2 \psi}{\partial \theta \partial t} = -\frac{\partial p}{\partial r} + \eta\left[\frac{\partial^2}{\partial r^2}\left(-\frac{1}{r}\frac{\partial \psi}{\partial \theta}\right) + \frac{1}{r}\frac{\partial}{\partial r}\left(-\frac{1}{r}\frac{\partial \psi}{\partial \theta}\right) + \frac{1}{r^3}\frac{\partial \psi}{\partial \theta} - \frac{1}{r^3}\frac{\partial^3 \psi}{\partial \theta^3} - \frac{2}{r^2}\frac{\partial^2 \psi}{\partial r \partial \theta}\right]. \tag{12}$$

Applying the chain rule leads to

$$-\frac{\rho}{r}\frac{\partial^2 \psi}{\partial \theta \partial t} = -\frac{\partial p}{\partial r} + \eta\left[-\frac{2}{r^3}\frac{\partial \psi}{\partial \theta} + \frac{2}{r^2}\frac{\partial^2 \psi}{\partial r \partial \theta} - \frac{1}{r}\frac{\partial^3 \psi}{\partial r^2 \partial \theta} + \frac{1}{r^3}\frac{\partial \psi}{\partial \theta} - \frac{1}{r^2}\frac{\partial^2 \psi}{\partial r \partial \theta} + \frac{1}{r^3}\frac{\partial \psi}{\partial \theta} - \frac{1}{r^3}\frac{\partial^3 \psi}{\partial \theta^3} - \frac{2}{r^2}\frac{\partial^2 \psi}{\partial r \partial \theta}\right], \tag{13}$$

where after reduction

$$-\frac{\rho}{r}\frac{\partial^2 \psi}{\partial \theta \partial t} = -\frac{\partial p}{\partial r} + \eta\left[-\frac{1}{r^2}\frac{\partial^2 \psi}{\partial r \partial \theta} - \frac{1}{r}\frac{\partial^3 \psi}{\partial r^2 \partial \theta} - \frac{1}{r^3}\frac{\partial^3 \psi}{\partial \theta^3}\right]. \tag{14}$$

Similarly, the second Navier-Stokes equation given in Eq. (8) is rewritten as

$$-r\rho\frac{\partial^2 \psi}{\partial r \partial t} = \frac{\partial p}{\partial \theta} - \eta\left[r\frac{\partial^3 \psi}{\partial r^3} + \frac{\partial^2 \psi}{\partial r^2} - \frac{1}{r}\frac{\partial \psi}{\partial r} + \frac{1}{r}\frac{\partial^3 \psi}{\partial r \partial \theta^2} - \frac{2}{r^2}\frac{\partial^2 \psi}{\partial \theta^2}\right]. \tag{15}$$

The pressure term can be eliminated by differentiating and equating Eq. (14) and Eq. (15). Differentiating Eq. (14) by θ results in

$$-\frac{\rho}{r}\frac{\partial^3\psi}{\partial\theta^2\partial t} = -\frac{\partial \mathrm{p}}{\partial r\partial\theta} + \eta\left[-\frac{1}{r^2}\frac{\partial^3\psi}{\partial r\partial\theta^2} - \frac{1}{r}\frac{\partial^4\psi}{\partial r^2\partial\theta^2} - \frac{1}{r^3}\frac{\partial^4\psi}{\partial\theta^4}\right], \tag{16}$$

while differentiating Eq. (15) by r results in

$$-\rho\frac{\partial}{\partial r}\left(r\frac{\partial^2\psi}{\partial r\partial t}\right) = \frac{\partial \mathrm{p}}{\partial r\partial\theta} - \eta\left[\frac{\partial}{\partial r}\left(r\frac{\partial^3\psi}{\partial r^3}\right) + \frac{\partial^3\psi}{\partial r^3} - \frac{\partial}{\partial r}\left(\frac{1}{r}\frac{\partial\psi}{\partial r}\right) + \frac{\partial}{\partial r}\left(\frac{1}{r}\frac{\partial^3\psi}{\partial r\partial\theta^2}\right) - 2\frac{\partial}{\partial r}\left(\frac{1}{r^2}\frac{\partial^2\psi}{\partial\theta^2}\right)\right]. \tag{17}$$

Eq. (17) can be expanded with the chain rule and simplified to

$$-\rho\frac{\partial^2\psi}{\partial r\partial t} - \rho r\frac{\partial^3\psi}{\partial r^2\partial t} = \frac{\partial \mathrm{p}}{\partial r\partial\theta} - \eta\left[r\frac{\partial^4\psi}{\partial r^4} + 2\frac{\partial^3\psi}{\partial r^3} - \frac{1}{r}\frac{\partial^2\psi}{\partial r^2} + \frac{1}{r^2}\frac{\partial\psi}{\partial r} - \frac{3}{r^2}\frac{\partial^3\psi}{\partial r\partial\theta^2} + \frac{1}{r}\frac{\partial^4\psi}{\partial r^2\partial\theta^2} + \frac{4}{r^3}\frac{\partial^2\psi}{\partial\theta^2}\right]. \tag{18}$$

Setting Eq. (16) equal to Eq. (18) through $\partial \mathrm{p}/(\partial r\partial\theta)$ and rearranging terms leads to

$$r\rho\frac{\partial}{\partial t}\left[\frac{1}{r^2}\frac{\partial^2\psi}{\partial\theta^2} + \frac{1}{r}\frac{\partial\psi}{\partial r} + \frac{\partial^2\psi}{\partial r^2}\right] + \eta\left[\frac{2}{r^2}\frac{\partial^3\psi}{\partial r\partial\theta^2} - \frac{2}{r}\frac{\partial^4\psi}{\partial r^2\partial\theta^2} - \frac{1}{r^3}\frac{\partial^4\psi}{\partial\theta^4} - \frac{4}{r^3}\frac{\partial^2\psi}{\partial\theta^2} - r\frac{\partial^4\psi}{\partial r^4} - 2\frac{\partial^3\psi}{\partial r^3} + \frac{1}{r}\frac{\partial^2\psi}{\partial r^2} - \frac{1}{r^2}\frac{\partial\psi}{\partial r}\right] = 0. \tag{19}$$

Note that the first bracketed term is the Laplace operator applied to the stream function ψ, i.e., the first term can be rewritten as

$$r\rho\frac{\partial}{\partial t}\left[\frac{1}{r^2}\frac{\partial^2\psi}{\partial\theta^2} + \frac{1}{r}\frac{\partial\psi}{\partial r} + \frac{\partial^2\psi}{\partial r^2}\right] = r\rho\frac{\partial}{\partial t}\nabla^2\psi. \tag{20}$$

The second bracketed term is more involved. First consider the expansion of $\nabla^4\psi$

$$\nabla^4\psi = \left(\frac{1}{r^2}\frac{\partial^2}{\partial\theta^2} + \frac{1}{r}\frac{\partial}{\partial r} + \frac{\partial^2}{\partial r^2}\right)\left(\frac{1}{r^2}\frac{\partial^2\psi}{\partial\theta^2} + \frac{1}{r}\frac{\partial\psi}{\partial r} + \frac{\partial^2\psi}{\partial r^2}\right), \tag{21}$$

which, when expanded gives

$$\nabla^4\psi = \left\{\frac{1}{r^4}\frac{\partial^4\psi}{\partial\theta^4} + \frac{1}{r^3}\frac{\partial^3\psi}{\partial r\partial\theta^2} + \frac{1}{r^2}\frac{\partial^4\psi}{\partial r^2\partial\theta^2}\right\} + \left\{\frac{1}{r}\frac{\partial}{\partial r}\left(\frac{1}{r^2}\frac{\partial^2\psi}{\partial\theta^2}\right) + \frac{1}{r}\frac{\partial}{\partial r}\left(\frac{1}{r}\frac{\partial\psi}{\partial r}\right) + \frac{1}{r}\frac{\partial^3\psi}{\partial r^3}\right\} + \left\{\frac{\partial^2}{\partial r^2}\left(\frac{1}{r^2}\frac{\partial^2\psi}{\partial\theta^2}\right) + \frac{\partial^2}{\partial r^2}\left(\frac{1}{r}\frac{\partial\psi}{\partial r}\right) + \frac{\partial^4\psi}{\partial r^4}\right\}. \tag{22}$$

Using the chain rule and combining terms results in

$$\nabla^4\psi = \frac{1}{r^4}\frac{\partial^4\psi}{\partial\theta^4} + \frac{4}{r^4}\frac{\partial^2\psi}{\partial\theta^2} - \frac{2}{r^3}\frac{\partial^3\psi}{\partial r\partial\theta^2} + \frac{2}{r^2}\frac{\partial^4\psi}{\partial r^2\partial\theta^2} + \frac{\partial^4\psi}{\partial r^4} + \frac{2}{r}\frac{\partial^3\psi}{\partial r^3} - \frac{1}{r^2}\frac{\partial^2\psi}{\partial r^2} + \frac{1}{r^3}\frac{\partial\psi}{\partial r}. \tag{23}$$

Multiplying both sides by r leads to

$$r\nabla^4\psi = \frac{1}{r^3}\frac{\partial^4\psi}{\partial\theta^4} + \frac{4}{r^3}\frac{\partial^2\psi}{\partial\theta^2} - \frac{2}{r^2}\frac{\partial^3\psi}{\partial r\partial\theta^2} + \frac{2}{r}\frac{\partial^4\psi}{\partial r^2\partial\theta^2} + r\frac{\partial^4\psi}{\partial r^4} + 2\frac{\partial^3\psi}{\partial r^3} - \frac{1}{r}\frac{\partial^2\psi}{\partial r^2} + \frac{1}{r^2}\frac{\partial\psi}{\partial r}. \tag{24}$$

Plugging Eq. (20) and (24) into Eq. (19) leads to

$$r\rho\frac{\partial}{\partial t}\nabla^2\psi - \eta[r\nabla^4\psi] = 0. \tag{25}$$

Or more simply

$$\nabla^4\psi - \frac{1}{\nu}\frac{\partial}{\partial t}\nabla^2\psi = \left(\nabla^2 - \frac{1}{\nu}\frac{\partial}{\partial t}\right)\nabla^2\psi = 0, \tag{26}$$

where the kinematic viscosity term, $\nu = \eta/\rho$, has been introduced. The general solution of Eq. (26) is [131]

$$\psi = \psi_1 + \psi_2, \tag{27}$$

Where ψ_1 and ψ_2 satisfy

$$\begin{aligned}\nabla^2\psi_1 &= \left(\frac{\partial^2}{\partial r^2} + \frac{1}{r}\frac{\partial}{\partial r} + \frac{1}{r^2}\frac{\partial^2}{\partial\theta^2}\right)\psi_1 = 0,\\ \left(\nabla^2 - \frac{1}{\nu}\frac{\partial}{\partial t}\right)\psi_2 &= \left(\frac{\partial^2}{\partial r^2} + \frac{1}{r}\frac{\partial}{\partial r} + \frac{1}{r^2}\frac{\partial^2}{\partial\theta^2} - \frac{1}{\nu}\frac{\partial}{\partial t}\right)\psi_2 = 0.\end{aligned} \tag{28}$$

Based on the boundary conditions (i.e. Eq. (10)), the general form of the solution is

$$\begin{aligned}\psi_1 &= e^{i\omega t}sin\theta * F_1(r),\\ \psi_2 &= e^{i\omega t}sin\theta * F_2(r).\end{aligned} \tag{29}$$

The task then becomes solving for the coefficients $F_1(r)$ and $F_2(r)$. Plugging Eq. (29) into the governing equations (i.e. Eq. (28)) results in

$$\begin{aligned}\frac{\partial^2 F_1(r)}{\partial r^2} + \frac{1}{r}\frac{\partial F_1(r)}{\partial r} - \frac{1}{r^2}F_1(r) &= 0,\\ \frac{\partial^2 F_2(r)}{\partial r^2} + \frac{1}{r}\frac{\partial F_2(r)}{\partial r} - \frac{1}{r^2}F_2(r) - \frac{i\omega}{\upsilon}F_2(r) &= 0.\end{aligned} \tag{30}$$

Using MATLAB (or equivalent the solutions to Eq. (30) can be found in a straightforward manner as

$$\begin{aligned}F_1(r) &= \frac{A}{r} + Br,\\ F_2(r) &= CI_1(kr) + EK_1(kr),\end{aligned} \tag{31}$$

where $k = \sqrt{(i\omega/\nu)}$, I_1 and K_1 are modified Bessel functions, and A, B, C, E are coefficients to be determined. Combining Eq. (31), Eq. (29), and Eq. (27) results in

$$\psi = \psi_1 + \psi_2 = \left(\frac{A}{r} + Br + CI_1(kr) + EK_1(kr)\right) e^{i\omega t} sin\theta. \tag{32}$$

Plugging Eq. (32) into Eq. (11) yields

$$\begin{aligned} \mathrm{v}_r &= -\frac{1}{r}\frac{\partial \psi}{\partial \theta} = \left(-\frac{A}{r^2} - B - \frac{1}{r}CI_1(kr) - \frac{1}{r}EK_1(kr)\right) e^{i\omega t} cos\theta, \\ \mathrm{v}_\theta &= \frac{\partial \psi}{\partial r} = \left(-\frac{A}{r^2} + B + C\left\{kI_0(kr) - \frac{1}{r}I_1(kr)\right\} + E\left\{-kK_0(kr) - \frac{1}{r}K_1(kr)\right\}\right) e^{i\omega t} sin\theta. \end{aligned} \tag{33}$$

Enforcing the boundary conditions of Eq. (10) on Eq. (33) leads to four equations with four unknowns

$$\begin{aligned} -\frac{A}{d^2} - B - \frac{1}{d}CI_1(kd) - \frac{1}{d}EK_1(kd) &= U_0, \\ -\frac{A}{d^2} + B + C\left\{kI_0(kd) - \frac{1}{d}I_1(kd)\right\} + E\left\{-kK_0(kd) - \frac{1}{d}K_1(kd)\right\} &= -U_0, \\ -\frac{A}{D^2} - B - \frac{1}{D}CI_1(kD) - \frac{1}{D}EK_1(kD) &= 0, \\ -\frac{A}{D^2} + B + C\left\{kI_0(kD) - \frac{1}{D}I_1(kD)\right\} + E\left\{-kK_0(kD) - \frac{1}{D}K_1(kD)\right\} &= 0. \end{aligned} \tag{34}$$

Solving this system of equations with MATLABs matrix solver results in

$$\begin{aligned} A &= \frac{A_{num}}{Den}\ ,\ B = \frac{B_{num}}{Den}\ ,\ C = \frac{C_{num}}{Den},\ E = \frac{E_{num}}{Den}, \\ A_{num} &= -DU_0 d[2I_1(dk)\{2K_1(Dk) + (Dk)K_0(Dk)\} - 2I_1(Dk)\{2K_1(dk) + \\ &\quad (dk)K_0(dk)\} - (dk)I_0(dk)\{2K_1(Dk) + (Dk)K_0(Dk)\} + (Dk)I_0(Dk)\{2K_1(dk) + \\ &\quad (dk)K_0(dk)\}], \\ B_{num} &= U_0 k[I_0(Dk)\{(2d)K_1(dk) - (2D)K_1(Dk) + (d^2k)K_0(dk)\} + \\ &\quad (2d)K_0(Dk)I_1(dk) - (2D)I_1(Dk)K_0(Dk) - (d^2k)K_0(Dk)I_0(dk)], \\ C_{num} &= 2U_0[(2D)K_1(kD) - (2d)K_1(kd) + (D^2k)K_0(kD) - (d^2k)K_0(kd)], \\ E_{num} &= -2U_0[(2D)I_1(kD) - (2d)I_1(kd) + (d^2k)I_0(kd) - (D^2k)I_0(kD)], \\ Den &= I_0(kD)\{(2Dk)K_1(kD) - (2dk)K_1(kd) + (k^2)(D^2 - d^2)K_0(kd)\} - \\ &\quad I_0(kd)\{(2Dk)K_1(kD) - (2dk)K_1(kd) + (k^2)(D^2 - d^2)K_0(kD)\} + \\ &\quad (2Dk)I_1(kD)\{K_0(kD) - K_0(kd)\} - (2dk)I_1(kd)\{K_0(kD) - K_0(kd)\}. \end{aligned} \tag{35}$$

With the coefficients A, B, C, E defined by Eq. (35), the velocity terms given in Eq. (33) are fully defined. The velocity terms (and their derivatives) can be calculated as

$$\mathrm{v}_\theta = \left(-\frac{A}{r^2} + B + C\left\{kI_0(kr) - \frac{1}{r}I_1(kr)\right\} + E\left\{-kK_0(kr) - \frac{1}{r}K_1(kr)\right\}\right)e^{i\omega t}sin\theta,$$

$$\frac{\partial \mathrm{v}_\theta}{\partial t} = i\omega\left(-\frac{A}{r^2} + B + C\left\{kI_0(kr) - \frac{1}{r}I_1(kr)\right\} + E\left\{-kK_0(kr) - \frac{1}{r}K_1(kr)\right\}\right)e^{i\omega t}sin\theta,$$

$$\frac{\partial \mathrm{v}_\theta}{\partial r} = \left(\frac{2A}{r^3} + C\left\{\left(k^2 + \frac{2}{r^2}\right)I_1(kr) - \frac{k}{r}I_0(kr)\right\} + E\left\{\left(k^2 + \frac{2}{r^2}\right)K_1(kr) + \frac{k}{r}K_0(kr)\right\}\right)e^{i\omega t}sin\theta,$$

$$\frac{\partial^2 \mathrm{v}_\theta}{\partial r^2} = \left(\frac{-6A}{r^4} + C\left\{\left(\frac{3k}{r^2} + k^3\right)I_0(kr) - \left(\frac{2k^2}{r} + \frac{6}{r^3}\right)I_1(kr)\right\} + E\left\{-\left(\frac{3k}{r^2} + k^3\right)K_0(kr) - \left(\frac{2k^2}{r} + \frac{6}{r^3}\right)K_1(kr)\right\}\right)e^{i\omega t}sin\theta, \quad (36)$$

$$\frac{\partial^2 \mathrm{v}_\theta}{\partial \theta^2} = -\left(-\frac{A}{r^2} + B + C\left\{kI_0(kr) - \frac{1}{r}I_1(kr)\right\} + E\left\{-kK_0(kr) - \frac{1}{r}K_1(kr)\right\}\right)e^{i\omega t}sin\theta,$$

$$\frac{\partial \mathrm{v}_r}{\partial \theta} = -\left(-\frac{A}{r^2} - B - \frac{1}{r}CI_1(kr) - \frac{1}{r}EK_1(kr)\right)e^{i\omega t}sin\theta.$$

To determine the fluid pressure, the second Navier-Stokes equation of Eq. (8) is rearranged as

$$\partial \mathrm{p} = \left(-\rho r\frac{\partial \mathrm{v}_\theta}{\partial t} + \eta r\left[\frac{\partial^2 \mathrm{v}_\theta}{\partial r^2} + \frac{1}{r}\frac{\partial \mathrm{v}_\theta}{\partial r} - \frac{\mathrm{v}_\theta}{r^2} + \frac{1}{r^2}\frac{\partial^2 \mathrm{v}_\theta}{\partial \theta^2} + \frac{2}{r^2}\frac{\partial \mathrm{v}_r}{\partial \theta}\right]\right)\partial\theta. \quad (37)$$

Using Eq. (36), Eq. (37) can be rewritten as

$$\begin{aligned}\partial \mathrm{p} = \Big[&(\rho i\omega)\left(\frac{A}{r} + Br\right)\\ &+ (\rho i\omega - k^2\eta)\{(-rk)(CI_0(kr) - EK_0(kr)) + CI_1(kr)\\ &+ EK_1(kr)\}\Big]e^{i\omega t}sin\theta\partial\theta\end{aligned} \quad (38)$$

which can be integrated over θ, resulting in

$$\mathrm{p} = \mathrm{p}_0 - \Big[(\rho i\omega)\left(\frac{A}{r} + Br\right) + (\rho i\omega - k^2\eta)\{(-rk)(CI_0(kr) - EK_0(kr)) + CI_1(kr) + EK_1(kr)\}\Big]e^{i\omega t}cos\theta. \quad (39)$$

With the pressure defined, the shear stresses from Eq. (9) can be calculated. Noting the derivatives defined by Eq. (36) and

$$\frac{\partial \mathrm{v}_r}{\partial r} = \left(\frac{2A}{r^3} + C\left\{\frac{2}{r^2}I_1(kr) - \frac{k}{r}I_0(kr)\right\} + E\left\{\frac{2}{r^2}K_1(kr) + \frac{k}{r}K_0(kr)\right\}\right)e^{i\omega t}cos\theta, \quad (40)$$

the resulting stress equations are

$$\begin{aligned}\sigma_{rr} = -\mathrm{p}_0 + \Big[&A\left\{\frac{\rho i\omega}{r} + \frac{4\eta}{r^3}\right\} + B\{-\rho i\omega r\} + C\left\{\left(-\rho i\omega kr + k^3r\eta - \frac{2\eta k}{r}\right)I_0(kr) + \left(\rho i\omega - k^2\eta + \frac{4\eta}{r^2}\right)I_1(kr)\right\} + E\left\{\left(\rho i\omega kr - k^3r\eta + \frac{2\eta k}{r}\right)K_0(kr) + \left(\rho i\omega - k^2\eta + \frac{4\eta}{r^2}\right)K_1(kr)\right\}\Big]e^{i\omega t}cos\theta,\end{aligned} \quad (41)$$

$$\sigma_{\theta\theta} = -\mathrm{p}_0 + \Big[A\left\{\frac{\rho i\omega}{r} + \frac{2\eta}{r^3}\right\} + B\left\{\rho i\omega r + \frac{2\eta}{r}\right\} + C\left\{(-\rho i\omega kr + k^3r\eta)I_0(kr) +\right.$$

$$\left(\rho i\omega - k^2\eta + \frac{2\eta}{r^2}\right) I_1(kr)\Big\} + E\left\{(\rho i\omega kr - k^3 r\eta)K_0(kr) + \left(\rho i\omega - k^2\eta + \frac{2\eta}{r^2}\right) K_1(kr)\right\}\Big] e^{i\omega t} cos\theta,$$

$$\tau_{r\theta} = \tau_{\theta r} = \eta\left[A\left\{\frac{4}{r^3}\right\} + C\left\{\left(\frac{-2k}{r}\right) I_0(kr) + \left(k^2 + \frac{4}{r^2}\right) I_1(kr)\right\} + E\left\{\left(\frac{2k}{r}\right) K_0(kr) + \left(k^2 + \frac{4}{r^2}\right) K_1(kr)\right\}\right] e^{i\omega t} sin\theta.$$

The resulting hydrodynamic force can be found by integrating the fluid pressure at the beam boundary (i.e. $r = d$) as [131]

$$f_{hydro} = d\int_0^{2\pi} (\sigma_{rr}|_{r=d} cos\theta - \tau_{r\theta}|_{r=d} sin\theta) d\theta \tag{42}$$

Note that the integration of Eq. (42) is over θ while the bracketed stress terms of Eq. (41) are not a function of θ. To simplify the mathematics, rewrite Eq. (41) as

$$\begin{aligned} \sigma_{rr} &= -\mathrm{p}_0 + [COEF\sigma_{rr}] e^{i\omega t} cos\theta, \\ \tau_{r\theta} &= [COEF\tau_{r\theta}] e^{i\omega t} sin\theta. \end{aligned} \tag{43}$$

where

$$\begin{aligned} COEF\sigma_{rr} = &\left[A\left\{\frac{\rho i\omega}{r} + \frac{4\eta}{r^3}\right\} + B\{-\rho i\omega r\} + C\left\{\left(-\rho i\omega kr + k^3 r\eta - \frac{2\eta k}{r}\right) I_0(kr) + \left(\rho i\omega - k^2\eta + \frac{4\eta}{r^2}\right) I_1(kr)\right\} + E\left\{\left(\rho i\omega kr - k^3 r\eta + \frac{2\eta k}{r}\right) K_0(kr) + \left(\rho i\omega - k^2\eta + \frac{4\eta}{r^2}\right) K_1(kr)\right\}\right], \\ COEF\tau_{r\theta} = &\eta\left[A\left\{\frac{4}{r^3}\right\} + C\left\{\left(\frac{-2k}{r}\right) I_0(kr) + \left(k^2 + \frac{4}{r^2}\right) I_1(kr)\right\} + E\left\{\left(\frac{2k}{r}\right) K_0(kr) + \left(k^2 + \frac{4}{r^2}\right) K_1(kr)\right\}\right]. \end{aligned} \tag{44}$$

Incorporating Eq. (43) into Eq. (42) leads to

$$f_{hydro} = -d\mathrm{p}_0 \int_0^{2\pi} cos\theta d\theta + d[COEF\sigma_{rr}|_{r=d}] e^{i\omega t} \int_0^{2\pi} cos^2\theta d\theta - d[COEF\tau_{r\theta}|_{r=d}] e^{i\omega t} \int_0^{2\pi} sin^2\theta d\theta. \tag{45}$$

Noting the first integral equates to zero and the latter two to π,

$$f_{hydro} = d\pi[COEF\sigma_{rr}|_{r=d} - COEF\tau_{r\theta}|_{r=d}] e^{i\omega t}. \tag{46}$$

Including the coefficients from Eq. (44) results in

$$f_{hydro} = d\pi e^{i\omega t}\left[A\left\{\frac{\rho i\omega}{d}\right\} + B\{-\rho i\omega d\} + C\{(-\rho i\omega kd + k^3 d\eta) I_0(kd) + (\rho i\omega - 2k^2\eta) I_1(kd)\} + E\{(\rho i\omega kd - k^3 d\eta) K_0(kd) + (\rho i\omega - 2k^2\eta) K_1(kd)\}\right]. \tag{47}$$

Including the terms from Eq. (35) leads to the final result

$$
\begin{gathered}
f_{hydro} = -i\rho\pi d^2\omega\Gamma U_0 e^{i\omega t}, \\
\Gamma = \frac{\Gamma_{num}}{\Gamma_{den}} - 1 = \Gamma_r - i\Gamma_i, \\
\Gamma_{num} = 2\alpha^2[I_0(\alpha)K_0(\beta) - I_0(\beta)K_0(\alpha)] - 4\alpha[I_1(\alpha)K_0(\beta) + I_0(\beta)K_1(\alpha)] + \\
4\alpha\gamma[I_0(\alpha)K_1(\beta) + I_1(\beta)K_0(\alpha)] - 8\gamma[I_1(\alpha)K_1(\beta) - I_1(\beta)K_1(\alpha)], \\
\Gamma_{den} = \alpha^2(1-\gamma^2)[I_0(\alpha)K_0(\beta) - I_0(\beta)K_0(\alpha)] + 2\alpha\gamma[I_0(\alpha)K_1(\beta) - I_1(\beta)K_0(\beta) + \\
I_1(\beta)K_0(\alpha) - I_0(\beta)K_1(\beta)] + 2\alpha\gamma^2[I_0(\beta)K_1(\alpha) - I_0(\alpha)K_1(\alpha) + I_1(\alpha)K_0(\beta) - \\
I_1(\alpha)K_0(\alpha)], \\
k = \sqrt{\frac{i\omega}{\nu}}; \quad \alpha = kd; \quad \beta = kD; \quad \gamma = \frac{d}{D}.
\end{gathered}
\tag{48}
$$

For the special case of an infinite viscous fluid the hydrodynamic function simplifies to

$$\Gamma = 1 + \frac{4K_1(\alpha)}{\alpha K_0(\alpha)}, \tag{49}$$

where after noting the Bessel function property

$$\frac{\partial K_\nu(z)}{\partial z} = -K_{\nu-1}(z) - \frac{\nu}{z}K_\nu(z), \tag{50}$$

Eq. (49) can be written as

$$\Gamma = 1 + \frac{4K_1(\alpha)}{\alpha K_0(\alpha)} = 1 - \frac{4K_1\left(\sqrt{\frac{i\omega d^2}{\nu}}\right)}{K_1\left(\sqrt{\frac{i\omega d^2}{\nu}}\right) + \sqrt{\frac{i\omega d^2}{\nu}}K_1{}'\left(\sqrt{\frac{i\omega d^2}{\nu}}\right)}, \tag{51}$$

which matches the result of Rosenhead (1963) [133]. The physical meaning of the various terms found in the hydrodynamic force are as follows [133]

- $\rho\pi d^2$ represents the mass of fluid (per unit length) displaced by the cylinder.
- Γ_r contributes an effective mass to the system.
- Γ_i contributes a viscous drag to the system.

To obtain the hydrodynamic function in the Fourier domain, the hydrodynamic loading of Eq.(48) is rewritten as

$$f_{hydro} = -i^2\rho\pi d^2\omega^2\Gamma\left[\frac{U_0}{i\omega}e^{i\omega t}\right], \tag{52}$$

where the bracketed term is recognized as the beam displacement, $w(x,t)$. Applying the Fourier transform to Eq. (52) leads to

$$\hat{F}_h(x,\omega) = \int_{-\infty}^{\infty} f_{hydro}e^{-i\omega t}dt = \int_{-\infty}^{\infty}[\rho\pi d^2\omega^2\Gamma w(x,t)]e^{-i\omega t}dt, \tag{53}$$

The non-time dependent terms can be removed from under the integral

$$\hat{F}_h(x,\omega) = \rho\pi d^2\omega^2\Gamma\int_{-\infty}^{\infty} w(x,t)e^{-i\omega t}dt, \tag{54}$$

where the integrated term, by definition, is $\widehat{W}(x,\omega)$. The final form of the hydrodynamic force in the frequency domain is

$$\hat{F}_h(x,\omega) = \rho\pi d^2\omega^2\Gamma\widehat{W}(x,\omega). \tag{55}$$

It is important to recognize the limits of applicability of Eq. (48). The fluid equations, representing the behavior of the viscous annulus fluid, were linearized by assuming small vibration amplitudes, permitting the form of Eq. (48) presented. For large beam motions or divergent behavior, the assumptions made in the derivation of the hydrodynamic forcing are violated and Eq. (48) is no longer valid. For instance, large deflections may cause the annulus fluid to separate from the pipe's outer surface thereby changing the flow regime and violating the derivation assumptions.

2.4. Solution Methodology

Since the equation of motion (i.e. Eq. (6)) is frequency dependent through the hydrodynamic forcing (i.e. Eq. (48)), a Green's function approach is used to determine the beams displacement time history. The equation of motion is converted into the frequency domain by utilizing Fourier transforms. The definition of the transform and the transform of the spatial derivative are

$$\begin{gathered}\int_{-\infty}^{\infty} w(x,t)e^{-i\omega t}dt = \widehat{W}(x,\omega),\\ \int_{-\infty}^{\infty} \frac{\partial^4 w(x,t)}{\partial x^4} e^{-i\omega t}dt = \frac{\partial^4}{\partial x^4}\left(\int_{-\infty}^{\infty} w(x,t)e^{-i\omega t}dt\right) = \frac{\partial^4}{\partial x^4}\widehat{W}(x,\omega).\end{gathered} \tag{56}$$

To calculate the temporal derivatives, use integration by parts where

$$\int v'(x)\, u(x)dx = v(x)u(x) - \int v(x)u'(x)\, dx, \tag{57}$$

with $'$ indicating a derivative. The temporal derivatives are then

$$\begin{gathered}\int_{-\infty}^{\infty} \frac{\partial w(x,t)}{\partial t} e^{-i\omega t}dt = we^{-i\omega t}\Big|_{-\infty}^{\infty} - \int_{-\infty}^{\infty} w(-i\omega e^{-i\omega t})\, dt = i\omega \int_{-\infty}^{\infty} we^{-i\omega t}\, dt = \\ i\omega\widehat{W}(x,\omega),\\ \int_{-\infty}^{\infty} \frac{\partial^2 w(x,t)}{\partial t^2} e^{-i\omega t}dt = (i\omega)^2\widehat{W} = -\omega^2\widehat{W}(x,\omega).\end{gathered} \tag{58}$$

Thus, the spatially normalized equation of motion in the frequency domain is written as

$$\frac{EI}{L^4}\frac{\partial^4\widehat{W}(x,\omega)}{\partial x^4} + ic\omega\widehat{W}(x,\omega) - (m + M_i)\omega^2\widehat{W}(x,\omega) = \hat{F}_d(x,\omega) + \hat{F}_h(x,\omega). \tag{59}$$

By incorporating Eq. (55) and rearranging terms,

$$\frac{EI}{L^4}\frac{\partial^4\widehat{W}(x,\omega)}{\partial x^4} - [(m + M_i)\omega^2 - ic\omega + \rho\pi d^2\omega^2\Gamma]\widehat{W}(x,\omega) = \hat{F}_d(x,\omega). \tag{60}$$

Note that Eq. (60) is an ordinary differential equation in non-dimensional x. Due to the inclusion of bracing elements in the motivating configuration, the beam is assumed fixed at both ends. The normalized boundary conditions can then be written as

$$\begin{gathered}\left[w(x,t) = \frac{\partial w(x,t)}{\partial x}\right]_{x=0} = 0,\\ \left[w(x,t) = \frac{\partial w(x,t)}{\partial x}\right]_{x=1} = 0,\end{gathered} \tag{61}$$

or in the frequency domain as

$$\begin{gathered}\left[\widehat{W}(x,\omega) = \frac{\partial\widehat{W}(x,\omega)}{\partial x}\right]_{x=0} = 0,\\ \left[\widehat{W}(x,\omega) = \frac{\partial\widehat{W}(x,\omega)}{\partial x}\right]_{x=1} = 0.\end{gathered} \tag{62}$$

For convenience, Eq. (60) can be written using two new terms as

$$\frac{\partial^4 \widehat{W}(x|\omega)}{\partial x^4} - B^4 \widehat{W}(x|\omega) = \hat{s}(x|\omega),$$

$$B^4 = \frac{L^4}{EI}[\mu\omega^2 - ic\omega + \rho\pi d^2\omega^2\Gamma], \tag{63}$$

$$\hat{s}(x|\omega) = \frac{L^4}{EI}\hat{F}_d(x|\omega).$$

The new governing equation (i.e. Eq. (63)) can be solved using Green's functions. The relevant equation can be written as

$$\frac{\partial^4 G(x,s|\omega)}{\partial x^4} - B^4 G(x,s|\omega) = \delta(x-s) \tag{64}$$

where s is a normalized spatial dimension. The boundary conditions are similar to Eq. (62) and can be written as

$$\begin{aligned} \left[G(x,s|\omega) = \frac{\partial G(x,s|\omega)}{\partial x}\right]_{x=0} &= 0, \\ \left[G(x,s|\omega) = \frac{\partial G(x,s|\omega)}{\partial x}\right]_{x=1} &= 0. \end{aligned} \tag{65}$$

For $x \neq s$ Eq. (64) becomes

$$\frac{\partial^4 G(x,s|\omega)}{\partial x^4} - B^4 G(x,s|\omega) = 0. \tag{66}$$

When $x < s$, Eq. (66) is solved with the first set of boundary conditions in Eq. (65) (i.e. at $x = 0$) while when $x > s$, Eq. (66) is solved with the second set of boundary conditions. This results in two equations with four remaining unknowns

$$\begin{aligned} G_{x<s} = C_{11}e^{Bx} + C_{12}e^{-Bx} - e^{-Bxi}\left[C_{11}\left(\frac{1}{2}+\frac{i}{2}\right) + C_{12}\left(\frac{1}{2}-\frac{i}{2}\right)\right] - e^{Bxi}\left[C_{11}\left(\frac{1}{2}-\frac{i}{2}\right) + \right. \\ \left. C_{12}\left(\frac{1}{2}+\frac{i}{2}\right)\right], \\ G_{x>s} = C_{13}e^{Bx} + C_{14}e^{-Bx} - e^{B(xi-i-1)}\left[C_{14}\left(\frac{1}{2}+\frac{i}{2}\right) + C_{13}e^{2B}\left(\frac{1}{2}-\frac{i}{2}\right)\right] - \\ e^{-B(xi-i+1)}\left[C_{14}\left(\frac{1}{2}-\frac{i}{2}\right) + C_{13}e^{2B}\left(\frac{1}{2}+\frac{i}{2}\right)\right]. \end{aligned} \tag{67}$$

The four unknowns (C_{11} to C_{14}) can be solved using the four continuity equations occurring at $x = s$

$$
\begin{gathered}
[G_{x>s} - G_{x<s} = 0]_{x=s}, \\
\left[\frac{\partial(G_{x>s})}{\partial x} - \frac{\partial(G_{x<s})}{\partial x} = 0\right]_{x=s}, \\
\left[\frac{\partial^2(G_{x>s})}{\partial x^2} - \frac{\partial^2(G_{x<s})}{\partial x^2} = 0\right]_{x=s}, \\
\left[\frac{\partial^3(G_{x>s})}{\partial x^3} - \frac{\partial^3(G_{x<s})}{\partial x^3} = 1\right]_{x=s}.
\end{gathered} \tag{68}
$$

After setting $x = s$ in Eq. (67), the four continuity equations and four unknowns can be placed into matrix form and solved via MATLAB as

$$
\begin{gathered}
C_i = \frac{C_{i_{num}}}{C_{DEN}}, \\
C_{DEN} = 4B^3\left[e^{B(s+2si+2)} + e^{B(-2i+s+2si)} - 4e^{B(-i+s+2si+1)} + e^{B(-2i+s+2si+2)} + e^{Bs(2i+1)}\right], \\
C_{11_{num}} = -\left[(1+i)\left\{e^{B(-2i+s+3si)} - e^{B(-i+s+3si+1)}\right\} + (i)\left\{e^{2Bs(i+1)} - e^{2B(-i+s+si)}\right\} + (1-i)\left\{e^{Bs(i+1)} - e^{B(-i+s+si+1)}\right\} + \left\{e^{2B(si+1)} - 2e^{B(-i+2si+1)} + e^{2B(-i+si+1)}\right\}\right], \\
C_{12_{num}} = (1+i)\left\{e^{B(s+si+2)} - e^{B(-i+s+si+1)}\right\} + (i)\left\{e^{2B(-i+si+1)} - e^{2B(si+1)}\right\} + (1-i)\left\{e^{B(-2i+s+3si+2)} - e^{B(-i+s+3is+1)}\right\} + \left\{e^{2B(-i+s+si)} - 2e^{B(-i+2s+2si+1)} + e^{2Bs(i+1)}\right\}, \\
C_{13_{num}} = (1+i)\left\{e^{B(-i+s+3si+1)} - e^{B(-2i+s+3si)}\right\} + (i)\left\{e^{2B(-i+s+si)} - e^{2Bs(i+1)}\right\} + (1-i)\left\{e^{B(-i+s+si+1)} - e^{Bs(i+1)}\right\} + \left\{e^{2Bi(s-1)} - 2e^{B(-i+2si+1)} + e^{2Bsi}\right\}, \\
C_{14_{num}} = -\left[(1+i)\left\{e^{B(-i+s+si+1)} - e^{B(s+si+2)}\right\} + (i)\left\{e^{2B(si+1)} - e^{2B(-i+si+1)}\right\} + (1-i)\left\{e^{B(-i+s+3si+1)} - e^{B(-2i+s+3si+2)}\right\} + \left\{e^{2B(s+si+1)} - 2e^{B(-i+2s+2si+1)} + e^{2B(-i+s+si+1)}\right\}\right].
\end{gathered} \tag{69}
$$

Plugging Eq. (69) into Eq. (67) results in the desired Green's functions. For the sake of space, the combined equation is not shown here. The combined Green's function can be written as

$$G(x, s|\omega) = G_{x<s}Heaviside(s - x) + G_{x>s}Heaviside(x - s). \tag{70}$$

The solution to the governing equation (i.e. Eq. (63)) is found by integrating over the domain as

$$\widehat{W}(x, \omega) = \int_0^1 G(x, s|\omega)\, \hat{s}(s|\omega) ds. \tag{71}$$

To determine the displacement response in the time domain, the inverse Fourier transform is taken

$$w(x,t) = \frac{1}{2\pi}\int_{-\infty}^{\infty} \widehat{W}(x,\omega)e^{i\omega t}d\omega. \quad (72)$$

In actual practice, the continuous Fourier response $\widehat{W}(x,\omega)$ is sampled and then discretely transformed into the time domain. This drastically reduces the computation time but requires a small amount of damping in the system (either viscous damping or damping generated by the hydrodynamic forcing) so that peaks in the frequency domain can be properly sampled. The sampling rate (ω_s) can be set to avoid aliasing, and balanced to minimize computational effort with time domain resolution. The discrete list of sampled frequencies ($\widehat{W}_{sampled}[a]$) can then be transformed using a discrete (or fast) Fourier transform

$$w[b] = \frac{\Omega_s}{2\pi n}\sum_{a=1}^{n} \widehat{W}_{sampled}[a]e^{2\pi(b-1)(a-1)/n}, \quad (73)$$

where $w[b]$ is the discrete displacement response at a specified location of interest, b and a are list positions, Ω_s is the size of the frequency range included in sampling, n is the number of samples, and $\widehat{W}_{sampled}[a]$ is a list of sampled values of the frequency response reordered so that the zero frequency term appears in position 1 of the list. The discrete displacement response can be plotted on the time axis using the time step $T = 2\pi/\Omega_s$. The Mathematica script implementing these calculations can be found in Appendix B.

2.5. Script Validation

Two cases are used to validate the Mathematica script.

2.5.1. Pseudo-Static Point Loading of a Fixed-Fixed Beam in a Vacuum

The displacement response of a fixed-fixed beam statically loaded at midspan with a point load is known to be

$$\Delta_{midspan} = \frac{PL^3}{192EI}. \quad (74)$$

Using the inputs provided in Table 3, the resulting midspan displacement is calculated as $4.018e-5m$.

Table 3. Pseudo-Static Beam: Model Inputs

Applied Force, P	100	N
Beam Length, L	6	m
Young's Modulus, E	$7e9$	N/m^2
Beam Inertia, I	$4e-4$	m^4

Using the Green's function model and Mathematica, a slowly varying harmonic load is placed at midspan. The frequency of the applied load is significantly smaller than the first natural frequency of the system resulting in a pseudo-static loading. A small amount of damping (1%) is included to allow the use of discrete Fourier transforms in determining the displacement time history. The frequency values used in the inverse DFT operation are $\omega_s = 0.05 rad/s$ and $\Omega_s = \pm 1000 rad/s$. The displacement time history found from the Green's function approach is shown in Figure 8. The peak displacement is $4.006e-5m$ (0.3% error). Note that when the load is removed after $10sec$, the beam is seen to freely vibrate until damping drives the displacement to zero.

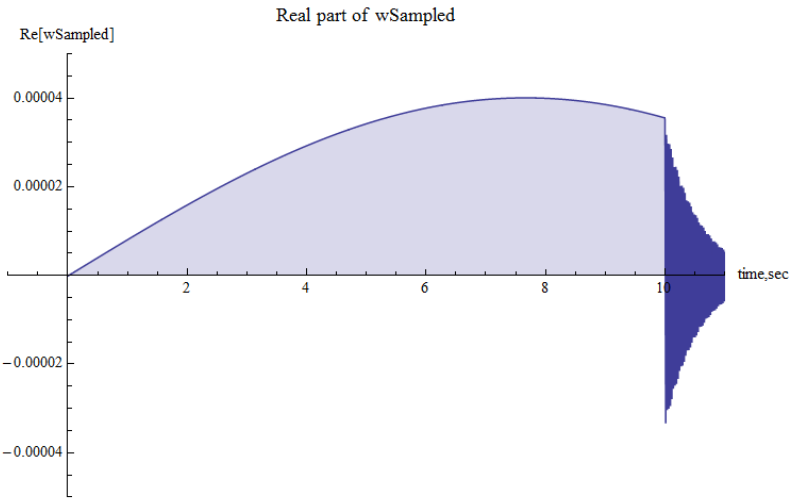

Figure 8. Pseudo-Static Beam: Displacement Time History

2.5.2. Triangular Loading of a Fixed-Fixed Beam Surrounded by an Unbounded Fluid

A fixed-fixed beam is dynamically loaded with an eccentric triangular load as shown in Figure 9. The model inputs are listed in Table 4. The frequency values used in the inverse DFT operation are $\omega_s = 0.05 rad/s$ and $\Omega_s = \pm 1000 rad/s$.

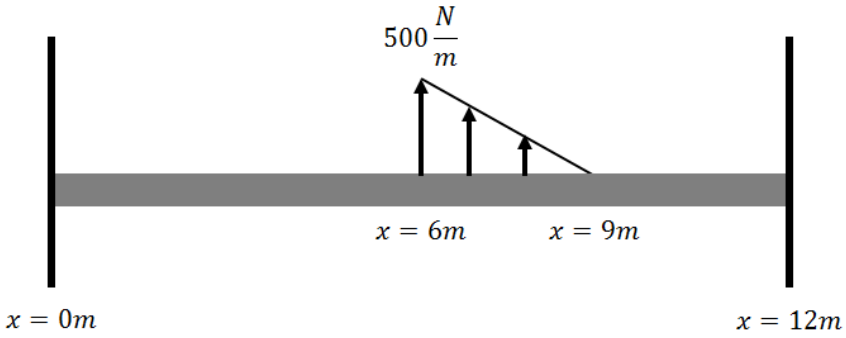

Figure 9. Loading Configuration

Table 4. System Properties

Young's Modulus, E	$2e11$	N/m^2
Beam Density, ρ	7800	kg/m^3
Beam Poisson's Ratio	0.33	-
Beam Outer Radius, d	0.06	m
Shell Radius, D	100000	m
Beam Length, L	12	m
Wall Thickness	0.007	m
Beam Area, A	$2.485e-3$	m^2
Beam Inertia, I	$3.982e-6$	m^4
Beam Mass, m	19.383	kg/m
Fluid Kinematic Viscosity	$1.00e-06$	m^2/s
Fluid Density, ρ	2000	kg/m^3
Viscous Damping Ratio	2%	-
Forcing Frequency	54.02	rad/s

The configuration is modeled using beam elements in ABAQUS as well as the Green's function approach outlined above. The steady-state midspan displacement response is plotted in Figure 10; the results show excellent agreement.

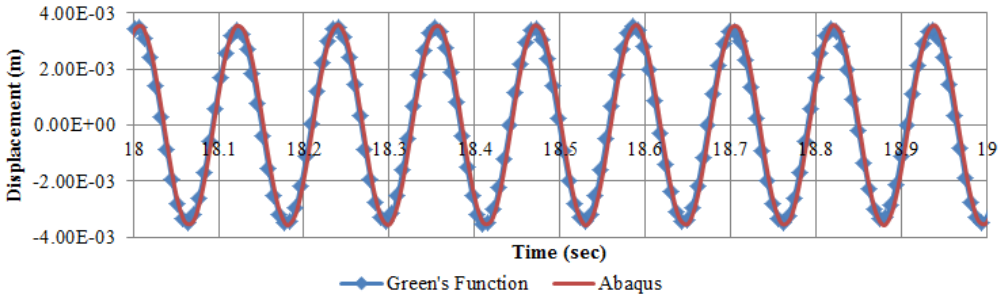

Figure 10. Model Comparison

2.6. Derivation of the Forcing Function

To estimate the time-varying distributed force applied to the production tube stemming from the pressure oscillations trailing a bluff body, a computational fluid dynamics (CFD) model is generated. The model is developed by the computational mechanics group within the structural engineering department. In total, three models are generated with the inputs listed in Table 5. Values for the fluid dynamic viscosity are taken as 0.2 Ns/m^2 , 0.02 Ns/m^2 , and 0.002 Ns/m^2.

Table 5. CFD Model Inputs

Conveyed Fluid Dynamic Viscosity	Varies	Ns/m^2
Conveyed Fluid Density	875	kg/m^3
Conveyed Fluid Velocity	1.5	m/s
Bluff Body Diameter	0.025	m
Production Tube Inner Radius	0.05	m
Length of Tube Considered	2	m
Bluff Body Position (Centerline)	0.3	m from inlet
Inlet Fluid Velocity Profile	Uniform	-

The only configuration to exhibit strong periodic behavior is the second model (with a fluid dynamic viscosity of 0.02 Ns/m^2). A graphical display of the output vorticity is shown in Figure 11.

Figure 11. CFD Vorticity Colored by Velocity Magnitude for Various Viscosities

The CFD pressure output from the second model is converted into a directional forcing at each finite element node. The nodal forces for each cross section are added and then spatially averaged to produce a force per unit length along the beam (for each time step). The result is 101 files (from time $6.0 - 7.0sec$ so that transients are eliminated) that contain oriented forces as shown in Figure 12.

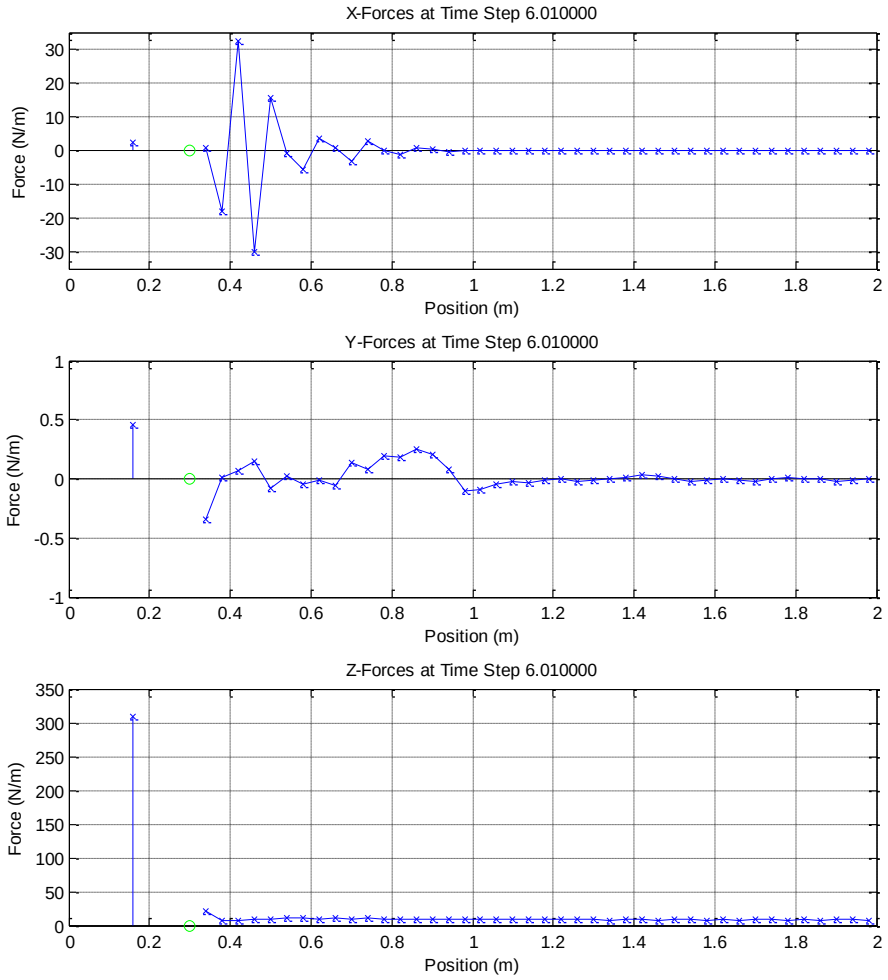

Figure 12. CFD Forcing Output

Note that the X-direction is orthogonal to the longitudinal axis of both the bluff body and production tube, the Y-direction is parallel to the longitudinal axis of the bluff body, and the Z-direction is parallel to the longitudinal axis of the production tube. The green circle indicates the location of the bluff body. The large force in the Z-direction between $0 - 0.3m$ is due to fluid pressure on the bluff body.

Due to the relatively small length over which the pressure oscillations act, the spatial forcing is integrated over the length of tube considered to determine an equivalent point force.

Figure 13 plots these equivalent point forces for all time steps. The maximum force is found to be $0.0964N$. A Fourier transform of the windowed time history indicates a forcing frequency of $124.4\ rad/s$. For the sake of future modeling, the load is simplified to $0.1N$ at $124\ rad/s$.

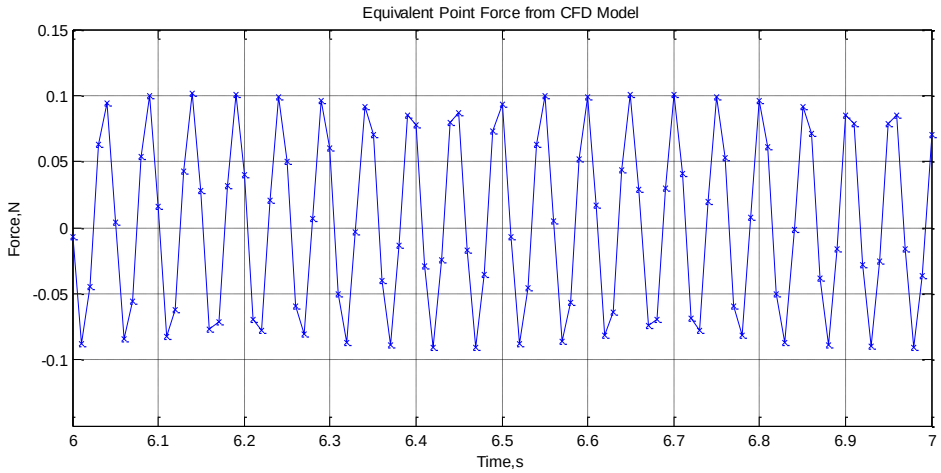

Figure 13. Time History of Equivalent Point Force

2.7. Results

The Green's function approach is used to model a baseline structural configuration with the intent of confirming or rejecting the assumptions used in the preliminary LANL calculations (i.e. that the achievable displacement magnitude is on the order of $\pm 5mm$). The model inputs are listed in Table 6. The potential effects of the connections, mass of the energy harvesting system, and shape of the structural housing (with respect to the hydrodynamic forcing) have been neglected for this preliminary analysis.

Table 6. Model Inputs

Young's Modulus, E	$2e11$	N/m^2
Beam Density, ρ	7800	kg/m^3
Beam Inner Radius	0.05	m
Shell Radius, D	0.108	m
Beam Length, L	10	m
Wall Thickness	0.007	m
Beam Area, A	$2.435e-3$	m^2
Beam Inertia, I	$3.382e-6$	m^4
Beam Mass, m	18.354	kg/m
Annulus Fluid Kinematic Viscosity	$1.00e-06$	m^2/s
Annulus Fluid Density, ρ	900	kg/m^3
Conveyed Fluid Density	875	kg/m^3
Conveyed Fluid Mass, M_i	6.872	kg/m
Viscous Damping Ratio	1%	-
Forcing Frequency	124.0	rad/s
Forcing Magnitude	0.1	N
DFT Sampling Frequency, ω_s	0.05	rad/s
DFT Sampling Range, Ω_s	± 1000	rad/s
Boundary Conditions	Fixed-Fixed	-

The steady-state displacement response is found to be negligibly small (on the order of $10^{-5}mm$). The forcing is increased fifty-fold to $5N$ with all other inputs unchanged. The resulting displacement response is shown in Figure 14 where the steady-state displacement amplitude is found to be $\pm 0.0112mm$. This is two orders of magnitude less than the displacement response assumed in the preliminary LANL calculations.

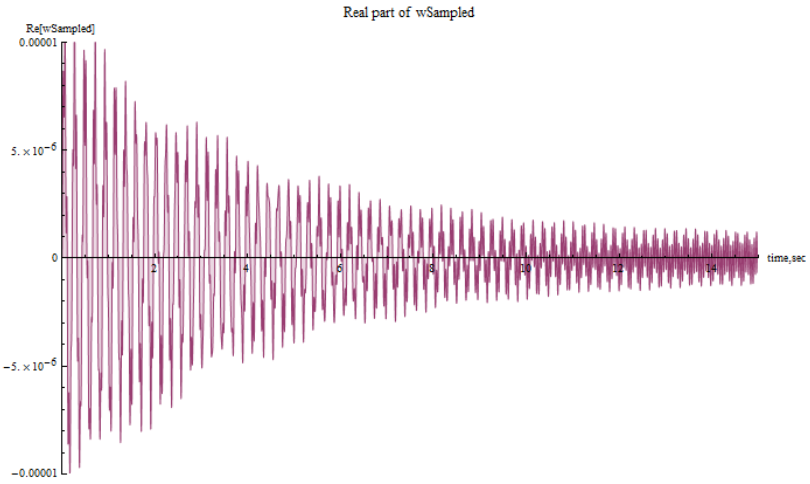

Figure 14. Displacement Response

The frequency response of the system is shown in Figure 15. The first and third modal responses are visible at 28.6 rad/s and 154.9 rad/s, respectively; the peak near 124 rad/s corresponds to the forcing frequency. The second natural frequency is not visible as, at the beam's midpoint, even modes do not contribute to the displacement response. To increase the displacement response, the stiffness of the system (i.e. the beam length) is altered so that the forcing frequency coincides with one of the systems natural frequencies (i.e. resonance). The results are shown in Table 7 where the forcing magnitude is reset to $0.1N$, the value determined from the CFD model.

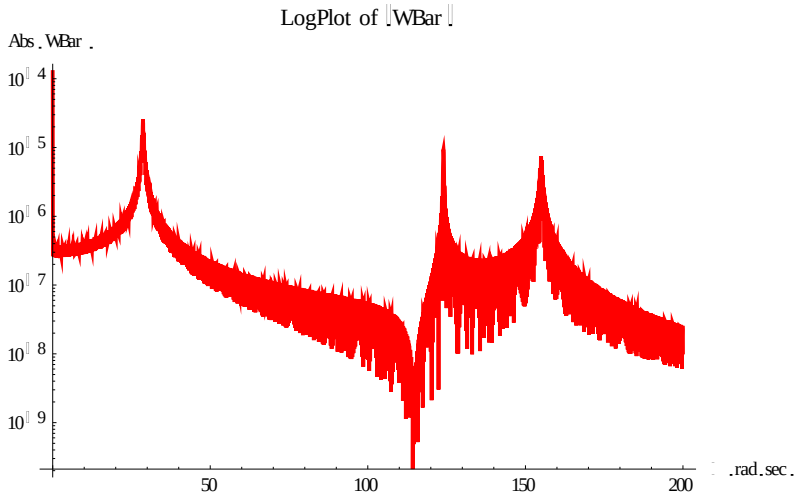

Figure 15. Frequency Response

Table 7. Steady State Displacement Magnitude for Various Cases

Resonant Mode	Beam Length (m)	Forcing Frequency (rad/s)	Steady State Displacement (mm)
1	4.81	124	± 0.0061
3	11.18	124	± 0.0065
5	17.57	124	± 0.0061
7	23.96	124	± 0.0052

In all four cases, the maximum resonant displacement is found to be nearly three orders of magnitude smaller than the displacement response assumed in the preliminary calculations.

Since the numeric models failed to prove that the assumed displacement response was realizable, industry practitioners were contacted in hopes of obtaining additional insights.

Unfortunately, those practitioners who would comment on the results provided no additional insights regarding the specific realization modeled, the assumed flow behavior, etc.

2.8. Moving Forward

While the current investigation failed to validate the assumed displacement response, the development of an energy harvester for downhole use is still thought to be valid. That is, mechanisms can be deployed to amplify ambient vibrations in the production tube and this mechanical energy can be harvested for future use in supporting low power electronic devices. The intellectual knowledge that can be contributed in the pursuit of such an energy harvesting system is:

- *Characterizing the dynamic behavior of the system.* Any acceleration driving an energy harvesting element will be colored by the natural frequency of the production tube and limited by the damping in the system. Since the system is non-trivially complex (a conveyed fluid inside of a pipe surrounded by another fluid), it is useful to understand how various parameters of interest affect the natural frequency and damping in the system.

- *Develop a tool to estimate harvestable power*. If the acceleration time-histories driving the production tube are known or can be reasonably approximated, an estimate of power output for a given energy harvester configuration can be developed. This preliminary estimate can be used by industry to decide whether an energy harvesting solution is viable for a specific hydrocarbon well of interest. If so, additional resources can be allocated to advance the design and fabrication of an energy harvesting tool.

Chapter 3

Characterizing Dynamic Behavior Using a Refined Analytical Model

3.1. Background

A model is needed to investigate the effects of various parameters of interest. An analytical model is specifically chosen so that a large input domain can be explored rapidly. A new equation of motion which captures conveyed fluid effects is derived. The equation of motion is then solved with the spectral element method as a Green's function approach is overly cumbersome when applied to the new equation of motion. The model is used to explore how changing various inputs effect the natural frequency and damping in the system.

3.1.1. Literature Review

Significant work has been done investigating the behavior of pipes conveying fluid [148]-[151], with special interest in cantilever pipes [152]-[153] due to their non-conservative nature. More general boundary conditions have also been considered. Kheiri et al. (2014) [154] investigated a fluid conveying pipe with flexible end restraints but did not account for a

confined external fluid. Bao (2014) [155] studied submerged fluid conveying pipes on elastic supports but neglected damping in the investigation.

Other work investigating the effects of nonlinear terms [156] and unsteady flow [157]-[160] in similar systems can also be found. However, these research efforts do not account for the possibility of a medium external to the pipe, such as a surrounding fluid or viscoelastic foundation, which may affect the dynamics of the system. When a viscoelastic foundation is included in the system model [161]-[163], some of the resulting behavior may be extrapolated to the configuration of interest; however, the problem formulation is fundamentally different with the clearest manifestation being the viscoelastic foundation model's failure to account for changing inertial effects. Such shortcomings become relevant as the dynamic behavior of beams vibrating in a viscous fluid is known to be altered due to both added mass and viscous effects [135], [140], [164].

The problem has been approached using a shell formulation where the treatment of inviscid fluid [165], viscous fluid flow [166], and the determination of added mass and damping terms [167] can be found in the literature. These formulations tend to be more complicated due to the use of the shell equation of motion which permits the inclusion of additional modes beyond those produced by a beam formulation. Conveniently, for typical production tube geometries where the effective pipe length is much larger than the pipe radius, the dynamic behavior of the two formulations converge [168]. Thus, for the application of interest, a beam formulation is not only plausible but preferred as its use allows further simplification of the problem since the effects of viscous friction from the conveyed fluid vanish from the equation of motion in a beam formulation [169].

3.2. The Equation of Motion

The following derivation of the governing equation of motion follows the work of Païdoussis and Issid (1974) [170] which is explored in greater depth in Païdoussis (2014) [169]. The assumptions used in the derivation are summarized in Table 8.

Table 8. Assumptions Used in the Derivation of the Equation of Motion

1	The length of the pipe greatly exceeds its nominal diameter.
2	The pipe is an isotropic linearly elastic solid.
3	The amplitude of vibration of the pipe is far smaller than any length scale in the pipe geometry.
4	The flexural stiffness is constant over the length of the pipe.
5	The Euler-Bernoulli approximation holds.
6	The conveyed fluid is incompressible with uniform flow profile (i.e. plug flow).
7	The pipe is thin walled.

3.2.1. Flow Profile

The conveyed fluid produced by an operating well may range from single-phase to a multiphase flow consisting of bubble, slug, transition, or mist flow. Although multiphase fluid flow is common in oil wells, predicting its behavior is complicated due to complex heat and mass transfer through the system [171]. Since the novel contribution of this study is the effects the annulus fluid has on the system, the inclusion of multiphase flow in the analytical model is unnecessarily burdensome; the produced fluid, which is expected to be turbulent, is modeled as a plug flow with either average viscous or inviscid characteristics.

3.2.2. Equilibrium

Consider the slender pipe shown in Figure 16 where s represents the curvilinear coordinate along the axis of the pipe and x, z represent the Cartesian coordinate system. The lateral displacement of the pipe is assumed to be much smaller than the pipes diameter ($w \ll 2d$), which itself is much smaller than the pipes length ($2d \ll L$). The axial displacement of the pipe is assumed to be much smaller than the lateral displacement of the pipe ($u \ll w$), permitting the assumption that $s \approx x$.

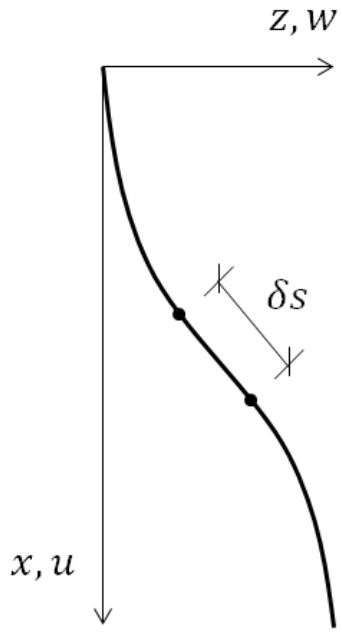

Figure 16. Coordinate System

Consider a differential element of length δs, shown in Figure 17. Forces on the fluid element include: fluid pressure ($A_i p$), self-weight ($M_i g \delta s$), and both normal ($F \delta s$) and tangential ($qS\delta s$) reaction forces between the fluid and pipe elements. The forces on the pipe element include: moment (M), shear (Q), tension (T), self-weight ($mg\delta s$), both normal ($F\delta s$) and tangential ($qS\delta s$) reaction forces between the fluid and pipe elements, viscous damping ($c\ \partial w/\partial t\ \delta s$), and a hydrodynamic force ($f_{hydro}\delta s$) which accounts for the effects of an external fluid surrounding the pipe.

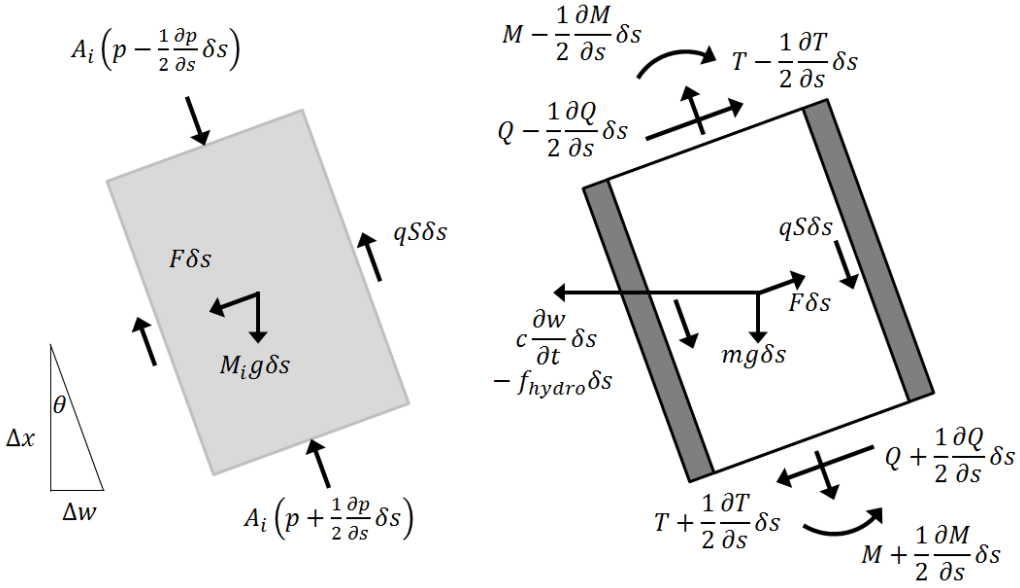

Figure 17. Differential Element: Fluid (Left) and Pipe (Right)

Applying vertical equilibrium to the fluid element results in

$$A_i\left[(pcos\theta)-\frac{1}{2}\frac{\partial}{\partial s}(pcos\theta)\delta s\right]-A_i\left[(pcos\theta)+\frac{1}{2}\frac{\partial}{\partial s}(pcos\theta)\delta s\right]-qS\delta s(cos\theta)+ M_i g\delta s+F\delta s(sin\theta)=M_i a_{fx}\delta s, \tag{75}$$

where for a small angle approximation one may take

$$cos\theta\approx 1,\quad sin\theta\approx\theta=\frac{\Delta w}{\Delta x}=\frac{\partial w}{\partial x}. \tag{76}$$

Combining Eq. (75) and Eq. (76) leads to

$$A_i\left[p-\frac{1}{2}\frac{\partial}{\partial s}p\delta s\right]-A_i\left[p+\frac{1}{2}\frac{\partial}{\partial s}p\delta s\right]-qS\delta s+M_i g\delta s+F\delta s\frac{\partial w}{\partial x}=M_i a_{fx}\delta s, \tag{77}$$

which, when incorporating the assumption that $s\approx x$, may be simplified to

$$-A_i\frac{\partial p}{\partial x}-qS+M_i g+F\frac{\partial w}{\partial x}=M_i a_{fx}, \tag{78}$$

Applying horizontal equilibrium to the fluid element results in

$$A_i\left[(psin\theta)-\frac{1}{2}\frac{\partial}{\partial s}(psin\theta)\delta s\right]-A_i\left[(psin\theta)+\frac{1}{2}\frac{\partial}{\partial s}(psin\theta)\delta s\right]-qS\delta s(sin\theta)- F\delta s(cos\theta)=M_i a_{fz}\delta s, \tag{79}$$

which may be similarly simplified to

$$-A_i\frac{\partial}{\partial x}\left(p\frac{\partial w}{\partial x}\right)-qS\frac{\partial w}{\partial x}-F=M_i a_{fz}. \tag{80}$$

Applying moment equilibrium to the pipe element leads to

$$\left(M+\frac{1}{2}\frac{\partial M}{\partial s}\delta s\right)-\left(M-\frac{1}{2}\frac{\partial M}{\partial s}\delta s\right)-\left(Q-\frac{1}{2}\frac{\partial Q}{\partial s}\delta s\right)\left(\frac{1}{2}\delta s\right)-\left(Q+\frac{1}{2}\frac{\partial Q}{\partial s}\delta s\right)\left(\frac{1}{2}\delta s\right)=0, \tag{81}$$

where rotary inertia has been neglected. Simplification leads to

$$Q=\frac{\partial M}{\partial s}=\frac{\partial M}{\partial x}=EI\frac{\partial^3 w}{\partial x^3}. \tag{82}$$

Applying vertical equilibrium results in

$$\begin{gathered}-\left[(Tcos\theta)-\frac{1}{2}\frac{\partial}{\partial s}(Tcos\theta)\delta s\right]-\left[(Qsin\theta)-\frac{1}{2}\frac{\partial}{\partial s}(Qsin\theta)\delta s\right]+\left[(Tcos\theta)+\right.\\ \left.\frac{1}{2}\frac{\partial}{\partial s}(Tcos\theta)\delta s\right]+\left[(Qsin\theta)+\frac{1}{2}\frac{\partial}{\partial s}(Qsin\theta)\delta s\right]+mg\delta s+qS\delta s(cos\theta)-F\delta s(sin\theta)=\\ ma_{px}\delta s,\end{gathered} \tag{83}$$

which can be simplified to

$$\frac{\partial T}{\partial x}+\frac{\partial}{\partial x}\left(Q\frac{\partial w}{\partial x}\right)+mg+qS-F\frac{\partial w}{\partial x}=ma_{px}. \tag{84}$$

The shear and acceleration terms of Eq. (84) can be neglected as higher order terms leading to

$$\frac{\partial T}{\partial x}+mg+qS-F\frac{\partial w}{\partial x}=0. \tag{85}$$

Lastly, horizontal equilibrium can be applied

$$\begin{gathered}-\left[(Tsin\theta)-\frac{1}{2}\frac{\partial}{\partial s}(Tsin\theta)\delta s\right]+\left[(Qcos\theta)-\frac{1}{2}\frac{\partial}{\partial s}(Qcos\theta)\delta s\right]+\left[(Tsin\theta)+\right.\\ \left.\frac{1}{2}\frac{\partial}{\partial s}(Tsin\theta)\delta s\right]-\left[(Qcos\theta)+\frac{1}{2}\frac{\partial}{\partial s}(Qcos\theta)\delta s\right]+qS\delta s(sin\theta)+F\delta s(cos\theta)-c\frac{\partial w}{\partial t}\delta s+\\ f_{hydro}\delta s=ma_{pz}\delta s,\end{gathered} \tag{86}$$

which can be simplified to

$$\frac{\partial}{\partial x}\left(T\frac{\partial w}{\partial x}\right)-\frac{\partial Q}{\partial x}+qS\frac{\partial w}{\partial x}+F-c\frac{\partial w}{\partial t}+f_{hydro}=ma_{pz}. \tag{87}$$

In summary, Eq. (78), Eq. (80), Eq. (82), Eq. (85), and Eq. (87) represent the relevant equilibrium equations.

3.2.3. Acceleration Terms

While the pipe acceleration is easily written as

$$a_{pz}=\frac{\partial^2 w}{\partial t^2}, \tag{88}$$

the fluid acceleration terms require additional analysis. A position vector for the pipe is defined as

$$\boldsymbol{r} = x\hat{\boldsymbol{\imath}} + z\hat{\boldsymbol{k}}. \tag{89}$$

The velocity of the pipe can then be written as

$$\boldsymbol{V}_p = \frac{\partial \boldsymbol{r}}{\partial t} = \dot{x}\hat{\boldsymbol{\imath}} + \dot{z}\hat{\boldsymbol{k}}, \tag{90}$$

where $(\dot{})$ represents a derivative with respect to time. The velocity of the conveyed fluid element is then

$$\boldsymbol{V}_f = \boldsymbol{V}_p + U\boldsymbol{\tau} = \left(\dot{x} + U\frac{\partial x}{\partial s}\right)\hat{\boldsymbol{\imath}} + \left(\dot{z} + U\frac{\partial z}{\partial s}\right)\hat{\boldsymbol{k}} = \left(\frac{\partial}{\partial t} + U\frac{\partial}{\partial s}\right)\boldsymbol{r} = \frac{D\boldsymbol{r}}{Dt}, \tag{91}$$

where $\boldsymbol{\tau}$ represents the unit vector tangential to the displaced pipe. For $z = w$, $\partial x/\partial s = cos\theta \approx 1$, and $\partial x/\partial t \approx 0$, Eq. (91) can be rewritten as

$$\boldsymbol{V}_f = (U)\hat{\boldsymbol{\imath}} + \left(\frac{\partial}{\partial t} + U\frac{\partial}{\partial s}\right)w\hat{\boldsymbol{k}}. \tag{92}$$

Taking the derivative of the fluid velocity results in the fluid acceleration

$$\boldsymbol{a_f} = \frac{D}{Dt}(\boldsymbol{V}_f) = \left(\frac{\partial}{\partial t} + U\frac{\partial}{\partial s}\right)\left[(U)\hat{\boldsymbol{\imath}} + \left(\frac{\partial}{\partial t} + U\frac{\partial}{\partial s}\right)w\hat{\boldsymbol{k}}\right]. \tag{93}$$

Expanding Eq. (93)

$$\boldsymbol{a_f} = \left[\frac{dU}{dt} + U\frac{dU}{ds}\right]\hat{\boldsymbol{\imath}} + \left[\frac{\partial^2 w}{\partial t^2} + U\frac{\partial^2 w}{\partial s \partial t} + \frac{dU}{dt}\frac{\partial w}{\partial s} + U\frac{\partial^2 w}{\partial s \partial t} + U\frac{dU}{ds}\frac{\partial w}{\partial s} + U^2\frac{\partial^2 w}{\partial s^2}\right]\hat{\boldsymbol{k}}, \tag{94}$$

where for an incompressible fluid, $dU/ds = 0$, leading to

$$\boldsymbol{a_f} = \frac{dU}{dt}\hat{\boldsymbol{\imath}} + \left[\frac{\partial^2 w}{\partial t^2} + 2U\frac{\partial^2 w}{\partial s \partial t} + \frac{dU}{dt}\frac{\partial w}{\partial s} + U^2\frac{\partial^2 w}{\partial s^2}\right]\hat{\boldsymbol{k}} = \frac{dU}{dt}\hat{\boldsymbol{\imath}} + \left[\frac{\partial}{\partial t} + U\frac{\partial}{\partial s}\right]^2 w\hat{\boldsymbol{k}}. \tag{95}$$

Recalling $s \approx x$, the fluid accelerations can be written as

$$a_{fz} = \left[\frac{\partial}{\partial t} + U\frac{\partial}{\partial x}\right]^2 w = \frac{\partial^2 w}{\partial t^2} + 2U\frac{\partial^2 w}{\partial x \partial t} + \frac{dU}{dt}\frac{\partial w}{\partial x} + U^2\frac{\partial^2 w}{\partial x^2}, \tag{96}$$

and

$$a_{fx} = \frac{dU}{dt}. \tag{97}$$

In summary, Eq. (88), Eq. (96), and Eq. (97) represent the relevant acceleration terms.

3.2.4. Assembling the Equation of Motion

Combining Eq. (80) and Eq. (87) leads to

$$-A_i \frac{\partial}{\partial x}\left(p \frac{\partial w}{\partial x}\right) + \frac{\partial}{\partial x}\left(T \frac{\partial w}{\partial x}\right) - \frac{\partial Q}{\partial x} - c \frac{\partial w}{\partial t} + f_{hydro} = M_i a_{fz} + m a_{pz}. \tag{98}$$

Incorporating Eq. (82), Eq. (88), and Eq. (96) then results in

$$-A_i \frac{\partial}{\partial x}\left(p \frac{\partial w}{\partial x}\right) + \frac{\partial}{\partial x}\left(T \frac{\partial w}{\partial x}\right) - \frac{\partial}{\partial x}\left(EI \frac{\partial^3 w}{\partial x^3}\right) - c \frac{\partial w}{\partial t} + f_{hydro} = M_i \left[\frac{\partial^2 w}{\partial t^2} + 2U \frac{\partial^2 w}{\partial x \partial t} + \frac{dU}{dt}\frac{\partial w}{\partial x} + U^2 \frac{\partial^2 w}{\partial x^2}\right] + m \frac{\partial^2 w}{\partial t^2}. \tag{99}$$

Combining terms and requiring that the flexural stiffness be constant over the length of pipe leads to

$$0 = -\frac{\partial}{\partial x}\left[(T - A_i p) \frac{\partial w}{\partial x}\right] + EI \frac{\partial^4 w}{\partial x^4} + c \frac{\partial w}{\partial t} - f_{hydro} + M_i \left[\frac{\partial^2 w}{\partial t^2} + 2U \frac{\partial^2 w}{\partial x \partial t} + \frac{dU}{dt}\frac{\partial w}{\partial x} + U^2 \frac{\partial^2 w}{\partial x^2}\right] + m \frac{\partial^2 w}{\partial t^2}. \tag{100}$$

Turning to the remaining equations of interest, Eq. (78) and Eq. (85) are combined as

$$-A_i \frac{\partial p}{\partial x} + (M_i + m) g + \frac{\partial T}{\partial x} = M_i a_{fx}. \tag{101}$$

Eq. (101) can be rewritten while simultaneously incorporating Eq. (97)

$$\frac{\partial}{\partial x}(T - A_i p) = M_i \frac{dU}{dt} - (M_i + m) g, \tag{102}$$

Integrating Eq. (102) from x to L leads to

$$(T - A_i p)|_L - (T - A_i p)|_x = \left(M_i \frac{dU}{dt} - (M_i + m) g\right)(L - x), \tag{103}$$

At $x = L$, there may be an applied external tension $(\overline{T})$ or mean pressure differential $(\overline{p})$ above the pressure required to overcome fluid friction. If the pipe is unable to displace axially, the pressurization along the length of the pipe may induce an additional axial force due to Poisson's effect. Consider the longitudinal and hoop stresses that develop in a thin-walled pipe. The hoop stress may be derived as (see Figure 18)

$$2d'\overline{p} = 2F = 2\sigma_h w_t \quad \rightarrow \quad \sigma_h = \frac{d'\overline{p}}{w_t} = \frac{2A_i \overline{p}}{A_p}, \tag{104}$$

while the resulting axial stress is

$$\sigma_a = \frac{T'}{A_p}. \tag{105}$$

The total longitudinal strain is written as

$$\varepsilon_l = \frac{1}{E}[\sigma_a - \upsilon\sigma_h] = \frac{1}{EA_p}[T' - \upsilon 2A_i\overline{p}]. \tag{106}$$

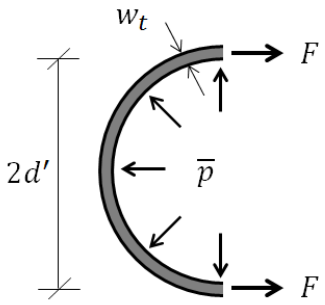

Figure 18. Hoop Forces in a Thin-Walled Pipe

If the pipe is not able to displace axially, $\int_0^L \varepsilon_l dx = 0$, leading to

$$T' = \upsilon 2A_i\overline{p}. \tag{107}$$

Eq. (103) can then be written as

$$T - A_i p = (T - A_i p)|_x = \overline{T} - A_i\overline{p}(1 - 2\nu\delta) + \left((M_i + m)g - M_i\frac{dU}{dt}\right)(L - x), \tag{108}$$

where $\delta = 0$ for unrestrained axial motion at $x = L$ and $\delta = 1$ if the axial motion is restrained at the boundaries. To arrive at the final form of the equation of motion, recall Eq. (100) and expand terms

$$\begin{aligned} 0 = -\left(\frac{\partial}{\partial x}(T - A_i p)\right)\frac{\partial w}{\partial x} - (T - A_i p)\frac{\partial^2 w}{\partial x^2} + EI\frac{\partial^4 w}{\partial x^4} + c\frac{\partial w}{\partial t} - f_{hydro} + M_i\frac{\partial^2 w}{\partial t^2} + \\ 2M_i U\frac{\partial^2 w}{\partial x \partial t} + M_i\frac{dU}{dt}\frac{\partial w}{\partial x} + M_i U^2\frac{\partial^2 w}{\partial x^2} + m\frac{\partial^2 w}{\partial t^2}. \end{aligned} \tag{109}$$

Noting that

$$\frac{\partial}{\partial x}(T - A_i p) = -\left((M_i + m)g - M_i\frac{dU}{dt}\right), \tag{110}$$

Eq. (108), Eq. (109), and Eq. (110) can be combined as

$$\begin{aligned} 0 = \left((M_i + m)g - M_i\frac{dU}{dt}\right)\frac{\partial w}{\partial x} - \left(\overline{T} - A_i\overline{p}(1 - 2\nu\delta) + \left((M_i + m)g - M_i\frac{dU}{dt}\right)(L - \right. \\ \left. x)\right)\frac{\partial^2 w}{\partial x^2} + EI\frac{\partial^4 w}{\partial x^4} + c\frac{\partial w}{\partial t} - f_{hydro} + M_i\frac{\partial^2 w}{\partial t^2} + 2M_i U\frac{\partial^2 w}{\partial x \partial t} + M_i\frac{dU}{dt}\frac{\partial w}{\partial x} + M_i U^2\frac{\partial^2 w}{\partial x^2} + \\ m\frac{\partial^2 w}{\partial t^2}, \end{aligned} \tag{111}$$

which can be simplified to

$$EI\frac{\partial^4 w}{\partial x^4} + \left[M_i U^2 - \overline{T} + A_i\overline{p}(1-2\nu\delta) - \left((M_i+m)g - M_i\frac{dU}{dt}\right)(L-x)\right]\frac{\partial^2 w}{\partial x^2} + 2M_i U\frac{\partial^2 w}{\partial x \partial t} + (M_i+m)g\frac{\partial w}{\partial x} + c\frac{\partial w}{\partial t} + (M_i+m)\frac{\partial^2 w}{\partial t^2} - f_{hydro} = 0. \tag{112}$$

In shorthand notation, where $(\dot{})$ and $()'$ represent temporal and spatial derivatives,

$$EIw'''' + \left\{M_i U^2 - \overline{T} + \bar{p}A_i(1-2\nu\delta) - \left[(M_i+m)g - M_i\dot{U}\right](L-x)\right\}w'' + 2M_i U\dot{w}' + (M_i+m)gw' + c\dot{w} + (M_i+m)\ddot{w} - f_{hydro} = 0. \tag{113}$$

Starting with the first term, the forces represented are a flexural restoring force, centrifugal force, externally applied tension force, tension stemming from a fluid pressure differential, gravity induced tension, time-varying flow effects, Coriolis force, gravity, external viscous damping, inertia, and a hydrodynamic forcing function.

3.3. Model Reduction

Two techniques are utilized to simplify the problem: (a) the equation of motion (i.e. Eq. (112) and Eq. (48)) is nondimensionalized and (b) real-world physical constraints are used in an attempt to reduce the parameters of interest.

3.3.1. Nondimensional Equation of Motion

The equation of motion has been derived as

$$EI\frac{\partial^4 w}{\partial x^4} + \left[M_i U^2 - \overline{T} + A_i\overline{p}(1-2\nu\delta) - \left((M_i+m)g - M_i\frac{dU}{dt}\right)(L-x)\right]\frac{\partial^2 w}{\partial x^2} + 2M_i U\frac{\partial^2 w}{\partial x \partial t} + (M_i+m)g\frac{\partial w}{\partial x} + c\frac{\partial w}{\partial t} + (M_i+m)\frac{\partial^2 w}{\partial t^2} + i\rho_e\pi d^2\omega\Gamma U_0 e^{i\omega t} = 0. \tag{114}$$

using Eq. (112) and Eq. (48) where the annulus fluid density (ρ) has been replaced with (ρ_e) to distinguish between the external (annulus) and internal (conveyed) fluids. Following the work of Païdoussis and Issid (1974) [170], define the following nondimensional terms

$$\xi = \frac{x}{L};\quad \eta = \frac{w}{L};\quad \tau = \left[\frac{EI}{M_i+m}\right]^{\frac{1}{2}}\frac{t}{L^2};\quad \Omega = \left[\frac{M_i+m}{EI}\right]^{\frac{1}{2}}\omega L^2 \tag{115}$$

where the last two terms represent nondimensional time and frequency. Alternatively,

$$x = \xi L; \quad w = \eta L; \quad t = \tau L^2 \left[\frac{M_i+m}{EI}\right]^{\frac{1}{2}}; \quad \omega = \frac{\Omega}{L^2}\left[\frac{EI}{M_i+m}\right]^{\frac{1}{2}}. \tag{116}$$

Since the equation of motion contains a number of derivatives, the dimensionless differential operators are needed. The spatial operators include

$$\begin{gathered}\frac{d}{dx} = \frac{d\xi}{dx}\frac{d}{d\xi} = \frac{1}{L}\frac{d}{d\xi}, \\ \frac{d^2}{dx^2} = \left(\frac{d}{dx}\right)^2 = \left(\frac{1}{L}\frac{d}{d\xi}\right)^2 = \frac{1}{L^2}\frac{d^2}{d\xi^2}, \\ \frac{d^3}{dx^3} = \frac{1}{L^3}\frac{d^3}{d\xi^3}, \\ \frac{d^4}{dx^4} = \frac{1}{L^4}\frac{d^4}{d\xi^4}.\end{gathered} \tag{117}$$

The temporal operators include

$$\begin{gathered}\frac{d}{dt} = \frac{d\tau}{dt}\frac{d}{d\tau} = \left[\frac{EI}{M_i+m}\right]^{\frac{1}{2}}\frac{1}{L^2}\frac{d}{d\tau}, \\ \frac{d^2}{dt^2} = \left(\frac{d}{dt}\right)^2 = \left(\left[\frac{EI}{M_i+m}\right]^{\frac{1}{2}}\frac{1}{L^2}\frac{d}{d\tau}\right)^2 = \left(\frac{EI}{M_i+m}\right)\frac{1}{L^4}\frac{d^2}{d\tau^2}.\end{gathered} \tag{118}$$

And lastly, the spatial-temporal operator is

$$\frac{\partial^2}{\partial x \partial t} = \left(\frac{\partial}{\partial x}\right)\left(\frac{\partial}{\partial t}\right) = \left(\frac{1}{L}\frac{\partial}{\partial \xi}\right)\left(\left[\frac{EI}{M_i+m}\right]^{\frac{1}{2}}\frac{1}{L^2}\frac{\partial}{\partial \tau}\right) = \left[\frac{EI}{M_i+m}\right]^{\frac{1}{2}}\frac{1}{L^3}\frac{\partial^2}{\partial \xi \partial \tau}. \tag{119}$$

The individual terms from Eq. (114) can be rewritten using Eq. (116) through Eq. (119). Flexural restoring force:

$$EI\frac{d^4(w)}{dx^4} = EI\frac{1}{L^4}\frac{d^4(\eta L)}{d\xi^4} = \frac{EI}{L^3}\left(\frac{d^4\eta}{d\xi^4}\right). \tag{120}$$

Centrifugal force:

$$M_i U^2\frac{d^2(w)}{dx^2} = M_i U^2\frac{1}{L^2}\frac{d^2(\eta L)}{d\xi^2} = \frac{M_i U^2}{L}\left(\frac{d^2\eta}{d\xi^2}\right). \tag{121}$$

Externally applied tension force:

$$\bar{T}\frac{d^2(w)}{dx^2} = \bar{T}\frac{1}{L^2}\frac{d^2(\eta L)}{d\xi^2} = \frac{\bar{T}}{L}\left(\frac{d^2\eta}{d\xi^2}\right). \tag{122}$$

Tension stemming from a fluid pressure differential:

$$\bar{p}A_i(1-2\nu\delta)\frac{d^2(w)}{dx^2} = \bar{p}A_i(1-2\nu\delta)\frac{1}{L^2}\frac{d^2(\eta L)}{d\xi^2} = \frac{\bar{p}A_i}{L}(1-2\nu\delta)\left(\frac{d^2\eta}{d\xi^2}\right). \tag{123}$$

Gravity induced tension and time-varying flow effects:

$$\begin{aligned}&\left[(M_i+m)g - M_i\frac{d(U)}{dt}\right](L-x)\frac{d^2(w)}{dx^2}\\ &= \left[(M_i+m)g - M_i\left[\frac{EI}{M_i+m}\right]^{\frac{1}{2}}\frac{1}{L^2}\frac{d(U)}{d\tau}\right]\left(L-(\xi L)\right)\frac{1}{L^2}\frac{d^2(\eta L)}{d\xi^2}\\ &= \left[(M_i+m)g - \frac{M_i}{L^2}\left[\frac{EI}{M_i+m}\right]^{\frac{1}{2}}\frac{dU}{d\tau}\right](1-\xi)\left(\frac{d^2\eta}{d\xi^2}\right).\end{aligned} \tag{124}$$

Coriolis force:

$$2M_iU\frac{\partial^2(w)}{\partial x\partial t} = 2M_iU\left[\frac{EI}{M_i+m}\right]^{\frac{1}{2}}\frac{1}{L^3}\frac{\partial^2(\eta L)}{\partial\xi\partial\tau} = \frac{2M_iU}{L^2}\left[\frac{EI}{M_i+m}\right]^{\frac{1}{2}}\left(\frac{\partial^2\eta}{\partial\xi\partial\tau}\right). \tag{125}$$

Gravity:

$$(M_i+m)g\frac{d(w)}{dx} = (M_i+m)g\frac{1}{L}\frac{d(\eta L)}{d\xi} = (M_i+m)g\left(\frac{d\eta}{d\xi}\right). \tag{126}$$

External viscous damping:

$$c\frac{d(w)}{dt} = c\left[\frac{EI}{M_i+m}\right]^{\frac{1}{2}}\frac{1}{L^2}\frac{d(\eta L)}{d\tau} = \frac{c}{L}\left[\frac{EI}{M_i+m}\right]^{\frac{1}{2}}\left(\frac{d\eta}{d\tau}\right). \tag{127}$$

Inertia:

$$(M_i+m)\frac{d^2(w)}{dt^2} = (M_i+m)\left(\frac{EI}{M_i+m}\right)\frac{1}{L^4}\frac{d^2(\eta L)}{d\tau^2} = \frac{EI}{L^3}\left(\frac{d^2\eta}{d\tau^2}\right). \tag{128}$$

Hydrodynamic forcing:

$$\begin{aligned}&i\rho_e\pi d^2\omega\Gamma U_0e^{i\omega t}\\ &= i\rho_e\pi d^2\left(\frac{\Omega}{L^2}\left[\frac{EI}{M_i+m}\right]^{\frac{1}{2}}\right)\Gamma U_0e^{i\left(\frac{\Omega}{L^2}\left[\frac{EI}{M_i+m}\right]^{\frac{1}{2}}\right)\left(\tau L^2\left[\frac{M_i+m}{EI}\right]^{\frac{1}{2}}\right)}\\ &= i\rho_e\pi d^2\frac{1}{L^2}\left[\frac{EI}{M_i+m}\right]^{\frac{1}{2}}\Omega\Gamma U_0e^{i\Omega\tau}.\end{aligned} \tag{129}$$

Using the previously defined shorthand notation, Eq. (114) is rewritten using Eq. (120) through Eq. (129)

$$\begin{aligned}&\frac{EI}{L^3}\eta'''' + \left\{\frac{M_iU^2}{L} - \frac{\bar{T}}{L} + \frac{\bar{p}A_i}{L}(1-2\nu\delta) - \left[(M_i+m)g - \frac{M_i}{L^2}\left[\frac{EI}{M_i+m}\right]^{\frac{1}{2}}\dot{U}\right](1-\xi)\right\}\eta'' +\\ &\frac{2M_iU}{L^2}\left[\frac{EI}{M_i+m}\right]^{\frac{1}{2}}\dot{\eta}' + (M_i+m)g\eta' + \frac{c}{L}\left[\frac{EI}{M_i+m}\right]^{\frac{1}{2}}\dot{\eta} + \frac{EI}{L^3}\ddot{\eta} + i\rho_e\pi d^2\frac{1}{L^2}\left[\frac{EI}{M_i+m}\right]^{\frac{1}{2}}\Omega\Gamma U_0e^{i\Omega\tau} = 0.\end{aligned} \tag{130}$$

Eq. (130) is then divided by EI/L^3 leading to

$$\eta'''' + \left\{\frac{L^3}{EI}\frac{M_i U^2}{L} - \frac{L^3}{EI}\frac{\bar{T}}{L} + \frac{L^3}{EI}\frac{\bar{p}A_i}{L}(1-2\nu\delta) - \left[\frac{L^3}{EI}(M_i+m)g - \frac{L^3}{EI}\frac{M_i}{L^2}\left[\frac{EI}{M_i+m}\right]^{\frac{1}{2}}\dot{U}\right](1-\xi)\right\}\eta'' + \frac{L^3}{EI}\frac{2M_i U}{L^2}\left[\frac{EI}{M_i+m}\right]^{\frac{1}{2}}\dot{\eta}' + \frac{L^3}{EI}(M_i+m)g\eta' + \frac{L^3}{EI}\frac{c}{L}\left[\frac{EI}{M_i+m}\right]^{\frac{1}{2}}\dot{\eta} + \ddot{\eta} + \frac{L^3}{EI}i\rho_e\pi d^2\frac{1}{L^2}\left[\frac{EI}{M_i+m}\right]^{\frac{1}{2}}\Omega\Gamma U_0 e^{i\Omega\tau} = 0. \quad (131)$$

Simplifying leads to

$$\eta'''' + \left\{\left(\left(\frac{M_i}{EI}\right)^{\frac{1}{2}}UL\right)^2 - \frac{\bar{T}L^2}{EI} + \frac{\bar{p}A_iL^2}{EI}(1-2\nu\delta) - \left[\frac{(M_i+m)gL^3}{EI} - \left(\frac{M_i}{M_i+m}\right)^{\frac{1}{2}}\left(\frac{M_i}{EI}\right)^{\frac{1}{2}}L\dot{U}\right](1-\xi)\right\}\eta'' + 2\left(\frac{M_i}{M_i+m}\right)^{\frac{1}{2}}\left(\frac{M_i}{EI}\right)^{\frac{1}{2}}LU\dot{\eta}' + \frac{(M_i+m)gL^3}{EI}\eta' + \frac{cL^2}{[EI(M_i+m)]^{\frac{1}{2}}}\dot{\eta} + \ddot{\eta} + \rho_e d^2 L\left[\frac{1}{EI(M_i+m)}\right]^{\frac{1}{2}}U_0 e^{i\Omega\tau}(i\pi\Omega\Gamma) = 0. \quad (132)$$

Or, using newly defined terms

$$\eta'''' + \left\{u^2 - \Lambda + \Pi(1-2\nu\delta) - \left[\gamma - \beta^{\frac{1}{2}}\dot{u}\right](1-\xi)\right\}\eta'' + 2\beta^{\frac{1}{2}}u\dot{\eta}' + \gamma\eta' + \sigma\dot{\eta} + \ddot{\eta} + \mathrm{X}(i\pi\Omega\Gamma) = 0, \quad (133)$$

where

$$u = \left(\frac{M_i}{EI}\right)^{\frac{1}{2}}UL;\quad \Lambda = \frac{\bar{T}L^2}{EI};\quad \Pi = \frac{\bar{p}A_iL^2}{EI};\quad \gamma = \frac{(M_i+m)gL^3}{EI};$$
$$\beta = \frac{M_i}{M_i+m};\quad \sigma = \frac{cL^2}{[EI(M_i+m)]^{\frac{1}{2}}};\quad \mathrm{X} = \rho_e d^2 L\left[\frac{1}{EI(M_i+m)}\right]^{\frac{1}{2}}U_0 e^{i\Omega\tau}. \quad (134)$$

These results indicate that each term will contribute to the dynamic behavior of the system.

3.3.2. Physical Constraints

The bracketed coefficients in Eq. (133) are seen to introduce tension into the system. If the applied axial force (Λ) is taken to be an order of magnitude larger than the combined effects of the gravity induced tension (γ) and the time-varying flow effects ($\beta^{\frac{1}{2}}\dot{u}$), the effect of these two forces may be neglected by using Λ as a bounded input when looking at axial force effects.

Deconstructing $\gamma - \beta^{\frac{1}{2}}\dot{u}$, the dimensional variables of interest are M_i, m, L, EI, and $\dot{U}$. The conveyed fluid mass (M_i) is a function of the pipes conveyed fluid area (A_i) and conveyed fluid density. All potential values for A_i can be determined for all standard production tube geometries using the list of standard geometries provided in API 5CT [113]. The conveyed

fluid density is assumed to be bounded between $0 kg/m^3$ for a gaseous fluid and $1500\ kg/m^3$ for a highly dense fluid. The pipe mass can be calculated using the standard tubing geometries provided in API 5CT [113] and an assumed steel density ranging from $7500\ kg/m^3$ to $8200\ kg/m^3$. The length of the system is assumed to range between $5m$ and $30m$, representing one to several lengths of production tubing [113]. The flexural stiffness is found using the pipes inertia (calculated using API 5CT [113] values) and an assumed Young's modulus of $200GPa$.

To estimate the maximum fluid acceleration, it is reasonable to assume the fluid will be produced using natural drive mechanisms, artificial lift mechanisms, and/or enhanced recovery methods. Generally speaking, natural drive mechanisms and enhanced recovery methods rely on reservoir fluid pressures to drive hydrocarbons up to the surface. The pressure at the reservoir layer may be due to natural mechanisms such as water drive or gravity drainage, or may be generated through reservoir enhancements such as waterflooding or gas injection. When utilizing these types of extraction methods, the conveyed fluid velocity slowly decays as the reservoir pressure dissipates due to fluid extraction. In these instances, it is reasonable to assume the conveyed fluid velocity is relatively unchanging (i.e. $dU/dt \approx 0$) over discrete time intervals. If the hydrocarons are extracted using artificial lift mechanisms, there are two paradigms to consider: constant velocity pumping (e.g. electric submersible pumps, jet pumps, etc.) and cyclical pumping (e.g. beam or other reciprocating rod pumps). While constant velocity pumping again leads to $dU/dt \approx 0$ as a reasonable assumption, cyclical pumping requires additional investigation. To estimate the peak acceleration of the conveyed fluid being produced by cyclical pumping, assume that the pump cycles at a known rate (strokes per minute; SPM) and with a known stroke length (SL). If the pump rod displacement profile is assumed to be sinusoidal, with the conveyed fluid displacement profile assumed to match, then

the displacement can be written as $(SL/2)sin(2\pi * SPM * 1min/60sec * t)$. The peak fluid acceleration can then be written as $(SL/2)\ (2\pi SPM/60)^2$. Using a practical relationship between SPM and SL provided by Cholet (2008) [172], the peak acceleration is estimated to be $-5\ m/s^2$ (or $5\ m/s^2$ upwards). These inputs are summarized in Table 9.

Table 9. Input Summary

Variable	Minimum Value	Maximum Value
Conveyed Fluid Area, $A_i\ (mm^2)$	279	7939
Conveyed Fluid Density, $\rho_i\ (kg/m^3)$	0	1500
Conveyed Fluid Mass, $M_i\ (kg/m)$	0	11.91
Pipe Cross Sectional Area, $A_p\ (mm^2)$	214	4941
Pipe Density, $\rho_p\ (kg/m^3)$	7500	8200
Pipe Mass, $m\ (kg/m)$	1.61	40.52
Supported Length, $L\ (m)$	5	30
Flexural Stiffness, $EI\ (Nm^2)$	$3.08e3$	$1.23e6$
Conveyed Fluid Acceleration, $\dot{U}\ (m/s^2)$	-5	0

Each permutation of these physically constrained, dimensioned variables can be used to determine a maximum value of $\gamma - \beta^{\frac{1}{2}}\dot{u}$ for each standard tubing geometry. This maximum value of $\gamma - \beta^{\frac{1}{2}}\dot{u}$ can be equated to Λ, allowing the peak tension force to be found. Based on the assumptions made above, the combined effects of the gravity induced tension and the time-varying flow effects is to induce a linearly varying tension force with a maximum peak amplitude of $14.48kN$. Thus, to bound the effects of the gravity induced tension and the time-varying flow, external axial forces ($\overline{T}$) greater than or equal to $\pm 145kN$ (one order of magnitude greater than $\overline{T}_{peak}$ in Table 10) will be considered when investigating axial force effects. A summary table is shown in Table 10.

Table 10. Bounded Tension Force

Tubing Outer Diameter (mm)	Tubing Wall Thickness (mm)	Flexural Stiffness, $EI\ (Nm^2)$	$\gamma - \beta^{\frac{1}{2}}\dot{u}$	$\bar{T}_{peak} = \left(\frac{EI}{L^2}\right)\left[\gamma - \beta^{\frac{1}{2}}\dot{u}\right]$ (kN)
26.67	2.87	$3.08E+03$	196.44	0.67
26.67	3.91	$3.73E+03$	193.27	0.80
33.40	3.38	$7.27E+03$	126.44	1.02
33.40	4.55	$8.79E+03$	123.35	1.21
42.16	3.18	$1.49E+04$	84.51	1.40
42.16	3.56	$1.62E+04$	82.20	1.48
42.16	4.85	$2.01E+04$	78.26	1.75
48.26	3.18	$2.30E+04$	67.22	1.72
48.26	3.68	$2.58E+04$	64.40	1.84
48.26	5.08	$3.26E+04$	60.39	2.19
48.26	6.35	$3.76E+04$	59.26	2.47
48.26	7.62	$4.16E+04$	59.31	2.74
52.40	3.96	$3.56E+04$	54.81	2.17
52.40	5.72	$4.64E+04$	51.03	2.63
60.32	4.24	$5.91E+04$	42.31	2.78
60.32	4.83	$6.53E+04$	40.83	2.96
60.32	6.45	$8.03E+04$	38.66	3.45
60.32	7.49	$8.85E+04$	38.11	3.75
60.32	8.53	$9.56E+04$	37.93	4.03
73.02	5.51	$1.34E+05$	28.38	4.23
73.02	7.01	$1.60E+05$	26.88	4.78
73.02	7.82	$1.73E+05$	26.44	5.07
73.02	8.64	$1.84E+05$	26.15	5.36
73.02	9.96	$2.01E+05$	25.94	5.80
73.02	11.18	$2.14E+05$	25.95	6.18
88.90	5.49	$2.51E+05$	20.46	5.71
88.90	6.45	$2.86E+05$	19.43	6.17
88.90	7.34	$3.15E+05$	18.78	6.58
88.90	9.52	$3.79E+05$	17.89	7.54
88.90	10.92	$4.15E+05$	17.63	8.12
88.90	12.09	$4.41E+05$	17.54	8.59
88.90	13.46	$4.68E+05$	17.53	9.12
101.60	5.74	$3.99E+05$	16.25	7.19
101.60	6.65	$4.49E+05$	15.41	7.69
101.60	8.38	$5.37E+05$	14.42	8.61
101.60	10.54	$6.33E+05$	13.79	9.70
101.60	12.70	$7.15E+05$	13.51	10.73
101.60	15.49	$8.02E+05$	13.45	11.98
114.30	6.88	$6.73E+05$	12.58	9.40
114.30	8.56	$8.00E+05$	11.72	10.42
114.30	9.65	$8.76E+05$	11.36	11.06
114.30	10.92	$9.58E+05$	11.07	11.79
114.30	12.70	$1.06E+06$	10.82	12.77
114.30	14.22	$1.14E+06$	10.70	13.58
114.30	16.00	$1.23E+06$	10.64	14.48

Critical values occurred when the conveyed fluid mass, pipe mass, and support lengths were maximized.

3.4. Solution Methodology

Simplifying the equation of motion using the physical constraints just described, Eq. (113) can be rewritten as

$$EIw'''' + \{M_i U^2 - \bar{T} + \bar{p}A_i(1-2\nu\delta)\}w'' + 2M_i U\dot{w}' + (M_i+m)gw' + c\dot{w} + (M_i+m)\ddot{w} - f_{hydro} = 0. \tag{135}$$

Since the equation of motion is frequency dependent through the hydrodynamic forcing (Eq. (48)), the spectral element method is used to solve for the desired outputs. Operating in the frequency domain, the spectral element method assembles element dynamic stiffness matrices into a global dynamic stiffness matrix using traditional finite element assembly techniques. Additional discussion of the spectral element method can be found in the works of Doyle (1989) [173], Lee (2009) [174], Lee et al. (2009) [175], and Lee and Oh (2003) [176]. The solution methodology, as applied to Eq. (135), is outlined in the next section.

3.4.1. Spectral Element Method

To implement the spectral element method, the governing equation of motion is transformed into the Fourier domain by taking the Fourier transform. The definitions of the transform, along with the transform of the spatial derivatives are

$$\begin{aligned}
\int_{-\infty}^{\infty} we^{-i\omega t}dt &= \widehat{W}(x,\omega) = \widehat{W}, \\
\int_{-\infty}^{\infty} w'e^{-i\omega t}dt &= \frac{\partial}{\partial x}\left(\int_{-\infty}^{\infty} w(x,t)e^{-i\omega t}dt\right) = \widehat{W}', \\
\int_{-\infty}^{\infty} w''e^{-i\omega t}dt &= \frac{\partial^2}{\partial x^2}\left(\int_{-\infty}^{\infty} w(x,t)e^{-i\omega t}dt\right) = \widehat{W}'', \\
\int_{-\infty}^{\infty} w''''e^{-i\omega t}dt &= \frac{\partial^4}{\partial x^4}\left(\int_{-\infty}^{\infty} w(x,t)e^{-i\omega t}dt\right) = \widehat{W}'''',
\end{aligned} \tag{136}$$

To the temporal derivatives are calculated using integration by parts

$$\int v'(x)\,u(x)dx = v(x)u(x) - \int v(x)u'(x)\,dx. \tag{137}$$

The temporal derivatives are

$$\int_{-\infty}^{\infty} \dot{w} e^{-i\omega t} dt = w e^{-i\omega t}\Big|_{-\infty}^{\infty} - \int_{-\infty}^{\infty} w(-i\omega e^{-i\omega t})\, dt = i\omega \int_{-\infty}^{\infty} w e^{-i\omega t}\, dt = i\omega \widehat{W},$$
$$\int_{-\infty}^{\infty} \ddot{w} e^{-i\omega t} dt = (i\omega)^2 \widehat{W} = -\omega^2 \widehat{W}. \tag{138}$$

The mixed-derivative is found as

$$\int_{-\infty}^{\infty} \dot{w}' e^{-i\omega t} dt = i\omega \widehat{W}'. \tag{139}$$

Using Eq. (55), Eq. (136), Eq. (138), and Eq. (139), Eq. (135) can be rewritten as

$$EI\widehat{W}'''' + \{M_i U^2 - \bar{T} + \bar{p} A_i (1 - 2\nu\delta)\}\widehat{W}'' + \{2i\omega M_i U + (M_i + m)g\}\widehat{W}' + \{i\omega c - (M_i + m)\omega^2 - \rho_e \pi d^2 \omega^2 \Gamma\}\widehat{W} = 0. \tag{140}$$

Assume the general solution of Eq. (140) to be

$$\widehat{W} = C e^{ikx} \tag{141}$$

where C is a constant and k is the wavenumber. Inserting Eq. (141) into Eq. (140) leads to the following dispersion relation

$$EIk^4 - \{M_i U^2 - \bar{T} + \bar{p} A_i (1 - 2\nu\delta)\}k^2 + \{2i\omega M_i U + (M_i + m)g\}ik + \{i\omega c - (M_i + m)\omega^2 - \rho_e \pi d^2 \omega^2 \Gamma\} = 0 \tag{142}$$

which can be solved for the four wavenumbers (k_r's), each a function of ω, allowing for Eq. (141) to be rewritten as

$$\widehat{W} = \sum_{r=1}^{4} C_r e^{ik_r x} = \boldsymbol{e}\boldsymbol{C}, \tag{143}$$

where

$$\boldsymbol{e} = \{e^{ik_1 x}\ e^{ik_2 x}\ e^{ik_3 x}\ e^{ik_4 x}\},$$
$$\boldsymbol{C} = \{C_1, C_2, C_3, C_4\}. \tag{144}$$

The nodal degrees of freedom and forces vectors for a single spectral element can be written as

$$\boldsymbol{d} = \{W_1, \Theta_1, W_2, \Theta_2\} = \{\widehat{W}(0), \widehat{W}'(0), \widehat{W}(L^e), \widehat{W}'(L^e)\},$$
$$\boldsymbol{f} = \{Q_1, M_1, Q_2, M_2\} = \{Q(0), -M(0), -Q(L^e), M(L^e)\}, \tag{145}$$

with the nodal orientation as shown in Figure 19.

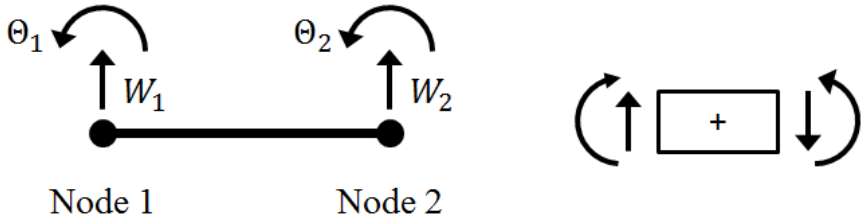

Figure 19. Spectral Element Convention [112]

The nodal degrees of freedom vector can be rewritten in terms of the constants vector through Eq. (143)

$$\boldsymbol{d} = \{\widehat{W}(0), \widehat{W}'(0), \widehat{W}(L^e), \widehat{W}'(L^e)\} = \{\boldsymbol{e}(0), \boldsymbol{e}'(0), \boldsymbol{e}(L^e), \boldsymbol{e}'(L^e)\}\boldsymbol{C} = \boldsymbol{HC}, \tag{146}$$

where

$$\boldsymbol{H} = \begin{bmatrix} 1 & 1 & 1 & 1 \\ ik_1 & ik_2 & ik_3 & ik_4 \\ e^{ik_1L^e} & e^{ik_2L^e} & e^{ik_3L^e} & e^{ik_4L^e} \\ ik_1e^{ik_1L^e} & ik_2e^{ik_2L^e} & ik_3e^{ik_3L^e} & ik_4e^{ik_4L^e} \end{bmatrix}. \tag{147}$$

Using the force relations

$$\begin{aligned} Q &= EI\widehat{W}''' - \bar{T}\widehat{W}', \\ M &= EI\widehat{W}'', \end{aligned} \tag{148}$$

the nodal forces vector can be written as

$$\boldsymbol{f} = \{Q(0), -M(0), -Q(L^e), M(L^e)\} = \boldsymbol{XC}, \tag{149}$$

where

$$\boldsymbol{X} = \begin{bmatrix} g_1 & g_2 & g_3 & g_4 \\ -h_1 & -h_2 & -h_3 & -h_4 \\ -g_1e^{ik_1L^e} & -g_2e^{ik_2L^e} & -g_3e^{ik_3L^e} & -g_4e^{ik_4L^e} \\ h_1e^{ik_1L^e} & h_2e^{ik_2L^e} & h_3e^{ik_3L^e} & h_4e^{ik_4L^e} \end{bmatrix}, \tag{150}$$

and

$$\begin{aligned} g_r &= -ik_r^3EI - ik_r\bar{T}, \\ h_r &= -k_r^2EI. \end{aligned} \tag{151}$$

The nodal degrees of freedom and forces vectors can be related through $\boldsymbol{C}$ using Eq. (146) and Eq. (149)

$$\boldsymbol{f} = \boldsymbol{XC} = \boldsymbol{X}(\boldsymbol{H}^{-1}\boldsymbol{d}) = \boldsymbol{Sd}, \tag{152}$$

where $\boldsymbol{S}$ is the spectral element matrix

$$\boldsymbol{S} = \boldsymbol{XH}^{-1}. \tag{153}$$

The individual spectral element matrices are assembled into a global dynamic stiffness matrix ($\boldsymbol{S_g}$) in a manner analogous to the finite element method. For a three-element model, as shown in Figure 20, the following assembly can be utilized

$$\boldsymbol{S_g} = \boldsymbol{A_1^T S^1 A_1} + \boldsymbol{A_2^T S^2 A_2} + \boldsymbol{A_3^T S^3 A_3}, \tag{154}$$

where

$$\boldsymbol{A_1} = \begin{bmatrix} 1 & 0 & 0 & 0 & 0 & 0 & 0 & 0 \\ 0 & 1 & 0 & 0 & 0 & 0 & 0 & 0 \\ 0 & 0 & 1 & 0 & 0 & 0 & 0 & 0 \\ 0 & 0 & 0 & 1 & 0 & 0 & 0 & 0 \end{bmatrix},$$

$$\boldsymbol{A_2} = \begin{bmatrix} 0 & 0 & 1 & 0 & 0 & 0 & 0 & 0 \\ 0 & 0 & 0 & 1 & 0 & 0 & 0 & 0 \\ 0 & 0 & 0 & 0 & 1 & 0 & 0 & 0 \\ 0 & 0 & 0 & 0 & 0 & 1 & 0 & 0 \end{bmatrix}, \tag{155}$$

$$\boldsymbol{A_3} = \begin{bmatrix} 0 & 0 & 0 & 0 & 1 & 0 & 0 & 0 \\ 0 & 0 & 0 & 0 & 0 & 1 & 0 & 0 \\ 0 & 0 & 0 & 0 & 0 & 0 & 1 & 0 \\ 0 & 0 & 0 & 0 & 0 & 0 & 0 & 1 \end{bmatrix},$$

and $\boldsymbol{S^1}$, $\boldsymbol{S^2}$, and $\boldsymbol{S^3}$ are the spectral element matrices for elements one, two, and three, respectively. This assembly leads to the global dynamic stiffness matrix

$$\boldsymbol{S_g} = \begin{bmatrix} S_{11}^1 & S_{12}^1 & S_{13}^1 & S_{14}^1 & 0 & 0 & 0 & 0 \\ S_{21}^1 & S_{22}^1 & S_{23}^1 & S_{24}^1 & 0 & 0 & 0 & 0 \\ S_{31}^1 & S_{32}^1 & S_{33}^1 + S_{11}^2 & S_{34}^1 + S_{12}^2 & S_{13}^2 & S_{14}^2 & 0 & 0 \\ S_{41}^1 & S_{42}^1 & S_{43}^1 + S_{21}^2 & S_{44}^1 + S_{22}^2 & S_{23}^2 & S_{24}^2 & 0 & 0 \\ 0 & 0 & S_{31}^2 & S_{32}^2 & S_{33}^2 + S_{11}^3 & S_{34}^2 + S_{12}^3 & S_{13}^3 & S_{14}^3 \\ 0 & 0 & S_{41}^2 & S_{42}^2 & S_{43}^2 + S_{21}^3 & S_{44}^2 + S_{22}^3 & S_{23}^3 & S_{24}^3 \\ 0 & 0 & 0 & 0 & S_{31}^3 & S_{32}^3 & S_{33}^3 & S_{34}^3 \\ 0 & 0 & 0 & 0 & S_{41}^3 & S_{42}^3 & S_{43}^3 & S_{44}^3 \end{bmatrix}. \tag{156}$$

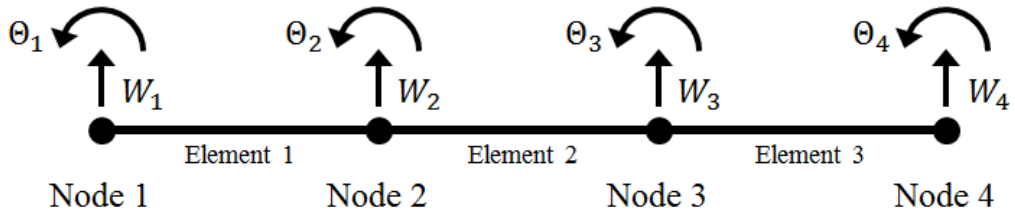

Figure 20. Three-Element Beam Model

The relevant spectral equation is given as

$$\boldsymbol{f_g} = \boldsymbol{S_g d_g}, \tag{157}$$

3.4.2. Incorporating Structural Boundary Conditions

Structural boundary conditions can be incorporated by (1) deleting the rows and columns corresponding to fixed boundaries or (2) adding nodal springs directly into the global dynamic stiffness matrix. The fluid boundary conditions are a function of the structural boundary conditions and are discussed in a later section.

3.4.2.1. Matrix Reduction

For each degree of freedom in which the displacement or rotation is prevented, the governing spectral equation (i.e. Eq. (157)) can be reduced by deleting the rows and columns corresponding to that specific degree of freedom. The spectral equation can be expanded for the three-element model given in Figure 20 as

$$\begin{bmatrix} Q_1 \\ M_1 \\ Q_2 \\ M_2 \\ Q_3 \\ M_3 \\ Q_4 \\ M_4 \end{bmatrix} = \begin{bmatrix} S_{11}^1 & S_{12}^1 & S_{13}^1 & S_{14}^1 & 0 & 0 & 0 & 0 \\ S_{21}^1 & S_{22}^1 & S_{23}^1 & S_{24}^1 & 0 & 0 & 0 & 0 \\ S_{31}^1 & S_{32}^1 & S_{33}^1 + S_{11}^2 & S_{34}^1 + S_{12}^2 & S_{13}^2 & S_{14}^2 & 0 & 0 \\ S_{41}^1 & S_{42}^1 & S_{43}^1 + S_{21}^2 & S_{44}^1 + S_{22}^2 & S_{23}^2 & S_{24}^2 & 0 & 0 \\ 0 & 0 & S_{31}^2 & S_{32}^2 & S_{33}^2 + S_{11}^3 & S_{34}^2 + S_{12}^3 & S_{13}^3 & S_{14}^3 \\ 0 & 0 & S_{41}^2 & S_{42}^2 & S_{43}^2 + S_{21}^3 & S_{44}^2 + S_{22}^3 & S_{23}^3 & S_{24}^3 \\ 0 & 0 & 0 & 0 & S_{31}^3 & S_{32}^3 & S_{33}^3 & S_{34}^3 \\ 0 & 0 & 0 & 0 & S_{41}^3 & S_{42}^3 & S_{43}^3 & S_{44}^3 \end{bmatrix} \begin{bmatrix} W_1 \\ \Theta_1 \\ W_2 \\ \Theta_2 \\ W_3 \\ \Theta_3 \\ W_4 \\ \Theta_4 \end{bmatrix}. \tag{158}$$

If the displacements and rotations at nodes 1 and 4 are set to zero (i.e. fixed-fixed boundaries), Eq. (158) can be reduced to

$$\begin{bmatrix} Q_2 \\ M_2 \\ Q_3 \\ M_3 \end{bmatrix} = \begin{bmatrix} S_{33}^1 + S_{11}^2 & S_{34}^1 + S_{12}^2 & S_{13}^2 & S_{14}^2 \\ S_{43}^1 + S_{21}^2 & S_{44}^1 + S_{22}^2 & S_{23}^2 & S_{24}^2 \\ S_{31}^2 & S_{32}^2 & S_{33}^2 + S_{11}^3 & S_{34}^2 + S_{12}^3 \\ S_{41}^2 & S_{42}^2 & S_{43}^2 + S_{21}^3 & S_{44}^2 + S_{22}^3 \end{bmatrix} \begin{bmatrix} W_2 \\ \Theta_2 \\ W_3 \\ \Theta_3 \end{bmatrix}. \tag{159}$$

3.4.2.2. Nodal Springs

Alternatively, consider the case shown in Figure 21 where nodal springs have been added to node 1 and 4. The springs, with stiffness K_{t1}, K_{r1}, K_{t2}, and K_{r2}, are attached at four new nodal points with degrees of freedom W_5, Θ_5, W_6, and Θ_6.

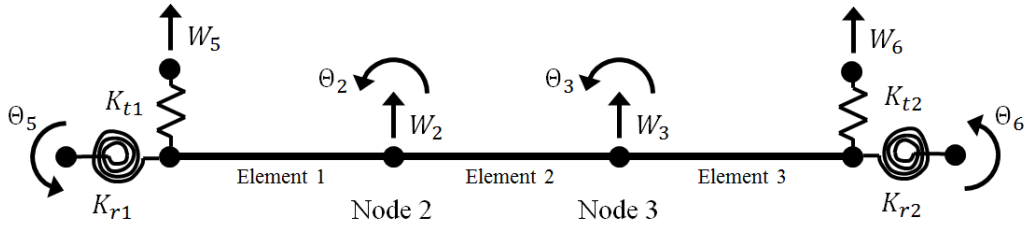

Figure 21. Three-Element Beam Model with Nodal Springs

Analyzing the translational springs shown in Figure 22, the resulting spring equations are

$$\begin{bmatrix} Q_1 \\ Q_5 \end{bmatrix} = \begin{bmatrix} K_{t1} & -K_{t1} \\ -K_{t1} & K_{t1} \end{bmatrix} \begin{bmatrix} W_1 \\ W_5 \end{bmatrix},$$
$$\begin{bmatrix} Q_4 \\ Q_6 \end{bmatrix} = \begin{bmatrix} K_{t2} & -K_{t2} \\ -K_{t2} & K_{t2} \end{bmatrix} \begin{bmatrix} W_4 \\ W_6 \end{bmatrix}. \tag{160}$$

Similarly, the rotational spring equations can be found as

$$\begin{bmatrix} M_1 \\ M_5 \end{bmatrix} = \begin{bmatrix} K_{r1} & -K_{r1} \\ -K_{r1} & K_{r1} \end{bmatrix} \begin{bmatrix} \Theta_1 \\ \Theta_5 \end{bmatrix},$$
$$\begin{bmatrix} M_4 \\ M_6 \end{bmatrix} = \begin{bmatrix} K_{r2} & -K_{r2} \\ -K_{r2} & K_{r2} \end{bmatrix} \begin{bmatrix} \Theta_4 \\ \Theta_6 \end{bmatrix}. \tag{161}$$

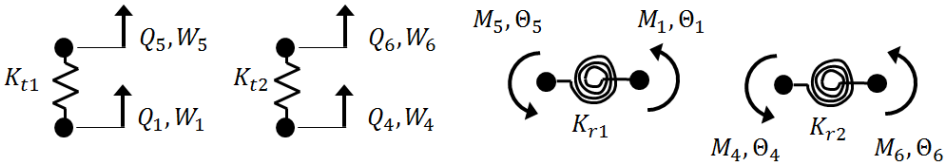

Figure 22. Free Body of Boundary Springs

Expanding the general spectral equation (Eq. (157)) for the new configuration leads to

$$\boldsymbol{f_g} = \begin{bmatrix} Q_1 \\ M_1 \\ Q_2 \\ M_2 \\ Q_3 \\ M_3 \\ Q_4 \\ M_4 \\ Q_5 \\ M_5 \\ Q_6 \\ M_6 \end{bmatrix}, \quad \boldsymbol{d_g} = \begin{bmatrix} W_1 \\ \Theta_1 \\ W_2 \\ \Theta_2 \\ W_3 \\ \Theta_3 \\ W_4 \\ \Theta_4 \\ W_5 \\ \Theta_5 \\ W_6 \\ \Theta_6 \end{bmatrix},$$

$$\boldsymbol{S_g} = \begin{bmatrix} S_{11}^1 + K_{t1} & S_{12}^1 & S_{13}^1 & S_{14}^1 & 0 & 0 & 0 & 0 & -K_{t1} & 0 & 0 & 0 \\ S_{21}^1 & S_{22}^1 + K_{r1} & S_{23}^1 & S_{24}^1 & 0 & 0 & 0 & 0 & 0 & -K_{r1} & 0 & 0 \\ S_{31}^1 & S_{32}^1 & S_{33}^1 + S_{11}^2 & S_{34}^1 + S_{12}^2 & S_{13}^2 & S_{14}^2 & 0 & 0 & 0 & 0 & 0 & 0 \\ S_{41}^1 & S_{42}^1 & S_{43}^1 + S_{21}^2 & S_{44}^1 + S_{22}^2 & S_{23}^2 & S_{24}^2 & 0 & 0 & 0 & 0 & 0 & 0 \\ 0 & 0 & S_{31}^2 & S_{32}^2 & S_{33}^2 + S_{11}^3 & S_{34}^2 + S_{12}^3 & S_{13}^3 & S_{14}^3 & 0 & 0 & 0 & 0 \\ 0 & 0 & S_{41}^2 & S_{42}^2 & S_{43}^2 + S_{21}^3 & S_{44}^2 + S_{22}^3 & S_{23}^3 & S_{24}^3 & 0 & 0 & 0 & 0 \\ 0 & 0 & 0 & 0 & S_{31}^3 & S_{32}^3 & S_{33}^3 + K_{t2} & S_{34}^3 & 0 & 0 & -K_{t2} & 0 \\ 0 & 0 & 0 & 0 & S_{41}^3 & S_{42}^3 & S_{43}^3 & S_{44}^3 + K_{r2} & 0 & 0 & 0 & -K_{r2} \\ -K_{t1} & 0 & 0 & 0 & 0 & 0 & 0 & 0 & K_{t1} & 0 & 0 & 0 \\ 0 & -K_{r1} & 0 & 0 & 0 & 0 & 0 & 0 & 0 & K_{r1} & 0 & 0 \\ 0 & 0 & 0 & 0 & 0 & 0 & -K_{t2} & 0 & 0 & 0 & K_{t2} & 0 \\ 0 & 0 & 0 & 0 & 0 & 0 & 0 & -K_{r2} & 0 & 0 & 0 & K_{r2} \end{bmatrix}, \tag{162}$$

where those terms that differ from those in Eq. (158) have been highlighted. If nodes 5 and 6 are fixed, matrix reduction can be used to reduce Eq. (162) to

$$\begin{bmatrix} Q_1 \\ M_1 \\ Q_2 \\ M_2 \\ Q_3 \\ M_3 \\ Q_4 \\ M_4 \end{bmatrix} = \begin{bmatrix} S_{11}^1 + K_{t1} & S_{12}^1 & S_{13}^1 & S_{14}^1 & 0 & 0 & 0 & 0 \\ S_{21}^1 & S_{22}^1 + K_{r1} & S_{23}^1 & S_{24}^1 & 0 & 0 & 0 & 0 \\ S_{31}^1 & S_{32}^1 & S_{33}^1 + S_{11}^2 & S_{34}^1 + S_{12}^2 & S_{13}^2 & S_{14}^2 & 0 & 0 \\ S_{41}^1 & S_{42}^1 & S_{43}^1 + S_{21}^2 & S_{44}^1 + S_{22}^2 & S_{23}^2 & S_{24}^2 & 0 & 0 \\ 0 & 0 & S_{31}^2 & S_{32}^2 & S_{33}^2 + S_{11}^3 & S_{34}^2 + S_{12}^3 & S_{13}^3 & S_{14}^3 \\ 0 & 0 & S_{41}^2 & S_{42}^2 & S_{43}^2 + S_{21}^3 & S_{44}^2 + S_{22}^3 & S_{23}^3 & S_{24}^3 \\ 0 & 0 & 0 & 0 & S_{31}^3 & S_{32}^3 & S_{33}^3 + K_{t2} & S_{34}^3 \\ 0 & 0 & 0 & 0 & S_{41}^3 & S_{42}^3 & S_{43}^3 & S_{44}^3 + K_{r2} \end{bmatrix} \begin{bmatrix} W_1 \\ \Theta_1 \\ W_2 \\ \Theta_2 \\ W_3 \\ \Theta_3 \\ W_4 \\ \Theta_4 \end{bmatrix}. \tag{163}$$

where the contribution from nodal springs at nodes one and four are apparent. In the limit that the boundary springs are set infinitely rigid, the displacements and rotations at nodes 1 and 4 become zero and, again using matrix reduction, Eq. (163) simplifies into the expected result of Eq. (159).

3.4.3. System Response

The natural frequencies of the system can be solved by setting the determinate of the global dynamic stiffness matrix ($\boldsymbol{S_g}$) to zero and solving for the frequency for each mode of interest

$$det\boldsymbol{S_g}(\omega) = 0. \tag{164}$$

For a forced dynamic response, the displacement at the free nodes can be determined by:

1. Transforming the nodal forces at the free nodes into the frequency domain and assemble $\boldsymbol{f_g}$.
2. Invert $\boldsymbol{S_g}$ and solve for $\boldsymbol{d_g}$ using Eq. (157).
3. Disassemble the global response into the element response (i.e. $\boldsymbol{d_g} \rightarrow \boldsymbol{d}$).
4. Calculate the $\boldsymbol{C}$ vector using Eq. (146) and Eq.(147) .
5. Calculate the frequency response $\widehat{W}$ using Eq. (143).
6. Apply an inverse Fourier transform to determine the displacement response in the time domain.

As was done in the Green's function approach, the inverse Fourier transform is done discretely to reduce computation time. The tradeoff, when compared to the continuous inverse transform, is the user must specify which frequencies to include from $\widehat{W}$ (i.e. Ω_s) and the frequency domain sampling rate (i.e. ω_s) [177]. The Mathematica script implementing these calculations can be found in Appendix C.

3.5. Script Validation

Five cases are used to validate the Mathematica script.

3.5.1. Deflection of a Fixed-Fixed Beam in a Confined, Slightly Viscous Fluid

A solid beam in a confined, slightly viscous fluid is subject to a harmonic point load applied at midspan. The modeled inputs are given in Table 11. No other damping is included in the system. The model is solved using both the spectral element model and the Green's

function approach previously described. The superimposed results are shown in Figure 23 to overlap.

Table 11. Beam in a Confined, Slightly Viscous Fluid: Input Parameters

Young's Modulus, E	$1e11$	N/m^2
Beam Density, ρ_p	7500	kg/m^3
Beam Outer Radius, d	0.02	m
Shell Inner Radius, D	0.06	m
Beam Length, L	1	m
Beam Area, A	$1.257e-3$	m^2
Beam Inertia, I	$1.257e-7$	m^4
Beam Mass, m	9.425	kg/m
Fluid Kinematic Viscosity, ν	$1.12e-06$	m^2/s
Fluid Density, ρ_e	999	kg/m^3
Coefficient of Gravity, g	9.81	m/s^2
Load Magnitude	1000	N
Forcing Frequency	400.02	rad/s
DFT Sampling Frequency, ω_s	0.1	rad/s
DFT Sampling Range, Ω_s	± 12500	rad/s
Boundary Conditions	Fixed-Fixed	-

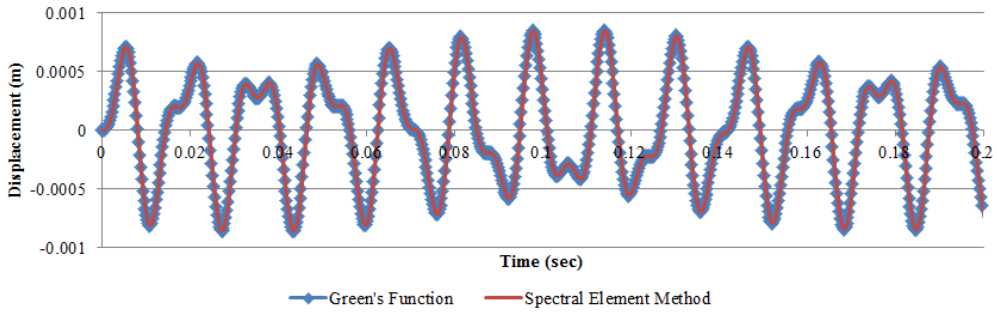

Figure 23. Beam in a Confined, Slightly Viscous Fluid: Superimposed Displacement Responses

3.5.2. Deflection of a Fixed-Fixed Beam in a Confined, Highly Viscous Fluid

A solid beam in a confined, highly viscous fluid is subject to a harmonic point load applied at midspan. The modeled inputs are given in Table 12. No other damping is included in the system. The model is solved using both the spectral element model and the Green's

function approach previously described. As in the slightly viscous case, the displacement results overlap (see Figure 24).

Table 12. Beam in a Confined, Highly Viscous Fluid: Input Parameters

Young's Modulus, E	$2e11$	N/m^2
Beam Density, ρ_p	8000	kg/m^3
Beam Outer Radius, d	0.06	m
Shell Inner Radius, D	0.07	m
Beam Length, L	10	m
Beam Area, A	$1.131e-2$	m^2
Beam Inertia, I	$1.018e-5$	m^4
Beam Mass, m	90.48	kg/m
Fluid Kinematic Viscosity, ν	$2e-04$	m^2/s
Fluid Density, ρ_e	1000	kg/m^3
Coefficient of Gravity, g	9.81	m/s^2
Load Magnitude	1000	N
Forcing Frequency	50.02	rad/s
DFT Sampling Frequency, ω_s	0.05	rad/s
DFT Sampling Range, Ω_s	± 600	rad/s
Boundary Conditions	Fixed-Fixed	-

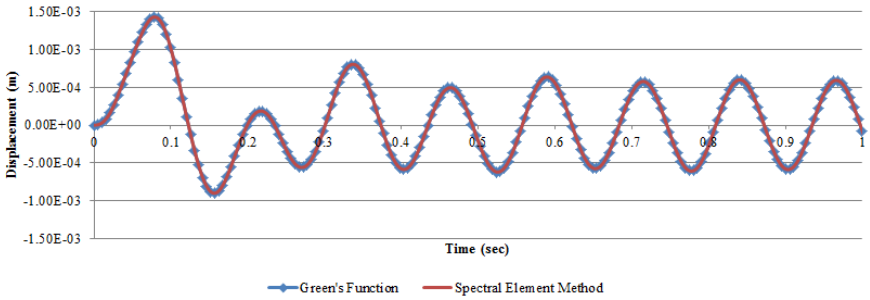

Figure 24. Beam in a Confined, Highly Viscous Fluid: Superimposed Displacement Responses

3.5.3. Natural Frequency of a Simply Supported Beam Under Axial Compression

A simply supported beam is subject to a compression load within a vacuum. The inputs are listed in Table 13. The first three natural frequencies of the beam are calculated using the spectral element method and the analytical solution, given by Rao (2007) [130] as

$$\omega_n = \pi^2 \left(\frac{EI}{mL^4}\right)^{\frac{1}{2}} \left(N^4 + \frac{N^2 PL^2}{\pi^2 EI}\right)^{\frac{1}{2}}, \tag{165}$$

where N corresponds to the mode of interest. The natural frequencies calculated from both methods are listed in Table 14 and are seen to match.

Table 13. Beam Under Axial Compression: Input Parameters

Young's Modulus, E	$2e11$	N/m^2
Beam Density, ρ_p	7800	kg/m^3
Beam Outer Radius, d	0.06	m
Beam Length, L	12	m
Beam Area, A	$1.131e-2$	m^2
Beam Inertia, I	$1.018e-5$	m^4
Beam Mass, m	88.22	kg/m
Coefficient of Gravity, g	9.81	m/s^2
Applied Compression, P	$5e4$	N
Boundary Conditions	Pinned-Pinned	-

Table 14. Natural Frequencies

Mode	Unloaded Natural Frequency (rad/s)	Compressed Natural Frequency (rad/s)		
		Spectral Element Method	Analytical	Error
1	10.41	8.34	8.34	0%
2	41.65	39.74	39.74	0%
3	93.71	91.82	91.82	0%

3.5.4. Critical Fluid Velocity of a Pipe Conveying Fluid in a Vacuum

The critical fluid velocity is defined as the fluid velocity (for a given mode) where the system loses stability by divergence. A single length of pipe is modeled with three ideal boundary conditions: pinned-pinned, pinned-fixed, and fixed-fixed. For each boundary condition, the critical fluid velocity of the first mode is calculated using the spectral element method and is then compared to the critical fluid velocity provided by Païdoussis (2014) [169]. The input parameters used are listed in Table 15. The critical fluid velocities for the three boundary conditions are listed in Table 16 and show excellent agreement. Note that the normalized fluid velocity is given by Eq. (134) and is repeated here for convenience.

$$u = \left(\frac{M_i}{EI}\right)^{\frac{1}{2}} UL. \tag{166}$$

Table 15. Critical Fluid Velocity of a Pipe Conveying Fluid: Input Parameters

Young's Modulus, E	$1.5e10$	N/m^2
Pipe Density, ρ_p	7000	kg/m^3
Conveyed Fluid Density, ρ_i	84.10	kg/m^3
Pipe Outer Radius, d	0.06	m
Pipe Wall Thickness, w_t	0.003	m
Pipe Length, L	20	m
Pipe Area, A_p	$1.103e-3$	m^2
Conveyed Fluid Area, A_i	$1.021e-2$	m^2
Pipe Inertia, I	$1.888e-6$	m^4
Pipe Mass, m	7.719	kg/m
Conveyed Fluid Mass, M_i	0.858	kg/m
Coefficient of Gravity, g	0	m/s^2
Applied Compression, P	0	N

Table 16. A Comparison of Critical Fluid Velocities

	Critical Fluid Velocity (m/s)	Normalized Critical Fluid Velocity		
Boundary Condition	Spectral Element Method	Spectral Element Method	Païdoussis (2014) [169]	Error
Pinned-Pinned	28.53	3.141	π	-0.006%
Pinned-Fixed	40.80	4.492	4.493	-0.001%
Fixed-Fixed	57.07	6.284	2π	0.011%

3.5.5. Damping Ratio of a Vibrating Fixed-Fixed Beam in a Viscous Fluid

A fixed-fixed beam is subject to a midspan harmonic point load (the system properties are given in Table 17). The forcing frequency is significantly lower than the first natural frequency such that the applied load is pseudo-static. After two-and-a-quarter cycles of loading the harmonic load is removed and the beam is allowed to freely vibrate. The resulting displacement time history is shown in Figure 25.

Table 17. Vibration of a Damped Beam: Input Parameters

Young's Modulus, E	$2e11$	N/m^2
Beam Density, ρ	4000	kg/m^3
Beam Outer Radius, d	0.05	m
Shell Inner Radius, D	0.057	m
Beam Length, L	9	m
Beam Area, A	$7.854 - 3$	m^2
Beam Inertia, I	$4.909e - 6$	m^4
Beam Mass, m	31.416	kg/m
Fluid Kinematic Viscosity, ν	$6e - 05$	m^2/s
Fluid Density, ρ_e	900	kg/m^3
Coefficient of Gravity, g	9.81	m/s^2
Load Magnitude, P	1000	N
Forcing Frequency	1.02	rad/s
DFT Sampling Frequency, ω_s	0.05	rad/s
DFT Sampling Range, Ω_s	± 200	rad/s
Boundary Conditions	Fixed-Fixed	-

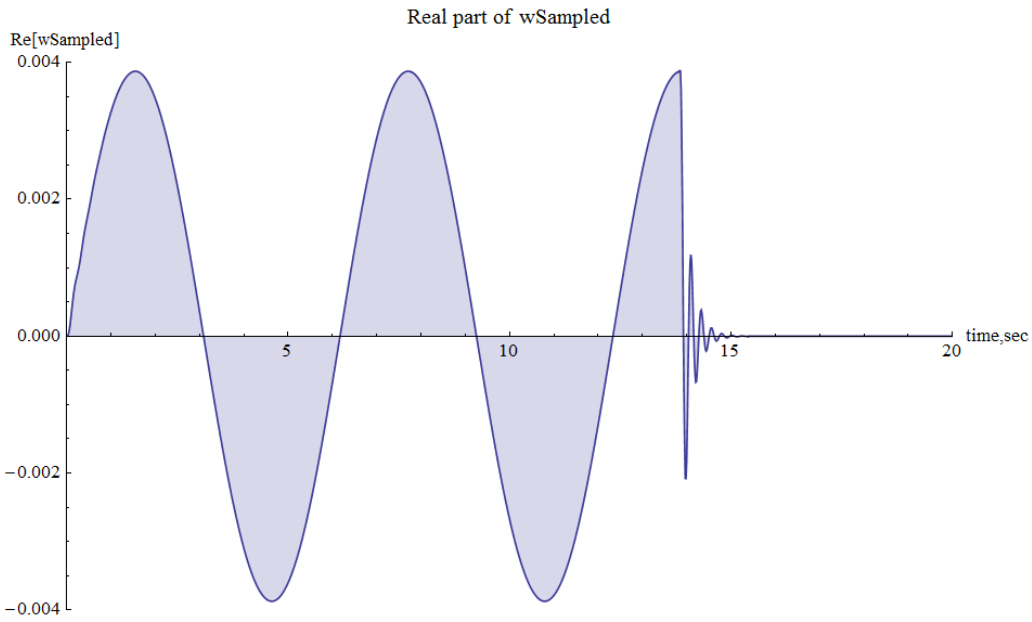

Figure 25. Vibration of a Damped Beam: Displacement Time History

The maximum analytical pseudo-static displacement is given by Eq. (74), reproduced here for convenience

$$\Delta_{midspan} = \frac{PL^3}{192EI}. \tag{167}$$

The maximum displacement given by the analytical equation shows excellent agreement with the results from the spectral element method ($3.87e-3m$ vs. $3.88e-3m$; error $= 0.3\%$).

The free-vibration response can be used to determine the natural frequency and damping ratio of the system. The free-vibration displacement is windowed and plotted in the Fourier domain (see Figure 26 where the first and third damped frequencies are visible; the second mode is not seen as the midpoint node is analyzed). The first damped frequency is found to be $\omega_d = 27.15\,rad/s$.

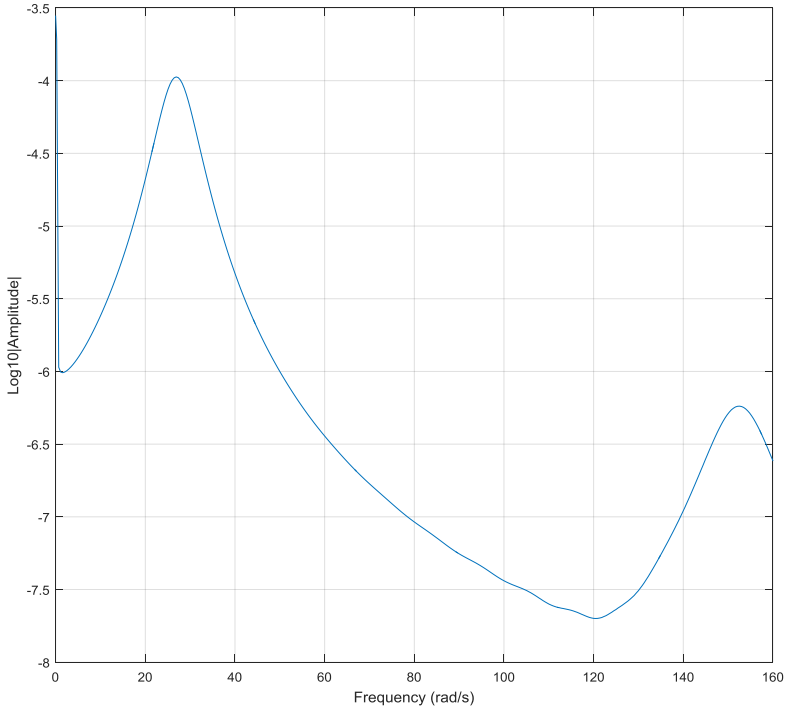

Figure 26. FFT of Windowed Displacement Response

Defining the logarithmic decrement to be the natural logarithm of the ratio between two successive displacement amplitudes

$$LD = ln\frac{w_1}{w_2}, \tag{168}$$

the same free vibration response can be used to calculate the average logarithmic decrement: $LD_{avg} = 1.137$. The logarithmic decrement can be used to find the damping ratio as

$$\zeta = \frac{LD}{\sqrt{4\pi^2 + LD^2}}. \tag{169}$$

Using the average logarithmic decrement, the damping ratio is calculated as $\zeta = 0.178$. With the damped frequency and the damping ratio known, the natural frequency and the imaginary component of the natural frequency can be calculated from

$$\begin{aligned} \omega_n &= \frac{\omega_d}{\sqrt{1-\zeta^2}}, \\ \omega_i &= \zeta\omega_n. \end{aligned} \tag{170}$$

with the numeric results $\omega_n = 27.59\,rad/s$ and $\omega_i = 4.91\,rad/s$. Table 18 compares the above frequency results with the output using Eq. (164); excellent agreement is seen.

Table 18. A Comparison of Outputs

	Results From…		Error
	Displacement Response	Eq. (164)	
ω_d	27.15	27.14	0.03%
ω_i	4.91	4.92	0.20%
ω_n	27.59	27.59	0%
ζ	0.178	0.178	0%

3.6. Parametric Study

As previously stated, it is assumed that the yet-to-be designed energy harvester will be included as part of the production string. In this configuration, the vibrational response of the production string acts as a ground motion input driving the energy harvester. These driving motions will be colored by the natural frequencies of the production string and limited by the damping in the system. Thus, it is important to understand how various inputs affect the natural frequencies and damping in the system. To this end, the analytical model developed using the spectral element method is used in a parametric study to characterize the dynamic behavior of

the production string. The inputs for the investigated cases are tabulated in Appendix D [178]. Only the first mode is investigated in each case as (1) the first mode often dominates the response of the system and (2) research indicates that three dimensional effects become non-trivial for higher order modes when employing a hydrodynamic function [142], [145]. In the outputs that follow, the conveyed fluid velocity and first natural frequency are nondimensionalized as

$$u = \left(\frac{M_i}{EI}\right)^{\frac{1}{2}} UL, \quad \Omega = \left(\frac{M_i+m}{EI}\right)^{\frac{1}{2}} \omega L^2. \tag{171}$$

3.6.1. Configuration

The assumed system configuration is shown in Figure 27 where elastic springs have been used as the boundary restraints. Changes in stiffness and mass due to the tubing connections are neglected for simplicity - while the analytical model can incorporate these connections, the simplified model is sufficient to illustrate the trends of interest. Since the final configuration of the structural housing is unknown, the structural housing is not included in the model.

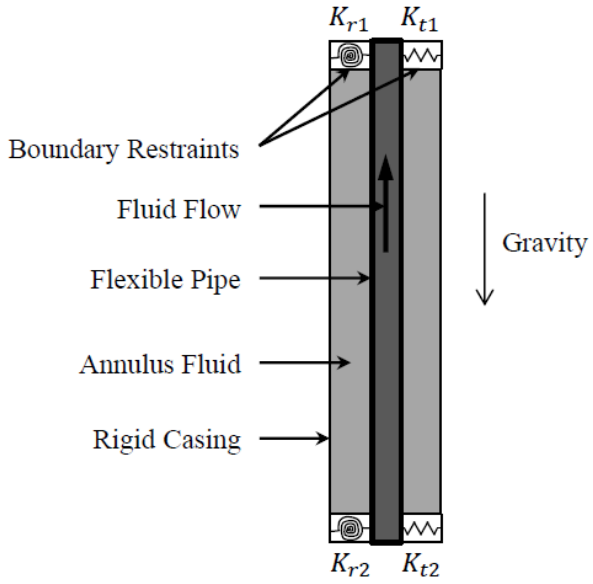

Figure 27. System Configuration

3.6.2. Fluid Boundary Conditions

The importance of the fluid boundary conditions have been illustrated by Kuiper et al. [179] and Païdoussis et al. [180], where it was shown that fluid boundary conditions may have a significant impact on the systems behavior. For the current study, the conveyed fluid at the inlet and outlet is assumed to be in a flow direction tangential to the deformed pipe, which is restrained from transverse displacements at the boundaries (i.e. the momentum of the fluid is assumed not to change at the boundaries – the fluid is imagined to be flowing into adjacent lengths of equally-pressurized pipe with slope continuity at the boundaries). While a larger multi-span model may provide a more realistic representation of the in-situ system, the added complexity distracts from the emphasis of the current findings, which are sufficiently conveyed with the simple model shown in Figure 27.

3.6.3. Practical Calculation of the Natural Frequency and Damping Ratio

By setting the determinant of the global dynamic stiffness matrix to zero

$$det\boldsymbol{S_g}(\omega) = 0, \tag{172}$$

the natural frequencies of the system can be determined; the frequencies are real for undamped systems and contain both real and imaginary parts for systems with damping. For undamped systems, the Mathematica root solver "FindRoot" is employed. For damped systems, the argument is taken to be complex

$$det\boldsymbol{S_g}(\omega_d + i\omega_i) = 0, \tag{173}$$

and a brute force method is used where ω_d (the damped frequency) and ω_i (corresponding to the rate of decay in the amplitude of vibration) are iterated until Eq. (173) is approximately satisfied.

For underdamped systems the relationship between ω_d, ω_i, ω_n, and ζ is generally known to be

$$\begin{aligned} \omega_d &= \sqrt{1-\zeta^2}\omega_n, \\ \omega_i &= \zeta\omega_n. \end{aligned} \tag{174}$$

Squaring and then adding both equations in Eq. (174) leads to

$$\omega_n = \sqrt{\omega_d^2 + \omega_i^2}, \tag{175}$$

which then allows the damping ratio to be calculated as

$$\zeta = \sqrt{1 - \left(\frac{\omega_d}{\omega_n}\right)^2} = \frac{\omega_i}{\omega_n}. \tag{176}$$

Alternatively, for specific cases the damping ratio can be estimated via the hydrodynamic function. For the cases used in the parametric study, where the translational displacement at the beam boundaries are restricted (i.e. $w(0) = w(L) = 0$ or alternatively $K_{t1} = K_{t2} = \infty$), the Coriolis force does no work [169], [181]. In such cases, and when the viscous damping term (c) is taken to be zero, damping arises solely from the hydrodynamic function. Once the natural frequency (ω_n) is calculated (i.e. Eq. (175)) the systems damping ratio can be found as [131]

$$\zeta = \frac{c_v}{c_{cr}}, \tag{177}$$

where at the natural frequency

$$\begin{aligned} c_v &= -\rho_e \pi d^2 \omega_n \Gamma_i, \\ c_{cr} &= 2(\Gamma_r \rho_e \pi d^2 + m + M_i)\omega_n, \end{aligned} \tag{178}$$

leading to

$$\zeta = \frac{-\rho_e \pi d^2 \Gamma_i}{2(\Gamma_r \rho_e \pi d^2 + m + M_i)}, \tag{179}$$

where ω_n is taken as the hydrodynamic function's argument.

Lastly, consider the scenario in which the argument of Eq. (173) is taken to be wholly real. The equality of Eq. (173) cannot be satisfied as only trivial values of the argument can drive both the real and imaginary output to zero, that is

$$det\boldsymbol{S_g}(\omega_{real}) = A + iB \neq 0, \tag{180}$$

where A and B are some constants. However, a wholly real frequency can be found that drives the real part of the determinant (i.e. A) to zero

$$\mathrm{Re}[det\boldsymbol{S_g}(\omega_{real})] = 0. \tag{181}$$

If ω_{real} is taken to be an approximation of the natural frequency ($\omega_{n.a}$), Eq. (179) can be used to find an approximation for the damping ratio (again assuming that damping arises solely from the hydrodynamic function).

To compare these various methods, three damped cases (i, ii, iii) are investigated. The inputs for each case are shown in Appendix E. For each case, the conveyed fluid velocity is incrementally increased up to the bifurcation velocity (i.e. $\zeta = 1$); the frequencies and damping ratios are recorded at each step. The results are plotted in Figure 28 through Figure 30.

Figure 28 plots the natural frequencies (based on ω_n found from Eq. (175) and $\omega_{n.a}$ found from Eq. (181)) versus the conveyed fluid velocity. Figure 29 plots three estimates of the damping ratio versus conveyed fluid velocity: (a) Eq. (176) utilizing ω_n, (b) Eq. (179) utilizing

ω_n, and (c) Eq. (179) utilizing $\omega_{n.a}$. Figure 30 plots discrete frequency-damping ratio pairs: (a) Eq. (176) utilizing ω_n, (b) Eq. (179) utilizing ω_n, and (c) Eq. (179) utilizing $\omega_{n.a}$. For reference, also included in Figure 30 are continuous lines generated by plotting Eq. (179) for arbitrary frequency values.

As the various methods are in general agreement, the third method (i.e. (c) Eq. (179) utilizing $\omega_{n.a}$) will be used in the parametric study. This method is selected as it requires the least computational effort as only one frequency variable needs to be solved.

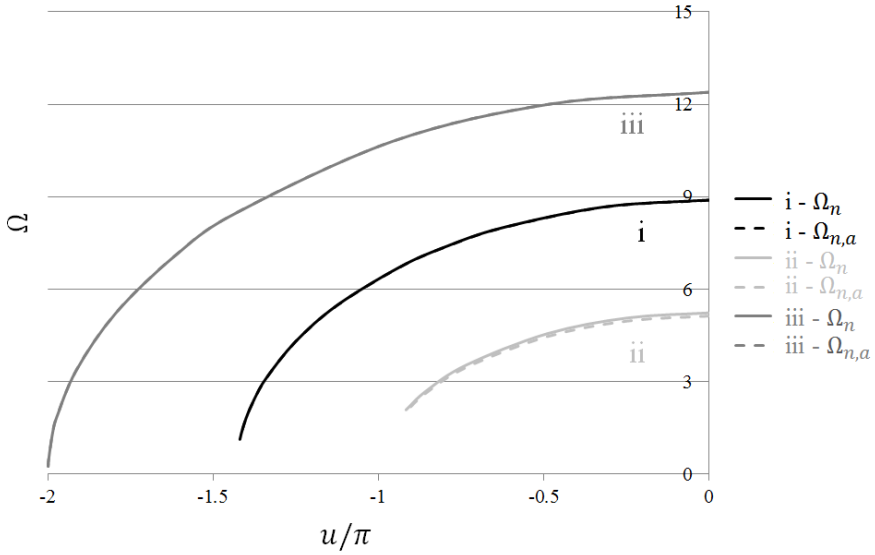

Figure 28. Fluid Velocity vs. Natural Frequency

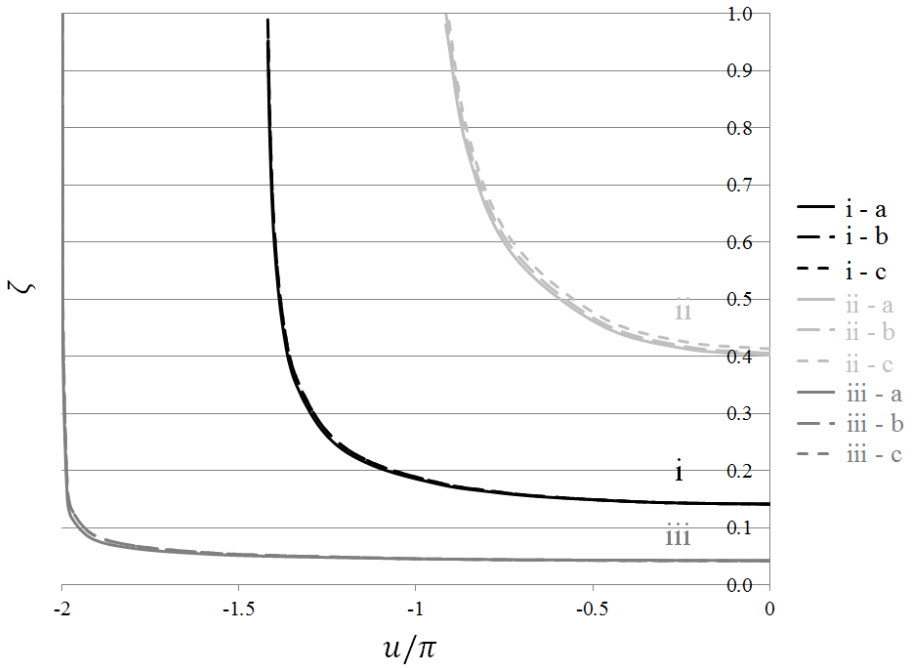

Figure 29. Fluid Velocity vs. Damping Ratio
(a) Eq. (176) utilizing ω_n, (b) Eq. (179) utilizing ω_n, and (c) Eq. (179) utilizing $\omega_{n.a}$

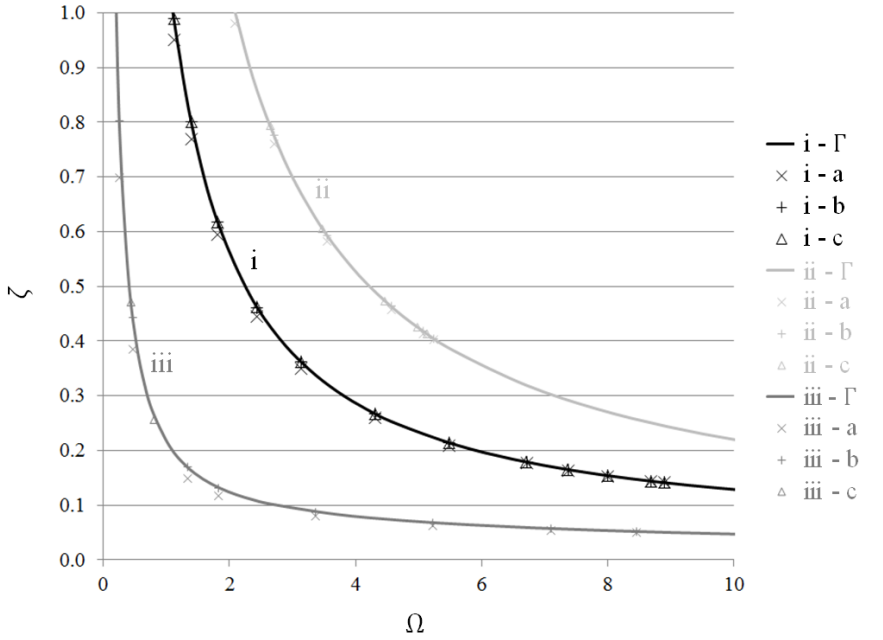

Figure 30. Natural Frequency vs. Damping Ratio
(a) Eq. (176) utilizing ω_n, (b) Eq. (179) utilizing ω_n, and (c) Eq. (179) utilizing $\omega_{n.a}$

3.6.4. Conveyed Fluid Velocity

Using the inputs from cases 1 and 2 (see Appendix D), the natural frequencies of a fixed-fixed and a pinned-pinned system (vibrating in a vacuum) are calculated as the conveyed fluid velocity is incrementally increased. The results are presented in Figure 31 and represent the baseline cases.

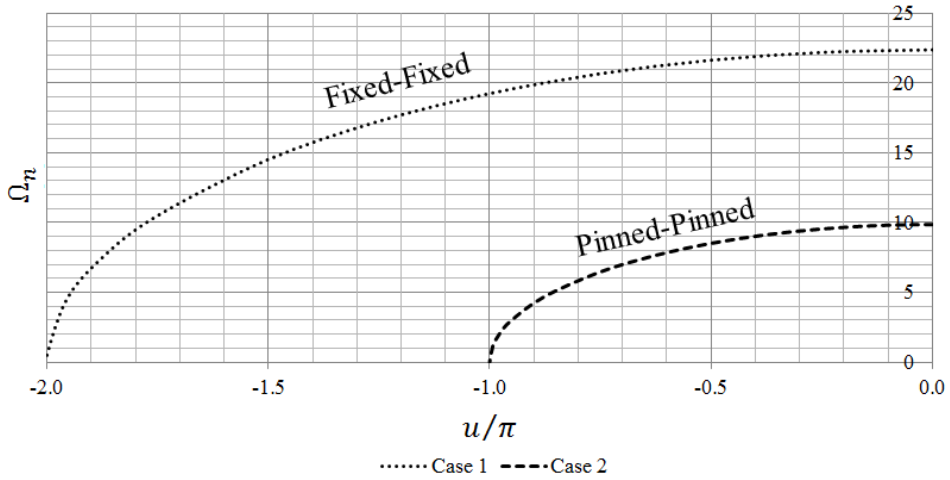

Figure 31. Conveyed Fluid Velocity: Flow Velocity vs. Natural Frequency [178]

The natural frequency is seen to decrease as the fluid velocity increases. This is due to an increasing compression in the system stemming from the centrifugal force generated by the conveyed fluid. Upon revisiting Eq. (135), specifically the second and third terms, the applied axial force is seen to be proportional to the conveyed fluid velocity squared ($\bar{T} \sim M_i U^2$): as the fluid velocity increases, the compression in the system increases. As the compression in the system approaches the Euler buckling load, the natural frequency approachs zero until, finally, divergence instability is reached at the critical fluid velocity (u_{cr}). For both cases, the nondimensional natural frequencies for zero fluid flow (22.37, 9.87) and critical flow velocity (-2π, $-\pi$) match published data [130], [169].

3.6.5. Axial Force

Cases 3 through 6 include external axial loads applied to the baseline systems ($150kN$ tension and $250kN$ compression) to investigate the effects of axial force. The systems first natural frequencies are plotted as a function of conveyed fluid velocity for cases 1 through 6 in Figure 32.

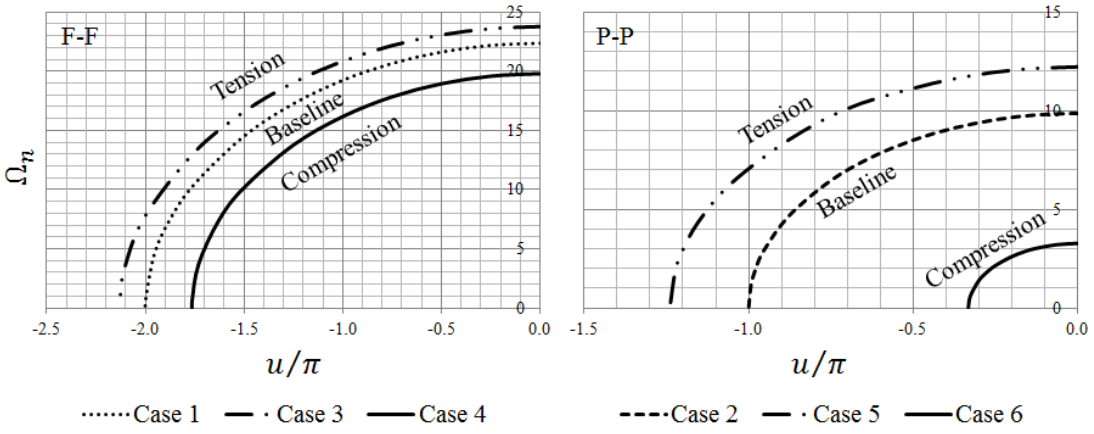

Figure 32. Axial Force Effects: Fixed-Fixed (Left) and Pinned-Pinned (Right) Boundaries [178]

The frequency offset at zero fluid flow is analogous to a beam under an applied tension or compression: the natural frequency of the beam will shift according to the applied axial load. For instance, consider the effect of the applied compression in case 4. Per Bolotin (1974) [182], the applied compressive force reduces the real part of the natural frequency as

$$\Omega_c = \Omega_n\sqrt{1 + \bar{T}/P_{Euler}}, \tag{182}$$

where P_{Euler} is the Euler buckling load of the pipe and $\Omega_n$for the unloaded case (i.e. case 1) was previously found to be 22.37. For the given inputs, the Euler buckling load can be calculated as $1123.9kN$, leading to a predicted natural frequency of $\Omega_c = 19.73$ which agrees well with the spectral element result of 19.80 (error = 0.3%).

The shift in the critical fluid velocity can also be calculated a priori. At the onset of the divergence instability, the applied compression in the system is limited to P_{Euler}. The critical fluid velocity can then be calculated from

$$M_i U_{cr}^2 = P_{Euler} + \bar{T}, \tag{183}$$

where for case 4 inputs the analytical calculation results in $U_{cr-case\,4} = -351.6 m/s$, or in non-dimensional form $u_{cr-case\,4} = -5.54$. These results (and the results from the three other axially loaded cases) agree well with the results produced by the spectral element model shown in Figure 32.

3.6.6. Annulus Fluid Density

The annulus fluid density manifests itself in the equation of motion as a multiplier of—but does not play a direct role in defining—the hydrodynamic function. It is, however, used to define the hydrodynamic force (see Eq. (48)). The annulus density could then be thought of as a sort of scaling factor applied to the effects of the hydrodynamic function where for $\rho_e = 0$ the hydrodynamic function plays no role while for $\rho_e \neq 0$ hydrodynamic effects will be included.

The zero flow case (i.e. $U = 0$) provides a useful realization in inviscid systems: the effects of the annulus fluid density can be directly observed through the added mass contributed by the hydrodynamic function. For inviscid systems, the hydrodynamic function is wholly real. Regrouping this inviscid hydrodynamic term within the equation of motion (i.e. Eq. (140)) leads to

$$\begin{gathered} EI\widehat{W}'''' + \{M_i U^2 - \bar{T} + \bar{p}A_i(1-2\nu\delta)\}\widehat{W}'' + \{2i\omega M_i U + (M_i + m)g\}\widehat{W}' + \\ \{i\omega c - (M_i + m + \rho_e \pi d^2 \Gamma_r)\omega^2\}\widehat{W} = 0. \end{gathered} \tag{184}$$

where the added mass term (i.e. $\rho_e \pi d^2 \Gamma_r$) becomes apparent. For case 1, where $\rho_e = 0$, the natural frequency of the system can be calculated as $\Omega_n = 22.37$ ($\omega_n = 67.18\, rad/s$). Note that the system mass includes both the conveyed fluid and pipe mass and can be written as

$M_i + m = 49.34\,kg/m$ (i.e. there is no added mass). The stiffness of case 1 (and in fact cases 7 and 8) can then be calculated as $K = \omega_n^2(M_i + m) = 222700\ kg/ms^2$. By selecting various fluid densities and hydrodynamic functions, the shift in natural frequency due to the added mass ($\rho_e \pi d^2 \Gamma_r$) can be analytically calculated as

$$\omega_n = \left(\frac{K}{M_i+m+\rho_e\pi d^2\Gamma_r}\right)^{\frac{1}{2}}, \quad \Omega_n = \left(\frac{K(M_i+m)}{EI(M_i+m+\rho_e\pi d^2\Gamma_r)}\right)^{\frac{1}{2}} L^2, \tag{185}$$

and compared with the spectral element output. Table 19 shows excellent agreement between the simplified method presented here and the spectral element estimates of the natural frequencies.

Table 19. The Role of Annulus Fluid Density [178]

Case	Γ_r	ρ_e (kg/m^3)	Added Mass, $\rho_e\pi d^2\Gamma_r$ (kg/m)	Total Mass (kg/m)	Natural Frequency, Ω_n		
					Analytical**	Spectral Element	Error
Fixed-Fixed Boundaries							
1*	1	0	0.00	49.34	22.37	22.37	0%
7	1	2000	26.55	75.89	18.04	18.04	0%
8	2	600	15.93	65.27	19.45	19.45	0%
Pinned-Pinned Boundaries							
2*	1	0	0.00	49.34	9.87	9.87	0%
9	3	1200	47.78	97.12	7.03	7.03	0%
10	2	600	15.93	65.27	8.58	8.58	0%

**Baseline case*

**$K_{fixed-fixed} = 222700\,kg/ms^2$; $K_{pinned-pinned} = 43300\,kg/ms^2$

3.6.7. Annulus Viscosity and Geometry

The annulus kinematic fluid viscosity (v) and annulus geometry (D, d) act to shape the hydrodynamic function in a complicated way (recall Eq. (48)). Rather than trying to understand the complex link between these three variables and the system response (i.e. natural frequency and damping ratio), it is easier to first examine the relationship between these variables and the hydrodynamic function and later observe how the hydrodynamic function affects the system response.

3.6.7.1. The Hydrodynamic Function

The hydrodynamic functions for different combinations of viscosity and geometry (see Table 20) are plotted in Figure 33 where ω is taken as purely real (the plotted frequency is not normalized as the hydrodynamic function is not a function of $E, I, L,$ etc.). Recall that the real part of the hydrodynamic function generates an added mass in the system while the imaginary part generates a viscous drag. For the range of inputs considered, the real part of the hydrodynamic function is dominated by effects stemming from the annulus geometry (i.e. the D/d ratio) while changes in the annulus viscosity result in only a small offset. In general:

- $Re[\Gamma]$ and $|Im[\Gamma]|$ decrease with an increasing D/d ratio.
- $Re[\Gamma]$ and $|Im[\Gamma]|$ increase with increasing viscosity, υ.

Table 20. Hydrodynamic Function Matrix [178]

		D/d	
		1.1	1.3
$\upsilon\left(\frac{m^2}{s}\right)$	$5e-5$	H1	H2
	$1e-5$	L1	L2

$d = 0.065m$

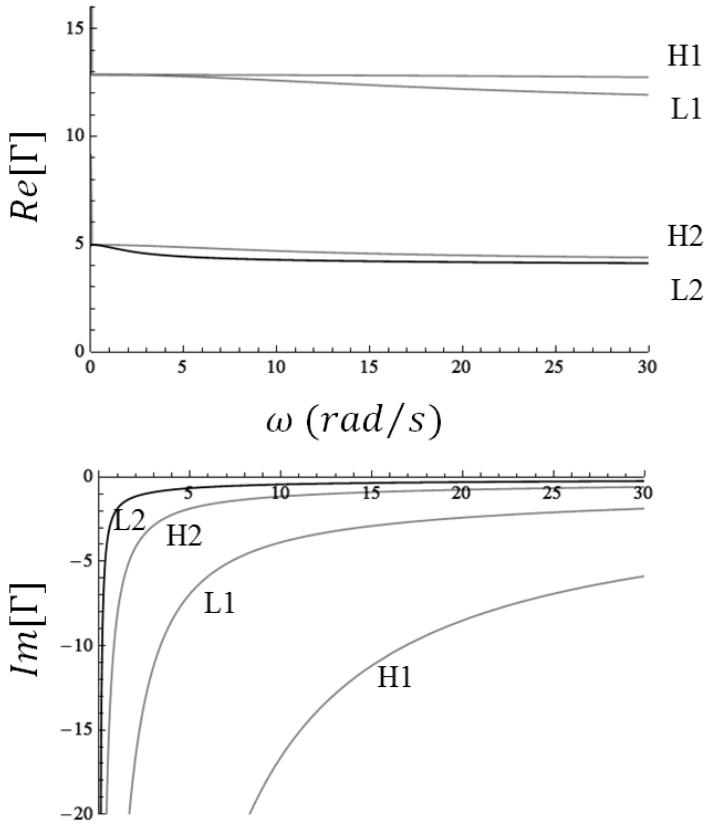

Figure 33. Hydrodynamic Functions: Real (Top) and Imaginary (Bottom) Parts [178]

3.6.7.2. Inviscid Systems

Taking $\upsilon = 0$ results in an inviscid system and a purely real hydrodynamic function with the reduced form [131]

$$\Gamma_{inviscid} = \frac{1+(d/D)^2}{1-(d/D)^2}. \tag{186}$$

To illustrate the effect of added mass, cases 11 through 14 are investigated with the spectral element results plotted in Figure 34. As was done in the previous section, the shifts in natural frequency for zero flow velocity can be predicted analytically and compared to the spectral element results. This is done in Table 21 with the results exhibiting excellent agreement between the two methods.

In each case, the inclusion of added mass does not change the critical flow velocity as divergence is a static phenomenon and is not dependent on inertial effects. This is illustrated in Figure 34 which shows the investigated cases converging to their respective critical flow velocities (-2π and $-\pi$, respectively).

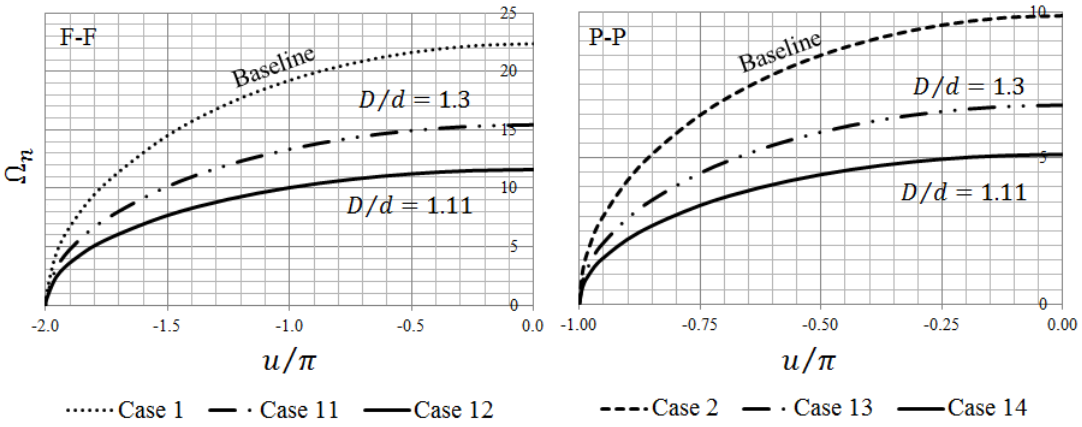

Figure 34. Inviscid Systems: Fixed-Fixed (Left) and Pinned-Pinned (Right) Boundaries [178]

Table 21. Added Mass Effects with Zero Flow [178]

Case	Γ_r	ρ_e (kg/m^3)	Added Mass, $\rho_e \pi d^2 \Gamma_r$ (kg/m)	Total Mass (kg/m)	Natural Frequency, Ω_n		
					Analytical**	Spectral Element	Error
Fixed-Fixed Boundaries							
1*	1	0	0.00	49.34	22.37	22.37	0%
11	3.90	1050	54.33	103.67	15.44	15.44	0%
12	9.62	1050	134.03	183.37	11.61	11.61	0%
Pinned-Pinned Boundaries							
2*	1	0	0.00	49.34	9.87	9.87	0%
13	3.90	1050	54.33	103.67	6.81	6.81	0%
14	9.62	1050	134.03	183.37	5.12	5.12	0%

**Baseline case*

**$K_{fixed-fixed} = 222700\, kg/ms^2$; $K_{pinned-pinned} = 43300\, kg/ms^2$

3.6.7.3. Viscous Systems

Six viscous cases (cases 15 through 20) are analyzed to observe how the full hydrodynamic function effects the system (i.e. $v \neq 0$). The resulting fluid velocity vs. damped frequency curves are shown in Figure 35; the benchmark cases are also included for reference.

The damping ratios, as a function of fluid velocity, are plotted in Figure 36 for each viscous case.

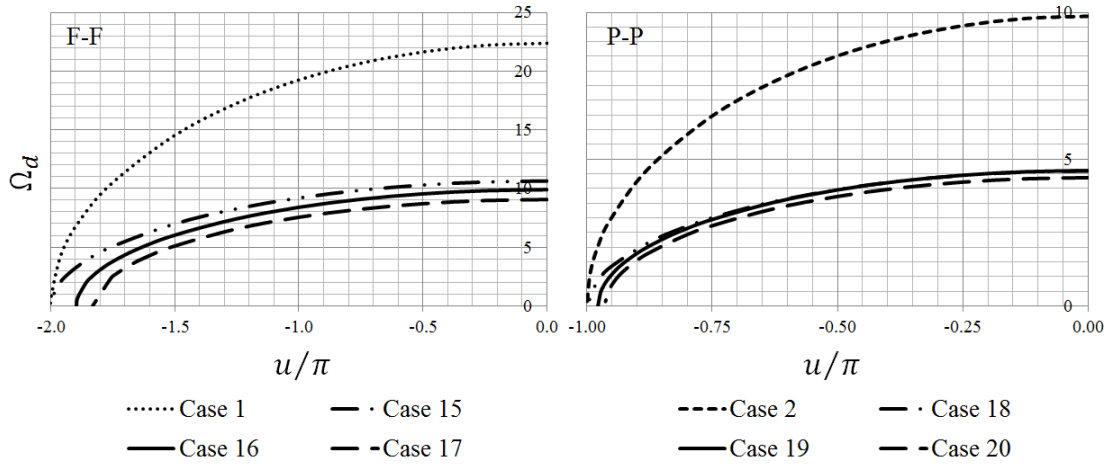

Figure 35. Viscous Systems: Fixed-Fixed (Left) and Pinned-Pinned (Right) Boundaries

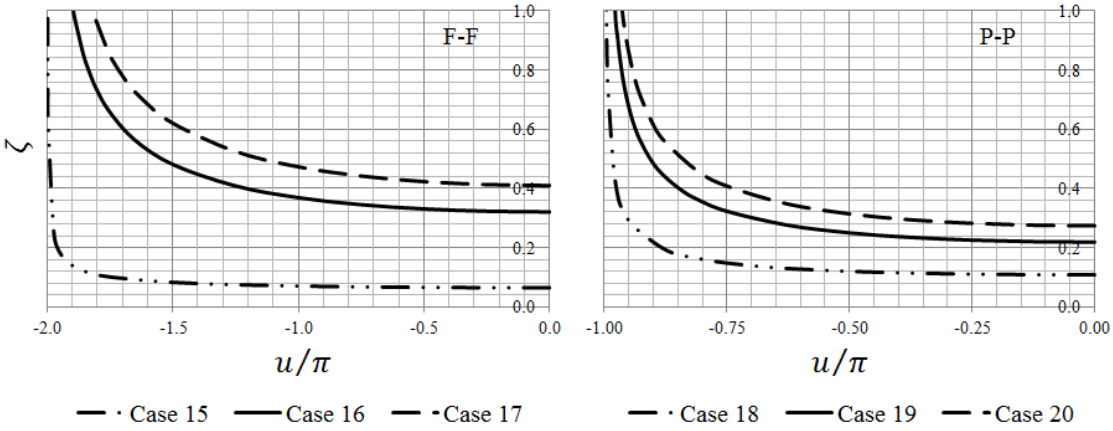

Figure 36. Viscous Systems: Fixed-Fixed (Left) and Pinned-Pinned (Right) Boundaries

Comparing Figure 35 and Figure 36, bifurcation is seen to occur in each viscous case when the damped frequency reaches zero. Once bifurcation is reached, the system behaves in an overdamped manner (i.e. $\zeta > 1$ as shown in Figure 36). The bifurcation velocity of each case differs due to the different levels of viscous drag in each case (as represented by the damping ratio in Figure 36). If the conveyed fluid velocity is incrementally increased past the

bifurcation velocity, eventually the system will diverge ($Re[\Omega] = Im[\Omega] = 0$); the system becomes unstable once divergence is reached.

Unlike the inviscid systems, the vertical shift in the real part of the natural frequency is now attributable to both added mass (stemming from $Re[\Gamma]$) and viscous drag (stemming from $Im[\Gamma]$). This difference can be illustrated by comparing cases 15 and 16. The added mass functions for these two cases are shown in Figure 37. The added mass in case 15 is seen to be larger than the added mass for case 16 which, if no other hydrodynamic effect existed, would have resulted in $\Omega_{d-case\ 15} < \Omega_{d-case\ 16}$. However, since the viscous drag associated with case 16 is much larger than that of case 15 (see Figure 36), the combined effect of the viscous annulus fluid is $\Omega_{d-case\ 15} > \Omega_{d-case\ 16}$, as seen in Figure 35.

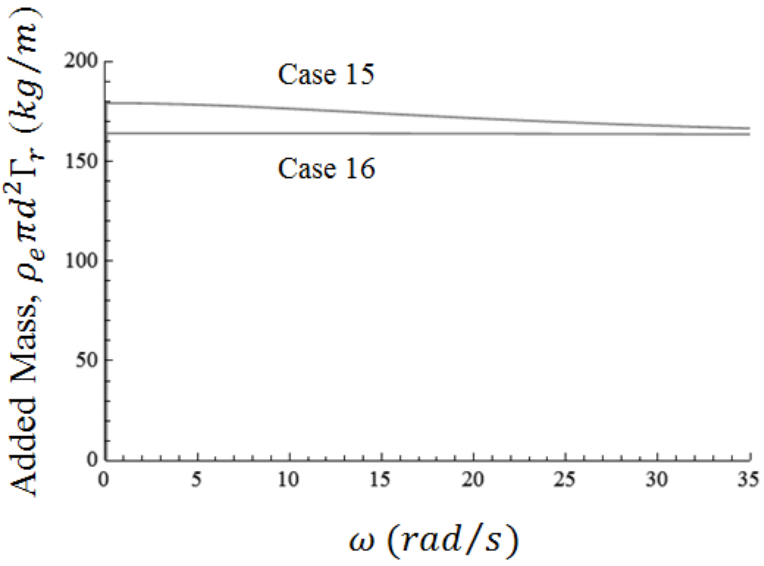

Figure 37. Added Mass

Lastly, compare the damping ratios of cases 15 and 18 for zero fluid flow: $\zeta_{case\ 15} = 0.065 < \zeta_{case\ 18} = 0.108$. Noting that the only difference in inputs between these two cases is the stiffness of the rotational boundary springs (case 15 models a fixed-fixed system while case

18 models a pinned-pinned system) the damping in each system is seen to be boundary condition dependent, or more specifically, frequency-dependent.

3.6.8. Frequency-Dependent Damping

In this section, after illustrating the damping ratios frequency-dependence through the hydrodynamic function, the conveyed fluid velocity is used as a parametric variable to demonstrate how changing a system's stiffness (and therefore its natural frequency) impacts the damping ratio. An illustrative example is included.

3.6.8.1. The Role of the Hydrodynamic Function

The damping ratios dependence on frequency is shown in Figure 38, where Eq. (179) and the relevant inputs from Appendix D have been used. It is apparent that the damping ratio is frequency dependent through the hydrodynamic function with systems operating at a higher frequency (e.g. those with stiff rotational boundary springs) experiencing less damping. Noting the relatively constant nature of Γ_r over the range of interest shown (see Figure 39), the change in damping is primarily attributed to the change in Γ_i where, as previously mentioned, Γ_i is known to contribute viscous drag to the system.

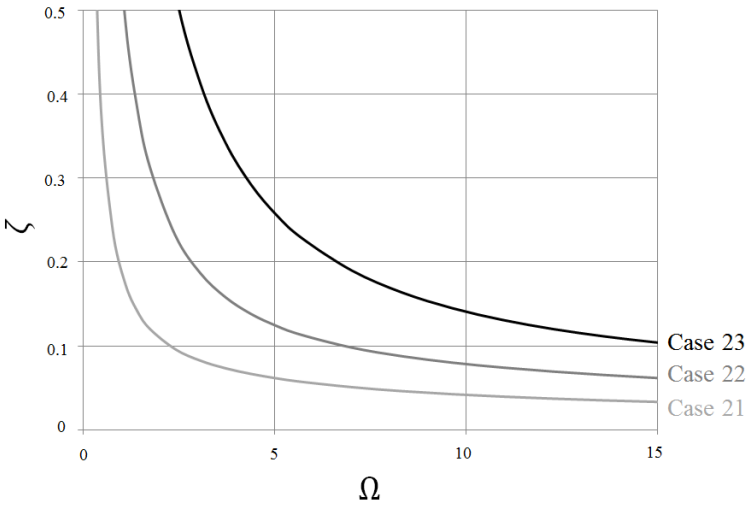

Figure 38. Damping Ratio per Eq. (179)

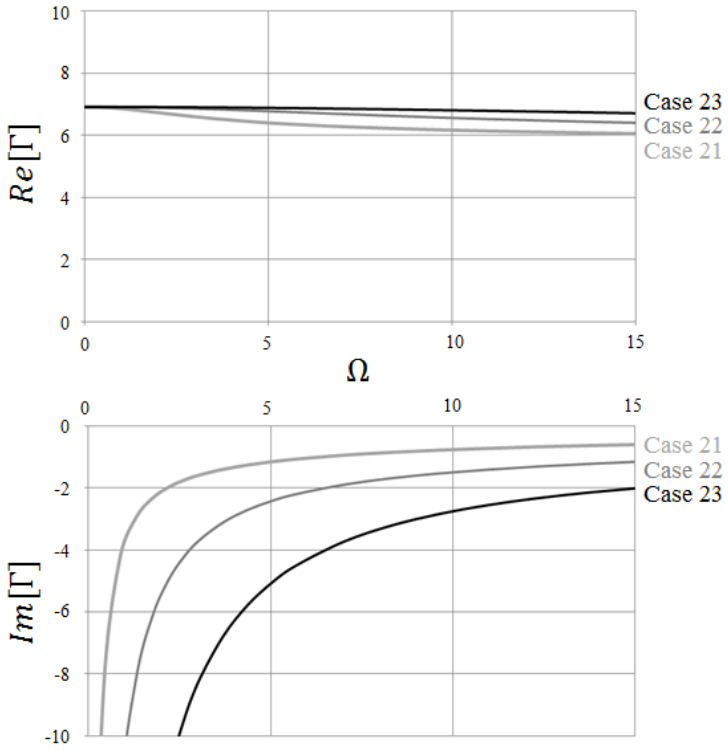

Figure 39. Hydrodynamic Functions: Real (Top) and Imaginary (Bottom) Parts

3.6.8.2. Damping for Zero Fluid Flow

Three different annulus fluid viscosities are investigated for the case of zero conveyed fluid velocity: low, moderate, and high viscosity fluids (cases 21, 22, and 23 respectively). For each system, the two rotational boundary springs are incrementally increased while the natural frequencies and damping ratios calculated. The results are three dimensional surfaces for each fluid viscosity relating the rotational boundary stiffness to the systems natural frequency and damping ratio. The three-dimensional surfaces for case 22 are shown in Figure 40 and Figure 41. Note that the four limiting boundary conditions (Pinned-Pinned, Fixed-Pinned, Pinned-Fixed, and Fixed-Fixed) are identified.

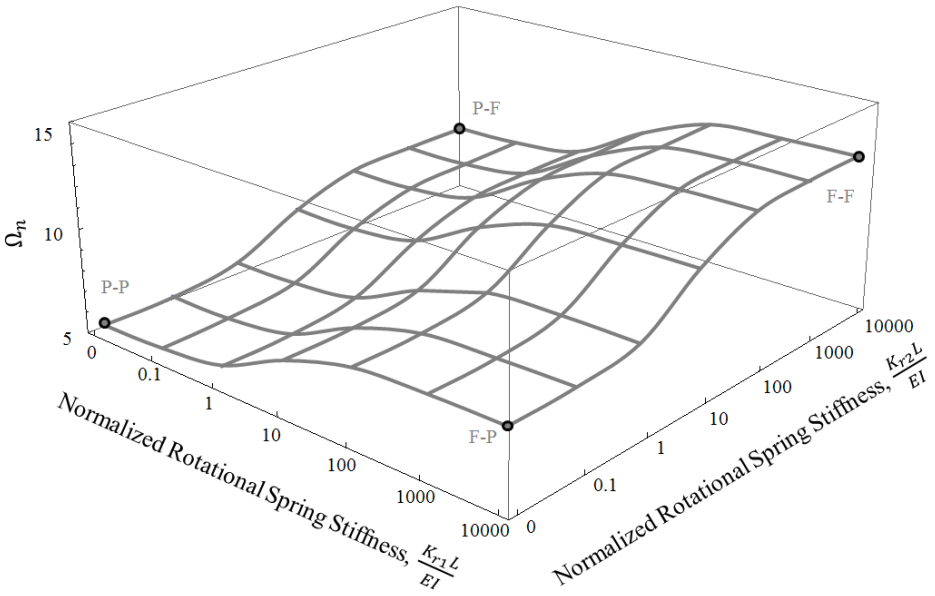

Figure 40. Rotational Spring Stiffness vs. Natural Frequency for Zero Fluid Velocity: Case 22

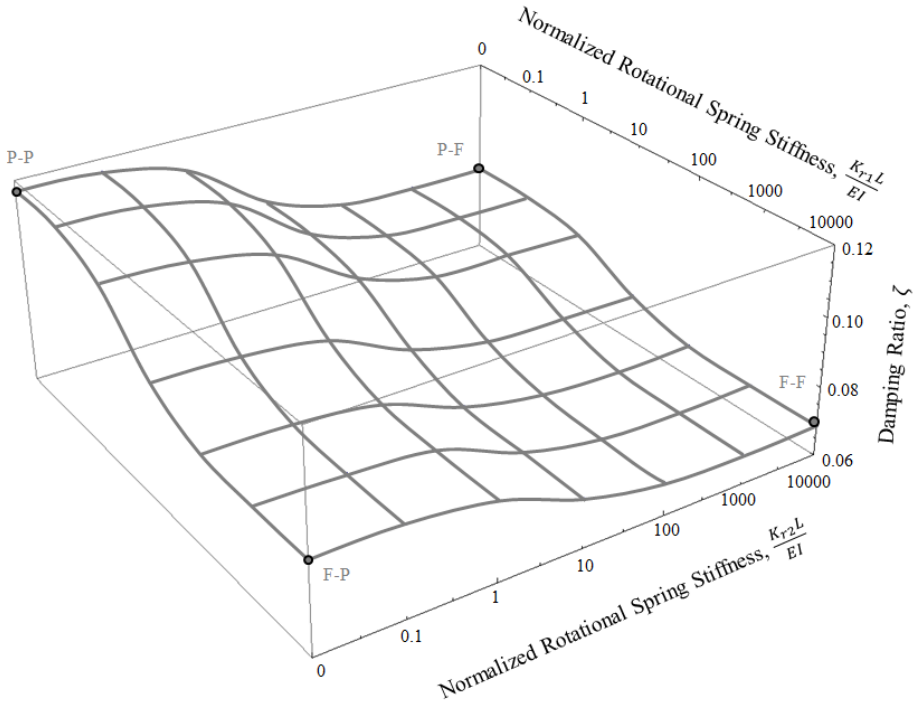

Figure 41. Rotational Spring Stiffness vs. Damping Ratio for Zero Fluid Velocity: Case 22

To better illustrate the behavior of the three cases, two dimensional plots are generated by taking three sections through each three dimensional surface. The results for all three

annulus fluid viscosities are presented in Figure 42 and Figure 43 where for the same fluid viscosity Figure 43 indicates stiffer systems result in lower damping ratios: $\zeta_{FF} < \zeta_{FP} = \zeta_{PF} < \zeta_{PP}$.

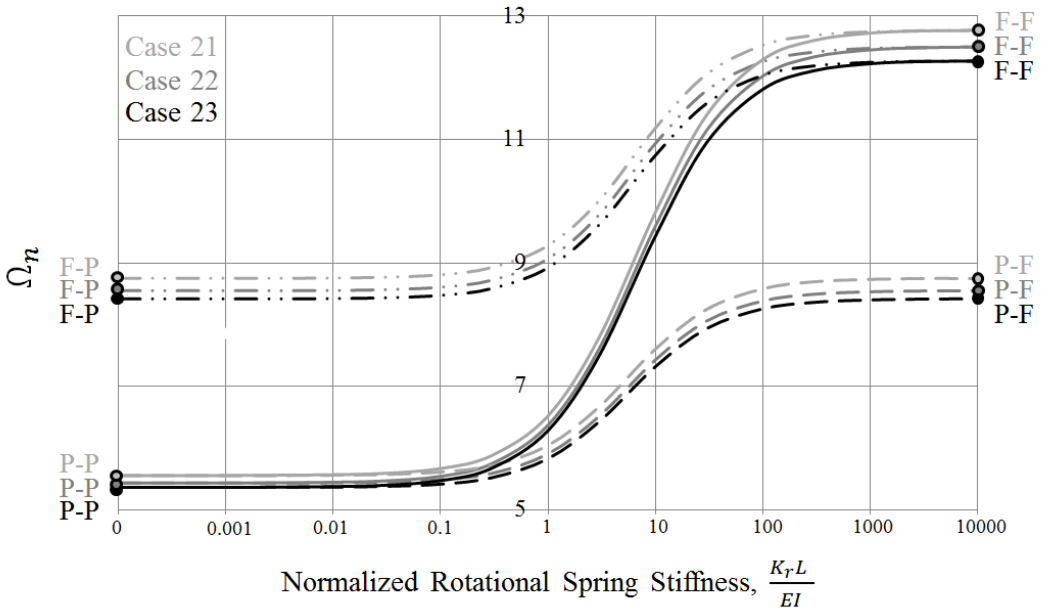

Figure 42. Rotational Spring Stiffness vs. Natural Frequency for Zero Fluid Velocity
——— , $K_{r_1} = K_{r_2} = K_r$; · — — — , $K_{r_1} = 0$ (Pinned) & $K_{r_2} = K_r$;
· — · · — , $K_{r_1} = 10000$ (Fixed) & $K_{r_2} = K_r$

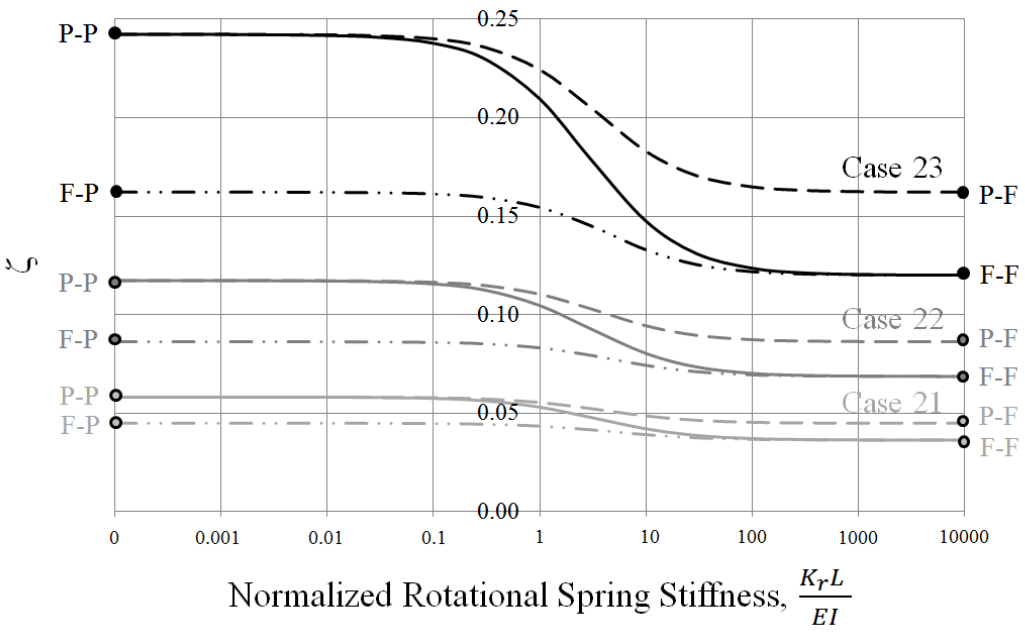

Figure 43. Rotational Spring Stiffness vs. Damping Ratio for Zero Fluid Velocity
——— , $K_{r1} = K_{r2} = K_r$; - - - - , $K_{r1} = 0$ (Pinned) & $K_{r2} = K_r$;
·—·— , $K_{r1} = 10000$ (Fixed) & $K_{r2} = K_r$

3.6.8.3. Damping for Non-Zero Fluid Flow

For non-zero fluid flow, the two-dimensional plots of Figure 42 and Figure 43 are expanded to include the conveyed fluid velocity as an additional variable. This results in new three-dimensional surfaces where the natural frequency and damping ratio are functions of both the stiffness of the rotational boundary springs and the conveyed fluid velocity. Figure 44 and Figure 45 plots two manifestations of these new surfaces for case 23. In Figure 44, the natural frequency is seen to decrease as the conveyed fluid velocity is increased. This behavior is explained by the induced compression stemming from the centrifugal force: as the fluid velocity increases, the induced compression increases resulting in a decreasing natural frequency. This decreasing natural frequency results in an increasing damping ratio due to the frequency-dependent nature of the hydrodynamic function (see Figure 38). This relationship is apparent in Figure 45 which shows the damping ratio increasing with increasing fluid velocity.

The damping ratio in Figure 45 is shown up to the systems bifurcation velocity after which the system no longer behaves in an underdamped manner (i.e. $\zeta > 1$ past the bifurcation velocity).

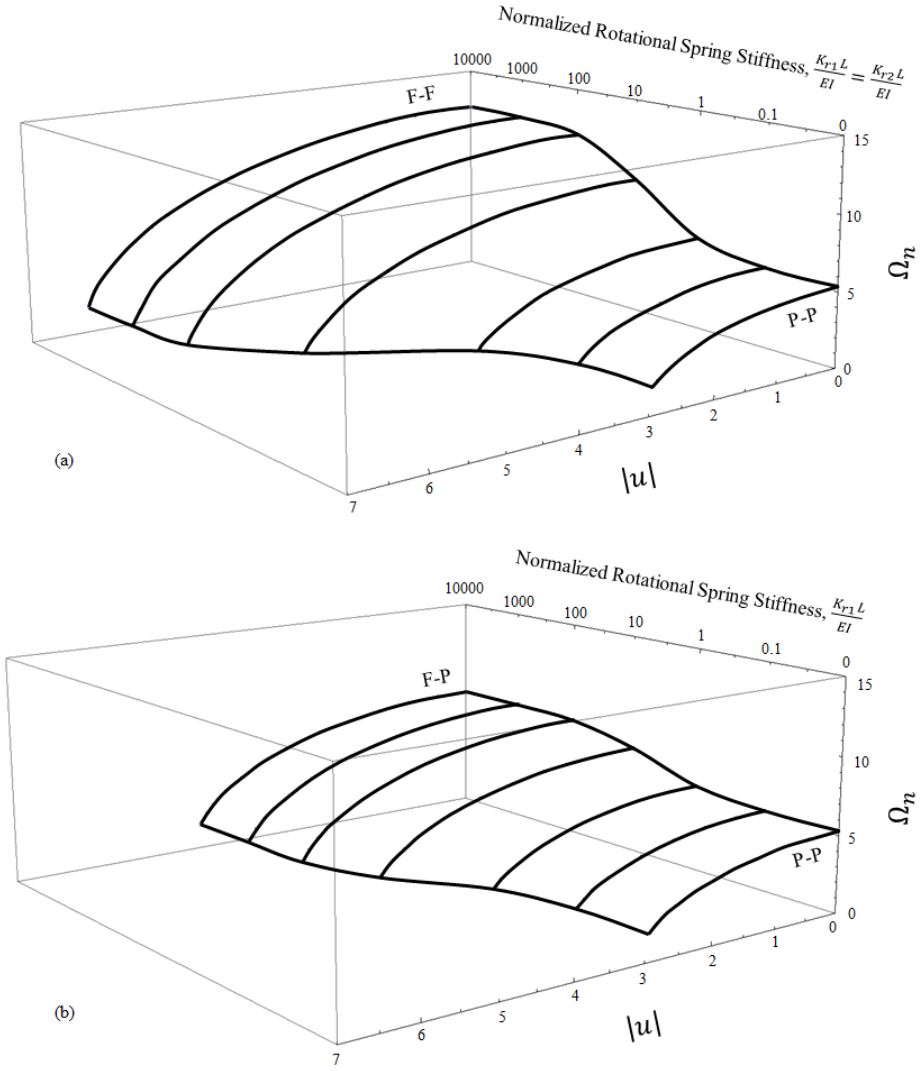

Figure 44. Fluid Velocity vs. Rotational Spring Stiffness vs. Natural Frequency – Case 23
(a) $K_{r1} = K_{r2} = K_r$; (b) $K_{r1} = K_r$ & $K_{r2} = 0$ (Pinned)

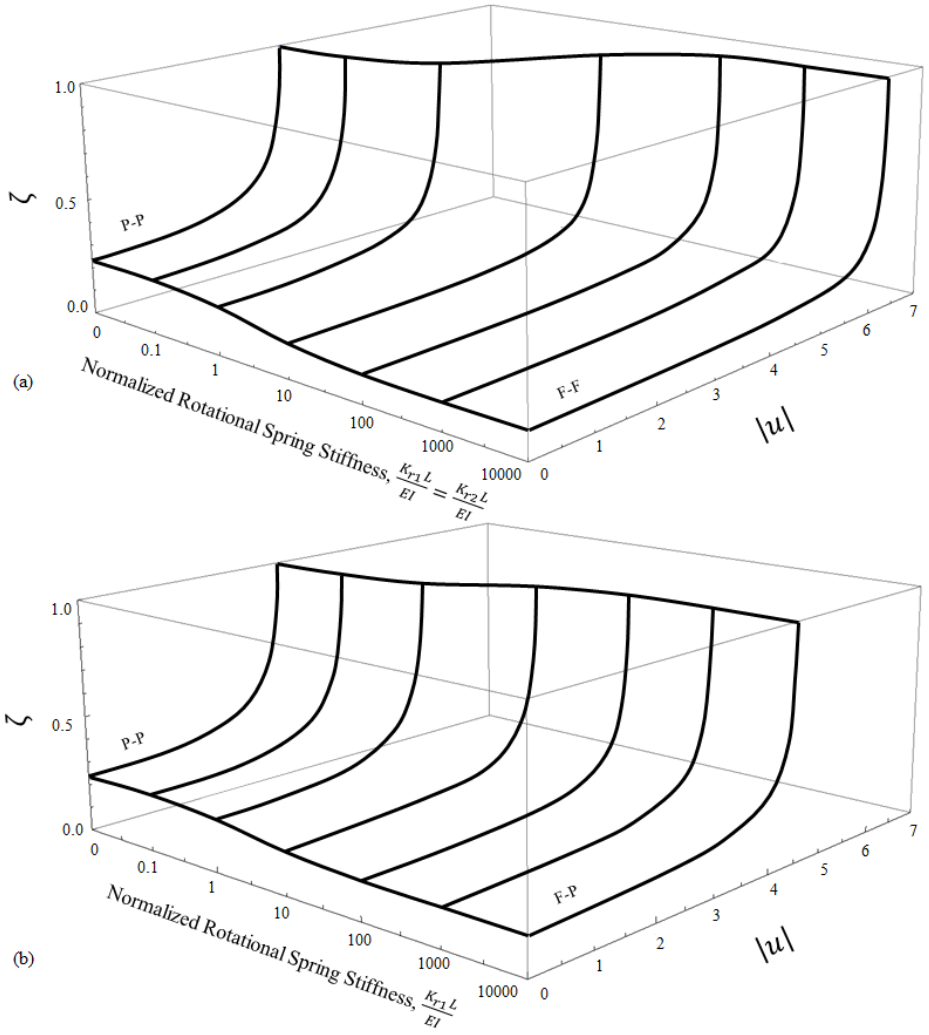

Figure 45. Fluid Velocity vs. Rotational Spring Stiffness vs. Damping Ratio – Case 23
(a) $K_{r1} = K_{r2} = K_r$; (b) $K_{r1} = K_r$ & $K_{r2} = 0$ (Pinned)

Since both the natural frequency and damping ratio are a function of the rotational stiffness of the boundary springs, Figure 44 and Figure 45 can be combined to directly relate the natural frequency, damping ratio, and conveyed fluid velocity. The resulting three-dimensional surfaces are shown in Figure 46 (note that some of the contours are nearly indistinguishable from each other). If the Figure 46 surfaces are collapsed onto the plane containing the natural frequency and damping ratio, the resulting two-dimensional projection is the same as that found in Figure 38.

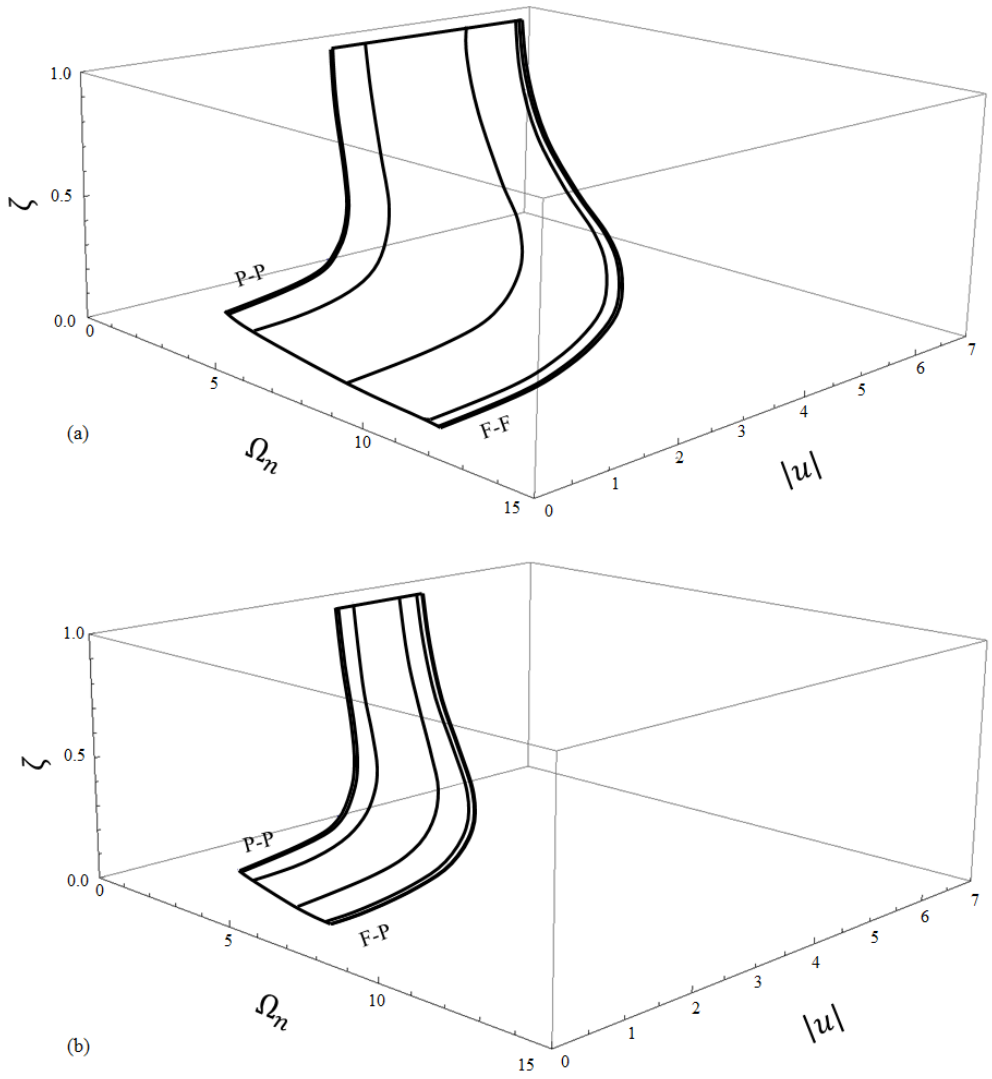

Figure 46. Fluid Velocity vs. Natural Frequency vs. Damping Ratio – Case 23
(a) $K_{r1} = K_{r2} = K_r$; (b) $K_{r1} = K_r$ & $K_{r2} = 0$ (Pinned)

Figure 47 shows the limiting cases of Figure 46 projected onto the plane containing the fluid velocity and damping ratio (cases 21 and 22 are also displayed). Several trends are noted:

- For the same boundary conditions and conveyed fluid velocity, higher viscosity systems have higher damping ratios.
- For the same annulus fluid viscosity and conveyed fluid velocity, systems with stiffer rotational boundary springs have lower damping ratios.

- For the same annulus fluid viscosity, the bifurcation velocity increases as the rotational boundary springs are stiffened.
- For the same boundary conditions, the bifurcation velocity decreases with increasing annulus fluid viscosity.
- As the fluid velocity increases, the rate at which the damping ratio changes increases.

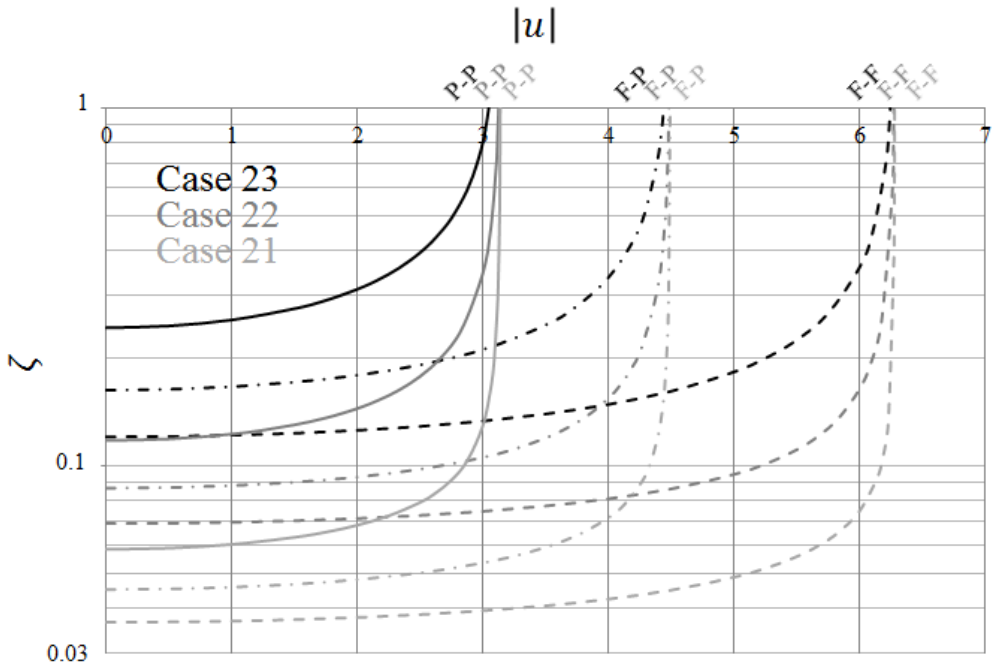

Figure 47. The Effect of Fluid Velocity on Damping for Three Limiting Cases

This last trend is further illustrated in Figure 48 where the percentage change in the damping ratios for the limiting cases are plotted; the damping ratios at $u = 0$ are taken as baseline values. Two additional trends are noted:

- For the same boundary conditions and conveyed fluid velocity, high-viscosity systems see a greater percentage change in damping ratio compared to their low viscosity counterparts.

- For the same annulus fluid viscosity and conveyed fluid velocity, systems with stiffer rotational boundary springs see a lower percentage change in damping ratio compared to systems with softer rotational springs.

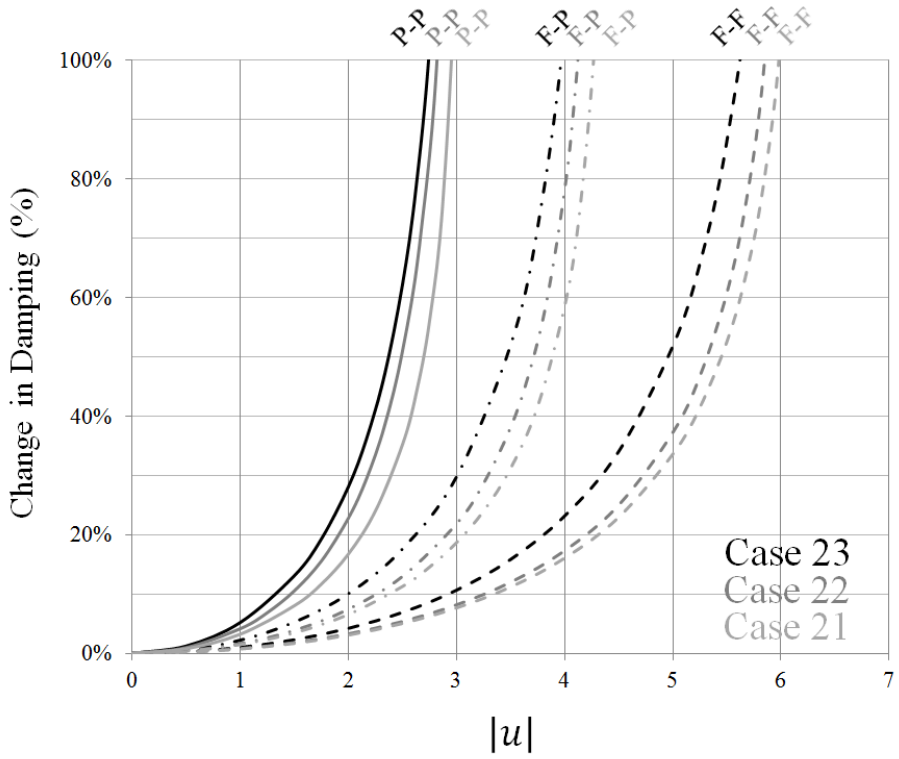

Figure 48. Change in Damping Ratio with Baseline at $u = 0$

3.6.8.4. An Illustrative Example

These results are especially relevant when there is uncertainty in the characterization of a system. Should the produced fluid velocity be greater than originally estimated or if the rotational stiffness of the boundary springs are initially over-predicted, Figure 47 has shown that the actual damping ratio will be higher than originally predicted. Additionally, Figure 48 has shown that such an error in estimating the damping ratio is exacerbated as the error in either the viscosity or fluid velocity increases.

As a numeric example assume a preliminary investigation of a system indicates a moderate viscosity annulus fluid (case 22), a normalized fluid velocity of one, rotational boundary springs with normalized stiffness of nine and other inputs as listed in Appendix D. The damping ratio for this system (case A) is calculated as 0.082 and is shown on the three dimensional domain of Figure 49.

If the system is actually operated at a normalized fluid velocity of two (case B; $\zeta = 0.086$) or has a normalized rotational stiffness of one (case C; $\zeta = 0.108$), the resulting error in estimating the damping ratio would be 4% and 31%, respectively. If the initial estimate of both the fluid velocity and spring stiffness's were in error (case D; $\zeta = 0.119$), the error jumps to 45%. The three dimensional surface of Figure 49 is compressed into a two dimensional plot in Figure 50 to more clearly illustrate the difference in the resulting damping ratios.

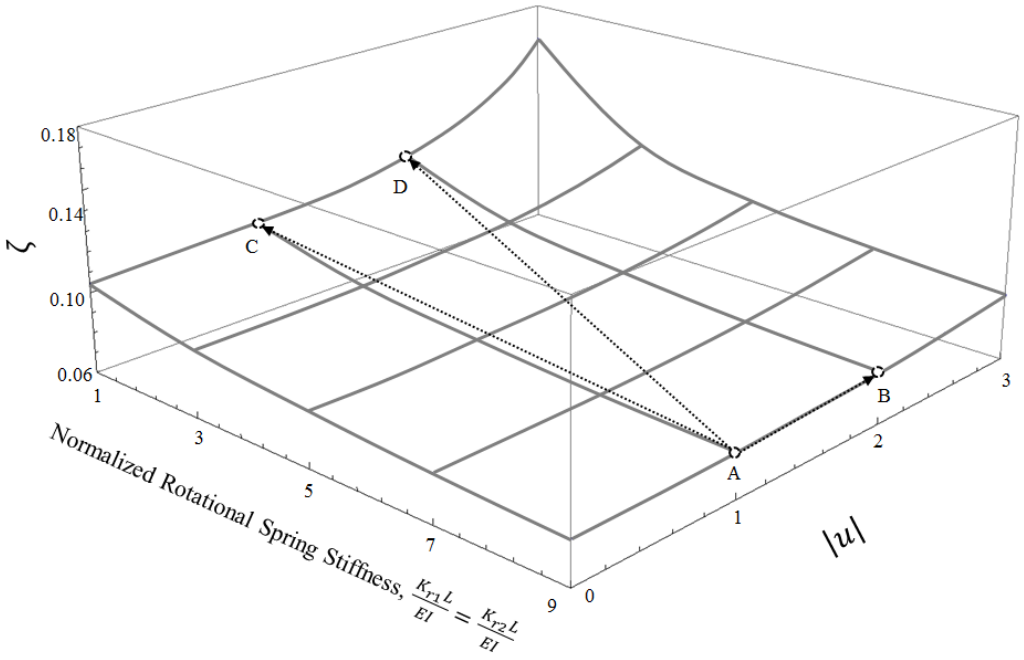

Figure 49. Damping Estimates: Potential Errors Stemming from Conveyed Fluid Velocity and/or Spring Stiffness's (3D)

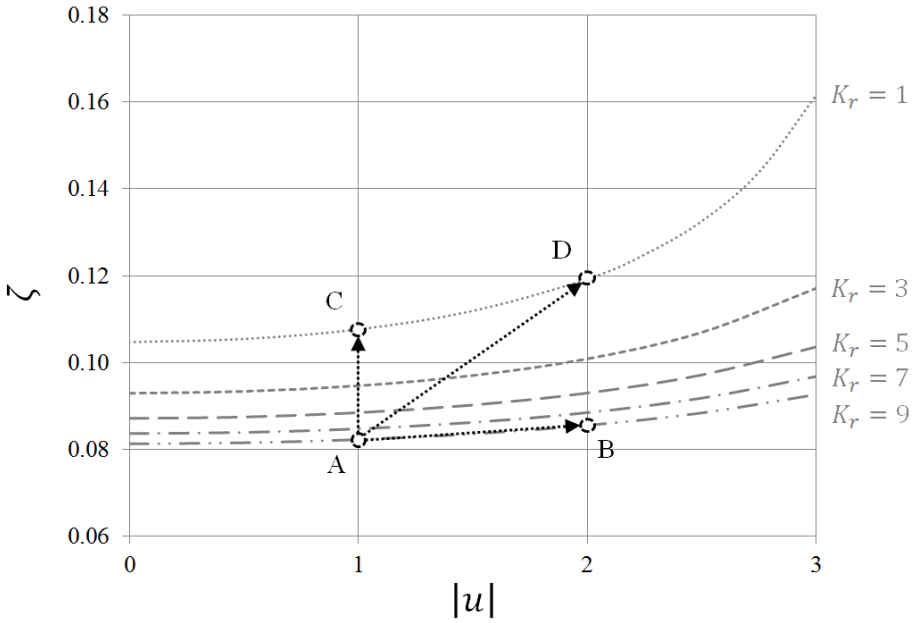

Figure 50. Damping Estimates: Potential Errors Stemming from Conveyed Fluid Velocity and/or Spring Stiffness's (2D)

If the annulus fluid viscosity is initially underestimated (i.e. case 22 was assumed in design but case 24 better represented the in-situ conditions), additional errors ensue. Figure 51 and Figure 52 depict the damping ratios in the new systems (A'-D') for an error in the annulus fluid viscosity (case A'; $\zeta = 0.099$); annulus fluid viscosity and conveyed fluid velocity (case B'; $\zeta = 0.104$); annulus fluid viscosity and rotational spring stiffness's (case C'; $\zeta = 0.134$); and annulus fluid viscosity, conveyed fluid velocity, and rotational spring stiffness's (case D'; $\zeta = 0.150$). The resulting errors (when compared to the baseline case A) are tabulated in Table 22 and in most cases are shown to be non-trivial.

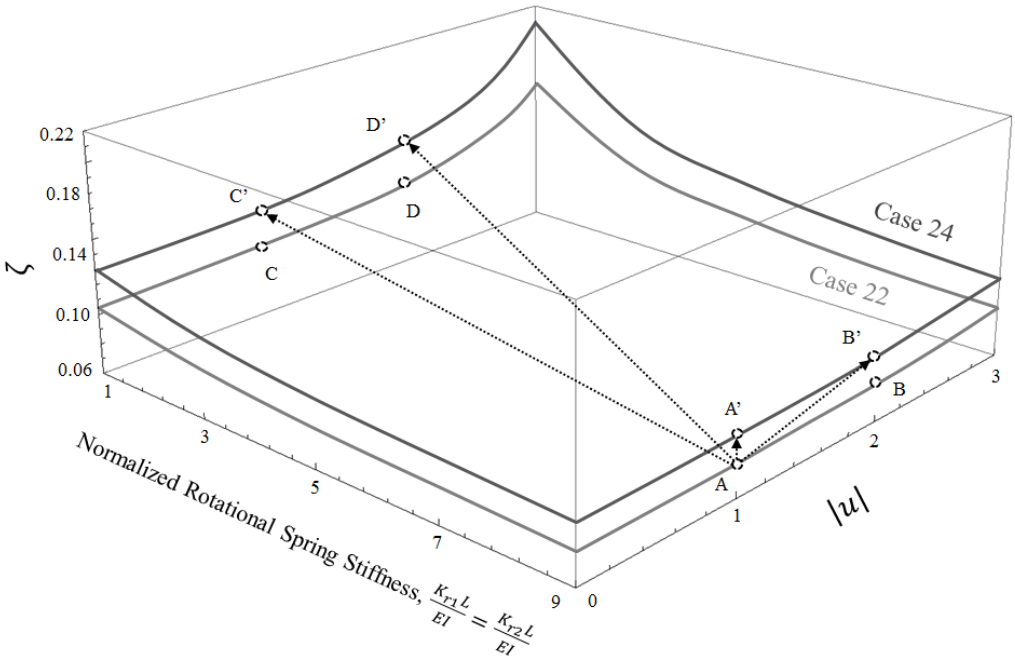

Figure 51. Potential Errors in Damping Estimates Stemming from Annulus Fluid Viscosity, Conveyed Fluid Velocity, and Spring Stiffness's (3D)

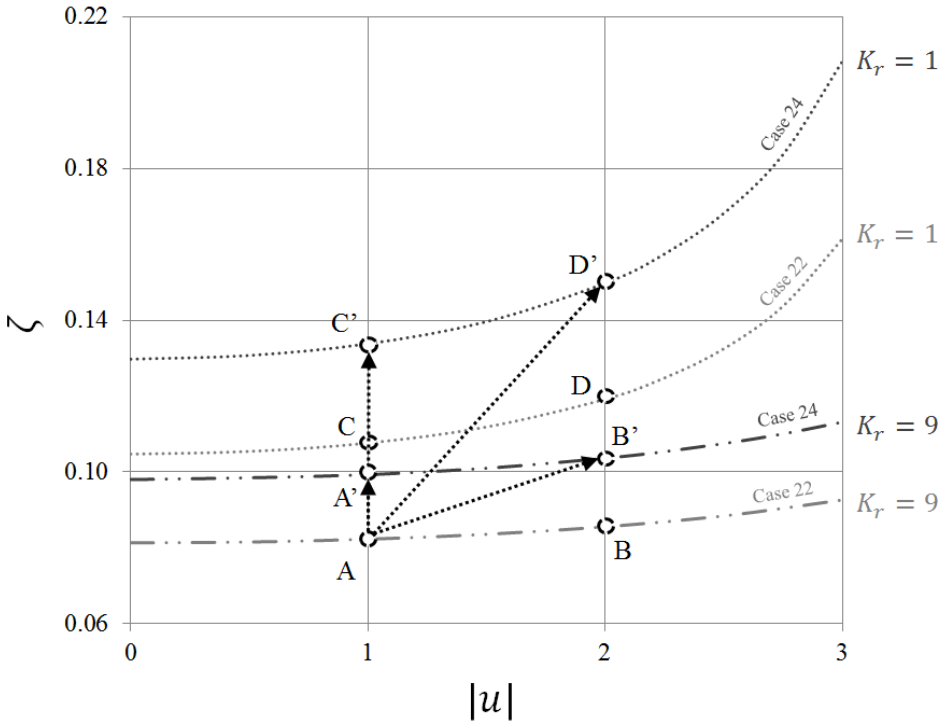

Figure 52. Potential Errors in Damping Estimates Stemming from Annulus Fluid Viscosity, Conveyed Fluid Velocity, and Spring Stiffness's (2D)

Table 22. Numeric Example: Damping Ratios and Corresponding Errors

Configuration	Damping Ratio	Error (%)
A	0.082	-
B	0.086	4%
C	0.108	31%
D	0.119	45%
A'	0.099	21%
B'	0.104	26%
C'	0.134	63%
D'	0.150	82%

3.6.9. Summary

To develop an optimal vibration based energy harvester for downhole deployment in a hydrocarbon well, it is important to accurately quantify the natural frequency and damping in the system since these parameters will affect the accelerations driving the energy harvesting system. To this end a parametric study was undertaken to investigate how changes in axial force, annulus geometry, annulus fluid properties, conveyed fluid velocity, and rotational boundary stiffness affect the dynamic behavior of a producing hydrocarbon well. The following results were found:

- Axial force acts to stiffen (tension) or soften (compression) a system.
- The annulus fluid density acts to scale the effect of the hydrodynamic function, in turn defining the hydrodynamic force.
- The effects of the hydrodynamic function are driven by the annulus fluid viscosity and annulus geometry.
- The real part of the hydrodynamic function contributes additional mass to the system, which causes a shift in the systems natural frequency but not in the velocity at which bifurcation occurs.

- The imaginary part of the hydrodynamic function acts to both shift the natural frequency of the system and the velocity at which bifurcation occurs.
- A shift in the bifurcation point is seen when the annulus fluid is viscous or externally applied axial forces are included in the system.
- Increasing the conveyed fluid velocity increases the systems damping ratio.
- Stiffer systems saw the damping ratio increase at a slower rate when compared to flexible systems as the conveyed fluid velocity was increased.

These findings give insight into the dynamic behavior of a submerged pipe conveying fluid, like what might be found in a hydrocarbon producing well. This study is a necessary step towards the development of a yet-to-be-designed energy harvester as the dynamics of the production string are expected to play a large role in the design of the energy harvester.

A portion of Chapter 3 has been published in SPIE Smart Structures and Materials+ Nondestructive Evaluation and Health Monitoring, Eric Kjolsing and Michael Todd, 2016. The title of this paper is "Gauging the Feasibility of a Downhole Energy Harvesting System Through a Proof-of-Concept Study". The dissertation author was the primary investigator and author of this paper.

Chapter 3 also includes content from four other publications, co-authored by Eric Kjolsing and Michael Todd. In each case the dissertation author was the primary investigator and author:

- "Shifts in the Fundamental Frequency of a Fluid Conveying Pipe Immersed in a Viscous Fluid for use in the Optimization of an Energy Harvesting System to be Deployed in a Producing Hydrocarbon Well", Society of Petroleum Engineers Western Regional Meeting, 2015.

- "A Frequency Study of a Clamped-Clamped Pipe Immersed in a Viscous Fluid Conveying Internal Steady Flow for use in Energy Harvester Development as Applied to Hydrocarbon Production Wells", SPIE Smart Structures and Materials+ Nondestructive Evaluation and Health Monitoring, 2015.
- "Frequency Response of a Fixed-Fixed Pipe Immersed in Viscous Fluids, Conveying Internal Steady Flow", Journal of Petroleum Science and Engineering, 2015.
- "The Impact of Boundary Conditions and Fluid Velocity on Damping for a Fluid Conveying Pipe in a Viscous Fluid", SPIE Smart Structures and Materials+ Nondestructive Evaluation and Health Monitoring, 2016.

A portion of Chapter 3 has been submitted for publication in the Journal of Sound and Vibration, Eric Kjolsing and Michael Todd, 2016. The title of this paper is "Damping of a Fluid-Conveying Pipe Surrounded by a Viscous Annulus Fluid". The dissertation author was the primary investigator and author of this paper.

Chapter 4
Preliminary Structural Housing Design

4.1. Overview

Using reasonable assumptions for an in-situ well configuration, a preliminary structural housing is designed to determine the maximum radial width available to house an energy harvesting system. This radial width dictates the maximum size of the energy harvesting elements and accompanying equipment (i.e. power storage elements, circuitry, etc.). The housings structural design accounts for American Petroleum Institute (API) loading scenarios [114] and uses standard API tubing geometries [113].

The following sections introduce the two preliminary design configurations considered, a demonstration case which walks through the design process, and the summarized results of the realizations investigated.

4.2. Preliminary Configurations

Two configurations are initially considered. Configuration A, shown in Figure 53, modifies a standard production tube geometry by welding into the string two custom machined

seating elements and an outer coaxial pipe. Configuration A requires that the outer coaxial pipe be split in two and then welded together around the production tube.

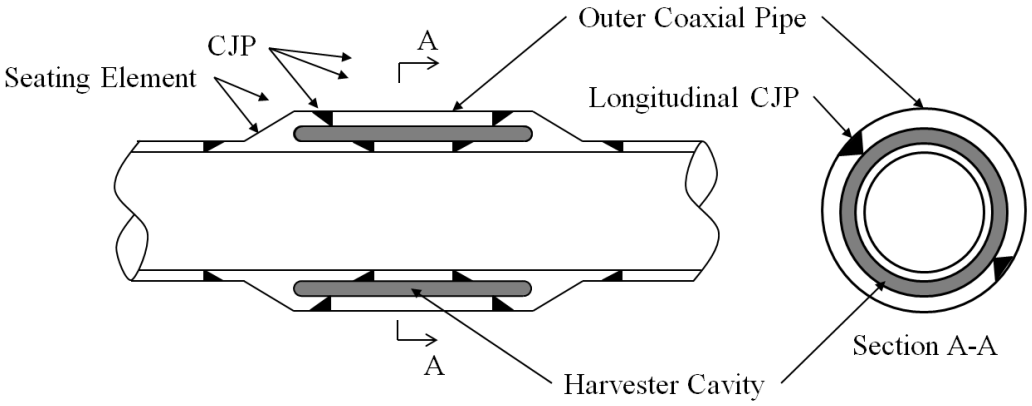

Figure 53. Configuration A

Configuration B, shown in Figure 54, mimics the structural design used by Schlumberger for their pressure and temperature gauges [183]-[184]. One possible construction sequence would have the production tube formed by protruding a thicker walled tube and then machining down to the required geometry. Smaller tubes (which contain the energy harvesters) can be fixed within the resulting longitudinal groves.

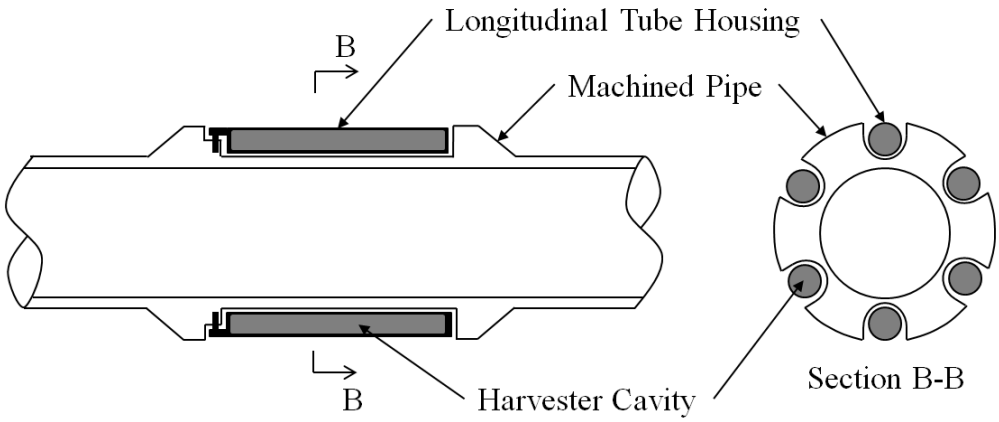

Figure 54. Configuration B

Both configurations are sub-optimal from a commercial perspective as neither permit easy access to the energy harvester cavity (the void in which the energy harvesting system will

be placed). However, the purpose of this proof-of-concept design is to determine the lower bound volumetric space available to house an energy harvesting system, not to provide a final production-ready design. In reality, any preliminary design will be modified and improved upon by industry prior to deployment to increase functionality and ease of use (e.g. the inclusion of threaded rather than welded connections).

4.3. Demonstration Case

The design process presented in this section begins by selecting a design operating pressure and temperature. Using a specific production tube outer diameter, the tubes wall thickness is selected so as to meet API load demands away from the structural housing (i.e. away from the modified length of tubing). The axial capacity of the production tube, when simultaneously subjected to the design fluid pressures, is then calculated (i.e. accounting for triaxial stress). At this point, the limits of the design loads on the unmodified production tube (both pressure loads and axial forces) have been quantified for the specific production tube geometry.

A preliminary housing configuration (i.e. the modified tube geometry) is then introduced. The housing is shown to provide sufficient capacity when loaded with the design loads by means of strength checks in-line with API requirements and Abaqus finite element models; in some cases, the targeted operating pressure or axial load carrying capacity is reduced to meet the allowable stress requirements. After the first demonstration housing is shown to be sufficient, other design pressures are selected and the process repeated. The various volumetric openings are tabulated. Design calculations are summarized in Appendix F.

4.3.1. Designing the Unmodified Production Tube

In industry, the production tube is selected by the well designer to optimize the production of hydrocarbons while simultaneously being structurally sufficient to withstand the load demands. An optimum production tube geometry cannot be selected without knowing numerous details about the well (which is beyond the scope of this work). Thus, an alternative selection method is required.

From API Specification 5CT (2005) [113], it is noted that standard production tubes come in ten outer diameters (or sizes), ranging from $1.050in$ to $4.50in$. Each of these sizes is available in a variety of wall thicknesses, end finishes, and steel grades. Of the ten sizes, the $3.50in$ diameter tubing offers the most commercially available options. As such, the $3.50in$ diameter tubing is assumed for the basis of the housing design. The steel grade is selected to be $L80$ ($80ksi$ yield strength) as it is commonly used in many oil and gas fields [185]. The wall thickness is initially assumed to be $0.375in$ (although this is the design variable) as it is the median available wall thickness for a $3.50in$-$L80$ production tube.

4.3.1.1. Design Pressure/Temperature

Based on the original capacity targeted by LANL, a design pressure of $10ksi$ and temperature of $210°F$ is selected. These values approach the upper limit of "conventional" wells with higher values being termed High-Pressure/High-Temperature (HPHT) wells [186].

In a global sense, the design temperature results in a thermal load whose effect will be to expand or contract the entire production string. This temperature loading will result in an axial force (if movement is prevented) or no axial force (if slip is allowed; this is common). Since this thermal load can be converted into a theoretically equivalent axial load, the thermal load may be included in the applied axial load.

4.3.1.2. Bursting

Bursting occurs when the internal tube pressure exceeds the external tube pressure, and the production tube wall begins to yield. The bursting pressure can be written as [114]

$$P_B = 0.875\left(\frac{Y_p w_t}{d}\right), \tag{187}$$

where P_B is the burst pressure, Y_p is the minimum yield strength, w_t is the nominal wall thickness, and d is the nominal outer radius. The 0.875 factor is included to reduce the effective wall thickness to account for a 12.5% manufacturing tolerance permitted by API Bulletin 5C2 [187]. For the geometry and steel grade selected, the minimum burst pressure is found to be $P_B = 15ksi$. A factor of safety (termed the design factor) is required and is given by

$$DF = \frac{P_B}{p_i}, \tag{188}$$

where p_i is the internal pressure (assuming zero external pressure, $p_o = 0ksi$). In practice the minimum design factor is selected by the designer; based on recommendations from the Society of Petroleum Engineers [188] a value of 1.25 is selected for this demonstration case. The actual design factor is then calculated as $DF_{actual} = 15ksi/10ksi = 1.50$. Thus, the selected geometry and strength exceeds the strength required ($DF_{actual} > DF_{required}$) under the scenario of a pressurized production tube and an empty annulus ($p_i = 10ksi, p_o = 0ksi$). Note that the next smallest wall thickness for a $3.50in$ production tube is $0.289in$ and would result in an insufficient bursting strength capacity ($DF_{actual} = 1.15$). A table summarizing the calculations can be found in Appendix F.

4.3.1.3. Collapse

Collapse occurs when the external tube pressure exceeds the internal tube pressure and the production tube begins to yield or loose load carrying capacity. There are four equations,

each representing different collapse mechanisms, governing the pressure differential that results in collapse: yield strength, plastic, transition, and elastic collapse. The equations used in determining the collapse limit can be found in API Bulletin 5C3 (2008) [114].

4.3.1.3.1. Yield Strength Collapse

Yield strength collapse occurs when the external pressure is sufficiently large to overcome the yield strength of the pipe. It can be written as

$$P_{Yp} = 2Y_p \left[\frac{(2d/w_t)-1}{(2d/w_t)^2}\right], \tag{189}$$

and only occurs when the $2d/w_t$ ratio is below a threshold specified in API Bulletin 5C3 (2008) [114]. For grade $L80$ steel, this threshold is 13.38. Since the actual $2d/w_t$ ratio is below this value ($9.33 < 13.38$), yield strength collapse is a possible failure mechanism. For the values selected in this demonstration case, $P_{Yp} = 15.31ksi$

4.3.1.3.2. Plastic Collapse

Plastic collapse is based on empirical testing of 2488 test cases [187]. The pressure at which plastic collapse occurs can be written as

$$P_p = Y_p \left[\frac{A}{(2d/w_t)} - B\right] - C, \tag{190}$$

where the coefficients A, B, and C are specified by API Bulletin 5C3 (2008) [114] and are dependent on the grade of steel. For grade $L80$ steel, these coefficients are $A = 3.071$, $B = 0.0667$, and $C = 1955$. For $L80$ steel, the range of $2d/w_t$ values for which plastic collapse occurs is $13.38 \leq 2d/w_t \leq 22.47$. Since the actual $2d/w_t$ ratio (9.33) does not fall within this range, plastic collapse will not occur for the selected geometry and steel grade.

4.3.1.3.3. Transition Collapse

Transition collapse represents a transitional (numeric) fit between the plastic and elastic collapse mechanisms [187]. It can be calculated as

$$P_T = Y_p \left[\frac{F}{(2d/w_t)} - G\right], \tag{191}$$

where the coefficients F and G are specified in in API Bulletin 5C3 (2008) [114] and are dependent on the grade of steel. For grade $L80$ steel, these coefficients are $F = 1.998$ and $G = 0.0434$. For $L80$ steel, the range of $2d/w_t$ values for which transition collapse occurs is $22.47 \leq 2d/w_t \leq 31.02$. Since the actual $2d/w_t$ ratio (9.33) does not fall within this range, transition collapse will not occur.

4.3.1.3.4. Elastic Collapse

Applicable to thin-wall pipes, elastic collapse is based on theoretical elastic instability failure. The elastic collapse pressure can be calculated as

$$P_E = \frac{46.95 \text{ x } 10^6}{(2d/w_t)[(2d/w_t)-1]^2}, \tag{192}$$

For grade $L80$ steel, elastic collapse occurs when $2d/w_t$ exceeds 31.02. Since the actual $2d/w_t$ ratio (9.33) does not exceed this value, elastic collapse will not occur.

4.3.1.3.5. Governing Collapse Case

Among the four potential collapse cases, yield strength collapse is seen to govern due to the actual $2d/w_t$ ratio falling within the appropriate bounds. Note that this result is in-line with the listed collapse resistance in Cholet (2008) [172]. Assuming a required collapse design factor of 1.1 [188], the actual collapse design factor is found to be sufficient from

$$DF = \frac{P_{Collapse}}{p_o}, \tag{193}$$

where p_o is the external pressure (assuming the internal pressure is zero; $p_i = 0ksi$, $p_o = 10ksi$) and $DF_{actual} = 1.53$. A table summarizing the calculations can be found in Appendix F.

4.3.1.4. Combined Stress

API requires the combined effect of axial load and fluid pressure to be taken into account to ensure satisfactory production tube performance. However, since there is no actual specific well currently being designed for this demonstration case, the design axial force is unknown. Instead of using the design pressure and axial force demands to check that the resulting stress demands are below the permitted values, the known material capacity (i.e. $80ksi$) and the design pressure forces (i.e. $10ksi$) are used to determine the maximum tension and compression forces that can be safely sustained by the system.

Four scenarios are investigated: two pressure conditions (bursting and collapse) and two axial force conditions (compression and tension). The typical design scenario is to ensure that the Von Mises stress demand that results from the triaxial loading is below the capacity of the system. API 5C3 (2008) [114] includes a separate check for the collapse/tension scenario which.

4.3.1.4.1. Collapse Pressure and Axial Tension

When calculating the collapse resistance of a pipe under tension loading, API reduces the collapse capacity by modifying the allowable yield stress. The yield strength of axial stress equivalent grade is given by as [114]

$$Y_{pa} = \left[\sqrt{1 - \frac{3}{4}\left(\frac{\sigma_z}{Y_p}\right)^2} - \frac{1}{2}\frac{\sigma_z}{Y_p}\right] Y_P, \tag{194}$$

where σ_z is the axial stress (tension is positive) and Y_{pa} is the yield strength of axial stress equivalent grade. To use this equation, the designer inputs σ_z and Y_P to determine Y_{pa}. The collapse resistance under axial stress is then calculated using formula factors with Y_{pa} (i.e. calculating the A, B, C, F, G coefficients used in the previous collapse calculations using Y_{pa} instead of Y_p). Based on a required design factor, the applied tension can be increased until the actual design factor equals (or is slightly larger than) the minimum required design factor. For the current configuration, the maximum applied tension while still meeting the collapse requirements is found to be $124kip$, as shown in Appendix F.

4.3.1.4.2. Burst Pressure and Axial Tension

The combined effect of burst pressure and tension stress is accounted for using a Von Mises (triaxial) stress check. The Von Mises equation is written as

$$\sigma_{VM} = \frac{1}{\sqrt{2}}\sqrt{(\sigma_t - \sigma_r)^2 + (\sigma_r - \sigma_z)^2 + (\sigma_z - \sigma_t)^2}, \tag{195}$$

where σ_{VM} is the Von Mises stress, σ_t is the tangential or hoop stress, σ_r is the radial stress, and σ_z is the axial stress. The stress components (Lame expressions) can be written as [189]

$$\begin{aligned} \sigma_t &= \frac{(d-w_t)^2 p_i - d^2 p_o}{d^2-(d-w_t)^2} + \frac{(p_i-p_o)(d-w_t)^2 d^2}{r^2(d^2-(d-w_t)^2)}, \\ \sigma_r &= \frac{(d-w_t)^2 p_i - d^2 p_o}{d^2-(d-w_t)^2} - \frac{(p_i-p_o)(d-w_t)^2 d^2}{r^2(d^2-(d-w_t)^2)}, \end{aligned} \tag{196}$$

where r is the radial distance (i.e. $r = d$ when investigating the outer diameter and $r = d - w_t$ when investigating the inner diameter of the production tube). For the specific geometry in question, the applied tension can be increased to $225kip$ before the combined burst and tension Von Mises stress exceeds the allowable capacity. A table summarizing the calculations can be found in Appendix F.

4.3.1.4.3. Collapse Pressure and Axial Compression

The same Von Mises stress check is used for the combined loading of collapse and compression. The compression can be set to $305kip$ (exceeding $A_{gross}Y_p$) before the combined collapse and compression Von Mises stress exceeds the allowable capacity. A table summarizing the calculations can be found in Appendix F.

4.3.1.4.4. Burst Pressure and Axial Compression

The same Von Mises stress check is used for the combined loading of bursting and compression. The compression can be set to $107kip$ before the combined bursting and compression Von Mises stress exceeds the allowable capacity. A table summarizing the calculations can be found in Appendix F.

4.3.2. Maximum Outer Diameter for the Structural Housing

The structural housing projects beyond the outer diameter of the production tube in order to provide space in which to place an energy harvesting system. The housings outer diameter is limited by the inner diameter of the casing. The selection of the casing outer diameter and wall thickness, like the selection of the production tube, is done by the well designer who has a number of geometries available [113]. To size the outer diameter of the casing in the current demonstration case, without having to analyze the casing for unknown soil loads, a suggested casing geometry provided by Renpu (2011) [190] is used. For a $3.50in$ production tube, an appropriate casing outer diameter is listed as $7.0in$. For this demonstration case, the casing wall thickness is selected as the median thickness for manufactured $7.0in$-$L80$ casing, which per API 5CT (2005) [113] is $0.453in$.

To account for tolerances and wobble in the well, the housings outer diameter should be limited to the diameter of the drift mandrel (a device lowered through the casing prior to

insertion of the production tube to ensure sufficient space). For casings with an outer diameter less than $9.625in$, API 5CT (2005) [113] indicates a standard drift mandrel diameter $0.125in$ less than the inner diameter of the casing. So, for a casing inner diameter of $6.094in$, an appropriate drift mandrel diameter is $5.969in$. Thus, to ensure sufficient space, the structural housings outer diameter is limited to $5.969in$.

4.3.3. Designing the Structural Housing – Configuration A

The design of the structural housing is done using both code equations and finite element models. The wall thickness of the outer coaxial pipe is sized using the API requirements previously presented. This ensures that the outer coaxial pipe has sufficient capacity away from any boundary effects induced by the seating element (see Figure 53). Since the seating element introduces boundary effects, the actual stress distribution near the seating element will differ from that assumed in the code equations. Once the wall thickness of the outer coaxial pipe is selected, finite element (FE) models are used to validate the design near the seating element.

4.3.3.1. Outer Diameter of Outer Coaxial Pipe

Based on the maximum housing outer diameter of $5.969in$, a housing outer diameter of $5.50in$ is selected; this outer diameter coincides with standard manufactured pipe geometry [113]. The three available wall thicknesses for this standard tubing diameter (grade $L80$) are $0.304in$, $0.361in$, and $0.415in$.

4.3.3.2. Sizing the Outer Coaxial Pipe Wall Thickness Using API Equations

The wall thickness of the outer coaxial pipe is sized using the API requirements previously presented in Sections 4.3.1.3, 4.3.1.4.1, and 4.3.1.4.3. Bursting is not considered as

the pressure within the harvester cavity is never expected to be greater than the external (annulus) fluid pressure.

4.3.3.2.1. Collapse

The calculations to size the outer coaxial pipe wall thickness to withstand collapse loading are identical to those performed in Section 4.3.1.3. Based on the calculations, the wall thickness is increased to $0.415in$ so as to maintain the minimum required design factor. A table summarizing the calculations can be found in Appendix F.

4.3.3.2.2. Collapse Pressure and Axial Loads

Under the combined loading scenario of collapse and axial force, two changes to the calculation set used in Section 4.3.1.4 are required. First, the nominal area used in the calculation is increased to include the cross sectional area of both the production tube and the outer coaxial pipe (see Figure 55). Since both elements are supporting axial load, the effective applied axial stress is reduced which will affect the Von Mises stress estimate.

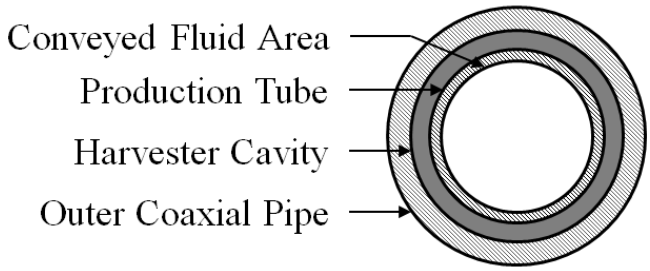

Figure 55. Nominal Area

Second, the compression induced by the annulus fluid is added to the applied axial force to arrive at an "actual" axial force. The need for this inclusion is apparent in Figure 56 where the protrusion of the outer coaxial pipe is seen to provide a projected area over which the annulus fluid induces compression.

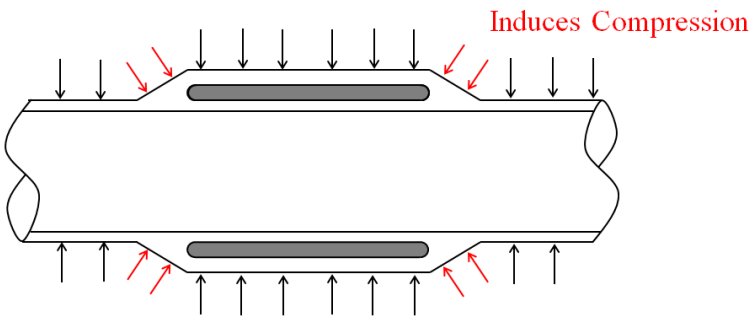

Figure 56. Induced Compression Stemming from External Fluid Pressure

The calculations show that the $0.415in$ wall thickness is capable of supporting both the $124kip$ tension and $305kip$ applied compression loads previously found in the design of the production tube (see Section 4.3.1.4). A table summarizing the calculations can be found in Appendix F.

4.3.3.3. Designing the Seating Element with Abaqus Finite Element Models

The seating element is designed using finite element models in Abaqus version 6.12. Following a mesh refinement study and an investigation into thermal effects, the seating element is analyzed to ensure sufficient strength when subjected to design loads. Two different geometric configurations are used in the analysis with the sole difference being the length of the harvester cavity (as shown in Figure 57). The $4in$ cavity length ("short span" model) represents the smallest housing that might be fabricated. The $22in$ cavity length ("long span" model) is sufficiently long that the Von Mises stress near the center of the harvester cavity converges to the results found from theoretical analysis of a uniform pipe (i.e. boundary effects become negligible). The internal radial fillets are dimensioned as $R_i = 0.3h$ and $R_o = 0.7h$, with h being the radial cavity width. This internal fillet geometry was determined based on preliminary analysis of four different fillet geometries under various load cases. Other preliminary calculations showed that an external radial fillet of $R = 3.0in$ produced reasonable results. Various Abaqus renderings and outputs are shown in Figure 58.

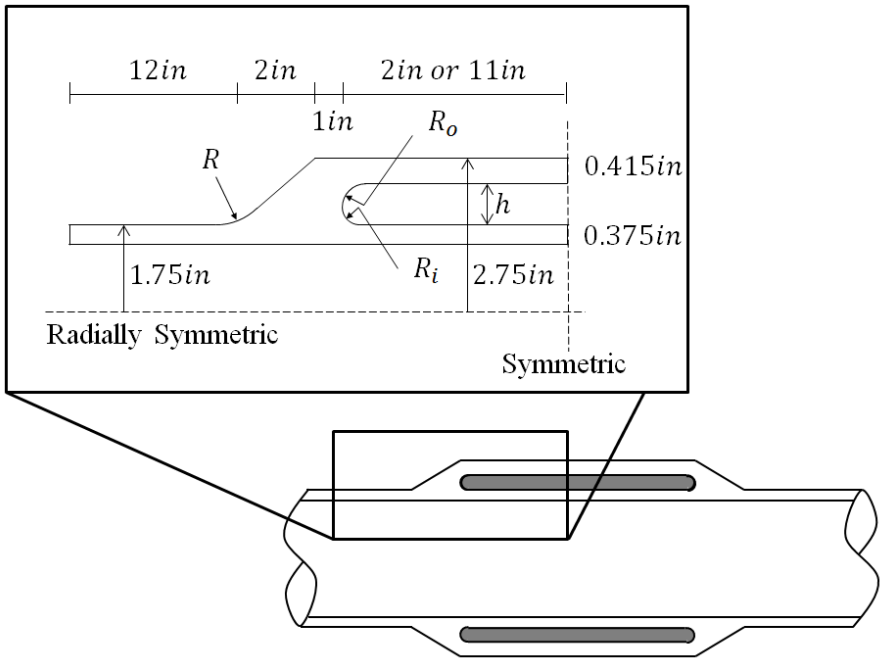

Figure 57. Model Geometry

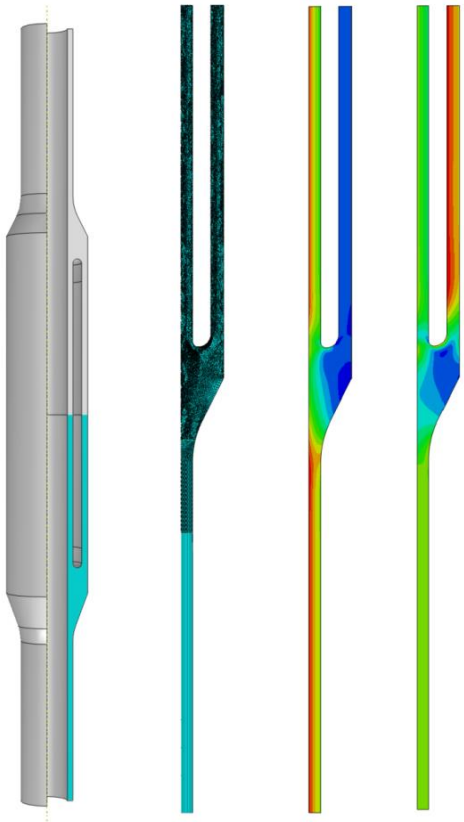

Figure 58. Abaqus Model. From Left to Right: 3/4 Model Rendering, Refined Mesh, Stress Outputs [191]

4.3.3.3.1. Mesh Refinement Study

A mesh refinement study is undertaken to ensure that the finite element mesh, which utilizes linear brick elements, is sufficiently refined in critical locations so as to accurately determine the Von Mises stresses under the design loads. The "short span" configuration shown in Figure 57 is discretized with a course mesh and then subjected to applied loads including $10ksi$ design pressures and axial forces equivalent to $\pm 100kip$. The resulting Von Mises stresses at six locations (see Figure 59) are recorded. The local mesh size at each location is then halved, the analysis re-run, and the new Von Mises stresses recorded. This process is repeated until the Von Mises stresses began to plateau, indicating that further mesh refinement will not significantly increase the models accuracy. The results of the mesh refinement study are shown in Figure 60 where the Von Mises stresses have been normalized by the course mesh model's output. The recommended local mesh sizes are shown in Table 23.

Figure 59. Mesh Refinement Study: Inspected Locations

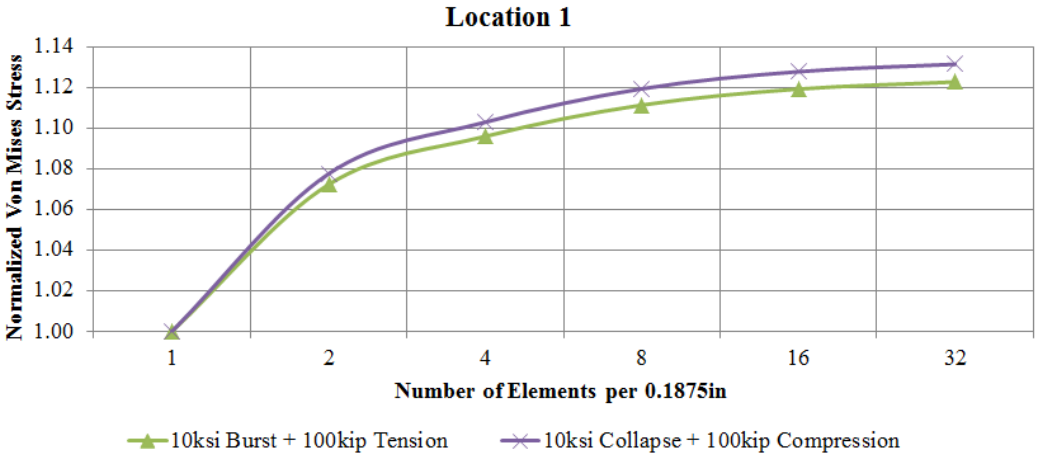

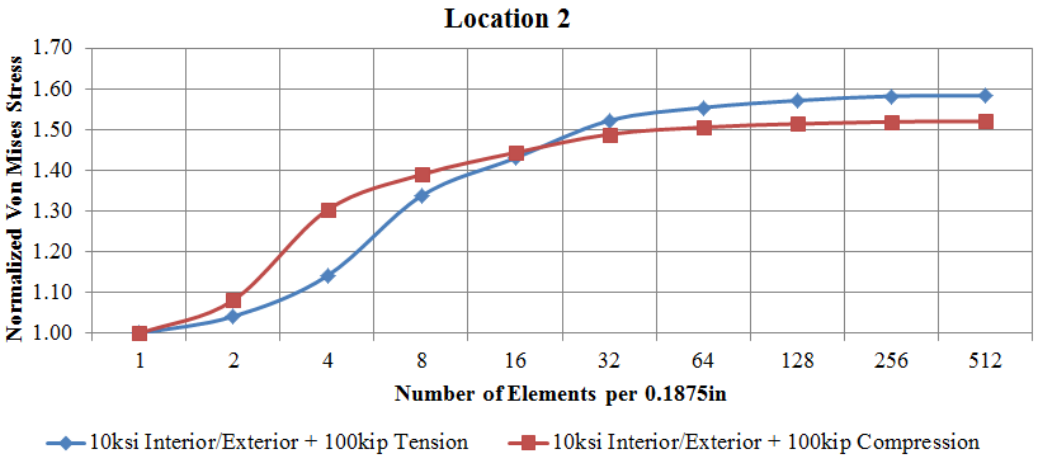

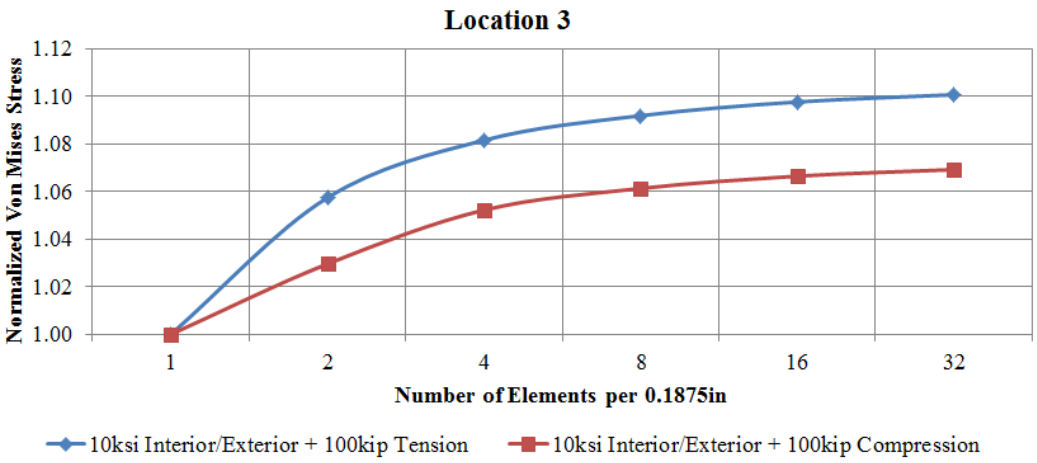

Figure 60. Mesh Refinement Study Results

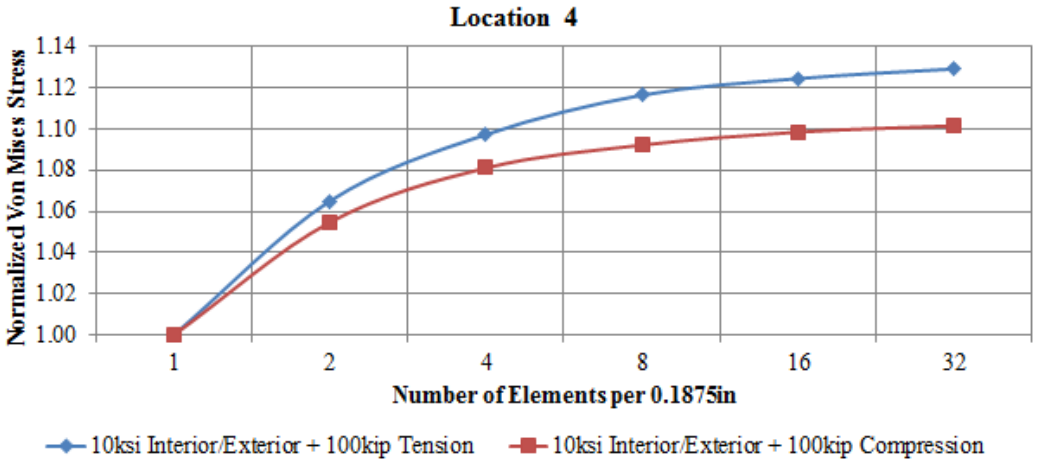

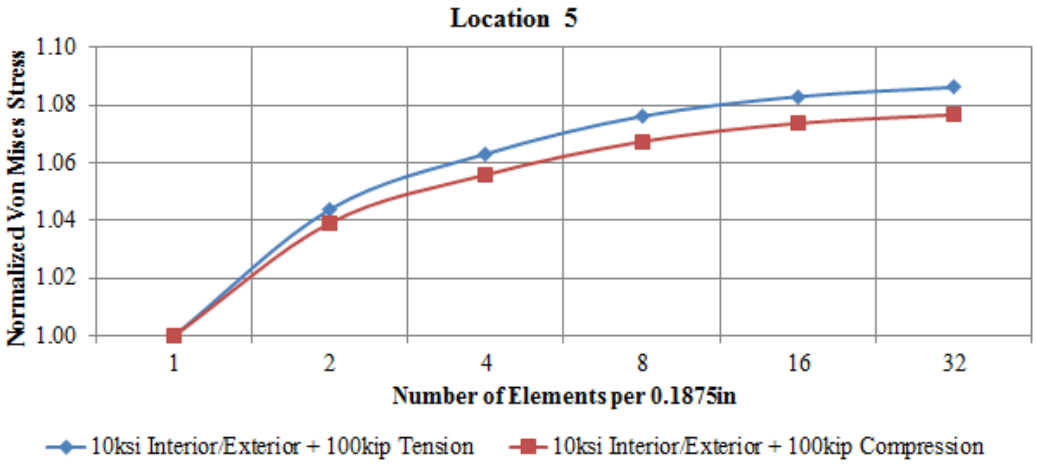

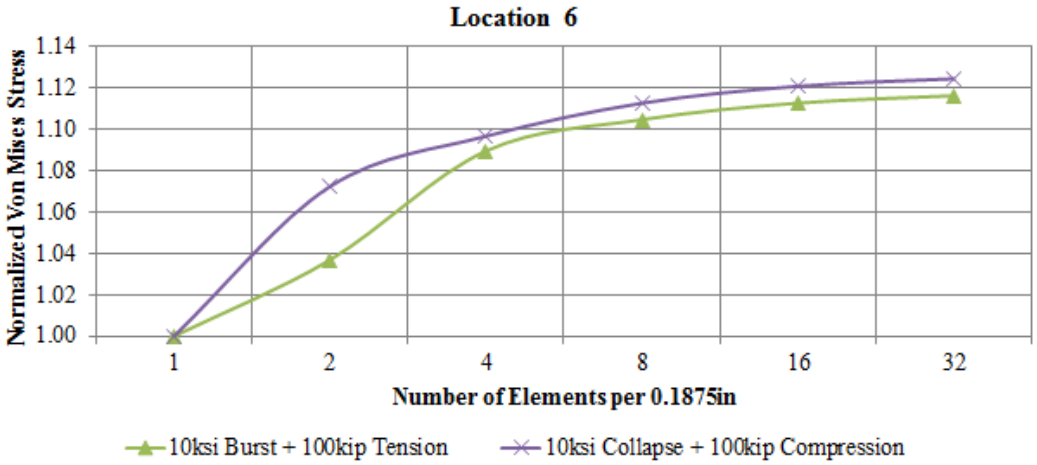

Figure 60. Mesh Refinement Study Results (Continued)

Table 23. Suggested Mesh Sizes

Location	No. of Elements per $0.1875in$	Local Mesh Size (in)
1	32	0.0059
2	256	0.0007
3	32	0.0059
4	32	0.0059
5	32	0.0059
6	32	0.0059

4.3.3.3.2. Thermal Effects

Thermal loading may result in:

- Induced axially forces within the production string (globally).
- Localized stresses within the structural housing.
- Radial displacements within the housing that may (1) reduce the available volume for the energy harvester or (2) cause the structural housing to contact the casings inner wall.
- A reduction in Young's modulus which may increase unwanted displacements.
- A reduction in yield strength necessitating lower design pressures or larger wall thicknesses.

An engineer with Chevron was contacted to better understand typical boundary conditions and code requirements. Based on this correspondence (A. Arrazola, personal communication, March 17, 2015), the following conclusions/design rationalizations were made:

- Expansion devices are commonly employed at the packer and can presumably be incorporated in the bracing elements adjacent to the energy harvester. This would allow the production tube to displace axially under thermal expansion and negate thermally induced axial loads.

- While the production tube/structural housing is free to expand axially, thermally induced internal forces may still develop in the seating element. Abaqus models will be used to determine what, if any, forces develop locally.
- Abaqus models will be used to quantify the radial displacement of the structural housing under various loading conditions.
- Abaqus models will be used to quantify the effects of reducing the Young's modulus due to temperature effects.
- Unlike HPHT wells where a reduction in yield strength is required [192], in practice, the use of a reduced yield strength is not universally applied to conventional wells. Physical tests have found that for ambient temperatures near $200°\text{F}$, steel may see the actual yield strength decrease by up to 5% [193]-[194]. However, in some design codes (e.g. the Eurocode 3 (1993) [195] and AISC Design Guide 19 (3002) [196]) the design yield strength is not reduced until temperatures exceed $212°\text{F}$ or more. For simplicity, no temperature-based reduction in yield strength is assumed in the current design.

Eight cases are investigated to determine (1) what, if any, forces develop locally in the structural housing due to temperature loads, (2) the radial displacement of the structural housing under various loading conditions, and (3) the effects of reducing the Young's modulus (due to temperature effects). The reduction in Young's modulus is assumed to be 10%, exceeding the reduction required by design codes [195]-[196] and similar to (or exceeding) the reduction seen in physical testing [193]-[194]. The coefficient of thermal expansion is taken to be $6.5e-6(1/°\text{F})$. No axial load is applied to the housing. The results from all eight cases are shown in Table 24 where the noted locations are the same as those shown in Figure 59.

Table 24. Thermal Modeling

Case	ΔT (°F)	E (ksi)	p_i (ksi)	p_o (ksi)	Von Mises Stress (ksi)				Displaced	
					Loc.1	Loc.2	Loc.3	Loc.4	Radial Width (in)	Outer Diameter (in)
1	0	$29e3$	10	10	10.00	64.14	64.49	48.97	0.578	NA
2	0	$26e3$	10	10	10.00	64.14	64.49	48.97	0.577	NA
3	200	$29e3$	10	10	10.00	64.14	64.49	48.97	0.578	NA
4	200	$26e3$	10	10	10.00	64.14	64.49	48.97	0.577	NA
5	200	$29e3$	0	0	NA	NA	NA	NA	NA	5.507
6	200	$26e3$	0	0	NA	NA	NA	NA	NA	5.507
7	200	$29e3$	10	0	NA	NA	NA	NA	NA	5.507
8	200	$26e3$	10	0	NA	NA	NA	NA	NA	5.507

In cases one through four, the Von Mises stress is seen not to change, indicating that the tabulated stresses are due solely to the unchanging pressure loading and not from temperature loads. The radial width (the distance between the outer diameter of the $3.50in$ production tube and the inner diameter of the $5.50in$ outer coaxial pipe) sees a maximum reduction of less than 1.5% when loaded. Cases five through eight indicate that the expansion due to thermal loading and internal fluid pressure is negligibly small. Effectively, these results imply that temperature effects are negligible in the current study.

4.3.3.3.3. Strength Cases

Finite element models are used to confirm the structural sufficiency of the housing configuration near the seating element. The eight load cases investigated are listed in Table 25. The reduced axial loads (which are less than those suggested in Section 4.3.1.4) are based on output from preliminary FE models.

Table 25. Strength Load Cases

Load Case	p_i (ksi)	p_o (ksi)	Axial Load* (kip)	Description
1	10	0	-90	Burst + Compression
2	10	0	115	Burst + Tension
3	0	10	-90	Collapse + Compression
4	0	10	115	Collapse + Tension
5	10	10	-90	Combined Loading
6	10	10	115	Combined Loading
7	0	0	-90	Pure Compression
8	0	0	115	Pure Tension

*$(+)$ = *Tension*

4.3.3.3.3.1. Von Mises Criteria

The Von Mises stress criteria can be used to check each load case except for case 4 (see Table 25) in which API uses the procedure outlined in Section 4.3.1.4.1 and Eq. (194) to determine structural sufficiency. The proper application of the API procedure becomes opaque when implementing FE models for the structural housing design. Fortunately, it can be shown that Eq. (194) is equivalent to satisfying a Von Mises stress criteria. Thus, when the structural housing collapse failure mechanism is expected to be yield strength collapse, a Von Mises stress check can be used directly. Following the work of Lubinski (1975) [197], consider a manipulation of the Von Mises stress criteria, re-written as

$$\sigma_{VM} = \frac{1}{\sqrt{2}}\sqrt{(\sigma_t - \sigma_r)^2 + (\sigma_r - \sigma_z)^2 + (\sigma_z - \sigma_t)^2}, \tag{197}$$

where the stress components (Lame expressions) can be written as

$$\begin{aligned} \sigma_t &= \frac{a^2 p_i - b^2 p_o}{b^2 - a^2} + \frac{(p_i - p_o)a^2 b^2}{r^2(b^2 - a^2)} = A + B, \\ \sigma_r &= \frac{a^2 p_i - b^2 p_o}{b^2 - a^2} - \frac{(p_i - p_o)a^2 b^2}{r^2(b^2 - a^2)} = A - B, \end{aligned} \tag{198}$$

where $a = d - w_t$, $b = d$, and

$$\begin{aligned} A &= \frac{a^2 p_i - b^2 p_o}{b^2 - a^2}, \\ B &= \frac{(p_i - p_o)a^2 b^2}{r^2(b^2 - a^2)}. \end{aligned} \tag{199}$$

The axial stress can be written as

$$\sigma_z = \Delta\sigma_z + \sigma_N = \Delta\sigma_z + A, \tag{200}$$

where $\Delta\sigma_z$ represents the excess axial stress above its neutral value and $\sigma_N = A$ represents the neutral axial stress [197]. Eq. (197) can be re-written as

$$\sigma_{VM} = \frac{1}{\sqrt{2}}\sqrt{\big(A + B - (A - B)\big)^2 + \big(A - B - (\Delta\sigma_z + A)\big)^2 + \big(\Delta\sigma_z + A - (A + B)\big)^2}, \tag{201}$$

which reduces to

$$\sigma_{VM} = \sqrt{3B^2 + \Delta{\sigma_z}^2}. \tag{202}$$

Expanding $3B^2$ leads to

$$3B^2 = \left[\sqrt{3}\left(\frac{a}{r}\right)^2 \frac{(p_i - p_o)b^2}{(b^2 - a^2)}\right]^2. \tag{203}$$

This can be simplified by defining a new term

$$F = 2\frac{b^2}{b^2 - a^2} = \frac{1}{2}\frac{\left({}^{2d}/_{w_t}\right)^2}{\left({}^{2d}/_{w_t} - 1\right)}. \tag{204}$$

This allows Eq. (203) to be written as

$$3B^2 = \left[\frac{\sqrt{3}}{2}\left(\frac{a}{r}\right)^2 (p_i - p_o)F\right]^2, \tag{205}$$

and Eq. (202) as

$$\sigma_{VM} = \sqrt{\left[\frac{\sqrt{3}}{2}\left(\frac{a}{r}\right)^2 (p_i - p_o)F\right]^2 + \Delta{\sigma_z}^2}. \tag{206}$$

Since yielding will occur first at the inner boundary [197] the location of interest is $r = a$. Additionally, since the Von Mises stress is to be below the minimum yield stress of the pipe (Y_p), Eq. (206) can be re-written as

$$\sqrt{\left[\frac{\sqrt{3}}{2}(p_i - p_o)F\right]^2 + \Delta{\sigma_z}^2} = \sigma_{VM} \leq Y_p. \tag{207}$$

Including Eq. (199) and Eq. (200) in Eq. (207), while writing p_o as $(p_o - p_i) + p_i$ leads to

$$\sqrt{\left[\frac{\sqrt{3}}{2}(p_i - p_o)F\right]^2 + \left[\sigma_z - \left\{\frac{a^2 p_i - b^2[(-p_i + p_o) + p_i]}{b^2 - a^2}\right\}\right]^2} = \sigma_{VM} \leq Y_p. \tag{208}$$

Expanding the second term leads to

$$\sqrt{\left[\frac{\sqrt{3}}{2}(p_i - p_o)F\right]^2 + \left[\sigma_z - \frac{a^2 p_i}{b^2 - a^2} - \frac{b^2(p_i - p_o)}{b^2 - a^2} + \frac{b^2 p_i}{b^2 - a^2}\right]^2} = \sigma_{VM} \leq Y_p. \tag{209}$$

Recalling Eq. (204) and noting $a^2/(b^2 - a^2) = 0.5F - 1$ leads to

$$\sqrt{(p_i - p_o)^2 F^2 + (p_o - p_i)F(\sigma_z + p_i) + (\sigma_z + p_i)^2} = \sigma_{VM} \leq Y_p. \tag{210}$$

A negative sign can be pulled out of the second term as

$$\sqrt{(p_i - p_o)^2 F^2 - (p_i - p_o)F(\sigma_z + p_i) + (\sigma_z + p_i)^2} = \sigma_{VM} \leq Y_p. \tag{211}$$

For simplicity, let $x = (p_i - p_o)F$ and $R = (\sigma_z + p_i)$. Using these terms and setting the yield criterion to be $\sigma_{VM} = Y_p$, Eq. (211) can be written as

$$x^2 - xR + R^2 = {Y_p}^2, \tag{212}$$

which can be rewritten as

$$x^2 - xR + \frac{1}{4}R^2 = {Y_p}^2 - \frac{3}{4}R^2, \tag{213}$$

and rearranged as

$$\left(-x + \frac{1}{2}R\right)^2 = {Y_p}^2 - \frac{3}{4}R^2. \tag{214}$$

The x term can be isolated as

$$-x = \sqrt{{Y_p}^2 - \frac{3}{4}R^2} - \frac{1}{2}R, \tag{215}$$

and after dividing both sides by Y_p,

$$-\frac{x}{Y_p} = \sqrt{1 - \frac{3}{4}\left(\frac{R}{Y_p}\right)^2} - \frac{1}{2}\frac{R}{Y_p}. \tag{216}$$

The values for x and R can be reinserted

$$-\frac{(p_i - p_o)F}{Y_p} = \sqrt{1 - \frac{3}{4}\left(\frac{\sigma_z + p_i}{Y_p}\right)^2} - \frac{1}{2}\frac{\sigma_z + p_i}{Y_p}. \tag{217}$$

For the collapse scenario take $p_i = 0$, leading to

$$\frac{p_o F}{Y_p} = \sqrt{1 - \frac{3}{4}\left(\frac{\sigma_z}{Y_p}\right)^2} - \frac{1}{2}\frac{\sigma_z}{Y_p}. \tag{218}$$

Recall the API equation for yield strength collapse, given in Eq. (189) and repeated here for convenience (where Eq. (204) has also been utilized)

$$P_{Yp} = 2Y_p\left[\frac{(2d/w_t) - 1}{(2d/w_t)^2}\right] = \frac{Y_p}{F}. \tag{219}$$

Inserting Eq. (219) into Eq. (218) leads to

$$\frac{p_o}{P_{Yp}} = \sqrt{1 - \frac{3}{4}\left(\frac{\sigma_z}{Y_p}\right)^2} - \frac{1}{2}\frac{\sigma_z}{Y_p}. \quad (220)$$

Note the similarity between Eq. (220) and the API code equation for the combined load state of collapse pressure and axial tension, given in Eq. (194), and re-written here for convenience

$$\frac{Y_{pa}}{Y_P} = \sqrt{1 - \frac{3}{4}\left(\frac{\sigma_z}{Y_p}\right)^2} - \frac{1}{2}\frac{\sigma_z}{Y_p}. \quad (221)$$

Thus, so long as the collapse mechanism is yield strength collapse, the intent of the API code appears to be a limitation of the Von Mises stress (σ_{VM}) to a value below the yield point (Y_P). Since the stress distribution of the seating element geometry is different than the ideal pipe case, it is reasonable to use FE analysis when the yield strength collapse case governs the individual pipe elements (i.e. the production tube and outer coaxial pipe) to determine the Von Mises stress directly. The observed Von Mises stress can then be compared to the material yield stress and the actual design factor obtained.

At this point it is relevant to note that each loading case of (1) collapse or (2) combined collapse and axial tension, for both the production tube and outer coaxial pipe in the demonstration case, were governed by the yield strength mechanism (see Appendix F). As such, the use of a Von Mises stress check in conjunction with FE analysis is justified for the design of the seating element.

4.3.3.3.3.2. Results

The results of the study are shown in Table 26 and Table 27 for the "short span" model and Table 28 and Table 29 for the "long span" model.

Table 26. Strength Cases: FE Based Stress Results for Short Span

Load Case	p_i (ksi)	p_o (ksi)	Axial Load* (kip)	Von Mises Stresses (ksi) at Location						Displaced Radial Width (in)
				1	2	3	4	5	6	
1	10	0	−90	60.6	34.0	20.2	51.3	44.6	61.6	0.583
2	10	0	115	47.5	34.0	10.5	46.1	38.1	48.9	0.583
3	0	10	−90	45.0	65.6	62.6	19.3	29.8	45.8	0.579
4	0	10	115	72.9	50.2	72.1	20.2	58.5	74.5	0.580
5	10	10	−90	14.4	73.1	62.3	55.4	14.9	15.0	0.577
6	10	10	115	41.2	67.1	71.8	47.9	43.1	43.1	0.578
7	0	0	−90	24.4	14.9	11.9	11.4	25.5	25.5	0.577
8	0	0	115	31.2	19.0	15.1	15.0	32.6	32.6	0.578

*(+) = *Tension*

Table 27. Strength Cases: FE Based Design Factors for Short Span

Load Case	Design Factor at Location											
	1		2		3		4		5		6	
	Req.	Actual	Req.	Actual	Req.	Actual	Req.	Actual	Req.	Actual	Req.	Actual
1	1.25	1.32	1.25	2.35	1.25	3.96	1.25	1.56	1.25	1.79	1.25	1.30
2	1.25	1.69	1.25	2.35	1.25	7.59	1.25	1.74	1.25	2.10	1.25	1.63
3	1.1	1.78	1.1	1.22	1.1	1.28	1.1	4.15	1.1	2.68	1.1	1.75
4	1.1	1.10	1.1	1.59	1.1	1.11	1.1	3.96	1.1	1.37	1.1	1.07
5	1.25	5.54	1.1	1.09	1.1	1.29	1.25	1.44	1.25	5.36	1.25	5.32
6	1.25	1.94	1.1	1.19	1.1	1.11	1.25	1.67	1.25	1.86	1.25	1.86
7	1.6	3.27	1.6	5.35	1.6	6.72	1.6	7.02	1.6	3.14	1.6	3.14
8	1.6	2.56	1.6	4.21	1.6	5.32	1.6	5.33	1.6	2.46	1.6	2.46

Table 28. Strength Cases: FE Based Stress Results for Long Span

Load Case	p_i (ksi)	p_o (ksi)	Axial Load* (kip)	Von Mises Stresses (ksi) at Location						Displaced Radial Width (in)
				1	2	3	4	5	6	
1	10	0	−90	60.7	30.8	21.5	49.8	44.5	61.7	0.583
2	10	0	115	47.6	33.4	9.8	45.5	38.1	49.0	0.583
3	0	10	−90	45.1	67.8	63.3	15.5	29.8	45.9	0.579
4	0	10	115	73.0	50.5	69.2	22.2	58.7	74.5	0.575
5	10	10	−90	14.4	76.8	63.2	51.7	14.7	15.1	0.578
6	10	10	115	41.2	64.5	68.2	46.2	43.3	43.1	0.578
7	0	0	−90	24.4	14.6	12.4	10.9	25.5	25.5	0.578
8	0	0	115	31.2	18.7	15.8	14.4	32.6	32.6	0.578

*(+) = *Tension*

Table 29. Strength Cases: FE Based Design Factors for Long Span

Load Case	Design Factor at Location											
	1		2		3		4		5		6	
	Req.	Actual	Req.	Actual	Req.	Actual	Req.	Actual	Req.	Actual	Req.	Actual
1	1.25	1.32	1.25	2.60	1.25	3.72	1.25	1.61	1.25	1.80	1.25	1.30
2	1.25	1.68	1.25	2.40	1.25	8.16	1.25	1.76	1.25	2.10	1.25	1.63
3	1.1	1.77	1.1	1.18	1.1	1.26	1.1	5.16	1.1	2.68	1.1	1.74
4	1.1	1.10	1.1	1.58	1.1	1.16	1.1	3.60	1.1	1.36	1.1	1.07
5	1.25	5.54	1.1	1.04	1.1	1.27	1.25	1.55	1.25	5.43	1.25	5.30
6	1.25	1.94	1.1	1.24	1.1	1.17	1.25	1.73	1.25	1.85	1.25	1.86
7	1.6	3.27	1.6	5.46	1.6	6.45	1.6	7.34	1.6	3.14	1.6	3.14
8	1.6	2.56	1.6	4.27	1.6	5.06	1.6	5.56	1.6	2.45	1.6	2.45

Note that for each span length, cases 4 and 5 violate the required design factor. For load case 5, the permitted axial compression has already been reduced to $90kip$ as $90kip$ represents the minimum load the housing will need to be able to support should the housing be deployed above a packer (A. Arrazola, personal communication, March 17, 2015). Although a refined analysis of the location 2 fillet may result in a satisfactory design factor, considering this is a preliminary design a more prudent route is to reduce the design pressure. This reduced design pressure will have the secondary benefit of improving the design factors for load case 4. The critical load cases, accounting for the updated design pressures, are shown in Table 30 and Table 31.

Table 30. Strength Cases: Updated FE Based Stress Results

Load Case**	p_i (ksi)	p_o (ksi)	Axial Load* (kip)	Von Mises Stresses (ksi) at Location					
				1	2	3	4	5	6
4, SS	0	9.3	115	69.5	46.5	67.5	19.8	56.4	71.1
5, SS	9.3	9.3	−90	15.1	68.7	57.7	51.9	15.7	15.8
4, LS	0	9.3	115	69.6	46.7	64.7	21.5	56.5	71.1
5, LS	9.3	9.3	−90	15.1	72.2	58.7	48.4	15.5	15.9

*$(+)$ = *Tension*

***SS = Short Span, LS = Long Span*

Table 31. Strength Cases: Updated FE Based Design Factors

Load Case**	Design Factor at Location											
	1		2		3		4		5		6	
	Req.	Actual	Req.	Actual	Req.	Actual	Req.	Actual	Req.	Actual	Req.	Actual
4, SS	1.1	1.15	1.1	1.72	1.1	1.19	1.1	4.04	1.1	1.42	1.1	1.13
5, SS	1.25	5.28	1.1	1.16	1.1	1.39	1.25	1.54	1.25	5.11	1.25	5.07
4, LS	1.1	1.15	1.1	1.71	1.1	1.24	1.1	3.73	1.1	1.42	1.1	1.12
5, LS	1.25	5.28	1.1	1.11	1.1	1.36	1.25	1.65	1.25	5.17	1.25	5.03

***SS = Short Span, LS = Long Span*

Since the design pressure has been lowered to $9.3ksi$, it is possible that a smaller wall thickness would have been selected by a well designer using the API equations (for the unmodified production tube away from the structural housing). Another design cycle, using a $9.3ksi$ design pressure, will show that reducing either the production tube or outer coaxial pipe wall thickness to the next lowest commercially available size (i.e. $0.375in \rightarrow 0.289in$ for the production tube and $0.415in \rightarrow 0.361in$ for the outer coaxial pipe) will result in a deficient

burst (production tube) or collapse (outer coaxial pipe) design factor. This means that a well designer, intending to design an unmodified well for a $9.3ksi$ design pressure, would still have selected a $0.375in$ production tube wall thickness (instead of a $0.289in$ thickness) so as to meet bursting requirements. This also means that the outer coaxial pipe still requires a $0.415in$ wall thickness (and not a $0.361in$ thickness) so as to meet collapse requirements.

Since the structural housing is capable of withstanding the minimum above-packer axial load of $90kip$, the preliminary design is considered satisfactory. A summary of the design is provided in Table 32.

Table 32. Configuration A Above Packer Design Summary

Production Tube Outer Diameter (in)	3.50
Production Tube Wall Thickness (in)	0.375
Casing Outer Diameter (in)	7.00
Casing Wall Thickness (in)	0.453
Outer Coaxial Pipe Outer Diameter (in)	5.50
Outer Coaxial Pipe Wall Thickness(in)	0.415
Steel Grade	$L80$
Yield Strength (ksi)	80
Design Pressure (ksi)	9.3
Maximum Tension (kip)	115
Maximum Compression (kip)	90
Unloaded Radial Width (in)	0.585
Loaded Radial Width (in)	0.573
Harvester Cavity Cross Sectional Area (in^2)	7.35

4.3.4. Designing the Structural Housing – Configuration A with Reduced Axial Loads

In the previous Section 4.3.3 the minimum axial load carrying capacity of the structural housing was set to $90kip$ to permit the energy harvesting system to be deployed above an axially set packer. Another possible deployment location would be below the packer. At this location significantly less axial capacity is required which may permit an increase in the design pressure and/or increase in the radial width.

To determine the required axial capacity of the system, assume the only demand at the housing elevation is the buoyant self-weight of the production string (including attached

equipment) and the end pressure generated by the reservoir fluid. An estimate of the required compressive capacity of $50kip$ is found by multiplying the production tube cross sectional area, by an assumed upperbound fluid pressure of $13ksi$ (this assumes the housing is near the bottom of the production string). The required tensile capacity is estimated to be $15kip$ which, when including 50% of the aforementioned fluid bearing pressure, represents the weight of over 3000 linear feet of $3.50in/0.375in$ tubing (this assumes the housing is some distance away from the bottom of the production string).

4.3.4.1. Results

An iterative design, following the design process outlined in Section 4.3.3, results in the final configuration shown in Table 33.

Table 33. Configuration A Below Packer Design Summary

Production Tube Outer Diameter (in)	3.50
Production Tube Wall Thickness (in)	0.375
Casing Outer Diameter (in)	7.00
Casing Wall Thickness (in)	0.453
Outer Coaxial Pipe Outer Diameter (in)	5.50
Outer Coaxial Pipe Wall Thickness (in)	0.415
Design Pressure (ksi)	10.1
Maximum Tension (kip)	15
Maximum Compression (kip)	50
Unloaded Radial Width (in)	0.585
Loaded Radial Width (in)	0.573
Harvester Cavity Cross Sectional Area (in^2)	7.35

4.3.5. Designing the Structural Housing – Configuration B

Since Configuration B does not include a cavity, the analysis is slightly simplified. In the following sections, the designs for two elements are considered:

- The longitudinal tube housing (LTH) accounting for both fixed-free and fixed-pinned boundaries.
- The machined pipe that will house the LTHs.

The assumptions outlined in the previous sections will be maintained (see Table 34). In addition, based on Section 4.3.3.3.2, temperature effects are assumed to be negligible.

Table 34. Geometric and Material Assumptions

Production Tube Outer Diameter (in)	3.50
Production Tube Wall Thickness (in)	0.375
Casing Outer Diameter (in)	7.00
Casing Wall Thickness (in)	0.453
Casing Inner Diameter (in)	6.094
Housing Outer Diameter (in)	5.50
Steel Grade	$L80$
Yield Strength (ksi)	80

The design of the LTH will assume a $0.8in$ outer diameter allowing for (1) a $0.1in$ gap between the production tube and LTH and (2) sufficient clearance such that external bodies contacting the housing will not contact the LTH (see Figure 61).

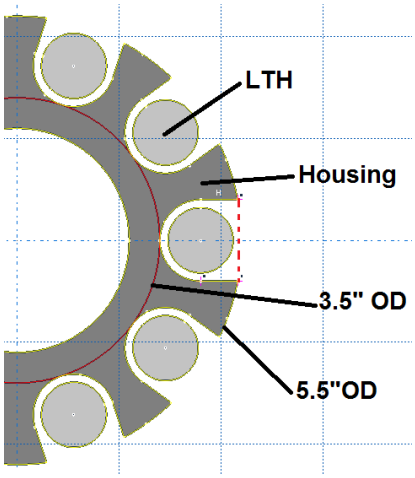

Figure 61. Partial Cross Section of Configuration B

4.3.5.1. Fixed-Free and Fixed-Pinned Longitudinal Tube Housing

The two proposed configurations are shown in Figure 62 and Figure 63. The boundary conditions are selected such that any axial load carried by the production string will not load the LTHs. The two configurations are similar with the exception that the tail of the fixed-pinned model reduces the effective length factor of the LTH, permitting a higher axial capacity. The three strength cases investigated include:

- Compressive strength for flexural buckling per the American Institute of Steel Construction (AISC; 2007) [198].
- Collapse and Collapse + Compression per API 5C3 (2008) [114].
- Von Mises stress stemming from FE analysis.

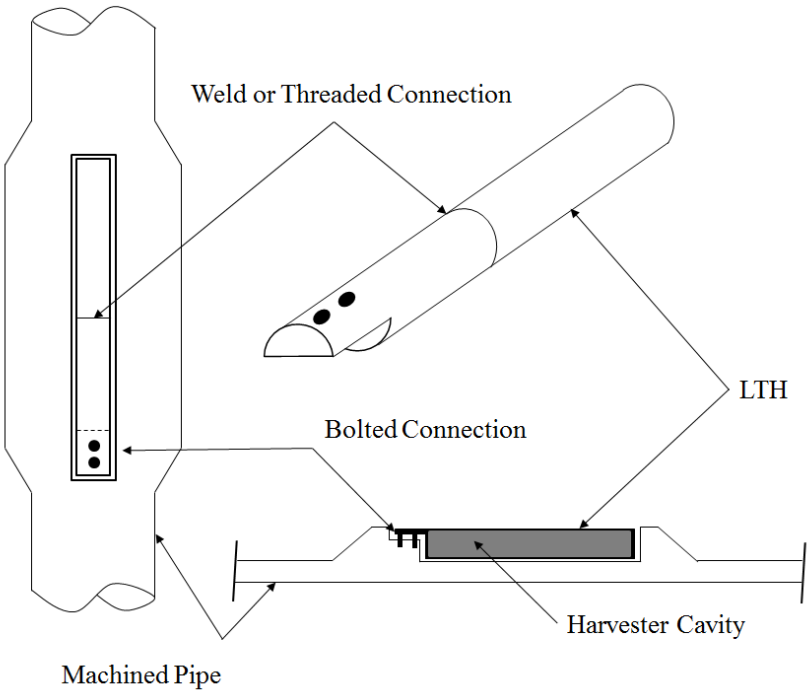

Figure 62. Fixed-Free LTH

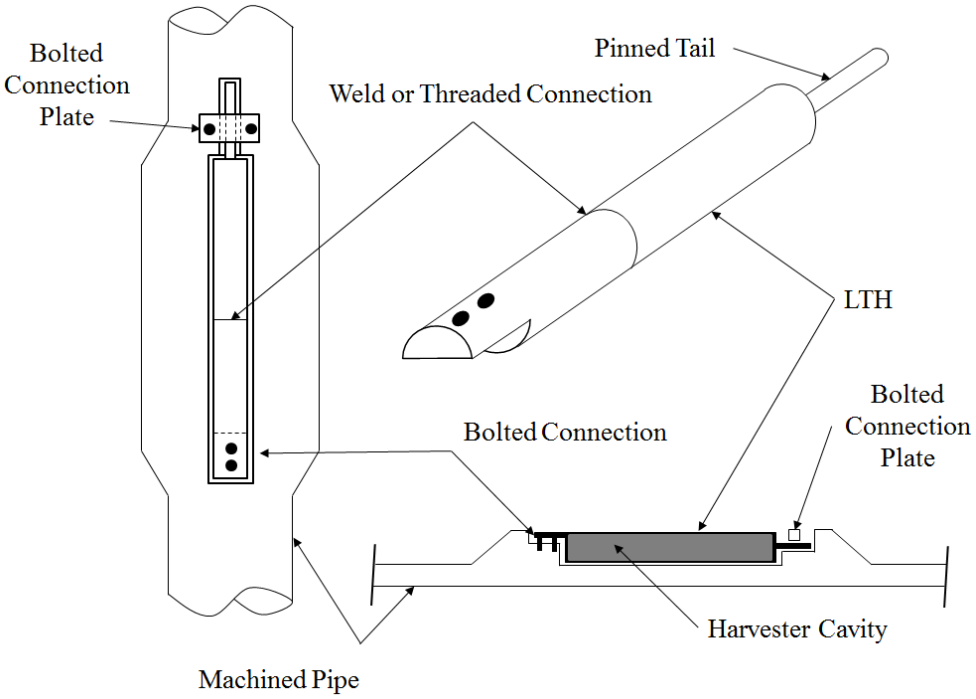

Figure 63. Fixed-Pinned LTH

4.3.5.1.1. AISC Criteria

AISC specifies the compressive strength of a non-slender compression member based on the limit state of flexural buckling. Consider the following sample calculation set (shown in Table 35) for a fixed-free LTH with an outer diameter (OD) of $0.8in$ and a $0.075in$ wall thickness. Note that the Young's modulus has been reduced due to the environments high operating temperature and that a capacity factor of 0.9 has been selected per AISC criteria.

Table 35. AISC LTH Sample Calculation

Outer Diameter (in)	0.8
Wall Thickness (in)	0.075
Nominal Area (in^2)	0.17
Length (in)	10.8
Young's Modulus (ksi)	27500
Yield Strength (ksi)	80
Inertia (in^4)	0.0113
Effective Length Factor, K [198]	2.1
Radius of Gyration, r (in)	0.26
KL/r	88.0
Is the System Slender?	No
Elastic/Plastic Limit	87.3
Elastic Critical Buckling Stress, F_e (ksi) [198]	35.04
Flexural Buckling Stress, F_{cr} (ksi) [198]	30.73
Compressive Demand (kip)	4.67
Capacity Factor [198]	0.9
Factored Compressive Strength (kip)	4.72
Demand ≤ Capacity	Yes

The calculation shows that a $10.8in$ long LTH is capable of withstanding the compressive demand ($4.67kip$) generated by the $9.3ksi$ design pressure on the ends (or caps) of the LTH ($9.3ksi$ design pressure is used so Configurations A and B could be compared directly). If the wall thickness of the LTH is increased, the length of the LTH can be increased. A wall thickness vs. length table is provided in Table 36 for both the fixed-free and fixed-pinned boundary conditions; the effective length factor for the fixed-pinned case is taken as $K = 0.8$.

Table 36. Wall Thickness vs. Length for Sufficient AISC Design ($0.8in$ OD)

Wall Thickness (in)	0.050	0.075	0.100	0.125	0.150	0.175
Fixed-Free Maximum Length (in)	8.7	10.8	11.9	12.7	13.3	13.7
Estimated Cavity Volume (in^3)	3.16	3.42	3.22	2.90	2.51	2.10
Fixed-Pinned Maximum Length (in)	23.0	28.5	31.3	33.4	34.9	35.9
Estimated Cavity Volume (in^3)	8.66	9.29	8.71	7.82	6.75	5.63

The volume listed is the cavity cross sectional area times the maximum length using the AISC code equations less $0.5in$ of length assumed occupied by the end caps of the LTH. In both boundary configurations the maximum available volume occurs with a $0.075in$ wall thickness. For prudence, the process is repeated using a $1.0in$ outer diameter LTH with the results shown in Table 37; the optimum wall thickness is seen to be $\sim 0.1in$.

Table 37. Wall Thickness vs. Length for Sufficient AISC Design ($1.0in$ OD)

Wall Thickness (in)	0.050	0.075	0.100	0.125	0.150	0.175
Fixed-Free Maximum Length (in)	8.9	12.3	13.8	14.9	15.7	16.3
Estimated Cavity Volume (in^3)	5.34	6.70	6.69	6.36	5.85	5.24
Fixed-Pinned Maximum Length (in)	23.5	32.2	36.4	39.2	41.3	42.9
Estimated Cavity Volume (in^3)	14.63	17.99	18.05	17.10	15.70	14.07

4.3.5.1.2. API Criteria

The LTH is checked against collapse and collapse + compression per the previously discussed API criteria. Although compression increases the collapse capacity, the annulus fluid pressure generates both loading simultaneously; collapse + compression is the more reasonable design case while collapse alone is the more conservative. The axial load is calculated by multiplying the cap area by a $9.3ksi$ fluid design pressure. The wall thicknesses at which a 1.1 design factor is achieved, for $0.8in$ and $1.0in$ OD LTHs, are provided in Table 38.

Table 38. API Collapse Calculations: Minimum Wall Thickness for 1.1 Design Factor

	Load Case	Minimum Wall Thickness (in)
$0.8in$ Outer Diameter	Collapse	0.058
	Collapse + $4.67kip$ Compression	0.048
$1.0in$ Outer Diameter	Collapse	0.072
	Collapse + $7.30kip$ Compression	0.059

4.3.5.1.3. Abaqus Finite Element Modeling

A finite element model of the $0.8in$ OD LTH with $0.075in$ wall thickness is generated. The connection details (i.e. bolted connection and tail) are not modeled as they do not contain a cavity and are simply triaxial loading of a volumetric block of steel. The model is generated in order to (1) confirm that the design factor is satisfactory and (2) determine the required fillet/geometry of the cap. The total length of the LTH is taken to be $10.4in$ and an applied pressure of $9.3ksi$ is used. The cap thickness is set to $0.25in$. The model output is shown in Figure 64. Utilizing a $1/8in$ radial fillet, the maximum Von Mises stress is found to be

$46.4ksi$, resulting in an acceptable design factor of 1.72. Although the cap thickness could be optimized, it is not done here.

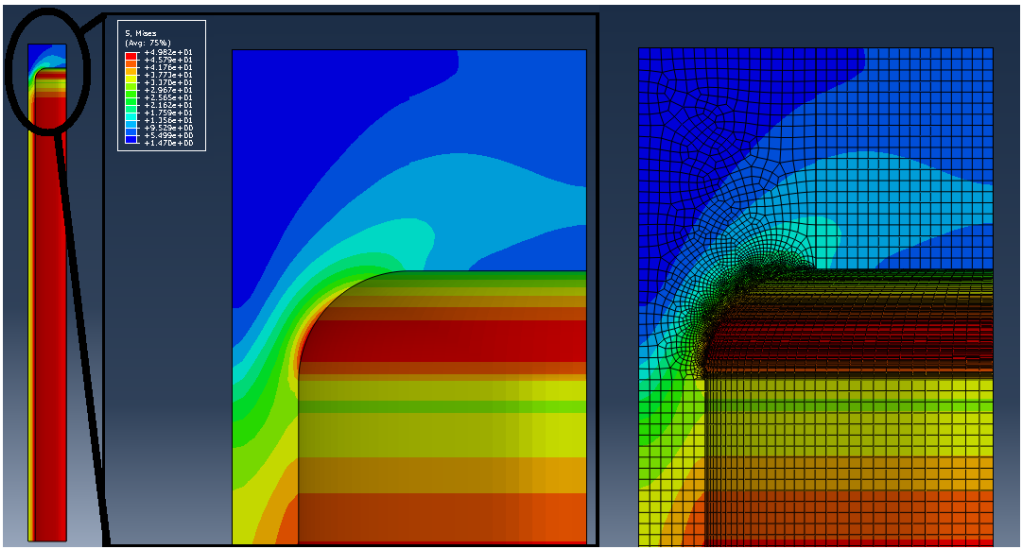

Figure 64. FE Model of $0.8in$ Outer Diameter LTH: Stress Results

4.3.5.2. Machined Pipe

The production tube is modified so as to house the LTHs. Since the production tube itself does not house a harvester cavity and a significant amount of material is being added to the production tube, the stress demand on the production tube is expected to decrease. To confirm this, a FE model is generated. A $10ksi$ design pressure is applied ($> 9.3ksi$ required). The geometry of the model is shown in Figure 65 and Figure 66. The cross section assumes 10 radially spaced LTHs (see Figure 61).

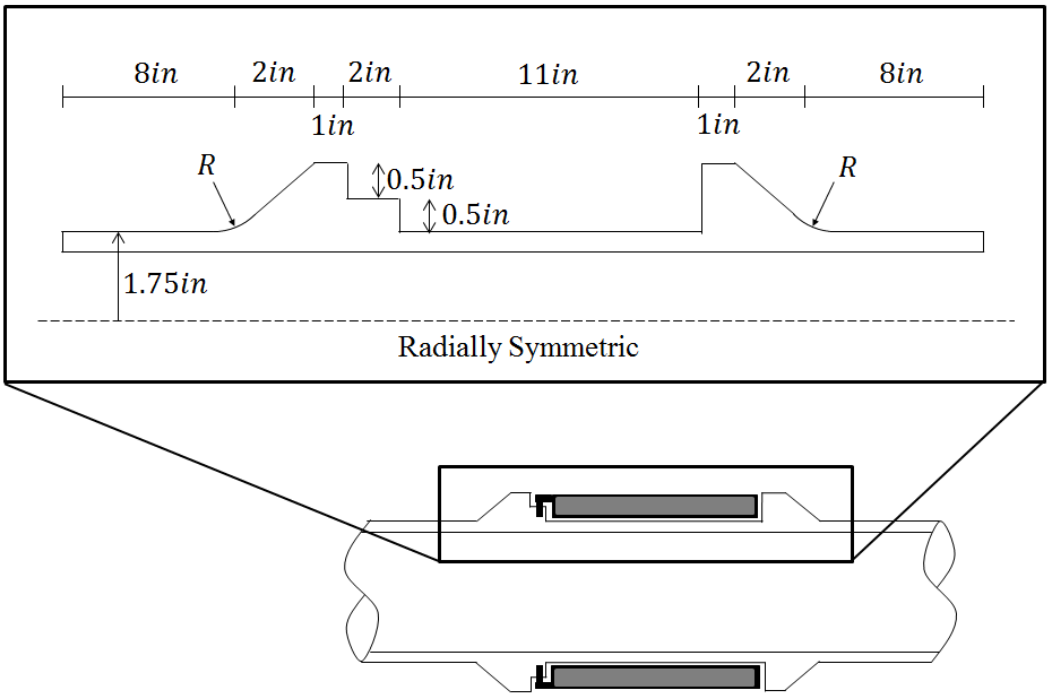

Figure 65. Modified Production Tube: Fixed-Free Geometry

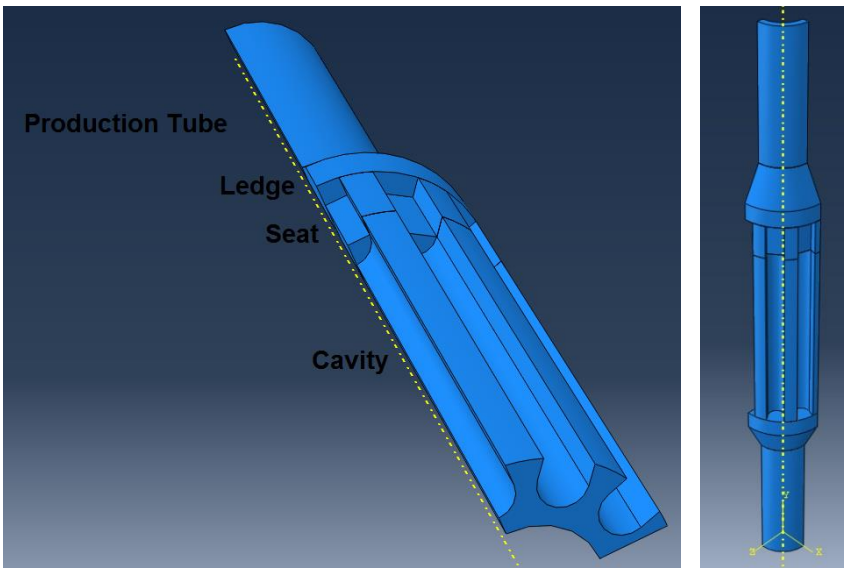

Figure 66. Modified Production Tube: Fixed-Free Abaqus Model

A course mesh is generated utilizing quadratic tetrahedral elements (element size ~0.125in); see Figure 67. The results for eight strength load cases are shown in Table 39.

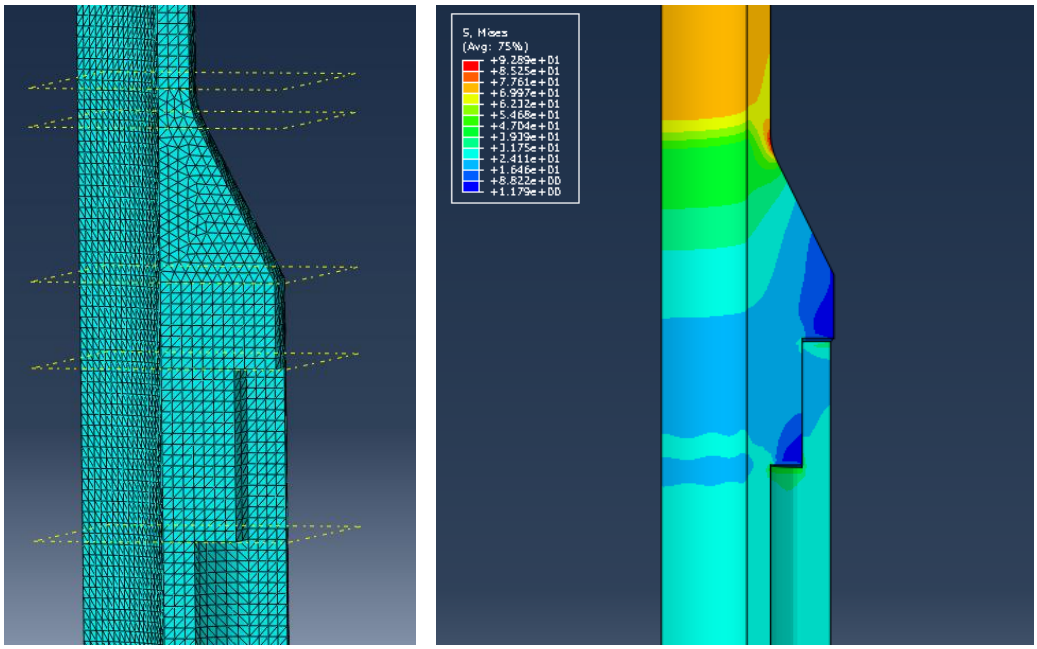

Figure 67. FE Course Tetrahedral Mesh (Left) and Sample Von Mises Stress Output (Right)

Table 39. Course Mesh Results

Load Case	p_i (ksi)	p_o (ksi)	Axial Load* (kip)	Von Mises Stresses (ksi)		
				Production Tube - Loc. 1	Fillet - Loc. 5	Seat/Cavity
1	10	0	225	63	78	47
2	10	0	−107	63	50	54
3	0	10	124	75	62	56
4	0	10	−305	72	88	44
5	10	10	225	71	91	30
6	10	10	−107	19	24	7
7	10	10	124	44	56	17
8	10	10	−305	73	93	30

*(+) = *Tension*

Radial Fillet: $2in$

Based on the results of Table 39 a refined mesh is generated: the element size is reduced to $\sim 0.0625in$ (i.e. half of the course mesh size) and the mesh is further refined near the fillet (~0.0208in); the refined mesh is shown in Figure 68. The refined mesh result for each load case is shown in Table 40. Although stress concentrations are still apparent at the fillet (i.e. location 5), the geometry of both the fillet and ledge is not limited, meaning that the geometry in this area can be adjusted to reduce the stress concentration.

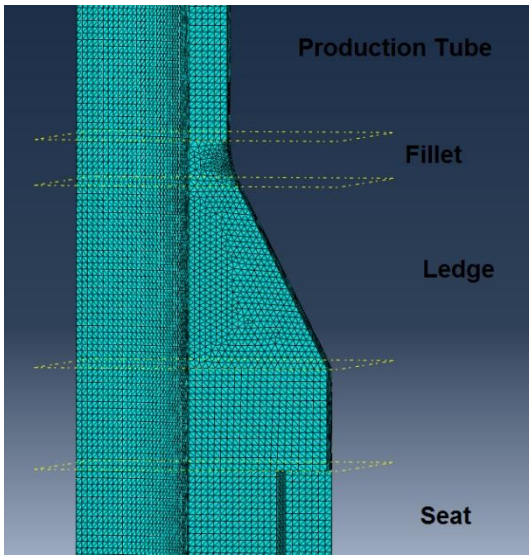

Figure 68. FE Refined Tetrahedral Mesh

Table 40. Refined Mesh Results

Load Case	p_i (ksi)	p_o (ksi)	Axial Load* (kip)	Von Mises Stresses (ksi)		
				Production Tube - Loc. 1	Fillet - Loc. 5	Seat/Cavity
1	10	0	225	64	78	50
2	10	0	−107	64	50	56
3	0	10	124	75	66	60
4	0	10	−305	72	90	51
5	10	10	225	71	89	29
6	10	10	−107	19	25	8
7	10	10	124	44	56	18
8	10	10	−305	73	91	30

*(+) = *Tension*
Radial Fillet: 2in

4.3.6. Comparing Configurations A and B

The harvester cavity cross sectional area provided by Configuration A was shown in Table 32 and Table 33 to be $7.35in^2$. For Configuration B, the available cross sectional areas were found to be $0.332in^2$ and $0.567in^2$ for $0.8in$ and $1.0in$ LTH outer diameters (for the optimal case of a $0.075in$ wall thickness; see Table 36 and Table 37). This equates to a total cross sectional area of $3.32in^2$ and $5.67in^2$ for 10 LTHs or $3.98in^2$ and $6.80in^2$ if 12 LTHs are used. In the limiting cases, Configuration A provides between 8% and 121% more cross sectional area than Configuration B and is not subject to the length restrictions imposed on

Configuration B LTHs. From a practical standpoint, the wiring together of 12 individual LTHs, which will be operating in a hostile downhole environment, is unattractive; all of the components for Configuration A can be wired together in the same harvester cavity behind the outer coaxial pipe. Since Configuration A provides (1) a larger cross sectional area in which to place an energy harvesting system and (2) a more robust design, the further design and investigation of Configuration B will not be pursued.

4.4. Design Summary

The Configuration A design process described in Section 4.3 was repeated for two additional steel grades: $J55$ ($55ksi$ yield strength) and $T95$ ($95ksi$ yield strength). A full design using $J55$ steel was quickly abandoned as the design pressure was found to be less than $5ksi$ (i.e. less than half of the LANL targeted design pressure; see Section 4.3.1.1). The results of the $L80$ and $T95$ cases are summarized in Table 41.

Table 41. Configuration A Design Summary

Material Grade		Above Packer	Below Packer
$L80$	Production Tube Outer Diameter (in)	3.50	3.50
	Production Tube Wall Thickness (in)	0.375	0.375
	Casing Outer Diameter (in)	7.00	7.00
	Casing Wall Thickness (in)	0.453	0.453
	Outer Coaxial Pipe Outer Diameter (in)	5.50	5.50
	Outer Coaxial Pipe Wall Thickness(in)	0.415	0.415
	Design Pressure (ksi)	9.3	10.1
	Maximum Tension (kip)	115	15
	Maximum Compression (kip)	90	50
	Unloaded Radial Width (in)	0.585	0.585
	Loaded Radial Width (in)	0.573	0.573
	Harvester Cavity Cross Sectional Area (in^2)	7.35	7.35
$T95$	Production Tube Outer Diameter (in)	3.50	3.50
	Production Tube Wall Thickness (in)	0.375	0.375
	Casing Outer Diameter (in)	7.00	7.00
	Casing Wall Thickness (in)	0.540	0.540
	Outer Coaxial Pipe Outer Diameter (in)	5.50	5.50
	Outer Coaxial Pipe Wall Thickness(in)	0.500	0.500
	Design Pressure (ksi)	12.6	13.2
	Maximum Tension (kip)	90	15
	Maximum Compression (kip)	90	55
	Unloaded Radial Width (in)	0.500	0.500
	Loaded Radial Width (in)	0.490	0.490
	Harvester Cavity Cross Sectional Area (in^2)	6.15	6.15

In most cases the load carrying capacity of the housing was limited by stress concentrations at the internal fillets (i.e. location 2 in Figure 59). While the fillet design could be optimized it is expected that the housing design, as a whole, will be improved during the next design iteration. Based on a conversation with a consultant in the oil and gas industry (W. Phillips, personal communication, May 15, 2015), two alternative designs were conceptualized and are presented in Figure 69. These design alternatives will likely alleviate the fillet stress concentrations found in Configuration A but introduce additional design complexity with the inclusion of threaded connections. Since the results from Table 41 provide reasonable lower bound geometries, specifically, maximum radial widths available to house an energy harvesting system, the design alternatives are not investigated here.

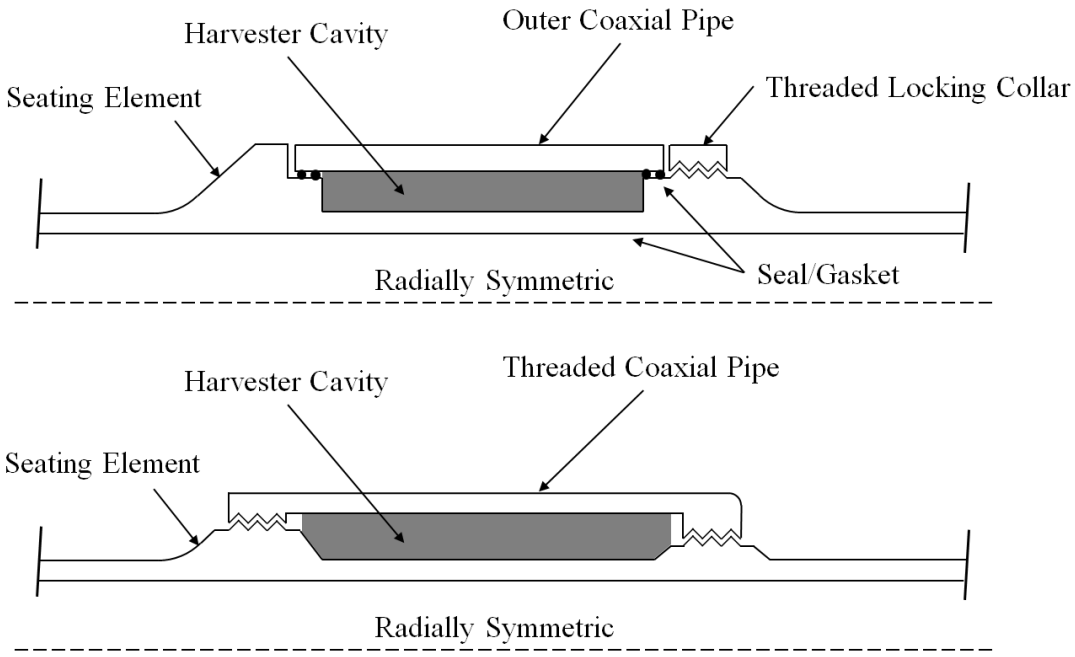

Figure 69. Configuration A Design Alternatives

A portion of Chapter 4 has been published in SPIE Smart Structures and Materials+ Nondestructive Evaluation and Health Monitoring, Eric Kjolsing and Michael Todd, 2016. The title of this paper is "Gauging the Feasibility of a Downhole Energy Harvesting System Through a Proof-of-Concept Study". The dissertation author was the primary investigator and author of this paper.

Chapter 5
Estimating Harvestable Power

5.1. Overview

Two scripts (programs written in MATLAB) are developed to estimate harvestable power for user-defined energy harvester configurations. The first script (FS) utlizes an uncoupled electromechanical model to analyze configurations with multiple energy harvesting elements. The second script (SS) utilizes coupled equations of motion to analyze a single energy harvesting element. By using coupled equations the SS results in a more accurate power estimate than the FS, but is more computationally expensive to execute. In addition, the inputs required to execute the SS are significant when compared to the FS, requiring the user to invest additional time in setting up the SS prior to execution. In practical application, the FS is intended to be an inexpensive order of magnitude power estimate. If the results from the FS look promising (i.e. the estimated power output is greater than the users required power output) than the user can invest resources in executing the SS. However, if the FS power output is significantly less than what the user requires, than the user can save resources by not executing the SS. If desired, the SS can be executed without executing the FS.

5.1.1. Transduction Mechanism

Subject to the stated assumptions and considered geometries, the minimum radial width available in which to place an energy harvesting system was found in Chapter 4 to be $0.49in$ (see Table 41). While miniaturized energy harvesting elements can be custom designed and fabricated to fit within this space, it is more cost effective to use commercially available harvesters.

From Section 1.2.4, the two transduction mechanisms under consideration are piezoelectric and electromagnetic transducers. While pizeoelectric transducers are available from a variety of manufacturers (e.g. Mide Corporation, American Piezo Ceramics, PI Ceramic, Piezo Systems, Micromechatronics, etc.), electromagnetic transducers are not as commerically available. In addition, those electromagnetic transducers that are commercially available were found with geometries exceeding the available radial width [199]; Chalasani and Conrad (2008) [21] noted that electromagnetic materials are bulky. Based on the available radial width, it is assumed that the deployed energy harvesting system will utilize cantilever piezoelectric elements driven by the vibration of the production tube.

It is important to note that when selecting commercially available piezoelectric energy harvesters, the user must ensure that the operational bounds perscribed by the manufacturer are not exceeded.

5.2. FS – Order of Magnitude Power Estimate

To generate an initial power estimate, the piezoelectric transducer is modeled as a single degree of freedom (SDOF) oscillator in a lumped parameter model. The power estimate is based on a viscous damping model where the maximum energy that might be extracted by the transducer is related to an “electric” viscous damping term included in the system. That is,

the mechanical power dissipated by the "electric" viscous damping term is considered the maximum power that might be harvested by the transducer. This type of model was introduced by Williams and Yates (1996) [200], and later used by Roundy et al. (2003) [201] and Trimble (2007) [202]. The model is widely used and is summarized by Kim et al. in Chapter 1 of Priya and Inman (2009) [28].

There are several limitations to this type of model. First, the model implicitly assumes that the majority of the power output stems from the transducers first mode of vibration as this is the only mode the SDOF oscillator can represent. Second, the transducer beam mass and tip mass are treated as a lumped term which may yield inaccurate results if the tip mass is small relative to the beam mass [203]. Lastly, the system neglects the coupling of the electric and mechanical equations of motion which may lead to an inaccurate prediction of the optimum load resistance and fails to predict the variation of the resonant frequency with changing load resistance [28]. The limitations of the model must be weighed against the models benefits, namely, simplicity and computational efficiency. Since the FS is used to explore a wide range of inputs quickly, and because the SS power estimate utilizes a more accurate model (i.e. coupled equations of motion), this simplified model is reasonable for its intended purpose.

The script returns the suggested base natural frequencies (i.e. the natural freuqency of each energy harvester on day zero at room temperature) and expected power output of the user-defined configuration.

5.2.1. Derivation of Power Estimate

Consider the SDOF oscillator shown in Figure 70 where m_{eq} represents the equivalent mass, $c_{eq} = c_m + c_e$ represents the equivalent viscous damping (mechanical and electric), c_a represents the damping due to the surrounding fluid, and k_{eq} represents the equivalent stiffness

[203]. The oscillator is excited by a base motion, $y(t)$, resulting in an absolute displacement, $x(t)$.

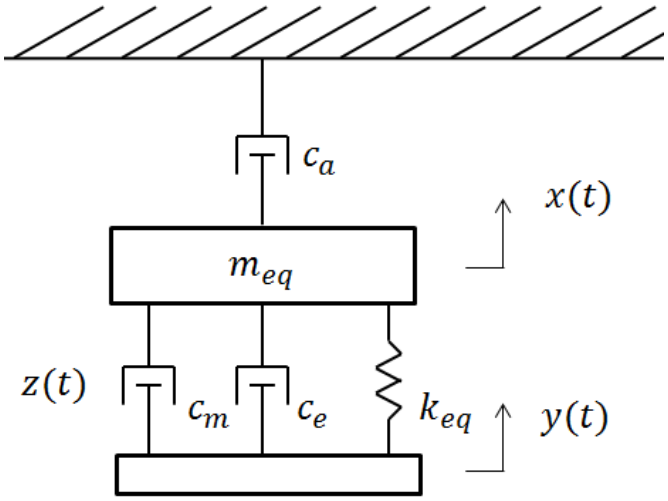

Figure 70. SDOF Oscillator

Force equilibrium leads to the familiar

$$m_{eq}\ddot{x}(t) + c_{eq}\big(\dot{x}(t) - \dot{y}(t)\big) + k_{eq}\big(x(t) - y(t)\big) + c_a\dot{x}(t) = 0. \tag{222}$$

Defining the relative displacement as

$$z(t) = x(t) - y(t), \tag{223}$$

Eq. (222) can be rewritten as

$$m_{eq}\ddot{z}(t) + \big(c_{eq} + c_a\big)\dot{z}(t) + k_{eq}z(t) = -m_{eq}\ddot{y}(t) - c_a\dot{y}(t). \tag{224}$$

Assuming zero initial conditions, taking the Laplace transform of Eq. (224) leads to

$$Z(s)\big[m_{eq}s^2 + \big(c_{eq} + c_a\big)s + k_{eq}\big] = -Y(s)[m_{eq}s^2 + c_as], \tag{225}$$

where $Z(s)$ and $Y(s)$ represent the Laplace transforms of $z(t)$ and $y(t)$, respectively. The transfer function is written as

$$H(s) = \frac{Z(s)}{Y(s)} = -\frac{m_{eq}s^2 + c_as}{m_{eq}s^2 + (c_{eq} + c_a)s + k_{eq}}. \tag{226}$$

For the case of light air damping (i.e. small c_a) the transfer function can be reduced to

$$H(s) = \frac{Z(s)}{Y(s)} = -\frac{m_{eq}s^2}{m_{eq}s^2 + c_{eq}s + k_{eq}}. \tag{227}$$

To return to the frequency domain let $s = i\omega$,

$$H(\omega) = \frac{m_{eq}\omega^2}{-m_{eq}\omega^2 + c_{eq}i\omega + k_{eq}}. \tag{228}$$

Dividing the numerator and denominator by m_{eq} and taking $\omega_n = \sqrt{(k_{eq}/m_{eq})}$ and $\zeta_{eq} = c_{eq}/(2m_{eq}\omega_n)$ to be the natural frequency and equivalent viscous damping ratio, the transfer function can be written as

$$H(\omega) = \frac{\omega^2}{(\omega_n^2 - \omega^2) + 2\zeta_{eq}\omega_n i\omega}. \tag{229}$$

The displacement response (in the frequency domain) can then be written as

$$Z(\omega) = H(\omega)Y(\omega), \tag{230}$$

where $Y(\omega)$ and $Z(\omega)$ are the Fourier transforms of the base motion $y(t)$ and relative motion $z(t)$, respectively. The relative motion can be found in the time domain by taking an inverse Fourier transform of $Z(\omega)$.

Turning to the power estimate, the instantaneous power related to the equivalent damper is written as

$$P_{inst}(t) = F_{damping}(t) * Velocity(t) = \left(c_{eq}\dot{z}(t)\right) * \dot{z}(t) = c_{eq}\left(\dot{z}(t)\right)^2. \tag{231}$$

The damping term can be split into its mechanical and electrical contributions, leading to the instantaneous power attributed to the electric damper as

$$P_{inst,e}(t) = c_e\left(\dot{z}(t)\right)^2. \tag{232}$$

The average power extracted by the electric damper over some time period T is then

$$P_{avg,e} = \frac{1}{T}\int_0^T P_{inst}(t)dt = \frac{c_e}{T}\int_0^T \left(\dot{z}(t)\right)^2 dt. \tag{233}$$

The maximum relative displacement of the mass is simply found as

$$z_{max} = Max[z(t)]. \tag{234}$$

5.2.1.1. Single Term Approximation

For arbitrary base motion, the power estimate of Eq. (233) is solved numerically. To facilitate an analytical discussion, consider the nature of the transfer function, $H(\omega)$, re-written as

$$H(\omega) = \frac{\omega^2}{(\omega_n^2-\omega^2)+2\zeta_{eq}\omega_n i\omega} = \frac{\left(\frac{\omega}{\omega_n}\right)^2}{\left(1-\left(\frac{\omega}{\omega_n}\right)^2\right)+2\zeta_{eq} i\left(\frac{\omega}{\omega_n}\right)} = \frac{r^2}{(1-r^2)+2\zeta_{eq} ir}. \tag{235}$$

where $r = \omega/\omega_n$ represents a frequency ratio. The magnitude of the transfer function is plotted in Figure 71 for various equivalent damping ratios (ζ_{eq}). The transfer function is seen to act like a narrow band-pass filter where only vibrations around $r \approx 1$ significantly contribute to the displacement response.

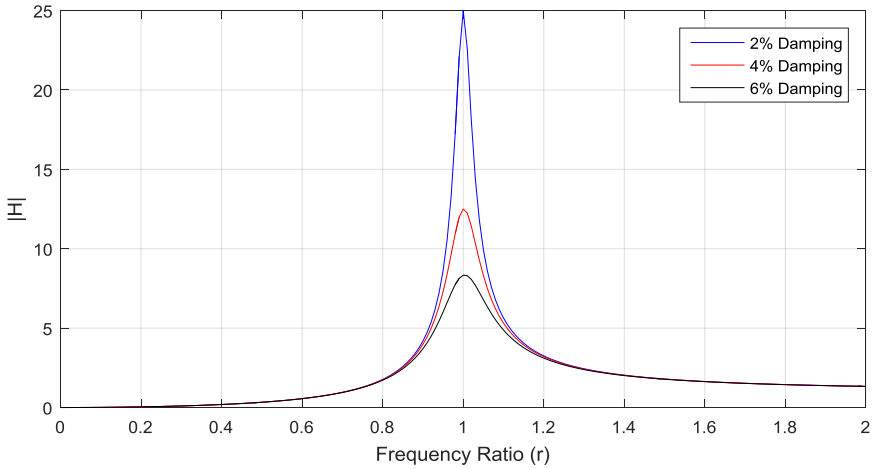

Figure 71. Transfer Function Magnitude

If the support acceleration is written in terms of a Fourier series

$$\ddot{y}(t) = \sum_{i=0}^{\infty} A_i \cos(\omega_i t), \tag{236}$$

the band-pass property of the SDOF system can be used to reduce the support acceleration to a single driving sinusoid ($\ddot{y}_s(t)$) with (a) the driving frequency set to the natural frequency of the SDOF oscillator and (b) the magnitude of acceleration set to that corresponding to the natural frequency, i.e.

$$\ddot{y}(t) = \sum_{i=0}^{\infty} A_i \cos(\omega_i t) \;\rightarrow\; \ddot{y}_s(t) = A\cos(\omega t)|_{A=A_n;\omega=\omega_n}. \tag{237}$$

Since the single term driving acceleration is sinusoidal, the resulting steady state motion of the SDOF oscillator will be a phase/amplitude shifted sinusoid at the same driving frequency, that is

$$\begin{aligned} z_s(t) &= B\cos(\omega t - \phi)|_{\omega=\omega_n} \\ \dot{z}_s(t) &= -B\omega\sin(\omega t - \phi)|_{\omega=\omega_n} \\ \ddot{z}_s(t) &= -B\omega^2\cos(\omega t - \phi)|_{\omega=\omega_n} \end{aligned} \tag{238}$$

Following the derivation by Rao (2004) [204] and taking c_a to be small, combine Eq. (224), Eq. (237) and Eq. (238)

$$\begin{aligned} m_{eq}\big(-B\omega^2\cos(\omega t - \phi)\big) + c_{eq}\big(-B\omega\sin(\omega t - \phi)\big) + k_{eq}\big(B\cos(\omega t - \phi)\big) = \\ -m_{eq}\big(A\cos(\omega t)\big). \end{aligned} \tag{239}$$

The terms can be grouped as

$$B\{[-m_{eq}\omega^2 + k_{eq}]\cos(\omega t - \phi) - [c_{eq}\omega]\sin(\omega t - \phi)\} = [-m_{eq}A]\cos(\omega t). \tag{240}$$

Noting the trigonometric relationships

$$\begin{aligned} \cos(\omega t - \phi) &= \cos(\omega t)\cos(\phi) + \sin(\omega t)\sin(\phi), \\ \sin(\omega t - \phi) &= \sin(\omega t)\cos(\phi) - \cos(\omega t)\sin(\phi), \end{aligned} \tag{241}$$

substitute Eq. (241) into Eq. (240)

$$\begin{aligned} B\{[-m_{eq}\omega^2 + k_{eq}]\big(\cos(\omega t)\cos(\phi) + \sin(\omega t)\sin(\phi)\big) - [c_{eq}\omega]\big(\sin(\omega t)\cos(\phi) - \\ \cos(\omega t)\sin(\phi)\big)\} = [-m_{eq}A]\cos(\omega t). \end{aligned} \tag{242}$$

The coefficients of $\cos(\omega t)$ and $\sin(\omega t)$ can be equated as

$$\begin{aligned} B\cos(\omega t)\{[-m_{eq}\omega^2 + k_{eq}]\cos(\phi) + [c_{eq}\omega]\sin(\phi)\} = [-m_{eq}A]\cos(\omega t), \\ B\sin(\omega t)\{[-m_{eq}\omega^2 + k_{eq}]\sin(\phi) - [c_{eq}\omega]\cos(\phi)\} = 0. \end{aligned} \tag{243}$$

The second equality in Eq. (243)

$$[-m_{eq}\omega^2 + k_{eq}]\sin(\phi) = [c_{eq}\omega]\cos(\phi), \tag{244}$$

leads to

$$\tan(\phi) = \frac{\sin(\phi)}{\cos(\phi)} = \frac{c_{eq}\omega}{-m_{eq}\omega^2 + k_{eq}} \;\rightarrow\; \phi = \arctan\left(\frac{c_{eq}\omega}{k_{eq} - m_{eq}\omega^2}\right). \tag{245}$$

Note the trigonometric relationships

$$\begin{aligned} \cos\big(\arctan(a)\big) &= \frac{1}{\sqrt{1+a^2}}, \\ \sin\big(\arctan(a)\big) &= \frac{a}{\sqrt{1+a^2}}. \end{aligned} \tag{246}$$

Having solved for ϕ in Eq. (245), Eq. (246) can be written as

$$\begin{aligned} \cos(\phi) &= \frac{1}{\sqrt{1+\left(\frac{c_{eq}\omega}{k_{eq}-m_{eq}\omega^2}\right)^2}} = \frac{k_{eq}-m_{eq}\omega^2}{\left[\left(k_{eq}-m_{eq}\omega^2\right)^2+\left(c_{eq}\omega\right)^2\right]^{\frac{1}{2}}}, \\ \sin(\phi) &= \frac{\frac{c_{eq}\omega}{k_{eq}-m_{eq}\omega^2}}{\sqrt{1+\left(\frac{c_{eq}\omega}{k_{eq}-m_{eq}\omega^2}\right)^2}} = \frac{c_{eq}\omega}{\left[\left(k_{eq}-m_{eq}\omega^2\right)^2+\left(c_{eq}\omega\right)^2\right]^{\frac{1}{2}}}. \end{aligned} \tag{247}$$

Eq. (247) and the first equality in Eq. (243) can be combined as

$$B\left\{\frac{\left(k_{eq}-m_{eq}\omega^2\right)^2}{\left[\left(k_{eq}-m_{eq}\omega^2\right)^2+\left(c_{eq}\omega\right)^2\right]^{\frac{1}{2}}} + \frac{\left(c_{eq}\omega\right)^2}{\left[\left(k_{eq}-m_{eq}\omega^2\right)^2+\left(c_{eq}\omega\right)^2\right]^{\frac{1}{2}}}\right\} = \left[-m_{eq}A\right]. \tag{248}$$

Simplifying the left hand side

$$B\left\{\left[\left(k_{eq} - m_{eq}\omega^2\right)^2 + \left(c_{eq}\omega\right)^2\right]^{\frac{1}{2}}\right\} = \left[-m_{eq}A\right], \tag{249}$$

leads to

$$B = \frac{-m_{eq}A}{\left[\left(k_{eq}-m_{eq}\omega^2\right)^2+\left(c_{eq}\omega\right)^2\right]^{\frac{1}{2}}}. \tag{250}$$

Having solved for the phase (Eq. (245)) and amplitude (Eq. (250)), the single-term SDOF response (Eq. (238)) is fully defined.

The instantaneous power estimate (i.e. Eq. (231)) is written as

$$P_{inst}(t) = c_{eq}\left(\dot{z}_s(t)\right)^2 = c_{eq}\left[\frac{-m_{eq}A}{\left[\left(k_{eq}-m_{eq}\omega^2\right)^2+\left(c_{eq}\omega\right)^2\right]^{\frac{1}{2}}}\right]^2 \omega^2\sin^2(\omega t - \phi), \tag{251}$$

where

$$\left(\dot{z}_s(t)\right)^2 = B^2\omega^2\sin^2(\omega t - \phi), \tag{252}$$

and Eq. (250) have been utilized. The average power over some time period T can be written as

$$P_{avg} = \frac{1}{T}\int_0^T P_{inst}(t)dt = \frac{c_{eq}{m_{eq}}^2 A^2\omega^2}{\left(k_{eq}-m_{eq}\omega^2\right)^2+\left(c_{eq}\omega\right)^2}\left[\frac{1}{T}\int_0^T \sin^2(\omega t-\phi)dt\right]. \tag{253}$$

Note that the bracketed term is simply the signal power of a single harmonic function and is equal to $1/2$. The average power can then be simplified to

$$P_{avg} = \frac{c_{eq}{m_{eq}}^2\omega^2}{\left(k_{eq}-m_{eq}\omega^2\right)^2+\left(c_{eq}\omega\right)^2}\left[\frac{A^2}{2}\right]. \tag{254}$$

Dividing the numerator and denominator by ${m_{eq}}^2$ leads to

$$P_{avg} = \frac{c_{eq}\omega^2}{\left(\frac{k_{eq}}{m_{eq}}-\omega^2\right)^2+\left(\frac{c_{eq}\omega}{m_{eq}}\right)^2}\left[\frac{A^2}{2}\right]. \tag{255}$$

Eq. (255) can be rewritten using $\omega_n = \sqrt{(k_{eq}/m_{eq})}$ and $c_{eq} = 2m_{eq}\omega_n\zeta_{eq}$ as

$$P_{avg} = \frac{(2m_{eq}\omega_n\zeta_{eq})\omega^2}{\left(\omega_n^2-\omega^2\right)^2+\left(\frac{(2m_{eq}\omega_n\zeta_{eq})\omega}{m_{eq}}\right)^2}\left[\frac{A^2}{2}\right]. \tag{256}$$

Dividing the numerator and denominator by $1/\omega_n^4$ leads to

$$P_{avg} = \frac{m_{eq}\zeta_{eq}\frac{\omega^2}{\omega_n^3}}{\left(1-\left(\frac{\omega}{\omega_n}\right)^2\right)^2+\left(2\zeta_{eq}\left(\frac{\omega}{\omega_n}\right)\right)^2}[A^2]. \tag{257}$$

Setting $\omega = \omega_n$ and $A = A_n$ (recall Eq. (237) and Eq. (238)) leads to

$$P_{avg} = \frac{m_{eq}\zeta_{eq}{A_n}^2}{4\omega_n\zeta_{eq}^2}. \tag{258}$$

Recall that the equivalent damper is composed of both a mechanical damper (which accounts for typical damping behavior) and an "electric" damper (which accounts for the energy extracted by the piezoelectric EH)

$$\begin{aligned} c_{eq} &= c_m + c_e, \\ \zeta_{eq} &= \zeta_m + \zeta_e. \end{aligned} \tag{259}$$

Rewrite Eq. (258) in terms of the two damping components

$$P_{avg} = \frac{m_{eq}(\zeta_m+\zeta_e)A_n{}^2}{4\omega_n(\zeta_m+\zeta_e)^2} = \frac{m_{eq}\zeta_m A_n{}^2}{4\omega_n(\zeta_m+\zeta_e)^2} + \frac{m_{eq}\zeta_e A_n{}^2}{4\omega_n(\zeta_m+\zeta_e)^2} = P_{avg,m} + P_{avg,e}, \tag{260}$$

where the first and second terms represents the average power dissipated by the mechanical and "electric" damper, respectively. The maximum power dissipated by the "electric" damper can be found from

$$\frac{dP_{avg,e}}{d\zeta_e} = 0, \tag{261}$$

leading to

$$\frac{d}{d\zeta_e}\left[\frac{m_{eq}\zeta_e A_n{}^2}{4\omega_n(\zeta_m+\zeta_e)^2}\right] = \frac{m_{eq}A_n{}^2}{4\omega_n}\left[\frac{-2\zeta_e}{(\zeta_m+\zeta_e)^3} + \frac{1}{(\zeta_m+\zeta_e)^2}\right] = 0. \tag{262}$$

From Eq. (262) the maximum power is seen to occur when $\zeta_m = \zeta_e$. Thus,

$$P_{avg,e-max} = \left.\frac{m_{eq}\zeta_e A_n{}^2}{4\omega_n(\zeta_m+\zeta_e)^2}\right|_{\zeta_m=\zeta_e} = \frac{m_{eq}A_n{}^2}{16\omega_n\zeta_m} = \frac{m_{eq}}{8\zeta_m}\left[\frac{A_n^2}{2\omega_n}\right] = \frac{m_{eq}}{8\zeta_m}\left[\frac{P_{signal}}{\omega_n}\right]. \tag{263}$$

Turning to the displacement, recall that the relative displacement of the mass is given by Eq. (238), repeated here for convenience

$$z_s(t) = B\cos(\omega t - \phi)|_{\omega=\omega_n}. \tag{264}$$

The maximum relative displacement occurs when $\cos(\omega t - \phi) = 1$, meaning that the maximum relative displacement is given by $|B|$

$$z_{s-max} = |B| = \left.\frac{|m_{eq}A|}{\left[\left(k_{eq}-m_{eq}\omega^2\right)^2+\left(c_{eq}\omega\right)^2\right]^{\frac{1}{2}}}\right|_{A=A_n;\omega=\omega_n} = \frac{|A_n|}{2\zeta_{eq}\omega_n^2}. \tag{265}$$

Recall that for the maximum power output $\zeta_m = \zeta_e$, thus

$$z_{s-max}|_{P_{avg,e-max}} = \frac{|A_n|}{4\zeta_m\omega_n^2}. \tag{266}$$

5.2.2. Practical Application

The user begins by entering acceleration time histories (also termed acceleration profiles) of the production tube at the harvester location, which represent the ground motions driving the attached energy harvesting elements. The acceleration time histories (a_x, a_y, and a_z) are entered for each global Cartesian coordinate (with the z-axis taken to be along the

longitudinal axis of the production string). The acceleration time histories can be defined by actual downhole accelerometer data or can be artificially generated as needed. Since the acceleration time histories are generally non-stationary over the life of the well (due to changes in production rate, hydrocarbon density, etc.), the acceleration profiles must be descretized by the user such that the profiles are locally stationary.

The user then enters an expected operating schedule that depicts (1) the expected temperature profile over the life of the well and (2) the time period over which each acceleration profile is valid. A sample schedule is shown in Figure 72 where three acceleration profiles are shown.

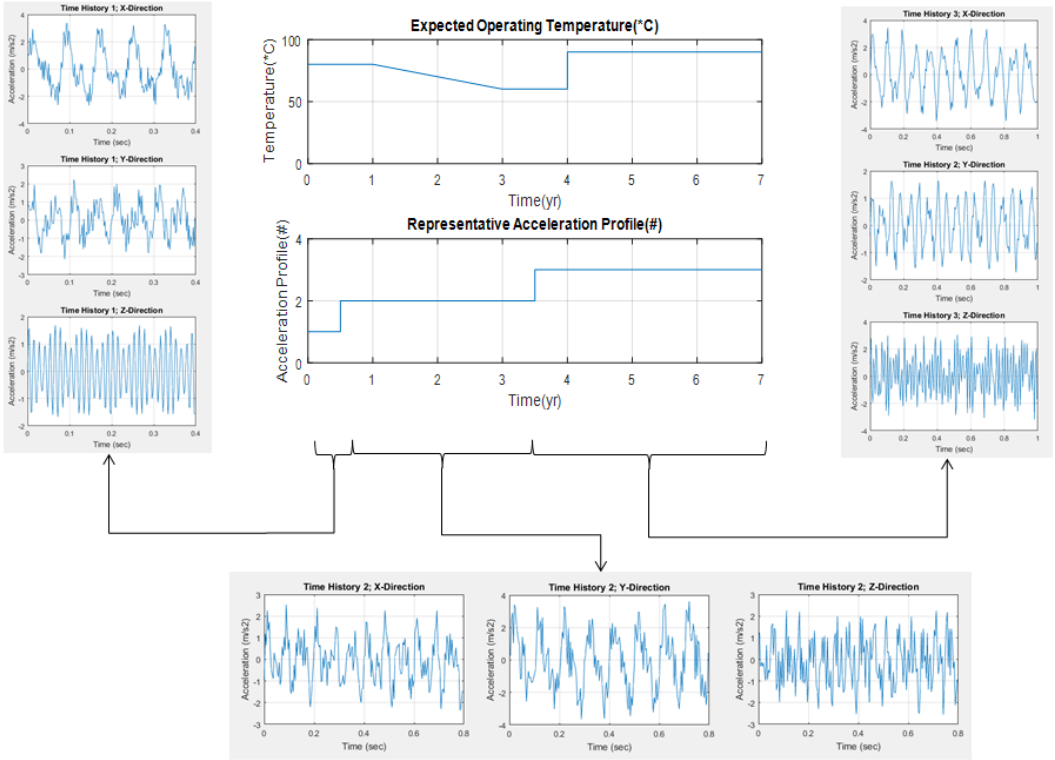

Figure 72. Sample Operating Schedule

For each acceleration profile, the global x- and y-axis acceleration time histories (a_x and a_y) are transformed to provide normal and tangential acceleration time histories at all relevant spatial locations (i.e. from $\theta = 0°:10°:350°$) as

$$a_n = a_x \cos(\theta) + a_y \sin(\theta)$$
$$a_t = -a_x \sin(\theta) + a_y \cos(\theta) \tag{267}$$

This results in 36 time histories ($\ddot{y}(t)$ in Eq. (224)) for each of the normal and tangential directions plus one time history for the z-direction (73 total time histories for each acceleration profile). A visual depicting the relevant coordinate system is provided in Figure 73.

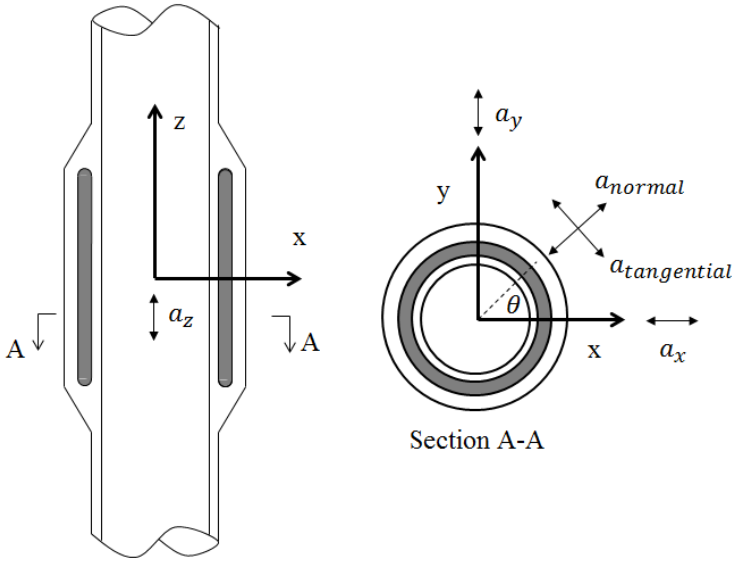

Figure 73. Relevant Coordinate System

Each of the 73 acceleration time histories are transformed into the frequency domain through a Fourier transform. To determine the displacement response in the frequency domain (i.e. $Y(\omega)$ of Eq. (230)) the Fourier transforms of the acceleration time histories are divided by $(i\omega)^2$, that is from Eq. (58)

$$Fourier\ Transform[\ddot{y}(t)] = (i\omega)^2\, Y(\omega), \tag{268}$$

or

$$Y(\omega) = \frac{Fourier\ Transform[\ddot{y}(t)]}{(i\omega)^2}. \tag{269}$$

Note that for low frequencies (as ω goes to zero) the denominator dominates the expression leading to erroneous displacement results. To correct for this, a rectangular window is used to

zero out Fourier coefficients for frequencies falling below a user specified truncation frequency. As an example, consider Figure 74 where the acceleration time history of interest is a simple sinusoid: $\ddot{y}(t) = (1\,m/s^2)\sin(2\pi(50Hz)t)\,;\ 0s \le t \le 7s$. When Eq. (269) is utilized the Fourier coefficients near the lower frequencies are seen to increase significantly. To obtain the correct displacement time history $(y(t))$, Fourier coefficients falling below $35Hz$ are set to zero. The resulting displacement time history is improved with the appropriate maximum displacement amplitude of $(1\,m/s^2)/(2\pi(50Hz))^2 = 1.01e-5m$ approximately obtained.

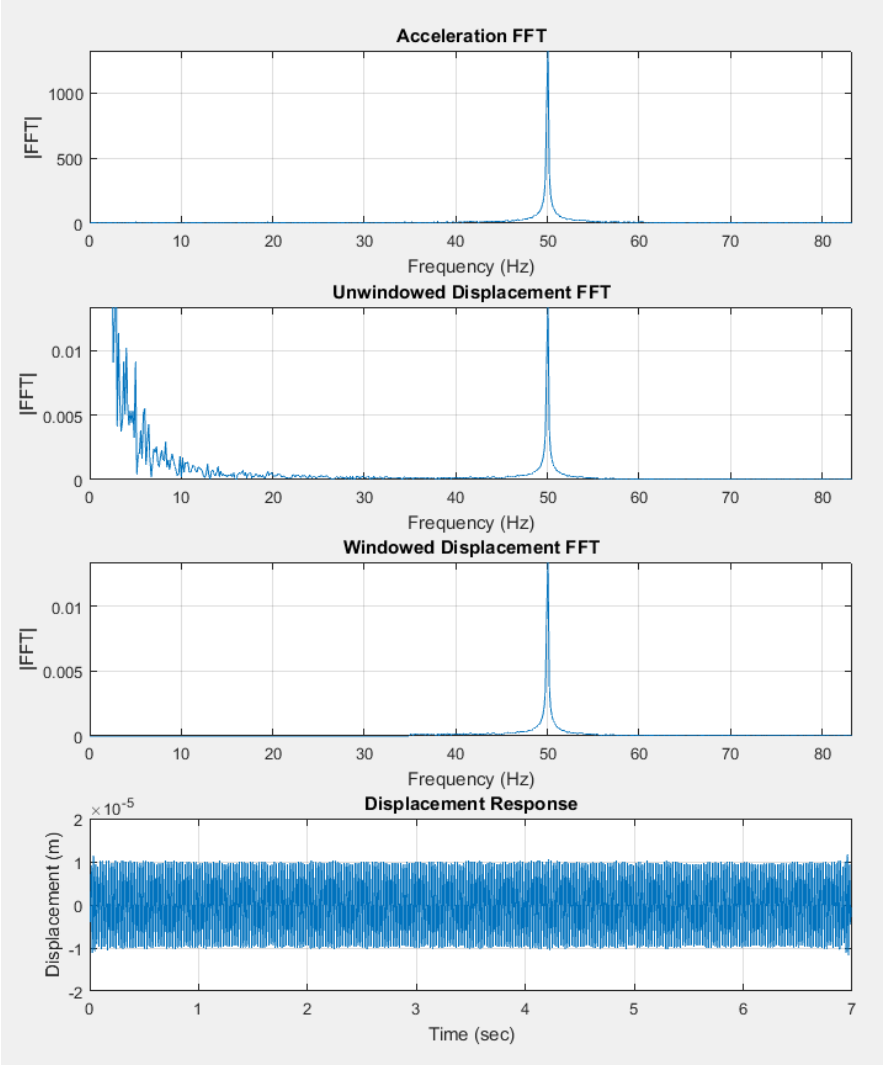

Figure 74. Correcting the Displacement Response in the Frequency Domain

The transfer function (Eq. (229)) is dependent on the equivalent damping ratio (ζ_{eq}) and natural frequency (ω_n) of the transducer. The user can specify one mechanical damping ratio (ζ_m) and several "electric" damping ratios (ζ_e) which combine to form the equivalent damping ratio ($\zeta_{eq} = \zeta_m + \zeta_e$). Since the natural frequency will change over time (due to degradation) and with changing temperature (softening of the system stiffness), the time and temperature dependent effects need to be accounted for. From Appendix G, changes to the Young's modulus, inertia, or beam length due to time or temperature are seen to cause a shift in the natural frequency of the transducer (the mass is assumed unchanging); the percent change in frequency was shown to be

$$\%\Delta\omega_n = \left[\sqrt{\frac{(\%E_i)(\%I_i)}{(\%L_i)^3}} - 1\right], \tag{270}$$

To account for these changes, the user is asked to define time and temperature dependent changes to the (1) Young's modulus, (2) inertia, and (3) beam length with input tables. Since this is a preliminary analysis the user may choose to use approximate values (as exact values may not yet be known) or assume any/all of the effects are negligible. A sample user input is provided in Figure 75.

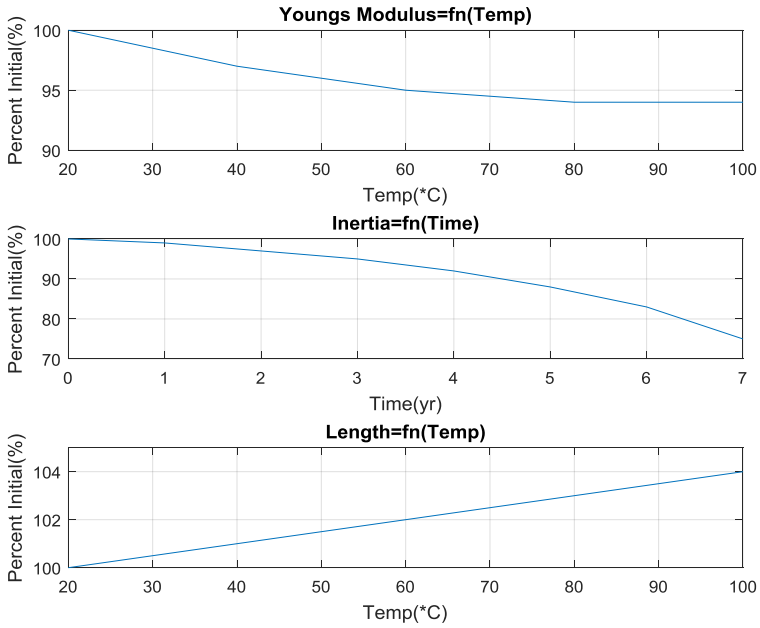

Figure 75. Time and Temperature Dependence: Sample Inputs

The final remaining user inputs are: (1) the window of time the user wants to maximize the power output $[T_{initial}: T_{final}]$, (2) the range of base frequencies and the discretization interval the user wishes to consider (these are the frequencies of the individual piezoelectric elements at day zero/room temperature) $[f_{n-lower}: df_n: f_{n-upper}]$, and (3) the location and orientation of each piezoelectric element. As an example of (3), a three element configuration designed to harvest tangential accelerations is shown in Figure 76 where the elements are spaced at $40°$, $120°$, and $350°$ from the global x-axis.

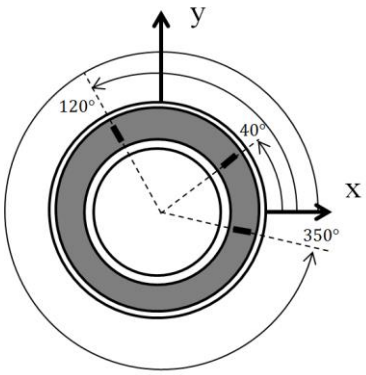

Figure 76. Example Three Harvester Configuration

5.2.2.1. Calculation Looping

The following analysis procedure describes the calculation sequence in the script. The first looping sequence calculates $\left(2\omega_{n,current}\right)/T * \int_0^T \left(\dot{z}(t)\right)^2 dt$ for all global angles, equivalent damping ratios, base frequencies of interest, and over the time domain of interest:

- The current time is set to the initial time specified by the user over which the user is interested in maximizing the power output ($T_{initial}$).
- Based on the current time the expected operating temperature and representative acceleration profiles are determined (see Figure 72).
- Based on the current time and operating temperature the percentage change in input parameters (Young's modulus, inertia, and beam length) are interpolated (see Figure 75).
- Use Eq. (270) to modify the base frequency (to account for time and temperature effects) and determine the frequency at the current time (i.e. the current natural frequency).
- Specify the equivalent damping ratio for the current realization.
- Using the current natural frequency and equivalent damping ratio, sample the transfer function ($H(\omega)$, Eq. (229)) at the same frequency spacing as the current Fourier transform ($Y(\omega)$) (corresponding to the representative acceleration profile at the current time step).
- For each global angle (θ), calculate the relative displacement response in the frequency domain ($Z(\omega)$) per Eq. (230).

- Calculate the inverse Fourier transform of $Z(\omega)$ to determine the displacement response in the time domain. Record the maximum absolute value (i.e. Eq. (234)).
- Calculate the relative velocity in the frequency domain as $(i\omega)(Z(\omega))$.
- Calculate the relative velocity in the time domain ($\dot{z}(t)$) by taking an inverse Fourier transform of $(i\omega)(Z(\omega))$.
- Square (point-wise) the relative velocity (i.e. $(\dot{z}(t))^2$).
- Use the trapezoidal rule to numerically integrate the relative velocity as $\frac{(2\omega_{n,current})}{T}\int_0^T \left(\dot{z}(t)\right)^2 dt$ (note Eq. (233)) where T is the duration of the signal.
- Repeat this looping through: (1) the time domain of interest $[T_{initial}: T_{final}]$, (2) the base frequencies of interest $[f_{n-lower}: f_{n-upper}]$, (3) the equivalent damping ratios considered, and (4) all global angles ($\theta = 0°: 10°: 350°$).

The second looping sequence generates a power estimate for each harvesting element. The output from the first looping sequence is multiplied by the equivalent mass of each harvester (m_{eq}) and the considered electric damping ratios (ζ_e,); the power estimates are made a function of $\alpha = 0°: 10°: 350°$, a global rotation angle illustrated in Figure 77.

In the third looping sequence, the power from each harvester, for each realization of α and ζ_e, is summed to provide an estimate of the total power all harvesters generate for that time period and configuration.

In the fourth looping sequence the power from each realization is integrated over the time domain of interest $[T_{initial}, T_{final}]$ to provide a scalar value. This scalar value is used as the optimization variable: for each global rotation angle α, the base frequencies and electric damping ratios that provide the largest scalar value is considered optimal as it maximizes the

total power over the entire time domain of interest (assuming the acceleration profiles are persistant).

This calculation sequence is best demonstrated with an example, which also provides an opportunity to verify the script.

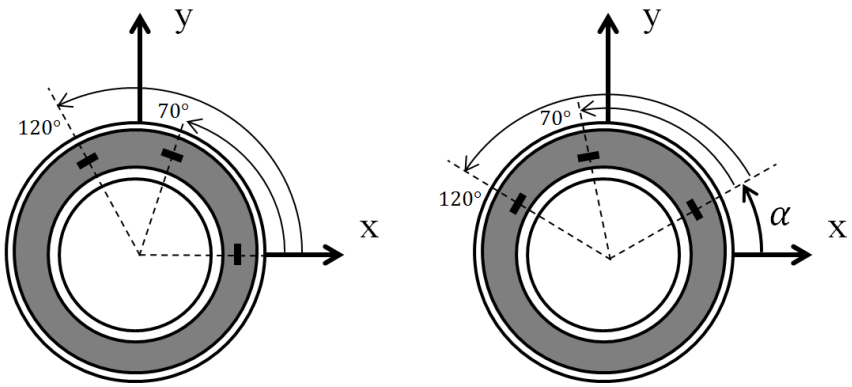

Figure 77. Global Pipe Rotation

5.2.3. Script Validation

The MATLAB script implementing these calculations can be found in Appendix H.

5.2.3.1. Inputs

Consider the case of bi-directional sinusoids in the x- and y-directions. The acceleration time histories for two acceleration profiles (APs) are written as

$$\begin{aligned} a_{x,AP1} &= \left(1.5\,\frac{m}{s^2}\right) * \sin(2\pi(14Hz)t), \quad a_{y,AP1} = \left(2.5\,\frac{m}{s^2}\right) * \sin(2\pi(18Hz)t); \\ a_{x,AP2} &= \left(3.0\,\frac{m}{s^2}\right) * \sin(2\pi(16Hz)t), \quad a_{y,AP2} = \left(2.0\,\frac{m}{s^2}\right) * \sin(2\pi(20Hz)t). \end{aligned} \tag{271}$$

The acceleration profiles are sampled at $0.002sec$ and $0.004sec$, and have durations of $7sec$ and $12sec$, respectively. The Young's modulus is assumed to see a 10.4% reduction ($\%E_i = 89.6\%$) if the operating temperature exceeds 50℃. The inertia and beam length are assumed independent of time and temperature (i.e. ($\%I_i = \%L_i = 100\%$). The operating schedule is

shown in Figure 78. Three piezoelectric elements are located at $\theta = 0°, 40°, 90°$ (for $\alpha = 0°$) and are oriented to harvest normal accelerations (see Figure 73). The equivalent mass of each of the three piezoelectrics is given in Table 42 and is based on

$$m_{eq} = \frac{33}{140} M_b + M_t. \tag{272}$$

The system is investigated for $\zeta_m = 3\%$ and $\zeta_e = 1\%, 3\%, 5\%, 7\%$ and 9%. The power output is to be optimized between year 1.5 and the start of year 3.0. The base frequencies considered range between $13Hz$ and $22Hz$ in $0.5Hz$ increments.

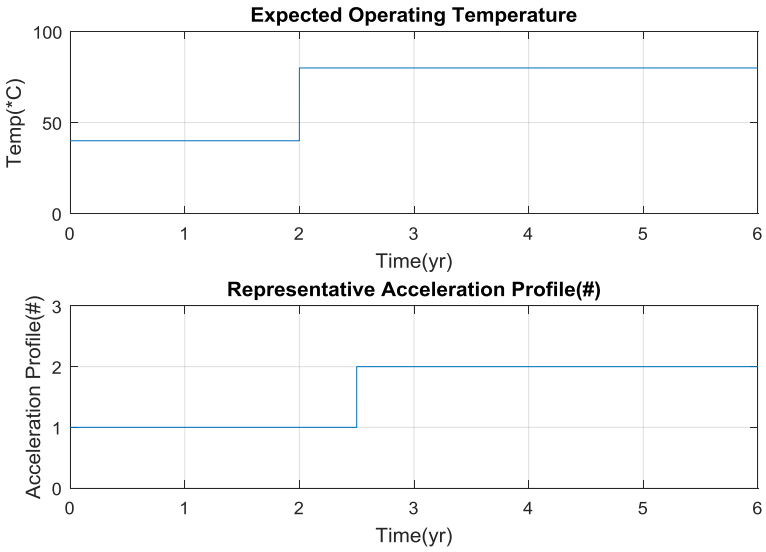

Figure 78. Expected Operating Schedule

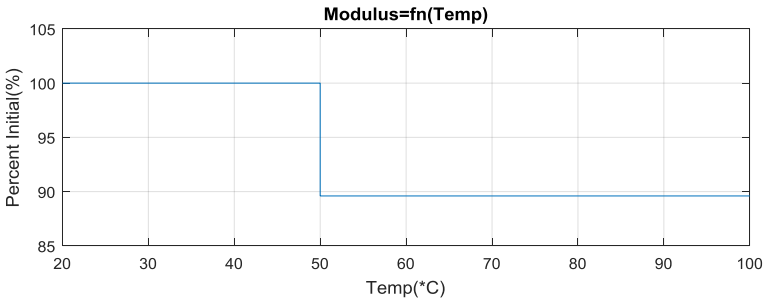

Figure 79. Temperature Dependent Young's Modulus

Transducer	Beam Mass, $M_b\ (kg)$	Tip Mass, $M_t\ (kg)$	Equivalent Mass, $m_{eq}\ (kg)$
1, $\theta = 0°$	0.04	0.15	0.1594
2, $\theta = 40°$	0.04	0.20	0.2094
3, $\theta = 90°$	0.04	0.20	0.2094

Table 42. Equivalent Masses

5.2.3.2. Representative Outputs

The first $0.4sec$ of the input acceleration time histories are shown in Figure 80.

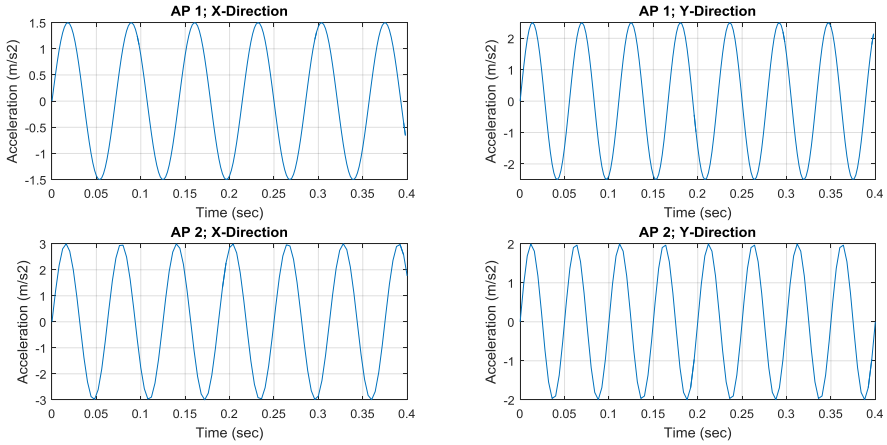

Figure 80. Acceleration Time Histories

Analytically, the acceleration time history for AP2 at $\theta = 40°$ can be written using Eq. (267) as

$$a_n = \left(2.298\,\frac{m}{s^2}\right)\sin(2\pi(16Hz)t) + \left(1.286\,\frac{m}{s^2}\right)\sin(2\pi(20Hz)t). \tag{273}$$

The corresponding output from the script is shown in Figure 81.

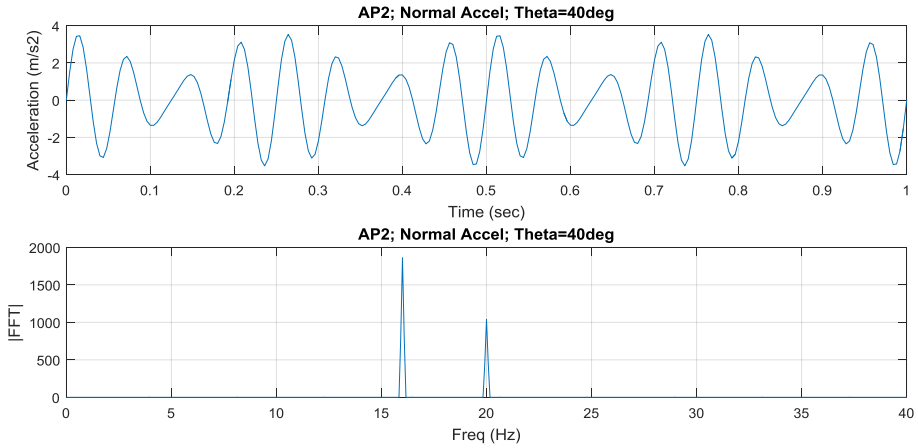

Figure 81. Transformed Acceleration Profile

Analytically, the displacement time history for AP1 in the x-direction can be found from the acceleration input $a_{x,AP1}$ as

$$d_{x,AP1} = \frac{-\left(1.5\frac{m}{s^2}\right)}{(2\pi(14Hz))^2} * \sin(2\pi(14Hz)t) = -(1.94e-4m)\sin(2\pi(14Hz)t). \quad (274)$$

Within the script, the acceleration time histories are converted to displacement time histories using Eq. (269) and the inverse Fourier transform. While in the frequency domain, the Fourier coefficients are truncated for frequencies less than $9Hz$. A sample output for AP1 is shown in Figure 82; the displacement matches the analytical result from Eq. (274).

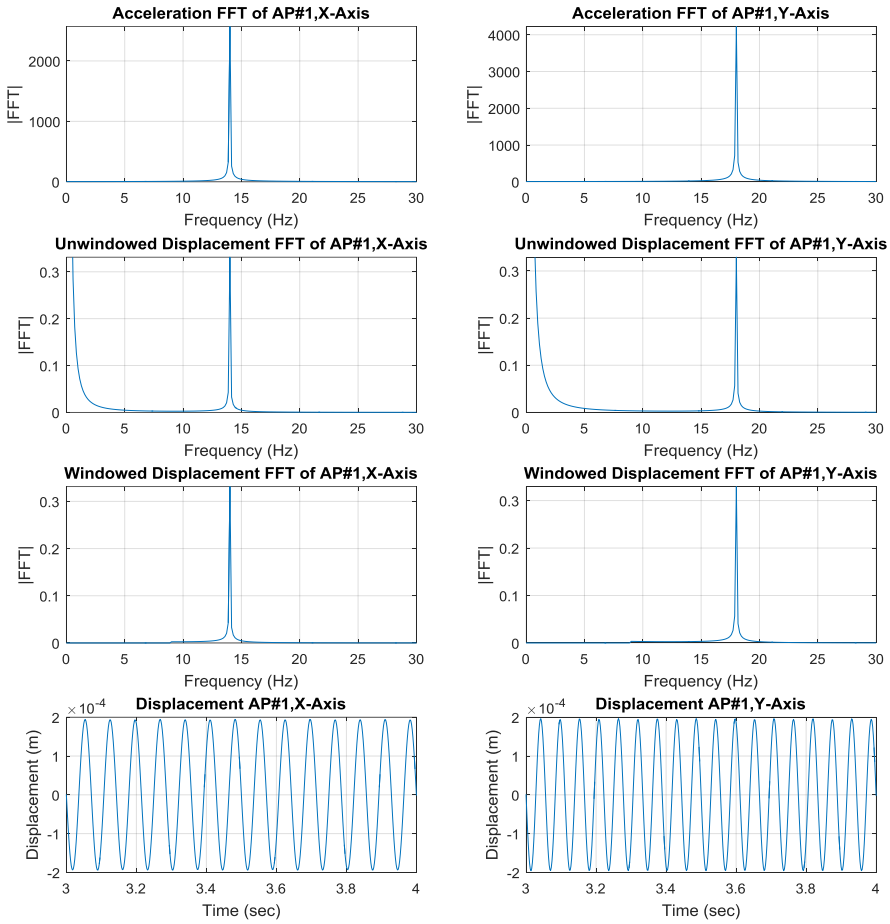

Figure 82. Driving Displacement Time History

The final output from the script is a table of optimal frequencies, their resulting uni-directional maximum displacements, and the optimal electric damping ratio for the three piezoelectric elements (subject to the models discretization resolution). The output for the previously described inputs is shown in Table 43. The first column (α) represents the global rotation angle of the pipe from the x-axis (see Figure 77). The second, fifth, and eighth columns (f_n) are the suggested baseline natural frequencies (the natural frequency at day zero/room temperature) for each piezoelectric element that will maximize the total harvested power over the time domain of interest. The third, sixth, and ninth columns (d_m) are the

maximum uni-directional displacement of the piezoelectric element (i.e. Eq. (234)) over the time domain of interest. The fourth, seventh, and tenth columns are the electrical damping ratio (ζ_e) that maximizes the harvesters power output over the time domain of interest. The last column is the electric power produced by all three piezoelectric elements integrated over the time domain of interest. The script also generates a plot of time vs. power and time vs. displacement for user specified values of α, f_{n1}, f_{n2}, and f_{n3}. Such a plot is provided in Figure 83.

Table 43. Suggested Frequencies

α (deg)	f_{n1} (Hz)	d_{m1} (mm)	ζ_{e1}	f_{n2} (Hz)	d_{m2} (mm)	ζ_{e2}	f_{n3} (Hz)	d_{m3} (mm)	ζ_{e3}	P_{tot} $(mW \cdot yr)$
0	17.0	2.45	3%	17.0	1.62	5%	18.5	1.19	5%	56.2
10	17.0	2.47	3%	17.5	1.14	7%	18.5	1.22	5%	54.7
20	17.0	2.41	3%	18.5	1.19	5%	18.5	1.22	5%	54.0
30	17.0	1.76	5%	18.5	1.22	5%	18.5	1.18	5%	52.9
40	17.0	1.62	5%	18.5	1.22	5%	17.5	1.14	7%	51.6
50	17.5	1.14	7%	18.5	1.19	5%	17.0	1.62	5%	52.1
60	18.5	1.19	5%	18.5	1.22	5%	17.0	1.76	5%	54.2
70	18.5	1.22	5%	18.5	1.22	5%	17.0	2.42	3%	55.9
80	18.5	1.22	5%	18.5	1.18	5%	17.0	2.47	3%	56.2
90	18.5	1.19	5%	17.5	1.14	7%	17.0	2.45	3%	55.6
100	18.5	1.22	5%	17.0	1.62	5%	17.0	2.47	3%	55.7
110	18.5	1.22	5%	17.0	1.76	5%	17.0	2.41	3%	55.3
120	18.5	1.18	5%	17.0	2.42	3%	17.0	1.76	5%	54.0
130	17.5	1.14	7%	17.0	2.47	3%	17.0	1.62	5%	52.7
140	17.0	1.62	5%	17.0	2.45	3%	17.5	1.14	7%	52.8
150	17.0	1.76	5%	17.0	2.47	3%	18.5	1.19	5%	54.9
160	17.0	2.42	3%	17.0	2.41	3%	18.5	1.22	5%	56.6
170	17.0	2.47	3%	17.0	1.76	5%	18.5	1.22	5%	57.0
180	17.0	2.45	3%	17.0	1.62	5%	18.5	1.19	5%	56.2
190	17.0	2.47	3%	17.5	1.14	7%	18.5	1.22	5%	54.7
200	17.0	2.41	3%	18.5	1.19	5%	18.5	1.22	5%	54.0
210	17.0	1.76	5%	18.5	1.22	5%	18.5	1.18	5%	52.9
220	17.0	1.62	5%	18.5	1.22	5%	17.5	1.14	7%	51.6
230	17.5	1.14	7%	18.5	1.19	5%	17.0	1.62	5%	52.1
240	18.5	1.19	5%	18.5	1.22	5%	17.0	1.76	5%	54.2
250	18.5	1.22	5%	18.5	1.22	5%	17.0	2.42	3%	55.9
260	18.5	1.22	5%	18.5	1.18	5%	17.0	2.47	3%	56.2
270	18.5	1.19	5%	17.5	1.14	7%	17.0	2.45	3%	55.6
280	18.5	1.22	5%	17.0	1.62	5%	17.0	2.47	3%	55.7
290	18.5	1.22	5%	17.0	1.76	5%	17.0	2.41	3%	55.3
300	18.5	1.18	5%	17.0	2.42	3%	17.0	1.76	5%	54.0
310	17.5	1.14	7%	17.0	2.47	3%	17.0	1.62	5%	52.7
320	17.0	1.62	5%	17.0	2.45	3%	17.5	1.14	7%	52.8
330	17.0	1.76	5%	17.0	2.47	3%	18.5	1.19	5%	54.9
340	17.0	2.42	3%	17.0	2.41	3%	18.5	1.22	5%	56.6
350	17.0	2.47	3%	17.0	1.76	5%	18.5	1.22	5%	57.0

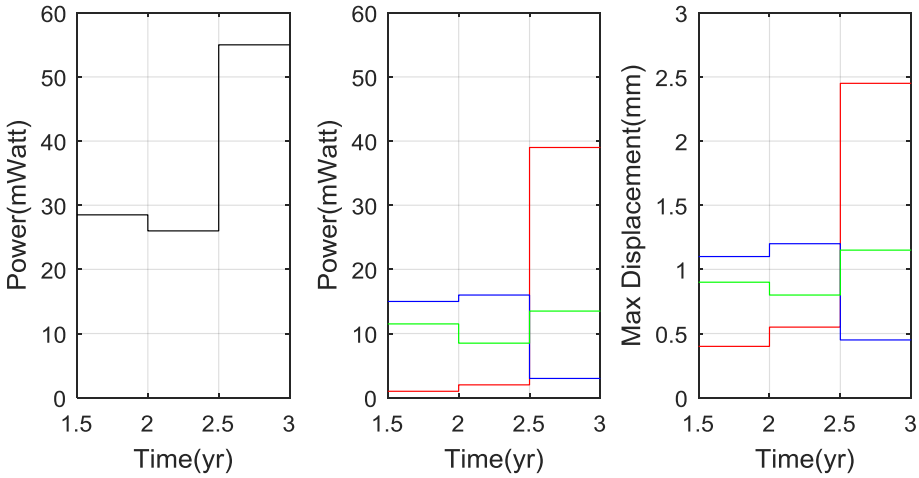

Figure 83. Power Output for a Single Realization ($\alpha = 90°$ from Table 43).
Piezo#1 = Blue; Piezo#2 = Green; Piezo#3 = Red.

Consider the first piezoelectric element (PE1) at year 2.2 in Figure 83 with a suggested base natural frequency of $18.5Hz$ and electric damping ratio of 5% ($\zeta_{eq} = \zeta_m + \zeta_e = 8\%$); the power output is estimated to be $15.80mW$ and the maximum displacement is estimated to be $1.19mm$. The script's output can be verified using alternative analytical equations.

The acceleration time history exciting PE1 in this configuration ($\alpha = 90°$) is

$$a_{y,AP1} = \left(2.5\frac{m}{s^2}\right)\sin(2\pi(18Hz)t). \tag{275}$$

This corresponds to a base motion displacement of

$$D_{y,AP1} = -\frac{\left(2.5\frac{m}{s^2}\right)}{(2\pi(18Hz))^2}\sin(2\pi(18Hz)t) = (-1.954e-4m)\sin(2\pi(18Hz)t). \tag{276}$$

where the amplitude of the motion is $d_{y,AP1} = -1.954e-4m$. For a base natural frequency of $18.5Hz$ the current natural frequency (at year 2.2) is adjusted by Eq. (270) as

$$f_{n,current} = \sqrt{\frac{(\%E_i)(\%I_i)}{(\%L_i)^3}}f_{n,base} = \sqrt{\frac{(0.896)(1)}{(1)^3}}18.5Hz = 17.51Hz. \tag{277}$$

The ratio of driving frequency to natural frequency is termed the frequency ratio and is given by

$$r = \frac{\omega}{\omega_{n,current}} = \frac{2\pi(18Hz)}{2\pi(17.51Hz)} = 1.028. \tag{278}$$

Since the base motion is a simple harmonic function, analytical solutions are readily available for the total displacement response of the oscillator. From Rao (1995) [204], the total displacement of the oscillator is given by

$$x = X\sin(\omega t - \phi) \tag{279}$$

where

$$\begin{aligned} X &= d_{y,AP1} * \left[\frac{1+\left(2\zeta_{eq}r\right)^2}{(1-r^2)^2+\left(2\zeta_{eq}r\right)^2}\right]^{0.5} = -1.139e-3m, \\ \phi &= \tan^{-1}\left[\frac{2\zeta_{eq}r^3}{1+\left(4\zeta_{eq}^2-1\right)r^2}\right] = 1.739rad. \end{aligned} \tag{280}$$

The relative displacement of the oscillator was given by Eq. (223) and is repeated here for convenience

$$z = x - y. \tag{281}$$

Combining Eq. (276), Eq. (279), Eq. (280), and Eq. (281) leads to the relative displacement response

$$z = x - D_{y,AP1} = X\sin(\omega t - \phi) - d_{y,AP1}\sin(\omega t), \tag{282}$$

while the derivative leads to the relative velocity response

$$\dot{z} = X\omega\cos(\omega t - \phi) - d_{y,AP1}\omega\cos(\omega t). \tag{283}$$

The maximum displacement occurs when

$$\dot{z} = 0 = X\omega\cos(\omega t - \phi) - d_{y,AP1}\omega\cos(\omega t). \tag{284}$$

Rearranging results in

$$\frac{d_{y,AP1}}{X} = \frac{\cos(\omega t-\phi)}{\cos(\omega t)} = \frac{\cos(\omega t)\cos(-\phi)-\sin(\omega t)\sin(-\phi)}{\cos(\omega t)}, \tag{285}$$

which leads to

$$\omega t = \tan^{-1}\left[\left(\frac{1}{-\sin(-\phi)}\right)\left(\frac{d_{y,AP1}}{X} - \cos(-\phi)\right)\right]. \tag{286}$$

Combining Eq. (282) and Eq. (286) results in

$$|z|_{max} = 1.19mm. \tag{287}$$

To develop a power estimate, the maximum relative velocity amplitude is needed. This occurs when

$$\ddot{z} = 0 = -X\omega^2 \sin(\omega t - \phi) + d_{y,AP1}\omega^2 \sin(\omega t). \tag{288}$$

Rearranging results in

$$\frac{d_{y,AP1}}{X} = \frac{\sin(\omega t - \phi)}{\sin(\omega t)} = \frac{\sin(\omega t)\cos(-\phi) + \cos(\omega t)\sin(-\phi)}{\sin(\omega t)}, \tag{289}$$

which leads to

$$\omega t = \tan^{-1}\left[\frac{\sin(-\phi)}{\frac{d_{y,AP1}}{X} - \cos(-\phi)}\right]. \tag{290}$$

Combining Eq. (283) and Eq. (290) results in

$$|\dot{z}|_{max} = 0.1343\,\frac{m}{s}. \tag{291}$$

Since the steady-state response of the oscillator will be harmonic, the power estimate (Eq. (233)) can be written as

$$P_{avg,e} = c_e(|\dot{z}|_{max})^2\left[\frac{1}{T}\int_0^T \sin^2(\omega t - \Phi)dt\right]. \tag{292}$$

Note that the bracketed term is simply the signal power of a single harmonic function and is equal to $1/2$. The power estimate is then

$$P_{avg,e} = \{c_e\}(|\dot{z}|_{max})^2[0.5] = \{2(0.1594kg)(2\pi(17.51Hz))(0.05)\}\left(0.1343\frac{m}{s}\right)^2[0.5] = 15.82mW. \tag{293}$$

Note that both the maximum uni-directional displacement (Eq. (287)) and power estimate (Eq. (293)) agree with the corresponding results from Figure 83. These calculations are repeated for the first and third piezoelectric element at other instances in time; the results are summarized in Table 44 and show excellent agreement.

Table 44. Script Validation

Piezoelectric Element	1	1	1	3	3	3
Time Instance (yr)	1.7	2.2	2.8	1.7	2.2	2.8
Acceleration Time History	$a_{y,AP1}$	$a_{y,AP1}$	$a_{y,AP2}$	$a_{x,AP1}$	$a_{x,AP1}$	$a_{x,AP2}$
Acceleration Amplitude (m/s^2)	2.5	2.5	2.0	1.5	1.5	3.0
Driving Frequency, f (Hz)	18	18	20	14	14	16
Base Motion Displacement (m)	$-1.954e-04$	$-1.954e-04$	$-1.267e-04$	$-1.939e-04$	$-1.939e-04$	$-2.968e-04$
$f_{n,base}$ (Hz)	18.5	18.5	18.5	17.0	17.0	17.0
$f_{n,current}$ (Hz)	18.50	17.51	17.51	17.00	16.09	16.09
Frequency Ratio, r	0.973	1.028	1.142	0.824	0.870	0.994
Mechanical Damping Ratio, ζ_m	3%	3%	3%	3%	3%	3%
Electrical Damping Ratio, ζ_e	5%	5%	5%	3%	3%	3%
Equivalent Damping Ratio, ζ_{eq}	8%	8%	8%	6%	6%	6%
Total Displacement Amplitude, X (m)	$-1.202e-03$	$-1.139e-03$	$-3.626e-4$	$-5.787e-04$	$-7.367e-4$	$-2.494e-03$
Phase Shift, ϕ (rad)	1.086	1.739	2.420	0.199	0.302	1.357
Oscillator Peak Displacement, $\lvert z\rvert_{max}$ (mm)	1.12	1.19	0.47	0.39	0.55	2.45
Script Peak Displacement Estimate (mm)	1.12	1.19	0.47	0.39	0.55	2.45
Error	0.0%	0.0%	0.0%	0.0%	0.0%	0.0%
Oscillator Peak velocity, $\lvert\dot{z}\rvert_{max}$ (m/s)	0.1272	0.1343	0.0585	0.0344	0.0488	0.2461
Average Extracted Power, $P_{avg,e}$ (mW)	14.98	15.82	3.00	0.79	1.51	38.49
Script Power Estimate (mW)	14.98	15.80	3.00	0.79	1.51	38.51
Error	0.0%	-0.1%	0.0%	0.0%	0.0%	0.1%

Note that for the realization in the last column, the driving frequency is very near the natural frequency (i.e. $r = 0.994$). In this case, and since $\zeta_m = \zeta_e$ was assumed, the single term approximation provided by Eq. (263) and Eq. (266) should provide a reasonable estimate (there will be some error as $r \neq 1$ and ζ_{eq} is relatively large). For the particular realization

$$P_{avg,e-max} \approx \frac{m_{eq}}{8\zeta_m}\left[\frac{A_n^2}{2\omega_n}\right] = \frac{0.2094kg}{8(0.03)}\left[\frac{\left(3\frac{m}{s^2}\right)^2}{2(2\pi 16.09Hz)}\right] = 38.84mW, \tag{294}$$

and

$$z_{s-max}\big|_{P_{avg,e-max}} \approx \frac{|A_n|}{4\zeta_m\omega_n^2} = \frac{\left|3\frac{m}{s^2}\right|}{4(0.03)(2\pi 16.09Hz)^2} = 2.44mm, \tag{295}$$

which compare reasonably well with the calculated values shown in Table 44 (errors of 0.9% and -0.4%, respectively).

5.3. SS – Refined Power Estimate

The underlying model imiplemented in the FS have several shortcomings, previously identified in Section 5.2. To generate an improved power estimate, a single piezoelectric

bimorph is modeled utilizing coupled electromechancial equations in a distributed system. The models derivation is shown in Section 5.3.1 and follows the work of Erturk and Inman (2011) [36]. The model has been experimentally validated and is discussed in Priya and Inman (2009) [28] and Erturk and Inman (2009) [205]. The same modeling approach has been applied to a unimorph piezoelectric element as described in Erturk and Inman (2008) [206] and Priya and Inman (2009) [28]. Following the models derivation, the practical application of the MATLAB script is described and several validation cases are shown. Lastly, demonstration cases illustrate how cyclic damage and temperature changes might effect the power output and displacement response of an excited bimorph.

5.3.1. Derivation of Power Estimate

5.3.1.1. Base Equation of Motion

Consider the uniform cantilever beam shown in Figure 84 where a tip mass has been included. The variables shown include the beam mass per unit length (m), beam length (L), tip mass (M_t), mass moment of inertia of the tip mass about $x = L$ (I_t), the relative displacement of the beam (w_R), and the base displacement (w_B). The beams total displacement for any spatial point (x) is the summation of the relative and base displacement, i.e. $w = w_R + w_B$.

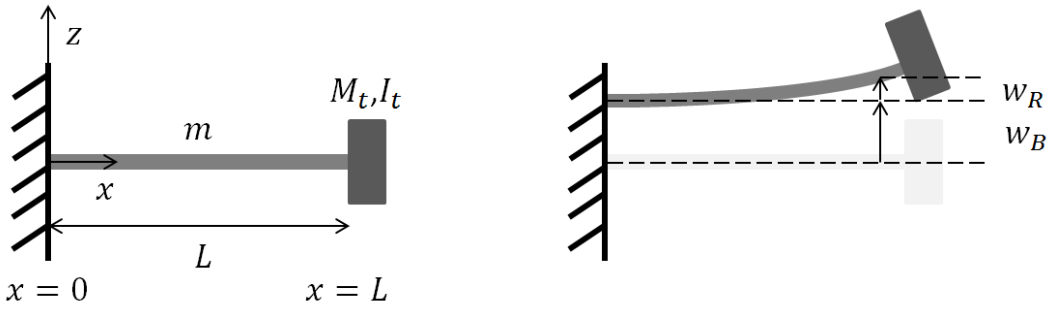

Figure 84. Uniform Cantilever Beam with Tip Mass: Initial (Left) and Displaced (Right) Shapes

Assuming Euler-Bernoulli beam theory, the kinetic energy of the system can be written as

$$KE = \int_0^L \left\{\frac{1}{2}(m + M_t\delta[x-L])\dot{w}^2\right\} + \left\{\frac{1}{2}I_t\delta[x-L](\dot{w}_R')^2\right\}dx, \tag{296}$$

where δ represents the Dirac delta function; $(\dot{\ })$ and $(\ )'$ represent temporal and spatial derivatives, respectively. The bracketed terms represent the translational kinetic energy of the system and the rotational kinetic energy of the tip mass, respectively. The bending strain energy can be written as

$$SE = \int_0^L \left\{\frac{1}{2}YI(w_R'')^2\right\}dx. \tag{297}$$

The Lagrangian is written as

$$\bar{\bar{L}} = KE - SE = \int_0^L \left\{\frac{1}{2}[m + M_t\delta(x-L)]\dot{w}^2\right\} + \left\{\frac{1}{2}I_t\delta(x-L)(\dot{w}_R')^2\right\} - \left\{\frac{1}{2}YI(w_R'')^2\right\}dx. \tag{298}$$

Applying Hamilton's principle

$$\int_{t_1}^{t_2} \underline{\delta}\bar{\bar{L}}dt = 0, \tag{299}$$

where the variation term ($\underline{\delta}$) has been underscored to distinguish it from the Dirac delta function of Eq. (296), leads to

$$\int_{t_1}^{t_2}\int_0^L \{[m + M_t\delta(x-L)]\dot{w}\underline{\delta}\dot{w}\} + \{I_t\delta(x-L)\dot{w}_R'\underline{\delta}\dot{w}_R'\} - \{YIw_R''\underline{\delta}w_R''\}dxdt = 0. \tag{300}$$

Looking at the three bracketed terms individually, the first term can be rearranged as

$$\int_0^L [m + M_t\delta(x-L)]\left\{\int_{t_1}^{t_2} \dot{w}\underline{\delta}\dot{w}\,dt\right\}dx. \tag{301}$$

Applying integration by parts to the bracketed integral leads to

$$\int_{t_1}^{t_2} \dot{w}\underline{\delta}\dot{w}\,dt = \dot{w}\underline{\delta}w\Big|_{t_1}^{t_2} - \int_{t_1}^{t_2} \ddot{w}\,\underline{\delta}w dt = -\int_{t_1}^{t_2} \ddot{w}\,\underline{\delta}w dt. \tag{302}$$

Eq. (301) can then be written as

$$-\int_{t_1}^{t_2}\int_0^L [m + M_t\delta(x-L)]\ddot{w}\,\underline{\delta}w dx\,dt. \tag{303}$$

The displacement (w) can be rewritten in terms of the relative and base displacement. Let $\ddot{w} = \ddot{w}_R + \ddot{w}_B$ and $\underline{\delta}w = \underline{\delta}w_R + \underline{\delta}w_B$ such that Eq. (303) can be written as

$$-\int_{t_1}^{t_2}\int_0^L [m + M_t\delta(x-L)]\left\{\ddot{w}_R\underline{\delta}w_R + \ddot{w}_B\underline{\delta}w_R + \ddot{w}_R\underline{\delta}w_B + \ddot{w}_B\underline{\delta}w_B\right\}dx\,dt. \tag{304}$$

A portion of this double integral (that corresponding to $\ddot{w}_R\underline{\delta}w_R$) can be expanded as

$$\int_0^L [m + M_t\delta(x-L)]\,\ddot{w}_R\underline{\delta}w_R dx = \int_0^L m\ddot{w}_R\underline{\delta}w_R dx + \int_0^L M_t\delta(x-L)\ddot{w}_R\underline{\delta}w_R dx. \tag{305}$$

Evaluating the second integral on the right hand side results in

$$\int_0^L M_t\delta(x-L)\ddot{w}_R\underline{\delta}w_R dx = M_t\ddot{w}_R(L)\underline{\delta}w_R. \tag{306}$$

Thus, the first bracketed term of Eq. (300) can be written as

$$-\int_{t_1}^{t_2}\left[\int_0^L\left[[m + M_t\delta(x-L)]\left\{\ddot{w}_B\underline{\delta}w_R + \ddot{w}_R\underline{\delta}w_B + \ddot{w}_B\underline{\delta}w_B\right\} + m\ddot{w}_R\underline{\delta}w_R\right]dx + M_t\ddot{w}_R(L)\underline{\delta}w_R\right]dt. \tag{307}$$

The second bracketed term of Eq. (300) can be rearranged as

$$\int_0^L I_t\delta(x-L)\left[\int_{t_1}^{t_2}\dot{w}_R'\underline{\delta}\dot{w}_R' dt\right]dx. \tag{308}$$

Applying integration by parts to the bracketed integral leads to

$$\int_{t_1}^{t_2}\dot{w}_R'\underline{\delta}\dot{w}_R' dt = \dot{w}_R'\underline{\delta}w_R'\Big|_{t_1}^{t_2} - \int_{t_1}^{t_2}\ddot{w}_R'\,\underline{\delta}w_R' dt = -\int_{t_1}^{t_2}\ddot{w}_R'\,\underline{\delta}w_R' dt. \tag{309}$$

Combining Eq. (308) and Eq. (309) leads to

$$-\int_{t_1}^{t_2}\left[\int_0^L I_t\delta(x-L)\ddot{w}_R'\underline{\delta}w_R'\,dx\right]dt, \tag{310}$$

which, after evaluating the spatial integral, can be written as

$$-\int_{t_1}^{t_2} I_t\ddot{w}_R'(L)\underline{\delta}w_R'\,dt. \tag{311}$$

Lastly, the third bracketed term of Eq. (300) can be written as

$$-\int_{t_1}^{t_2}\int_0^L YIw_R''\underline{\delta}w_R''\,dx\,dt = -\int_{t_1}^{t_2}\int_0^L M\underline{\delta}w_R''\,dx\,dt. \tag{312}$$

where YIw_R'' has been replaced with a generalized moment term (M). Applying integration by parts to the spatial integral leads to

$$-\int_{t_1}^{t_2}\int_0^L M\underline{\delta}w_R''\,dx\,dt = -\int_{t_1}^{t_2}\left[M\underline{\delta}w_R'\Big|_0^L - \int_0^L M'\underline{\delta}w_R' dx\right]dt. \tag{313}$$

Again applying integration by parts to the spatial integral results in

$$-\int_{t_1}^{t_2}\left[M\underline{\delta}w_R'\Big|_0^L - \int_0^L M'\underline{\delta}w_R' dx\right]dt = -\int_{t_1}^{t_2}\left[M\underline{\delta}w_R'\Big|_0^L - \left\{M'\underline{\delta}w_R\Big|_0^L - \int_0^L M''\underline{\delta}w_R dx\right\}\right]dt. \tag{314}$$

Eq. (300) can then be written in terms of Eq. (307), Eq. (311) and Eq. (314)

$$\begin{gathered} -\int_{t_1}^{t_2}\left[\int_0^L\left[[m+M_t\delta(x-L)]\{\ddot{w}_B\underline{\delta}w_R+\ddot{w}_R\underline{\delta}w_B+\ddot{w}_B\underline{\delta}w_B\}+m\ddot{w}_R\underline{\delta}w_R\right]dx+\right. \\ \left.M_t\ddot{w}_R(L)\underline{\delta}w_R\right]dt-\int_{t_1}^{t_2}I_t\ddot{w}_R'(L)\underline{\delta}w_R'\,dt-\int_{t_1}^{t_2}\left[M\underline{\delta}w_R'\Big|_0^L-\left\{M'\underline{\delta}w_R\Big|_0^L-\right.\right. \\ \left.\left.\int_0^L M''\underline{\delta}w_R dx\right\}\right]dt=0. \end{gathered} \tag{315}$$

Regrouping terms

$$\int_{t_1}^{t_2}\begin{bmatrix} M_t\ddot{w}_R(L)\underline{\delta}w_R+I_t\ddot{w}_R'(L)\underline{\delta}w_R'+M\underline{\delta}w_R'\Big|_0^L-M'\underline{\delta}w_R\Big|_0^L \\ +\int_0^L[m\ddot{w}_R+[m+M_t\delta(x-L)]\ddot{w}_B+M'']\underline{\delta}w_R dx \\ +\int_0^L\left[[m+M_t\delta(x-L)](\ddot{w}_R+\ddot{w}_B)\right]\underline{\delta}w_B dx \end{bmatrix}dt=0, \tag{316}$$

where $\underline{\delta}w_B=0$ since the base acceleration is known.

The equation of motion can be extracted as

$$m\ddot{w}_R+[m+M_t\delta(x-L)]\ddot{w}_B+M''=0, \tag{317}$$

or equivalently

$$M''+m\ddot{w}_R=-[m+M_t\delta(x-L)]\ddot{w}_B. \tag{318}$$

The boundary conditions can be extracted as

$$\begin{gathered} w_R=0 \quad \& \quad w_R'=0 \quad @x=0; \\ M'-M_t\ddot{w}_R=0 \quad \& \quad M+I_t\ddot{w}_R'=0 \quad @x=L. \end{gathered} \tag{319}$$

5.3.1.2. Inclusion of Piezoelectric Effects

To incorporate piezoelectric effects, the generalized moment (M) is expanded. The following derivations are based on the beam cross section shown in Figure 85 where the x, y, and z-axis correspond to the 1, 2, and 3-direction.

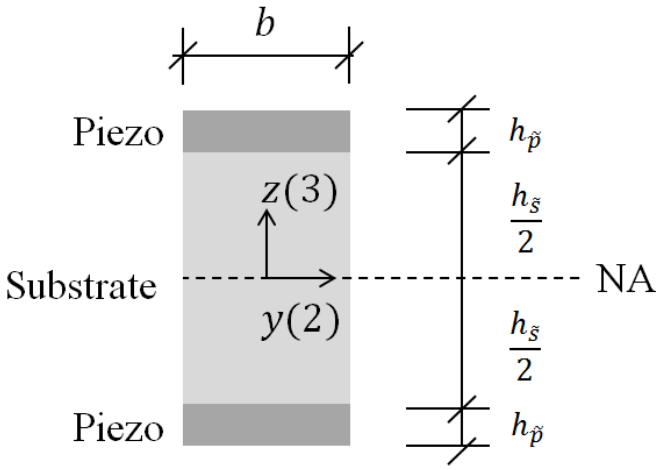

Figure 85. Beam Cross Section

5.3.1.2.1. Parallel Connection

The internal bending moment is defined as [207]

$$M = -\int_A zT_1 dA, \tag{320}$$

where T_1 is the axial stress in the cross section. For the cross section shown in Figure 85, Eq. (320) can be expanded as

$$M = -b\left[\int_{-h_{\tilde{p}}-h_{\tilde{s}}/2}^{-h_{\tilde{s}}/2} T_1^{\tilde{p}-L} z dz + \int_{-h_{\tilde{s}}/2}^{h_{\tilde{s}}/2} T_1^{\tilde{s}} z dz + \int_{h_{\tilde{s}}/2}^{h_{\tilde{s}}/2+h_{\tilde{p}}} T_1^{\tilde{p}-U} z dz\right], \tag{321}$$

where $T_1^{\tilde{p}-L}$, $T_1^{\tilde{s}}$, and $T_1^{\tilde{p}-U}$ are the x-component stresses in the lower piezoelectric, substrate, and upper piezoelectric layers, respectively. For the substrate (with no piezoelectric properties), the x-component stress is

$$T_1^{\tilde{s}} = Y_{\tilde{s}} S_1^{\tilde{s}}, \tag{322}$$

where $Y_{\tilde{s}}$ is the Young's modulus of the substrate and $S_1^{\tilde{s}}$ is the axial strain in the substrate. In general, the axial strain is related to curvature as

$$S_1 = -zw_R''. \tag{323}$$

For piezoelectric elements connected in parallel and polarized as shown in Figure 86, the x-component stresses can be written for the piezoelectric elements as [32]

$$T_1^{\tilde{p}-U} = c_{11}^E S_1^{\tilde{p}-U} - \bar{e}_{31} E_3^U, \tag{324}$$

and

$$T_1^{\tilde{p}-L} = c_{11}^E S_1^{\tilde{p}-L} - \bar{e}_{31} E_3^L. \tag{325}$$

Note that c_{11}^E is the elastic modulus of the piezoelectric at constant electric field, $\bar{e}_{31}$ is the effective piezoelectric stress constant, and E_3 is the electric field component in the z-direction.

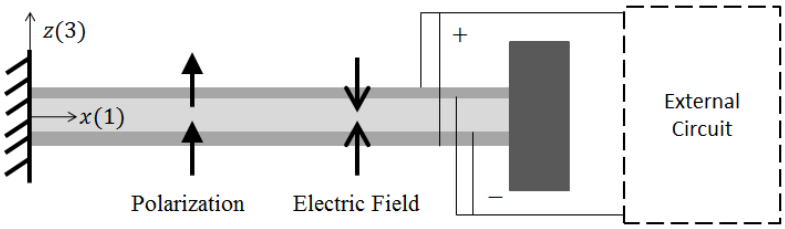

Figure 86. Parallel Connection

Eq. (321) can be expanded as

$$M = -b\left[\int_{-h_{\tilde{p}}-h_{\tilde{s}}/2}^{-h_{\tilde{s}}/2}(c_{11}^E(-zw_R'') - \bar{e}_{31}E_3^L)zdz + \int_{-h_{\tilde{s}}/2}^{h_{\tilde{s}}/2} Y_{\tilde{s}}(-zw_R'')zdz + \int_{h_{\tilde{s}}/2}^{h_{\tilde{s}}/2+h_{\tilde{p}}}(c_{11}^E(-zw_R'') - \bar{e}_{31}E_3^U)zdz\right]. \tag{326}$$

The mechanical integrals can be isolated as

$$M = -b\left[-c_{11}^E w_R'' \int_{-h_{\tilde{p}}-h_{\tilde{s}}/2}^{-h_{\tilde{s}}/2} z^2dz - Y_{\tilde{s}} w_R'' \int_{-h_{\tilde{s}}/2}^{h_{\tilde{s}}/2} z^2dz - c_{11}^E w_R'' \int_{h_{\tilde{s}}/2}^{h_{\tilde{s}}/2+h_{\tilde{p}}} z^2dz\right], \tag{327}$$

which reduces to

$$M = -b\left[-\frac{c_{11}^E w_R''}{3}\left[\left(h_{\tilde{p}} + \frac{h_{\tilde{s}}}{2}\right)^3 - \left(\frac{h_{\tilde{s}}}{2}\right)^3\right] - \frac{Y_{\tilde{s}} w_R''}{3}\left[\frac{h_{\tilde{s}}^3}{4}\right] - \frac{c_{11}^E w_R''}{3}\left[\left(h_{\tilde{p}} + \frac{h_{\tilde{s}}}{2}\right)^3 - \left(\frac{h_{\tilde{s}}}{2}\right)^3\right]\right]. \tag{328}$$

Eq. (328) can be simplified to

$$M = \frac{2b}{3}\left[c_{11}^E\left[\left(h_{\tilde{p}} + \frac{h_{\tilde{s}}}{2}\right)^3 - \frac{h_{\tilde{s}}^3}{8}\right] + Y_{\tilde{s}}\left[\frac{h_{\tilde{s}}^3}{8}\right]\right] w_R'' = YI w_R''. \tag{329}$$

where the sections weighted flexural rigidity is given by

$$YI = \frac{2b}{3}\left[c_{11}^E\left[\left(h_{\tilde{p}} + \frac{h_{\tilde{s}}}{2}\right)^3 - \frac{h_{\tilde{s}}^3}{8}\right] + Y_{\tilde{s}}\left[\frac{h_{\tilde{s}}^3}{8}\right]\right]. \tag{330}$$

Note that an analysis of a purely mechanical composite beam would result in the same flexural rigidity. The electric integrals can be isolated as

$$M = b\left[\bar{e}_{31}E_3^L\int_{-h_{\tilde{p}}-h_{\tilde{s}}/2}^{-h_{\tilde{s}}/2} z dz + \bar{e}_{31}E_3^U\int_{h_{\tilde{s}}/2}^{h_{\tilde{s}}/2+h_{\tilde{p}}} z dz\right], \tag{331}$$

which simplifies to

$$M = b\left[\frac{\bar{e}_{31}E_3^L}{2}\left[\frac{h_{\tilde{s}}^2}{4} - \left(h_{\tilde{p}} + \frac{h_{\tilde{s}}}{2}\right)^2\right] + \frac{\bar{e}_{31}E_3^U}{2}\left[\left(h_{\tilde{p}} + \frac{h_{\tilde{s}}}{2}\right)^2 - \frac{h_{\tilde{s}}^2}{4}\right]\right]. \tag{332}$$

For the parallel case, the electric fields can be written as $E_3^U = -v_p/h_{\tilde{p}}$ and $E_3^L = v_p/h_{\tilde{p}}$. Eq. (332) is then written as

$$M = b\left[-\frac{\bar{e}_{31}}{2}\left(\frac{v_p}{h_{\tilde{p}}}\right)\left[\left(h_{\tilde{p}} + \frac{h_{\tilde{s}}}{2}\right)^2 - \frac{h_{\tilde{s}}^2}{4}\right] + \frac{\bar{e}_{31}}{2}\left(-\frac{v_p}{h_{\tilde{p}}}\right)\left[\left(h_{\tilde{p}} + \frac{h_{\tilde{s}}}{2}\right)^2 - \frac{h_{\tilde{s}}^2}{4}\right]\right], \tag{333}$$

or

$$M = -\frac{b\bar{e}_{31}}{h_{\tilde{p}}}\left[\left(h_{\tilde{p}} + \frac{h_{\tilde{s}}}{2}\right)^2 - \frac{h_{\tilde{s}}^2}{4}\right]v_p = -\vartheta_p v_p, \tag{334}$$

where

$$\vartheta_p = \frac{b\bar{e}_{31}}{h_{\tilde{p}}}\left[\left(h_{\tilde{p}} + \frac{h_{\tilde{s}}}{2}\right)^2 - \frac{h_{\tilde{s}}^2}{4}\right] = 2b\bar{e}_{31}\left(\frac{h_{\tilde{p}}+h_{\tilde{s}}}{2}\right). \tag{335}$$

The electrical term must be multiplied by $[H(x) - H(x-L)]$ so that it survives the spatial differentiation where $H(x)$ is the Heaviside function [36]. Eq. (321) is then equal to

$$M = YIw_R'' - \vartheta_p v_p[H(x) - H(x-L)], \tag{336}$$

where ϑ_p is given by Eq. (335). For the case of parallel connection, Eq. (318) is then written as

$$YIw_R^{p\prime\prime\prime\prime} - \vartheta_p v_p\left[\frac{d\delta(x)}{dx} - \frac{d\delta(x-L)}{dx}\right] + m\ddot{w}_R^p = -[m + M_t\delta(x-L)]\ddot{w}_B. \tag{337}$$

5.3.1.2.2. Series Connection

For piezoelectric elements connected in series and polarized as shown in Figure 87, the x-component stresses can be written for the upper piezoelectric element as

$$T_1^{\tilde{p}-U} = c_{11}^E S_1^{\tilde{p}-U} - \bar{e}_{31}E_3^U, \tag{338}$$

and

$$T_1^{\tilde{p}-L} = c_{11}^E S_1^{\tilde{p}-L} + \bar{e}_{31}E_3^L, \tag{339}$$

for the lower piezoelectric element. Note that the only difference between the series and parallel system is the sign of the electrical component in Eq. (339) (compare to Eq. (325)). This will result in a sign change in Eq. (332), which is written for the series connection as

$$M = b\left[-\frac{\bar{e}_{31}E_3^L}{2}\left[\frac{h_{\tilde{s}}^2}{4} - \left(h_{\tilde{p}} + \frac{h_{\tilde{s}}}{2}\right)^2\right] + \frac{\bar{e}_{31}E_3^U}{2}\left[\left(h_{\tilde{p}} + \frac{h_{\tilde{s}}}{2}\right)^2 - \frac{h_{\tilde{s}}^2}{4}\right]\right]. \tag{340}$$

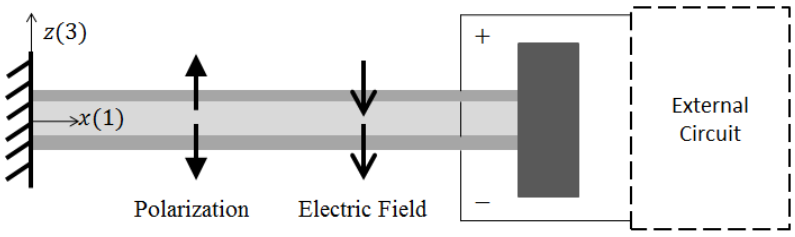

Figure 87. Series Connection

For the series case, the electric fields can be written as $E_3^U = E_3^L = -v_s/(2h_{\tilde{p}})$. Eq. (340) is rewritten as

$$M = b\left[+\frac{\bar{e}_{31}}{2}\left(-\frac{v_s}{2h_{\tilde{p}}}\right)\left[\left(h_{\tilde{p}} + \frac{h_{\tilde{s}}}{2}\right)^2 - \frac{h_{\tilde{s}}^2}{4}\right] + \frac{\bar{e}_{31}}{2}\left(-\frac{v_s}{2h_{\tilde{p}}}\right)\left[\left(h_{\tilde{p}} + \frac{h_{\tilde{s}}}{2}\right)^2 - \frac{h_{\tilde{s}}^2}{4}\right]\right]. \tag{341}$$

or more simply

$$M = -\frac{b\bar{e}_{31}}{2h_{\tilde{p}}}\left[\left(h_{\tilde{p}} + \frac{h_{\tilde{s}}}{2}\right)^2 - \frac{h_{\tilde{s}}^2}{4}\right]v_s = -\vartheta_s v_s, \tag{342}$$

where

$$\vartheta_s = \frac{b\bar{e}_{31}}{2h_{\tilde{p}}}\left[\left(h_{\tilde{p}} + \frac{h_{\tilde{s}}}{2}\right)^2 - \frac{h_{\tilde{s}}^2}{4}\right] = b\bar{e}_{31}\left(\frac{h_{\tilde{p}}+h_{\tilde{s}}}{2}\right). \tag{343}$$

Again, the electrical term must be multiplied by $[H(x) - H(x-L)]$ so that it survives the spatial differentiation where $H(x)$ is the Heaviside function [36]. Eq. (321) is then equal to

$$M = YIw_R'' - \vartheta_s v_s[H(x) - H(x-L)], \tag{344}$$

where ϑ_s is given by Eq. (343). For the case of series connection, Eq. (318) is then written as

$$YIw_R^{s\prime\prime\prime\prime} - \vartheta_s v_s\left[\frac{d\delta(x)}{dx} - \frac{d\delta(x-L)}{dx}\right] + m\ddot{w}_R^s = -[m + M_t\delta(x-L)]\ddot{w}_B. \tag{345}$$

5.3.1.3. Damped Equation of Motion

Both Kelvin-Voigt and viscous damping can be incorporated into the model. For Kelvin-Voigt (or strain-rate) damping, the effective modulus is replaced by

$$Y = Y + c_s \frac{\partial}{\partial t}. \tag{346}$$

The updated equations of motion for both the parallel and series configurations are then

$$YIw_R^{p\prime\prime\prime\prime} + c_s I\dot{w}_R^{p\prime\prime\prime\prime} + c_a\dot{w}_R^p - \vartheta_p \upsilon_p \left[\frac{d\delta(x)}{dx} - \frac{d\delta(x-L)}{dx}\right] + m\ddot{w}_R^p = -[m + M_t\delta(x-L)]\ddot{w}_B, \tag{347}$$

and

$$YIw_R^{s\prime\prime\prime\prime} + c_s I\dot{w}_R^{s\prime\prime\prime\prime} + c_a\dot{w}_R^s - \vartheta_s \upsilon_s \left[\frac{d\delta(x)}{dx} - \frac{d\delta(x-L)}{dx}\right] + m\ddot{w}_R^s = -[m + M_t\delta(x-L)]\ddot{w}_B, \tag{348}$$

respectively. Note that the viscous damping term has been added directly and its contribution to the driving force has been neglected [203]. Assuming proportional damping, the eigenfunctions can be found from the corresponding undamped system.

5.3.1.4. Eigenvalue Analysis of Undamped System

Consider the free vibration of Eq. (318) where $M = YIw_R''$

$$YIw_R'''' + m\ddot{w}_R = 0. \tag{349}$$

The corresponding boundary conditions can be written as

$$\begin{gathered} w_R = 0 \quad \& \quad w_R' = 0 \quad @x = 0; \\ YIw_R''' - M_t\ddot{w}_R = 0 \quad \& \quad YIw_R'' + I_t\ddot{w}_R' = 0 \quad @x = L. \end{gathered} \tag{350}$$

Using separation of variables take

$$w_R(x,t) = \phi(x)\eta(t). \tag{351}$$

Eq. (349) becomes

$$YI\phi''''\eta + m\phi\ddot{\eta} = 0, \tag{352}$$

or

$$\frac{YI}{m}\frac{\phi''''}{\phi} = -\frac{\ddot{\eta}}{\eta}, \tag{353}$$

Since the left hand side is spatially dependent while the right hand side is solely dependent on time, both sides must be equal to the same constant

$$\frac{YI}{m}\frac{\phi''''}{\phi} = -\frac{\ddot{\eta}}{\eta} = \gamma. \tag{354}$$

Eq. (354) can then be rewritten as two equations

$$\begin{gathered}\phi'''' - \frac{\gamma m}{YI}\phi = 0, \\ \ddot{\eta} + \gamma\eta = 0.\end{gathered} \tag{355}$$

The form of the temporal equation implies a harmonic solution, requiring that the constant γ be positive and permitting the expression $\gamma = \omega^2$. The general solutions to Eq. (355) are known to be [130]

$$\begin{gathered}\phi = C_1\cos\left(\frac{\lambda}{L}x\right) + C_2\cosh\left(\frac{\lambda}{L}x\right) + C_3\sin\left(\frac{\lambda}{L}x\right) + C_4\sinh\left(\frac{\lambda}{L}x\right), \\ \eta = C_5\cos(\omega t) + C_6\sin(\omega t)\end{gathered} \tag{356}$$

where

$$\lambda^4 = \frac{\omega^2 m L^4}{YI}. \tag{357}$$

The temporal solution in Eq. (356) can be combined with Eq. (351) to rewrite the boundary conditions of Eq. (350) as

$$\begin{gathered}\phi = 0 \quad \& \quad \phi' = 0 \quad @x = 0; \\ YI\phi'''\eta - M_t\phi(-\omega^2\eta) = 0 \rightarrow YI\phi''' + \omega^2 M_t\phi = 0 \quad @x = L; \\ YI\phi''\eta + I_t\phi'(-\omega^2\eta) = 0 \rightarrow YI\phi'' - \omega^2 I_t\phi' = 0 \quad @x = L.\end{gathered} \tag{358}$$

The unknown spatial coefficients of Eq. (356) (i.e. C_1 to C_4) can be solved from the spatial boundary conditions provided in Eq. (358). The displacement boundary condition at $x = 0$ results in

$$\phi(0) = C_1\cos(0) + C_2\cosh(0) + C_3\sin(0) + C_4\sinh(0) = C_1 + C_2 = 0. \tag{359}$$

The slope boundary condition at $x = 0$ results in

$$\phi'(0) = -C_1\frac{\lambda}{L}\sin(0) + C_2\frac{\lambda}{L}\sinh(0) + C_3\frac{\lambda}{L}\cos(0) + C_4\frac{\lambda}{L}\cosh(0) = C_3 + C_4 = 0. \tag{360}$$

Since $C_1 = -C_2$ and $C_3 = -C_4$, the spatial equation in Eq. (356) can be written as

$$\phi = C_1\left[\cos\left(\frac{\lambda}{L}x\right) - \cosh\left(\frac{\lambda}{L}x\right)\right] + C_3\left[\sin\left(\frac{\lambda}{L}x\right) - \sinh\left(\frac{\lambda}{L}x\right)\right]. \tag{361}$$

The third boundary condition of Eq. (358) leads to

$$\begin{gathered} YI\frac{\lambda^3}{L^3}\{C_1[\sin(\lambda) - \sinh(\lambda)] + C_3[-\cos(\lambda) - \cosh(\lambda)]\} \\ +\omega^2 M_t\{C_1[\cos(\lambda) - \cosh(\lambda)] + C_3[\sin(\lambda) - \sinh(\lambda)]\} = 0, \end{gathered} \tag{362}$$

or, after dividing through by $YI\lambda^3/L^3$

$$\begin{gathered} \{C_1[\sin(\lambda) - \sinh(\lambda)] + C_3[-\cos(\lambda) - \cosh(\lambda)]\} \\ +\frac{\lambda M_t}{Lm}\{C_1[\cos(\lambda) - \cosh(\lambda)] + C_3[\sin(\lambda) - \sinh(\lambda)]\} = 0, \end{gathered} \tag{363}$$

The fourth boundary condition of Eq. (358) leads to

$$\begin{gathered} YI\frac{\lambda^2}{L^2}\{C_1[-\cos(\lambda) - \cosh(\lambda)] + C_3[-\sin(\lambda) - \sinh(\lambda)]\} \\ -\omega^2 I_t\frac{\lambda}{L}\{C_1[-\sin(\lambda) - \sinh(\lambda)] + C_3[\cos(\lambda) - \cosh(\lambda)]\} = 0. \end{gathered} \tag{364}$$

or, after dividing through by $YI\,\lambda^2/L^2$

$$\begin{gathered} \{C_1[-\cos(\lambda) - \cosh(\lambda)] + C_3[-\sin(\lambda) - \sinh(\lambda)]\} \\ -\frac{\lambda^3 I_t}{L^3 m}\{C_1[-\sin(\lambda) - \sinh(\lambda)] + C_3[\cos(\lambda) - \cosh(\lambda)]\} = 0. \end{gathered} \tag{365}$$

Eq. (363) and Eq. (365) can be put into matrix form as

$$\begin{bmatrix} a_{11} & a_{12} \\ a_{21} & a_{22} \end{bmatrix}\begin{bmatrix} C_1 \\ C_3 \end{bmatrix} = \begin{bmatrix} 0 \\ 0 \end{bmatrix}, \tag{366}$$

where

$$\begin{aligned} a_{11} &= [\sin(\lambda) - \sinh(\lambda)] + \frac{\lambda M_t}{Lm}[\cos(\lambda) - \cosh(\lambda)], \\ a_{12} &= [-\cos(\lambda) - \cosh(\lambda)] + \frac{\lambda M_t}{Lm}[\sin(\lambda) - \sinh(\lambda)], \\ a_{21} &= [-\cos(\lambda) - \cosh(\lambda)] - \frac{\lambda^3 I_t}{L^3 m}[-\sin(\lambda) - \sinh(\lambda)], \\ a_{22} &= [-\sin(\lambda) - \sinh(\lambda)] - \frac{\lambda^3 I_t}{L^3 m}[\cos(\lambda) - \cosh(\lambda)]. \end{aligned} \tag{367}$$

For a nontrivial solution of C_1 and C_3, the determinant of the coefficient matrix must be equal to zero. This leads to the characteristic equation

$$\begin{gathered} -1 - \frac{\lambda^4 M_t I_t}{L^4 m^2} + \cosh(\lambda)\left[\left(\frac{\lambda^4 M_t I_t}{L^4 m^2} - 1\right)\cos(\lambda) + \left(\frac{\lambda M_t}{Lm} + \frac{\lambda^3 I_t}{L^3 m}\right)\sin(\lambda)\right] - \left(\frac{\lambda M_t}{Lm} - \right. \\ \left. \frac{\lambda^3 I_t}{L^3 m}\right)\cos(\lambda)\sinh(\lambda) = 0, \end{gathered} \tag{368}$$

which can be solved for the eigenvalues of each mode r of interest (i.e. λ_r). After noting the relationship $C_3 = -C_1(a_{11}/a_{12})$ from Eq. (366), the eigenfunction of each mode r can be written as

$$\phi_r = C_1\left\{\left[\cos\left(\frac{\lambda_r}{L}x\right) - \cosh\left(\frac{\lambda_r}{L}x\right)\right] + \varsigma_r\left[\sin\left(\frac{\lambda_r}{L}x\right) - \sinh\left(\frac{\lambda_r}{L}x\right)\right]\right\}. \tag{369}$$

where

$$\varsigma_r = -\frac{a_{11}}{a_{12}} = \frac{[\sin(\lambda_r)-\sinh(\lambda_r)]+\frac{\lambda_r M_t}{Lm}[\cos(\lambda_r)-\cosh(\lambda_r)]}{[\cos(\lambda_r)+\cosh(\lambda_r)]-\frac{\lambda_r M_t}{Lm}[\sin(\lambda_r)-\sinh(\lambda_r)]}. \tag{370}$$

The undamped natural frequency for mode r can then be determined from Eq. (357) as

$$\omega_r = \lambda_r^2\sqrt{\frac{YI}{mL^4}}. \tag{371}$$

5.3.1.5. Mass-Normalized Eigenfunctions

The coefficient C_1 of Eq. (369) can be determined by normalizing the eigenfunctions. Consider the governing spatial equation given in Eq. (355)

$$\phi'''' - \frac{\gamma m}{YI}\phi = 0. \tag{372}$$

Taking ϕ_r and ϕ_s to be the solutions at modes r and s

$$\begin{aligned} YI\phi_r'''' &= \omega_r^2 m\phi_r, \\ YI\phi_s'''' &= \omega_s^2 m\phi_s. \end{aligned} \tag{373}$$

Mulitplying the first equation in Eq. (373) by ϕ_s and integrating over the length of the beam leads to

$$YI\int_0^L \phi_s\phi_r''''\,dx = \omega_r^2 m\int_0^L \phi_s\phi_r dx. \tag{374}$$

Use integration by parts to expand the left hand side spatial integral as

$$\int_0^L \phi_s\phi_r''''\,dx = \phi_s\phi_r'''|_0^L - \int_0^L \phi_s'\phi_r'''dx. \tag{375}$$

Use integration by parts to expand the right hand side spatial integral of Eq. (375) as

$$\int_0^L \phi_s'\phi_r'''dx = \phi_s'\phi_r''|_0^L - \int_0^L \phi_s''\phi_r''dx. \tag{376}$$

Eq. (374) can then be rewritten as

$$YI\left[\phi_s\phi_r'''|_0^L - \phi_s'\phi_r''|_0^L + \int_0^L \phi_s''\phi_r'' dx\right] = \omega_r^2 m \int_0^L \phi_s\phi_r dx. \tag{377}$$

Incorporating the boundary conditions from Eq. (358) leads to

$$YI\left[\phi_s(L)\left\{\frac{\omega_r^2 M_t}{YI}\left(-\phi_r(L)\right)\right\} - \phi_s'(L)\left\{\frac{\omega_r^2 I_t}{YI}\phi_r'(L)\right\} + \int_0^L \phi_s''\phi_r'' dx\right] = \omega_r^2 m \int_0^L \phi_s\phi_r dx, \tag{378}$$

which can be rearranged as

$$YI\int_0^L \phi_s''\phi_r'' dx = \omega_r^2\left[m\int_0^L \phi_s\phi_r dx + M_t\phi_s(L)\phi_r(L) + I_t\phi_s'(L)\phi_r'(L)\right]. \tag{379}$$

Similarly

$$YI\int_0^L \phi_r''\phi_s'' dx = \omega_s^2\left[m\int_0^L \phi_r\phi_s dx + M_t\phi_r(L)\phi_s(L) + I_t\phi_r'(L)\phi_s'(L)\right]. \tag{380}$$

Subtracting Eq. (380) from Eq. (379) leads to

$$0 = (\omega_r^2 - \omega_s^2)\left[m\int_0^L \phi_s\phi_r dx + M_t\phi_s(L)\phi_r(L) + I_t\phi_s'(L)\phi_r'(L)\right]. \tag{381}$$

Since $\omega_r^2 \neq \omega_s^2$, the orthogonality condition arises

$$0 = m\int_0^L \phi_s\phi_r dx + M_t\phi_s(L)\phi_r(L) + I_t\phi_s'(L)\phi_r'(L). \tag{382}$$

The eigenfunction amplitude (i.e. C_1) can be found from

$$m\int_0^L \phi_s\phi_r dx + M_t\phi_s(L)\phi_r(L) + I_t\phi_s'(L)\phi_r'(L) = \delta_{rs}, \tag{383}$$

where δ_{rs} is the Kronecker delta. Substituting Eq. (383) into Eq. (379) leads to the alternative form

$$YI\int_0^L \phi_s''\phi_r'' dx = \omega_r^2\delta_{rs}. \tag{384}$$

5.3.1.6. Coupled Electrical Equation for a Piezoelectric Element

A piezoelectric element can be represented as a current source in parallel with its internal capacitance [208]. Applying Kirchoff's law to the circuit shown in Figure 88 leads to

$$i_{\tilde{p}} = C_{\tilde{p}}\dot{v} + \frac{v}{R}. \tag{385}$$

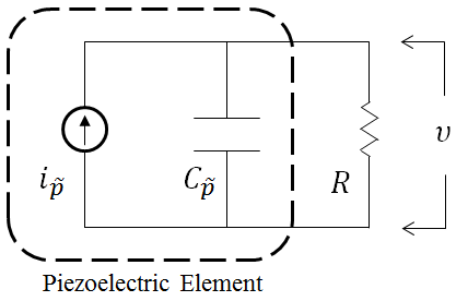

Figure 88. Piezoelectric Circuit Model

The electric displacement (D) can be used to relate this circuit equation to the mechanical system [32]

$$\int_A n_i \dot{D}_i \, dA = \bar{Y} v, \tag{386}$$

where the circuit admittance is $\bar{Y} = 1/R$ and the integral is over the surface area of the piezoelectric. Expanding Eq. (386)

$$\int_A \dot{D}_3 \, dA = \int_A \frac{d}{dt}\left[\bar{e}_{31} S_1^{\tilde{p}} + \bar{\varepsilon}_{33}^S E_3\right] dA = \frac{v}{R}, \tag{387}$$

Where $\bar{\varepsilon}_{33}^S$ is the permittivity component at constant strain. Taking the average stress in the piezoelectric layer to be

$$S_1^{\tilde{p}} = -\left(\frac{h_{\tilde{p}} + h_{\tilde{s}}}{2}\right) w_R'', \tag{388}$$

Eq. (388) can be expanded as

$$\int_A \left[-\bar{e}_{31}\left(\frac{h_{\tilde{p}} + h_{\tilde{s}}}{2}\right) \dot{w}_R'' + \bar{\varepsilon}_{33}^S \dot{E}_3\right] dA = \frac{v}{R}. \tag{389}$$

Utilizing Eq. (351) and taking $E_3 = -v/h_{\tilde{p}}$

$$\int_A \left[\sum_{r=1}^{\infty}\left(-\bar{e}_{31}\left(\frac{h_{\tilde{p}} + h_{\tilde{s}}}{2}\right) \dot{\eta}_r \phi_r''\right) - \bar{\varepsilon}_{33}^S \frac{\dot{v}}{h_{\tilde{p}}}\right] dA = \frac{v}{R}. \tag{390}$$

Expanding the integral and rearranging terms leads to

$$-\sum_{r=1}^{\infty} \bar{e}_{31}\left(\frac{h_{\tilde{p}} + h_{\tilde{s}}}{2}\right) \dot{\eta}_r \int_A \phi_r'' \, dA = \bar{\varepsilon}_{33}^S \frac{\dot{v}}{h_{\tilde{p}}} \int_A dA + \frac{v}{R}. \tag{391}$$

Integrating over the surface area of the electrode results in

$$-\sum_{r=1}^{\infty} \dot{\eta}_r \left[\bar{e}_{31}\left(\frac{h_{\tilde{p}} + h_{\tilde{s}}}{2}\right) b \phi_r'(L)\right] = \bar{\varepsilon}_{33}^S \frac{\dot{v}}{h_{\tilde{p}}} bL + \frac{v}{R}, \tag{392}$$

or equivalently

$$-\sum_{r=1}^{\infty}\kappa_r\dot{\eta}_r = \frac{\bar{\varepsilon}_{33}^{S}bL}{h_{\tilde{p}}}\dot{v} + \frac{v}{R}, \tag{393}$$

where the modal coupling coefficient (κ_r) is defined as

$$\kappa_r = \bar{e}_{31}\left(\frac{h_{\tilde{p}}+h_{\tilde{s}}}{2}\right)b\phi_r'(L). \tag{394}$$

Comparing Eq. (385) and Eq. (394), the current stemming from the piezoelectric and the piezoelectric's internal capacitance are

$$i_{\tilde{p}} = -\sum_{r=1}^{\infty}\kappa_r\dot{\eta}_r \quad \text{and} \quad C_{\tilde{p}} = \frac{\bar{\varepsilon}_{33}^{S}bL}{h_{\tilde{p}}}. \tag{395}$$

5.3.1.7. Coupled Electrical Equation for a Piezoelectric Bimorph

The electrical circuit for a parallel and series connection are shown in Figure 89 [36]. Applying Kirchoff's laws leads to

$$i_{\tilde{p}}^{p} = C_{\tilde{p}}\dot{v}^{p} + \frac{v^{p}}{2R}, \tag{396}$$

for the parallel connection and

$$i_{\tilde{p}}^{s} = \frac{C_{\tilde{p}}\dot{v}^{s}}{2} + \frac{v^{s}}{R}, \tag{397}$$

for the series connection.

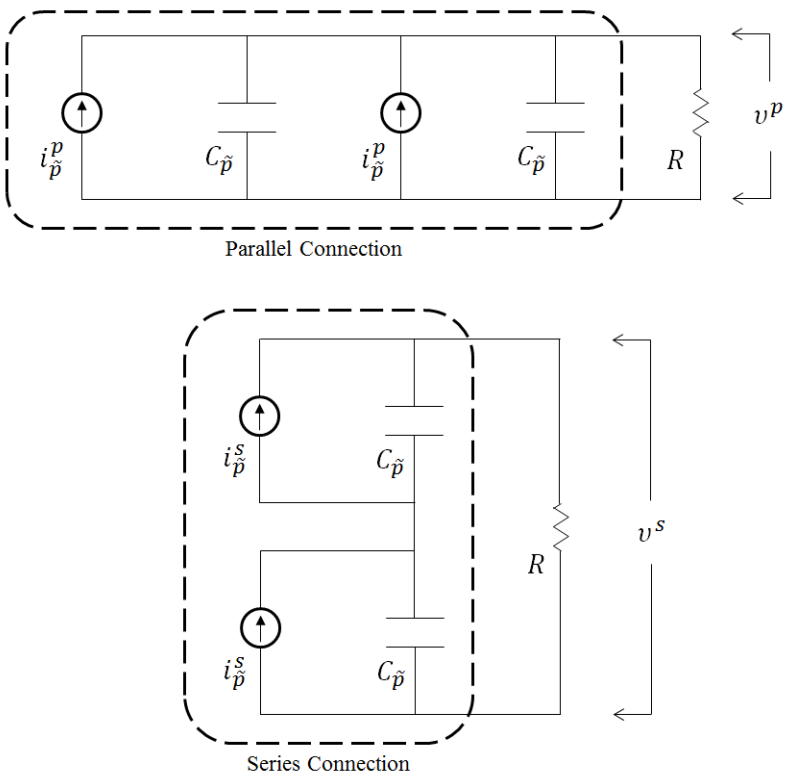

Figure 89. Electrical Circuits for Piezoelectric Bimorph [36]

5.3.1.8. System Response to Harmonic Loading

After substituting Eq. (351) into Eq. (347) or Eq. (348) and applying the orthogonality conditions, the governing modal equation can be written in general terms as [36]

$$\ddot{\eta}_r + 2\zeta_r\omega_r\dot{\eta}_r + \omega_r^2\eta_r - \Theta_r v = f_r, \tag{398}$$

where the modal electromechancial coupling term and modal forcing terms are written as

$$\Theta_r = \vartheta\phi_r'(L), \tag{399}$$

and

$$f_r = \left[-m\int_0^L \phi_r dx - M_t\phi_r(L)\right]\ddot{w}_B. \tag{400}$$

In the case of a parallel connection, where Eq. (335) is noted,

$$\Theta_r^p = \vartheta^p\phi_r'(L) = 2b\bar{e}_{31}\left(\frac{h_{\tilde{p}}+h_{\tilde{s}}}{2}\right)\phi_r'(L). \tag{401}$$

The relevant circuit equation, given by Eq. (396) is expanded using Eq. (395)

$$i_{\tilde{p}}^{p} = -\sum_{r=1}^{\infty} \kappa_r \dot{\eta}_r^{p} = C_{\tilde{p}} \dot{v}^{p} + \frac{v^{p}}{2R}. \tag{402}$$

Multiplying through by 2 and introducing the modal coupling coefficient (Eq. (394)) results in

$$-\sum_{r=1}^{\infty} \left\{ 2\bar{e}_{31} \left(\frac{h_{\tilde{p}} + h_{\tilde{s}}}{2} \right) b \phi_r'(L) \right\} \dot{\eta}_r^{p} = 2C_{\tilde{p}} \dot{v}^{p} + \frac{v^{p}}{R}. \tag{403}$$

Note that the bracketed term is equivalent to Θ_r^{p} given by Eq. (401). Turning to the series connection, the modal electromechanical coupling term is

$$\Theta_r^{s} = \vartheta^{s} \phi_r'(L) = b\bar{e}_{31} \left(\frac{h_{\tilde{p}} + h_{\tilde{s}}}{2} \right) \phi_r'(L). \tag{404}$$

where Eq. (343) has been utilized. The relevant circuit equation, given by Eq. (397) is expanded using Eq. (395)

$$i_{\tilde{p}}^{s} = -\sum_{r=1}^{\infty} \kappa_r \dot{\eta}_r^{s} = \frac{C_{\tilde{p}} \dot{v}^{s}}{2} + \frac{v^{s}}{R}, \tag{405}$$

Introducing the modal coupling coefficient (Eq. (394)) results in

$$-\sum_{r=1}^{\infty} \left\{ \bar{e}_{31} \left(\frac{h_{\tilde{p}} + h_{\tilde{s}}}{2} \right) b \phi_r'(L) \right\} \dot{\eta}_r^{s} = \frac{C_{\tilde{p}} \dot{v}^{s}}{2} + \frac{v^{s}}{R}, \tag{406}$$

where the bracketed term is equivalent to Θ_r^{s} given by Eq. (404).

The equivalent electromechanical equations, representing both the parallel and series configurations, can thus be written as

$$\begin{aligned} \ddot{\eta}_r + 2\zeta_r \omega_r \dot{\eta}_r + \omega_r^2 \eta_r - \Theta_r v &= f_r, \\ -\sum_{r=1}^{\infty} \Theta_r \dot{\eta}_r &= C_{\tilde{p}}^{eq} \dot{v} + \frac{v}{R}, \end{aligned} \tag{407}$$

where

$$\begin{aligned} \Theta_r &= 2\bar{e}_{31} \left(\frac{h_{\tilde{p}} + h_{\tilde{s}}}{2} \right) b \phi_r'(L), \\ C_{\tilde{p}}^{eq} &= 2C_{\tilde{p}} = 2\frac{\bar{\varepsilon}_{33}^{S} bL}{h_{\tilde{p}}}, \end{aligned} \tag{408}$$

for a parallel connection and

$$\begin{aligned} \Theta_r &= \bar{e}_{31} \left(\frac{h_{\tilde{p}} + h_{\tilde{s}}}{2} \right) b \phi_r'(L), \\ C_{\tilde{p}}^{eq} &= \frac{C_{\tilde{p}}}{2} = \frac{\bar{\varepsilon}_{33}^{S} bL}{2h_{\tilde{p}}}, \end{aligned} \tag{409}$$

for a series connection.

Assuming the driving base motion is harmonic and of the form

$$w_b = \bar{W}_B e^{i\omega t}, \tag{410}$$

where $\bar{W}_B$ is the translation amplitude and ω is the excitation frequency, the harmonic forcing function given by Eq. (400) is written as

$$f_r = \left[-m\int_0^L \phi_r dx - M_t\phi_r(L)\right](-\omega^2\bar{W}_B)e^{i\omega t}, \tag{411}$$

or

$$f_r = F_r e^{i\omega t}, \tag{412}$$

where

$$\begin{gathered} F_r = \left[-m\int_0^L \phi_r dx - M_t\phi_r(L)\right](-\omega^2\bar{W}_B) = \sigma_r(-\omega^2\bar{W}_B). \\ \sigma_r = -m\int_0^L \phi_r dx - M_t\phi_r(L). \end{gathered} \tag{413}$$

For a harmonic base motion, the steady-state mechanical response and voltage response of the beam are assumed to be harmonic and of the form

$$\eta_r = \mathrm{H}_r e^{i\omega t} \quad \text{and} \quad \upsilon = \bar{V} e^{i\omega t} \tag{414}$$

Rewriting Eq. (407) in terms of Eq. (412) and Eq. (414)

$$\begin{gathered} -\omega^2\mathrm{H}_r + 2\zeta_r\omega_r i\omega\mathrm{H}_r + \omega_r^2\mathrm{H}_r - \Theta_r\bar{V} = F_r, \\ -\sum_{r=1}^{\infty}\Theta_r i\omega\mathrm{H}_r = C_{\tilde{p}}^{eq} i\omega\bar{V} + \frac{\bar{V}}{R}, \end{gathered} \tag{415}$$

Equating the two electromechanical equations through H_r leads to

$$-\sum_{r=1}^{\infty}\Theta_r i\omega\left[\frac{F_r+\Theta_r\bar{V}}{(-\omega^2+2\zeta_r\omega_r i\omega+\omega_r^2)}\right] = \left[C_{\tilde{p}}^{eq} i\omega + \frac{1}{R}\right]\bar{V}. \tag{416}$$

Expanding Eq. (416)

$$-\sum_{r=1}^{\infty}\frac{\Theta_r i\omega F_r}{(-\omega^2+2\zeta_r\omega_r i\omega+\omega_r^2)} - \sum_{r=1}^{\infty}\frac{i\omega\Theta_r^2\bar{V}}{(-\omega^2+2\zeta_r\omega_r i\omega+\omega_r^2)} = \left[C_{\tilde{p}}^{eq} i\omega + \frac{1}{R}\right]\bar{V}, \tag{417}$$

and reordering leads to

$$\bar{V} = \frac{-\sum_{r=1}^{\infty} \frac{\Theta_r i\omega F_r}{(-\omega^2 + 2\zeta_r \omega_r i\omega + \omega_r^2)}}{\sum_{r=1}^{\infty} \frac{i\omega \Theta_r^2}{(-\omega^2 + 2\zeta_r \omega_r i\omega + \omega_r^2)} + \left[C_{\tilde{p}}^{eq} i\omega + \frac{1}{R}\right]}. \tag{418}$$

The steady-state time-dependent voltage can be found with Eq. (414) and Eq. (418). Having obtained values for F_r and $\bar{V}$ by means of Eq. (413) and Eq. (418), H_r can be calculated through Eq. (415)

$$\mathrm{H}_r = \frac{F_r + \Theta_r \bar{V}}{(-\omega^2 + 2\zeta_r \omega_r i\omega + \omega_r^2)} = \left\{ F_r - \Theta_r \frac{\sum_{r=1}^{\infty} \frac{\Theta_r i\omega F_r}{(-\omega^2 + 2\zeta_r \omega_r i\omega + \omega_r^2)}}{\sum_{r=1}^{\infty} \frac{i\omega \Theta_r^2}{(-\omega^2 + 2\zeta_r \omega_r i\omega + \omega_r^2)} + \left[C_{\tilde{p}}^{eq} i\omega + \frac{1}{R}\right]} \right\} \frac{1}{(-\omega^2 + 2\zeta_r \omega_r i\omega + \omega_r^2)}. \tag{419}$$

Utilizing Eq. (414), the relative displacement response can then be calculated as

$$w_R(x,t) = \sum_{r=1}^{\infty} \phi(x)\, \eta_r(t). \tag{420}$$

Or in expanded form

$$w_R = \sum_{r=1}^{\infty} \left\{ F_r - \Theta_r \frac{\sum_{r=1}^{\infty} \frac{\Theta_r i\omega F_r}{(-\omega^2 + 2\zeta_r \omega_r i\omega + \omega_r^2)}}{\sum_{r=1}^{\infty} \frac{i\omega \Theta_r^2}{(-\omega^2 + 2\zeta_r \omega_r i\omega + \omega_r^2)} + \left[C_{\tilde{p}}^{eq} i\omega + \frac{1}{R}\right]} \right\} \frac{\phi(x) e^{i\omega t}}{(-\omega^2 + 2\zeta_r \omega_r i\omega + \omega_r^2)}. \tag{421}$$

Frequency response functions (FRFs) can be defined to relate the input base acceleration ($\ddot{w}_B$) to output voltage (v) or relative displacement (w_R). Define a FRF for the voltage as α

$$v = \alpha \ddot{w}_B. \tag{422}$$

Utilizing Eq. (410) and Eq. (414)

$$\bar{V} e^{i\omega t} = \alpha(-\omega^2 \bar{W}_B) e^{i\omega t}. \tag{423}$$

Rearranging terms and incorporating Eq. (413) and Eq. (418)

$$\alpha(\omega) = \frac{\bar{V}}{-\omega^2 \bar{W}_B} = \frac{-\sum_{r=1}^{\infty} \frac{\Theta_r i\omega \sigma_r}{(-\omega^2 + 2\zeta_r \omega_r i\omega + \omega_r^2)}}{\sum_{r=1}^{\infty} \frac{i\omega \Theta_r^2}{(-\omega^2 + 2\zeta_r \omega_r i\omega + \omega_r^2)} + \left[C_{\tilde{p}}^{eq} i\omega + \frac{1}{R}\right]}. \tag{424}$$

Define a FRF for the relative displacement as β

$$w_R = \beta \ddot{w}_B. \tag{425}$$

Rearranging terms and incorporating Eq. (413), Eq. (414), Eq. (419), and Eq. (420)

$$\beta(\omega,x)=\frac{\sum_{r=1}^{\infty}\phi(x)\mathrm{H}_r}{-\omega^2\bar{W}_B}=\sum_{r=1}^{\infty}\left\{\sigma_r-\Theta_r\frac{\sum_{r=1}^{\infty}\frac{\Theta_r i\omega\sigma_r}{(-\omega^2+2\zeta_r\omega_r i\omega+\omega_r^2)}}{\sum_{r=1}^{\infty}\frac{i\omega\Theta_r^2}{(-\omega^2+2\zeta_r\omega_r i\omega+\omega_r^2)}+\left[C_{\tilde{p}}^{eq}i\omega+\frac{1}{R}\right]}\right\}\frac{\phi(x)}{(-\omega^2+2\zeta_r\omega_r i\omega+\omega_r^2)}. \quad (426)$$

5.3.1.9. Extension to Periodic Loading

A periodic base motion can be approximated by a truncated Fourier series as [204]

$$\ddot{w}_B(t)\cong\frac{a_0}{2}+\sum_{n=1}^{N}a_n\cos\left(n\frac{2\pi}{T}t\right)+b_n\sin\left(n\frac{2\pi}{T}t\right), \quad (427)$$

where the series coefficients are defined as

$$\begin{aligned}a_0&=\frac{2}{T}\int_0^T\ddot{w}_B(t)dt,\\ a_n&=\frac{2}{T}\int_0^T\ddot{w}_B(t)\cos\left(n\frac{2\pi}{T}t\right)dt,\\ b_n&=\frac{2}{T}\int_0^T\ddot{w}_B(t)\sin\left(n\frac{2\pi}{T}t\right)dt,\end{aligned} \quad (428)$$

and the length of the signal is given by T. For all typical structural systems with near-zero mean acceleration over the time interval of interest, $a_0\approx 0$. Using the FRF given in Eq. (424) the voltage output is found as

$$v(t)=\sum_{n=1}^{N}\left|\alpha\left(n\frac{2\pi}{T}\right)\right|\left[a_n\cos\left[\left(n\frac{2\pi}{T}t\right)+\Phi\left(n\frac{2\pi}{T}\right)\right]+b_n\sin\left[\left(n\frac{2\pi}{T}t\right)+\Phi\left(n\frac{2\pi}{T}\right)\right]\right], \quad (429)$$

where $|\alpha(2\pi n/T)|$ and $\Phi(2\pi n/T)$ are the modulus and phase angle of the FRF. Similarly, the relative displacement response can be found as

$$w_R(x,t)=\sum_{n=1}^{N}\left|\beta\left(n\frac{2\pi}{T}\right)\right|\left[a_n\cos\left[\left(n\frac{2\pi}{T}t\right)+\Psi\left(n\frac{2\pi}{T}\right)\right]+b_n\sin\left[\left(n\frac{2\pi}{T}t\right)+\Psi\left(n\frac{2\pi}{T}\right)\right]\right]. \quad (430)$$

The instantaneous power output is found as

$$P_{inst}(t)=\frac{v(t)^2}{R}. \quad (431)$$

The average power output is found as

$$P_{avg}=\frac{1}{T}\int_0^T P_{inst}(t)dt. \quad (432)$$

5.3.2. Practical Application

The user begins by entering acceleration time histories (also termed acceleration profiles) of the production tube at the harvester location, which represent the ground motions driving the attached piezoelectric energy harvester. Each acceleration profile is then represented by a Fourier series (see Eq. 428) to facilitate future calculation of the voltage and relative tip displacement responses (see Eq. 429 and Eq. 430). The acceleration profiles are unidirectional as, unlike the FS analysis, only a single piezoelectric element is analyzed in the SS due to the increased computational effort of the coupled equations of motion. The acceleration time histories can be based on actual downhole accelerometer data or can be artificially generated as needed. Since the acceleration time histories are generally non-stationary over the life of the well (due to changes in production rate, hydrocarbon density, etc.), the acceleration profiles must be discretized by the user such that the profiles are locally stationary. The user defines an operating schedule which specifies when each acceleration profile is active in the model.

The user then defines constant inputs such as the beam mass (m), the density of the tip mass, the number of modes to be considered, etc. Next, the range and discretization step of each parameter is specified: the tip mass (M_t) and resistive load (R) are variables of interest in maximizing the power output over the user specified time domain of interest. Variables that are expected to change over time and/or temperature are included in separate sub-functions.

5.3.2.1. Variable Dependence

Since the operating environment may change over time, several inputs are made dependent on other variables. For instance, the mass moment of inertia of the tip mass is made a function of the tip mass (an optimization variable), an assumed density of the tip mass, and an assumed geometry (see Figure 90) [209]

$$I_t = \frac{5}{12} M_t a^2 = \frac{5}{12} \frac{M_t^2}{\rho_t b}. \tag{433}$$

Other dependencies include:

- The thermal expansion coefficient of certain piezoelectric materials has been shown to increase with increasing temperature, implying a nonlinear relationship between beam length and temperature [210]-[211].
- The modal damping ratio is known to be sensitive to both temperature and frequency [212]-[213].
- Several researchers have shown that the piezoelectric elastic modulus ($\bar{c}_{11}^E = 1/s_{11}^E$) decreases with increasing temperature [211]. Other tests have shown that this trend will eventually reverse course: at a certain thermal load the elastic modulus will begin to increase with increasing temperature [214]-[215].
- The elastic modulus of glass-epoxy laminates (often used as a substrate layer [216]) has been shown to steadily decrease with increasing temperature (when below the glass transition temperature) [217]. Since the elastic modulus of both the substrate and piezoelectric show temperature dependence, the flexural rigidity of the harvester is temperature dependent.
- It is well known that load cycling of structural elements leads to the development of microcracks which, when orthogonal to the longitudinal axis of the energy harvester, will reduce the sections effective inertia. The flexural rigidity of the energy harvester is then dependent on the number and amplitude of load cycles.

- The magnitude of the piezoelectric strain constant ($d_{31} = \bar{e}_{31}/\bar{c}_{11}^{E}$) has been shown to increase with increasing temperature [214]-[215], [218]-[219], decrease 4-10% per decade due to aging [220]-[222], and decrease when electrically cycled [218].

- The piezoelectric capacitance (Eq. 395) can be written in terms of the permittivity component at constant strain ($\bar{\varepsilon}_{33}^{S}$) or constant stress ($\bar{\varepsilon}_{33}^{T}$) as [36]

$$C_{\tilde{p}} = \frac{\bar{\varepsilon}_{33}^{S} bL}{h_{\tilde{p}}} = \frac{[\bar{\varepsilon}_{33}^{T} - \bar{c}_{11}^{E}(d_{31})^2]bL}{h_{\tilde{p}}}. \tag{434}$$

  Researchers have found that the relative permittivity at constant stress increases with increasing temperature[214]-[215], [218]-[519]; several manufacturers have shown that capacitance increases with increasing temperature [223]-[225]. Capacitance has also been shown to age [225] and slightly degrade when mechanically cycled [226].

  The included dependencies are summarized in Table 45.

Table 45. Variable Dependencies

Variable*	Temperature**	Time	Load Cycle
Beam Length (L)	X		
Modal Damping Ratio (ζ_r)***	X		
Piezoelectric Elastic Modulus ($\bar{c}_{11}^{E}$)	X		
Flexural Rigidity (YI)	X		X
Piezoelectric Strain Constant (d_{31})	X	X	X
Piezoelectric Capacitance ($C_{\tilde{p}}$)	X	X	X

** The tip mass inertia is dependent on the tip mass.*
***The operating temperature is dependent on time.*
**** The modal damping ratio is dependent on the undamped natural frequency.*

These dependencies are defined by the user in tabular form within MATLAB sub-functions. When called upon by the script, the current temperature and time are used as input arguments; the current value of the variable of interest is returned. The variable is then modified based on the amount of accumulated damage stemming from load cycling (as applicable).

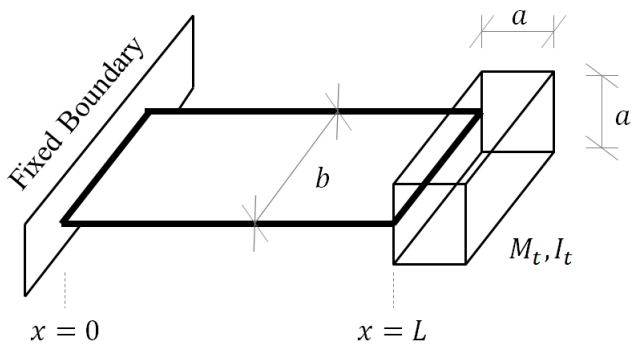

Figure 90. Assumed Tip Mass Geometry

5.3.2.2. Damage Accumulation

5.3.2.2.1. Background

In Section 5.3.2.1 it was noted that several properties degrade as the cumulative load cycles increase. For example, the accumulation of microcracking in the energy harvester will cause a decrease in its flexural rigidity and a subsequent change in the system's natural frequency. This may result in the system falling into or out of resonance, directly impacting the power output. To account for such changes, a damage metric and a damage model are needed.

One common damage metric is stress: a test element is cycled at a constant stress level until failure with element properties observed throughout the course of testing. The results are often plotted as property (i.e. flexural rigidity) vs. cycles and for multiple tests, stress vs. cycles to failure (an illustration is provided in Figure 91).

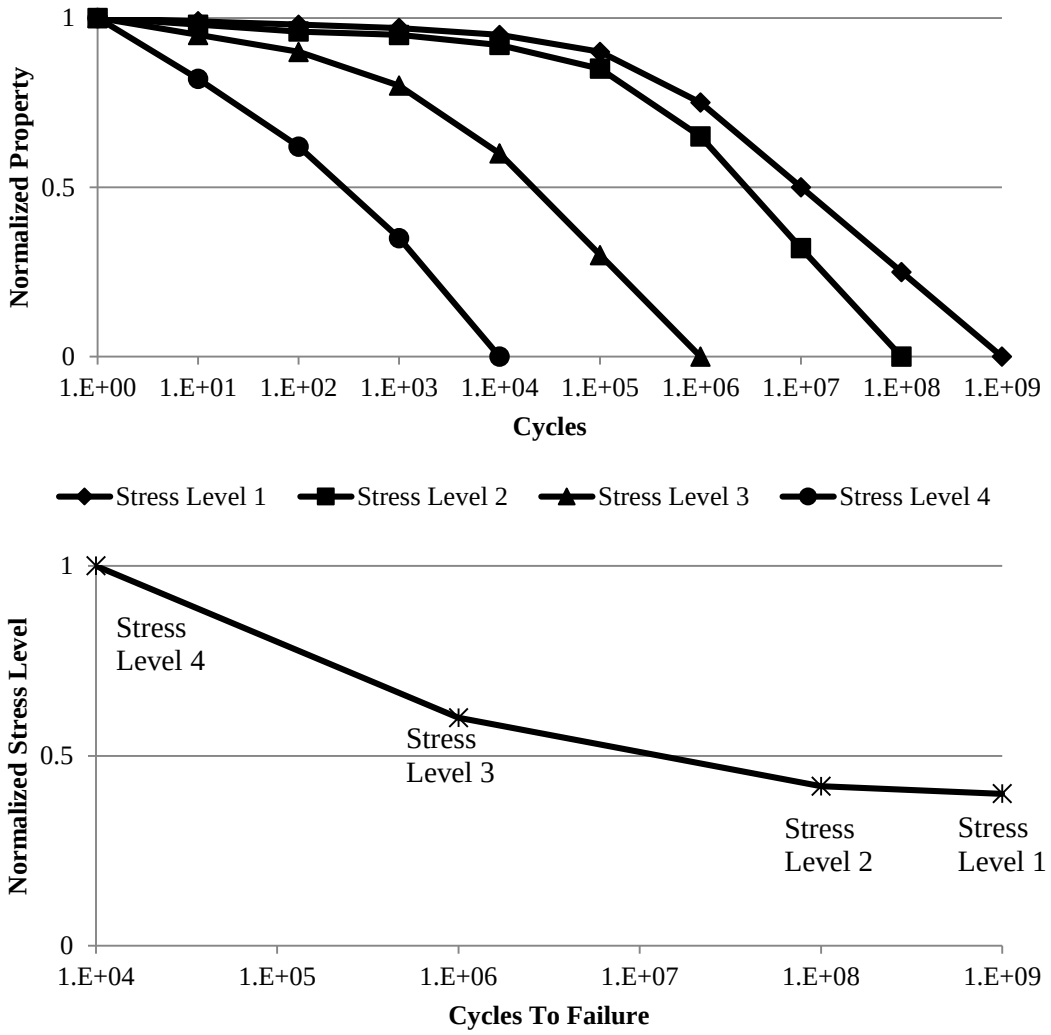

Figure 91. Stress Cycling

This metric becomes difficult to incorporate in conjunction with the SS model previously derived as the relative displacement output from the model (w_R) is based on a spatially uniform (or average) flexural rigidity. While the beam curvature (and subsequently a flexural stress term) can be calculated from this output, the output cannot account for any local damage (i.e. amplified curvature) that might be occurring - this is analogous to a linear analysis failing to capture localized curvature in the plastic hinge of a column.

An alternative metric is the relative tip displacement of the beam ($w_R(x = L)$): rather than cycling a test element to a specified stress level, the element can be cycled to a specified

displacement amplitude. As before, element properties can be observed throughout the course of testing and plotted as property vs. cycles and for multiple tests, amplitude vs. cycles to failure.

Consider the testing of Q identical piezoelectric bimorphs with each bimorph subject to a harmonic base acceleration resulting in a relative tip displacement amplitude A_k ($k = 1{:}\,Q$). After n cycles the cyclic loading is stopped and the relevant properties (V^a, V^b, etc.) of each bimorph tested. The Q bimorphs are again cyclically loaded and the process repeated until a property of interest degrades to failure at N_k cycles. A graphic depicting this process is shown in Figure 92.

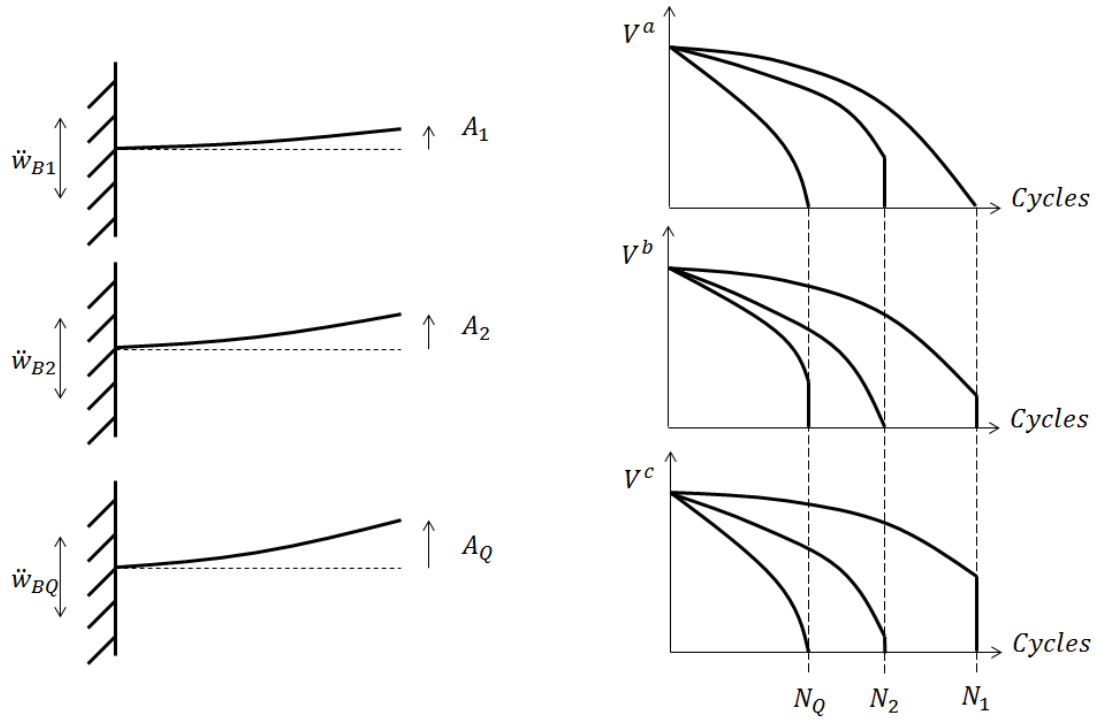

Figure 92. Cyclic Testing of Q Bimorphs

For a given property V with initial value V_i a representative output is enlarged in Figure 93. The damage from source k after n_k cycles is ΔV_k while the maximum possible damage

from source k is seen to be V_i and occurs after N_k cycles. Assume the damage from each load cycle is linearly additive such that

$$\Delta V_1 + \Delta V_2 + \Delta V_Q = \sum_{k=1}^{Q} \Delta V_k = C * V_i, \tag{435}$$

where C is a damage index representing the percent accumulated damage of variable V after n_k cycles at amplitude A_k $(k = 1{:}\,Q)$. Eq. (435) can be rewritten as

$$\sum_{k=1}^{Q} \frac{\Delta V_k}{V_i} = C \leq 1, \tag{436}$$

which is seen to be a weighted form of Miner's rule [227]. An equivalent interpretation is

$$\sum_{k=1}^{Q} D_k \leq \bar{D}, \tag{437}$$

where $\bar{D}$ is the total damage property V can sustain and D_k is damage to property V stemming from the k^{th} source (i.e. n_k cycles at amplitude A_k). Eq. (437) can be rewritten as

$$\sum_{k=1}^{Q} \frac{D_k}{\bar{D}} = C \leq 1. \tag{438}$$

where C again represents the percent accumulated damage. After n_k cycles at amplitude A_k $(k = 1{:}\,Q)$, the value of the damaged property is then

$$V_{damaged} = (1 - C)V_i. \tag{439}$$

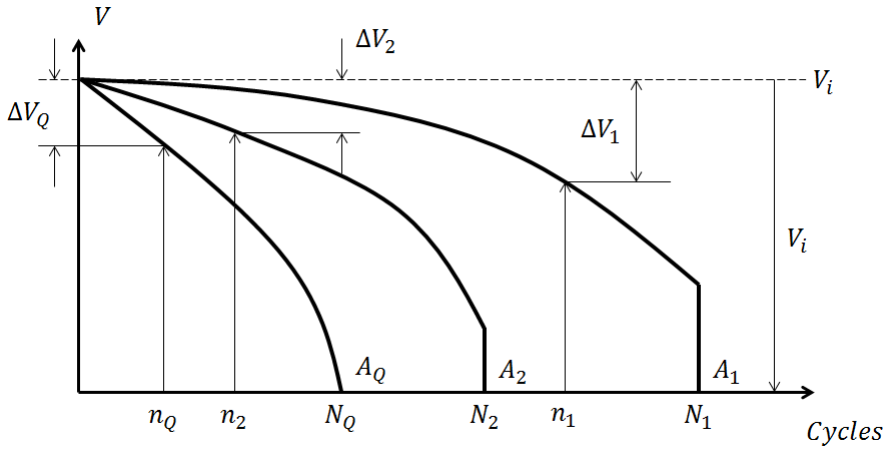

Figure 93. Cyclic Lifespan of Property V

5.3.2.2.2. Application

Prior to executing the script, the user specifies property degradation as a function of load cycles within a sub-function (see Figure 92). The relative tip displacement is calculated per Eq. 430 based on current system properties. A rainflow analysis is performed using the MATLAB toolbox RAINFLOW [228]-[229] to determine the number of cycles and the corresponding cycle amplitudes of the relative tip displacement for the current loading. To utilize the test data (Figure 92) the rainflow output is regrouped into the amplitudes specified by the user (i.e. the A_k's) in the sub-function and the corresponding cycles (i.e. the n_k's) counted. The just-calculated cycle counts are scaled to account for the total duration the given acceleration time history acts on the system and then added to the cumulative cycle counts from all previous loading (see Figure 94). The cumulative data is used to interpolate the damage (i.e. ΔV_k's) for each property allowing for the calculation of the damage index per Eq. (436) (Figure 93). At the start of the next loading cycle the system properties are modified per Eq. (439) after accounting for other variable dependencies.

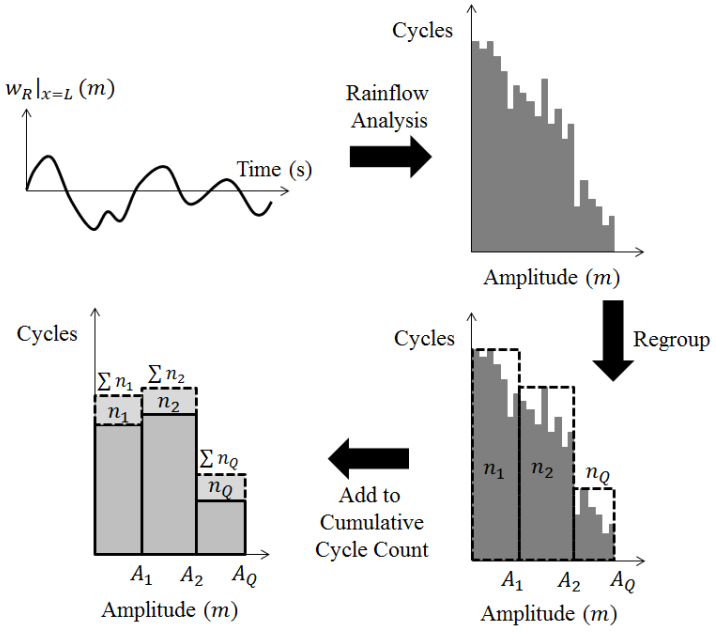

Figure 94. Regrouping Rainflow Output

5.3.2.3. Calculation Looping

The following analysis procedure describes the calculation sequence in the script. The calculations occur within three 'for' loops covering the tip masses, resistive loads, and time increments specified by the user.

- For the current time determine the current temperature (sub-function).
- For the current temperature determine the current beam length (sub-function), piezoelectric elastic modulus (sub-function), and undamaged flexural rigidity (sub-function).
- For the current time and temperature determine the undamaged piezoelectric strain constant (sub-function) and piezoelectric capacitance (sub-function).
- Modify the undamaged flexural rigidity, piezoelectric strain constant, and piezoelectric capacitance by their respective damage accumulation factors (C's from a sub-function; see Eq. (439)).
- Calculate the effective piezoelectric stress constant ($\bar{e}_{31} = d_{31}\bar{c}_{11}^{E}$).
- Determine the eigenvalues (λ_r's) per Eq. (368).
- Calculate the unnormalized eigenfunction per Eq. (369) and Eq. (370).
- Normalize the eigenfunction per Eq. (383).
- Calculate the undamped natural frequency per Eq. (371).
- For the current temperature and undamped natural frequency determine the current damping ratio (sub-function).
- Calculate the forcing coefficients (σ_r's) per Eq. (413).

- Based on the user specified circuit connection calculate the coupling coefficients (Θ_r's) and equivalent capacitance ($C_{\tilde{p}}^{eq}$) per Eq. (408) or Eq. (409).
- Calculate the transfer functions for the voltage (α) and relative tip displacement (β) per Eq. (424) and Eq. (426).
- For the current time determine the current acceleration profile.
- Calculate the voltage, relative tip displacement, and instantaneous power output per Eq. (429), Eq. (430), and Eq. (431).
- Truncate the relative tip displacement and instantaneous power output time histories to eliminate initial transient effects.
- Calculate the average power output with the truncated instantaneous power output time history per Eq. (432).
- Perform a rainflow analysis (MATLAB toolbox) with the truncated relative tip displacement time history to determine load cycles and corresponding amplitudes. Scale the cycle counts based on the duration the relative tip displacement time history is applicable.
- Based on the rainflow analysis, calculate the cumulative damage (C's) to the flexural rigidity, piezoelectric strain constant, and piezoelectric capacitance (sub-function).
- Step forward in time. Use the new damage accumulation factors in the next time step.

5.3.3. Script Validation

The MATLAB script implementing these calculations can be found in Appendix I. The sub-functions performing the cumulative damage calculations and containing the variable

dependence for the piezoelectric strain constant are provided in Appendix J for reference. Four cases are used to validate the MATLAB script.

5.3.3.1. Fourier Series

Consider a square sine wave defined as

$$f(x) = 2\left(H\left(\frac{x}{L}\right) - H\left(\frac{x}{L} - 1\right)\right) - 1, \tag{440}$$

over $[0,2L]$ where H represents the Heaviside function. Since the function is odd the Fourier coefficients can be calculated from

$$b_n = \frac{1}{L}\int_0^{2L} f(x) sin\left(\frac{n\pi x}{L}\right) dx, \tag{441}$$

which reduces to [230]

$$b_n = \frac{4}{n\pi}\begin{cases} 0 & n = even \\ 1 & n = odd \end{cases}. \tag{442}$$

The analytical Fourier series for $f(x)$ is then

$$f(x) = \frac{4}{\pi}\sum_{n=1,3,5\ldots}^{n=\infty} \frac{1}{n} sin\left(\frac{n\pi x}{L}\right). \tag{443}$$

Taking $L = 1000$, the analytical expansion of Eq. (443) is truncated at $n = N$ and plotted in Figure 95 against the original function and the scripts Fourier expansion. The analytical and script outputs show excellent agreement. Both models show the expected convergence.

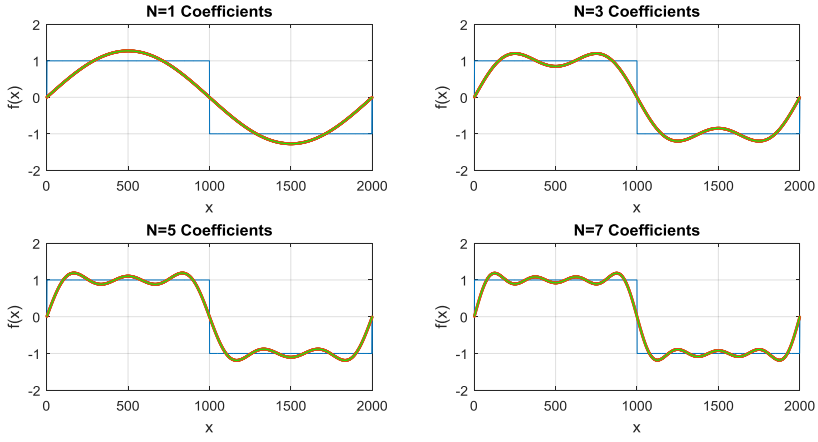

Figure 95. Fourier Series Comparison
Original Function (Blue), Analytical Expansion (Green), and Script Expansion (Red)

5.3.3.2. Modal Analysis

The modal frequencies and mode shapes calculated by the script are compared to results found using ABAQUS finite element analysis. Three cases are analyzed with the relevant inputs listed in Table 46. The calculated natural frequencies are compared in Table 47 while the mode shapes (after being normalized to unit magnitude) are compared in Figure 96, Figure 97, and Figure 98. The results show excellent agreement.

Table 46. Modal Analysis Comparison: Inputs

Case	1	2	3
Length L, (m)	0.01		
Width b, (m)	0.005		
Height (m)	0.0001		
Modes Considered	3		
Tip Mass M_t, (kg)	0	0.01	0.01
Tip Inertia I_t, $(kgm\text{^}2)$	0	0	$1.388e-6$
Beam Mass m, $(kg\ /\ m)$	0.0025		
Modulus Y, $(N\ /\ m\text{^}2)$	$4e11$		
Flexural Rigidity YI, $(Nm\text{^}2)$	$1.667e-4$		
Number of Elements (ABAQUS)	50		

Table 47. Natural Frequency Comparison

	Natural Frequency (Hz)								
Case	1			2			3		
Mode	Script	FEM	|Error|	Script	FEM	|Error|	Script	FEM	|Error|
1	14.45	14.45	0.00%	1.12	1.12	0.00%	1.10	1.10	0.00%
2	90.55	90.50	0.06%	63.46	63.46	0.00%	11.08	11.08	0.00%
3	253.53	253.36	0.07%	205.42	205.50	0.04%	92.80	92.82	0.02%

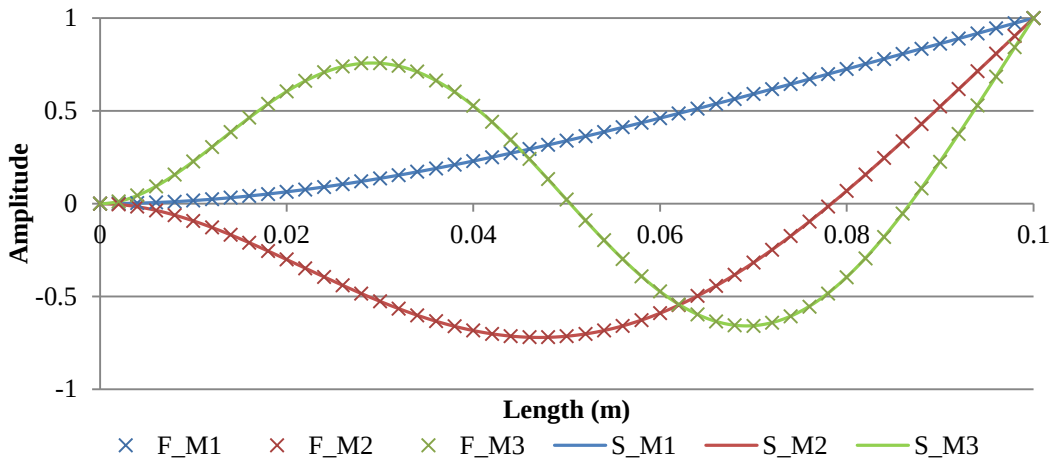

Figure 96. Case 1 Mode Shape Comparison
F=FEM; S=Script; M=Mode

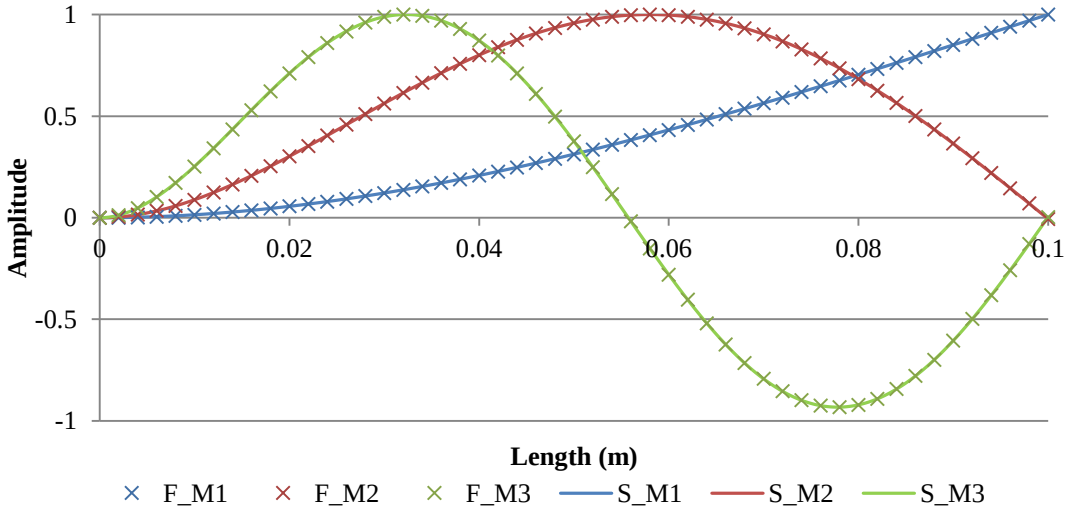

Figure 97. Case 2 Mode Shape Comparison
F=FEM; S=Script; M=Mode

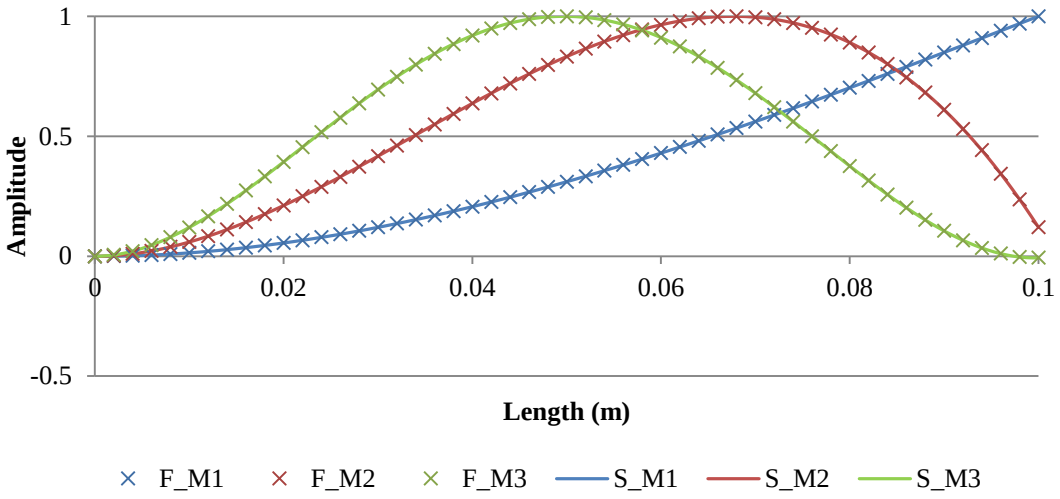

Figure 98. Case 3 Mode Shape Comparison
F=FEM; S=Script; M=Mode

5.3.3.3. Frequency Response Functions

The coded frequency response functions can be compared to results published by Erturk and Inman (2011) [36]. For the inputs listed in Table 48 the frequency response functions (FRFs) are calculated using seven different resistance values (see Table 49). Following the published format [36], the results are normalized by the gravitational constant and are plotted in Figure 99 and Figure 100. The script results show excellent agreement with the publishd figures and the same trends noted by Erturk and Inman (2011) [36] are seen: voltage output is seen to increase with increasing resistance and the resonance frequency is seen to shift with the external load resistance. Lastly, Table 50 compares the resonant frequencies for the undamped, short-circuit ($R = 0.01\Omega \sim 0$), and open-circuit ($R = 1e10\Omega \sim \infty$) cases; excellent agreement is seen.

Table 48. FRF Comparison: Inputs

Length L, (m)	0.030
Width b, (m)	0.005
Distance to Neutral Axis $\frac{h_{\tilde{p}}+h_{\tilde{s}}}{2}$, (m)	$1e-4$
Modes Considered	3
Damping Ratios, Modes $1-3$	$0.010, 0.012, 0.030$
PZT Material	PZT-5A
Substrate Material	Aluminum
Tip Mass M_t, (kg)	0
Tip Inertia I_t, (kgm^2)	0
Damage Index C	0 (no damage)
Beam Mass m, (kg/m)	0.0123
Flexural Rigidity YI, (Nm^2)	$1.090e-3$
Piezoelectric Elastic Modulus c_{11}^E, (N/m^2)	$61e9$
Piezoelectric Constant d_{31}, (m/V)	$-171e-12$
Piezoelectric Capacitance $C_{\tilde{p}}$, (F)	$1.33e-8$
Piezoelectric Configuration	Series

Table 49. Resistance Used in Analysis with Color Coding

Resistance (Ω)	Plotting Color
100	Blue
1000	Green
10000	Cyan
100000	Black
1000000	Magenta
10000000	Red

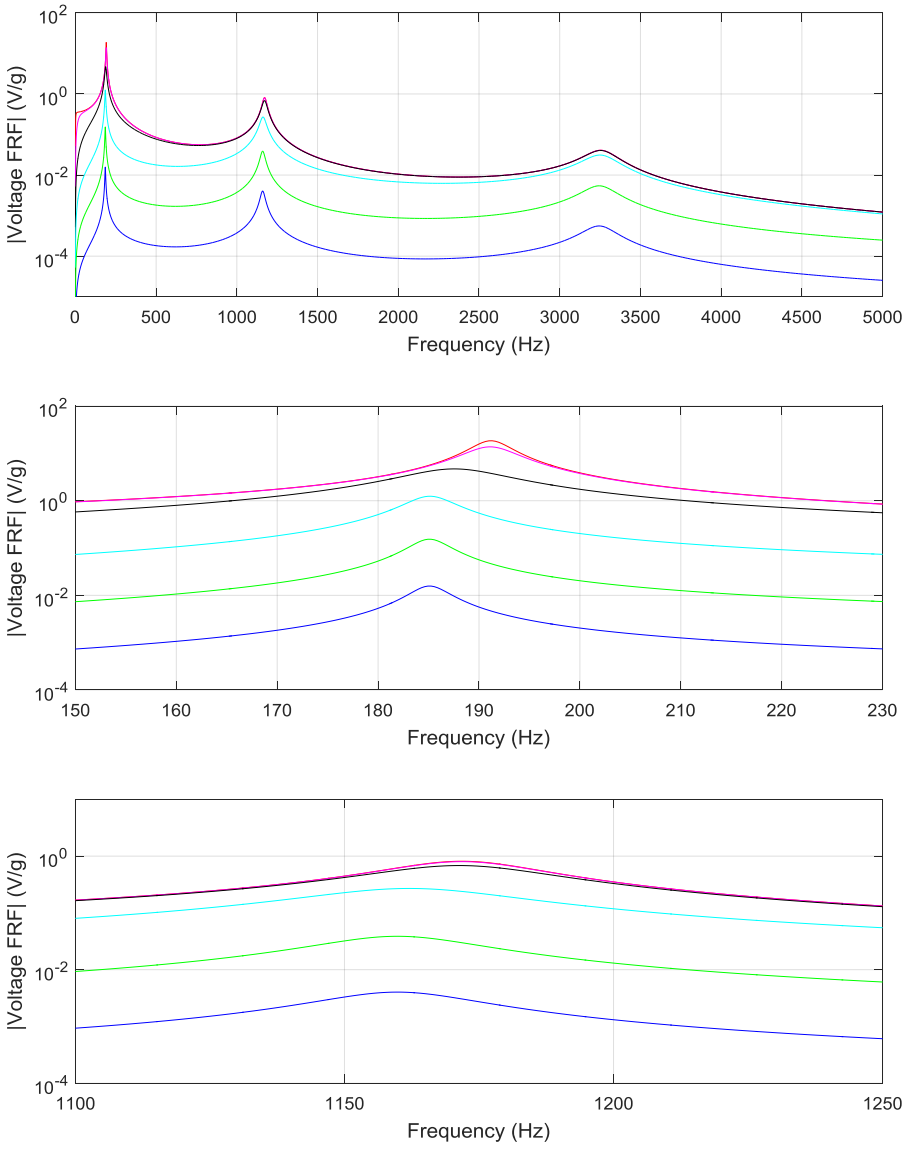

Figure 99. Voltage FRFs for Various Resistance

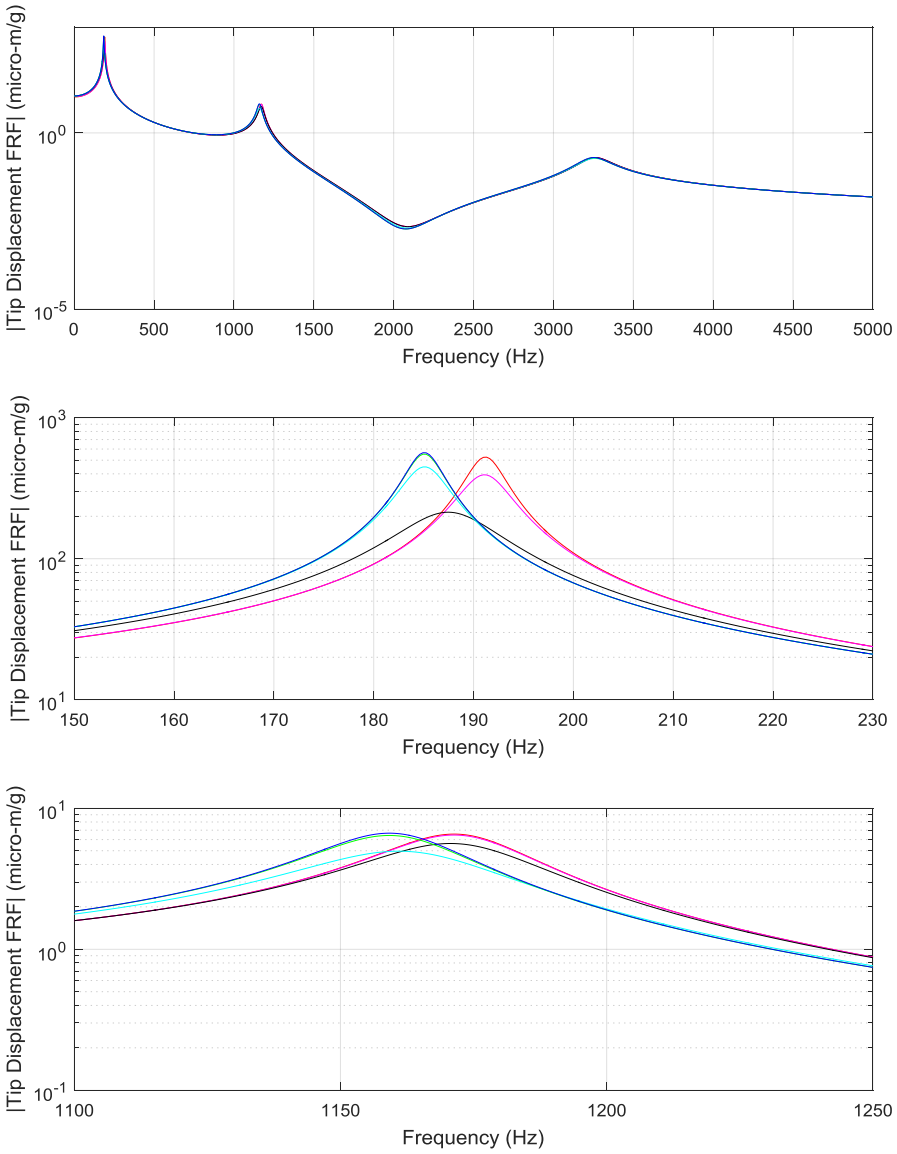

Figure 100. Tip Displacement FRFs for Various Resistance

Table 50. Resonant Frequency Comparison

Mode	Undamped Resonance Frequency f_r (Hz)			Short-Circuit Resonance Frequency f_r^{sc} (Hz)			Open-Circuit Resonance Frequency f_r^{oc} (Hz)		
	Script	E & I [36]	|Error|	Script	E & I [36]	|Error|	Script	E & I [36]	|Error|
1	185.1	185.1	0.00%	185.1	185.1	0.00%	191.1	191.1	0.00%
2	1159.9	1159.8	0.01%	1159.6	1159.7	0.01%	1171.6	1171.6	0.00%
3	3247.9	3247.6	0.01%	3247.8	3245.3	0.08%	3258.2	3254.1	0.13%

5.3.3.4. Damage Accumulation

The natural frequencies of a given system can be tracked over time to observe the effects of accumulated damage. Consider an uncoupled structural system defined by the inputs given in Table 51. The system is subjected to the operating schedule and harmonic loading shown in Table 52. The damage to the flexural rigidity is based on cyclic fatigue testing per Table 53, the contents of which are plotted in Figure 101 (note that these are arbitrary values for illustration purposes).

Table 51. Damage Accumulation: Inputs

Length L, (m)	0.15
Width b, (m)	0.01
Modes Considered	1
Damping Ratio	0.06
Tip Mass M_t, (kg)	0
Tip Inertia I_t, (kgm^2)	0
Damage Index C	Varies
Beam Mass m, (kg/m)	0.05
Initial Flexural Rigidity YI, (Nm^2)	$1.090e-3$
Piezoelectric Elastic Modulus c_{11}^E, (N/m^2)	0
Piezoelectric Constant d_{31}, (m/V)	0
Piezoelectric Capacitance $C_{\tilde{p}}$, (F)	0
Resistance R, (Ω)	~ 0

Table 52. Loading Schedule

Start Time (year)	Loading Amplitude (m/s^2)	Loading Frequency (Hz)	Loading Frequency (rad/s)	End Time (year)	Loading Cycles
0	1.0	5	31.42	0.1	$1.58e7$
0.1	1.5	10	62.83	0.2	$3.15e7$
0.2	2.0	5	31.42	0.3	$1.58e7$
0.3	0.5	20	125.66	0.4	$6.31e7$
0.4	1.25	15	94.25	0.5	$4.73e7$
0.5	0.5	20	125.66	0.6	$6.31e7$
0.6	2.0	5	31.42	0.7	$1.58e7$
0.7	0.5	20	125.66	0.8	$6.31e7$
0.8	1.25	15	94.25	0.9	$4.73e7$

Table 53. Residual Flexural Rigidity as a Function of Cycle Count and Amplitude

		Cycle Count			
		$1e7$	$5.5e7$	$1e8$	$5.5e8$
Tested Amplitude (mm)	1	0.95	0.9	0.85	0.80
	2	0.94	0.89	0.84	0.76
	3	0.94	0.89	0.84	0.76
	4	0.92	0.87	0.82	0.74
	5	0.87	0.82	0.77	0.69
	6	0.77	0.72	0.67	0.59
	7	0.70	0.65	0.60	0.52

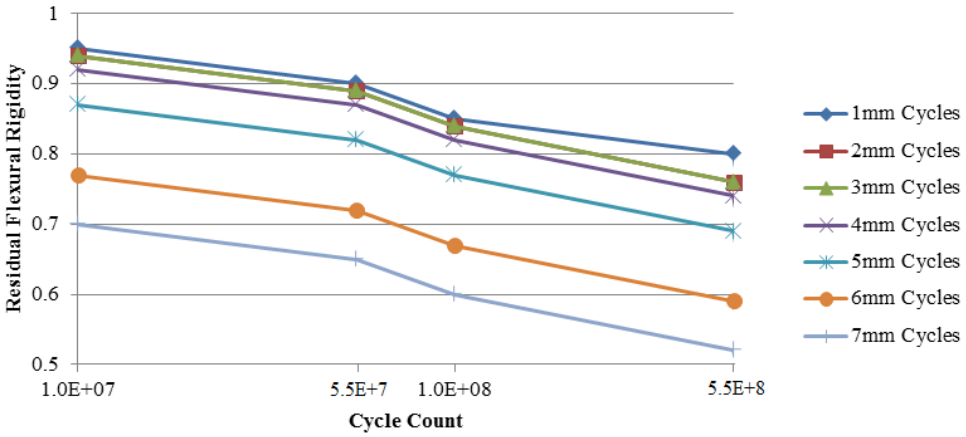

Figure 101. Residual Flexural Rigidity as a Function of Cycle Count and Amplitude

The mass normalized eigenfunction, which can be found analytically [130] or through the use of finite element analysis, is shown in Figure 102. Its integral is found as

$$\int_0^L \phi_1 dx = -1.3562. \tag{444}$$

Noting Eq. (413)

$$\sigma_1 = -m\int_0^L \phi_1 dx = 0.0678. \tag{445}$$

Using Eq. (445), and knowing the loading frequency (ω, see Table 52), damping ratio (0.06, see Table 51), and mode shape ($\phi_1(L) = -23.09$, see Figure 102), the relative tip displacement transfer function can be calculated (for a given system natural frequency ω_1) using Eq. (426) as

$$\beta(\omega, L) = \sigma_1 \frac{\phi_1(L)}{(-\omega^2 + 2\zeta_r\omega_1 i\omega + \omega_1^2)}. \tag{446}$$

Using an iterative calculation scheme, the relative tip displacement can be calculated using Eq. (446) and Table 52 as

$$w_R(L,t) = \beta(\omega, L)\ddot{w}_B. \tag{447}$$

Using the calculated tip displacement (Eq. (447)) and the cumulative loading cycles (see Table 52), the reduction in flexural rigidity can be calculated from Table 53 or Figure 101. The damage at the end of each $0.1yr$ time increment is used to modify the flexural rigidity at the beginning of the next loading cycle (thereby reducing the first natural frequency and changing the tip displacement FRF). Truncated sample calculations are provided in Table 54. These results can be compared to the script output (which utilizes a rainflow analysis to count the loading cycles and interpolates the damage through a MATLAB sub-routine). The results from the two methodologies are shown in Figure 103 and Figure 104 where the first natural frequencies and relative displacement response are compared, respectively. The results show excellent agreement.

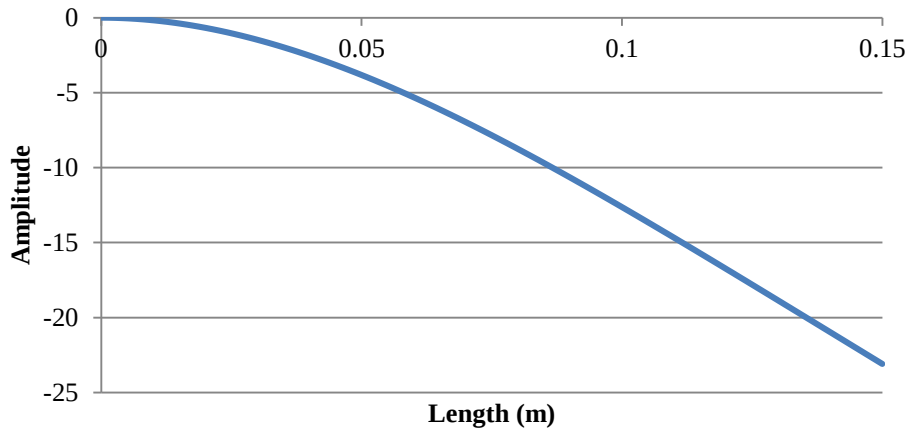

Figure 102. Mass Normalized Eigenfunction of the First Mode

Table 54. Damage Accumulation

	Start Time (yr)	0	0.1	0.2	0.3	0.4
	Current YI (Nm^2)	$1.09e-3$	$9.96e-4$	$9.15e-4$	$6.58e-4$	$5.81e-4$
	Current Nat. Freq. (rad/s)	23.1	22.1	21.1	17.9	16.8
	Relative Disp. (mm)	3.4	0.7	5.7	0.1	0.2
$1mm$ Amplitude	Cycles	0	$3.15e+7$	$3.15e+7$	$9.46e+7$	$1.42e+8$
	Damage	0	0.074	0.074	0.144	0.155
$4mm$ Amplitude	Cycles	$1.58e+7$	$1.58e+7$	$1.58e+7$	$1.58e+7$	$1.58e+7$
	Damage	0.086	0.086	0.086	0.086	0.086
$5mm$ Amplitude	Cycles	0	0	0	0	0
	Damage	0	0	0	0	0
$6mm$ Amplitude	Cycles	0	0	$1.58e+7$	$1.58e+7$	$1.58e+7$
	Damage	0	0	0.236	0.236	0.236
	Cumulative Damage	0.086	0.160	0.397	0.467	0.477

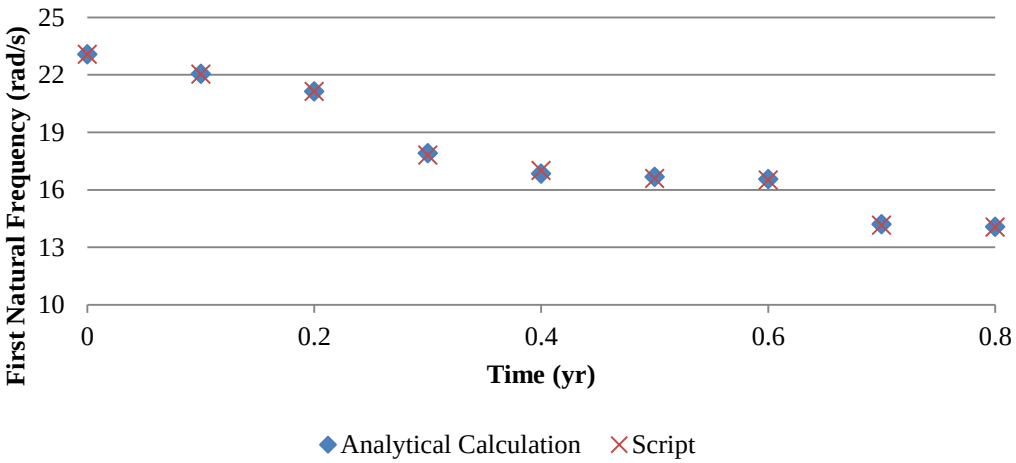

Figure 103. Comparing Natural Frequencies

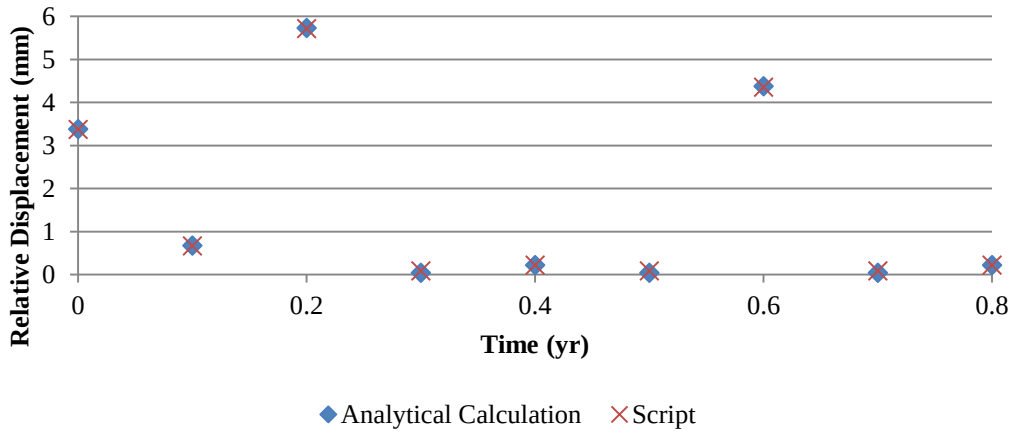

Figure 104. Comparing Relative Displacement

5.3.4. Demonstration Cases

Four cases are used to demonstrate the script. In the first case, a baseline analysis is presented in which an optimal tip mass and resistive load are selected for a specified loading schedule. Damage and time/temperature dependence are not included in the baseline case. In the second case, a damage model is incorporated, resulting in a shift in the optimal tip mass and resistive load. In the third case, temperature dependence is included in the baseline model, again leading to a shift in the optimal tip mass and resistive load. Finally, the full script is demonstrated by including both the damage model and temperature dependence in the analysis. Trends are noted in each case.

5.3.4.1. Optimal Tip Mass and Resistive Load: Baseline Case

A piezoelectric element, characterized by the properties in Table 55, is subject to time-dependent harmonic loading given by Table 56. No time or temperature dependence is included in the model. Damage is assumed not to accumulate. For each loading regime the maximum relative tip displacement (MRTD) and average power output are calculated over a range of tip masses and resistive loads. The results are presented in Figure 105, Figure 106, Figure 107, and Figure 108.

Table 55. Inputs

Length L, (m)	0.030
Width b, (m)	0.005
Distance to Neutral Axis $\frac{h_{\tilde{p}}+h_{\tilde{s}}}{2}$, (m)	$1e-4$
Modes Considered	1
Damping Ratio	0.010
Tip Mass M_t, (kg)	Optimized Variable
Tip Mass Density (kg/m^3)	6000
Tip Inertia I_t, (kgm^2)	Varies
Damage Index C	0 (No Damage)
Beam Mass m, (kg/m)	0.02
Operating Temperature (℃)	Constant Temp.
Flexural Rigidity YI, (Nm^2)	$1.090e-3$
Piezoelectric Elastic Modulus c_{11}^E, (N/m^2)	$61e9$
Piezoelectric Constant d_{31}, (m/V)	$-171e-12$
Piezoelectric Capacitance $C_{\tilde{p}}$, (F)	$1.33e-8$
Piezoelectric Configuration	Series
Resistive Load R, (Ω)	Optimized Variable

Table 56. Loading Schedule

Start Time (year)	Loading Regime	Loading Amplitude (m/s^2)	Loading Frequency (Hz)	Loading Frequency (rad/s)	End Time (year)
0	1	2	20	125.66	0.3
0.3	2		30	188.50	0.6
0.6	3		25	157.08	0.9

For low resistive loads ($R \approx 0\Omega$; short-circuit condition) the MRTD approaches that of the electromechanically uncoupled system where a maximum response is seen as the undamped natural frequency (ω_r) and the loading frequency converge. As the resistive load is increased, the system shifts from a short-circuit to open-circuit condition, leading to a shift in the systems resonant frequency. The introduction of a resistive load results in piezoelectric power generation and power dissipation in the resistor due to Joule heating [36]. Unlike viscous damping, the observed frequency shift, which is due to the changing electrical boundary condition (i.e. an increased resistive load), causes an upward frequency shift (as was shown in the frequency response function of Figure 100). For the current scenario (where the loading frequency is specified), as the systems resonant frequency increases due to changing resistance the tip mass that maximizes the displacement response must increase (thereby lowering the

resonant frequency) such that the resonant frequency and loading frequency coincide. This upwards shift in optimal tip mass is apparent in each plot of Figure 106.

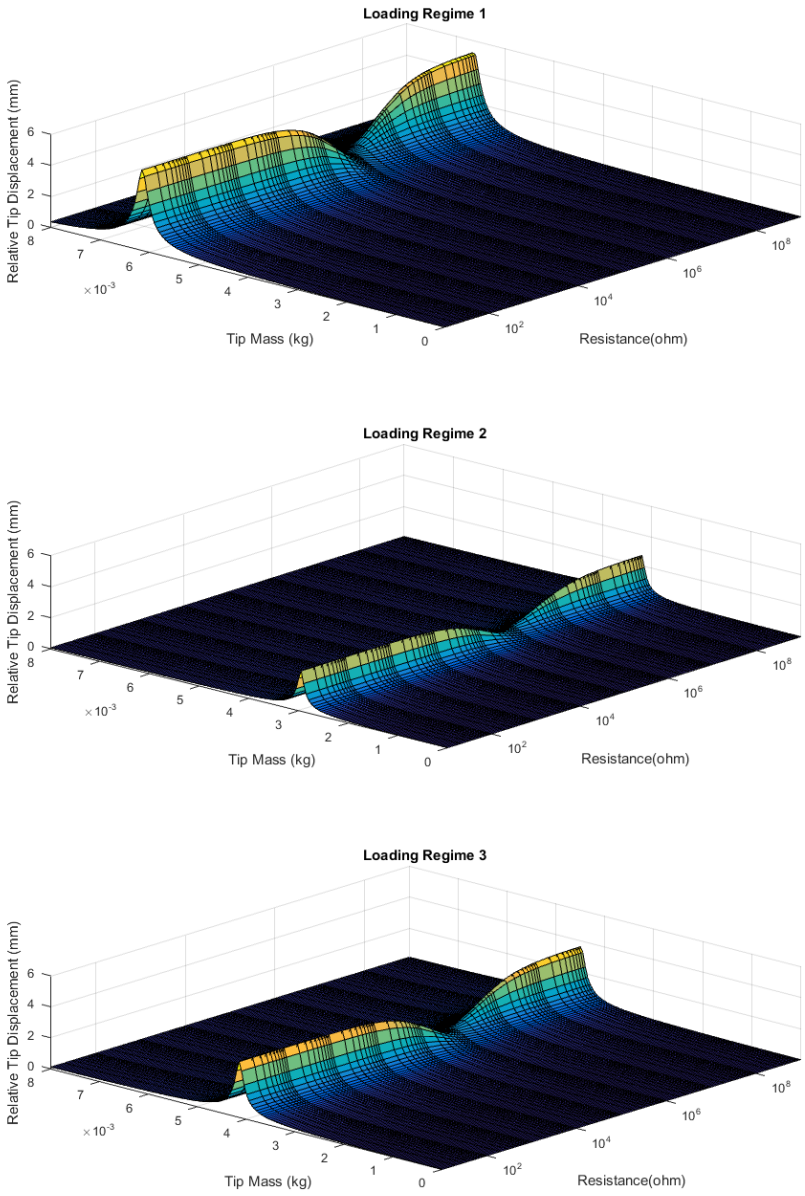

Figure 105. Maximum Relative Tip Displacement (MRTD): Baseline Case Loading Regime One (Top), Two (Middle), and Three (Bottom) Shown

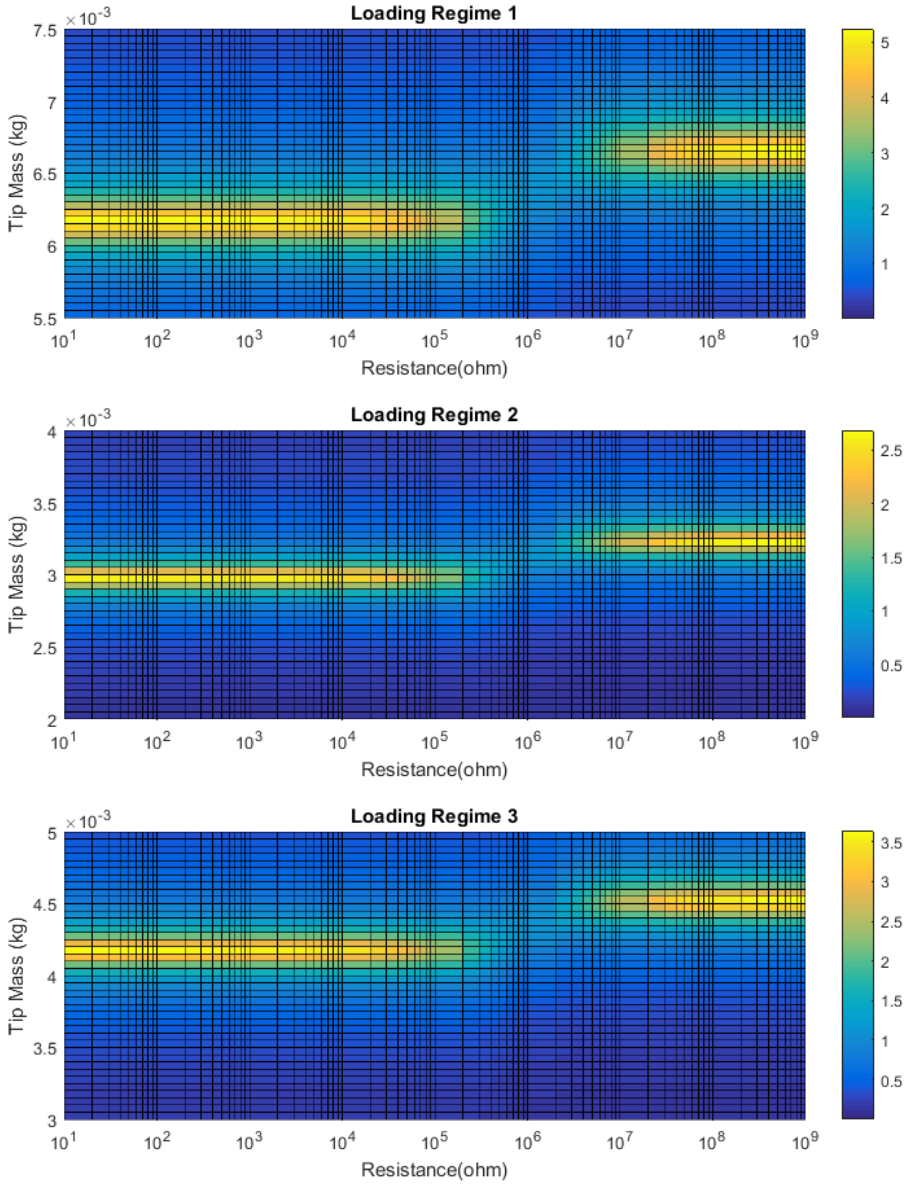

Figure 106. Maximum Relative Tip Displacement (MRTD) Contours (mm): Baseline Case Loading Regime One (Top), Two (Middle), and Three (Bottom) Shown

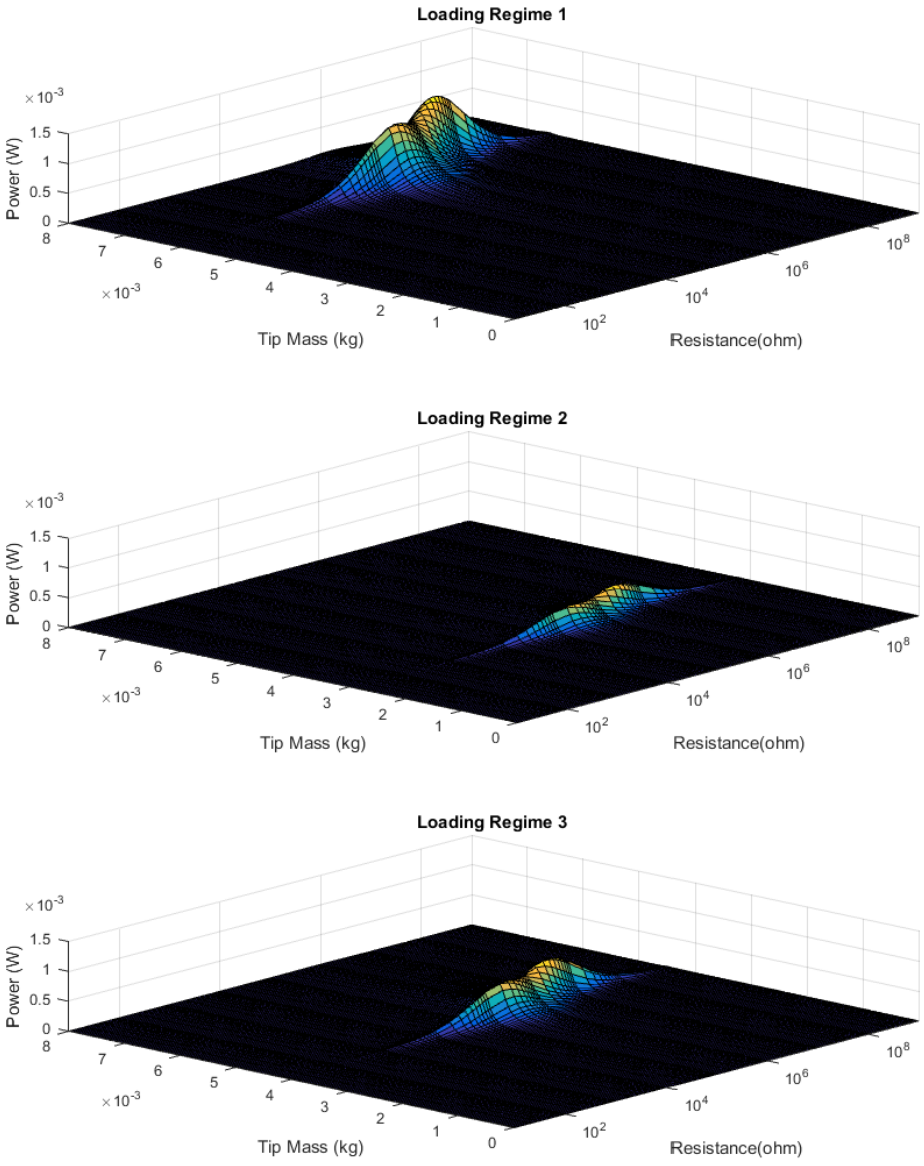

Figure 107. Average Power: Baseline Case
Loading Regime One (Top), Two (Middle), and Three (Bottom) Shown

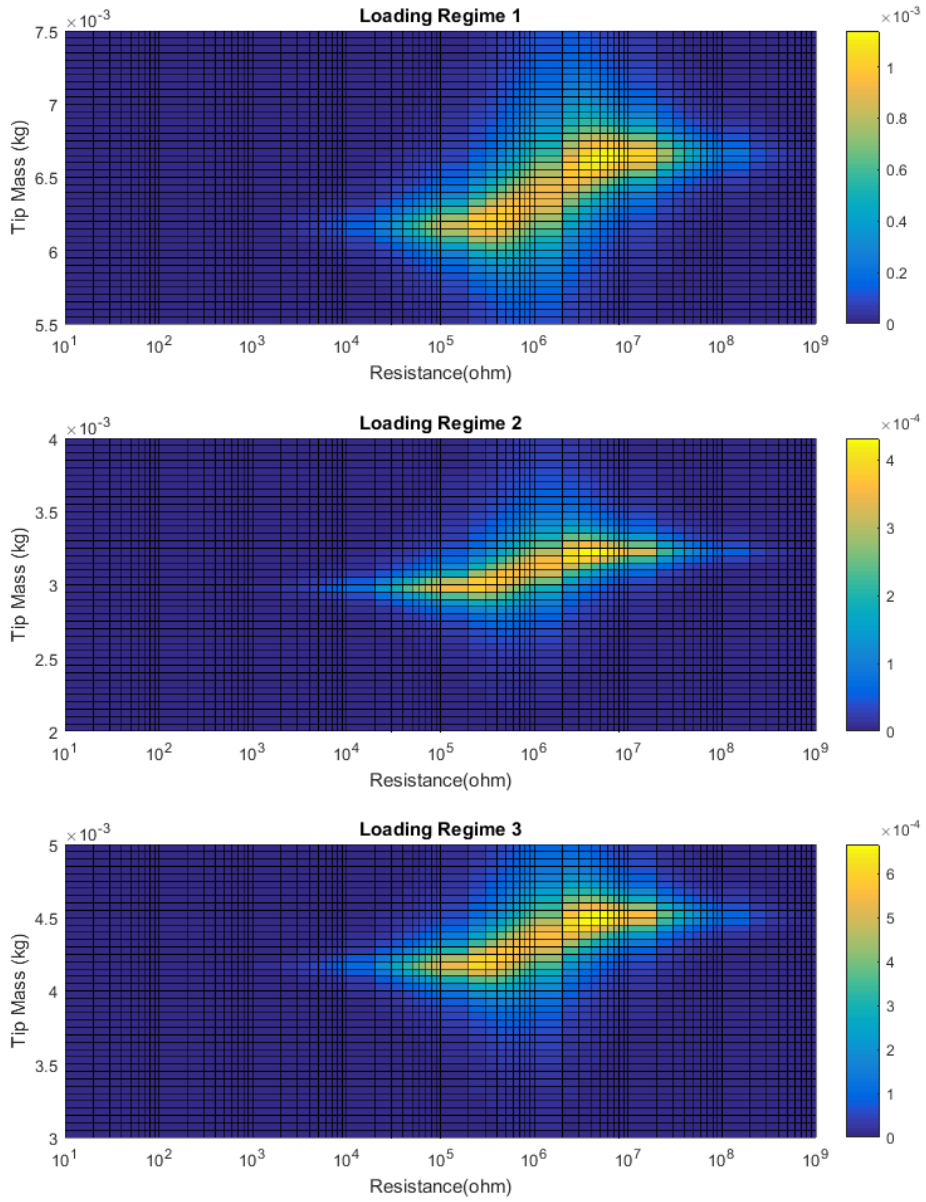

Figure 108. Average Power Contours (W): Baseline Case
Loading Regime One (Top), Two (Middle), and Three (Bottom) Shown

Turning to the average power output of Figure 107, two local maxim are observable. As previously described, increasing the resistive load results in an increase in the resonant frequency leading to a shift in the optimal tip mass. The difference in local maxim is attributed

to the changing tip mass. To demonstrate this, several power output FRFs are shown in Figure 109 for resistive loads near the local maximums under loading regime one. Note that: (1) for a fixed resistive load the magnitude of the power FRF increases with increasing tip mass, (2) as the tip mass increases the resonant frequency of the system decreases, and (3) as the resistive load increases the resonant frequency of the system increases.

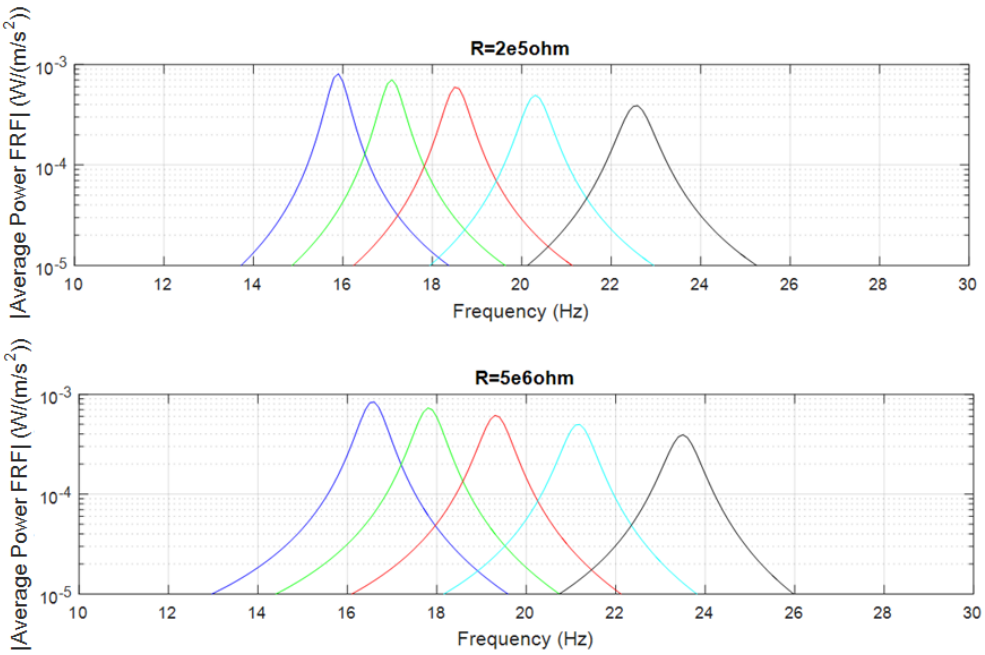

Figure 109. Average Power Frequency Response Functions for Various Resistive Loads and Tip Masses $0.009kg$ (Blue), $0.008kg$ (Green), $0.007kg$ (Red), $0.006kg$ (Cyan), $0.005kg$ (Black)

To determine the optimal tip mass and resistive load that maximizes the average power output over all three loading regimes (i.e. from year 0 to 0.9), the average power output from each realization for each loading regime (given in Figure 107 and Figure 108) is integrated over the regimes duration resulting in a scalar value that can be used as an optimization metric. The resulting metric is plotted in Figure 110. The total average power output is found to be maximized when $M_t = 0.0066kg$, $R = 5e6\Omega$ and results in an average power output of $1.14mW$, $1.14\mu W$, and $5.56\mu W$ for loading regime one, two, and three, respectively. Note that this realization produces over 99% of its total average power output during the first loading

regime due to resonant behavior. The corresponding MRTDs are $2.64mm$, $0.08mm$, and $0.18mm$. These results are plotted over time in Figure 111.

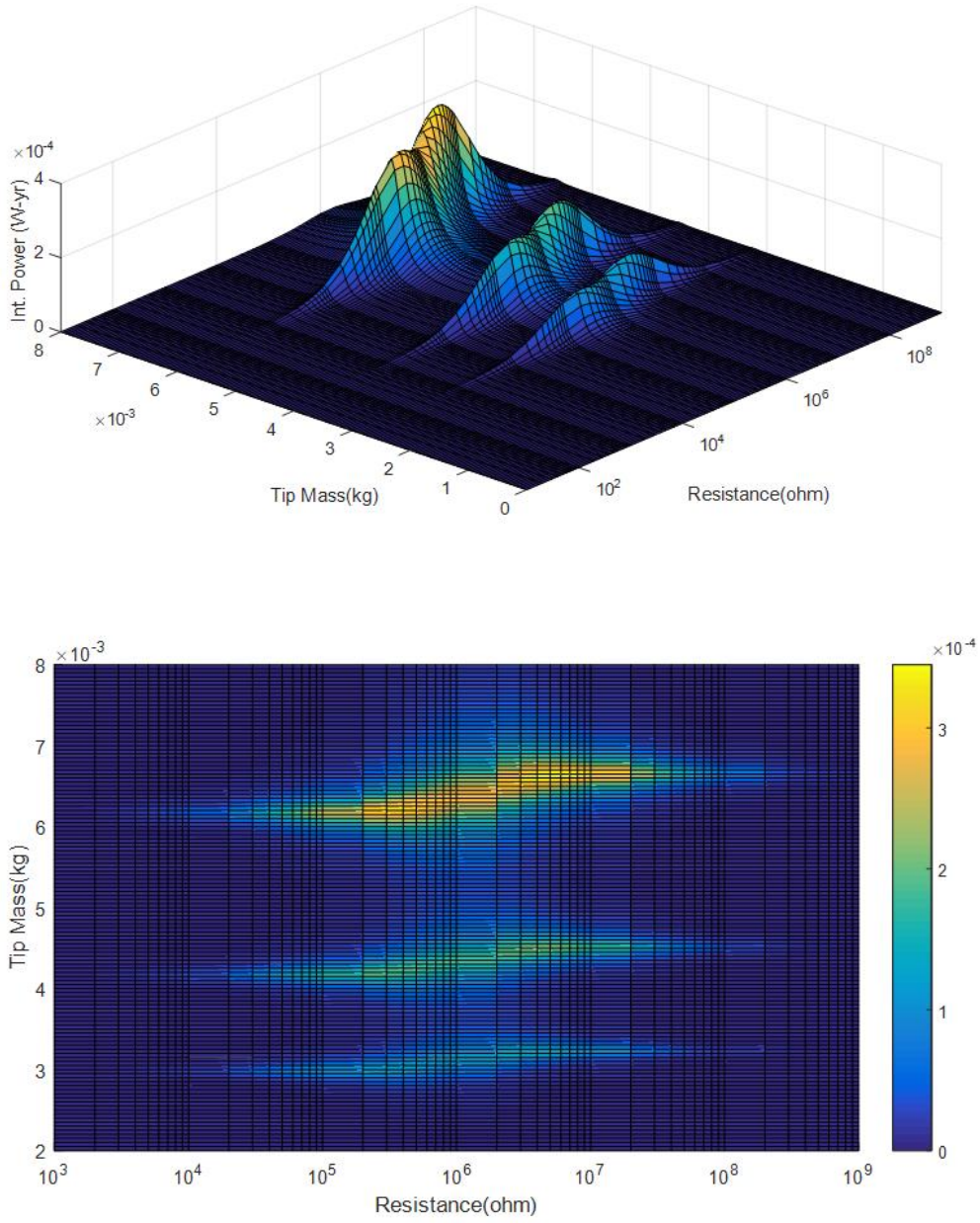

Figure 110. Integrated Power Metric (Wyr)

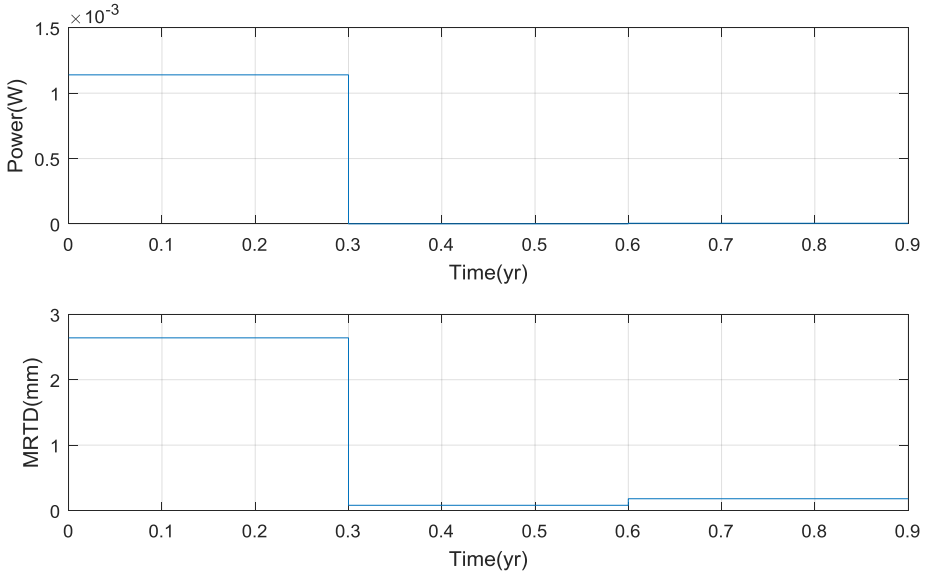

Figure 111. Average Power Output and Maximum Relative Tip Displacement (MRTD) for Maximum Power Case

5.3.4.2. Optimal Tip Mass and Resistive Load: Incorporating Damage

The baseline model of the piezoelectric element used in Section 5.3.4.1 is now expanded to incorporate the linear cumulative damage model described in Section 5.3.2.2. The inputs and loading schedule are repeated for convenience in Table 57 and Table 58. No time or temperature dependence is included in the model. As before, the maximum relative tip displacement (MRTD) and average power output are calculated over a range of tip masses and resistive loads. Since damage accumulation is dependent on load cycles which accumulate over time, the analysis must be discretized in time: the time discretization used in this analysis is $0.05yr$. The mechanical and electrical terms are first investigated separately to demonstrate their individual effects. Following this, their combined effects are demonstrated as an optimal tip mass and resistive load are selected.

Table 57. Inputs

Length L, (m)	0.030
Width b, (m)	0.005
Distance to Neutral Axis $\frac{h_{\tilde{p}}+h_{\tilde{s}}}{2}$, (m)	$1e-4$
Modes Considered	1
Damping Ratio	0.010
Tip Mass M_t, (kg)	Optimized Variable
Tip Mass Density (kg/m^3)	6000
Tip Inertia I_t, (kgm^2)	Varies
Damage Index C	Varies
Beam Mass m, (kg/m)	0.02
Operating Temperature (℃)	Constant Temp.
Flexural Rigidity YI, (Nm^2)	$1.090e-3$ & Varies
Piezoelectric Elastic Modulus c_{11}^E, (N/m^2)	$61e9$
Piezoelectric Constant d_{31}, (m/V)	$-171e-12$ & Varies
Piezoelectric Capacitance $C_{\tilde{p}}$, (F)	$1.33e-8$ & Varies
Piezoelectric Configuration	Series
Resistive Load R, (Ω)	Optimized Variable

Table 58. Loading Schedule

Start Time (year)	Loading Regime	Loading Amplitude (m/s^2)	Loading Frequency (Hz)	Loading Frequency (rad/s)	End Time (year)
0	1	2	20	125.66	0.3
0.3	2		30	188.50	0.6
0.6	3		25	157.08	0.9

5.3.4.2.1. Degradation of Flexural Rigidity During the First Loading Regime

The degradation of flexural rigidity is based on load cycling data shown in Figure 112; while trends outlined in Section 5.3.2.1 have been followed, arbitrary values have been used. The piezoelectric terms are held constant (i.e. d_{31} and $C_{\tilde{p}}$ are assumed not to degrade).

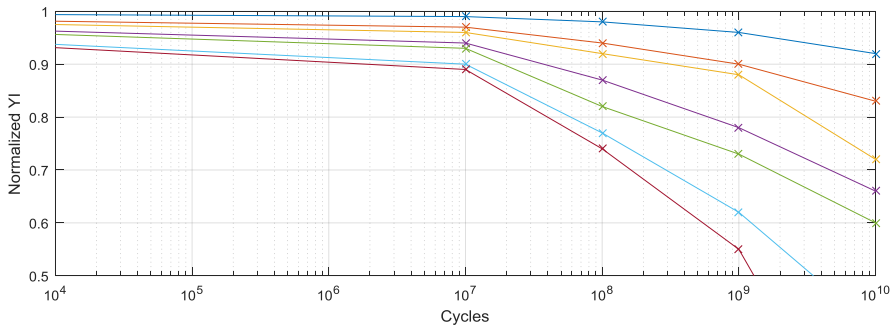

Figure 112. Normalized Degradation of Flexural Rigidity From Cycling at Specified Amplitudes $A_1 = 0.5mm$ (Blue), $A_2 = 1mm$ (Orange), $A_3 = 1.5mm$ (Yellow), $A_4 = 2mm$ (Purple), $A_5 = 3mm$ (Green), $A_6 = 5mm$ (Cyan), $A_7 = 7mm$ (Red)

The MRTD is plotted in Figure 113 for various tip masses and resistive loads. The cumulative damage to the flexural stiffness is plotted in Figure 114. As damage is accumulated, the flexural stiffness of the system is reduced. This results in a decrease in the systems resonant frequencies. Since the driving frequency is fixed ($20Hz$ in the first loading regime) the tip mass maximizing the MRTD (i.e. the tip mass corresponding to the largest MRTD) must be reduced as damage is accumulated, thereby offsetting the reduction in system stiffness. This trend is visible in Figure 113 where the tip mass maximizing the MRTD is seen to shift downwards over time (or more accurately, as cyclic damage accumulates). Since the maximum MRTD now occurs for a new (and smaller) tip mass realization, damage will accumulate to a greater degree at the new tip mass realization during the next loading cycle. This can be seen in Figure 114 where damage is seen to accumulate for smaller tip masses in each subsequent time increment.

A second visible trend in Figure 113 is the reduction in the maximum MRTD as the tip mass decreases. This trend is explained by Figure 115 which plots FRFs for the relative tip displacement (assuming constant stiffness). Note that: (1) for a fixed resistive load the magnitude of the displacement FRF decreases with decreasing tip mass, (2) as the tip mass decreases the resonant frequency of the system increases, and (3) as the resistive load increases the resonant frequency of the system increases.

The average power output is shown in Figure 116 where the trends seen in the MRTD contours of Figure 113 are visible. The downward shift in tip mass corresponding to the maximum average power output can again be attributed to damage accumulation. As damage is accumulated, the flexural stiffness of the system is reduced. This results in a decrease in the systems resonant frequencies. Since the driving frequency is fixed ($20Hz$ in the first loading regime) the tip mass maximizing the average power output must be reduced as damage is

accumulated, thereby offsetting the reduction in system stiffness. Lastly, the reduction in power output can be explained by the inherent nature of the power FRF; see Figure 109 where a decreasing tip mass was shown to lead to a reduced power FRF.

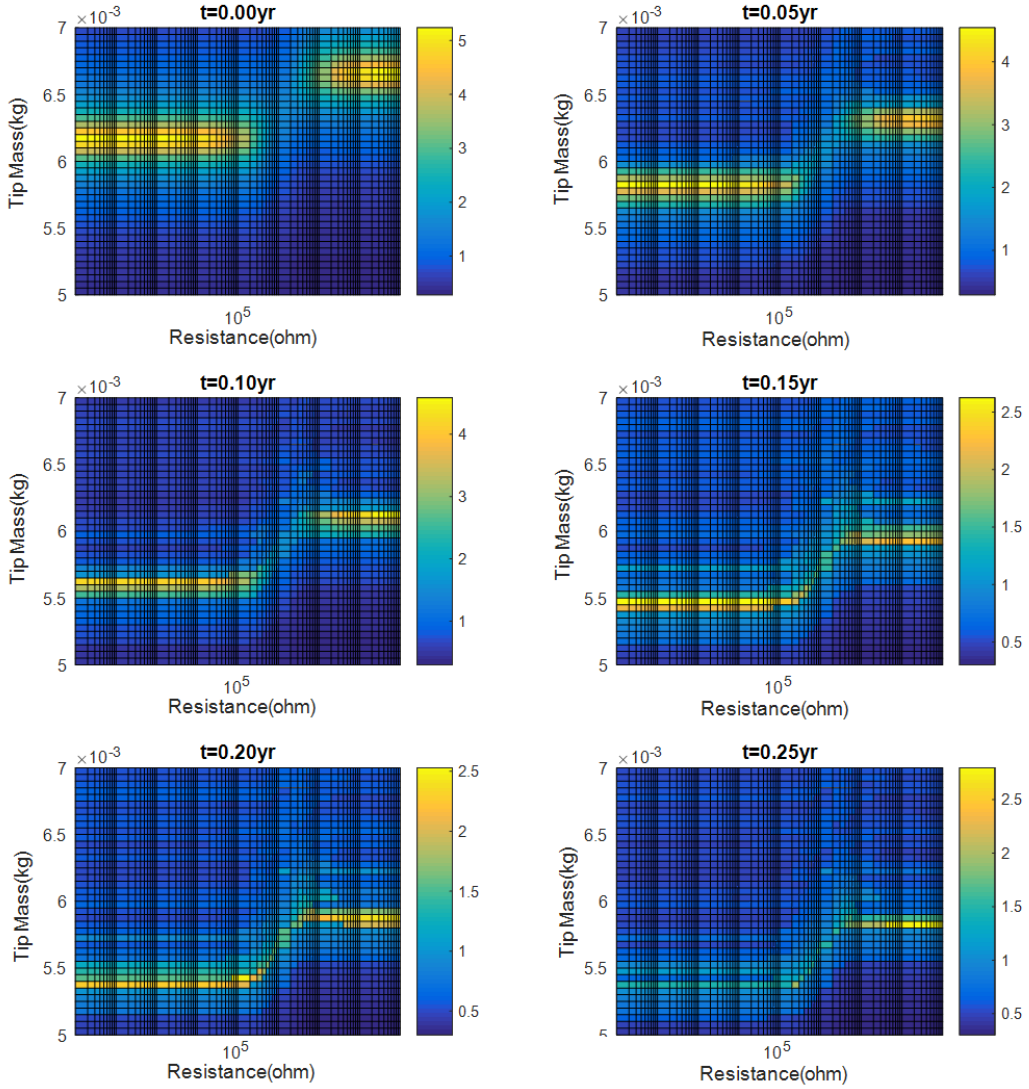

Figure 113. Maximum Relative Tip Displacement (MRTD) Contours (mm) Based on Degradation of Flexural Rigidity. Results Applicable for $0.05yr$ from the Initial Time Indicated

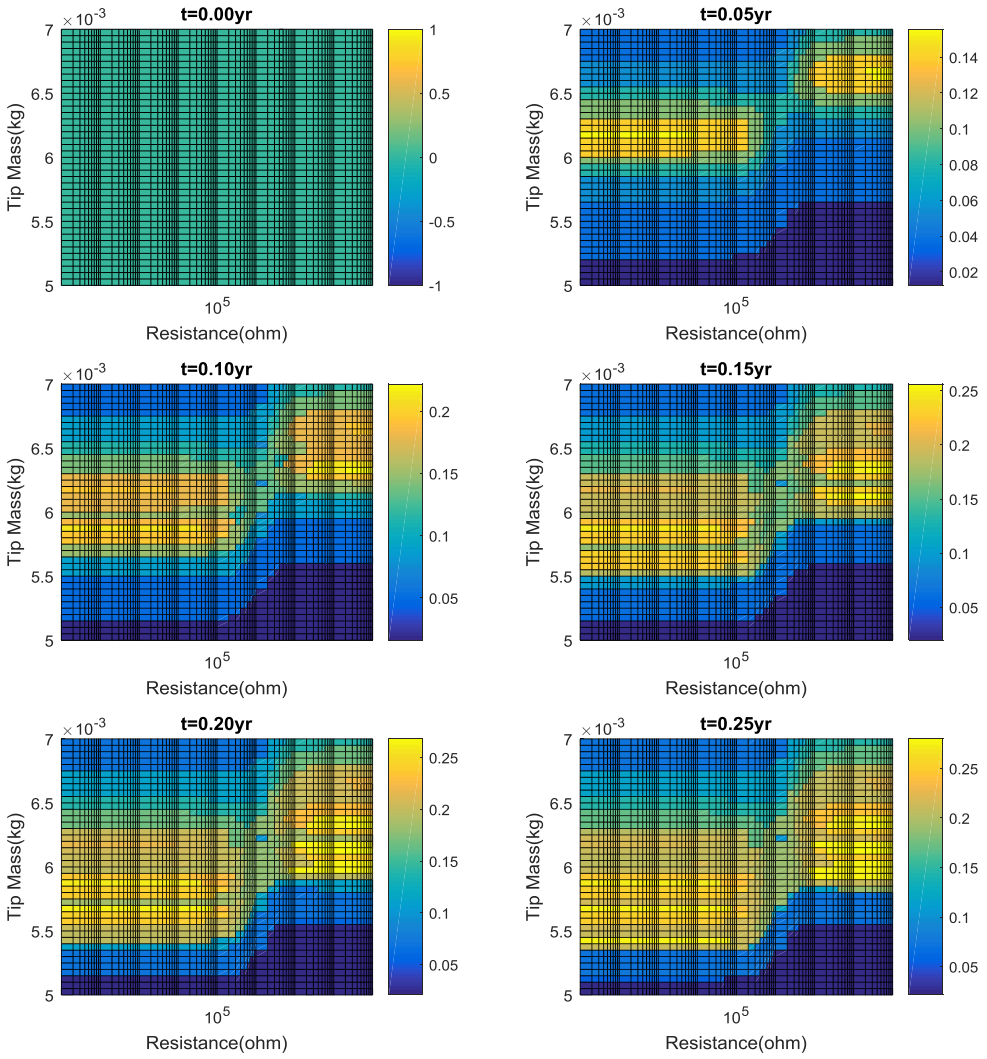

Figure 114. Cumulative Damage Contours (C) Based on Degradation of Flexural Rigidity. Results Applicable for $0.05yr$ from the Initial Time Indicated

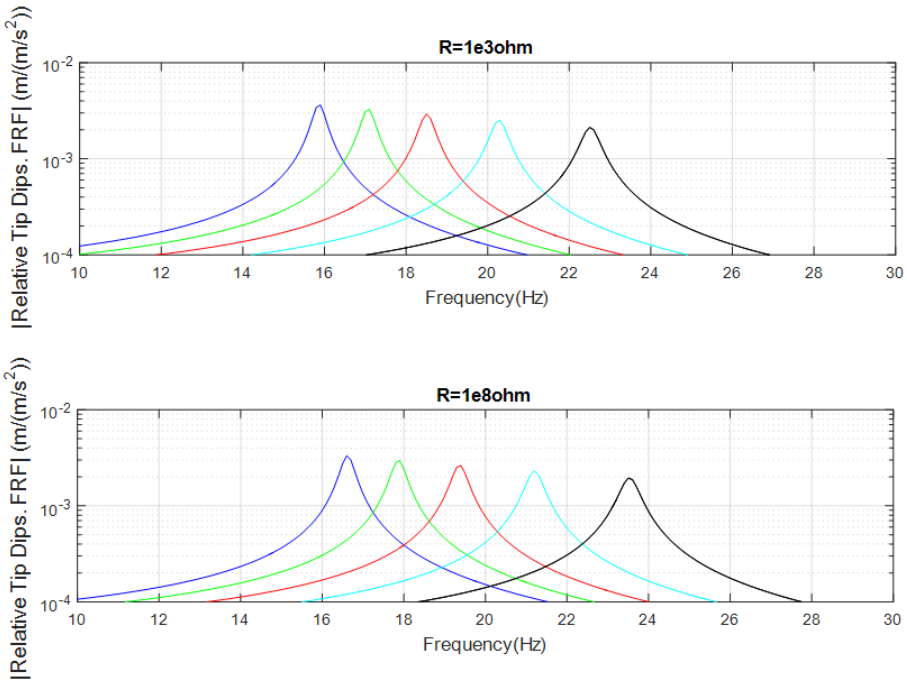

Figure 115. Relative Tip Displacement FRFs for Various Resistive Loads and Tip Masses $0.009kg$ (Blue), $0.008kg$ (Green), $0.007kg$ (Red), $0.006kg$ (Cyan), $0.005kg$ (Black)

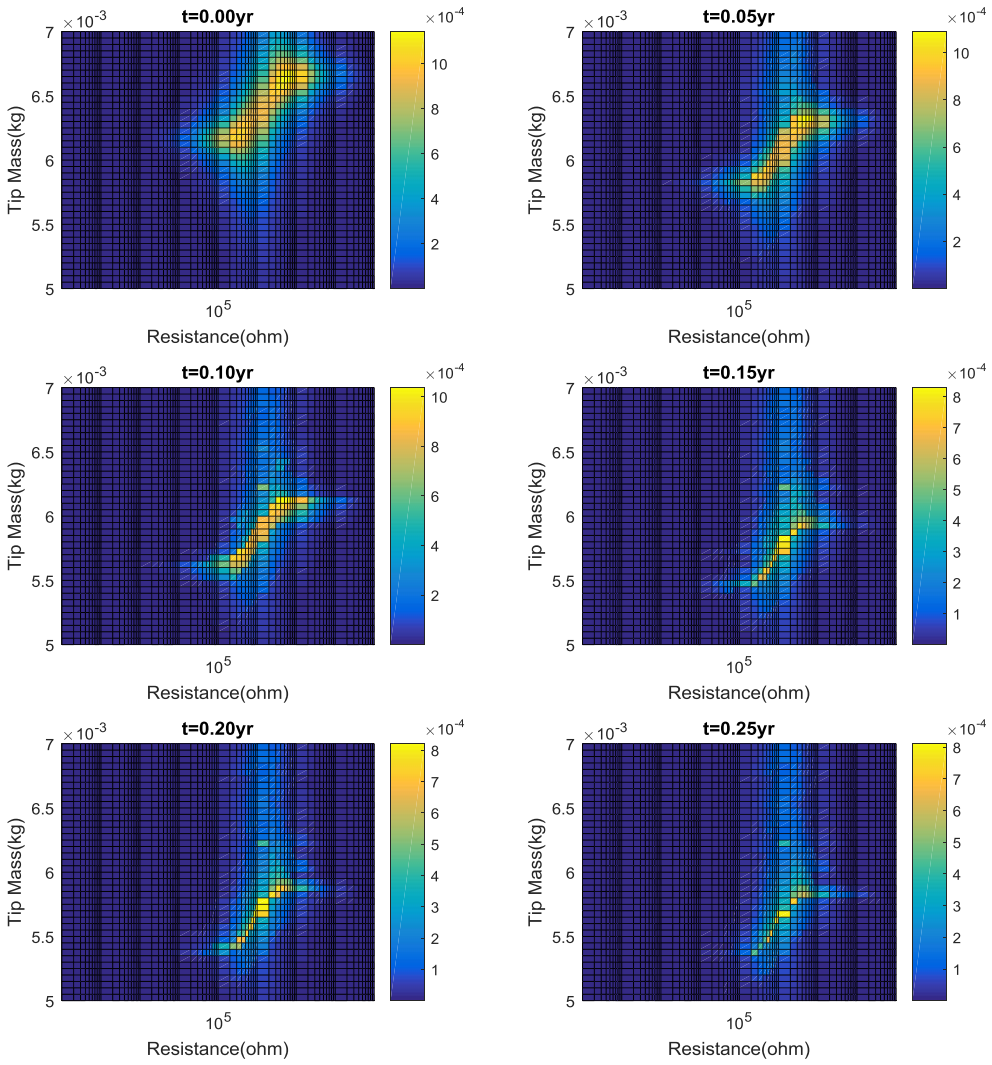

Figure 116. Average Power Contours (W) Based on Degradation of Flexural Rigidity. Results Applicable for $0.05yr$ from the Initial Time Indicated

5.3.4.2.2. Degradation of Piezoelectric Terms During the First Loading Regime

The degradation of the piezoelectric terms (d_{31} and $C_{\tilde{p}}$) are based on load cycling data shown in Figure 117; while trends outlined in Section 5.3.2.1 have been followed, arbitrary values have been used. The flexural rigidity is held constant and assumed not to degrade.

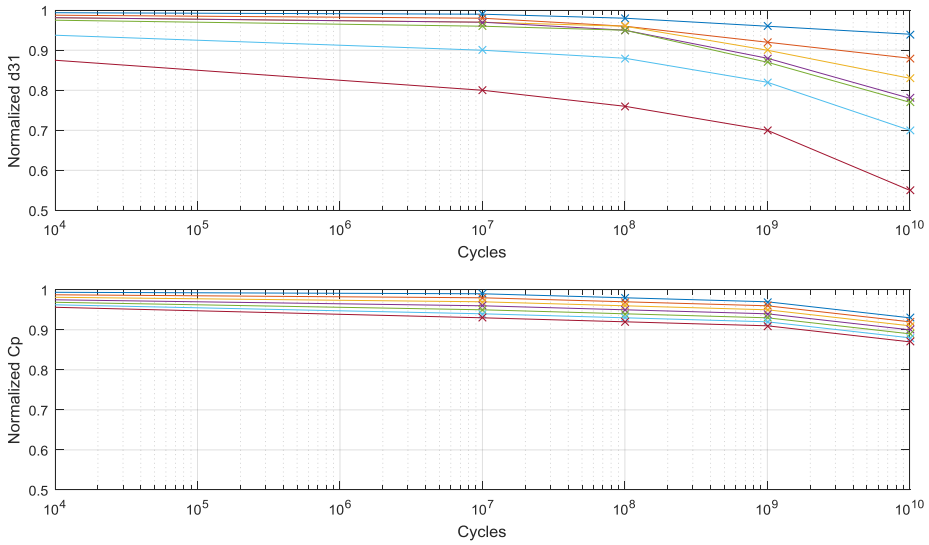

Figure 117. Normalized Degradation of Piezoelectric Properties From Cycling at Specified Amplitudes $A_1 = 0.5mm$ (Blue), $A_2 = 1mm$ (Orange), $A_3 = 1.5mm$ (Yellow), $A_4 = 2mm$ (Purple), $A_5 = 3mm$ (Green), $A_6 = 5mm$ (Cyan), $A_7 = 7mm$ (Red)

The MRTD is plotted in Figure 118 for various tip masses and resistive loads. The cumulative damage to each piezoelectric term is plotted in Figure 119 and Figure 120. As noted by the relatively unchanging optimal tip mass in Figure 118, the degradation of the piezoelectric terms is seen to have a significantly smaller impact on the shift of resonance frequency (relative to the degradation of flexural rigidity) This leads to damage being concentrated in those realizations with high relative MRTD. In other words, damage to the piezoelectric terms is localized where the MRTD is high and the realizations for which the MRTD are high are relatively constant.

As previously noted, for low resistive loads ($R \approx 0\Omega$; short-circuit condition) the MRTD approaches that of the electromechanically uncoupled system where a maximum response is seen as the undamped natural frequency (ω_r) and the loading frequency converge. Under the short-circuit condition, then, degradation of the piezoelectric terms has a small impact on the MRTD as the system is dominated by the governing mechanical equations. For high resistive loads (e.g. open-circuit condition), the shift in resonance frequency is due to the

inclusion of the governing electrical equations. When the piezoelectric terms degrade, the induced shift in the resonance frequency will once again shift (back towards a mechanically governed system) causing a change in the optimal tip mass. These trends can be seen in Figure 118: the MRTD is relatively constant for low resistive loads while for high resistive loads, damage to the piezoelectric terms results in a slight downward shift in the tip mass maximizing the MRTD.

The average power output is shown in Figure 121. Note that damage to the piezoelectric terms is based on the MRTD and, for the investigated cases, the realizations with high MRTD do not overlap with realizations with high average power output. This means that realizations with significant damage do not coincide with realizations with high average power output (compare Figure 119/Figure 120 and Figure 121). This results in the average power output appearing relatively constant through each time increment.

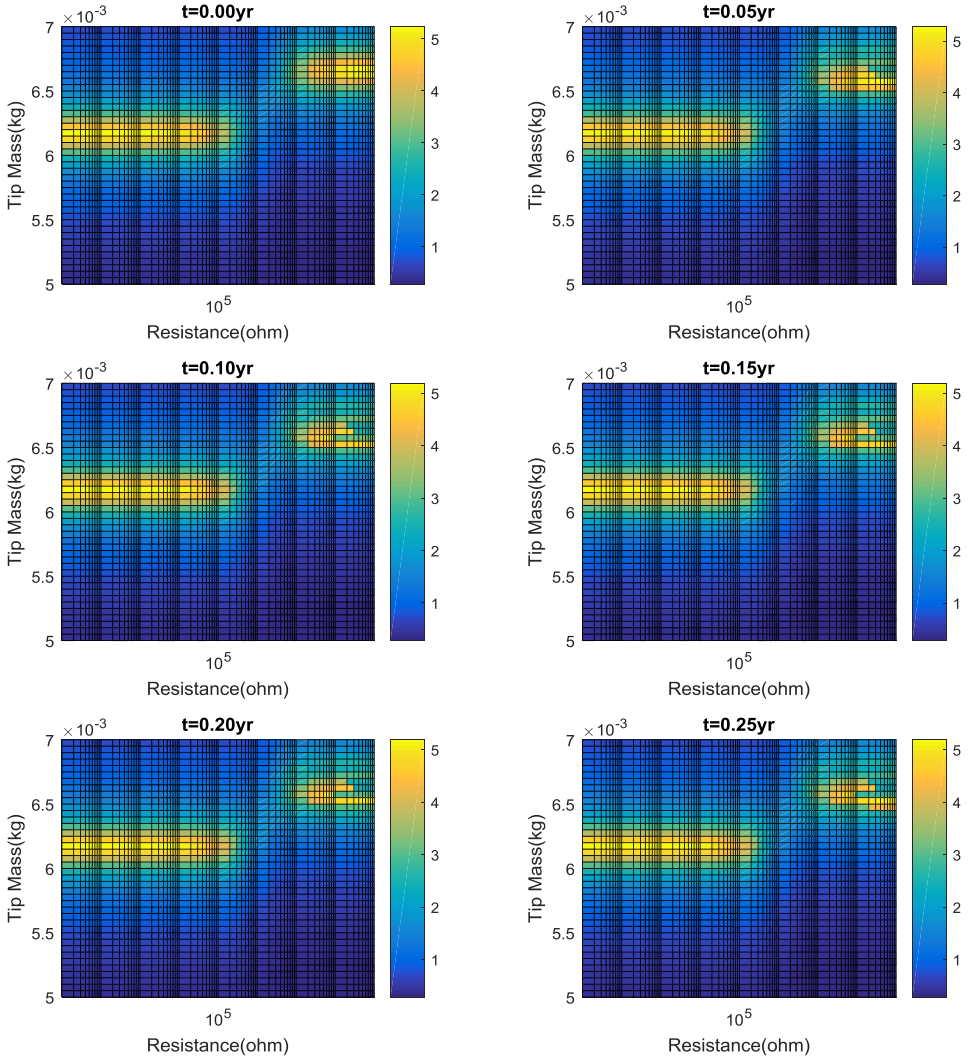

Figure 118. Maximum Relative Tip Displacement (MRTD) Contours (mm) Based on Degradation of Piezoelectric Terms. Results Applicable for $0.05yr$ from the Initial Time Indicated

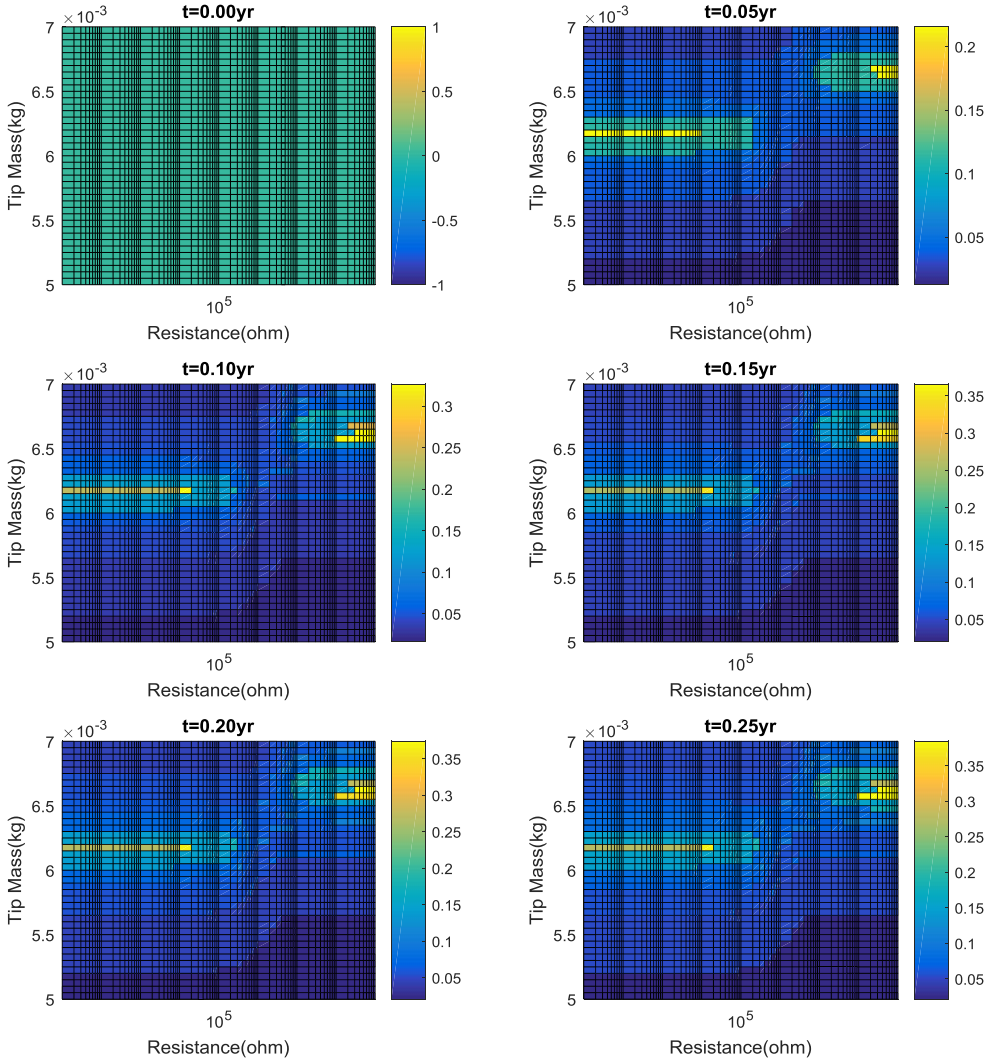

Figure 119. Cumulative Damage Contours (C) of d_{31}Based on Degradation of Piezoelectric Terms. Results Applicable for $0.05yr$ from the Initial Time Indicated

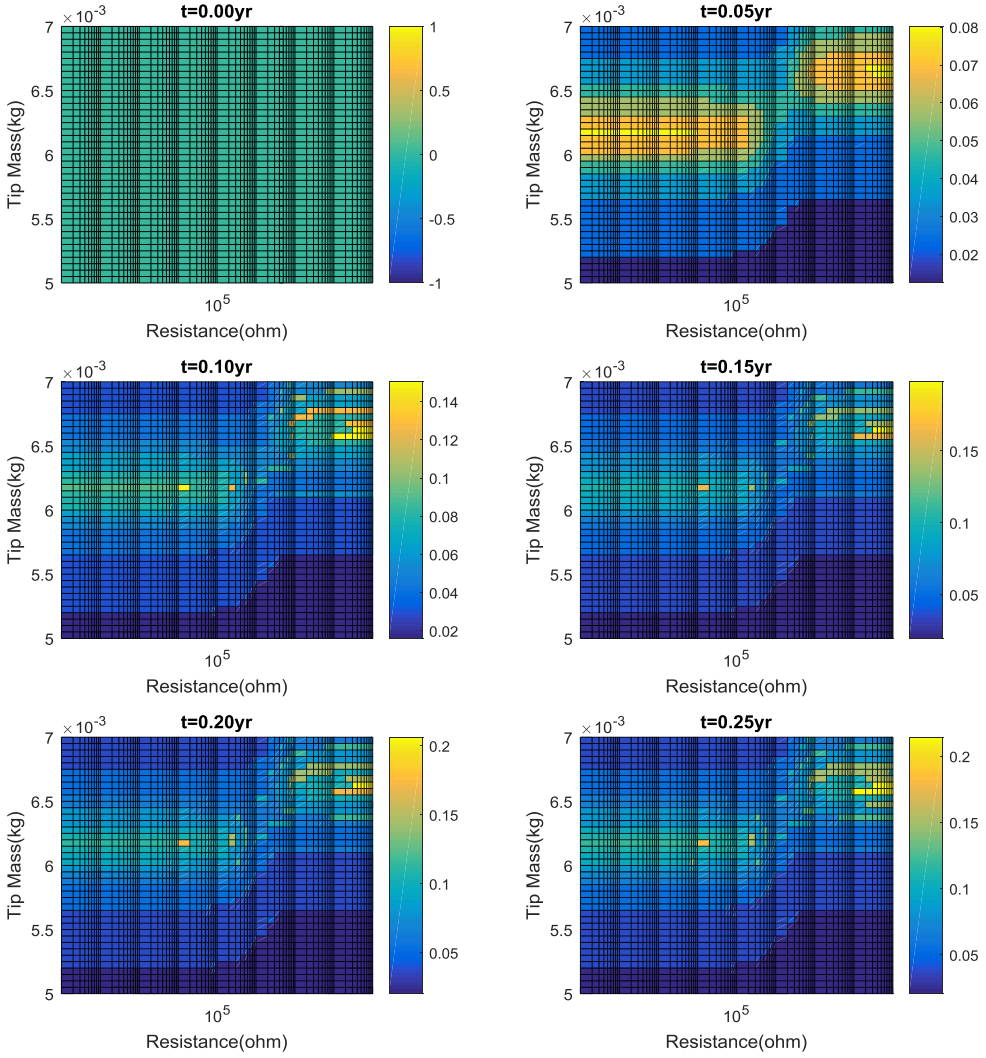

Figure 120. Cumulative Damage Contours (C) of $C_{\tilde{p}}$ Based on Degradation of Piezoelectric Terms. Results Applicable for $0.05yr$ from the Initial Time Indicated

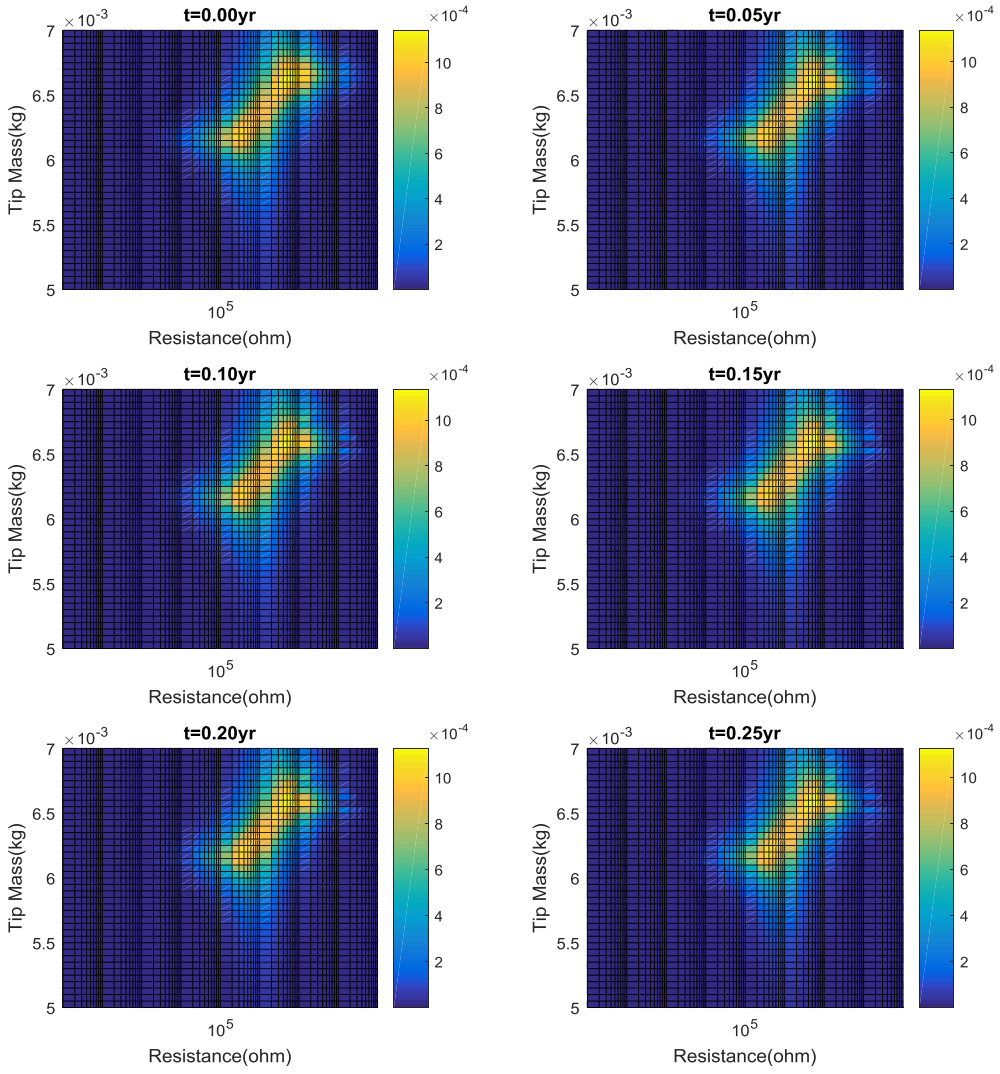

Figure 121. Average Power Contours (W) Based on Degradation of Piezoelectric Terms. Results Applicable for $0.05yr$ from the Initial Time Indicated

5.3.4.2.3. Combined Degradation Over all Three Loading Regimes

All three degradation models (Figure 112 and Figure 117) are included in a final analysis covering all three loading regimes (recall Table 58). The resulting MRTD and average power output are shown in Figure 122 and Figure 123. The trends identified in Section 5.3.4.2.1 and Section 5.3.4.2.2 are apparent in all three loading regimes. The downward shift of

tip mass (corresponding to maximum response) between each loading regime is due to the changing loading frequency between each regime: as the loading frequency changes ($20Hz$, $30Hz$, $25Hz$) the tip mass corresponding to resonant behavior changes.

Two interesting results are seen in the damage contours shown in Figure 124, Figure 125, and Figure 126. First, since the degredation of flexural rigidity causes a noticeable shift in the tip mass corresponding to maximum response, degradation of the piezoelectric terms is seen to spread to other tip mass realizations to a greater degree (unlike the concentrated damage shown in Figure 119 and Figure 120). Second, damage accumulation is stratified and, for the inputs considered, shows little overlap between each loading regime. As a physical example consider two different tip mass realizations: the first corresponds to a resonant frequency around $20Hz$ (e.g. $M_t \approx 0.0062kg$) while the second corresponds to a resonant frequency around $30Hz$ (e.g. $M_t \approx 0.003kg$). During the first loading regime the first realization is excited near resonance, resulting in relatively significant damage accumulation, while the second realization is not near resonance, resulting in relatively little damage accumulation. During the second loading regime the shift in loading frequency results in the second realization being excited near resonance while the first realization is no longer excited near resonance. Thus, during the second loading regime the additive damage to the first realization is small while the additive damage to the second realization is large. This explains the stratified nature of the damage and its evolution over time/cyclic loading.

To determine the tip mass and resistive load that maximizes the average power output over all three loading regimes (i.e. from year 0 to 0.9), the average power output from each realization is integrated over each time step and summed, resulting in a scalar value that can be used as an optimization metric. The resulting metric is plotted in Figure 127. The total average power output is found to be maximized when $M_t = 0.0062kg$, $R = 1e6\Omega$. The average power

output and corresponding MRTD are shown in Figure 128. For comparison purposes, Figure 128 also includes the average power output and corresponding MRTD for (1) the maximized result found in the baseline case ($M_t = 0.0066kg, R = 5e6\Omega$) and (2) the same realization ($M_t = 0.0066kg, R = 5e6\Omega$) but when damage is incorporated. When degradation is included in the analysis the power output from the originally optimal realization ($M_t = 0.0066kg, R = 5e6\Omega$) drops off rapidly due to a shift in the resonance frequency (i.e. the large initial MRTD leads to significant damage during the first time step which leads to a larger frequency shift in the next time step). The new optimal realization ($M_t = 0.0062kg, R = 1e6\Omega$) is seen to accumulate less damage (note the smaller initial MRTD) resulting in a smaller shift of the resonant frequency away from the loading frequency. This allows for a moderate power output over a greater duration compared to the large output over a short duration from the originally optimal realization.

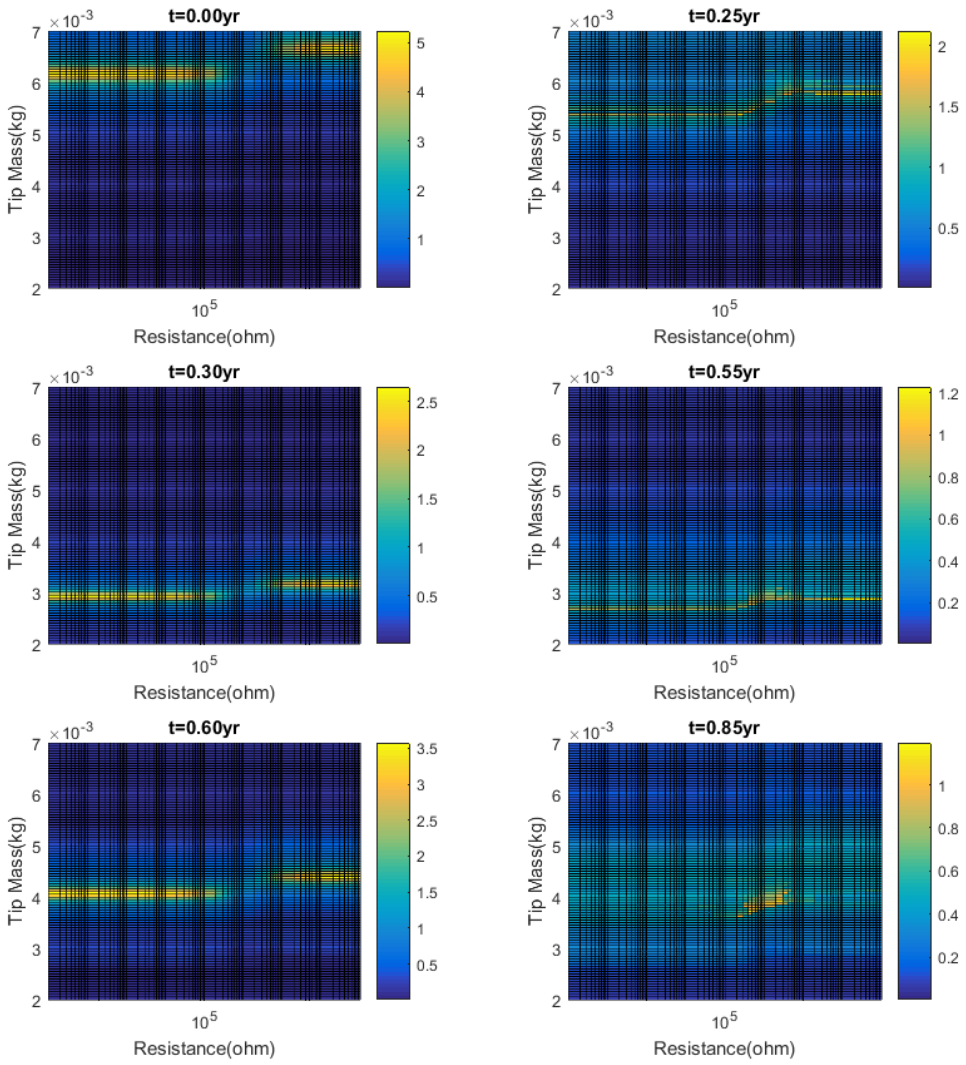

Figure 122. Maximum Relative Tip Displacement (MRTD) Contours (mm) Based on Full Degradation Model. Results Applicable for $0.05yr$ from the Initial Time Indicated

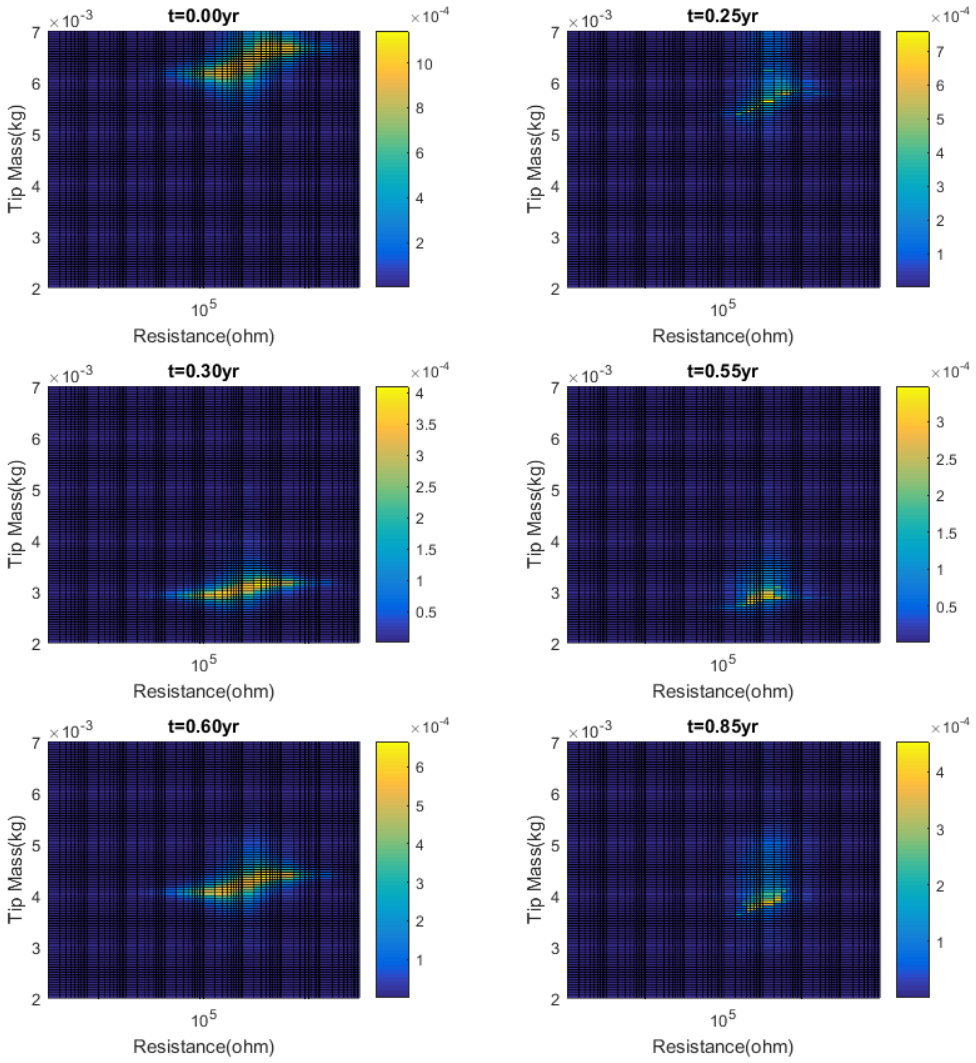

Figure 123. Average Power Contours (W) Based on Full Degradation Model. Results Applicable for $0.05yr$ from the Initial Time Indicated

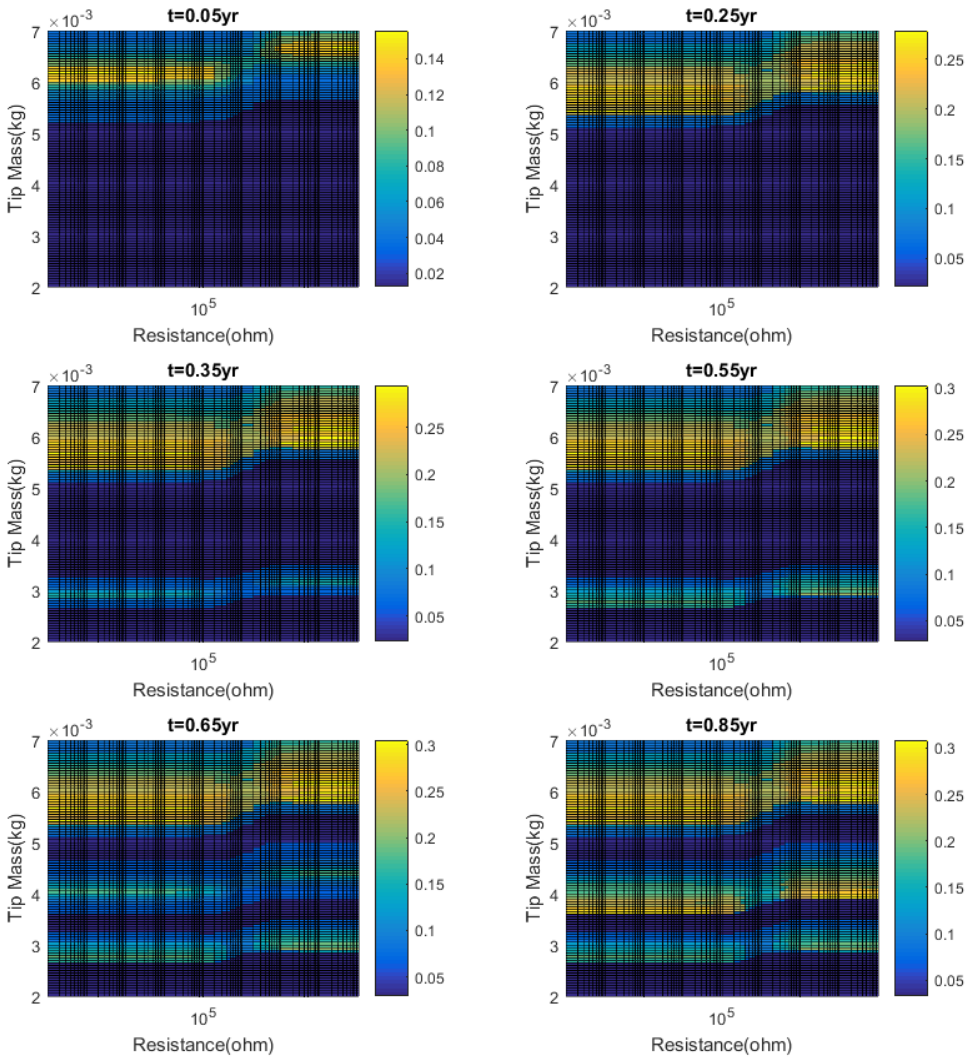

Figure 124. Cumulative Damage Contours (C) of Flexural Rigidity Based on Full Degradation Model. Results Applicable for $0.05yr$ from the Initial Time Indicated

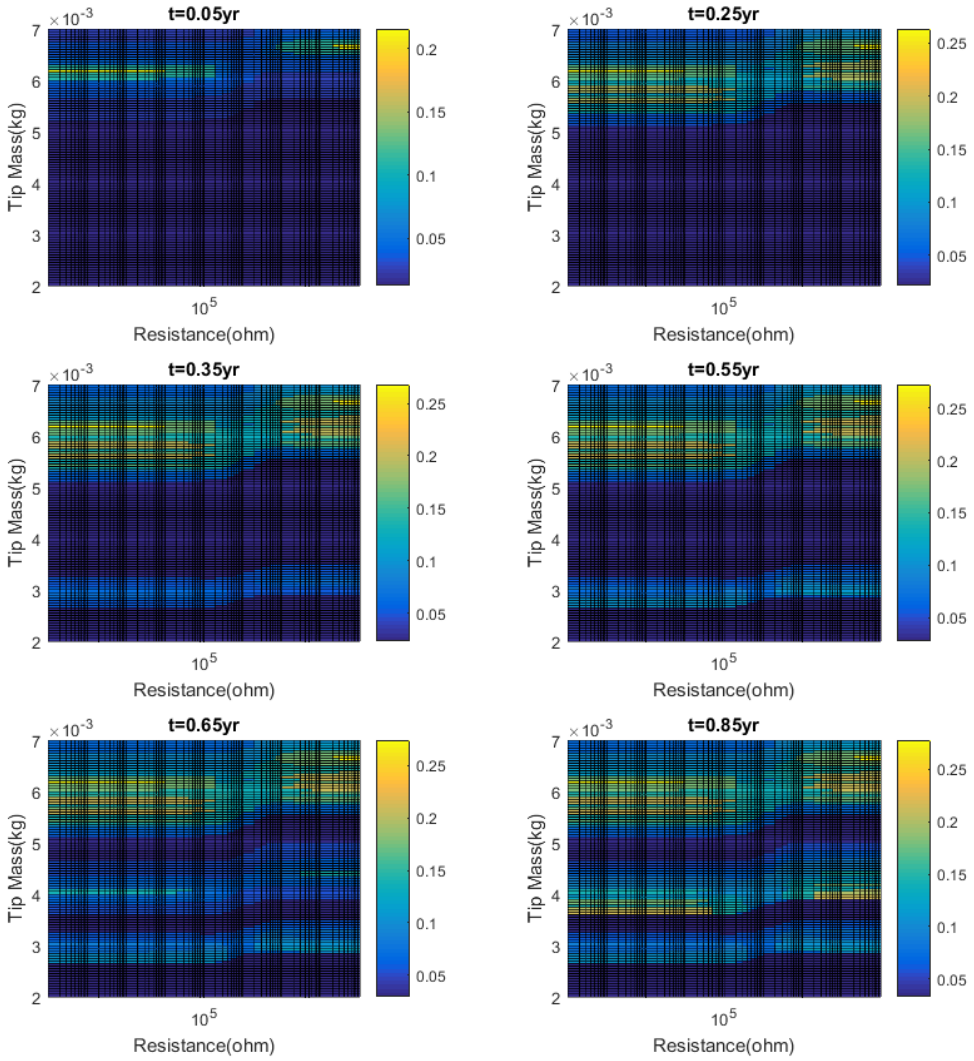

Figure 125. Cumulative Damage Contours (C) of d_{31} Based on Full Degradation Model. Results Applicable for $0.05yr$ from the Initial Time Indicated

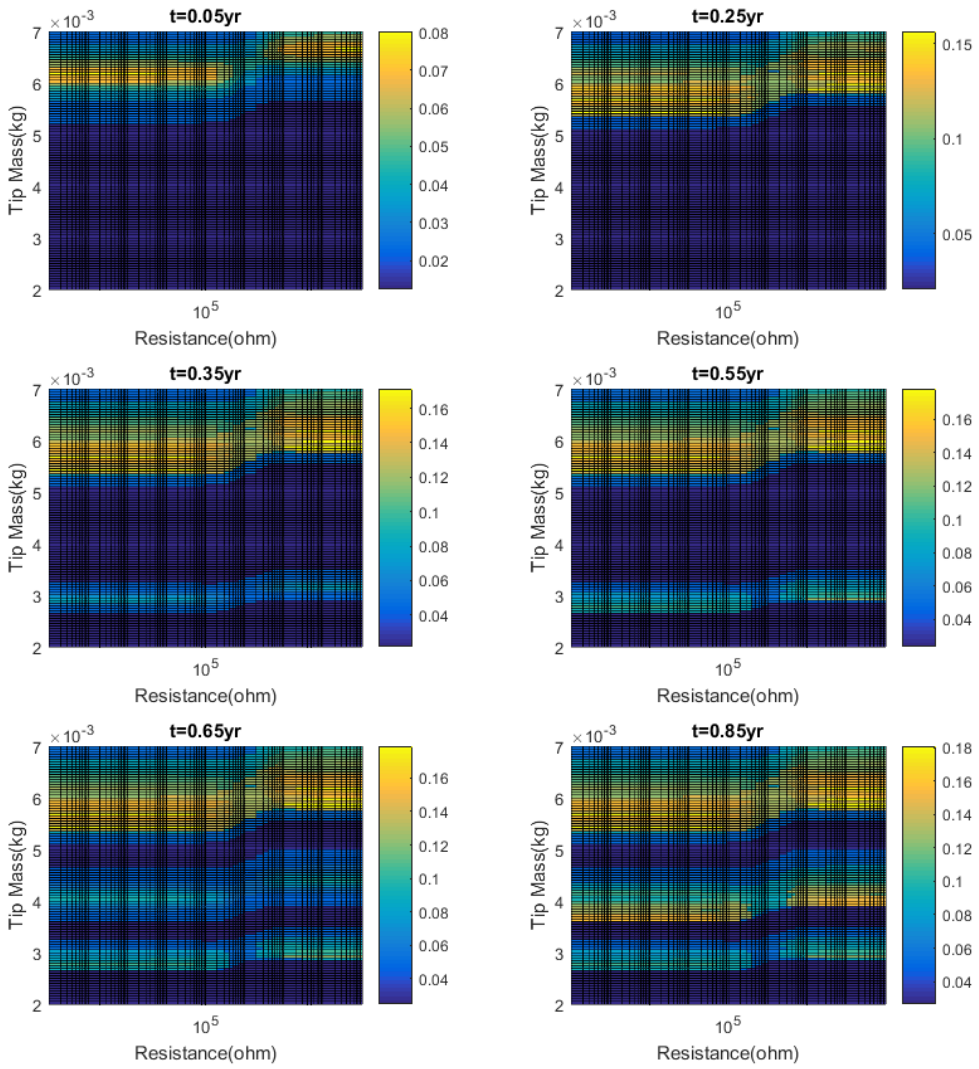

Figure 126. Cumulative Damage Contours (C) of $C_{\tilde{p}}$ Based on Full Degradation Model. Results Applicable for $0.05yr$ from the Initial Time Indicated

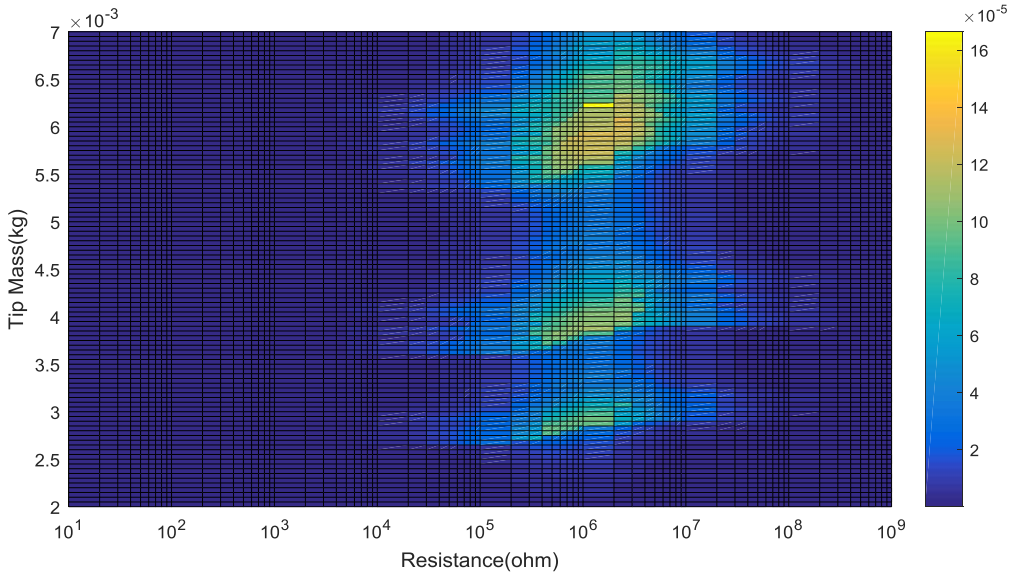

Figure 127. Integrated Power Metric (Wyr)

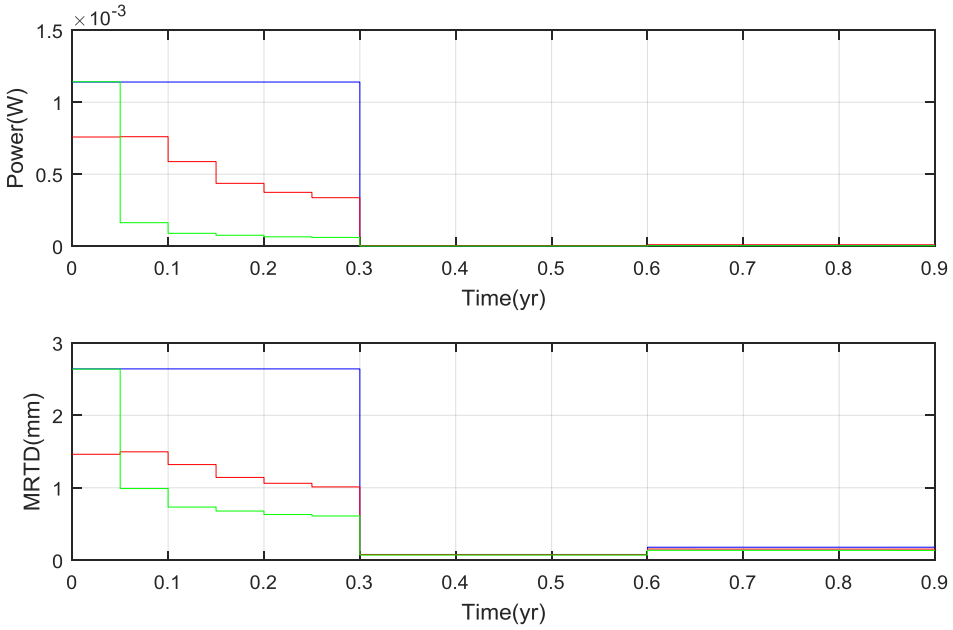

Figure 128. Average Power Output and Maximum Relative Tip Displacement (MRTD)
$M_t = 0.0066kg$, $R = 5e6\Omega$ with No Damage (Baseline; Blue)
$M_t = 0.0066kg$, $R = 5e6\Omega$ with Damage (Green)
$M_t = 0.0062kg$, $R = 1e6\Omega$ with Damage (New Optimum; Red)

5.3.4.3. Optimal Tip Mass and Resistive Load: Incorporating Temperature Dependency

The baseline model of the piezoelectric element is now expanded to include temperature effects. The inputs and loading schedule are repeated for convenience in Table 59 and Table 60. Damage is not included in the model and the piezoelectric terms are assumed not to degrade with time (the effect of time on the piezoelectric constant and piezoelectric capacitance are small for the given loading schedule and neglected for the entire analysis). The time-dependent operating temperature is shown in Figure 129. As before, the maximum relative tip displacement (MRTD) and average power output are calculated over a range of tip masses and resistive loads. The mechanical and electrical terms are first investigated separately to demonstrate their individual effects. Following this, their combined effects are demonstrated as an optimal tip mass and resistive load are selected.

Table 59. Inputs

Length L, (m)	0.030 & Varies
Width b, (m)	0.005
Distance to Neutral Axis $\frac{h_{\tilde{p}}+h_{\tilde{s}}}{2}$, (m)	$1e-4$
Modes Considered	1
Damping Ratio	0.010
Tip Mass M_t, (kg)	Optimized Variable
Tip Mass Density (kg/m^3)	6000
Tip Inertia I_t, (kgm^2)	Varies
Damage Index C	0 (No Damage)
Beam Mass m, (kg/m)	0.02
Operating Temperature (℃)	Varies
Flexural Rigidity YI, (Nm^2)	$1.090e-3$ & Varies
Piezoelectric Elastic Modulus c_{11}^E, (N/m^2)	$61e9$ & Varies
Piezoelectric Constant d_{31}, (m/V)	$-171e-12$ & Varies
Piezoelectric Capacitance $C_{\tilde{p}}$, (F)	$1.33e-8$ & Varies
Piezoelectric Configuration	Series
Resistive Load R, (Ω)	Optimized Variable

**Values shown are at baseline* 20℃

Table 60. Loading Schedule

Start Time (year)	Loading Regime	Loading Amplitude (m/s^2)	Loading Frequency (Hz)	Loading Frequency (rad/s)	End Time (year)
0	1	2	20	125.66	0.3
0.3	2		30	188.50	0.6
0.6	3		25	157.08	0.9

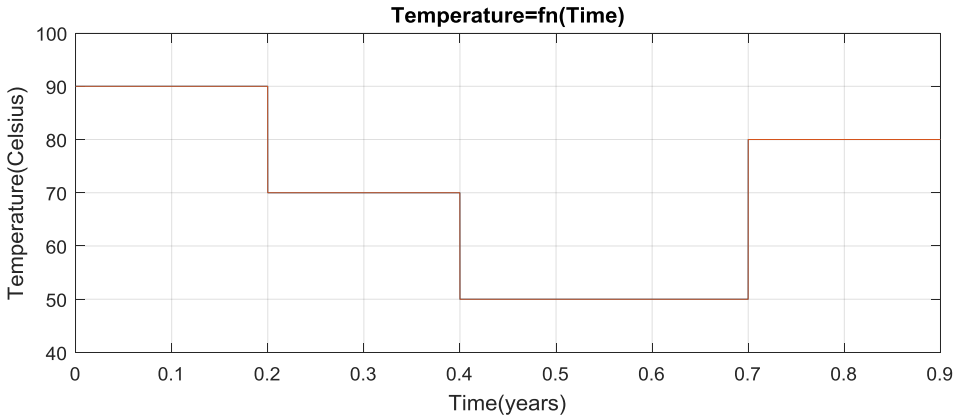

Figure 129. Time-Dependent Operating Temperature

5.3.4.3.1. Temperature Dependent Mechanical Properties During the First Loading Regime

The beam length and flexural rigidity are made to be temperature dependent with the assumed dependencies shown in Figure 130; while trends outlined in Section 5.3.2.1 have been followed, arbitrary values have been used. The modal damping ratio, piezoelectric constant, piezoelectric capacitance, and piezoelectric elastic modulus are made constant (0.01, $-171e-12\,m/V$, $1.33e-8F$, $61e9\,N/m^2$, respectively). Note that while the piezoelectric elastic modulus is a mechanical term, within the current model its sole use is in the definition of the effective piezoelectric stress constant ($\bar{e}_{31}$) which helps define the modal electromechanical coupling (Θ_r). As such, it is not included as a dependent variable in the current section and instead is incorporated in Section 5.3.4.3.2.

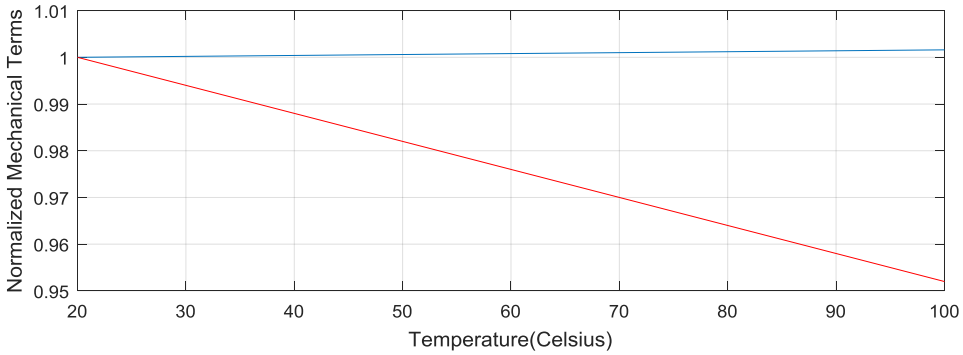

Figure 130. Normalized Temperature Dependence of the Beam Length (Blue) and Flexural Rigidity (Red)

The MRTD for the two temperature loads within the first loading regime are shown in Figure 131. Also included in Figure 131 is the baseline result at room temperature (i.e. the first plot in Figure 106). By increasing the operating temperature (20℃ to 90℃) the beam length increases and the flexural rigidity decreases. Both changes result in a decrease in the natural frequency of the system. Since the loading frequency is constant within the first loading regime, resonant behavior occurs at a lower tip mass as the temperature increases. This can be seen in the first two plots of Figure 131. When the temperature decreases (90℃ to 70℃) the reverse occurs and the tip mass corresponding to maximum MRTD is seen to increase. Analogous behavior is seen in the power output of Figure 132.

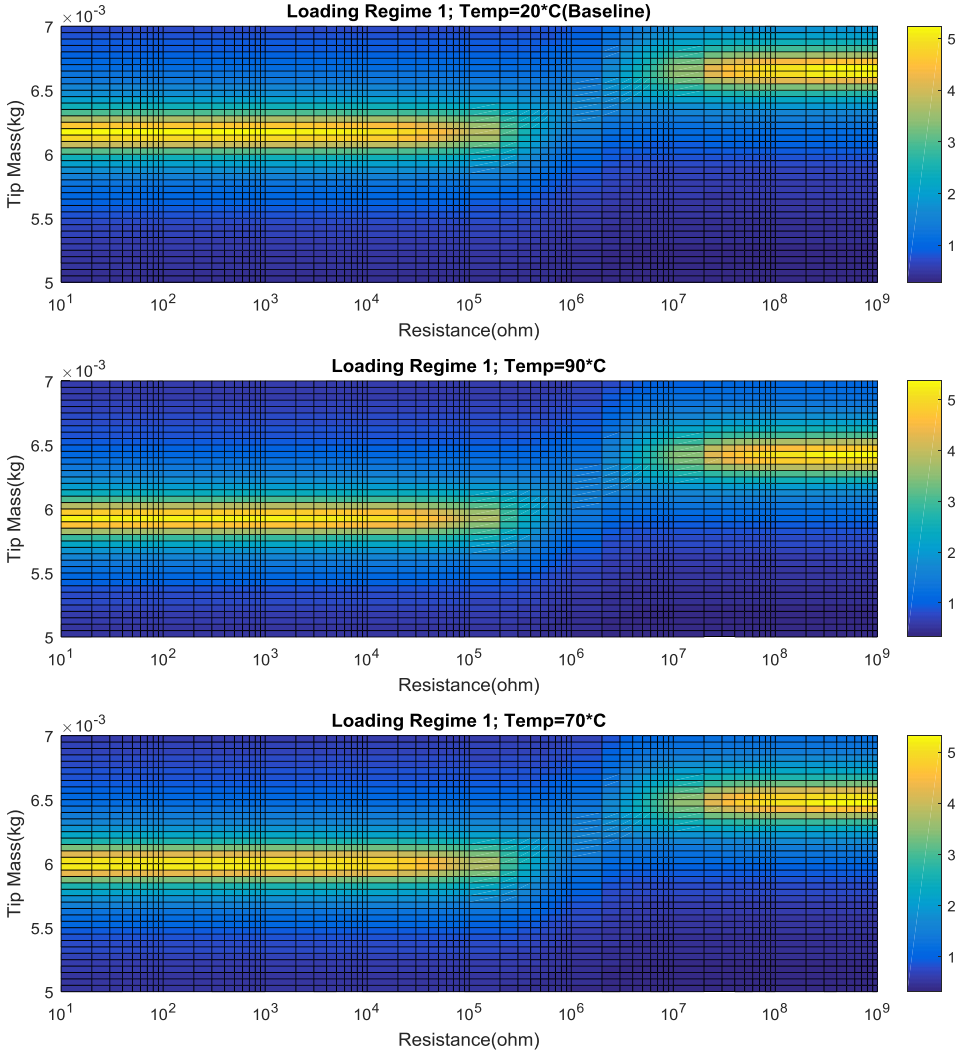

Figure 131. Maximum Relative Tip Displacement (MRTD) Contours (mm) Including Mechanical Temperature Effects

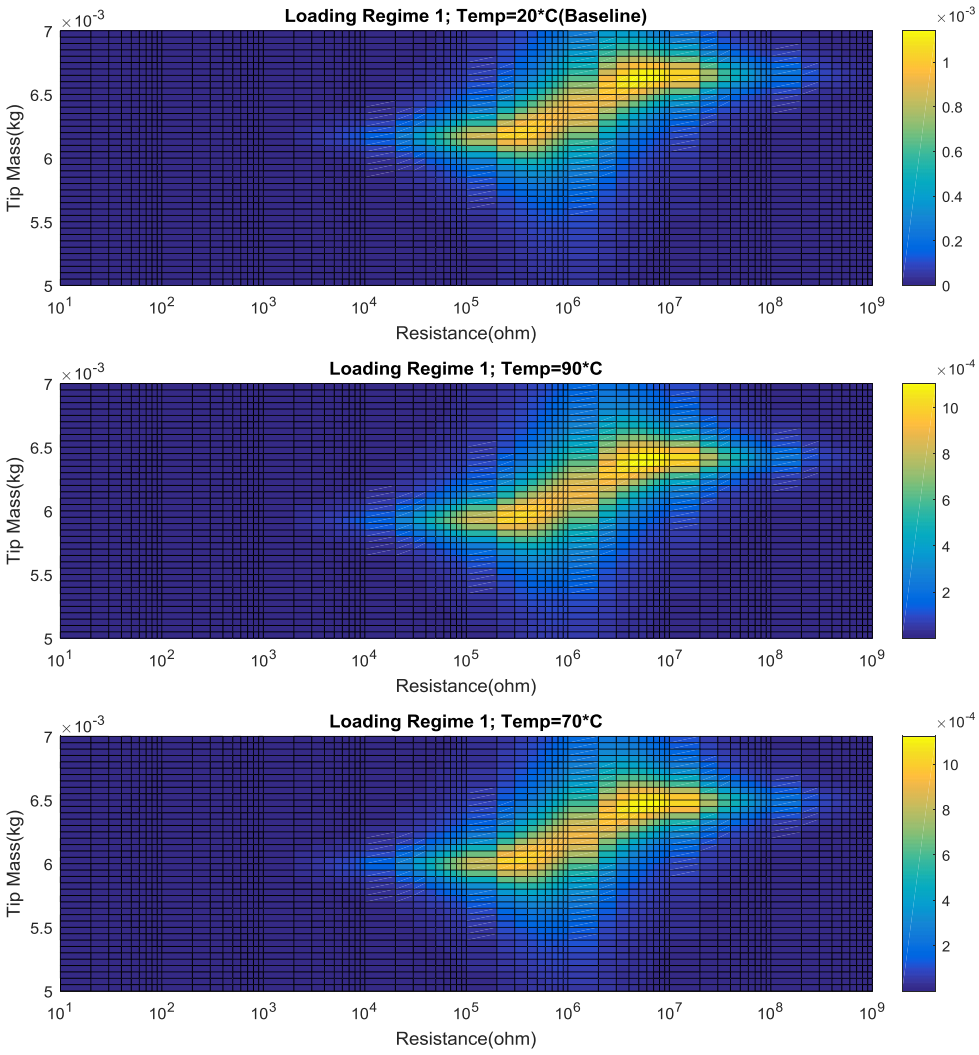

Figure 132. Average Power Contours (W) Including Mechanical Temperature Effects

5.3.4.3.2. Temperature Dependent Piezoelectric Properties During the First Loading Regime

The piezoelectric constant, piezoelectric capacitance, and piezoelectric elastic modulus are made to be temperature dependent with the assumed dependencies shown in Figure 133; while trends outlined in Section 5.3.2.1 have been followed, arbitrary values have been used.

The modal damping ratio, beam length, and flexural rigidity are made constant (0.01, $0.03m$ and $1.09e-3\ Nm^2$, respectively).

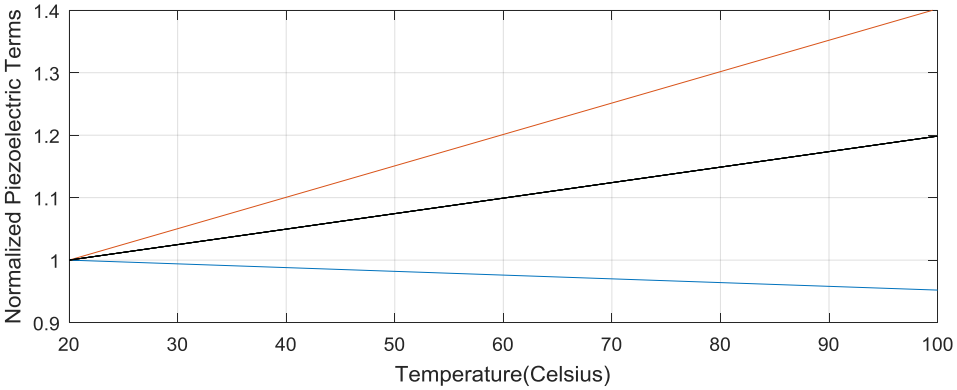

Figure 133. Normalized Temperature Dependence of the Piezoelectric Properties
Piezoelectric Constant (Red), Piezoelectric Capacitance (Black),
and Piezoelectric Elastic Modulus (Blue)

The MRTD for the two temperature loads within the first loading regime are shown in Figure 134. Also included in Figure 134 is the baseline result at room temperature (i.e. the first plot in Figure 106). For low resistive loads the coupled electromechanical system is dominated by the mechanical equation of motion. So, even for large changes in the piezoelectric terms (due to changing temperature) the MRTD at low resistance levels is expected to be relatively constant. At higher resistive loads, in general, the governing electrical equations cause a shift in the resonance frequency. Thus, if a temperature increase causes the magnitude of the piezoelectric terms to increase (recall $\bar{e}_{31} = d_{31}\bar{c}_{11}^{E}$), the shift in the resonance frequency is expected to be more severe. As the resonance frequency shifts, the tip mass corresponding to the maximum MRTD must also shift as the loading frequency is constant in the first loading regime. These trends are apparent in Figure 134. Analogous arguments can be made for the power output shown in Figure 135 where the tip mass corresponding to the maximum power output is relatively constant for low resistive loads (e.g. $R < 3e5\Omega$) but is seen to shift for higher resistive loads (e.g. $R > 4e6\Omega$).

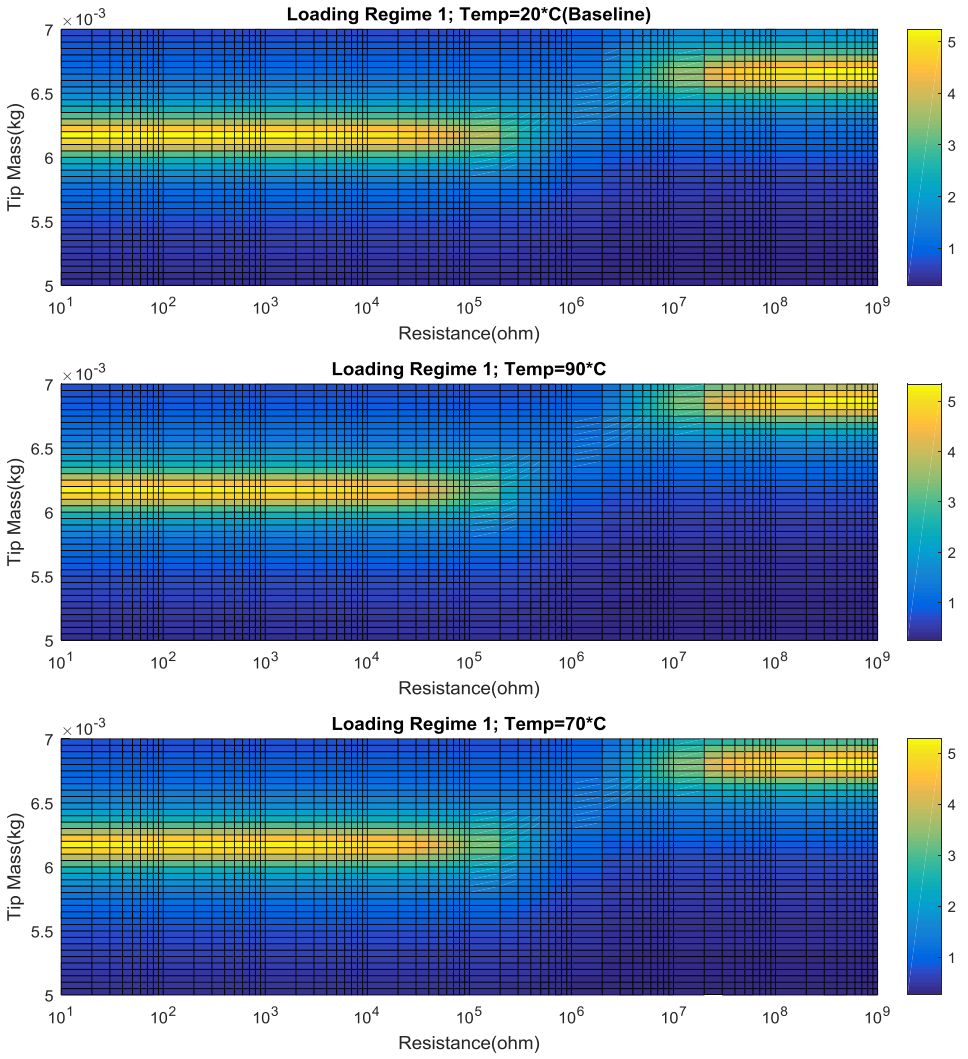

Figure 134. Maximum Relative Tip Displacement (MRTD) Contours (mm) Including Piezoelectric Temperature Effects

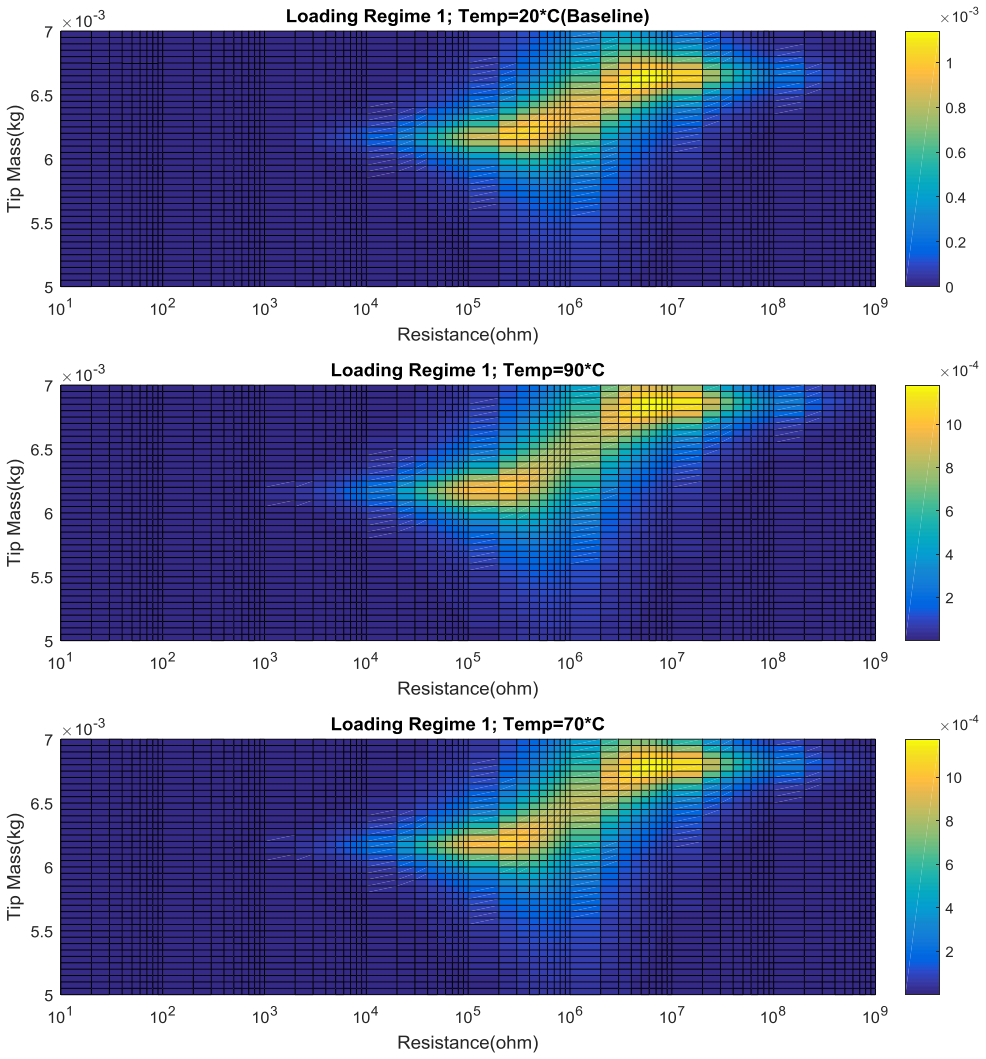

Figure 135. Average Power Contours (W) Including Piezoelectric Temperature Effects

5.3.4.3.3. Combined Temperature Effects Over all Three Loading Regimes

The combined temperature effects of all five variables (see Figure 130 and Figure 133) are included in an analysis spanning all three loading regimes. The resulting MRTD and average power output are shown in Figure 136 and Figure 137. The previously identified trends are apparent in all three loading regimes.

To determine the tip mass and resistive load that maximizes the average power output over all three loading regimes (i.e. from year 0 to 0.9), the average power output from each realization is integrated over each time step and summed, resulting in a scalar value that can be used as an optimization metric. The resulting metric is plotted in Figure 138. The total average power output is found to be maximized when $M_t = 0.0066kg$, $R = 7e6\Omega$. The average power output and corresponding MRTD are shown in Figure 139. For comparison purposes, Figure 139 also includes the average power output and corresponding MRTD for (1) the maximized result found in the baseline case ($M_t = 0.0066kg$, $R = 5e6\Omega$) and (2) the same realization ($M_t = 0.0066kg$, $R = 5e6\Omega$) but when temperature effects are included. For the assumed dependencies and thermal loads, temperature is seen to have a significantly smaller effect on the systems power output than damage accumulation (compare Figure 128 and Figure 139).

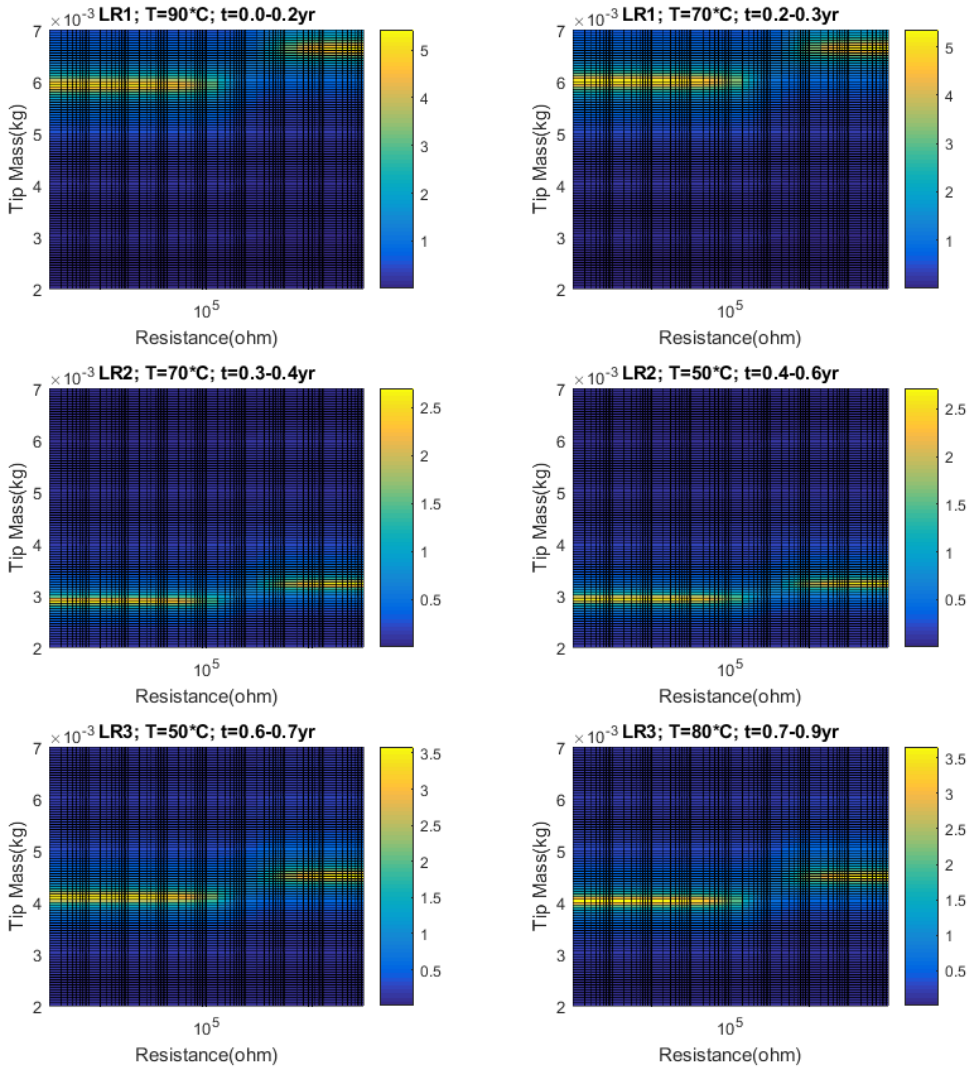

Figure 136. Maximum Relative Tip Displacement (MRTD) Contours (mm) Based on Full Temperature Effects

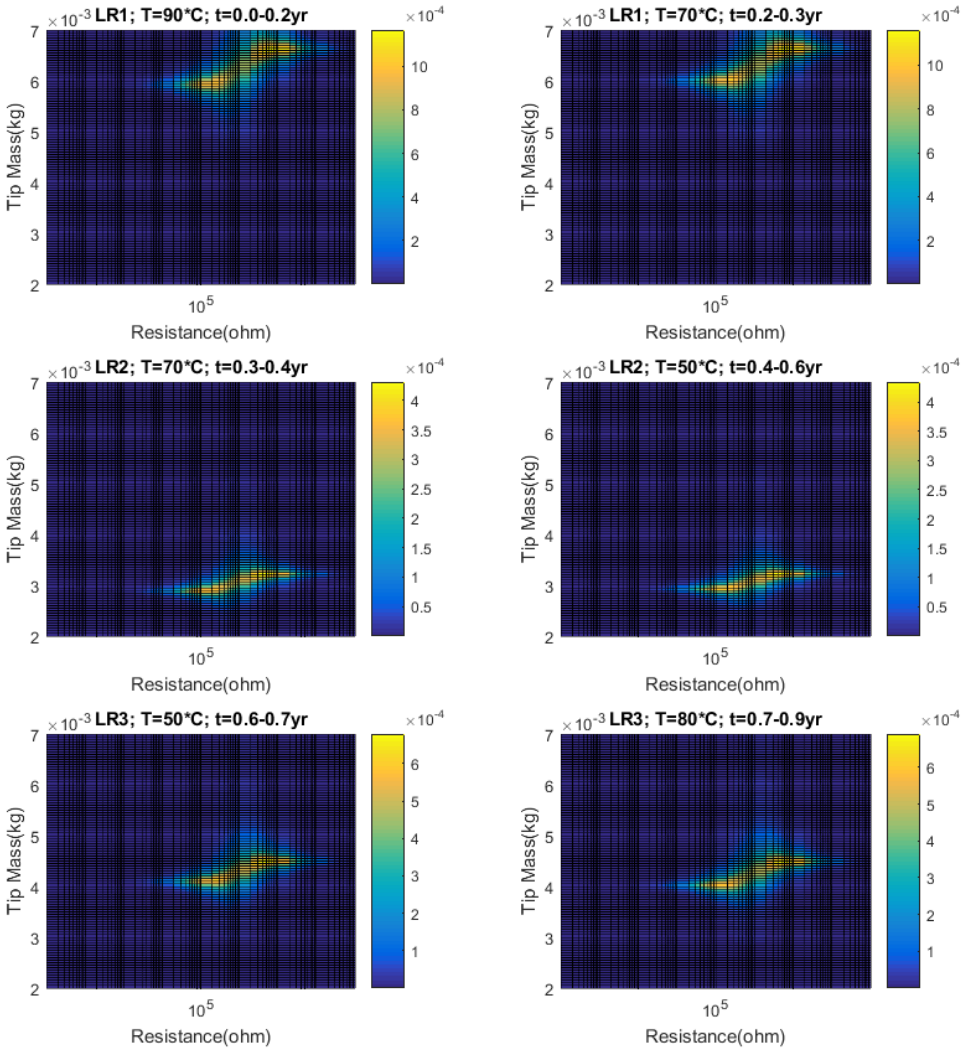

Figure 137. Average Power Contours (W) Based on Full Temperature Effects

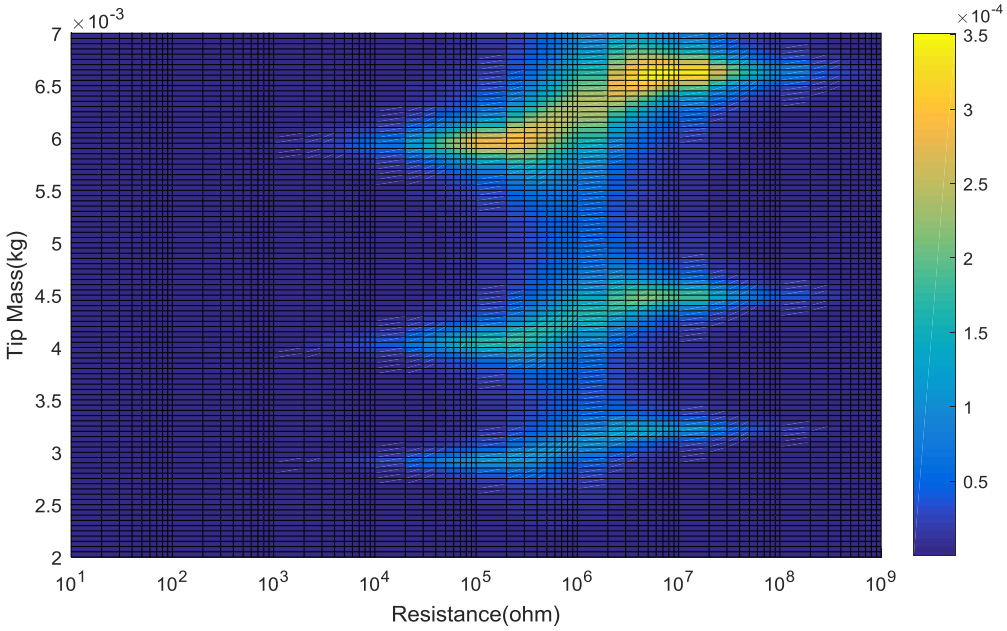

Figure 138. Integrated Power Metric (Wyr)

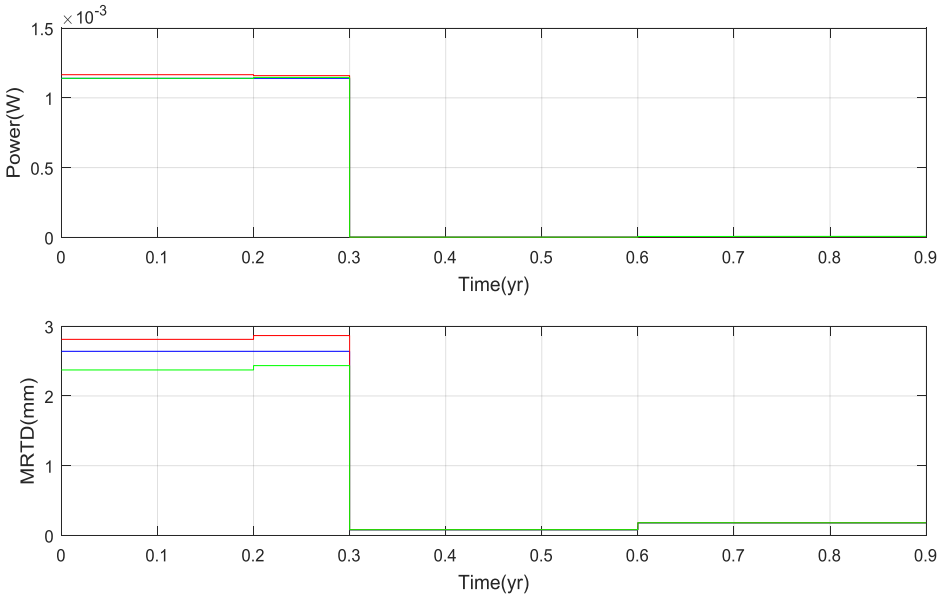

Figure 139. Average Power Output and Maximum Relative Tip Displacement (MRTD)
$M_t = 0.0066kg$, $R = 5e6\Omega$ with No Temperature Effects (Baseline; Blue)
$M_t = 0.0066kg$, $R = 5e6\Omega$ with Temperature Effects (Green)
$M_t = 0.0066kg$, $R = 7e6\Omega$ with Temperature Effects (New Optimum; Red)

5.3.4.4. Optimal Tip Mass and Resistive Load: Incorporating Damage and Temperature Effects

Both damage accumulation and temperature effects can be included in a single model to determine an optimal configuration (i.e. tip mass and resistive load). Using the same inputs, loading schedule, and expected operating temperature as before (repeated in Table 61, Table 62, and Figure 140) the tip mass which maximizes the total average power output can be calculated. The time discretization is taken to be $0.05yr$. The damage and temperature dependencies are repeated in Figure 141 and Figure 142 for convenience. The resulting MRTD, cumulative damage contours, and average power output for select time instances are shown in Figure 143, Figure 144, Figure 145, respectively. The power metric is shown in Figure 146 and indicates that the optimal realization is $M_t = 0.0061kg$, $R = 2e6\Omega$. The average power output and corresponding MRTD are shown in Figure 147. The previously noted trends are apparent.

Table 61. Inputs

Length L, (m)	0.030 & Varies
Width b, (m)	0.005
Distance to Neutral Axis $\frac{h_{\tilde{p}}+h_{\tilde{s}}}{2}$, (m)	$1e-4$
Modes Considered	1
Damping Ratio	0.010
Tip Mass M_t, (kg)	Optimized Variable
Tip Mass Density (kg/m^3)	6000
Tip Inertia I_t, (kgm^2)	Varies
Damage Index C	Varies
Beam Mass m, (kg/m)	0.02
Operating Temperature (℃)	Varies
Flexural Rigidity YI, (Nm^2)	$1.090e-3$ & Varies
Piezoelectric Elastic Modulus c_{11}^E, (N/m^2)	$61e9$ & Varies
Piezoelectric Constant d_{31}, (m/V)	$-171e-12$ & Varies
Piezoelectric Capacitance $C_{\tilde{p}}$, (F)	$1.33e-8$ & Varies
Piezoelectric Configuration	Series
Resistive Load R, (Ω)	Optimized Variable

**Values shown are at baseline* 20℃

Table 62. Loading Schedule

Start Time (year)	Loading Regime	Loading Amplitude (m/s^2)	Loading Frequency (Hz)	Loading Frequency (rad/s)	End Time (year)
0	1	2	20	125.66	0.3
0.3	2		30	188.50	0.6
0.6	3		25	157.08	0.9

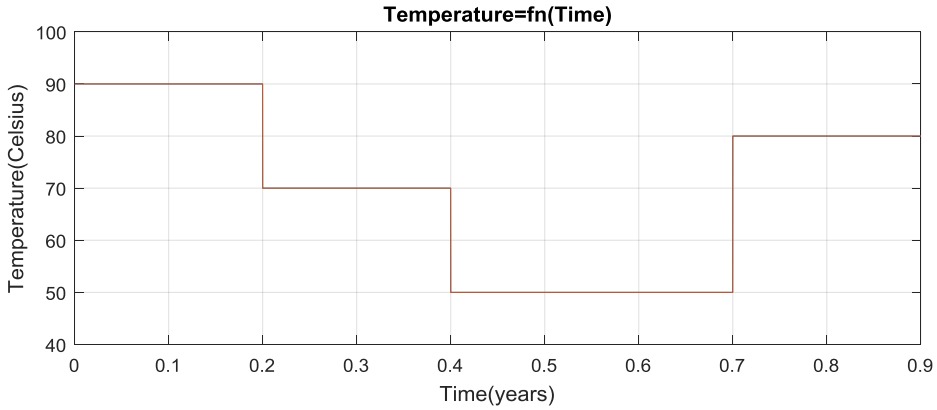

Figure 140. Time-Dependent Operating Temperature

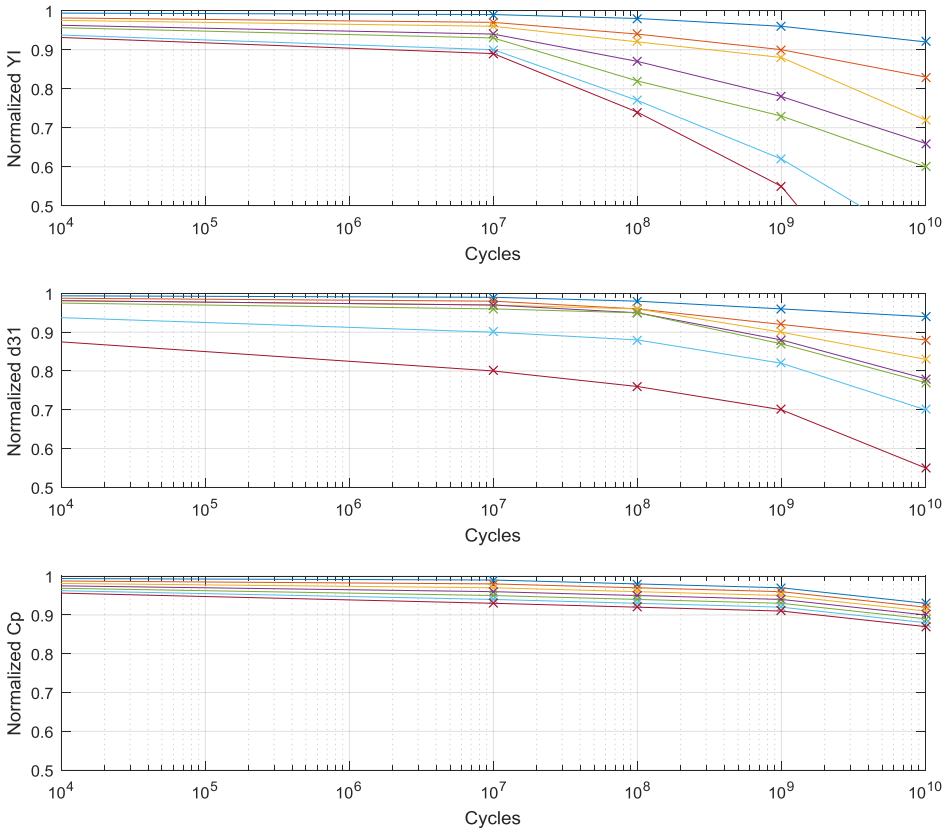

Figure 141. Normalized Degradation of From Cycling at Specified Amplitudes
$A_1 = 0.5mm$ (Blue), $A_2 = 1mm$ (Orange), $A_3 = 1.5mm$ (Yellow), $A_4 = 2mm$ (Purple), $A_5 = 3mm$ (Green), $A_6 = 5mm$ (Cyan), $A_7 = 7mm$ (Red)

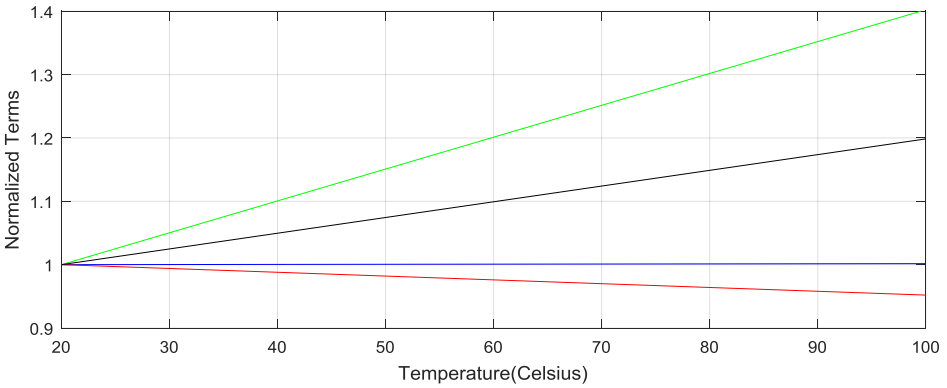

Figure 142. Normalized Temperature Dependence
Beam Length (Blue), Flexural Rigidity and Piezoelectric Elastic Modulus (Red), Piezoelectric Constant (Green), and the Piezoelectric Capacitance (Black)

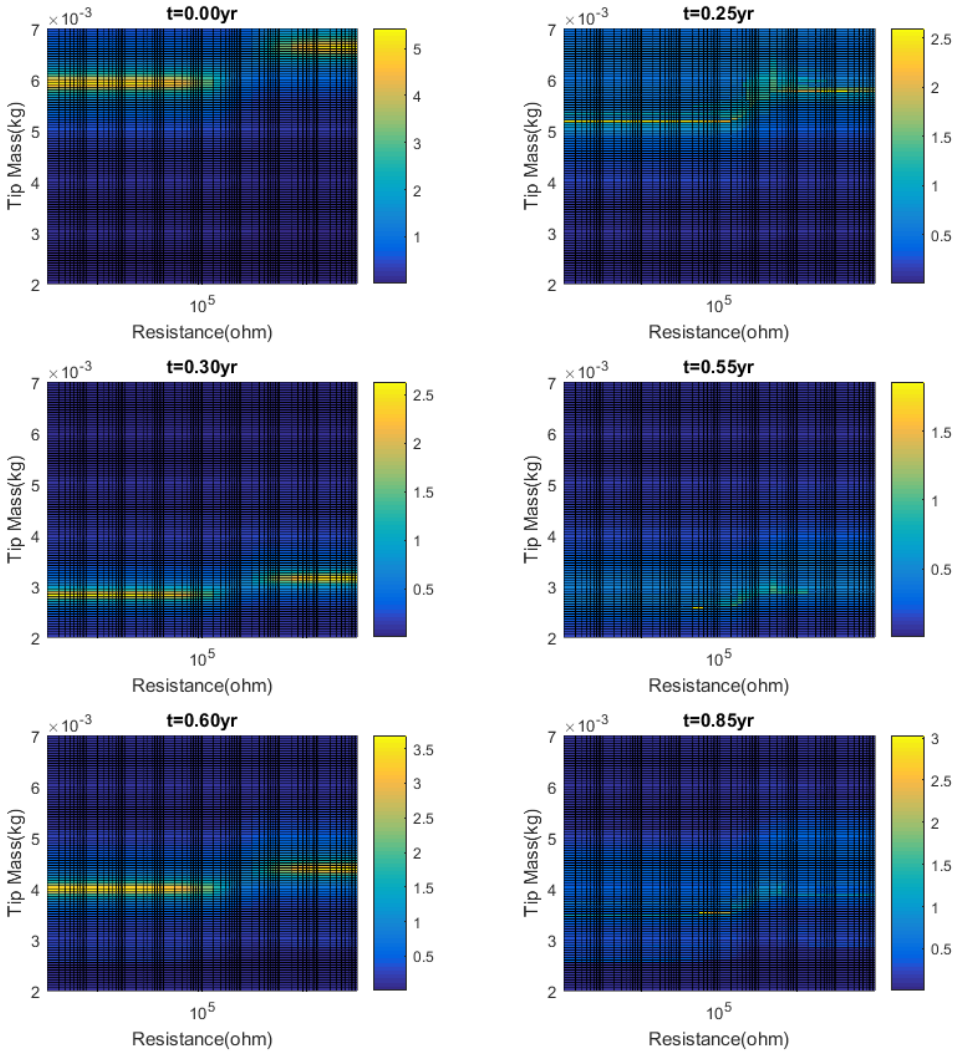

Figure 143. Maximum Relative Tip Displacement (MRTD) Contours (mm) Including Damage and Temperature Effects: Select Instances in Time

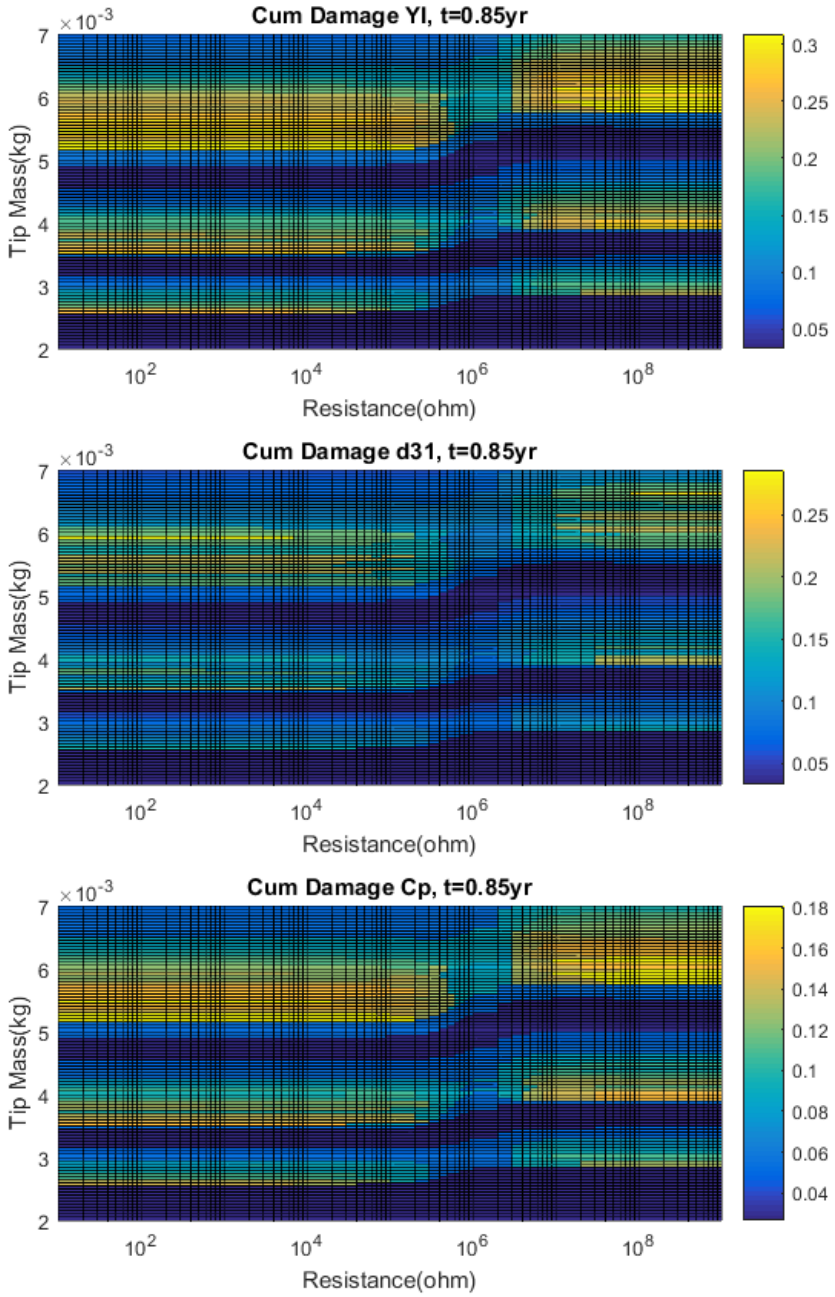

Figure 144. Cumulative Damage Contours (C) of Flexural Rigidity (YI), Piezoelectric Constant (d_{31}), and Piezoelectric Capacitance ($C_{\tilde{p}}$) Including Damage and Temperature Effects: Select Instances in Time

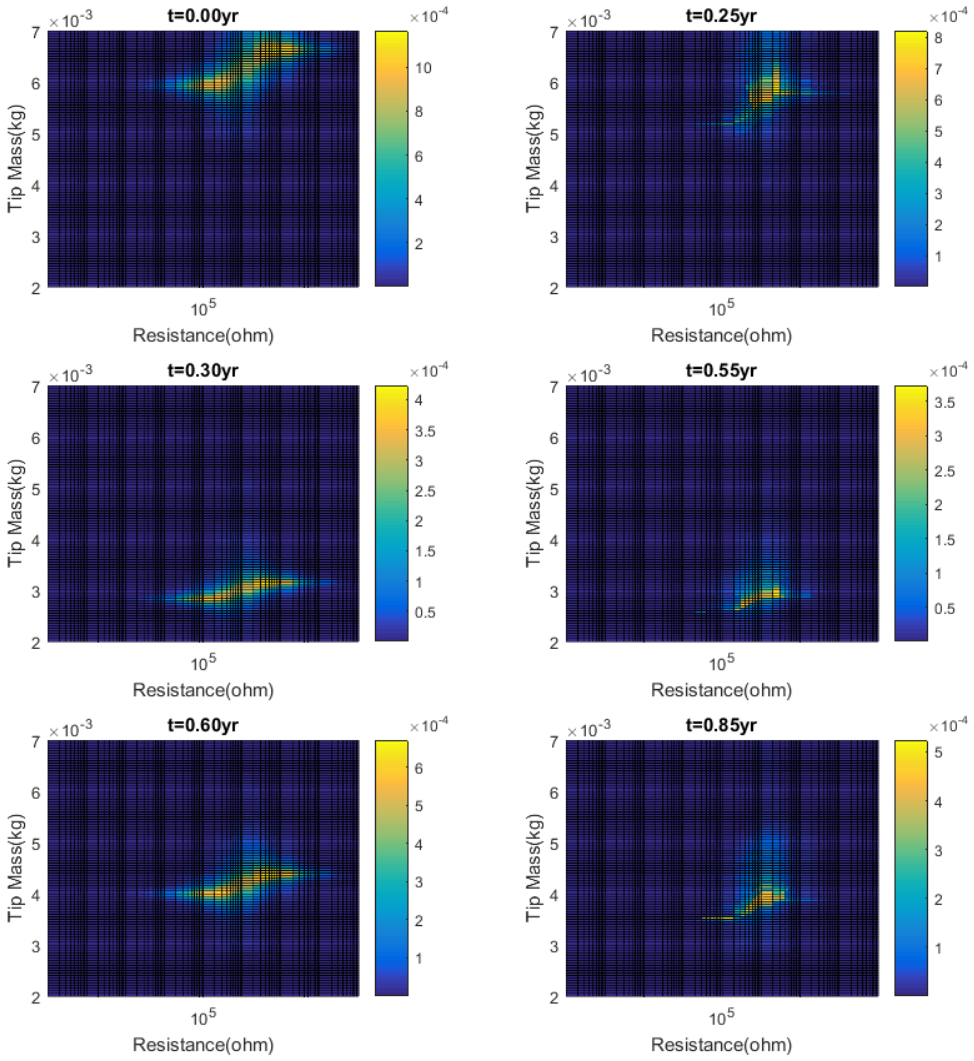

Figure 145. Average Power Contours (W) Including Damage and Temperature Effects: Select Instances in Time

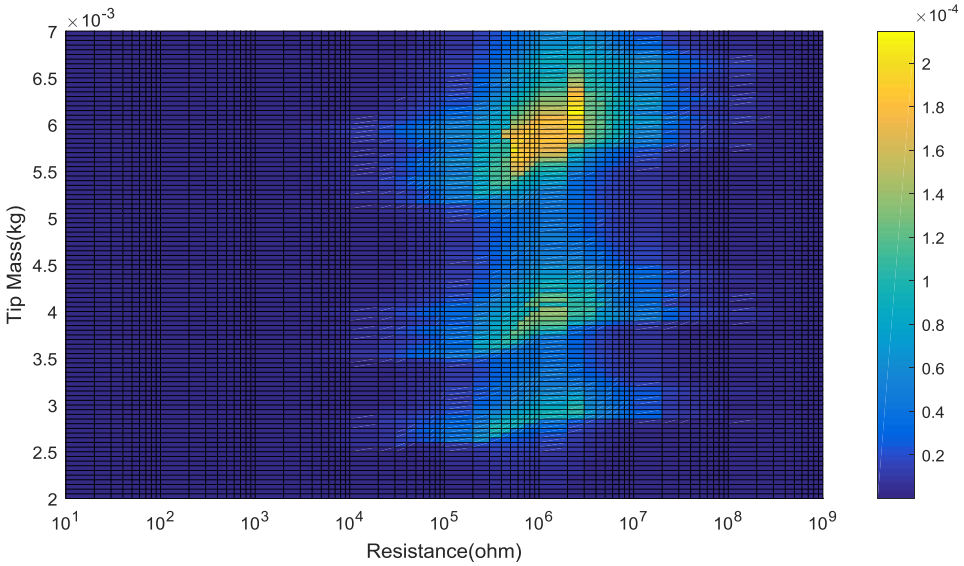

Figure 146. Integrated Power Metric (Wyr)

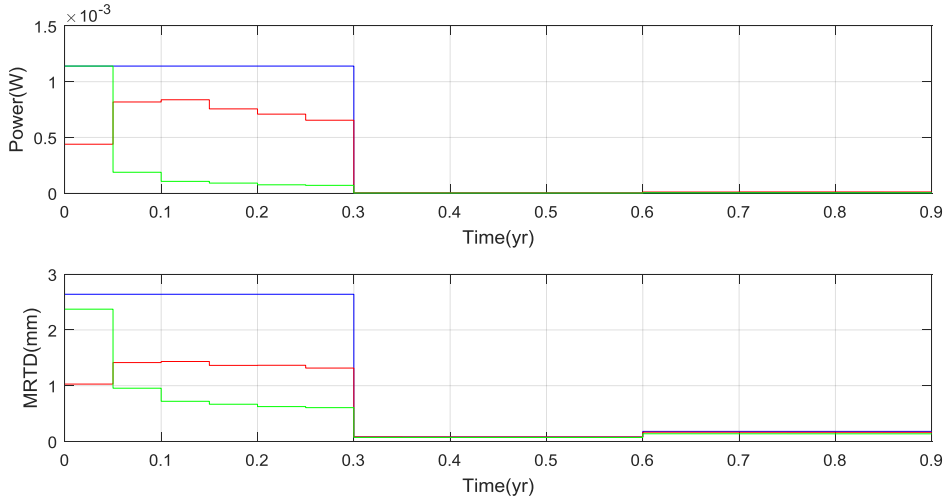

Figure 147. Average Power Output and Maximum Relative Tip Displacement (MRTD)
$M_t = 0.0066kg$, $R = 5e6\Omega$ with No Effects (Baseline; Blue)
$M_t = 0.0066kg$, $R = 5e6\Omega$ with Full Effects (Green)
$M_t = 0.0061kg$, $R = 2e6\Omega$ with Full Effects (New Optimum; Red)

5.3.5. Summary

Beyond providing a useful tool for practitioners, the SS (specifically the demonstration cases) revealed several interesting results. For the inputs considered, the following trends are noted. From the baseline model with constant loading (i.e. within the first loading regime):

- For low resistive loads the MRTD approaches that of the electromechanically uncoupled system where a maximum response is seen as the undamped natural frequency (ω_r) and the loading frequency converge. As the resistive load is increased there is an upwards shift in the systems resonant frequency and a corresponding upwards shift in the tip mass maximizing the MRTD.
- The power generated by the energy harvester is dependent on the tip mass and, for the resonance case, increases with increasing tip mass.

From the damage accumulation models with constant loading:

- Damage to the flexural rigidity leads to a reduction in the resonant frequency across all resistive loads. The reduced resonant frequency results in a reduced optimal tip mass and, since the power output is dependent on the tip mass, a reduced power output.
- Damage to the piezoelectric terms does not significantly affect the tip mass corresponding to the maximum MRTD for low resistive loads but has some impact for high resistive loads. Degradation of the piezoelectric terms is concentrated in those tip mass realizations where the MRTD is high; in this study the realizations where the MRTD was high did not correspond to the realizations where the power output was high. Thus, degradation of the piezoelectric terms was not seen to significantly affect the maximum power output.

From the temperature dependent models with constant loading:

- Temperature-based changes to the mechanical terms leads to changes in the resonant frequency (and thus the optimal tip mass) across all resistive loads.

- Temperature-based changes to the piezoelectric terms negligibly impacts the optimal tip mass for low resistive loads (for which the mechanical equations of motion dominate the systems behavior) but does cause shifts in the optimal tip mass for high resistive loads.

Across all models:

- Damage accumulation is seen to have a non-trivial impact on the optimal realization (i.e. tip mass and resistive load) and maximum average power output.
- A majority of the power generated by an optimized piezoelectric energy harvester will likely be generated during a single acceleration profile if the user-inputted acceleration time histories are sufficiently dissimilar. This likely necessitates the use of a broadband (or similar) energy harvesting system for practical applications.

A portion of Chapter 5 has been published in SPIE Smart Structures and Materials+ Nondestructive Evaluation and Health Monitoring, Eric Kjolsing and Michael Todd, 2016. The title of this paper is “Gauging the Feasibility of a Downhole Energy Harvesting System Through a Proof-of-Concept Study”. The dissertation author was the primary investigator and author of this paper.

Chapter 6
Summary of Research and Future Work

The research presented in this dissertation stems from a design project originating at Los Alamos National Laboratory. The original goal of the project was to design and fabricate a vibration energy harvesting system that could be used to replace or supplement conventional power sources in downhole applications. The goal of the project changed during the projects lifetime, as explained below.

In Chapter 2, an analytical model was developed to investigate critical assumptions made in the initial proof of concept design calculations. The configuration of interest consisted of a bluff body within a fluid conveying pipe which itself was surrounded by a viscous annulus fluid. The analytical model representing this configuration was based on an Euler-Bernoulli beam model paired with a hydrodynamic forcing function which represented the inertial and viscous effects of the annulus fluid. The analytical model used Green's functions to calculate the translational displacement of the pipe due to an applied harmonic point force (representing the pressure oscillation stemming from the conveyed fluid/bluff body interaction). The investigation found the maximum resonant displacement was orders of magnitude less than that

assumed in the preliminary calculations. With the preliminary design in question, the project changed directions: rather than design and fabricate a vibration energy harvesting system, investigations that would support the future design of a downhole energy harvesting system were pursued.

Since the power generated by vibration based energy harvesters is sensitive to the natural frequency and damping of the supporting structure, Chapter 3 parametrically explored the dynamic behavior of a production string using a new equation of motion. The hydrodynamic function utilized in Chapter 2 was paired with the equation of motion of a fluid conveying pipe. The spectral element method was used to solve for the natural frequency and damping ratio in the system as parameters of interest were varied. Parameters included the conveyed fluid velocity, axial force, annulus fluid properties, annulus geometry, and rotational boundary springs.

In Chapter 4, a preliminary structural housing was designed so as to determine the radial width available to house an energy harvesting system. Hand calculations and finite element models were used in conjunction with American Petroleum Institute loading scenarios and tubing geometries to design the housing. This work was a necessary precursor to the work in Chapter 5 as the available radial width dictated which commercially available transduction mechanisms might be employed.

In Chapter 5, two approaches were developed to estimate harvestable power for user-defined piezoelectric energy harvester configurations. The first approach utilizes an uncoupled electromechanical lumped parameter model to produce a computationally inexpensive order of magnitude power estimate. The second approach utilizes coupled electromechanical equations in a distributed system to generate an improved power output estimate. So as to provide a more domain-specific tool, the second program specifically accounts for the accumulation of damage

and variable dependencies. Through four demonstration cases, it was shown how damage accumulation and temperature variations might affect the power output of a piezoelectric energy harvester. The investigations results are especially important when designing for the downhole environment where replacing an energy harvesting system would be expensive.

The main contributions found in this dissertation include:

A parametric study describing how variables of interest affect the natural frequency and damping ratio of a braced production string.

Investigations demonstrating how damage accumulation and temperature variations might affect the power output of a piezoelectric energy harvester.

Design software which facilitates the optimal design of a piezoelectric energy harvester so as to maximize power output.

Additional work may prove beneficial in advancing the design of a downhole vibration based energy harvesting system.

- The preliminary harvester design relied on pressure oscillations (stemming from the conveyed fluid/bluff body interaction) to harmonically displace the production tube, thus exciting the energy harvesting system. However, the magnitude of the tube displacement found in Chapter 2 was smaller than what was assumed in the proof of concept calculations. In order to determine the power output for a vibration energy harvesting system, the displacement (or acceleration) time history exciting the harvester is needed. Representative downhole acceleration time histories should be developed or acquired from downhole measurements. The development of mechanical amplifiers would also prove useful if the ambient vibrations do not result in sufficient power output.

- While the preliminary housing design of Chapter 4 provided a radial width (enabling the development of the MATLAB programs in Chapter 5), the housing design is not optimized. Design alternatives which would reduce stress concentrations and/or improve access to the energy harvesting system, like those shown in Figure 69, should be developed.
- Relatively little literature is available describing the degradation of the mechanical and piezoelectric terms when subjected to mechanical cycling. Commercially available bimorphs should be mechanically cycled to various displacement amplitudes so as to determine the degradation of various properties (thus enabling the utilization of the damage accumulation model described in Chapter 5).
- In Chapter 5, damage accumulation was seen to play a significant role in determining the tip mass and resistive load corresponding to the maximum average power output. Damage is dependent on the amplitude and cycle count of the relative tip displacement (for the damage model utilized in this study), which is dependent on the driving acceleration time histories which excite the energy harvester. The SS model should be expanded to include uncertainty in the loading. After assigning probabilities as to when each acceleration profile is active, Monte Carlo analysis can be performed to determine the damage-dependent power output over time. Statistical analysis can then be used to determine the average power output for a user-specified confidence interval.

Appendix A – LANL Initial Power Estimates

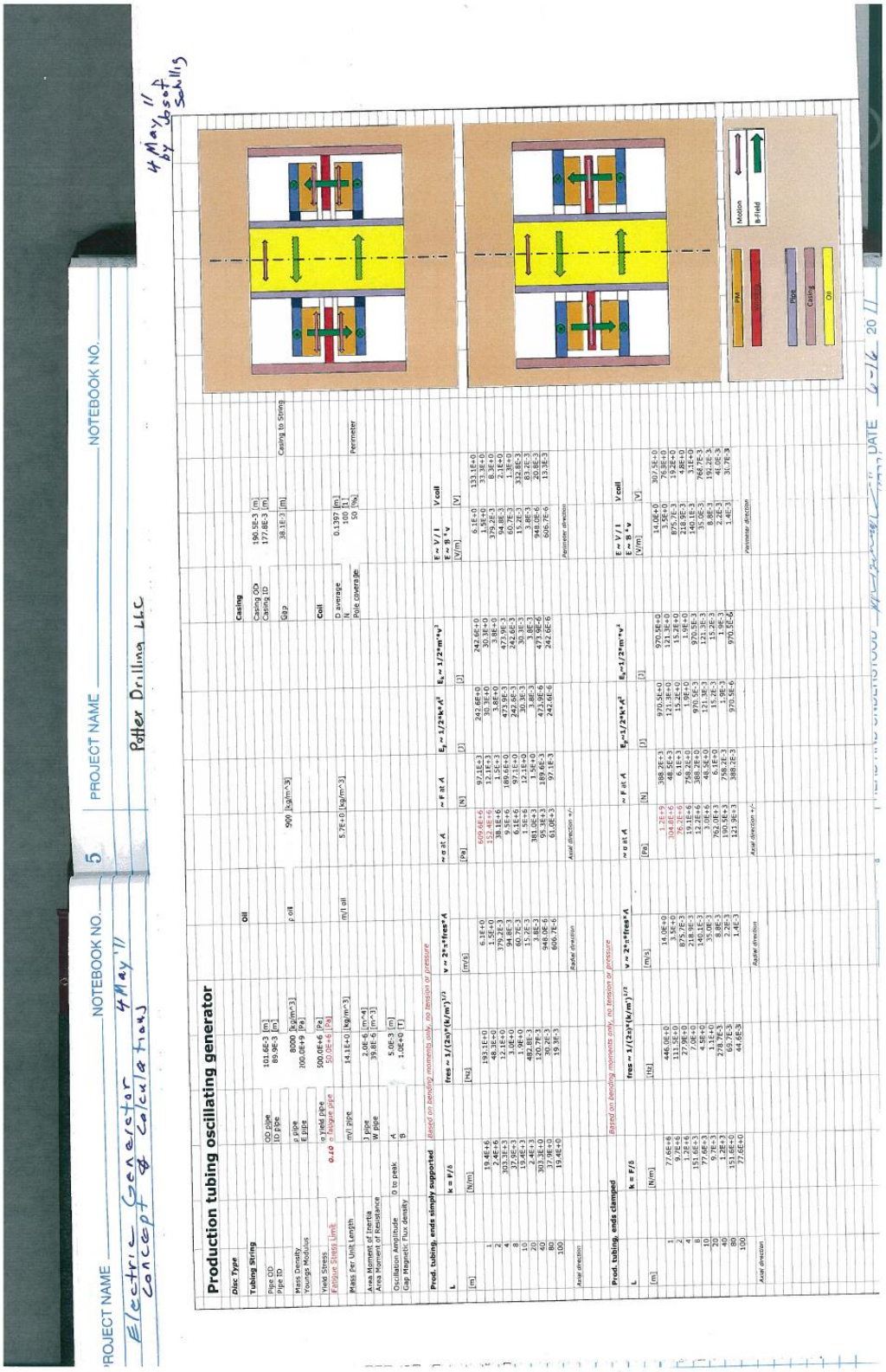

Figure A.1 – LANL Proof of Concept Calculations (Part 1 of 2)

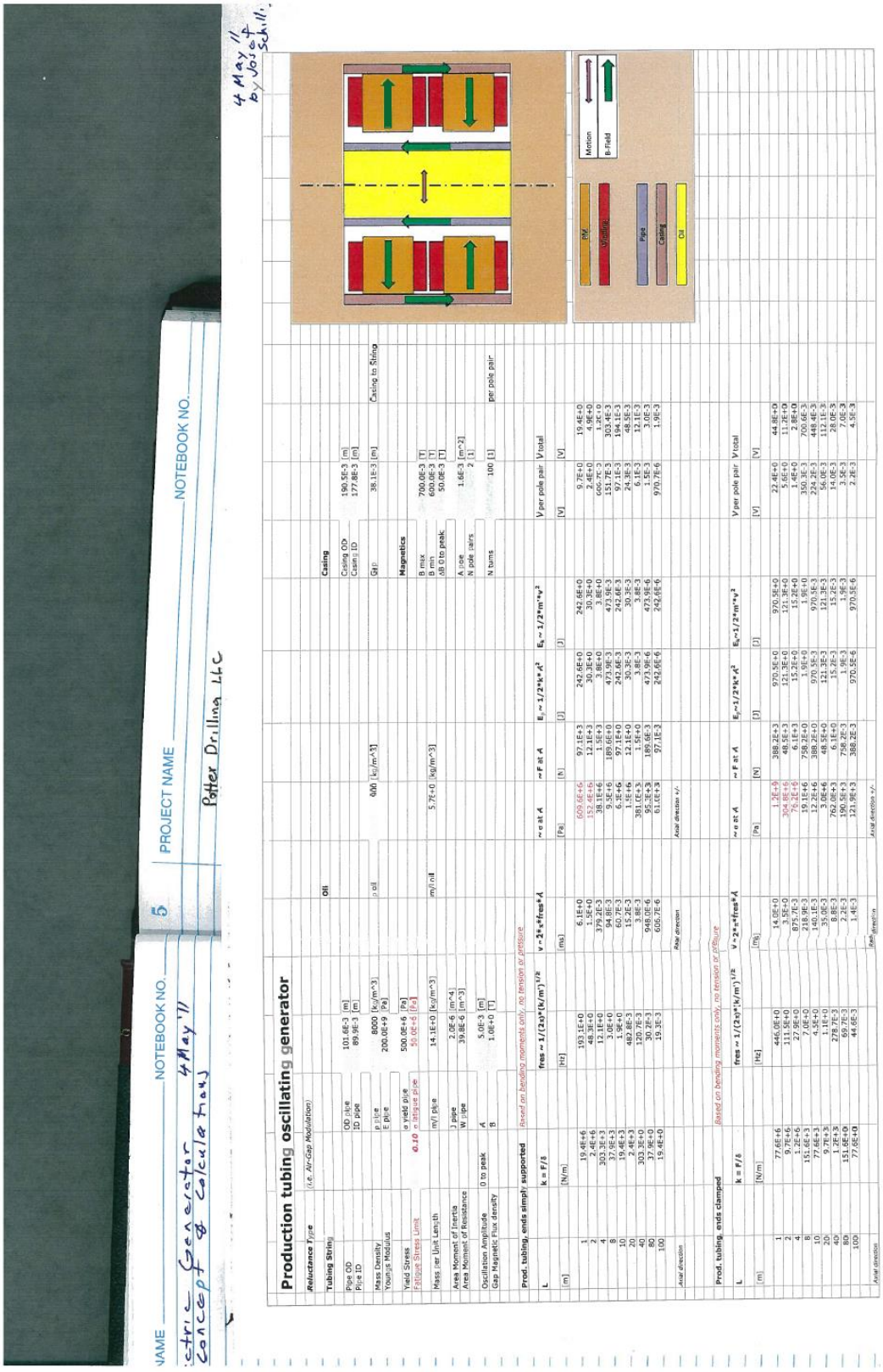

Figure A.2 – LANL Proof of Concept Calculations (Part 2 of 2)

Appendix B – Mathematica Script Supporting Green's Function Analysis

CFD_Pt_Load

Problem Description

```
(*Using the equivalent point load generated from the CFD results, analyze possible systems*)
```

Miscellaneous *Mathematica* Initialization

```
(*MISCELLANEOUS INITIALIZATION----------*)
LaunchKernels[];(*Launch Kernels for parallel processing*)
<<"FourierSeries`"(*load FourierSeries package*)
SetOptions[FourierTransform,FourierParameters→{1,-1}]; (*set options for FT*)
SetOptions[InverseFourierTransform,FourierParameters→{1,-1}]; (*set options for FT*)
SetOptions[Fourier,FourierParameters→{1,-1}]; (*set options for FT*)
SetOptions[InverseFourier,FourierParameters→{1,-1}]; (*set options for FT*)
```

Define Material and Geometric Terms

```
(*CLEAR VARIABLES----------*)
Clear[nu,rho,eta];(*Annulus Fluid Properties*)
Clear[YoungsModulus,PipeInnerRadius,PipeWallThickness,PipeOuterRadius,SteelDensity,PipeSteelAre
a,PipeFluidArea,c,d,ShellD,BeamLength,BeamArea,DensityBeam,BeamInertia,mew];(*Structural
Properties*)
Clear[i];(*Miscellaneous*)

(*ANNULUS FLUID PROPERTIES----------*)
nu=1*10^-6;(*Fluid kinematic viscosity, m^2/s*)
rho=875;(*Fluid Density, kg/m^3*)
eta=nu*rho;(*Fluid Dynamic Viscosity, N*s/m^2*)

(*STRUCTURAL PROPERTIES----------*)
YoungsModulus=2*10^11;(*N/m^2*)
PipeInnerRadius=0.05;(*m*)
PipeWallThickness=0.007;(*m*)
PipeOuterRadius=PipeInnerRadius+PipeWallThickness;(*m*)
SteelDensity=7800;(*kg/m^3*)
```

```
PipeSteelArea=Pi*(PipeOuterRadius^2-PipeInnerRadius^2);(*m^2*)
PipeFluidArea=Pi*PipeInnerRadius^2;(*m^2*)
c=0; (*Rayleigh Damping Coefficient*)
d=PipeOuterRadius;(*Beam Outer Radius, m*)
ShellD=0.108;(*Casing/Screen Inner Radius, m*)
BeamLength=23.96;(*m*)
BeamArea=Pi*PipeOuterRadius^2-Pi*PipeInnerRadius^2;(*m^2*)
DensityBeam=(PipeSteelArea*SteelDensity+PipeFluidArea*rho)/BeamArea;(*kg/m^3*)
BeamInertia=Pi*(PipeOuterRadius^4-PipeInnerRadius^4)/4;(*Based on pipe alone,m^4*)
mew=BeamArea*DensityBeam;(*Beam mass per unit length,kg/m*)

(*Miscellaneous----------*)
i=(-1)^0.5;(*imaginary unit*)
```

Define the Hydrodynamic Function and the B Term - Used To Determine System Natural Frequencies via Green's Function for Setting Forcing Definition

Calculations

```
(*CLEAR VARIABLES----------*)
Clear[ k,ω,alpha,beta,gamma,hfNum,hfDen,hf];(*Hydrdynamic Function*)
Clear[B];(*B Term*)

(*DEFINE THE HYDRODYNAMIC FUNCTION (WCJ EQUATION)----------*)
k=(i*ω/nu)^0.5;(*Define term for convenience*)
alpha=k*d;(*Define term for convenience*)
beta=k*ShellD;(*Define term for convenience*)
gamma=d/ShellD;(*Define term for convenience*)
hfNum=2*alpha^2*(BesselI[0,alpha]*BesselK[0,beta]-BesselI[0,beta]*BesselK[0,alpha])-
4*alpha*(BesselI[1,alpha]*BesselK[0,beta]+BesselI[0,beta]*BesselK[1,alpha])+4*alpha*gamma*(Bessel
I[0,alpha]*BesselK[1,beta]+BesselI[1,beta]*BesselK[0,alpha])-
8*gamma*(BesselI[1,alpha]*BesselK[1,beta]-BesselI[1,beta]*BesselK[1,alpha]);
hfDen=alpha^2*(1-gamma^2)*(BesselI[0,alpha]*BesselK[0,beta]-
BesselI[0,beta]*BesselK[0,alpha])+2*alpha*gamma*(BesselI[0,alpha]*BesselK[1,beta]-
BesselI[1,beta]*BesselK[0,beta]+BesselI[1,beta]*BesselK[0,alpha]-
BesselI[0,beta]*BesselK[1,beta])+2*alpha*gamma^2*(BesselI[0,beta]*BesselK[1,alpha]-
BesselI[0,alpha]*BesselK[1,alpha]+BesselI[1,alpha]*BesselK[0,beta]-
BesselI[1,alpha]*BesselK[0,alpha]);
hf=hfNum/hfDen-1;(*Hydrodynamic Function*)

(*DEFINE B TERM----------*)
B=((BeamLength^4/(YoungsModulus*BeamInertia))*(mew*ω^2-i*c*ω+rho*Pi*d^2*ω^2*hf))^0.25;
```

Plots

```
(*CLEAR VARIABLES----------*)
Clear[ωmax,h1,h2];(*Hydrdynamic Function*)

(*PLOT THE HYDRODYNAMIC FUNCTION----------*)
ωmax=800;(*absolute value of frequency range for plotting*)
h1=Plot[Re[hf],{ω,0,ωmax},PlotLabel→"Real part of Hydrodynamic Function",AxesLabel→{"ω
(rad/sec)","Re[hf]"}];
h2=Plot[Im[hf],{ω,0,ωmax},PlotLabel→"Imaginary part of Hydrodynamic Function",AxesLabel→{"ω
(rad/sec)","Im[hf]"}];
Table[{h1,h2}]
```

Define the Fixed-Fixed Green's Function - Used To Determine System Natural Frequencies for Forcing Definition

Calculations

```
(*CLEAR VARIABLES-----------------------------------------------------------------*)
Clear[C11,C12,C13,C14,s];(*coefficients*)
Clear[GXLessS,x,GXGreaterS,GreensFunction];(*green's function*)

(*DEFINE THE COEFFICIENTS---------------------------------------------------------*)
(*Note the equations solved for in the MATLAB file 'Greens_Function_Solver_Fixed_Fixed'*)
C11=(-((1+i)*(Exp[B*(-2*i+s+3*s*i)]-Exp[B*(-i+s+3*s*i+1)])+(i)*(Exp[2*B*s*(i+1)]-Exp[2*B*(-
i+s+s*i)])+(1-i)*(Exp[B*s*(i+1)]-Exp[B*(-i+s+s*i+1)])+(Exp[2*B*(s*i+1)]-2*Exp[B*(-
i+2*s*i+1)]+Exp[2*B*(-i+s*i+1)])))/(4*B^3*(Exp[B*(s+2*s*i+2)]+Exp[B*(-2*i+s+2*s*i)]-4*Exp[B*(-
i+s+2*s*i+1)]+Exp[B*(-2*i+s+2*s*i+2)]+Exp[B*s*(2*i+1)]));
C12=((1+i)*(Exp[B*(s+s*i+2)]-Exp[B*(-i+s+s*i+1)])+(i)*(Exp[2*B*(-i+s*i+1)]-Exp[2*B*(s*i+1)])+(1-
i)*(Exp[B*(-2*i+s+3*s*i+2)]-Exp[B*(-i+s+3*s*i+1)])+(Exp[2*B*(-i+s+s*i)]-2Exp[B*(-
i+2*s+2*s*i+1)]+Exp[2*B*s*(i+1)]))/(4*B^3*(Exp[B*(s+2*s*i+2)]+Exp[B*(-2*i+s+2*s*i)]-4*Exp[B*(-
i+s+2*s*i+1)]+Exp[B*(-2*i+s+2*s*i+2)]+Exp[B*s*(2*i+1)]));
C13=((1+i)*(Exp[B*(-i+s+3*s*i+1)]-Exp[B*(-2*i+s+3*s*i)])+(i)*(Exp[2*B*(-i+s+s*i)]-
Exp[2*B*s*(i+1)])+(1-i)*(Exp[B*(-i+s+s*i+1)]-Exp[B*s*(i+1)])+(Exp[2*B*i*(s-1)]-2*Exp[B*(-
i+2*s*i+1)]+Exp[2*B*s*i]))/(4*B^3*(Exp[B*(s+2*s*i+2)]+Exp[B*(-2*i+s+2*s*i)]-4*Exp[B*(-
i+s+2*s*i+1)]+Exp[B*(-2*i+s+2*s*i+2)]+Exp[B*s*(2*i+1)]));
C14=(-((1+i)*(Exp[B*(-i+s+s*i+1)]-Exp[B*(s+s*i+2)])+(i)*(Exp[2*B*(s*i+1)]-Exp[2*B*(-
i+s*i+1)])+(1-i)*(Exp[B*(-i+s+3*s*i+1)]-Exp[B*(-2*i+s+3*s*i+2)])+(Exp[2*B*(s+s*i+1)]-2*Exp[B*(-
i+2*s+2*s*i+1)]+Exp[2*B*(-i+s+s*i+1)])))/(4*B^3*(Exp[B*(s+2*s*i+2)]+Exp[B*(-2*i+s+2*s*i)]-
4*Exp[B*(-i+s+2*s*i+1)]+Exp[B*(-2*i+s+2*s*i+2)]+Exp[B*s*(2*i+1)]));

(*DEFINE THE GREEN'S FUNCTIONS----------------------------------------------------*)
GXLessS=C11*Exp[B*x]+C12*Exp[-B*x]-Exp[-B*x*i]*(C11*(1/2+i/2)+C12*(1/2-i/2))-
Exp[B*x*i]*(C11*(1/2-i/2)+C12*(1/2+i/2));
GXGreaterS=C13*Exp[B*x]+C14*Exp[-B*x]-Exp[B*(x*i-i-1)]*(C14*(1/2+i/2)+C13*Exp[2*B]*(1/2-
i/2))-Exp[-B*(x*i-i+1)]*(C14*(1/2-i/2)+C13*Exp[2*B]*(1/2+i/2));

(*DEFINE THE COMBINED GREEN'S FUNCTION--------------------------------------*)
GreensFunction=GXLessS*HeavisideTheta[s-x]+GXGreaterS*HeavisideTheta[x-s];
```

General Plots

```
(*CLEAR VARIABLES-----------------------------------------------------------------------*)
Clear[x,ωhigh,ωlow,recursionLimit,g1,g2];(*plotting*)

(*DEFINE PLOTTING PARAMETERS-----------------------------------------------------*)
x=0.01;(*select spatial point of interest*)
ωhigh=126;(*absolute value of frequency range for plotting*)
ωlow=122;(*absolute value of frequency range for plotting*)
recursionLimit=3;(*the maximum number of recursions*)

(*DEFINE GREEN'S FUNCTION PLOTS OF INTEREST-------------------------------*)
g1=Timing[ContourPlot[Re[GXLessS],{ω,ωlow,ωhigh},{s,0.02,1},PlotLegends→Automatic,MaxRecurs
ion→recursionLimit]];(*Real part of Green's Function*)
g2=Timing[ContourPlot[Im[GXLessS],{ω,ωlow,ωhigh},{s,0.02,1},PlotLegends→Automatic,MaxRecurs
ion→recursionLimit]];(*Imaginary part of Green's Function*)
Clear[x];(*clear  spatial point of interest*)
```

```
(*SHOW PLOTS OF INTEREST----------*)
Table[{g1[[2]],g2[[2]]}](*show plots*)
Table[{g1[[1]],g2[[1]]}](*show time it took to calculate plots*)
```

Localized Plots

```
(*CLEAR VARIABLES----------*)
Clear[x,gL1,gL2,gL3];(*plotting*)

(*DEFINE PLOTTING PARAMETERS----------*)
x=0.01;(*select spatial point of interest*)

(*DEFINE PLOTS OF INTEREST----------*)
gL1=Timing[Plot3D[Re[GXLessS],{ω,110,140},{s,0.02,1}]];(*Real Part*)
gL2=Timing[Plot3D[Im[GXLessS],{ω,110,140},{s,0.02,1}]];(*Im Part*)
gL3=Timing[Plot3D[Abs[GXLessS],{ω,110,140},{s,0.02,1}]];(*Im Part*)
Clear[x];(*clear  spatial point of interest*)

(*SHOW PLOTS OF INTEREST----------*)
Table[{gL1[[2]],gL2[[2]],gL3[[2]]}] (*show plots*)
Table[{gL1[[1]],gL2[[1]],gL3[[1]]}](*show time it took to calculate plots*)
```

Define Forcing Function

Calculations

```
(*CLEAR VARIABLES----------*)
Clear[mag,omd,duration,Slope,sStart,sEnd,fHarmonic,t,s,FHarmonic,ω,fHarmonicCheck];(*Forcing
Function*)
Clear[sHat];(*normalized function*)

(*DEFINE FORCING FUNCTION AND TRANSFORMS----------*)
mag=Rationalize[2.09];(*Maximum Magnitude of Distributed Load,N/m*)
omd=Rationalize[124.005];(*Radial Frequency of the Forcing Function,rad/s*)
duration=Rationalize[40.0];(*sec, time duration of continuous function*)
(*Slope=Rationalize[4/3];(*spatial slope of the forcing function*)*)
sStart=Rationalize[0.499];(*where the forcing begins*)
sEnd=Rationalize[0.501];(*where the forcing ends*)
(*Define the harmonic forcing function()
!!!!!!!!!define space as a function of s to match integral definition of WBar!!!!!!!*)
fHarmonic[t_,s_]=mag*Sin[omd*t]*UnitStep[t,duration-t]*UnitStep[s-sStart,sEnd-s];(*forcing
function*)
FHarmonic=Timing[FourierTransform[fHarmonic[t,s],t,ω]/.HeavisideTheta→UnitStep];(*Continuous FT
of the forcing function*)
fHarmonicCheck=Timing[N[InverseFourierTransform[FHarmonic[[2]],ω,t]]/.HeavisideTheta→UnitStep/
.Sign'→Sign];
(*IFT used for checking proper transforms*)

(*DEFINE THE TRANSFORMED AND NORMALIZED FORCING FUNCTION---*)
sHat=(BeamLength^4/(YoungsModulus*BeamInertia))*FHarmonic[[2]];(*Normalize the Continuous FT*)

(*OUTPUTS OF INTEREST----------*)
sHat(*scaled forcing function in fourier domain*)
Table[{FHarmonic[[1]],fHarmonicCheck[[1]]}](*time to calculate transforms*)
```

Plots

```
(*CLEAR VARIABLES-----------------------------------------------------------------------*)
Clear[s,trange,ωrange];(*plotting parameters*)
Clear[diracDelta,x,f1,f2,f3,f4,f5,f6];(*plots*)

(*DEFINE PLOTTING PARAMETERS-----------------------------------------------------------*)
s=0.5;(*select spatial point of interest*)
trange=1;(*absolute value of EXCESS time range for plotting*)
ωrange=250;(*absolute value of frequency range for plotting*)

(*DEFINE CONTINUOUS PLOTS OF INTEREST---------------------------------------*)
diracDelta[x_]=PDF[NormalDistribution[0,1/100],x];(*Define a delta function for plotting purposes*)
f1=Timing[Plot[fHarmonic[t,s],{t,-trange,trange+duration},PlotLabel→"fHarmonic",AxesLabel→{"t
(sec)","Amplitude"}]];(*input function*)
f2=Timing[Plot[Re[fHarmonicCheck[[2]]],{t,-
trange,trange+duration},PlotLabel→"Re[fHarmonicCheck]",AxesLabel→{"t
(sec)","Amplitude"}]];(*transformed input function*)
f3=Timing[Plot[Im[fHarmonicCheck[[2]]],{t,-
trange,trange+duration},PlotLabel→"Im[fHarmonicCheck]",AxesLabel→{"t
(sec)","Amplitude"}]];(*transformed input function*)
f4=Timing[Plot[Re[sHat]/.DiracDelta→diracDelta,{ω,-ωrange,ωrange},PlotStyle→
{Thick,Red},PlotLabel→"Real part of sHat",AxesLabel→{"ω (rad/sec)","Re[sHat]"}]];(*Real part of
sHat*)
f5=Timing[Plot[Im[sHat]/.DiracDelta→diracDelta,{ω,-ωrange,ωrange},PlotStyle→
{Thick,Red},PlotLabel→"Imaginary part of sHat",AxesLabel→{"ω (rad/sec)","Im[sHat]"}]];(*Im part of
sHat*)
f6=Timing[Plot[Abs[sHat]/.DiracDelta→diracDelta,{ω,-ωrange,ωrange},PlotStyle→
{Thick,Red},PlotLabel→"|sHat|",AxesLabel→{"ω (rad/sec)","Abs[sHat]"}]];(*Abs[sHat]*)
Clear[s];(*clear spatial point of interest*)

(*SHOW CONTINUOUS PLOTS OF INTEREST-----------------------------------------*)
Table[{f1[[2]],f2[[2]],f3[[2]]}] (*show plots*)
Table[{f1[[1]],f2[[1]],f3[[1]]}](*show time it took to calculate plots*)
Table[{f4[[2]],f5[[2]],f6[[2]]}](*show plots*)
Table[{f4[[1]],f5[[1]],f6[[1]]}](*show time it took to calculate plots*)
```

Localized Plots - Set ωs Based on Side Lob Widths of sHat

```
(*CLEAR VARIABLES-----------------------------------------------------------------------*)
Clear[s,fL1];


(*DEFINE PLOTTING PARAMETERS-----------------------------------------------------------*)
s=0.5;(*select spatial point of interest*)

(*DEFINE PLOTS OF INTEREST-------------------------------------------------------------*)
fL1=Timing[Plot[Abs[sHat]/.DiracDelta→diracDelta,{ω,120,130},PlotStyle→
{Thick,Red},PlotLabel→"|sHat|",AxesLabel→{"ω
(rad/sec)","Abs[sHat]"},PlotRange→{{123,125},{0,5}}]];(*Abs[sHat]*)
Clear[s];(*clear  spatial point of interest*)

(*SHOW PLOTS OF INTEREST---------------------------------------------------------------*)
```

```
Table[{fL1[[2]]}] (*show plots*)
Table[{fL1[[1]]}](*show time it took to calculate plots*)
```

Clear B and Re-Define Green's Function Symbolically in B to Reduce Calculation Time for the Continuous Fourier Response

Clear the B Term

```
(*CLEAR VARIABLES-----------------------------------------------------------------------*)
Clear[B];
```

Redefine Green's Function as Symbolic in B

```
(*CLEAR VARIABLES-----------------------------------------------------------------------*)
Clear[C11,C12,C13,C14,s];(*coefficients*)
Clear[GXLessS,x,GXGreaterS,GreensFunction];(*green's function*)

(*DEFINE THE COEFFICIENTS---------------------------------------------------------------*)
C11=(-((1+i)*(Exp[B*(-2*i+s+3*s*i)]-Exp[B*(-i+s+3*s*i+1)])+(i)*(Exp[2*B*s*(i+1)]-Exp[2*B*(-
i+s+s*i)])+(1-i)*(Exp[B*s*(i+1)]-Exp[B*(-i+s+s*i+1)])+(Exp[2*B*(s*i+1)]-2*Exp[B*(-
i+2*s*i+1)]+Exp[2*B*(-i+s*i+1)])))/(4*B^3*(Exp[B*(s+2*s*i+2)]+Exp[B*(-2*i+s+2*s*i)]-4*Exp[B*(-
i+s+2*s*i+1)]+Exp[B*(-2*i+s+2*s*i+2)]+Exp[B*s*(2*i+1)]));
C12=((1+i)*(Exp[B*(s+s*i+2)]-Exp[B*(-i+s+s*i+1)])+(i)*(Exp[2*B*(-i+s*i+1)]-Exp[2*B*(s*i+1)])+(1-
i)*(Exp[B*(-2*i+s+3*s*i+2)]-Exp[B*(-i+s+3*s*i+1)])+(Exp[2*B*(-i+s+s*i)]-2Exp[B*(-
i+2*s+2*s*i+1)]+Exp[2*B*s*(i+1)]))/(4*B^3*(Exp[B*(s+2*s*i+2)]+Exp[B*(-2*i+s+2*s*i)]-4*Exp[B*(-
i+s+2*s*i+1)]+Exp[B*(-2*i+s+2*s*i+2)]+Exp[B*s*(2*i+1)]));
C13=((1+i)*(Exp[B*(-i+s+3*s*i+1)]-Exp[B*(-2*i+s+3*s*i)])+(i)*(Exp[2*B*(-i+s+s*i)]-
Exp[2*B*s*(i+1)])+(1-i)*(Exp[B*(-i+s+s*i+1)]-Exp[B*s*(i+1)])+(Exp[2*B*i*(s-1)]-2*Exp[B*(-
i+2*s*i+1)]+Exp[2*B*s*i]))/(4*B^3*(Exp[B*(s+2*s*i+2)]+Exp[B*(-2*i+s+2*s*i)]-4*Exp[B*(-
i+s+2*s*i+1)]+Exp[B*(-2*i+s+2*s*i+2)]+Exp[B*s*(2*i+1)]));
C14=(-((1+i)*(Exp[B*(-i+s+s*i+1)]-Exp[B*(s+s*i+2)])+(i)*(Exp[2*B*(s*i+1)]-Exp[2*B*(-
i+s*i+1)])+(1-i)*(Exp[B*(-i+s+3*s*i+1)]-Exp[B*(-2*i+s+3*s*i+2)])+(Exp[2*B*(s+s*i+1)]-2*Exp[B*(-
i+2*s+2*s*i+1)]+Exp[2*B*(-i+s+s*i+1)])))/(4*B^3*(Exp[B*(s+2*s*i+2)]+Exp[B*(-2*i+s+2*s*i)]-
4*Exp[B*(-i+s+2*s*i+1)]+Exp[B*(-2*i+s+2*s*i+2)]+Exp[B*s*(2*i+1)]));

(*DEFINE THE GREEN'S FUNCTIONS----------------------------------------------------------*)
GXLessS=C11*Exp[B*x]+C12*Exp[-B*x]-Exp[-B*x*i]*(C11*(1/2+i/2)+C12*(1/2-i/2))-
Exp[B*x*i]*(C11*(1/2-i/2)+C12*(1/2+i/2));
GXGreaterS=C13*Exp[B*x]+C14*Exp[-B*x]-Exp[B*(x*i-i-1)]*(C14*(1/2+i/2)+C13*Exp[2*B]*(1/2-
i/2))-Exp[-B*(x*i-i+1)]*(C14*(1/2-i/2)+C13*Exp[2*B]*(1/2+i/2));

(*DEFINE THE COMBINED GREEN'S FUNCTION--------------------------------------*)
GreensFunction=GXLessS*HeavisideTheta[s-x]+GXGreaterS*HeavisideTheta[x-s];
```

Calculate the Continuous Fourier Response (symbolic in B)

```
(*CLEAR VARIABLES-----------------------------------------------------------------------*)
Clear[Argument,WBar,s];(*Fourier Response*)

(*DETERMINE FOURIER RESPONSE------------------------------------------------------------*)
Argument=GreensFunction*sHat;(*argument for the integration to follow*)
WBar[x_,ω_,B_]=Timing[Chop[N[Integrate[Argument,{s,0,1}]]]];(*Determine Fourier Response*)

(*Show Timing---------------------------------------------------------------------------*)
Table[{WBar[x,w,B][[1]] }](*show time it took to calculate*)
```

Re-Define the B Term (WBar=fn{B})

```
(*CLEAR VARIABLES-----------------------------------------------------------------------*)
Clear[B];

(*DEFINE B TERM-------------------------------------------------------------------------*)
B=((BeamLength^4/(YoungsModulus*BeamInertia))*(mew*ω^2-i*c*ω+rho*Pi*d^2*ω^2*hf))^0.25;
```

Plot/Investigate the Continuous Fourier Response

Plots

```
 (*CLEAR VARIABLES-----------------------------------------------------------------------*)
Clear[x,freqUpper,freqLower,W1,W2];(*plotting*)

(*DEFINE PLOTTING PARAMETERS-----------------------------------------------------------*)
x=0.5;(*select spatial point of interest*)
freqUpper=200;(*upper frequency for plotting purposes*)
freqLower=0;(*lower frequency for plotting purposes*)


(*DEFINE WBAR PLOTS OF INTEREST--------------------------------------------------------*)
W1=Timing[Plot[Abs[WBar[x,ω,B][[2]]],{ω,freqLower,freqUpper},PlotStyle→
{Thick,Red},PlotLabel→"|WBar|",AxesLabel→{"ω (rad/sec)","Abs[WBar]"}]];(*Abs[WBar]*)
W2=Timing[LogPlot[Abs[WBar[x,ω,B][[2]]],{ω,freqLower,freqUpper},PlotStyle→
{Thick,Red},PlotLabel→"LogPlot of |WBar|",AxesLabel→{"ω
(rad/sec)","Abs[WBar]"}]];(*Abs[WBar]*)
Clear[x];(*clear  spatial point of interest*)

(*SHOW PLOTS OF INTEREST---------------------------------------------------------------*)
Table[{W1[[2]],W2[[2]]}](*show plots*)
Table[{W1[[1]],W2[[1]]}](*show time it took to calculate plots*)
```

Localized Plots

```
(*CLEAR VARIABLES-----------------------------------------------------------------------*)
Clear[x,WL1];

(*DEFINE PLOTTING PARAMETERS-----------------------------------------------------------*)
x=0.5;(*select spatial point of interest*)

(*DEFINE PLOTS OF INTEREST-------------------------------------------------------------*)
WL1=Timing[Plot[Abs[WBar[x,ω,B][[2]]],{ω,120,130},PlotStyle→
{Thick,Red},PlotLabel→"|WBar|",AxesLabel→{"ω
(rad/sec)","Abs[WBar]"},PlotRange→{{120,130},{0,2*10^-5}}]];(*Abs[WBar]*)
Clear[x];

(*SHOW PLOTS OF INTEREST---------------------------------------------------------------*)
Table[{WL1[[2]]}](*show plots*)
Table[{WL1[[1]]}](*show time it took to calculate plots*)
```

Determine Local Maximum

```
(*CLEAR VARIABLES-----------------------------------------------------------------------*)
Clear[xPOI,ωPOI];

(*DEFINE POINTS OF INTEREST------------------------------------------------------------*)
xPOI=0.5;(*spatial point of interest*)
```

```
ωPOI=124;(*starting point for frequency point of interest*)

(*DETERMINE MAXIMUM----------*)
FindArgMax[Abs[WBar[xPOI,ω,B][[2]]],{ω,ωPOI}](*frequency*)
FindMaxValue[Abs[WBar[xPOI,ω,B][[2]]],{ω,ωPOI}](*value*)
Clear[xPOI,ωPOI];
```

Sample the Continuous Fourier Response at a Specific Spatial Location

Calculations

```
(*CLEAR VARIABLES----------*)
Clear[x,ωs,Os];(*user inputs*)
Clear[WBarSampled1,ω,WBarSampled2,WBarSampled3,WBarSampled];(*sampling*)

(*USER INPUTS----------*)
x=0.5;(*Determine the spatial location where the displacement time history will be determined*)
(*!!!!!!!!!!!!!!!!!!Set ωs Based on Side Lob Widths of WBar to avoid Aliasing!!!!!!!!!!!!!!!*)
(*!!!!!!!!!!!Make sure to not sample on the driving frequency to avoid a singularity!!!!!!!!*)
ωs=0.05;(*Define the frequency sampling rate*)
Os=2000;(*Determine the TOTAL range of frequencies to be included in sampling*)

(*SAMPLE THE CONTINUOUS SIGNAL AND REORDER SO AS TO PERFORM THE DISCRETE FT----------*)
WBarSampled1=Timing[Chop[Table[WBar[x,ω,B][[2]],{ω,-Os/2+ωs,-ωs,ωs}]]];(*Sampled WBar for ω<0*)
ω=ωs;(*Define offset point to avoid sampling singularity*)
WBarSampled2=Timing[Chop[WBar[x,ω,B][[2]]]];(*Sampled WBar at ω~0*)
Clear[ω];(*Clear offset point*)
WBarSampled3=Timing[Chop[Table[WBar[x,ω,B][[2]],{ω,ωs,Os/2,ωs}]]];(*Sampled WBar for ω>0*)
(*Combine the three lists in an order appropriate for discrete transforms*)
WBarSampled=Timing[Flatten[Join[{WBarSampled2[[2]]},{WBarSampled3[[2]]},{WBarSampled1[[2]]}]]];

(*SHOW TIME FOR SAMPLING----------*)
Table[{WBarSampled1[[1]],WBarSampled2[[1]],WBarSampled3[[1]],WBarSampled[[1]]}](*show timing*)
```

Plots

```
(*CLEAR VARIABLES----------*)
Clear[WS1,WS2,WS3];(*plotting*)

(*DEFINE PLOTS OF INTEREST----------*)
WS1=Timing[ListPlot[Re[WBarSampled[[2]]],Filling→Axis,Joined→True,PlotLabel→"Real part of WBarSampled",AxesLabel→{"Sample,k","Re[WBarSampled]"},PlotStyle→Red]];(*Real part of WBarSampled*)
WS2=Timing[ListPlot[Im[WBarSampled[[2]]],Filling→Axis,Joined→True,PlotLabel→"Imag. part of WBarSampled",AxesLabel→{"Sample,k","Im[WBarSampled]"},PlotStyle→Red]];(*Imaginary part of WBarSampled*)
WS3=Timing[ListPlot[Abs[WBarSampled[[2]]],Filling→Axis,Joined→True,PlotLabel→"|WBarSampled|",AxesLabel→{"Sample,k","Abs[WBarSampled]"},PlotStyle→Red]];(*Abs[WBarSampled]*)

(*SHOW PLOTS OF INTEREST----------*)
```

```
Table[{WS1[[2]],WS2[[2]],WS3[[2]]}](*show plots*)
Table[{WS1[[1]],WS2[[1]],WS3[[1]]}](*show time it took to calculate plots*)
```

Local Plots

```
(*CLEAR VARIABLES----------*)
Clear[WSL1];

(*DEFINE PLOTS OF INTEREST----------*)
(*!!!!!!!!!!!!!!!!Note that x was previously defined when we sampled WBar!!!!!!!!!!!!!!!!!!*)
WSL1=Timing[ListPlot[Abs[WBarSampled[[2]]],Filling→Axis,Joined→True,PlotLabel→"|WBarSampl
ed|",AxesLabel→{"Sample,k","Abs[WBarSampled]"},PlotRange→{{0,40000},{0,0.00005}},PlotStyle
→Red]];(*Abs[WBar]*)

(*SHOW PLOTS OF INTEREST----------*)
Table[{WSL1[[2]]}](*show plots*)
Table[{WSL1[[1]]}](*show time it took to calculate plots*)
```

Superimposed Plots

```
(*CLEAR VARIABLES----------*)
Clear[ωL,ωH,AmpMax,WLCont,WLDisc];

(*DEFINE PLOTTING PARAMETERS----------*)
ωL=120;(*plotting low frequency*)
ωH=130;(*plotting high frequency*)
AmpMax=0.0004;(*plotting amplitude*)

(*DEFINE PLOTS OF INTEREST----------*)
WLCont=Timing[Plot[Abs[WBar[x,ω,B][[2]]],{ω,ωL,ωH},PlotStyle→
{Thick,Red},PlotLabel→"|WBar|",AxesLabel→{"ω
(rad/sec)","Abs[WBar]"},PlotRange→{{ωL,ωH},{0,AmpMax}}]];(*Abs[WBar]*)
WLDisc=Timing[ListPlot[Abs[WBarSampled[[2]]],Filling→Axis,Joined→False,PlotLabel→"|WBarSam
pled|",AxesLabel→{"ω
(rad/sec)","Abs[WBarSampled]"},PlotRange→{{ωL,ωH},{0,AmpMax}},PlotStyle→Blue,DataRange→
{0,Os-ωs}]];(*the data is scaled from k→ω for plotting purposes*)

(*SHOW PLOTS OF INTEREST----------*)
Show[{WLCont[[2]],WLDisc[[2]]},AxesLabel→{"ω (rad/sec)","Magnitude"},PlotLabel→"|WBar| &
|WBarSampled|"](*superimpose the two plots*)
Table[{WLCont[[1]],WLDisc[[1]]}](*show time it took to calculate plots*)
```

Calculate the Displacement Response

Calculations

```
(*CLEAR VARIABLES----------*)
Clear[wSampled];

(*TAKE THE IFT OF WBAR TO DETERMINE THE DISPLACEMENT RESPONSE IN DISCRETE
FORM----------*)
wSampled=Timing[(Os/(2*Pi))*Chop[N[InverseFourier[WBarSampled[[2]]]]]];

(*SHOW TIME FOR CALCULATION----------*)
Table[{wSampled[[1]]}](*show time it took to calculate*)
```

Plot/Investigate the Displacement Response

Plots

```
(*CLEAR VARIABLES-----------------------------------------------------------------------*)
Clear[dispMag,w1,w2,w3];

(*DEFINE PLOTTING PARAMETERS-------------------------------------------------------*)
dispMag=10^-5;(*Maximum expected displacement magnitude*)

(*DEFINE DISPLACEMENT PLOTS OF INTEREST-------------------------------------*)
w1=Timing[ListPlot[Re[wSampled[[2]]],PlotRange→{{-trange,trange+duration},{-
dispMag,dispMag}},Filling→Axis,PlotLabel→"Real part of
wSampled",AxesLabel→{"time,sec","Re[wSampled]"},Joined→True,DataRange→{0,2*Pi/ωs}]];(*Real
part*)
w2=Timing[ListPlot[Im[wSampled[[2]]],PlotRange→{{-trange,trange+duration},{-
dispMag,dispMag}},Filling→Axis,PlotLabel→"Imag. part of
wSampled",AxesLabel→{"time,sec","Im[wSampled]"},Joined→True,DataRange→{0,2*Pi/ωs}]];(*Real
part*)
w3=Timing[ListPlot[Abs[wSampled[[2]]],PlotRange→{{-trange,trange+duration},{-
dispMag,dispMag}},Filling→Axis,PlotLabel→"Abs part of
wSampled",AxesLabel→{"time,sec","Abs[wSampled]"},Joined→True,DataRange→{0,2*Pi/ωs}]];(*Re
al part*)

(*SHOW PLOTS OF INTEREST-----------------------------------------------------------*)
Table[{w1[[2]],w2[[2]],w3[[2]]}](*show plots*)
Table[{w1[[1]],w2[[1]],w3[[1]]}](*show time it took to calculate plots*)
```

Local Plots

```
(*CLEAR VARIABLES-----------------------------------------------------------------------*)
Clear[wL1];

(*DEFINE PLOTS OF INTEREST---------------------------------------------------------*)
wL1=Timing[ListPlot[Re[wSampled],PlotRange→{{0,15},{-10^-8,3*10^-
6}},Filling→Axis,PlotLabel→"Real part of
wSampled",AxesLabel→{"time,sec","Re[wSampled]"},Joined→True,DataRange→{0,2*Pi/ωs}]];(*Real
part*)(*Abs[WBar]*)

(*SHOW PLOTS OF INTEREST-----------------------------------------------------------*)
Table[{wL1[[2]]}](*show plots*)
Table[{wL1[[1]]}](*show time it took to calculate plots*)
```

Appendix C – Mathematica Script Supporting Spectral Element Analysis

Determine the Response of a System on the Extended EOM Using SEM

Problem Description
Use the Spectral Element Method to solve the extended equation of motion of a fixed-fixed beam under harmonic forcing.

Miscellaneous *Mathematica* Initialization

MISCELLANEOUS INITIALIZATION;

```
LaunchKernels[];(*Launch Kernels for parallel processing*)
<<"FourierSeries`"(*load FourierSeries package*)
SetOptions[FourierTransform,FourierParameters→{1,-1}]; (*set options for FT*)
SetOptions[InverseFourierTransform,FourierParameters→{1,-1}]; (*set options
for FT*)
SetOptions[Fourier,FourierParameters→{1,-1}]; (*set options for FT*)
SetOptions[InverseFourier,FourierParameters→{1,-1}]; (*set options for FT*)
```

Define Material and Geometric Terms

CLEAR VARIABLES;

```
Clear[Young,do,wt,di,Inertia1,Inertia2,Inertia3,Ap,Ai,rhop,m,nup,cote,L,ShellD
];(*Structural Properties*)
Clear[nue,rhoe,eta];(*Annulus Fluid Properties*)
Clear[rhoi,Mi,U];(*Conveyed Fluid Properties*)
Clear[elL1,elL2,elL3];(*SEM Properties*)
Clear[kd1,kd2,kd3];(*SEM Properties*)
Clear[T,p,ΔT,g,i];(*Miscellaneous Terms*)
```

STRUCTURAL PROPERTIES;

```
Young=Rationalize[3*10^11];(*N/m^2, Young's Modulus*)
do=Rationalize[0.08];(*m, Radius to Outer Edge of Pipe*)
wt=Rationalize[0.08];(*m, Pipe Wall Thickness*)
di=do-wt;(*m,Radius to Inner Edge of Pipe*)
Inertia1=Pi*(do^4-di^4)/4;(*m^4, Moment of Inertia*)
Inertia2=1*Inertia1;
Inertia3=1*Inertia1;
```

```
Inertia=Inertia1; (*for rayleigh damping estimate*)
Ap=Pi*(do^2-di^2);(*m2, Pipe Cross Sectional Area*)
Ai=Pi*(di^2);(*m2, Flow Area*)
rhop=Rationalize[6000];(*kg/m3, Pipe Density*)
m=Rationalize[Ap*rhop];(*kg/m, Mass per Unit Length of Pipe*)
nup=Rationalize[0.33];(*Poisson Ratio of Pipe*)
cote=Rationalize[11*10^-6];(*1/K, Coefficient of Thermal Expansion*)
ShellD=Rationalize[100];(*m, Casing/Screen Inner Radius*)
```

ANNULUS FLUID PROPERTIES;

```
nue=Rationalize[1.0*10^-8];(*m2/s, Annulus Fluid Kinematic Viscosity*)
rhoe=Rationalize[0.001];(*kg/m3, Density of Annulus Fluid*)
eta=Rationalize[nue*rhoe];(*Ns/m2, Annulus Fluid Dynamic Viscosity*)
```

CONVEYED FLUID PROPERTIES;

```
rhoi=Rationalize[000];(*kg/m3, Density of Conveyed Fluid*)
Mi=Rationalize[Ai*rhoi];(*kg/m, Mass per Unit Length of Conveyed Fluid*)
U=Rationalize[0];(*m/s, Mean Axial Flow Velocity*)
```

SEM TERMS;

```
elL1=6;(*L/2;(*m, Element Length*)*)
elL2=6;
L=elL1+elL2;(*m, Beam Length*)
```

DISTRIBUTED SPRINGS;

```
kd1=0; (*N/m2*)
kd2=0;(*N/m2*)
```

MISCELLANEOUS TERMS;

```
T=Rationalize[0];(*N, Externally Applied Tension, (+)=T, (-)=C*)
p=Rationalize[0];(*N/m2, Mean Pressure Differential, (+)=interior p>exterior
p*)
ΔT=Rationalize[0];(*Kelvin, Temperature Differential*)
g=Rationalize[9.81];(*m/s2, Gravitational Constant*)
i=Sqrt[-1];(*Imaginary Unit*)
```

Define Rayleigh Damping Coefficient Based Solely on Beam (Fixed-Fixed/First Mode)

CLEAR VARIABLES;

```
Clear[xi1,ω1,c];(*Damping Properties*)
```

DESIRED DAMPING RATIO FOR FIRST TWO MODES;

```
xi1=Rationalize[0.15];(*Desired damping ratio for first mode*)
```

APPROXIMATE FIRST UNDAMPED NATURAL FREQUENCy OF BEAM IN VACUUM;

```
ω1=(4.7300)^2*(Young*Inertia/((m+Mi)*L^4))^0.5;(*first nat freq*)
```

VISCOUS DAMPING COEFFICIENT;

```
c=2*m*ω1*xi1
```

Solve EOM for Wavenumbers 1

CLEAR VARIABLES;

```
Clear[G1,ω,k,hf,k11,k12,k13,k14];
```

SOLVE FOR WAVENUMBERS AS A FUNCTION OF ω AND HYDRODYNAMIC FORCE;

```
G1=Timing[Solve[(Young*Inertia1)*k^4-(Mi*U^2-T+p*Ai*(1-
2*nup)+Young*Ap*cote*ΔT)*k^2+(2*i*ω*Mi*U+(Mi+m)*g)*i*k+(i*ω*c-(Mi+m)*ω^2-
rhoe*Pi*do^2*ω^2*hf+kd1)□0,k]];

(*REASSIGN THE CALCUALTED K'S INTO FOUR VARIABLES-------------------*)
k11=Part[Part[Part[G1[[2]],1],1],2];
k12=Part[Part[Part[G1[[2]],2],1],2];
k13=Part[Part[Part[G1[[2]],3],1],2];
k14=Part[Part[Part[G1[[2]],4],1],2];
```

SHOW TIMING;

```
G1[[1]]
```

Create Exponential Vectors 1

CLEAR VARIABLES;

```
Clear[x,evector1,devector1,ddevector1,dddevector1]
```

CREATE VECTORS;

```
evector1[x_]={Exp[i*k11*x],Exp[i*k12*x],Exp[i*k13*x],Exp[i*k14*x]};
devector1[x_]={i*k11*Exp[i*k11*x],i*k12*Exp[i*k12*x],i*k13*Exp[i*k13*x],i*k14*
Exp[i*k14*x]};(*spatial derivative of evector*)
ddevector1[x_]={-k11^2*Exp[i*k11*x],-k12^2*Exp[i*k12*x],-k13^2*Exp[i*k13*x],-
k14^2*Exp[i*k14*x]};(*second spatial derivative of evector*)
dddevector1[x_]={-i*k11^3*Exp[i*k11*x],-i*k12^3*Exp[i*k12*x],-
i*k13^3*Exp[i*k13*x],-i*k14^3*Exp[i*k14*x]};(*third spatial derivative of
evector*)
```

Assemble Hinverse Matrix (from Displacements) 1

CLEAR VARIABLES;

```
Clear[H1,Hinv1];
```

ASSEMBLE Hinv MATRIX;

```
H1={evector1[0],devector1[0],evector1[elL1],devector1[elL1]};
Hinv1=Timing[Inverse[H1]];(*Take the matrix inverse*)
```

SHOW TIMING;

```
Hinv1[[1]](*Show time required to calculate Hinv*)
```

Assemble X Matrix (from Forces) 1

CLEAR VARIABLES;

```
Clear[Q1,x,M1,X1];
```

DEFINE FORCE RELATIONS;

```
Q1[x_]=Young*Inertia1*dddevector1[x]-T*devector1[x];(*Shear*)
M1[x_]=Young*Inertia1*ddevector1[x];(*Moment*)
```

ASSEMBLE X MATRIX;

```
X1=Timing[{Q1[0],-M1[0],-Q1[elL1],M1[elL1]}];
```

SHOW TIMING;

```
X1[[1]](*Show time required to calculate X*)
```

Calcualte Spectral Element Matrix 1

CLEAR VARIABLES;

```
Clear[Sb1];
```

CALCULATE SPECTRAL ELEMENT MATRIX;

```
Sb1=Timing[X1[[2]].Hinv1[[2]]];
```

SHOW TIMING;

```
Sb1[[1]](*Show time required to calculate Sb*)
```

Solve EOM for Wavenumbers 2

CLEAR VARIABLES;

```
Clear[G2,ω,k,hf,k21,k22,k23,k24];
```

SOLVE FOR WAVENUMBERS AS A FUNCTION OF ω AND HYDRODYNAMIC FORCE;

```
G2=Timing[Solve[(Young*Inertia2)*k^4-(Mi*U^2-T+p*Ai*(1-
2*nup)+Young*Ap*cote*ΔT)*k^2+(2*i*ω*Mi*U+(Mi+m)*g)*i*k+(i*ω*c-(Mi+m)*ω^2-
rhoe*Pi*do^2*ω^2*hf+kd2)□0,k]];
```

(*REASSIGN THE CALCUALTED K'S INTO FOUR VARIABLES----------*)

```
k21=Part[Part[Part[G2[[2]],1],1],2];
k22=Part[Part[Part[G2[[2]],2],1],2];
k23=Part[Part[Part[G2[[2]],3],1],2];
k24=Part[Part[Part[G2[[2]],4],1],2];
```

SHOW TIMING;

```
G2[[1]]
```

Create Exponential Vectors 2

CLEAR VARIABLES;

```
Clear[x,evector2,devector2,ddevector2,dddevector2]
```

CREATE VECTORS;

```
evector2[x_]={Exp[i*k21*x],Exp[i*k22*x],Exp[i*k23*x],Exp[i*k24*x]};
devector2[x_]={i*k21*Exp[i*k21*x],i*k22*Exp[i*k22*x],i*k23*Exp[i*k23*x],i*k24*
Exp[i*k24*x]};(*spatial derivative of evector*)
ddevector2[x_]={-k21^2*Exp[i*k21*x],-k22^2*Exp[i*k22*x],-k23^2*Exp[i*k23*x],-
k24^2*Exp[i*k24*x]};(*second spatial derivative of evector*)
dddevector2[x_]={-i*k21^3*Exp[i*k21*x],-i*k22^3*Exp[i*k22*x],-
i*k23^3*Exp[i*k23*x],-i*k24^3*Exp[i*k24*x]};(*third spatial derivative of
evector*)
```

Assemble Hinverse Matrix (from Displacements) 2

CLEAR VARIABLES;

```
Clear[H2,Hinv2];
```

ASSEMBLE Hinv MATRIX;

```
H2={evector2[0],devector2[0],evector2[elL2],devector2[elL2]};
Hinv2=Timing[Inverse[H2]];(*Take the matrix inverse*)
```

SHOW TIMING;

```
Hinv2[[1]](*Show time required to calculate Hinv*)
```

Assemble X Matrix (from Forces) 2

CLEAR VARIABLES;

```
Clear[Q2,x,M2,X2];
```

DEFINE FORCE RELATIONS;

```
Q2[x_]=Young*Inertia2*dddevector2[x]-T*devector2[x];(*Shear*)
```

```
M2[x_]=Young*Inertia2*ddevector2[x];(*Moment*)
```

ASSEMBLE X MATRIX;

```
X2=Timing[{Q2[0],-M2[0],-Q2[elL2],M2[elL2]}];
```

SHOW TIMING;

```
X2[[1]](*Show time required to calculate X*)
```

Calcualte Spectral Element Matrix 2

CLEAR VARIABLES;

```
Clear[Sb2];
```

CALCULATE SPECTRAL ELEMENT MATRIX;

```
Sb2=Timing[X2[[2]].Hinv2[[2]]];
```

SHOW TIMING;

```
Sb2[[1]](*Show time required to calculate Sb*)
```

Assemble 2-Element Global Matrix

CLEAR VARIABLES;

```
Clear[A1,A2,K1,K2,Sg];
```

DEFINE ASSEMBLY MATRICIES;

```
A1={{0,0},{0,0},{1,0},{0,1}};
A2={{1,0},{0,1},{0,0},{0,0}};
```

ELEMENT CONTRIBUTION TO GLOBAL MATRIX;

```
K1=Timing[Transpose[A1].Sb1[[2]].A1];
K2=Timing[Transpose[A2].Sb2[[2]].A2];
```

DEFINE GLOBAL MATRIX;

```
Sg[ω_,hf_]=K1[[2]]+K2[[2]];
```

SHOW TIMING;

```
Table[{K1[[1]],K2[[1]]}](*Show time required to calculate terms*)
```

Determine Natural Frequencies

Define the General Hydrodynamic Function

CLEAR VARIABLES;

```
Clear[ kb,ω,alpha,beta,gamma,hfNum,hfDen,hf];
```

DEFINE THE HYDRODYNAMIC FUNCTION;

```
kb=(i*ω/nue)^0.5;(*Define term for convenience*)
alpha=kb*do;(*Define term for convenience*)
beta=kb*ShellD;(*Define term for convenience*)
gamma=do/ShellD;(*Define term for convenience*)
hfNum=2*alpha^2*(BesselI[0,alpha]*BesselK[0,beta]-
BesselI[0,beta]*BesselK[0,alpha])-
4*alpha*(BesselI[1,alpha]*BesselK[0,beta]+BesselI[0,beta]*BesselK[1,alpha])+4*
alpha*gamma*(BesselI[0,alpha]*BesselK[1,beta]+BesselI[1,beta]*BesselK[0,alpha]
)-8*gamma*(BesselI[1,alpha]*BesselK[1,beta]-BesselI[1,beta]*BesselK[1,alpha]);
hfDen=alpha^2*(1-gamma^2)*(BesselI[0,alpha]*BesselK[0,beta]-
BesselI[0,beta]*BesselK[0,alpha])+2*alpha*gamma*(BesselI[0,alpha]*BesselK[1,be
ta]-BesselI[1,beta]*BesselK[0,beta]+BesselI[1,beta]*BesselK[0,alpha]-
BesselI[0,beta]*BesselK[1,beta])+2*alpha*gamma^2*(BesselI[0,beta]*BesselK[1,alp
```

```
ha]-BesselI[0,alpha]*BesselK[1,alpha]+BesselI[1,alpha]*BesselK[0,beta]-
BesselI[1,alpha]*BesselK[0,alpha]);
hf[ω_]=hfNum/hfDen-1;(*Hydrodynamic Function*)
```

Plot the General Hydrodynamic Function

CLEAR VARIABLES;

```
Clear[ωmax,h1,h2];
```

PLOT THE HYDRODYNAMIC FUNCTION;

```
ωmax=34;(*Maximum frequency for plotting*)
h1=Plot[Re[hf[ω]],{ω,0,ωmax},PlotLabel→"Real part of Hydrodynamic
Function",AxesLabel→{"ω (rad/sec)","Re[hf]"}];
h2=Plot[Im[hf[ω]],{ω,0,ωmax},PlotLabel→"Imaginary part of Hydrodynamic
Function",AxesLabel→{"ω (rad/sec)","Im[hf]"}];
Table[{h1,h2}]
```

Calculations - Plot to Refine Range of REAL Frequency

CLEAR VARIABLES;

```
Clear[ωL,ωH,ωdesc,detSg1,s1,s2,s3];
```

DEFINE PARAMETERS FOR PLOTTING INVESTIGATION;

```
ωL=5;(*First frequency where Det[Sg] is investigated*)
ωH=55;(*Last frequency where Det[Sg] is investigated*)
ωdesc=5;(*Descretization size*)
magExpected=1*10^50;(*Y-axis magnitude of plot*)
```

CREATE A LIST OF DET[SG];

```
detSg1=Timing[Table[Det[Sg[ω,hf[ω]]],{ω,ωL,ωH,ωdesc}]];
```

PLOT THE ABSOLUTE VALUE OF DET[SG];

```
s1=ListPlot[Re[detSg1[[2]]],Filling→Axis,Joined→True,PlotRange→{{ωL,ωH},{-
magExpected,magExpected}},DataRange→{ωL,ωH},PlotLabel→"Re[Det[Sg]]",AxesLabel
→{"ω (rad/sec)","Re[Det[Sg]]"}]
s2=ListPlot[Im[detSg1[[2]]],Filling→Axis,Joined→True,PlotRange→{{ωL,ωH},{-
magExpected,magExpected}},DataRange→{ωL,ωH},PlotLabel→"Im[Det[Sg]]",AxesLabel
→{"ω (rad/sec)","Im[Det[Sg]]"}];
s3=ListPlot[Abs[detSg1[[2]]],Filling→Axis,Joined→True,PlotRange→{{ωL,ωH},{0,
magExpected}},DataRange→{ωL,ωH},PlotLabel→"Abs[Det[Sg]]",AxesLabel→{"ω
(rad/sec)","Abs[Det[Sg]]"}]
Table[{s1,s2}](*show plots*)
```

SHOW TIMING;

```
detSg1[[1]]
```

Calculations - Plot to Refine Range of Imaginary Frequency

CLEAR VARIABLES;

```
Clear[ωLreal,ωHreal,ωdescreal,ωLimag,ωHimag,ωdescimag,detSg2,s1,s2,s3];
```

DEFINE PARAMETERS FOR PLOTTING INVESTIGATION;

```
ωLreal=16;(*First frequency where Det[Sg] is investigated*)
ωHreal=22;(*Last frequency where Det[Sg] is investigated*)
ωdescreal=1;(*Descretization size*)
ωLimag=0.5;(*First frequency where Det[Sg] is investigated*)
```

```
ωHimag=3.5;(*Last frequency where Det[Sg] is investigated*)
ωdescimag=1;(*Descretization size*)
```

CREATE A LIST OF DET[SG];

```
detSg2=Timing[Table[Det[Sg[ωr+i*ωi,hf[ωr+i*ωi]]],{ωi,ωLimag,ωHimag,ωdescimag}
,{ωr,ωLreal,ωHreal,ωdescreal}]];
```

PLOT THE ABSOLUTE VALUE OF DET[SG];

```
ListPlot3D[Abs[detSg2[[2]]]/magExpected,DataRange→{{ωLreal,ωHreal},{ωLimag,ωH
imag}},PlotLabel→"Abs[detSg2]",AxesLabel→{"Real","Imag"}]
```

SHOW TIMING;

```
detSg2[[1]]
```

Iterate Natural Frequency

CLEAR VARIABLES;

```
Clear[ω];
```

CALCULATE THE DETERMINATE OF SG AT SPECIFIED FREQUENCY - DRIVE IT TO ZERO;

```
ω=43.448+6.59168*i;(*Frequency of interest*)
-0.5*((rhoe*Pi*do^2)/(Re[hf[ω]]*rhoe*Pi*do^2+m+Mi))*Im[hf[ω]]
Det[Sg[ω,hf[ω]]](*Calcualte Det[Sg] at FOI*)
hf[ω]
hf[Sqrt[Re[ω]^2+Im[ω]^2]]
Clear[ω];(*Clear FOI*)
```

Root Solver to Find Natural Frequency

CLEAR VARIABLES;

```
Clear[R1];
```

FIND ROOT;

```
R1=Timing[Chop[SetPrecision[FindRoot[Det[Sg[ω,hf[ω]]],{ω,40}],10]]];
R1[[2]](*Find root*)
```

Define Nodal Forcing

CLEAR VARIABLES;

```
Clear[mag,ωd,duration,fHarmonic,t,FHarmonic,ω,range,f1,f2,f3,f4]
mag=Rationalize[2000];(*N, magnitude of load*)
ωd=Rationalize[1.015];(*rad/sec, frequency of forcing*)
duration=Rationalize[13.928];(*s, duration of load*)
fHarmonic[t_]=(mag*UnitStep[t,duration-t])*Sin[ωd*t];(*N*)
FHarmonic=Timing[FourierTransform[fHarmonic[t],t,ω]/.HeavisideTheta→UnitStep]
;(*Continuous FT of the forcing function*)
```

PLOT THE FORCING FUNCTION;

```
range=600;(*rad/sec, frequency range for plotting*)
f1=Timing[Plot[fHarmonic[t],{t,-
1,1+duration},PlotLabel→"fHarmonic",AxesLabel→{"t
(sec)","Amplitude"}]];(*input function*)
f2=Timing[Plot[Re[FHarmonic[[2]]]/.DiracDelta→diracDelta,{ω,-
range,range},PlotStyle→ {Thick,Red},PlotLabel→"Real part of
FHarmonic",AxesLabel→{"ω (rad/sec)","Re[FHarmonic]"}]];(*Real part of
FHarmonic*)
```

```
f3=Timing[Plot[Im[FHarmonic[[2]]]/.DiracDelta→diracDelta,{ω,-
range,range},PlotStyle→ {Thick,Red},PlotLabel→"Imaginary part of
FHarmonic",AxesLabel→{"ω (rad/sec)","Im[FHarmonic]"}]];(*Im part of
FHarmonic*)
f4=Timing[Plot[Abs[FHarmonic[[2]]]/.DiracDelta→diracDelta,{ω,-
range,range},PlotStyle→ {Thick,Red},PlotLabel→"|FHarmonic|",AxesLabel→{"ω
(rad/sec)","Abs[FHarmonic]"}]];(*Abs[FHarmonic]*)
```

SHOW CONTINUOUS PLOTS;

```
Table[f1[[2]]] (*show plots*)
Table[f1[[1]]](*show time it took to calculate plots*)
Table[{f2[[2]],f3[[2]],f4[[2]]}](*show plots*)
Table[{f2[[1]],f3[[1]],f4[[1]]}](*show time it took to calculate plots*)
(*show time it took to calculate plots*)
```

Plot Forcing

```
Plot[Abs[FHarmonic[[2]]]/.DiracDelta→diracDelta,{ω,-range,range},PlotStyle→
{Thick,Red},PlotLabel→"|FHarmonic|",AxesLabel→{"ω
(rad/sec)","Abs[FHarmonic]"},PlotRange→{{-
100,100},{0,2000}}](*Abs[FHarmonic]*)
```

Assemble the Global Spectral Nodal Forcing Vector (Fixed-Fixed)

CLEAR VARIABLES;

```
Clear[fg];
```

ASSEMBLE THE GLOBAL FORCE VECTOR;

```
fg={FHarmonic[[2]],0};
```

Calculate the Global Spectral Nodal DOF Vector

CLEAR VARIABLES;

```
Clear[Sg,ω,Sginv,dg];
```

REDEFINE THE GLOBAL MATRIX (IE PULL THE HYDRODYNAMIC FUNCTION OUT);

```
Sg[ω_,hf_]=K1[[2]]+K2[[2]];
```

CALCULATE THE GLOBAL SPECTRAL MATRIX;

```
Sginv[ω_,hf_]=Inverse[Sg[ω,hf]];
```

CALCULATE THE GLOBAL SPECTRAL NODAL DOF VECTOR;

```
dg[ω_,hf_]=Sginv[ω,hf].fg;
```

Determine Displacement Response Based on First Element

Calculate the Continuous Frequency Response for the First Element

CLEAR VARIABLES;

```
Clear[d,ω,Cvector,Wvector];
```

DISTRIBUTE DG TO THE ELEMENT LEVEL;

```
d[ω_,hf_]={0,0,Part[dg[ω,hf][[1]]],Part[dg[ω,hf][[1,2]]]};
```

CALCULATE THE C VECTOR NEEDED TO ASSEMBLE THE FOURIER COEFFICIENT EQUATION;

```
Cvector[ω_,hf_]=Hinv1[[2]].d[ω,hf];
```

ASSEMBLE THE FOURIER COEFFIECIENT EQUATION;

```
Wvector[ω_,hf_]=evector1[x].Cvector[ω,hf];
```

Calculate the Continuous Frequency Response for the Second Element

CLEAR VARIABLES;

```
Clear[dR,CvectorR,WvectorR];
```

DISTRIBUTE DG TO THE ELEMENT LEVEL;

```
dR[ω_,hf_]={Part[dg[ω,hf][[1]]],Part[dg[ω,hf][[1,2]]],0,0};
```

CALCULATE THE C VECTOR NEEDED TO ASSEMBLE THE FOURIER COEFFICIENT EQUATION;

```
CvectorR[ω_,hf_]=Hinv2[[2]].dR[ω,hf];
```

ASSEMBLE THE FOURIER COEFFIECIENT EQUATION;

```
WvectorR[ω_,hf_]=evector2[x].CvectorR[ω,hf];
```

Plot the Continuous Frequency Responses Around The Forcing Frequency

CLEAR VARIABLES;

```
Clear[x,ωL,ωH, W1,W1R];
```

PLOT THE FREQUENCY RESPONSE FOR THE FIRST ELEMENT;

```
ωL=1;
ωH=3;
x=elL1;
W1=Timing[LogPlot[Abs[Wvector[ω,hf[ω]]],{ω,ωL,ωH},PlotStyle→{Thick,Red},PlotL
abel→"|Wvector|",AxesLabel→{"ω (rad/sec)","Abs[Wvector]"}]];
Clear[x];
```

PLOT THE FREQUENCY RESPONSE FOR THE SECOND ELEMENT;

```
x=0;
W1R=Timing[LogPlot[Abs[WvectorR[ω,hf[ω]]],{ω,ωL,ωH},PlotStyle→{Thick,Blue},Pl
otLabel→"|Wvector|",AxesLabel→{"ω (rad/sec)","Abs[Wvector]"}]];
Clear[x];
```

SUPERIMPOSE PLOTS;

```
Show[{W1[[2]],W1R[[2]]},AxesLabel→{"ω
(rad/sec)","Magnitude"},PlotLabel→"|Wvector|:1st Element=Red, 2nd
Element=Blue"]
Table[{W1[[2]],W1R[[2]]}]
Table[{W1[[1]],W1R[[1]]}]
```

Sample the Continuous Frequency Response (Use First Element Moving Forward)

CLEAR VARIABLES;

```
Clear[x,ωs,Ωs,WBarSampled1,ω,WvectorRR,WvectorLL,WBarSampled2,WBarSampled3,WBa
rSampled];
```

SAMPLING PARAMETERS;

```
x=elL1;(*spatial point of interest*)
ωs=0.025;(*Define the frequency s
ampling rate*)
(*!!!!!!!!!!!!!!!!!!Set ωs Based on Side Lob Widths to avoid
Aliasing!!!!!!!!!!!!!!!!*)
(*!!!!!!Make sure to not sample on the driving frequency to avoid a
singularity!!!!!*)
Ωs=400;(*Determine the TOTAL range of frequencies to be included in sampling*)
```

SAMPLE THE CONTINUOUS SIGNAL AND REORDER SO AS TO PERFORM THE DISCRETE FT;

```
WBarSampled1=Timing[Table[Wvector[ω,hf[ω]],{ω,-Ωs/2+ωs,-ωs,ωs}]];(*Sampled
Wvector for ω<0*)
ω=ωs;(*Define offset point to avoid sampling at zero frequency*)
WvectorRR=Wvector[ω,hf[ω]];(*Sample at zero+*)
Clear[ω];(*Clear offset point*)
ω=-ωs;(*Define offset point to avoid sampling at zero frequency*)
WvectorLL=Wvector[ω,hf[ω]];(*Sample at zero-*)
Clear[ω];(*Clear offset point*)
WBarSampled2=Timing[(WvectorRR+WvectorLL)/2];(*Sampled Wvector at ω~0*)
WBarSampled3=Timing[Table[Wvector[ω,hf[ω]],{ω,ωs,Ωs/2,ωs}]];(*Sampled Wvector
for ω>0*)
(*Combine the three lists in an order appropriate for discrete transforms*)
WBarSampled=Timing[Flatten[Join[{WBarSampled2[[2]]},{WBarSampled3[[2]]},{WBarS
ampled1[[2]]}]]];
```

SHOW TIME FOR SAMPLING;

```
Table[{WBarSampled1[[1]],WBarSampled2[[1]],WBarSampled3[[1]],WBarSampled[[1]]}
]
```

Plot the Sampled Frequency Response

CLEAR VARIABLES;

```
Clear[ωLs,ωHs,AmpMax,WLDisc];
```

DEFINE PLOTTING PARAMETERS;

```
ωLs=2(*plotting low frequency*)
ωHs=3;(*plotting high frequency*)
AmpMax=0.1;(*plotting amplitude*)
```

DEFINE PLOTS OF INTEREST;

```
WLDisc=Timing[ListPlot[Abs[WBarSampled[[2]]],Filling→Axis,Joined→False,PlotLa
bel→"|WBarSampled|",AxesLabel→{"ω
(rad/sec)","Abs[WBarSampled]"},PlotRange→{{ωLs,ωHs},{0,AmpMax}},PlotStyle→Blu
e,DataRange→{0,Ωs-ωs}]];(*the data is scaled from k→ω for plotting
purposes*)

(*SHOW PLOTS OF INTEREST------------------------------------------*)
Show[WLDisc[[2]],AxesLabel→{"ω (rad/sec)","Magnitude"},PlotLabel→"|Wvector| &
|WBarSampled|"]
Table[WLDisc[[1]]](*show time it took to calculate plots*)
```

Plot the Continuous and Sampled Frequency Response (Superimposed)

CLEAR VARIABLES;

```
Clear[AmpMax,WLCont,WLDisc2];
```

DEFINE PLOTTING PARAMETERS;

```
AmpMax=0.01;(*plotting amplitude*)
ωL=2;
ωH=3;
```

DEFINE PLOTS OF INTEREST;

```
WLCont=Timing[Plot[Abs[Wvector[ω,hf[ω]]],{ω,ωL,ωH},PlotStyle→
{Thick,Red},PlotLabel→"|Wvector|",AxesLabel→{"ω
(rad/sec)","Abs[Wvector]"},PlotRange→{{ωL,ωH},{0,AmpMax}}]];(*Abs[Wvector]*)
```

```
WLDisc2=Timing[ListPlot[Abs[WBarSampled[[2]]],Filling→Axis,Joined→False,PlotL
abel→"|WBarSampled|",AxesLabel→{"ω
(rad/sec)","Abs[WBarSampled]"},PlotRange→{{ωL,ωH},{0,AmpMax}},PlotStyle→Blue,
DataRange→{0,Ωs-ωs}]];(*the data is scaled from k→ω for plotting purposes*)
```

SHOW PLOTS OF INTEREST;

```
Show[{WLCont[[2]],WLDisc2[[2]]},AxesLabel→{"ω
(rad/sec)","Magnitude"},PlotLabel→"|Wvector| & |WBarSampled|"](*superimpose
the two plots*)
Table[{WLCont[[1]],WLDisc2[[1]]}](*show time it took to calculate plots*)
```

Calculate the Displacement Response as the iFFT of Wvector

CLEAR VARIABLES;

```
Clear[wSampled];
```

TAKE THE IFFT OF Wvector TO DETERMINE THE DISPLACEMENT RESPONSE IN DISCRETE FORM;

```
wSampled=Timing[(Ωs/(2*Pi))*N[InverseFourier[WBarSampled[[2]]]]];
```

SHOW TIME FOR CALCULATION;

```
Table[{wSampled[[1]]}](*show time it took to calculate*)
```

Plot the Displacement Response

CLEAR VARIABLES;

```
Clear[ti,tf,dispMag,w1,w2,w3];
```

DEFINE PLOTTING PARAMETERS;

```
ti=0;(*starting time*)
tf=20;(*final time*)
dispMag=0.002;(*Maximum expected displacement magnitude*)
```

DEFINE DISPLACEMENT PLOTS OF INTEREST;

```
w1=Timing[ListPlot[Re[wSampled[[2]]],PlotRange→{{ti,tf},{-
dispMag,dispMag}},Filling→Axis,PlotLabel→"Real part of
wSampled",AxesLabel→{"time,sec","Re[wSampled]"},Joined→True,DataRange→{0,2*P
i/ωs}]];(*Real part*)
w2=Timing[ListPlot[Im[wSampled[[2]]],PlotRange→{{ti,tf},{-
dispMag,dispMag}},Filling→Axis,PlotLabel→"Imag. part of
wSampled",AxesLabel→{"time,sec","Im[wSampled]"},Joined→True,DataRange→{0,2*P
i/ωs}]];(*Imaginary part*)
w3=Timing[ListPlot[Abs[wSampled[[2]]],PlotRange→{{ti,tf},{-
dispMag,dispMag}},Filling→Axis,PlotLabel→"Abs part of
wSampled",AxesLabel→{"time,sec","Abs[wSampled]"},Joined→True,DataRange→{0,2*
Pi/ωs}]];(*Absolute*)
```

SHOW PLOTS OF INTEREST;

```
Table[w1[[2]]]
Table[{w2[[2]],w3[[2]]}](*show plots*)
Table[{w1[[1]],w2[[1]],w3[[1]]}](*show time it took to calculate plots*)
```

Appendix D – Parametric Study Inputs

Table D.1. Parametric Study: Inputs [178]

		Conveyed Fluid Velocity	
		Case	
Variable	Units	1	2
Young's Modulus, E	N/m^2	$2e11$	
Pipe Outer Radius, d	m	0.065	
Pipe Wall Thickness, w_t	m	0.015	
Pipe Inertia, I	m^4	$9.11e-6$	
Pipe Area, A_p	m^2	$5.42e-3$	
Conveyed Fluid Flow-Area, A_i	m^2	$7.85e-3$	
Poisson's Ratio, ν	-	0	
Pipe Density, ρ_p	kg/m^3	7800	
Pipe Mass, m	kg/m	42.27	
Coefficient of Gravity, g	m/s^2	9.81	
Pipe Length, L	m	8	
Conveyed Fluid Density, ρ_i	kg/m^3	900	
Annulus Fluid Density, ρ_e	kg/m^3	0	
Casing Inner Radius, D	m	∞	
Annulus Fluid Kinematic Viscosity, υ	m^2/s	0	
Conveyed Fluid Mass, M_i	kg/m	7.07	
Conveyed Fluid Velocity, U	m/s	Varies*	
Externally Applied Tension, $\bar{T}$	N	0	
Mean Pressure Differential, $\bar{p}$	N/m^2	0	
Viscous Damping, c	kg/s	0	
Translational Spring Stiffness, $K_{t1} = K_{t2}$	N/m	∞	
Rotational Spring Stiffness, K_{r1}	Nm/rad	∞	0
Rotational Spring Stiffness, K_{r2}	Nm/rad	∞	0

**The flow velocity is taken to be negative, indicating flow in the direction opposite gravity*

Table D.1. Parametric Study: Inputs (Continued) [178]

		Axial Force			
		Case			
Variable	Units	3	4	5	6
Young's Modulus, E	N/m^2	$2e11$			
Pipe Outer Radius, d	m	0.065			
Pipe Wall Thickness, w_t	m	0.015			
Pipe Inertia, I	m^4	$9.11e-6$			
Pipe Area, A_p	m^2	$5.42e-3$			
Conveyed Fluid Flow-Area, A_i	m^2	$7.85e-3$			
Poisson's Ratio, ν	-	0			
Pipe Density, ρ_p	kg/m^3	7800			
Pipe Mass, m	kg/m	42.27			
Coefficient of Gravity, g	m/s^2	9.81			
Pipe Length, L	m	8			
Conveyed Fluid Density, ρ_i	kg/m^3	900			
Annulus Fluid Density, ρ_e	kg/m^3	0			
Casing Inner Radius, D	m	∞			
Annulus Fluid Kinematic Viscosity, υ	m^2/s	0			
Conveyed Fluid Mass, M_i	kg/m	7.07			
Conveyed Fluid Velocity, U	m/s	Varies*			
Externally Applied Tension, $\bar{T}$	N	$1.5e5$	$-2.5e5$	$1.5e5$	$-2.5e5$
Mean Pressure Differential, $\bar{p}$	N/m^2	0			
Viscous Damping, c	kg/s	0			
Translational Spring Stiffness, $K_{t1} = K_{t2}$	N/m	∞			
Rotational Spring Stiffness, K_{r1}	Nm/rad	∞		0	
Rotational Spring Stiffness, K_{r2}	Nm/rad	∞		0	

**The flow velocity is taken to be negative, indicating flow in the direction opposite gravity*

Table D.1. Parametric Study: Inputs (Continued) [178]

		Annulus Fluid Density			
		Case			
Variable	Units	7	8	9	10
Young's Modulus, E	N/m^2	$2e11$			
Pipe Outer Radius, d	m	0.065			
Pipe Wall Thickness, w_t	m	0.015			
Pipe Inertia, I	m^4	$9.11e-6$			
Pipe Area, A_p	m^2	$5.42e-3$			
Conveyed Fluid Flow-Area, A_i	m^2	$7.85e-3$			
Poisson's Ratio, ν	-	0			
Pipe Density, ρ_p	kg/m^3	7800			
Pipe Mass, m	kg/m	42.27			
Coefficient of Gravity, g	m/s^2	9.81			
Pipe Length, L	m	8			
Conveyed Fluid Density, ρ_i	kg/m^3	900			
Annulus Fluid Density, ρ_e	kg/m^3	2000	600	1200	600
Casing Inner Radius, D	m	∞	0.113	0.092	0.113
Annulus Fluid Kinematic Viscosity, υ	m^2/s	0			
Conveyed Fluid Mass, M_i	kg/m	7.07			
Conveyed Fluid Velocity, U	m/s	0			
Externally Applied Tension, $\bar{T}$	N	0			
Mean Pressure Differential, $\bar{p}$	N/m^2	0			
Viscous Damping, c	kg/s	0			
Translational Spring Stiffness, $K_{t1} = K_{t2}$	N/m	∞			
Rotational Spring Stiffness, K_{r1}	Nm/rad	∞		0	
Rotational Spring Stiffness, K_{r2}	Nm/rad	∞		0	

Table D.1. Parametric Study: Inputs (Continued) [178]

		Inviscid Systems			
		Case			
Variable	Units	11	12	13	14
Young's Modulus, E	N/m^2	$2e11$			
Pipe Outer Radius, d	m	0.065			
Pipe Wall Thickness, w_t	m	0.015			
Pipe Inertia, I	m^4	$9.11e-6$			
Pipe Area, A_p	m^2	$5.42e-3$			
Conveyed Fluid Flow-Area, A_i	m^2	$7.85e-3$			
Poisson's Ratio, ν	-	0			
Pipe Density, ρ_p	kg/m^3	7800			
Pipe Mass, m	kg/m	42.27			
Coefficient of Gravity, g	m/s^2	9.81			
Pipe Length, L	m	8			
Conveyed Fluid Density, ρ_i	kg/m^3	900			
Annulus Fluid Density, ρ_e	kg/m^3	1050			
Casing Inner Radius, D	m	$1.30d$	$1.11d$	$1.30d$	$1.11d$
Annulus Fluid Kinematic Viscosity, υ	m^2/s	0			
Conveyed Fluid Mass, M_i	kg/m	7.07			
Conveyed Fluid Velocity, U	m/s	Varies*			
Externally Applied Tension, $\bar{T}$	N	0			
Mean Pressure Differential, $\bar{p}$	N/m^2	0			
Viscous Damping, c	kg/s	0			
Translational Spring Stiffness, $K_{t1} = K_{t2}$	N/m	∞			
Rotational Spring Stiffness, K_{r1}	Nm/rad	∞		0	
Rotational Spring Stiffness, K_{r2}	Nm/rad	∞		0	

**The flow velocity is taken to be negative, indicating flow in the direction opposite gravity*

Table D.1. Parametric Study: Inputs (Continued) [178]

		Viscous Systems					
		Case					
Variable	Units	15	16	17	18	19	20
Young's Modulus, E	N/m^2	$2e11$					
Pipe Outer Radius, d	m	0.065					
Pipe Wall Thickness, w_t	m	0.015					
Pipe Inertia, I	m^4	$9.11e-6$					
Pipe Area, A_p	m^2	$5.42e-3$					
Conveyed Fluid Flow-Area, A_i	m^2	$7.85e-3$					
Poisson's Ratio, ν	-	0					
Pipe Density, ρ_p	kg/m^3	7800					
Pipe Mass, m	kg/m	42.27					
Coefficient of Gravity, g	m/s^2	9.81					
Pipe Length, L	m	8					
Conveyed Fluid Density, ρ_i	kg/m^3	900					
Annulus Fluid Density, ρ_e	kg/m^3	1050					
Casing Inner Radius, D	m	$1.10d$	$1.11d$	$1.10d$	$1.10d$	$1.11d$	$1.10d$
Annulus Fluid Kinematic Viscosity, υ	m^2/s	$1.2e-5$	$1.2e-4$		$1.2e-5$	$3.6e-5$	
Conveyed Fluid Mass, M_i	kg/m	7.07					
Conveyed Fluid Velocity, U	m/s	Varies*					
Externally Applied Tension, $\bar{T}$	N	0					
Mean Pressure Differential, $\bar{p}$	N/m^2	0					
Viscous Damping, c	kg/s	0					
Translational Spring Stiffness, $K_{t1} = K_{t2}$	N/m	∞					
Rotational Spring Stiffness, K_{r1}	Nm/rad	∞			0		
Rotational Spring Stiffness, K_{r2}	Nm/rad	∞			0		

**The flow velocity is taken to be negative, indicating flow in the direction opposite gravity*

Table D.1. Parametric Study: Inputs (Continued) [178]

		Frequency Dependent Damping			
		Case			
Variable	Units	21	22	23	24
Young's Modulus, E	N/m^2	$2e11$			
Pipe Outer Radius, d	m	0.05			
Pipe Wall Thickness, w_t	m	0.007			
Pipe Inertia, I	m^4	$2.22e-6$			
Pipe Area, A_p	m^2	$2.05e-3$			
Conveyed Fluid Flow-Area, A_i	m^2	$5.81e-3$			
Poisson's Ratio, ν	-	0			
Pipe Density, ρ_p	kg/m^3	7800			
Pipe Mass, m	kg/m	15.95			
Coefficient of Gravity, g	m/s^2	9.81			
Pipe Length, L	m	8			
Conveyed Fluid Density, ρ_i	kg/m^3	850			
Annulus Fluid Density, ρ_e	kg/m^3	900			
Casing Inner Radius, D	m	$1.2d$			
Annulus Fluid Kinematic Viscosity, υ	m^2/s	$1e-05$	$3e-05$	$7e-05$	$4e-05$
Conveyed Fluid Mass, M_i	kg/m	4.94			
Conveyed Fluid Velocity, U	m/s	Varies*			
Externally Applied Tension, $\bar{T}$	N	0			
Mean Pressure Differential, $\bar{p}$	N/m^2	0			
Viscous Damping, c	kg/s	0			
Translational Spring Stiffness, $K_{t1} = K_{t2}$	N/m	∞			
Rotational Spring Stiffness, K_{r1}	Nm/rad	Varies			
Rotational Spring Stiffness, K_{r2}	Nm/rad	Varies			

**The flow velocity is taken to be negative, indicating flow in the direction opposite gravity*

Appendix E – Damping Ratio Comparison

Table E.1 Inputs

		Case		
Variable	Units	i	ii	iii
Viscous Damping, c	kg/s	0		
Pipe Outer Radius, d	m	0.040	0.050	0.055
Coefficient of Gravity, g	m/s^2	9.81		
Pipe Mass, m	kg/m	10.60	16.36	9.32
Mean Pressure Differential, $\bar{p}$	N/m^2	0		
Conveyed Fluid Flow-Area, A_i	m^2	$3.85e-3$	$5.81e-3$	$8.17e-3$
Casing Inner Radius, D	m	0.05	0.06	0.07
Young's Modulus, E	N/m^2	$1.80e11$	$2.10e11$	$2.00e11$
Pipe Inertia, I	m^4	$8.32e-7$	$2.22e-6$	$1.87e-6$
Rotational Spring Stiffness, K_{r1}	Nm/rad	∞	0	∞
Rotational Spring Stiffness, K_{r2}	Nm/rad	0	0	∞
Translational Spring Stiffness, $K_{t1} = K_{t2}$	N/m	∞	∞	∞
Pipe Length, L	m	10	13	9
Conveyed Fluid Mass, M_i	kg/m	2.31	4.07	6.53
Externally Applied Tension, $\bar{T}$	N	0		
Conveyed Fluid Velocity, U	m/s	Varies*		
Annulus Fluid Density, ρ_e	kg/m^3	900	950	800
Annulus Fluid Kinematic Viscosity, υ	m^2/s	$3.00e-5$	$4.50e-5$	$2.00e-5$
Poisson's Ratio, ν	-	0		

**The flow velocity is taken to be negative, indicating flow in the direction opposite gravity*

Appendix F – Structural Housing Design Calculations

Table F.1. Production Tube Summary – Bursting

Outer Diameter, $2d\ (in)$	3.50
Wall Thickness, $w_t\ (in)$	0.375
Yield Strength, $Y_p\ (psi)$	80000
Unfactored Burst Pressure, $P_B\ (psi)$	15000
Internal Pressure, $p_i\ (psi)$	10000
External Pressure, $p_o\ (psi)$	0
Required Design Factor, $DF_{required}$	1.25
Actual Design Factor, DF_{actual}	1.50
Burst Design Sufficient?	Yes

Table F.2. Production Tube Summary – Collapse

Outer Diameter, $2d\ (in)$	3.50
Wall Thickness, $w_t\ (in)$	0.375
Yield Strength, $Y_p\ (psi)$	80000
$(2d/w_t)_{actual}$	9.33
Yield Strength Collapse Upperbound, $(2d/w_t)_{Y_p}$	13.38
Yield Strength Collapse Possible?	Yes
Yield Strength Collapse Pressure, $P_{Yp}\ (psi)$	15306
Plastic Collapse Variable, A	3.071
Plastic Collapse Variable, B	0.0667
Plastic Collapse Variable, C	1955
Plastic Collapse Lowerbound, $(2d/w_t)_{Y_p,p}$	13.38
Plastic Collapse Upperbound, $(2d/w_t)_{p,T}$	22.47
Plastic Collapse Possible?	No
Plastic Collapse Pressure, $P_p\ (psi)$	N/A
Transition Collapse Variable, F	1.998
Transition Collapse Variable, G	0.0434
Transition Collapse Lowerbound, $(2d/w_t)_{p,T}$	22.47
Transition Collapse Upperbound, $(2d/w_t)_{T,E}$	31.02
Transition Collapse Possible?	No
Transition Collapse Pressure, $P_T\ (psi)$	N/A
Elastic Collapse Lowerbound, $(2d/w_t)_{T,E}$	31.02
Elastic Collapse Possible?	No
Elastic Collapse Pressure, $P_E\ (psi)$	N/A
Min Collapse Pressure Differential (psi)	15306
Internal Pressure, $p_i\ (psi)$	0
External Pressure, $p_o\ (psi)$	10000
Required Design Factor, $DF_{required}$	1.1
Actual Design Factor, DF_{actual}	1.53
Collapse Design Sufficient?	Yes

Table F.3. Production Tube Summary – Collapse + Tension

Outer Diameter, $2d\ (in)$	3.50
Wall Thickness, $w_t\ (in)$	0.375
Yield Strength, $Y_p\ (psi)$	80000
$(2d/w_t)_{actual}$	9.33
Applied Tension (lb)	124000
Actual Tension (lb)	124000
Nominal Cross Sectional Area, $A_p\ (in^2)$	3.68
Axial Stress, $\sigma_z\ (psi)$	33681
Yield Strength of ASEG, $Y_{pa}\ (psi)$	57652
Yield Strength Collapse Upperbound, $(2d/w_t)_{Y_p}$	14.61
Yield Strength Collapse Possible?	Yes
Yield Strength Collapse Pressure, $P_{Yp}\ (psi)$	11030
Plastic Collapse Variable, A	2.998
Plastic Collapse Variable, B	0.0554
Plastic Collapse Variable, C	1286
Plastic Collapse Lowerbound, $(2d/w_t)_{Y_p,p}$	14.61
Plastic Collapse Upperbound, $(2d/w_t)_{p,T}$	24.69
Plastic Collapse Possible?	No
Plastic Collapse Pressure, $P_p\ (psi)$	N/A
Transition Collapse Variable, F	1.985
Transition Collapse Variable, G	0.0367
Transition Collapse Lowerbound, $(2d/w_t)_{p,T}$	24.69
Transition Collapse Upperbound, $(2d/w_t)_{T,E}$	36.41
Transition Collapse Possible?	No
Transition Collapse Pressure, $P_T\ (psi)$	N/A
Elastic Collapse Lowerbound, $(2d/w_t)_{T,E}$	36.41
Elastic Collapse Possible?	No
Elastic Collapse Pressure, $P_E\ (psi)$	N/A
Min Collapse Pressure Differential (psi)	11030
Internal Pressure, $p_i\ (psi)$	0
External Pressure, $p_o\ (psi)$	10000
Required Design Factor, $DF_{required}$	1.1
Actual Design Factor, DF_{actual}	1.10
Collapse + Tension Design Sufficient?	Yes

Table F.4. Production Tube Summary – Burst + Tension

Outer Diameter, $2d\ (in)$	3.50
Wall Thickness, $w_t\ (in)$	0.375
Yield Strength, $Y_p\ (psi)$	80000
Applied Tension (lb)	225000
Actual Tension (lb)	225000
Nominal Cross Sectional Area, $A_p\ (in^2)$	3.68
Axial Stress, $\sigma_z\ (psi)$	61115
Outer Wall Radius, $d\ (in)$	1.75
Inner Wall Radius, $d - w_t\ (in)$	1.375
Internal Pressure, $p_i\ (psi)$	10000
External Pressure, $p_o\ (psi)$	0
Tangential Stress at Inner Wall, $\sigma_t\ (psi)$	42267
Radial Stress at Inner Wall, $\sigma_r\ (psi)$	-10000
Von Mises Stress at Inner Wall, $\sigma_{VM}\ (psi)$	63814
Tangential Stress at Outer Wall, $\sigma_t\ (psi)$	32267
Radial Stress at Outer Wall, $\sigma_r\ (psi)$	0
Von Mises Stress at Outer Wall, $\sigma_{VM}\ (psi)$	52955
Governing Von Mises Stress (psi)	63814
Required Design Factor, $DF_{required}$	1.25
Actual Design Factor, DF_{actual}	1.25
Burst + Tension Design Sufficient?	Yes

Table F.5. Production Tube Summary – Collapse + Compression

Outer Diameter, $2d\ (in)$	3.50
Wall Thickness, $w_t\ (in)$	0.375
Yield Strength, $Y_p\ (psi)$	80000
Applied Compression (lb)	-305000
Actual Compression (lb)	-305000
Nominal Cross Sectional Area, $A_p\ (in^2)$	3.68
Axial Stress, $\sigma_z\ (psi)$	-82845
Outer Wall Radius, $d\ (in)$	1.75
Inner Wall Radius, $d - w_t\ (in)$	1.375
Internal Pressure, $p_i\ (psi)$	0
External Pressure, $p_o\ (psi)$	10000
Tangential Stress at Inner Wall, $\sigma_t\ (psi)$	-52267
Radial Stress at Inner Wall, $\sigma_r\ (psi)$	0
Von Mises Stress at Inner Wall, $\sigma_{VM}\ (psi)$	72561
Tangential Stress at Outer Wall, $\sigma_t\ (psi)$	-42267
Radial Stress at Outer Wall, $\sigma_r\ (psi)$	-10000
Von Mises Stress at Outer Wall, $\sigma_{VM}\ (psi)$	63223
Governing Von Mises Stress (psi)	72561
Required Design Factor, $DF_{required}$	1.1
Actual Design Factor, DF_{actual}	1.10
Collapse + Compression Design Sufficient?	Yes

Table F.6. Production Tube Summary – Burst + Compression

Outer Diameter, $2d\ (in)$	3.50
Wall Thickness, $w_t\ (in)$	0.375
Yield Strength, $Y_p\ (psi)$	80000
Applied Compression (lb)	-107000
Actual Compression (lb)	-107000
Nominal Cross Sectional Area, $A_p\ (in^2)$	3.68
Axial Stress, $\sigma_z\ (psi)$	-29064
Outer Wall Radius, $d\ (in)$	1.75
Inner Wall Radius, $d - w_t\ (in)$	1.375
Internal Pressure, $p_i\ (psi)$	10000
External Pressure, $p_o\ (psi)$	0
Tangential Stress at Inner Wall, $\sigma_t\ (psi)$	42267
Radial Stress at Inner Wall, $\sigma_r\ (psi)$	-10000
Von Mises Stress at Inner Wall, $\sigma_{VM}\ (psi)$	63966
Tangential Stress at Outer Wall, $\sigma_t\ (psi)$	32267
Radial Stress at Outer Wall, $\sigma_r\ (psi)$	0
Von Mises Stress at Outer Wall, $\sigma_{VM}\ (psi)$	53138
Governing Von Mises Stress (psi)	63966
Required Design Factor, $DF_{required}$	1.25
Actual Design Factor, DF_{actual}	1.25
Burst + Compression Design Sufficient?	Yes

Table F.7. Outer Coaxial Pipe Summary – Collapse

Outer Diameter, $2d\ (in)$	5.50
Wall Thickness, $w_t\ (in)$	0.415
Yield Strength, $Y_p\ (psi)$	80000
$(2d/w_t)_{actual}$	13.25
Yield Strength Collapse Upperbound, $(2d/w_t)_{Y_p}$	13.38
Yield Strength Collapse Possible?	Yes
Yield Strength Collapse Pressure, $P_{Yp}\ (psi)$	11161
Plastic Collapse Variable, A	3.071
Plastic Collapse Variable, B	0.0667
Plastic Collapse Variable, C	1955
Plastic Collapse Lowerbound, $(2d/w_t)_{Y_p,p}$	13.38
Plastic Collapse Upperbound, $(2d/w_t)_{p,T}$	22.47
Plastic Collapse Possible?	No
Plastic Collapse Pressure, $P_p\ (psi)$	N/A
Transition Collapse Variable, F	1.998
Transition Collapse Variable, G	0.0434
Transition Collapse Lowerbound, $(2d/w_t)_{p,T}$	22.47
Transition Collapse Upperbound, $(2d/w_t)_{T,E}$	31.02
Transition Collapse Possible?	No
Transition Collapse Pressure, $P_T\ (psi)$	N/A
Elastic Collapse Lowerbound, $(2d/w_t)_{T,E}$	31.02
Elastic Collapse Possible?	No
Elastic Collapse Pressure, $P_E\ (psi)$	N/A
Min Collapse Pressure Differential (psi)	11161
Internal Pressure, $p_i\ (psi)$	0
External Pressure, $p_o\ (psi)$	10000
Required Design Factor, $DF_{required}$	1.1
Actual Design Factor, DF_{actual}	1.12
Collapse Design Sufficient?	Yes

Table F.8. Outer Coaxial Pipe Summary – Collapse + Tension

Outer Diameter, $2d\ (in)$	5.50
Wall Thickness, $w_t\ (in)$	0.415
Yield Strength, $Y_p\ (psi)$	80000
$(2d/w_t)_{actual}$	13.25
Projected Housing Area (in^2)	14.14
Annulus Induced Compression (lb)	-141372
Applied Tension (lb)	124000
Actual Tension (lb)	-17372
Combined Nominal Cross Sectional Area (in^2)	10.31
Axial Stress, $\sigma_z\ (psi)$	-1685
Yield Strength of ASEG, $Y_{pa}\ (psi)$	80829
Yield Strength Collapse Upperbound, $(2d/w_t)_{Y_p}$	13.35
Yield Strength Collapse Possible?	Yes
Yield Strength Collapse Pressure, $P_{Yp}\ (psi)$	11276
Plastic Collapse Variable, A	3.074
Plastic Collapse Variable, B	0.0671
Plastic Collapse Variable, C	1980
Plastic Collapse Lowerbound, $(2d/w_t)_{Y_{p,p}}$	13.35
Plastic Collapse Upperbound, $(2d/w_t)_{p,T}$	22.40
Plastic Collapse Possible?	No
Plastic Collapse Pressure, $P_p\ (psi)$	N/A
Transition Collapse Variable, F	1.999
Transition Collapse Variable, G	0.0437
Transition Collapse Lowerbound, $(2d/w_t)_{p,T}$	22.40
Transition Collapse Upperbound, $(2d/w_t)_{T,E}$	30.85
Transition Collapse Possible?	No
Transition Collapse Pressure, $P_T\ (psi)$	N/A
Elastic Collapse Lowerbound, $(2d/w_t)_{T,E}$	30.85
Elastic Collapse Possible?	No
Elastic Collapse Pressure, $P_E\ (psi)$	N/A
Min Collapse Pressure Differential (psi)	11276
Internal Pressure, $p_i\ (psi)$	0
External Pressure, $p_o\ (psi)$	10000
Required Design Factor, $DF_{required}$	1.1
Actual Design Factor, DF_{actual}	1.13
Collapse + Tension Design Sufficient?	Yes

Table F.9. Outer Coaxial Pipe Summary – Collapse + Compression

Outer Diameter, $2d\ (in)$	5.50
Wall Thickness, $w_t\ (in)$	0.415
Yield Strength, $Y_p\ (psi)$	80000
Projected Housing Area (in^2)	14.14
Annulus Induced Compression (lb)	-141372
Applied Compression (lb)	-305000
Actual Compression (lb)	-446372
Nominal Cross Sectional Area, $A_p\ (in^2)$	10.31
Axial Stress, $\sigma_z\ (psi)$	-43292
Outer Wall Radius, $d\ (in)$	2.75
Inner Wall Radius, $d - w_t\ (in)$	2.335
Internal Pressure, $p_i\ (psi)$	0
External Pressure, $p_o\ (psi)$	10000
Tangential Stress at Inner Wall, $\sigma_t\ (psi)$	-71679
Radial Stress at Inner Wall, $\sigma_r\ (psi)$	0
Von Mises Stress at Inner Wall, $\sigma_{VM}\ (psi)$	62522
Tangential Stress at Outer Wall, $\sigma_t\ (psi)$	-61679
Radial Stress at Outer Wall, $\sigma_r\ (psi)$	-10000
Von Mises Stress at Outer Wall, $\sigma_{VM}\ (psi)$	45372
Governing Von Mises Stress (psi)	62522
Required Design Factor, $DF_{required}$	1.1
Actual Design Factor, DF_{actual}	1.28
Collapse + Compression Design Sufficient?	Yes

Appendix G – Linear Sensitivity Analysis

The natural frequency of a SDOF oscillator can be written as

$$\omega_n = \sqrt{\frac{k}{m}}, \tag{G.1}$$

where for a cantilever configuration

$$\omega_n = \sqrt{\frac{3EI}{mL^3}}. \tag{G.2}$$

Assuming that the mass does not erode over time or change with changing temperature, the natural frequencies time/temperature dependence is a function of the Young's modulus, inertia, and beam length. Taking the derivative of the natural frequency with respect to each variable

$$\begin{aligned}
\frac{\partial \omega_n}{\partial E} &= \frac{\sqrt{3}I}{2mL^3}\left(\frac{EI}{mL^3}\right)^{-0.5} = \frac{1}{2}\sqrt{\frac{3EI}{mL^3}}\frac{1}{E} = \frac{\omega_n}{2E}, \\
\frac{\partial \omega_n}{\partial I} &= \frac{\sqrt{3}E}{2mL^3}\left(\frac{EI}{mL^3}\right)^{-0.5} = \frac{1}{2}\sqrt{\frac{3EI}{mL^3}}\frac{1}{I} = \frac{\omega_n}{2I}, \\
\frac{\partial \omega_n}{\partial L} &= \frac{-3\sqrt{3}EI}{2mL^4}\left(\frac{EI}{mL^3}\right)^{-0.5} = \frac{-3}{2}\sqrt{\frac{3EI}{mL^3}}\frac{1}{L} = \frac{-3\omega_n}{2L}.
\end{aligned} \tag{G.3}$$

A perturbation of the natural frequency leads to

$$\Delta\omega_n = \frac{\partial\omega_n}{\partial E}\Delta E = \omega_n\left(\frac{1}{2}\frac{\Delta E}{E}\right) \quad \rightarrow \quad \frac{\Delta\omega_n}{\omega_n} = \left(\frac{1}{2}\frac{\Delta E}{E}\right),$$

$$\Delta\omega_n = \frac{\partial\omega_n}{\partial I}\Delta I = \omega_n\left(\frac{1}{2}\frac{\Delta I}{I}\right) \quad \rightarrow \quad \frac{\Delta\omega_n}{\omega_n} = \left(\frac{1}{2}\frac{\Delta I}{I}\right), \tag{G.4}$$

$$\Delta\omega_n = \frac{\partial\omega_n}{\partial L}\Delta L = \omega_n\left(\frac{-3}{2}\frac{\Delta L}{L}\right) \quad \rightarrow \quad \frac{\Delta\omega_n}{\omega_n} = -3\left(\frac{1}{2}\frac{\Delta L}{L}\right).$$

While all three variables are seen to affect the natural frequency, the change in beam length appears to have the largest impact. To calculate the percentage change in natural frequency for given perturbations of Young's modulus, inertia, and beam length, consider the following. Assume the initial state is

$$\omega_{n,initial} = \sqrt{\frac{k_i}{m}} = \sqrt{\frac{3E_iI_i}{mL_i^3}}. \tag{G.6}$$

At the final stage (i.e. after accounting for changes in material properties/geometry)

$$\omega_{n,final} = \sqrt{\frac{k_f}{m}} = \sqrt{\frac{3E_fI_f}{mL_f^3}}, \tag{G.7}$$

where

$$E_f = (\%E_i)E_i; \quad I_f = (\%I_i)I_i; \quad L_f = (\%L_i)L_i. \tag{G.8}$$

Eq. (G.7) can then be written as

$$\omega_{n,final} = \sqrt{\frac{3E_fI_f}{mL_f^3}} = \sqrt{\frac{3(\%E_i)E_i(\%I_i)I_i}{m[(\%L_i)L_i]^3}}\sqrt{\frac{3E_iI_i}{mL_i^3}\frac{(\%E_i)(\%I_i)}{(\%L_i)^3}} = \omega_{n,initial}\sqrt{\frac{(\%E_i)(\%I_i)}{(\%L_i)^3}}. \tag{G.9}$$

The change in natural frequency is then

$$\Delta\omega_n = \omega_{n,final} - \omega_{n,initial} = \left[\sqrt{\frac{(\%E_i)(\%I_i)}{(\%L_i)^3}} - 1\right]\omega_{n,initial}. \tag{G.10}$$

The percentage change in natural frequency is then

$$\%\Delta\omega_n = \frac{\Delta\omega_n}{\omega_{n,initial}} = \left[\sqrt{\frac{(\%E_i)(\%I_i)}{(\%L_i)^3}} - 1\right]. \tag{G.11}$$

As an numeric example, consider the situation where

$$E_i = 2e8\frac{N}{m_2}; \quad I_i = 3e-10m^4; \quad L_i = 0.03m; \quad m = 0.1kg;$$
$$\%E_i = 95\%; \quad \%I_i = 104\%; \quad \%L_i = 106\%; \tag{G.12}$$

leading to

$$E_f = 1.9e8\frac{N}{m_2}; \quad I_f = 3.12e-10m^4; \quad L_f = 0.0318m. \tag{G.13}$$

The natural frequencies provided by Eq. (G.6) and Eq. (G.7) can be calculated as

$$\begin{aligned} \omega_{n,initial} &= \sqrt{\frac{3E_iI_i}{mL_i^3}} = \sqrt{\frac{3\left(2e8\frac{N}{m_2}\right)(3e-10m^4)}{(0.1kg)(0.03m)^3}} = 258.20\frac{rad}{s}, \\ \omega_{n,final} &= \sqrt{\frac{3E_fI_f}{mL_f^3}} = \sqrt{\frac{3\left(1.9e8\frac{N}{m_2}\right)(3.12e-10m^4)}{(0.1kg)(0.0318m)^3}} = 235.17\frac{rad}{s}. \end{aligned} \tag{G.14}$$

The percentage change in natural frequency is then

$$\%\Delta\omega_n = \frac{\Delta\omega_n}{\omega_{n,initial}} = \frac{\omega_{n,final}-\omega_{n,initial}}{\omega_{n,initial}} = -8.92\%. \tag{G.15}$$

Using Eq. (G.11)

$$\%\Delta\omega_n = \frac{\Delta\omega_n}{\omega_{n,initial}} = \left[\sqrt{\frac{(0.95)(1.04)}{(1.06)^3}} - 1\right] = -8.92\%, \tag{G.16}$$

the same result is found.

Appendix H – MATLAB Script Supporting FS Analysis

```
%Using a SDOF model and the full vibrational input, determine a power
%estimate.
clear;clc;
i=sqrt(-1); %imaginary unit
%%
%Reference in the representative user defined acceleration time history
%profiles.  For this work, three acceleration profiles will be used.
 %The time histories should be even length
%The user must input the acceleration_input.txt

%The first line of the input file should contain the time step
%Numeric entries should start on the fourth line
%Column 1 - Time
%Column 2 - Acceleration in x-direction (in m/s2)
%Column 3 - Acceleration in y-direction (in m/s2)
%Column 4 - Acceleration in z-direction (in m/s2)
%The +x direction corresponds to theta=0 (transverse to the pipe axis)
%The +y direction corresponds to theta=90 (transverse to the pipe axis)
%The +z direction points upwards along the length of the pipe

%------Acceleration Time History #1---------
%Reference the file
filename1='Acceleration_Input_1.txt'; %define the file name
delimiterIn='\t'; %define the spacing in the file
%Import the time step (dt)
headerlinesIn=0; %define the number of header lines
s1=importdata(filename1,delimiterIn,headerlinesIn); %import data
dt_1=s1.data; %Pull the data into a matrix form
fs_1=1/dt_1; %Hz, the sampling rate obtained from the input file
%Import acceleration data
headerlinesIn=3; %define the number of header lines
s1=importdata(filename1,delimiterIn,headerlinesIn); %import data
S1=s1.data; %Pull the data into a matrix form
T_1=S1(:,1); %time
Ax_1=S1(:,2); %m/s2, acceleration in the x-direction
Ay_1=S1(:,3); %m/s2, acceleration in the y-direction
Az_1=S1(:,4); %m/s2, acceleration in the z-direction
```

```
%------Acceleration Time History #2---------
%Reference the file
filename2='Acceleration_Input_2.txt'; %define the file name
delimiterIn='\t'; %define the spacing in the file
%Import the time step (dt)
headerlinesIn=0; %define the number of header lines
s2=importdata(filename2,delimiterIn,headerlinesIn); %import data
dt_2=s2.data; %Pull the data into a matrix form
fs_2=1/dt_2; %Hz, the sampling rate obtained from the input file
%Import acceleration data
headerlinesIn=3; %define the number of header lines
s2=importdata(filename2,delimiterIn,headerlinesIn); %import data
S2=s2.data; %Pull the data into a matrix form
T_2=S2(:,1); %time
Ax_2=S2(:,2); %m/s2, acceleration in the x-direction
Ay_2=S2(:,3); %m/s2, acceleration in the y-direction
Az_2=S2(:,4); %m/s2, acceleration in the z-direction

%------Acceleration Time History #3---------
%Reference the file
filename3='Acceleration_Input_3.txt'; %define the file name
delimiterIn='\t'; %define the spacing in the file
%Import the time step (dt)
headerlinesIn=0; %define the number of header lines
s3=importdata(filename3,delimiterIn,headerlinesIn); %import data
dt_3=s3.data; %Pull the data into a matrix form
fs_3=1/dt_3; %Hz, the sampling rate obtained from the input file
%Import acceleration data
headerlinesIn=3; %define the number of header lines
s3=importdata(filename3,delimiterIn,headerlinesIn); %import data
S3=s3.data; %Pull the data into a matrix form
T_3=S3(:,1); %time
Ax_3=S3(:,2); %m/s2, acceleration in the x-direction
Ay_3=S3(:,3); %m/s2, acceleration in the y-direction
Az_3=S3(:,4); %m/s2, acceleration in the z-direction


% %--------Plot the raw time histories------------
% figure(100)
% subplot(2,2,1);plot(T_1(1:200),Ax_1(1:200));grid on;axis([0 0.4 -1.5 1.5])
% title('AP 1; X-Direction');xlabel('Time (sec)');ylabel('Acceleration (m/s2)');
% subplot(2,2,2);plot(T_1(1:200),Ay_1(1:200));grid on;axis([0 0.4 -2.5 2.5])
% title('AP 1; Y-Direction');xlabel('Time (sec)');ylabel('Acceleration (m/s2)');
% subplot(2,2,3);plot(T_2(1:101),Ax_2(1:101));grid on;axis([0 0.4 -3 3])
% title('AP 2; X-Direction');xlabel('Time (sec)');ylabel('Acceleration (m/s2)');
% subplot(2,2,4);plot(T_2(1:101),Ay_2(1:101));grid on;axis([0 0.4 -2 2])
% title('AP 2; Y-Direction');xlabel('Time (sec)');ylabel('Acceleration (m/s2)');
%
% %Plot the raw time histories
% figure(1) %Acceleration Profile #1
% subplot(3,2,1);plot(T_1,Ax_1);grid on;
% title('Time History 1; X-Direction');xlabel('Time (sec)');ylabel('Acceleration (m/s2)');
% subplot(3,2,2);plot(T_1(1:200),Ax_1(1:200));grid on;
% title('Time History 1; X-Direction');xlabel('Time (sec)');ylabel('Acceleration (m/s2)');
% subplot(3,2,3);plot(T_1,Ay_1);grid on;
% title('Time History 1; Y-Direction');xlabel('Time (sec)');ylabel('Acceleration (m/s2)');
% subplot(3,2,4);plot(T_1(1:200),Ay_1(1:200));grid on;
% title('Time History 1; Y-Direction');xlabel('Time (sec)');ylabel('Acceleration (m/s2)');
% subplot(3,2,5);plot(T_1,Az_1);grid on;
% title('Time History 1; Z-Direction');xlabel('Time (sec)');ylabel('Acceleration (m/s2)');
```

```
% subplot(3,2,6);plot(T_1(1:200),Az_1(1:200));grid on;
% title('Time History 1; Z-Direction');xlabel('Time (sec)');ylabel('Acceleration (m/s2)');
%
% figure(2) %Acceleration Profile #2
% subplot(3,2,1);plot(T_2,Ax_2);grid on;
% title('Time History 2; X-Direction');xlabel('Time (sec)');ylabel('Acceleration (m/s2)');
% subplot(3,2,2);plot(T_2(1:200),Ax_2(1:200));grid on;
% title('Time History 2; X-Direction');xlabel('Time (sec)');ylabel('Acceleration (m/s2)');
% subplot(3,2,3);plot(T_2,Ay_2);grid on;
% title('Time History 2; Y-Direction');xlabel('Time (sec)');ylabel('Acceleration (m/s2)');
% subplot(3,2,4);plot(T_2(1:200),Ay_2(1:200));grid on;
% title('Time History 2; Y-Direction');xlabel('Time (sec)');ylabel('Acceleration (m/s2)');
% subplot(3,2,5);plot(T_2,Az_2);grid on;
% title('Time History 2; Z-Direction');xlabel('Time (sec)');ylabel('Acceleration (m/s2)');
% subplot(3,2,6);plot(T_2(1:200),Az_2(1:200));grid on;
% title('Time History 2; Z-Direction');xlabel('Time (sec)');ylabel('Acceleration (m/s2)');
%
% figure(3) %Acceleration Profile #3
% subplot(3,2,1);plot(T_3,Ax_3);grid on;
% title('Time History 3; X-Direction');xlabel('Time (sec)');ylabel('Acceleration (m/s2)');
% subplot(3,2,2);plot(T_3(1:200),Ax_3(1:200));grid on;
% title('Time History 3; X-Direction');xlabel('Time (sec)');ylabel('Acceleration (m/s2)');
% subplot(3,2,3);plot(T_3,Ay_3);grid on;
% title('Time History 3; Y-Direction');xlabel('Time (sec)');ylabel('Acceleration (m/s2)');
% subplot(3,2,4);plot(T_3(1:200),Ay_3(1:200));grid on;
% title('Time History 2; Y-Direction');xlabel('Time (sec)');ylabel('Acceleration (m/s2)');
% subplot(3,2,5);plot(T_3,Az_3);grid on;
% title('Time History 3; Z-Direction');xlabel('Time (sec)');ylabel('Acceleration (m/s2)');
% subplot(3,2,6);plot(T_3(1:200),Az_3(1:200));grid on;
% title('Time History 3; Z-Direction');xlabel('Time (sec)');ylabel('Acceleration (m/s2)');

%%

%Upload the acceleration-temp operating schedule.
 %The user must input the schedule.txt file
%The first entry of the input file contains the time step (yr)
%The second entry contains the base/room temperature(*C)
%Column numeric entries should start on the fifth line
%Column 1 - Time (yr)
%Column 2 - Expected operating temperature (*C)
%Column 3 - Acceleration profile (this is the number corresponding to the
%acceleration profiles above (i.e. 1 = acceleration profile 1)

%Reference the file
filenameS='Schedule.txt'; %define the file name
delimiterIn='\t'; %define the spacing in the file
%Import the time step (dt)
headerlinesIn=1; %define the number of header lines
sS=importdata(filenameS,delimiterIn,headerlinesIn); %import data
dt_S=sS.data(1); %year, time step
T0=sS.data(2); %*C, base/room temperature
%Import analysis data
headerlinesIn=4; %define the number of header lines
sS=importdata(filenameS,delimiterIn,headerlinesIn); %import data
SS=sS.data; %Pull the data into a matrix form
T_S=SS(:,1); %year
Op_Temp=SS(:,2); %*C, operating temperature
Accel_Profile=SS(:,3); %acceleration profile to be used for the given time

% %--------Plot the analysis data----------
```

```
% figure(4)
% subplot(2,1,1);stem(T_S,Op_Temp);hold on;stem(T_S,Op_Temp-T0,'r');grid on;
% title('Expected Operating Temperature (Blue); Delta-Temp (Red); (*C)')
% xlabel('Time (yr)'); ylabel('Temperature (*C)');
% subplot(2,1,2);stem(T_S,Accel_Profile,'black');grid on;
% title('Representative Acceleration Profile (#)')
% xlabel('Time (yr)'); ylabel('Acceleration Profile (#)');

%%

%Calculate the normal and tangential acceleration components in 10 degree
%increments for each of the acceleration profiles

%------------------Acceleration Time History #1----------------
An_1(length(Ax_1),35)=0; %initialize the array, set all cells to zero
At_1(length(Ax_1),35)=0; %initialize the array, set all cells to zero
for ii=1:1:36
An_1(:,ii)=Ax_1*cos((ii-1)*10*(pi/180))+Ay_1*sin((ii-1)*10*(pi/180));
At_1(:,ii)=-Ax_1*sin((ii-1)*10*(pi/180))+Ay_1*cos((ii-1)*10*(pi/180));
end
%------------------Acceleration Time History #2----------------
An_2(length(Ax_2),35)=0; %initialize the array, set all cells to zero
At_2(length(Ax_2),35)=0; %initialize the array, set all cells to zero
for ii=1:1:36
An_2(:,ii)=Ax_2*cos((ii-1)*10*(pi/180))+Ay_2*sin((ii-1)*10*(pi/180));
At_2(:,ii)=-Ax_2*sin((ii-1)*10*(pi/180))+Ay_2*cos((ii-1)*10*(pi/180));
end
%------------------Acceleration Time History #3----------------
An_3(length(Ax_3),35)=0; %initialize the array, set all cells to zero
At_3(length(Ax_3),35)=0; %initialize the array, set all cells to zero
for ii=1:1:36
An_3(:,ii)=Ax_3*cos((ii-1)*10*(pi/180))+Ay_3*sin((ii-1)*10*(pi/180));
At_3(:,ii)=-Ax_3*sin((ii-1)*10*(pi/180))+Ay_3*cos((ii-1)*10*(pi/180));
end

% %Plot for output comparison
% L=length(An_2(:,5));
% An40=hamming(L).*An_2(:,5);
% An40_w=fftshift(fft(An40));
% df=fs_2/L;%Hz, the frequency bin width
% f_2=df*((-L/2):1:(L/2)-1);%frequencies corresponding to shifted fft
%
% figure(99)
% subplot(2,1,1);plot(T_2,An_2(:,5));grid on;axis([0 1 -4 4])
% title('AP2; Normal Accel; Theta=40deg');xlabel('Time (sec)');ylabel('Acceleration (m/s2)');
% subplot(2,1,2);plot(f_2,abs(An40_w));grid on;axis([0 40 0 2000])
% title('AP2; Normal Accel; Theta=40deg');xlabel('Freq (Hz)');ylabel('|FFT|');


%%

%Convert the acceleration time histories into displacement Fourier
%transforms
 %The user must input f_truncate
%Amplitudes under f_trancate (Hz) will be set to zero during
%the transformation to avoid the scaling that occurs when dividing the
%acceleration spectrum by -omega^2
f_truncate_1=9;
f_truncate_2=9;
f_truncate_3=9;
```

```
%------------------Acceleration Time History #1---------------
L=length(An_1);%number of time steps
An_1(length(An_1),:)=0;%set the last data point to zero
an_1=fft(An_1);%take fft of time history
an_1_shift=fftshift(an_1);%shift the fft for plotting purposes
df=fs_1/L;%Hz, the frequency bin width
f_1=df*((-L/2):1:(L/2)-1);%frequencies corresponding to shifted fft

%calculate the displacement FFT
d_1_shift=zeros(size(an_1_shift));
for ii=1:1:36 %cycle over all angles 0:10:350
d_1_shift(:,ii)=an_1_shift(:,ii)./((1i*(2*pi*f_1')).^2); %convert the acceleration FFT into a displacement FFT
end

%zero out amplitudes between the +/-frequencies defined by f_truncate
n=round(f_truncate_1/df);
d_1_shift_t=d_1_shift;%define a new variable for truncation
d_1_shift_t(L/2-n:L/2+n,:)=0;%zero out terms that fall within f_truncate

%Calculate displacement response
D1=ifft(fftshift(d_1_shift_t));

% %Plot the FFT's
% figure(5)
% subplot(4,2,1);plot(f_1,abs(an_1_shift(:,1)));grid on;axis([0 max(f_1) 0 max(abs(an_1(:,1)))])
% xlabel('Frequency (Hz)');ylabel('|FFT|');title('Acceleration FFT of AP#1,X-Axis');
% subplot(4,2,3);plot(f_1,abs(d_1_shift(:,1)));grid on;axis([0 max(f_1) 0 max(abs(d_1_shift_t(:,1)))])
% xlabel('Frequency (Hz)');ylabel('|FFT|');title('Unwindowed Displacement FFT of AP#1,X-Axis');
% subplot(4,2,5);plot(f_1,abs(d_1_shift_t(:,1)));grid on;axis([0 max(f_1) 0 max(abs(d_1_shift_t(:,1)))])
% xlabel('Frequency (Hz)');ylabel('|FFT|');title('Windowed Displacement FFT of AP#1,X-Axis');
% subplot(4,2,7);plot(T_1,real(D1(:,1)));grid on;
% xlabel('Time (sec)');ylabel('Displacement (m)');title('Displacement AP#1,X-Axis');
% subplot(4,2,2);plot(f_1,abs(an_1_shift(:,10)));grid on;axis([0 max(f_1) 0 max(abs(an_1(:,10)))])
% xlabel('Frequency (Hz)');ylabel('|FFT|');title('Acceleration FFT of AP#1,Y-Axis');
% subplot(4,2,4);plot(f_1,abs(d_1_shift(:,10)));grid on;axis([0 max(f_1) 0 max(abs(d_1_shift_t(:,10)))])
% xlabel('Frequency (Hz)');ylabel('|FFT|');title('Unwindowed Displacement FFT of AP#1,Y-Axis');
% subplot(4,2,6);plot(f_1,abs(d_1_shift_t(:,10)));grid on;axis([0 max(f_1) 0 max(abs(d_1_shift_t(:,10)))])
% xlabel('Frequency (Hz)');ylabel('|FFT|');title('Windowed Displacement FFT of AP#1,Y-Axis');
% subplot(4,2,8);plot(T_1,real(D1(:,10)));grid on;
% xlabel('Time (sec)');ylabel('Displacement (m)');title('Displacement AP#1,Y-Axis');


%------------------Acceleration Time History #2---------------
L=length(An_2);%number of time steps
An_2(length(An_2),:)=0;%set the last data point to zero
an_2=fft(An_2);%take fft of time history
an_2_shift=fftshift(an_2);%shift the fft for plotting purposes
df=fs_2/L;%Hz, the frequency bin width
f_2=df*((-L/2):1:(L/2)-1);%frequencies corresponding to shifted fft

%calculate the displacement FFT
d_2_shift=zeros(size(an_2_shift));
for ii=1:1:36 %cycle over all angles 0:10:350
d_2_shift(:,ii)=an_2_shift(:,ii)./((1i*(2*pi*f_2')).^2); %convert the acceleration FFT into a displacement FFT
end

%zero out amplitudes between the +/-frequencies defined by f_truncate
n=round(f_truncate_2/df);
d_2_shift_t=d_2_shift;%define a new variable for truncation
```

```
d_2_shift_t(L/2-n:L/2+n,:)=0;%zero out terms that fall within f_truncate

%Calculate displacement response
D2=ifft(fftshift(d_2_shift_t));
%
% %Plot the FFT's
% figure(6)
% subplot(4,2,1);plot(f_2,abs(an_2_shift(:,1)));grid on;axis([0 max(f_2) 0 max(abs(an_2(:,1)))])
% xlabel('Frequency (Hz)');ylabel('|FFT|');title('Acceleration FFT of AP#2,X-Axis');
% subplot(4,2,3);plot(f_2,abs(d_2_shift(:,1)));grid on;axis([0 max(f_2) 0 max(abs(d_2_shift_t(:,1)))])
% xlabel('Frequency (Hz)');ylabel('|FFT|');title('Unwindowed Displacement FFT of AP#2,X-Axis');
% subplot(4,2,5);plot(f_2,abs(d_2_shift_t(:,1)));grid on;axis([0 max(f_2) 0 max(abs(d_2_shift_t(:,1)))])
% xlabel('Frequency (Hz)');ylabel('|FFT|');title('Windowed Displacement FFT of AP#2,X-Axis');
% subplot(4,2,7);plot(T_2,real(D2(:,1)));grid on;
% xlabel('Time (sec)');ylabel('Displacement (m)');title('Displacement AP#2,X-Axis');
% subplot(4,2,2);plot(f_2,abs(an_2_shift(:,10)));grid on;axis([0 max(f_2) 0 max(abs(an_2(:,10)))])
% xlabel('Frequency (Hz)');ylabel('|FFT|');title('Acceleration FFT of AP#2,Y-Axis');
% subplot(4,2,4);plot(f_2,abs(d_2_shift(:,10)));grid on;axis([0 max(f_2) 0 max(abs(d_2_shift_t(:,10)))])
% xlabel('Frequency (Hz)');ylabel('|FFT|');title('Unwindowed Displacement FFT of AP#2,Y-Axis');
% subplot(4,2,6);plot(f_2,abs(d_2_shift_t(:,10)));grid on;axis([0 max(f_2) 0 max(abs(d_2_shift_t(:,10)))])
% xlabel('Frequency (Hz)');ylabel('|FFT|');title('Windowed Displacement FFT of AP#2,Y-Axis');
% subplot(4,2,8);plot(T_2,real(D2(:,10)));grid on;
% xlabel('Time (sec)');ylabel('Displacement (m)');title('Displacement AP#2,Y-Axis');

%------------------Acceleration Time History #3----------------
L=length(An_3);%number of time steps
An_3(length(An_3),:)=0;%set the last data point to zero
an_3=fft(An_3);%take fft of time history
an_3_shift=fftshift(an_3);%shift the fft for plotting purposes
df=fs_3/L;%Hz, the frequency bin width
f_3=df*((-L/2):1:(L/2)-1);%frequencies corresponding to shifted fft

%calculate the displacement FFT
d_3_shift=zeros(size(an_3_shift));
for ii=1:1:36 %cycle over all angles 0:10:350
d_3_shift(:,ii)=an_3_shift(:,ii)./((1i*(2*pi*f_3')).^2); %convert the acceleration FFT into a displacement FFT
end

%zero out amplitudes between the +/-frequencies defined by f_truncate
n=round(f_truncate_3/df);
d_3_shift_t=d_3_shift;%define a new variable for truncation
d_3_shift_t(L/2-n:L/2+n,:)=0;%zero out terms that fall within f_truncate

%Calculate displacement response
D3=ifft(fftshift(d_3_shift_t));

% %Plot the FFT's
% figure(7)
% subplot(4,2,1);plot(f_3,abs(an_3_shift(:,1)));grid on;axis([0 max(f_3) 0 max(abs(an_3(:,1)))])
% xlabel('Frequency (Hz)');ylabel('|FFT|');title('Acceleration FFT of AP#3,X-Axis');
% subplot(4,2,3);plot(f_3,abs(d_3_shift(:,1)));grid on;axis([0 max(f_3) 0 max(abs(d_3_shift_t(:,1)))])
% xlabel('Frequency (Hz)');ylabel('|FFT|');title('Unwindowed Displacement FFT of AP#3,X-Axis');
% subplot(4,2,5);plot(f_3,abs(d_3_shift_t(:,1)));grid on;axis([0 max(f_3) 0 max(abs(d_3_shift_t(:,1)))])
% xlabel('Frequency (Hz)');ylabel('|FFT|');title('Windowed Displacement FFT of AP#3,X-Axis');
% subplot(4,2,7);plot(T_3,real(D3(:,1)));grid on;
% xlabel('Time (sec)');ylabel('Displacement (m)');title('Displacement AP#3,X-Axis');
% subplot(4,2,2);plot(f_3,abs(an_3_shift(:,10)));grid on;axis([0 max(f_3) 0 max(abs(an_3(:,10)))])
% xlabel('Frequency (Hz)');ylabel('|FFT|');title('Acceleration FFT of AP#3,Y-Axis');
% subplot(4,2,4);plot(f_3,abs(d_3_shift(:,10)));grid on;axis([0 max(f_3) 0 max(abs(d_3_shift_t(:,10)))])
% xlabel('Frequency (Hz)');ylabel('|FFT|');title('Unwindowed Displacement FFT of AP#3,Y-Axis');
```

```
% subplot(4,2,6);plot(f_3,abs(d_3_shift_t(:,10)));grid on;axis([0 max(f_3) 0 max(abs(d_3_shift_t(:,10)))])
% xlabel('Frequency (Hz)');ylabel('|FFT|');title('Windowed Displacement FFT of AP#3,Y-Axis');
% subplot(4,2,8);plot(T_3,real(D3(:,10)));grid on;
% xlabel('Time (sec)');ylabel('Displacement (m)');title('Displacement AP#3,Y-Axis');
%%
%Define the window of time the user wants to maximize the possible energy
%production.  This could be the entire life-cycle or some smaller window
%(e.g. from 3.4yr - 4.6yr).  For example T_opt=[2.1;3.3] means that the
%user wants to optimize the energy output starting at year 2.1 and ending
%at the start of year 3.3.
 %The user must update T_opt

T_opt=[1.5;3.0];%years, window of time the user wants to optimize energy output

%extract the times of interest
T_initial=T_opt(1); %year, isolate the initial time increment to analyze
T_final=T_opt(2); %year, isolate the final time increment to analyze.
%Note that we'll end up integrating over the final dt_S which gives us the
%user desired 'final' operating time

%%
%User defines the number of harvesters and the relative locations (of their
%base) for(1)normal, (2)tangential, and (3) vertical piezoelectric
%orientations.  Angle the piezoelectric in 10 degree increments.  Use only
%positive angles.

P_o_n=[1 0; 2 40; 3 90]; %a matrix representing the number (first column)
%and orientation angle alpha (second column) for normally configured
%piezoelectrics: P_o_n=[1 40; 2 120; 3 350] means piezoelectric #2 is
%120degrees from the global X-axis

%based on the user specified EH locations, determine relative location of
%EH when the pipe is rotated through 360deg
E1_loc_index=zeros(1,36);
E2_loc_index=zeros(1,36);
E3_loc_index=zeros(1,36);
for alpha_index=1:1:36
alpha=(alpha_index)*10; %deg, pipe rotation angle
E1_loc=P_o_n(1,2)+alpha; %deg, location of EH1 including pipe rotation
if E1_loc>365
E1_loc=E1_loc-360; %adjust angle to 0:360
end
E1_loc_index(alpha_index)=E1_loc/10;% index location of EH1 including pipe rotation

E2_loc=P_o_n(2,2)+alpha; %deg, location of EH1 including pipe rotation
if E2_loc>365
E2_loc=E2_loc-360; %adjust angle to 0:360
end
E2_loc_index(alpha_index)=E2_loc/10;% index location of EH1 including pipe rotation

E3_loc=P_o_n(3,2)+alpha; %deg, location of EH1 including pipe rotation
if E3_loc>365
E3_loc=E3_loc-360; %adjust angle to 0:360
end
E3_loc_index(alpha_index)=E3_loc/10;% index location of EH1 including pipe rotation
end

%%
%specify the harvester base frequencies of interest
%The user must update f_n_lower, f_n_limit, d_f_n
```

```
%----------------Harvesters Oriented in Normal Direction----------------
f_n_lower=13;%Hz, this is the minimum EH frequency at room temp. considered
f_n_limit=22;%Hz, this is the maximum EH frequency at room temp. considered
d_f_n=0.5;%Hz, this is the increment the EH base frequencies are cycled through

%%

%specify the damping ratios to be considered

zeta_m=0.03;%mechanical damping ratio (single scalar)
zeta_e_lower=0.01;%lower limit of electric damping
zeta_e_upper=0.09;%upper limit of electric damping
zeta_e_diff=0.02;%descritization of electric damping
zeta_e=zeta_e_lower:zeta_e_diff:zeta_e_upper; %electric damping ratio

zeta_eq=zeta_m*ones(length(zeta_e),1)+zeta_e'; %equivalent damping ratio

%%

%Loop over all relevant frequencies, accounting for time/temperature
%effects based on the given temperature profile to determine terms needed
%to calculate power

%initialize matricies
EH_wn_adj=zeros(round((T_final-T_initial)/dt_S+1),round((f_n_limit-f_n_lower)/d_f_n+1));
z_max=zeros(round((T_final-T_initial)/dt_S+1),round((f_n_limit-f_n_lower)/d_f_n+1),length(zeta_eq),36);
P_int=zeros(round((T_final-T_initial)/dt_S+1),round((f_n_limit-f_n_lower)/d_f_n+1),length(zeta_eq),36);
P_avg_nome=zeros(round((T_final-T_initial)/dt_S+1),round((f_n_limit-f_n_lower)/d_f_n+1),length(zeta_eq),36);


for time_index=1:1:round((T_final-T_initial)/dt_S+1) %time in terms of the array index number
time=T_initial+(time_index-1)*dt_S; %years, represents current time
C_Temp=Op_Temp(round(time/dt_S+1)); %*C, the current operating temperature
AP=Accel_Profile(round(time/dt_S+1));%Identify the current accel profile

%Young's Modulus adjustment factor for time/temperature effects
d_M=MODULUS_TimeTempDependence(time,C_Temp)/100;%Percent of inital
%Inertia adjustment factor for time/temperature effects
d_I=INERTIA_TimeTempDependence(time,C_Temp)/100;%Percent of inital
%Length accounting for time/temperature effects
d_L=LENGTH_TimeTempDependence(time,C_Temp)/100;%Percent of inital

%Loop over the basic/room temperature natural frequencies
for EH_fn_index=1:1:round((f_n_limit-f_n_lower)/d_f_n+1) %loop over all base/unaltered nat freq.
%convert the index number to the actual base frequency investigated
EH_fn=(EH_fn_index-1)*d_f_n+f_n_lower; %Hz

%adjust current natural frequency for time/temp dependence
EH_fn_adj=EH_fn*(sqrt(d_M*d_I/d_L^3)); %Hz;
EH_wn_adj(time_index,EH_fn_index)=2*pi*EH_fn_adj; %rad/sec...
%this is stored as it will be needed for c_eq calc

%determine the frequency spacing and Fourier coefficients of Y(w)
%corresponding to the current acceleration profile (AP)
if AP==1
fnn=f_1; %Hz, frequencies corresponding to Fourier coefficients
Y_w=d_1_shift_t; %Fourier coefficients (truncated at lower freqs)
dt=dt_1; %sec, time step for displacement and velocity
end
```

```
if AP==2
fnn=f_2; %Hz, frequencies corresponding to Fourier coefficients
Y_w=d_2_shift_t; %Fourier coefficients (truncated at lower freqs)
dt=dt_2; %sec, time step for displacement and velocity
end
if AP==3
fnn=f_3; %Hz, frequencies corresponding to Fourier coefficients
Y_w=d_3_shift_t; %Fourier coefficients (truncated at lower freqs)
dt=dt_3; %sec, time step for displacement and velocity
end
%convert the frequency spacing to radial frequency
wnn=2*pi*fnn; %rad/s
t_range=(0:1:length(wnn)-1)*dt;

%Loop over the considered damping ratios (zeta_eq)
for zeta_indexEQ=1:1:length(zeta_eq)
zetaEQ=zeta_eq(zeta_indexEQ);%the current equivalent damping ratio in %

%calculate the transfer functions at a frequency spacing
%corresponding to the Fourier coefficients
H_w=wnn.^2./((EH_wn_adj(time_index,EH_fn_index)^2-
wnn.^2)+2*zetaEQ*EH_wn_adj(time_index,EH_fn_index)*1i.*wnn);

%loop over all global angle axis (i.e. global pipe rotation).  The angles
%considered are 0:10:350 degrees which, for 10 degree increments corresponds
%to 1:1:36
for theta_index=1:1:36 %global angle index
theta=(theta_index-1)*10; %degrees, global angle

%Calculate the displacement response in frequency domain Z(w)
Z_w=H_w'.*Y_w(:,theta_index);

%Calculate the displacement response in the time domain
%z(t)
z=ifft(fftshift(Z_w));%m

%truncate the displacement response so that anomalies near
%the start/end are not included; this is a consequence of
%calculating Y(w) in the frequency domain
z_t=z(round(0.05*length(z)):round(0.95*length(z)));%m
%store the maximum amplitude displacement
z_max(time_index,EH_fn_index,zeta_indexEQ,theta_index)=max(max(real(z_t)),abs(min(real(z_t))));%m

%calculate the velocity of z in the frequency domain
Z_w_velo=i*wnn'.*Z_w;

%calculate the velocity of z in the time domain
z_velo=ifft(fftshift(Z_w_velo));%m/s

%truncate the displacement response so that anomalies near
%the start/end are not included; this is a consequence of
%calculating Y(w) in the frequency domain
z_velo_t=z_velo(round(0.05*length(z_velo)):round(0.95*length(z_velo)));%m/s
%calculate the point-wise square of the velocity
z_velo_t_s=real(z_velo_t).^2;%m/s
%summerize the times of interest
t_t=(0:1:length(z_velo_t_s)-1)*dt;%s, the time window corresponding to z_velo_t_s
t_f=(length(z_velo_t_s)-1)*dt;%s, the final time corresponding to z_velo_t_s

%calc the average power integral over the truncated range
```

```
%(i.e., P_avg,e = c_eq * P_int
P_int(time_index,EH_fn_index,zeta_indexEQ,theta_index)=trapz(t_t,z_velo_t_s)/t_f;

%Determine the mass and electric damping ratio -normalized electric power for all global angles (theta)
%this is the integral of velocity squared, divided by T,
%multiplied by 2 * current natural frequency
P_avg_nome(time_index,EH_fn_index,zeta_indexEQ,theta_index)=2*EH_wn_adj(time_index,EH_fn_index)*P_int(
time_index,EH_fn_index,zeta_indexEQ,theta_index);
end
end
end
end


%%

%Define the equivalent mass for each EH.  For initial estimates (when
%determining the ideal natural frequency) you can use m_e1=1.  Once you
%know the base frequency and have looked at commercially available
%products (and know the actuall stiffness), re-run with the actual mass to
%improve power estimates.

m_tip1=0.15;%kg
m_beam1=0.04;%kg
m_eq1=(33/140)*m_beam1+m_tip1;%kg

m_tip2=0.2;%kg
m_beam2=0.04;%kg
m_eq2=(33/140)*m_beam2+m_tip2;%kg

m_tip3=0.2;%kg
m_beam3=0.04;%kg
m_eq3=(33/140)*m_beam3+m_tip3;%kg


%%
%Determine the power estimate for each EH as a function of alpha - include
%the equivalent mass and electric damping ratio for each EH.

P_avg_me_1=zeros(round((T_final-T_initial)/dt_S+1),round((f_n_limit-f_n_lower)/d_f_n+1),length(zeta_eq),36);
P_avg_me_2=zeros(round((T_final-T_initial)/dt_S+1),round((f_n_limit-f_n_lower)/d_f_n+1),length(zeta_eq),36);
P_avg_me_3=zeros(round((T_final-T_initial)/dt_S+1),round((f_n_limit-f_n_lower)/d_f_n+1),length(zeta_eq),36);

for zeta_index=1:1:length(zeta_eq) %loop over all damping ratios.  Since the equivalent damping and
for EH_fn_index=1:1:round((f_n_limit-f_n_lower)/d_f_n+1) %loop over all base/unaltered nat freq.
for time_index=1:1:round((T_final-T_initial)/dt_S+1) %time in terms of the array index number
for alpha_index=1:1:36 %global angle index
P_avg_me_1(time_index,EH_fn_index,zeta_index,alpha_index)=m_eq1*zeta_e(zeta_index)*P_avg_nome(time_inde
x,EH_fn_index,zeta_index,E1_loc_index(alpha_index));
P_avg_me_2(time_index,EH_fn_index,zeta_index,alpha_index)=m_eq2*zeta_e(zeta_index)*P_avg_nome(time_inde
x,EH_fn_index,zeta_index,E2_loc_index(alpha_index));
P_avg_me_3(time_index,EH_fn_index,zeta_index,alpha_index)=m_eq3*zeta_e(zeta_index)*P_avg_nome(time_inde
x,EH_fn_index,zeta_index,E3_loc_index(alpha_index));
end
end
end
end

%%
```

```
%determine the total power estimate for each alpha realization
%time,fn1,fn2,fn3,zeta_e1,zeta_e2,zeta_e3,alpha
P_avg_me_tot=zeros(round((T_final-T_initial)/dt_S+1),round((f_n_limit-f_n_lower)/d_f_n+1),round((f_n_limit-
f_n_lower)/d_f_n+1),round((f_n_limit-f_n_lower)/d_f_n+1),length(zeta_e),length(zeta_e),length(zeta_e),36);

for zeta_index1=1:1:length(zeta_e) %loop over all damping ratios for EH1
for zeta_index2=1:1:length(zeta_e) %loop over all damping ratios for EH2
for zeta_index3=1:1:length(zeta_e) %loop over all damping ratios for EH3
for time_index=1:1:round((T_final-T_initial)/dt_S+1) %time in terms of the array index number
for alpha_index=1:1:36 %global angle index
for EH_fn1_index=1:1:round((f_n_limit-f_n_lower)/d_f_n+1) %loop over all base/unaltered nat freq.
for EH_fn2_index=1:1:round((f_n_limit-f_n_lower)/d_f_n+1) %loop over all base/unaltered nat freq.
for EH_fn3_index=1:1:round((f_n_limit-f_n_lower)/d_f_n+1) %loop over all base/unaltered nat freq.
P_avg_me_tot(time_index,EH_fn1_index,EH_fn2_index,EH_fn3_index,zeta_index1,zeta_index2,zeta_index3,alpha_
index)=P_avg_me_1(time_index,EH_fn1_index,zeta_index1,alpha_index)+P_avg_me_2(time_index,EH_fn2_index,
zeta_index2,alpha_index)+P_avg_me_3(time_index,EH_fn3_index,zeta_index3,alpha_index);
end
end
end
end
end
end
end
end

%%

%integrate the total power over time
%fn1,fn2,fn3,zeta_e1,zeta_e2,zeta_e3,alpha
P_avg_me_tot_int=zeros(round((f_n_limit-f_n_lower)/d_f_n+1),round((f_n_limit-
f_n_lower)/d_f_n+1),round((f_n_limit-f_n_lower)/d_f_n+1),length(zeta_e),length(zeta_e),length(zeta_e),36);

for zeta_index1=1:1:length(zeta_e) %loop over all damping ratios for EH1
for zeta_index2=1:1:length(zeta_e) %loop over all damping ratios for EH2
for zeta_index3=1:1:length(zeta_e) %loop over all damping ratios for EH3
for alpha_index=1:1:36 %global angle index
for EH_fn1_index=1:1:round((f_n_limit-f_n_lower)/d_f_n+1) %loop over all base/unaltered nat freq.
for EH_fn2_index=1:1:round((f_n_limit-f_n_lower)/d_f_n+1) %loop over all base/unaltered nat freq.
for EH_fn3_index=1:1:round((f_n_limit-f_n_lower)/d_f_n+1) %loop over all base/unaltered nat freq.
P_avg_me_tot_int(EH_fn1_index,EH_fn2_index,EH_fn3_index,zeta_index1,zeta_index2,zeta_index3,alpha_index)=
trapz(P_avg_me_tot(:,EH_fn1_index,EH_fn2_index,EH_fn3_index,zeta_index1,zeta_index2,zeta_index3,alpha_inde
x))*dt_S;
end
end
end
end
end
end
end

%%

%determine optimal base natural frequencies for global angles alpha

%initialize vectors
Optimal_Base_Freq1=zeros(36,1);
Optimal_Base_Freq2=zeros(36,1);
Optimal_Base_Freq3=zeros(36,1);
Optimal_zeta_e1=zeros(36,1);
Optimal_zeta_e2=zeros(36,1);
```

```
Optimal_zeta_e3=zeros(36,1);
P_avg_me_tot_opt=zeros(36,1);


for alpha_index=1:1:36 %global angle index
%determine the frequency index and zeta_e for EH1, 2, 3

%corresponds to zeta_e for EH3
[Pn6,In6]=max(max(max(max(max(max(P_avg_me_tot_int(:,:,:,:,:,:,:,alpha_index)))))));
%corresponds to zeta_e for EH2
[Pn5,In5]=max(max(max(max(max(P_avg_me_tot_int(:,:,:,:,:,In6,alpha_index))))));
%corresponds to zeta_e for EH3
[Pn4,In4]=max(max(max(max(P_avg_me_tot_int(:,:,:,:,In5,In6,alpha_index)))));
%corresponds to fnbase for EH3
[Pn3,In3]=max(max(max(P_avg_me_tot_int(:,:,:,In4,In5,In6,alpha_index))));
%corresponds to fnbase for EH2
[Pn2,In2]=max(max(P_avg_me_tot_int(:,:,In3,In4,In5,In6,alpha_index)));
%corresponds to fnbase for EH1
[Pn1,In1]=max(P_avg_me_tot_int(:,In2,In3,In4,In5,In6,alpha_index));


%convert frequency index to actual frequencies (Hz)
Optimal_Base_Freq1(alpha_index)=((In1-1)*d_f_n+f_n_lower); %Hz
Optimal_Base_Freq2(alpha_index)=((In2-1)*d_f_n+f_n_lower); %Hz
Optimal_Base_Freq3(alpha_index)=((In3-1)*d_f_n+f_n_lower); %Hz
Optimal_zeta_e1(alpha_index)=zeta_e(In4);
Optimal_zeta_e2(alpha_index)=zeta_e(In5);
Optimal_zeta_e3(alpha_index)=zeta_e(In6);
%Power output at optimal base frequencies
P_avg_me_tot_opt(alpha_index)=P_avg_me_tot_int(In1,In2,In3,In4,In5,In6,alpha_index);

end


%%
%plot table of results
Alpha_deg=[0:10:350]'; %degrees, global rotation angle
fn_1_Hz=Optimal_Base_Freq1(:); %Hz, optimal base frequencies
fn_2_Hz=Optimal_Base_Freq2(:); %Hz, optimal base frequencies
fn_3_Hz=Optimal_Base_Freq3(:); %Hz, optimal base frequencies
Zeta_e1=Optimal_zeta_e1(:);%optimal electric damping ratio
Zeta_e2=Optimal_zeta_e2(:);%optimal electric damping ratio
Zeta_e3=Optimal_zeta_e3(:);%optimal electric damping ratio
Tot_Avg_E_Power_mWattYr=(1000)*P_avg_me_tot_opt(:); %Watt, power output

%determine maximum displacements
EH_fn_index1=(fn_1_Hz-f_n_lower)/d_f_n+1;%determine index number for frequencies
EH_fn_index2=(fn_2_Hz-f_n_lower)/d_f_n+1;%determine index number for frequencies
EH_fn_index3=(fn_3_Hz-f_n_lower)/d_f_n+1;%determine index number for frequencies
zeta_e_index1=round((Zeta_e1-zeta_e_lower)/zeta_e_diff+1);%determine index number for damping
zeta_e_index2=round((Zeta_e2-zeta_e_lower)/zeta_e_diff+1);%determine index number for damping
zeta_e_index3=round((Zeta_e3-zeta_e_lower)/zeta_e_diff+1);%determine index number for damping
%initialize vectors
Max_Disp1=zeros(36,1);
Max_Disp2=zeros(36,1);
Max_Disp3=zeros(36,1);
for ii=1:1:36
Max_Disp1(ii)=max(z_max(:,EH_fn_index1(ii),zeta_e_index1(ii),E1_loc_index(ii)));
Max_Disp2(ii)=max(z_max(:,EH_fn_index2(ii),zeta_e_index2(ii),E2_loc_index(ii)));
Max_Disp3(ii)=max(z_max(:,EH_fn_index3(ii),zeta_e_index3(ii),E3_loc_index(ii)));
```

```
end
%reorient for table/plotting purposes
 Max_Disp1_mm=(1000)*Max_Disp1;
 Max_Disp2_mm=(1000)*Max_Disp2;
 Max_Disp3_mm=(1000)*Max_Disp3;

T=table(Alpha_deg,fn_1_Hz,Max_Disp1_mm,Zeta_e1,fn_2_Hz,Max_Disp2_mm,Zeta_e2,fn_3_Hz,Max_Disp3_mm
,Zeta_e3,Tot_Avg_E_Power_mWattYr)

%%
%plot power as a function of time for a given realization

alpha_index=10;%determine index number for rotation angle alpha

EH_fn1_index=12;%determine index number for frequency
EH_fn2_index=10;%determine index number for frequency
EH_fn3_index=9;%determine index number for frequency

zeta_e_index1=3;%determine index number for damping
zeta_e_index2=4;%determine index number for damping
zeta_e_index3=2;%determine index number for damping

figure(100)
%total power (mWatt)
subplot(1,3,1);plot(T_initial:dt_S:T_final,1000*P_avg_me_tot(:,EH_fn1_index,EH_fn2_index,EH_fn3_index,zeta_e
_index1,zeta_e_index2,zeta_e_index3,alpha_index),'black');grid on;
xlabel('Time (yr)');ylabel('Power (mWatt)');axis([T_initial T_final 0 60])
%individual harvester power
subplot(1,3,2);plot(T_initial:dt_S:T_final,1000*P_avg_me_1(:,EH_fn1_index,zeta_e_index1,alpha_index),'b'); hold
on; grid on;
xlabel('Time (yr)');ylabel('Power (mWatt)');axis([T_initial T_final 0 60]);
plot(T_initial:dt_S:T_final,1000*P_avg_me_2(:,EH_fn2_index,zeta_e_index2,alpha_index),'g');hold on;
plot(T_initial:dt_S:T_final,1000*P_avg_me_3(:,EH_fn3_index,zeta_e_index3,alpha_index),'r'); hold on;
%individual harvester max uni-directional displacement
subplot(1,3,3);plot(T_initial:dt_S:T_final,1000*z_max(:,EH_fn1_index,zeta_e_index1,
E1_loc_index(alpha_index)),'b'); hold on; grid on;
xlabel('Time (yr)');ylabel('Max Displacement (mm)');axis([T_initial T_final 0 3]);
plot(T_initial:dt_S:T_final,1000*z_max(:,EH_fn2_index,zeta_e_index2,E2_loc_index(alpha_index)),'g');hold on;
plot(T_initial:dt_S:T_final,1000*z_max(:,EH_fn3_index,zeta_e_index3,E3_loc_index(alpha_index)),'r'); hold on;
```

Appendix I – MATLAB Script Supporting SS Analysis

```
clear;clc;
tic%start timer to determine duration of script
i=sqrt(-1); %imaginary unit
%%
%Reference in the representative user defined periodic acceleration time
%history profiles.  For this work, three acceleration profiles will be used.

%THE TIME HISTORIES SHOULD BE EVEN LENGTH (I.E. NOT ODD)

%The first line of the input file should contain the time step
%Numeric entries should start on the fourth line
%Column 1 - Time
%Column 2 - Acceleration (in m/s2)

%------Acceleration Time History #1---------
%Reference the file
filename1='Acceleration_Input_1_p2.txt'; %define the file name
delimiterIn='\t'; %define the spacing in the file
%Import the time step (dt)
headerlinesIn=0; %define the number of header lines
s1=importdata(filename1,delimiterIn,headerlinesIn); %import data
dt_1=s1.data(1); %Pull the data into a matrix form
fs_1=1/dt_1; %Hz, the sampling rate obtained from the input file
%Import acceleration data
headerlinesIn=3; %define the number of header lines
s1=importdata(filename1,delimiterIn,headerlinesIn); %import data
S1=s1.data; %Pull the data into a matrix form
T_1=S1(:,1); %time
A_1=S1(:,2); %m/s2, acceleration

%------Acceleration Time History #2---------
%Reference the file
filename2='Acceleration_Input_2_p2.txt'; %define the file name
delimiterIn='\t'; %define the spacing in the file
%Import the time step (dt)
headerlinesIn=0; %define the number of header lines
s2=importdata(filename2,delimiterIn,headerlinesIn); %import data
dt_2=s2.data(1); %Pull the data into a matrix form
```

```
fs_2=1/dt_2; %Hz, the sampling rate obtained from the input file
%Import acceleration data
headerlinesIn=3; %define the number of header lines
s2=importdata(filename2,delimiterIn,headerlinesIn); %import data
S2=s2.data; %Pull the data into a matrix form
T_2=S2(:,1); %time
A_2=S2(:,2); %m/s2, acceleration

%------Acceleration Time History #3---------
%Reference the file
filename3='Acceleration_Input_3_p2.txt'; %define the file name
delimiterIn='\t'; %define the spacing in the file
%Import the time step (dt)
headerlinesIn=0; %define the number of header lines
s3=importdata(filename3,delimiterIn,headerlinesIn); %import data
dt_3=s3.data(1); %Pull the data into a matrix form
fs_3=1/dt_3; %Hz, the sampling rate obtained from the input file
%Import acceleration data
headerlinesIn=3; %define the number of header lines
s3=importdata(filename3,delimiterIn,headerlinesIn); %import data
S3=s3.data; %Pull the data into a matrix form
T_3=S3(:,1); %time
A_3=S3(:,2); %m/s2, acceleration

%------Acceleration Time History #4---------
%Reference the file
filename4='Acceleration_Input_4_p2.txt'; %define the file name
delimiterIn='\t'; %define the spacing in the file
%Import the time step (dt)
headerlinesIn=0; %define the number of header lines
s4=importdata(filename4,delimiterIn,headerlinesIn); %import data
dt_4=s4.data(1); %Pull the data into a matrix form
fs_4=1/dt_4; %Hz, the sampling rate obtained from the input file
%Import acceleration data
headerlinesIn=3; %define the number of header lines
s4=importdata(filename4,delimiterIn,headerlinesIn); %import data
S4=s4.data; %Pull the data into a matrix form
T_4=S4(:,1); %time
A_4=S4(:,2); %m/s2, acceleration

%------Acceleration Time History #5---------
%Reference the file
filename5='Acceleration_Input_5_p2.txt'; %define the file name
delimiterIn='\t'; %define the spacing in the file
%Import the time step (dt)
headerlinesIn=0; %define the number of header lines
s5=importdata(filename5,delimiterIn,headerlinesIn); %import data
dt_5=s5.data(1); %Pull the data into a matrix form
fs_5=1/dt_5; %Hz, the sampling rate obtained from the input file
%Import acceleration data
headerlinesIn=3; %define the number of header lines
s5=importdata(filename5,delimiterIn,headerlinesIn); %import data
S5=s5.data; %Pull the data into a matrix form
T_5=S5(:,1); %time
A_5=S5(:,2); %m/s2, acceleration

% %--------Plot the raw time histories------------
% figure(1) %Acceleration Profiles
% subplot(5,2,1);plot(T_1,A_1);grid on;
% axis([0 T_1(length(T_1)) min(A_1) max(A_1)]);
```

```
% title('Time History 1');xlabel('Time (sec)');ylabel('Acceleration (m/s^2)');
% subplot(5,2,2);plot(T_1(1:500),A_1(1:500));grid on;
% axis([0 1 min(A_1) max(A_1)]);
% title('Time History 1');xlabel('Time (sec)');ylabel('Acceleration (m/s^2)');
% subplot(5,2,3);plot(T_2,A_2);grid on;
% axis([0 T_2(length(T_2)) min(A_2) max(A_2)]);
% title('Time History 2');xlabel('Time (sec)');ylabel('Acceleration (m/s^2)');
% subplot(5,2,4);plot(T_2(1:500),A_2(1:500));grid on;
% axis([0 1 min(A_2) max(A_2)]);
% title('Time History 2');xlabel('Time (sec)');ylabel('Acceleration (m/s^2)');
% subplot(5,2,5);plot(T_3,A_3);grid on;
% axis([0 T_3(length(T_3)) min(A_3) max(A_3)]);
% title('Time History 3');xlabel('Time (sec)');ylabel('Acceleration (m/s^2)');
% subplot(5,2,6);plot(T_3(1:500),A_3(1:500));grid on;
% axis([0 1 min(A_3) max(A_3)]);
% title('Time History 3');xlabel('Time (sec)');ylabel('Acceleration (m/s^2)');
% subplot(5,2,7);plot(T_4,A_4);grid on;
% axis([0 T_4(length(T_4)) min(A_4) max(A_4)]);
% title('Time History 4');xlabel('Time (sec)');ylabel('Acceleration (m/s^2)');
% subplot(5,2,8);plot(T_4(1:500),A_4(1:500));grid on;
% axis([0 1 min(A_4) max(A_4)]);
% title('Time History 4');xlabel('Time (sec)');ylabel('Acceleration (m/s^2)');
% subplot(5,2,9);plot(T_5,A_5);grid on;
% axis([0 T_5(length(T_5)) min(A_5) max(A_5)]);
% title('Time History 5');xlabel('Time (sec)');ylabel('Acceleration (m/s^2)');
% subplot(5,2,10);plot(T_5(1:500),A_5(1:500));grid on;
% axis([0 1 min(A_5) max(A_5)]);
% title('Time History 5');xlabel('Time (sec)');ylabel('Acceleration (m/s^2)');

%--------Clear Variables------------
clearvars filename1 delimiterIn headerlinesIn s1 S1
clearvars filename2 delimiterIn headerlinesIn s2 S2
clearvars filename3 delimiterIn headerlinesIn s3 S3
clearvars filename4 delimiterIn headerlinesIn s4 S4
clearvars filename5 delimiterIn headerlinesIn s5 S5
%%
clearvars N1 nmax1 T1 a1 b1 A_1est nn kk
clearvars N2 nmax2 T2 a2 b2 A_2est nn kk
clearvars N3 nmax3 T3 a3 b3 A_3est nn kk
clearvars N4 nmax4 T4 a4 b4 A_4est nn kk
clearvars N5 nmax5 T5 a5 b5 A_5est nn kk

%Calculate Fourier Series coefficients for periodic signal. a_0 is assumed
%to be zero.

%------Acceleration Time History #1---------
N1=500;%The number of coefficient pairs (exact for N=nmax)
nmax1=length(T_1);%number of samples in the signal
T1=T_1(length(T_1));%s, the maximum time included in the signal
%initialize matricies
a1(:)=zeros(1,N1);%a Fourier Series coefficients
b1(:)=zeros(1,N1);%b Fourier Series coefficients
A_1est=zeros(1,nmax1);%Fourier Series estimate of signal
%calculatute Fourier Series coefficients
for nn=1:1:nmax1
for kk=1:1:N1
a1(kk)=a1(kk)+(2/nmax1)*(A_1(nn)*cos(2*(kk)*pi*nn/nmax1));
b1(kk)=b1(kk)+(2/nmax1)*(A_1(nn)*sin(2*(kk)*pi*nn/nmax1));
end
end
```

```
%calculateFourier Series estimate of signal
for nn=1:1:nmax1
for kk=1:1:N1
A_1est(nn)=A_1est(nn)+a1(kk)*cos(2*(kk)*pi*nn/nmax1)+b1(kk)*sin(2*(kk)*pi*nn/nmax1);
end
end

%------Acceleration Time History #2---------
N2=600;%The number of coefficient pairs (exact for N=nmax)
nmax2=length(T_2);%number of samples in the signal
T2=T_2(length(T_2));%s, the maximum time included in the signal
%initialize matricies
a2(:)=zeros(1,N2);%a Fourier Series coefficients
b2(:)=zeros(1,N2);%b Fourier Series coefficients
A_2est=zeros(1,nmax2);%Fourier Series estimate of signal
%calculatute Fourier Series coefficients
for nn=1:1:nmax2
for kk=1:1:N2
a2(kk)=a2(kk)+(2/nmax2)*(A_2(nn)*cos(2*(kk)*pi*nn/nmax2));
b2(kk)=b2(kk)+(2/nmax2)*(A_2(nn)*sin(2*(kk)*pi*nn/nmax2));
end
end
%calculateFourier Series estimate of signal
for nn=1:1:nmax2
for kk=1:1:N2
A_2est(nn)=A_2est(nn)+a2(kk)*cos(2*(kk)*pi*nn/nmax2)+b2(kk)*sin(2*(kk)*pi*nn/nmax2);
end
end

%------Acceleration Time History #3---------
N3=600;%The number of coefficient pairs (exact for N=nmax)
nmax3=length(T_3);%number of samples in the signal
T3=T_3(length(T_3));%s, the maximum time included in the signal
%initialize matricies
a3(:)=zeros(1,N3);%a Fourier Series coefficients
b3(:)=zeros(1,N3);%b Fourier Series coefficients
A_3est=zeros(1,nmax3);%Fourier Series estimate of signal
%calculatute Fourier Series coefficients
for nn=1:1:nmax3
for kk=1:1:N3
a3(kk)=a3(kk)+(2/nmax3)*(A_3(nn)*cos(2*(kk)*pi*nn/nmax3));
b3(kk)=b3(kk)+(2/nmax3)*(A_3(nn)*sin(2*(kk)*pi*nn/nmax3));
end
end
%calculateFourier Series estimate of signal
for nn=1:1:nmax3
for kk=1:1:N3
A_3est(nn)=A_3est(nn)+a3(kk)*cos(2*(kk)*pi*nn/nmax3)+b3(kk)*sin(2*(kk)*pi*nn/nmax3);
end
end

%------Acceleration Time History #4---------
N4=500;%The number of coefficient pairs (exact for N=nmax)
nmax4=length(T_4);%number of samples in the signal
T4=T_4(length(T_4));%s, the maximum time included in the signal
%initialize matricies
a4(:)=zeros(1,N4);%a Fourier Series coefficients
b4(:)=zeros(1,N4);%b Fourier Series coefficients
A_4est=zeros(1,nmax4);%Fourier Series estimate of signal
%calculatute Fourier Series coefficients
```

```
for nn=1:1:nmax4
for kk=1:1:N4
a4(kk)=a4(kk)+(2/nmax4)*(A_4(nn)*cos(2*(kk)*pi*nn/nmax4));
b4(kk)=b4(kk)+(2/nmax4)*(A_4(nn)*sin(2*(kk)*pi*nn/nmax4));
end
end
%calculateFourier Series estimate of signal
for nn=1:1:nmax4
for kk=1:1:N4
A_4est(nn)=A_4est(nn)+a4(kk)*cos(2*(kk)*pi*nn/nmax4)+b4(kk)*sin(2*(kk)*pi*nn/nmax4);
end
end

%------Acceleration Time History #5---------
N5=500;%The number of coefficient pairs (exact for N=nmax)
nmax5=length(T_5);%number of samples in the signal
T5=T_5(length(T_5));%s, the maximum time included in the signal
%initialize matricies
a5(:)=zeros(1,N5);%a Fourier Series coefficients
b5(:)=zeros(1,N5);%b Fourier Series coefficients
A_5est=zeros(1,nmax5);%Fourier Series estimate of signal
%calculatute Fourier Series coefficients
for nn=1:1:nmax5
for kk=1:1:N5
a5(kk)=a5(kk)+(2/nmax5)*(A_5(nn)*cos(2*(kk)*pi*nn/nmax5));
b5(kk)=b5(kk)+(2/nmax5)*(A_5(nn)*sin(2*(kk)*pi*nn/nmax5));
end
end
%calculateFourier Series estimate of signal
for nn=1:1:nmax5
for kk=1:1:N5
A_5est(nn)=A_5est(nn)+a5(kk)*cos(2*(kk)*pi*nn/nmax5)+b5(kk)*sin(2*(kk)*pi*nn/nmax5);
end
end

% %--------Plot the Estimated Time Histories------------
% %plot the time histories to ensure sufficient coefficient pairs used.  IF
% %there is a poor match, increase the size N.
% figure(2)
% subplot(5,1,1);plot(T_1,A_1);hold on;grid on;
% plot(T_1,A_1est,'r-.');
% title('Time History 1; B=Actual; R=Estimate');
% xlabel('Time (sec)');ylabel('Acceleration (m/s^2)');
% subplot(5,1,2);plot(T_2,A_2);hold on;grid on;
% plot(T_2,A_2est,'r-.');
% title('Time History 2; B=Actual; R=Estimate');
% xlabel('Time (sec)');ylabel('Acceleration (m/s^2)');
% subplot(5,1,3);plot(T_3,A_3);hold on;grid on;
% plot(T_3,A_3est,'r-.');
% title('Time History 3; B=Actual; R=Estimate');
% xlabel('Time (sec)');ylabel('Acceleration (m/s^2)');
% subplot(5,1,4);plot(T_4,A_4);hold on;grid on;
% plot(T_4,A_4est,'r-.');
% title('Time History 4; B=Actual; R=Estimate');
% xlabel('Time (sec)');ylabel('Acceleration (m/s^2)');
% subplot(5,1,5);plot(T_5,A_5);hold on;grid on;
% plot(T_5,A_5est,'r-.');
% title('Time History 5; B=Actual; R=Estimate');
% xlabel('Time (sec)');ylabel('Acceleration (m/s^2)');
```

```
%--------Clear Variables------------
clearvars A_1est nn kk nmax1
clearvars A_2est nn kk nmax2
clearvars A_3est nn kk nmax3
clearvars A_4est nn kk nmax4
clearvars A_5est nn kk nmax5


%%

%Upload the acceleration operating schedule.

%The first entry of the input file contains the time step (yr)
%The second entry contains the base/room temperature(*C)
%Column numeric entries should start on the fifth line
%Column 1 - Time (yr)
%Column 2 - Expected operating temperature (*C)
%Column 3 - Acceleration profile (this is the number corresponding to the
%acceleration profiles above (i.e. 1 = acceleration profile 1)

%Reference the file
filenameS='Schedule_p2.txt'; %define the file name
delimiterIn='\t'; %define the spacing in the file
%Import the time step (dt)
headerlinesIn=1; %define the number of header lines
sS=importdata(filenameS,delimiterIn,headerlinesIn); %import data
dt_S=sS.data(1); %year, time step
%Import analysis data
headerlinesIn=4; %define the number of header lines
sS=importdata(filenameS,delimiterIn,headerlinesIn); %import data
SS=sS.data; %Pull the data into a matrix form
T_S=SS(:,1); %year
Accel_Profile=SS(:,3); %acceleration profile to be used for the given time

% %--------Plot the analysis data------------
% figure(3)
% plot(T_S,Accel_Profile,'oblack');grid on;
% axis([0 6 0 5]);
% title('Representative Acceleration Profile (#)')
% xlabel('Time (yr)'); ylabel('Acceleration Profile (#)');

%--------Clear Variables------------
clearvars filenameS delimiterIn headerlinesIn sS SS

%%
%Define the window of time the user wants to maximize the possible energy
%production.  This could be the entire life-cycle or some smaller window
%(e.g. from 3.4yr - 4.6yr).  For example T_opt=[2.1;3.3] means that the
%user wants to optimize the energy output starting at year 2.1 and ending
%at the start of year 3.3.

T_opt=[0;0.9];%years, window of time the user wants to optimize energy output

%extract the times of interest
T_initial=T_opt(1); %year, isolate the initial time increment to analyze
T_final=T_opt(2); %year, isolate the final time increment to analyze.

%%
%Define Constant Inputs
m=0.02;%kg/m, beam mass per unit length
```

```
rho_tip=6000;%kg/m^3, density of material used for tip mass
b=0.005;%m, width of piezoelectric
n_modes=1;%number of eigenmodes considered (not to exceed 3)
Connection='Series'; %how the piezoelectric is connected. 'Series' or 'Parallel'
hps=0.0001;%m, distance between neutral axis and mid-height of piezo layer
k=7;%number of piezoelectric bimorphs tested for fatigue (see CUM_DAMAGE)

%%
%Define range of tip masses considered
dMt=0.00005;%kg, the differential mass investigated
MtCases=12;%the number of differential masses investigated
%(i.e. Mtip=0:dMtip:(MtipCases-1)*dMtip)

%%
%Define range of load resistances considered
dR=521052;%ohm, the differential resistance investigated
RCases=13;%the number of differential resistances investigated
%(i.e. R=dR:dR:(RCases)*dR)

%%
%Monte Carlo inputs

%number of realizations in the monte carlo analysis
MC_Temp=1;%temp

%Type of uncertainty in analysis
% 'N' for normal ; 'U' for uniform dist.; 'None' for no uncertainty
Type='None';

%%
%List of subroutines that define other necessary inputs

%----------RETURNS NUMERIC VALUES--------NO UNCERTAINTY-------------
%Damping ratios for modes 1-3
%   MODAL_1_DAMP=fn(mode 1 natural frequency, Temp)
%   MODAL_2_DAMP=fn(mode 2 natural frequency, Temp)
%   MODAL_3_DAMP=fn(mode 3 natural frequency, Temp)
%Beam Properties
%   BEAM_LENGTH=fn(Temp)
%   UNDAMAGED_FLEXURAL_STIFFNESS=fn(Temp)
%Circuits
%   UNDAMAGED_PIEZO_CAPACITANCE=fn(Temp,Time)
%   UNDAMAGED_PIEZO_CONSTANT_D=fn(Temp,Time)
%   PIEZO_ELASTIC_MOD=fn(Temp)
%Damage
%   CUM_DAMAGE=fn(cumulative cycle count, new rainflow amplitude, new rainflow cycles)

%----------MATLAB TOOLBOX FUNCTIONS------NO UNCERTAINTY-----------
%Rainflow analysis for cumulative damage calculations
% http://www.mathworks.com/matlabcentral/fileexchange/...
%                           3026-rainflow-counting-algorithm
%   sig2ext
%   rainflow
%   rfmatrix

%----------RETURNS NUMERIC VALUES---------UNCERTAINTY-------------
%Schedule
%   TEMP=fn(Time,Distribution Type)

%%
```

```
%define constant variables---------
desc=200;%number of descretizations in eigenmode calculations
%define a range of lambdas to consider
delta=0.001; dl=(0:delta:50)';
RFBin=100;%number of histogram bins in rainflow analysis
test_cases=7;%number of experimental cases used in CUM_DAMAGE

%Initialize Matricies-----------------
Mt=zeros(1,length(MtCases));%kg, tip mass
It=zeros(1,length(MtCases));%kg*m2, tip inertia about x=L
R=zeros(1,length(RCases));%ohm, resistance
MCT=zeros(1,length(MC_Temp));%number of monte carlo simulations
Pavg=zeros(MtCases,MC_Temp,round(T_final/dt_S),RCases);%W,average power
%maximum relative tip displacement
wR_tip_max=zeros(MtCases,MC_Temp,round(T_final/dt_S),RCases);%m
%damage terms
%arguments(ii,MCT,jj,kk)=(Mtip,MonteCarlo,time(yr),resistance)
C_YIm=zeros(MtCases,MC_Temp,round(T_final/dt_S)+1,RCases);
C_d31m=zeros(MtCases,MC_Temp,round(T_final/dt_S)+1,RCases);
C_Cpm=zeros(MtCases,MC_Temp,round(T_final/dt_S)+1,RCases);
nk_count=zeros(MtCases,MC_Temp,round(T_final/dt_S)+1,RCases,test_cases);


TESTcnt=zeros(15,150);
TESTamp=zeros(15,150);
TESTwr=zeros(15,5500);

%-----------------------------------------------------
%Loop over the tip masses (Mtip)
for ii=1:1:MtCases
Mt(ii)=(ii-1)*dMt+0.0055;%kg,tip mass
It(ii)=(5/12)*Mt(ii)^2/(rho_tip*b);%kg*m2, tip inertia about x=L

%-----------------------------------------------------
%Loop over trial resistances
for kk=1:1:RCases
R(kk)=3.3*(10^(kk+1));%ohm, resistance value

%-----------------------------------------------------
%Loop over temperatures in a monte carlo analysis
for MCT=1:1:MC_Temp

%zero out variables for next calculation cycle
clearvars sum_nk_previous
sum_nk_previous=zeros(1,test_cases);%cumulative cycles
clearvars C_YI C_d31 C_Cp

%-----------------------------------------------------
%Loop over time
%need to start with day zero since we need to calculate accumulated
%damge (i.e. the C's)
for jj=1:1:round(T_final/dt_S)

%-----------------------------------------------------
%zero out variables for next calculation cycle
clearvars time C_Temp L c11E
clearvars d31_U Cp_U YI_U d31 Cp YI
clearvars e31
clearvars fun scinter ninter aa Lambda_r
```

```
Lambda_r=zeros(1,n_modes);%eigenvalues for mode r
clearvars Sr_num Sr_den Sr Phi_rU aa dx
clearvars PHI_RU Phi_r_U_L Phi_r_prime_U_L
PHI_RU=zeros(desc+1,n_modes);%unnormalized eigenmodes
Phi_r_U_L=zeros(1,n_modes);%unnormalized eigenmode at L
Phi_r_prime_U_L=zeros(1,n_modes);%unnormalized eigenmode slope at L
clearvars dx x aa
clearvars C1 PHI_R Phi_r_L Phi_r_prime_L wr
C1=zeros(1,n_modes);%eigenmode normalizing coefficient
PHI_R=zeros(desc+1,n_modes);%normalized eigenmodes
Phi_r_L=zeros(1,n_modes);%normalized eigenmode at L
Phi_r_prime_L=zeros(1,n_modes);%normalized eigenmode slope at L
wr=zeros(1,n_modes);%rad/s, nat frequency
clearvars zeta1 zeta2 zeta3 zeta
clearvars sigma_r Theta_r_equiv
sigma_r=zeros(1,n_modes);%frequency-domain force coefficient
Theta_r_equiv=zeros(1,n_modes);%equivalent modal electromechancial coupling
clearvars Cp_equiv
clearvars alpha beta xx NN ee g w_test
clearvars AP
clearvars tInc t n
clearvars cnt amp

%-------------------------------------------------------
time=(jj-1)*dt_S; %years, represents current time
C_Temp=TEMP(time,Type);%Celsius, current temperature
L=BEAM_LENGTH(C_Temp);%m, beam length
c11E=PIEZO_ELASTIC_MOD(C_Temp);%N/m2, elastic modulus of piezoceramic

%-------------------------------------------------------
%incorporate damage

%Cp_U and Cp do not yet account for 'Parallel' or Series'
%connection type

%undamaged values
d31_U=UNDAMAGED_PIEZO_CONSTANT_D(C_Temp,time);%m/V or C/N
Cp_U=UNDAMAGED_PIEZO_CAPACITANCE(C_Temp,time);%Farad(F) or sec/Ohm
YI_U=UNDAMAGED_FLEXURAL_STIFFNESS(C_Temp);%N/m2

%damaged values
d31=d31_U*(1-C_d31m(ii,MCT,jj,kk));%m/V or C/N
Cp=Cp_U*(1-C_Cpm(ii,MCT,jj,kk));%Farad(F) or sec/Ohm
YI=YI_U*(1-C_YIm(ii,MCT,jj,kk));%N/m2

%-------------------------------------------------------
%other piezoelectric properties
%effective piezoelectric stress constant
e31=d31*c11E; %C/m2, this is based on damaged terms

%-------------------------------------------------------
%Calculate the eigenvalues

%define the Eigenvalue equation
fun=@(lam)-1-lam.^4*Mt(ii)*It(ii)/(L^4*m^2)+cosh(lam).*...
((lam.^4*Mt(ii)*It(ii)/(L^4*m^2)-1).*cos(lam)+(lam.*Mt(ii)/(L*m)...
+lam.^3*It(ii)/(L^3*m)).*sin(lam))-(lam.*Mt(ii)/(L*m)-lam.^3*It(ii)/(L^3*m)).*...
cos(lam).*sinh(lam);

%               %plot when the Eigenvalue equation changes sign
```

```
%           figure(1)
%           plot(dl,sign(fun(dl)));xlabel('Lambda');grid on;

%find the approximate locations where the eigenvalue eqn crosses the 0-axis
scinter=(find(diff(sign(fun(dl))))-1)*delta;
ninter=length(scinter);%number of times EigEqn crosses the 0-axis

%if there are fewer than 'n_modes' roots have MATLAB come back with an error - the
%user will need to update dl above to encompass a broader range so as to
%capture multiple eigenvalues
if ninter<n_modes
display('Error in Eigenvalue Calculation: Less than "n_modes" roots found; adjust search range "dl" or number of
modes considered.');
end

%calculate the Eigenvalues (Lambda's)
for aa = 1:n_modes
Lambda_r(aa) = fzero(fun,dl(round((scinter(aa)/delta+1))));
end

%ensure that the Lambdas are sufficiently seperated that the delta used is
%appropriate (so that we've identified where the EigEqn crosses the 0-axis
if n_modes>1
if Lambda_r(2)-Lambda_r(1)<10*delta
display('Error in Eigenvalue Calculation: The lambdas may be too closely spaced; adjust spacing "delta".');
end
end

%-----------------------------------------------------------
%Calculate the UNNORMALIZED eigenfunctions

%calculate SIGMA_r
Sr_num=sin(Lambda_r)-sinh(Lambda_r)+Mt(ii)/(m*L)*Lambda_r.*(cos(Lambda_r)-cosh(Lambda_r));%numerator
Sr_den=cos(Lambda_r)+cosh(Lambda_r)-Mt(ii)/(m*L)*Lambda_r.*(sin(Lambda_r)-sinh(Lambda_r));%denominator
Sr=Sr_num./Sr_den;%SIGMA_r

%UNNORMALIZED eigenfunction (i.e. doesn't include coefficient)
Phi_rU=@(x)cos(Lambda_r./L*x)-cosh(Lambda_r./L*x)+Sr.*(sin(Lambda_r./L*x)-sinh(Lambda_r./L*x));

%put the UNNORMALIZED eigenfunctions in matrix form (position,mode)
for aa=1:1:desc+1
   dx=L*(aa-1)/desc;%m, spatial descretization
   PHI_RU(aa,:)=Phi_rU(dx);
end

%-----------------------------------------------------------
%Calculate the UNNORMALIZED eigenfunctions at L
Phi_r_U_L=Phi_rU(L);

%-----------------------------------------------------------
%Calculate the slope of the UNNORMALIZED eigenfunctions at L
Phi_r_prime_U_L=(Lambda_r./L).*(-sin(Lambda_r)-sinh(Lambda_r)+...
   Sr.*(cos(Lambda_r)-cosh(Lambda_r)));

% -----------------------------------------------------------
%Calculate the COEFFICIENTS TO NORMALIZE the mode shapes

dx=L/desc;%m, spatial descretization (note the calc of PHI_RU).
x=0:dx:L;%m, descretized length
```

```
%calculate normalization coefficients C1
for aa=1:1:n_modes
C1(aa)=sqrt(1./(m*trapz(x,PHI_RU(:,aa).^2)+...
Mt(ii)*Phi_r_U_L(aa).^2+It(ii)*Phi_r_prime_U_L(aa).^2));
end

%---------------------------------------------------------
%NORMALIZE the eigenfunction outputs
for aa=1:1:n_modes
PHI_R(:,aa)=C1(aa).*PHI_RU(:,aa);%eigenfunctions
Phi_r_L(aa)=C1(aa)*Phi_r_U_L(aa);%at x=L
Phi_r_prime_L(aa)=C1(aa)*Phi_r_prime_U_L(aa);%slope at x=L
end

%---------------------------------------------------------
%for each eigenvalue Lambda (i.e. for each mode) calc the
%current undamped natural frequency of the rth mode in
%short-circuit conditions (R_l=0)
wr=Lambda_r.^2.*sqrt(YI/(m*L^4));

%---------------------------------------------------------
%Calc the damping ratios for the current nat freq./temp
zeta1=MODAL_1_DAMP(wr(1),C_Temp);%mode 1
zeta=zeta1;%group into single damping array
if n_modes==2
zeta2=MODAL_2_DAMP(wr(2),C_Temp);%mode 2
zeta=[zeta1;zeta2];%group into single damping array
end
if n_modes==3
zeta2=MODAL_2_DAMP(wr(2),C_Temp);%mode 2
zeta3=MODAL_3_DAMP(wr(3),C_Temp);%mode 3
zeta=[zeta1;zeta2;zeta3];%group into single damping array
end

%---------------------------------------------------------
%Calculate sigma_r (the frequency-domain force coefficient)
sigma_r=-m*trapz(x,PHI_R)-Mt(ii)*Phi_r_L;

%---------------------------------------------------------
%account for bimorph connection
if strcmp(Connection,'Parallel')==1
Theta_r_equiv=2*e31*hps*b*Phi_r_prime_L;
Cp_equiv=2*Cp;%Farad(F) or sec/Ohm
%Cp is damaged at this point
else
if strcmp(Connection,'Series')==1
Theta_r_equiv=e31*hps*b*Phi_r_prime_L;
Cp_equiv=Cp/2;%Farad(F) or sec/Ohm
%Cp is damaged at this point
end
end

%---------------------------------------------------------
%Calculate transfer functions alpha=fn(frequency, resistance)
%and beta=fn(frequency,resistance); beta will also be spatially
%descretized.

if n_modes==1
alpha=@(w)(...
((-i*w*Theta_r_equiv(1)*sigma_r(1))/(wr(1)^2-w^2+i*2*zeta(1)*wr(1)*w))/...
```

```
((i*w*Theta_r_equiv(1)^2)/(wr(1)^2-w^2+i*2*zeta(1)*wr(1)*w)+...
i*w*Cp_equiv+1/R(kk)));
beta=@(w)(...
(sigma_r(1)+Theta_r_equiv(1)*alpha(w))*...
(PHI_R(:,1)/(wr(1)^2-w^2+i*2*zeta(1)*wr(1)*w)));
end
if n_modes==2
alpha=@(w)(...
((-i*w*Theta_r_equiv(1)*sigma_r(1))/(wr(1)^2-w^2+i*2*zeta(1)*wr(1)*w)+...
(-i*w*Theta_r_equiv(2)*sigma_r(2))/(wr(2)^2-w^2+i*2*zeta(2)*wr(2)*w))/...
((i*w*Theta_r_equiv(1)^2)/(wr(1)^2-w^2+i*2*zeta(1)*wr(1)*w)+...
(i*w*Theta_r_equiv(2)^2)/(wr(2)^2-w^2+i*2*zeta(2)*wr(2)*w)+...
i*w*Cp_equiv+1/R(kk)));
beta=@(w)(...
(sigma_r(1)+Theta_r_equiv(1)*alpha(w))*...
(PHI_R(:,1)/(wr(1)^2-w^2+i*2*zeta(1)*wr(1)*w))+...
(sigma_r(2)+Theta_r_equiv(2)*alpha(w))*...
(PHI_R(:,2)/(wr(2)^2-w^2+i*2*zeta(2)*wr(2)*w)));
end
if n_modes==3
alpha=@(w)(...
((-i*w*Theta_r_equiv(1)*sigma_r(1))/(wr(1)^2-w^2+i*2*zeta(1)*wr(1)*w)+...
(-i*w*Theta_r_equiv(2)*sigma_r(2))/(wr(2)^2-w^2+i*2*zeta(2)*wr(2)*w)+...
(-i*w*Theta_r_equiv(3)*sigma_r(3))/(wr(3)^2-w^2+i*2*zeta(3)*wr(3)*w))/...
((i*w*Theta_r_equiv(1)^2)/(wr(1)^2-w^2+i*2*zeta(1)*wr(1)*w)+...
(i*w*Theta_r_equiv(2)^2)/(wr(2)^2-w^2+i*2*zeta(2)*wr(2)*w)+...
(i*w*Theta_r_equiv(3)^2)/(wr(3)^2-w^2+i*2*zeta(3)*wr(3)*w)+...
i*w*Cp_equiv+1/R(kk)));

beta=@(w)(...
(sigma_r(1)+Theta_r_equiv(1)*alpha(w))*...
(PHI_R(:,1)/(wr(1)^2-w^2+i*2*zeta(1)*wr(1)*w))+...
(sigma_r(2)+Theta_r_equiv(2)*alpha(w))*...
(PHI_R(:,2)/(wr(2)^2-w^2+i*2*zeta(2)*wr(2)*w))+...
(sigma_r(3)+Theta_r_equiv(3)*alpha(w))*...
(PHI_R(:,3)/(wr(3)^2-w^2+i*2*zeta(3)*wr(3)*w)));

end

%           %plot transfer functions to observe behavior
%           for dx=0:1:1000
%              xx(dx+1)=dx;%rad/s, frequency range
%              NN(dx+1)=alpha(dx);%combined
%           end
%           %plot the transfer function at (1) the beam tip and (2) at the
%           %beam midspan for an array of frequencies.  The first plot
%           %indicates that the first mode governs the tip displacement.
%           %The second plot indicates that the second and third modes are
%           %slightly contributing.
%           for ee=0:5:1000
%              g=beta(ee);%beta for an array of frequencies
%              subplot(2,1,1);semilogy(ee,abs(g(length(beta(ee)))),'bo');hold on;grid on;
%              xlabel('Frequency(rad/s)');ylabel('|Beta|');title('x=L');
%              subplot(2,1,2);semilogy(ee,abs(g(round(0.5*length(beta(ee))))),'bo');hold on;grid on;
%              xlabel('Frequency(rad/s)');ylabel('|Beta|');title('x=0.5*L');
%           end
%           w_test=50;%test frequency for plotting beta
%           figure(6);
%           subplot(4,1,1);semilogy(xx,abs(NN));grid on;
%           xlabel('Frequency (rad/s)');ylabel('|Alpha|');
```

```
%               subplot(4,1,2);plot(xx,angle(NN));grid on;
%               xlabel('Frequency (rad/s)');ylabel('Phase Angle of Alpha');
%               subplot(4,1,3);plot(0:L/desc:L,abs(beta(w_test)));grid on;
%               xlabel('Spatial Location (m)');ylabel('|Beta|');
%               subplot(4,1,4);plot(0:L/desc:L,angle(beta(w_test)));grid on;
%               xlabel('Spatial Location (m)');ylabel('Phase Angle of Beta');

%-------------------------------------------------------
%Determine which Fourier Coefficients to use in the voltage,
%relative displacement, and power calculations

AP=Accel_Profile(jj);%the current acceleration profile
%specify the Fourier Coefficients
if AP==1
an=a1;bn=b1;N=N1;tt=T_1;T=T1;dt=dt_1;
%an,bn=Fourier coefficients
%N=number of Fourier coefficients
%tt=time array of base acceleration
%T=maximum(t)
%dt=differential time step in time array
end
if AP==2
an=a2;bn=b2;N=N2;tt=T_2;T=T2;dt=dt_2;
end
if AP==3
an=a3;bn=b3;N=N3;tt=T_3;T=T3;dt=dt_3;
end
if AP==4
an=a4;bn=b4;N=N4;tt=T_4;T=T4;dt=dt_4;
end
if AP==5
an=a5;bn=b5;N=N5;tt=T_5;T=T5;dt=dt_5;
end
if AP>5
display('Error: Acceleration profiles exceed 5; expand code');
end


%-------------------------------------------------------
%Compare the maximum frequency used in the Fourier Series
%with the natural frequency of the system. If the Fourier
%series doesn't capture the natural frequency of interest,
%notify the user.

if n_modes==1
if wr(1)>((2*pi)/(2*dt))
display('Warning, the first natural frequency exceeds the Nyquist freqency of the acceleration profile (AP)');disp(AP)
end
end
%if two modes specified
if n_modes==2
if wr(1)>(N*2*pi/T)
display('Warning, the first natural frequency exceeds the Nyquist freqency of the acceleration profile (AP)');disp(AP)
end
if wr(2)>(N*2*pi/T)
display('Warning, the second natural frequency exceeds the Nyquist freqency of the acceleration profile
(AP)');disp(AP)
end
end
%if three modes specified
```

```
if n_modes==3
if wr(1)>(N*2*pi/T)
display('Warning, the first natural frequency exceeds the Nyquist freqency of the acceleration profile (AP)');disp(AP)
end
if wr(2)>(N*2*pi/T)
display('Warning, the second natural frequency exceeds the Nyquist freqency of the acceleration profile
(AP)');disp(AP)
end
if wr(3)>(N*2*pi/T)
display('Warning, the third natural frequency exceeds the Nyquist freqency of the acceleration profile
(AP)');disp(AP)
end
end

%-------------------------------------------------------
%Calculate voltage, relative displacement, and power

%initialize vectors
clearvars FVar alpha_AMP alpha_PH beta_AMP beta_AMP_L
clearvars beta_PH beta_PH_L v wr_L Pinst
clearvars wR_L_trunc v_trunc Pinst_trunc tt_trunc T_trunc
FVar=zeros(1,N);%frequency variable
alpha_AMP=zeros(1,N);%alpha-amplitude coefficient
alpha_PH=zeros(1,N);%alpha-phase
beta_AMP=zeros(1,length(PHI_R));%beta-amplitude coefficient
beta_AMP_L=zeros(1,N);%beta-amplitude coefficient at x=L
beta_PH=zeros(1,length(PHI_R));%beta-phase
beta_PH_L=zeros(1,N);%beta-phase at x=L
v=zeros(1,round((T/dt)+1));%V, voltage
wR_L=zeros(1,round((T/dt)+1));%m, relative displacement
Pinst=zeros(1,round((T/dt)+1));%W,power

%loop over base acceleration time array
for tInc=1:1:round((T/dt)+1)
t=(tInc-1)*dt;%sec, time
%loop over Fourier Coefficients
for n=1:1:N
FVar(n)=n*(2*pi/T);%frequency variable

%voltage calculations-----
alpha_AMP(n)=abs(alpha(FVar(n)));%amplitude coefficient
alpha_PH(n)=angle(alpha(FVar(n)));%phase
v(tInc)= v(tInc)+alpha_AMP(n)*(an(n)*cos(FVar(n)*t+alpha_PH(n))+...
bn(n)*sin(FVar(n)*t+alpha_PH(n)));%voltage

%relative tip displacement calculations-----
%spatially dependent amplitude coefficient
beta_AMP=abs(beta(FVar(n)));
%amplitude coefficient at x=L
beta_AMP_L(n)=beta_AMP(length(beta_AMP));
%spatially dependent phase
beta_PH=angle(beta(FVar(n)));
%amplitude coefficient at x=L
beta_PH_L(n)=beta_PH(length(beta_AMP));
%Relative displacement at x=L
wR_L(tInc)=wR_L(tInc)+beta_AMP_L(n)*(an(n)*cos(FVar(n)*t+beta_PH_L(n))+...
bn(n)*sin(FVar(n)*t+beta_PH_L(n)));%m
end %n - fourier coefficients
Pinst(tInc)=v(tInc)^2/R(kk);%instantaneous Power
end %tInc- time (sec)
```

```
%           %plot full results
%           figure(7)
%           subplot(3,1,1);plot(tt,wR_L);grid on;
%           xlabel('Time(s)');
%           ylabel('Relative Tip Displacement(m)');
%           subplot(3,1,2);plot(tt,v);grid on;
%           xlabel('Time(s)');
%           ylabel('Voltage(V)');
%           subplot(3,1,3);plot(tt,Pinst);grid on;
%           xlabel('Time(s)');
%           ylabel('Instantaneous Power(W)');

%-------------------------------------------------------
%Truncate/shift the voltage, relative displacement, and
%power to account for initial transients

%Since the base acceleration starts with zero initial
%conditions there will be some transient response for the
%voltage and relative displacement output.  Truncate the
%sequences by removing the the initial data points that
%correspond to a 95% reduction in transient response based
%on the first mode
percent_reduction=0.95;
TOI=-log(1-percent_reduction)/(zeta(1)*wr(1));%sec,time at
%which the first mode transient response will have decayed
%by percent_reduction
trunc=round(TOI/dt);%corresponding sample number

%if the truncation is too large we may be eliminating most
%of the system response.  In such cases, notify the user
if TOI>0.5*T
display('Warning, the transient response truncation is eliminating more than 50% of the system response (see
"trunc")');
end
if TOI>0.8*T
display('Warning, the transient response truncation is eliminating more than 80% of the system response (see
"trunc")');
end
if TOI>0.99*T
display('Warning, the transient response truncation eliminated more than 99% of the system response (see "trunc")');
end

%truncate the sequences to remove transient responses
wR_L_trunc=wR_L(trunc:length(wR_L));%m,truncated relative tip disp
v_trunc=v(trunc:length(v));%V,truncated voltage
Pinst_trunc=Pinst(trunc:length(Pinst));%W,truncated inst power
tt_trunc=0:dt:(length(tt)-trunc)*dt;%sec,shifted time array
T_trunc=max(tt_trunc);%s,maximum truncated time

%           %plot truncated results
%           figure(8)
%           subplot(3,1,1);plot(tt_trunc,wR_L_trunc);grid on;
%           xlabel('Truncated/Shifted Time(s)');
%           ylabel('Truncated Relative Tip Displacement(m)');
%           subplot(3,1,2);plot(tt_trunc,v_trunc);grid on;
%           xlabel('Truncated/Shifted Time(s)');
%           ylabel('Voltage(V)');
%           subplot(3,1,3);plot(tt_trunc,Pinst_trunc);grid on;
%           xlabel('Truncated/Shifted Time(s)');
```

```
%               ylabel('Truncated Instantaneous Power(W)');

%--------------------------------------------------------
%store outputs that will be displayed post-analysis

%maximum tip displacement
%arguments(ii,MCT,jj,kk)=(Mtip,MonteCarlo,time(yr),resistance)
wR_tip_max(ii,MCT,jj,kk)=max(abs(wR_L_trunc));%m

%average power for an AP
%arguments(ii,MCT,jj,kk)=(Mtip,MonteCarlo,time(yr),resistance)
Pavg(ii,MCT,jj,kk)=(1/T_trunc)*trapz(tt_trunc,Pinst_trunc);%W

%--------------------------------------------------------
%Perform a rainflow analysis on the relative tip
%displacement for damage accumulation purposes

[cnt,ampB]=rfmatrix(rainflow(sig2ext(wR_L_trunc)),RFBin,1,'ampl');
%cnt=number of cycles for truncated time history
%amp= amplitude of cycles corresponding to cnt

%               %plot the rainflow output
%               figure(9)
%               stem(amp,cnt)%plot the histogram of amplitudes
%               xlabel('Amplitude (m)');ylabel('Count');

%scale the cycle count (sec) as it acts over the time scale
%dt_S (yr)
cnt_S=(dt_S*365*24*60*60/T_trunc)*cnt;


%--------------------------------------------------------
%calculate the cumulative damage to YI,d31,Cp

[C_YI,C_d31,C_Cp,nk_addl]=CUM_DAMAGE(sum_nk_previous,ampB,cnt_S);
%increment the number of cycles at each amplitude in test_cases
sum_nk_previous=sum_nk_previous+nk_addl;

%track damage for ploting at the end
C_YIm(ii,MCT,jj+1,kk)=C_YI;
C_d31m(ii,MCT,jj+1,kk)=C_d31;
C_Cpm(ii,MCT,jj+1,kk)=C_Cp;
nk_count(ii,MCT,jj+1,kk,:)=sum_nk_previous;
%arguments(ii,MCT,jj,kk)=(Mtip,MonteCarlo,time(yr),resistance)

PPP(ii,kk)=Pavg(ii,MCT,jj,kk);
WWW(ii,kk)=wR_tip_max(ii,MCT,jj,kk);

end   %jj - time (yr)
end   %MCT - monte carlo simulation
end   %kk - resistance
end   %ii - Mtip

 toc %stop timer to determine duration of script
```

Appendix J – Sample MATLAB Sub-Functions Supporting SS Analysis

Cumulative Damage

```
function[C_YI,C_d31,C_Cp,nk_new]=CUM_DAMAGE(nk_old,amp,cnt)

%Calculate the amount of damage that has accumulated for the flexural
%stiffness (YI), piezoelectric constant (d31), and piezoelectric
%capacitence (Cp).

%Outputs
%   C_YI,C_d31,C_Cp = percent damage of YI, d31, Cp for the next cycle
%   nk_updated = updated cycle counts for each of the Ak amplitudes
%Inputs
%   nk_old=cumulative cycle counts from the previous load cycles
%   amp=amplitudes from rainflow analysis of current time history
%   cnt=bin counts from rainflow analysis of current time history
%%

%Define user tables FROM PHYSICAL TESTING for each Ak case----------------

%Tested amplitudes {from lowest (1) to highest (k)}
Ak=[
0.0005  ;
0.0010  ;
0.0015  ;
0.0020  ;
0.0030  ;
0.0050  ;
0.0070  ];%m

%number of cycles each data point was collected at
cyc=[
0   ,   1.00E+07   ,   1.00E+08   ,   1.00E+09   ,   1.00E+10   ,   1.00E+11   ;   %Ak(1)
0   ,   1.00E+07   ,   1.00E+08   ,   1.00E+09   ,   1.00E+10   ,   1.00E+11   ;   %Ak(2)
0   ,   1.00E+07   ,   1.00E+08   ,   1.00E+09   ,   1.00E+10   ,   1.00E+11   ;   %Ak(3)
0   ,   1.00E+07   ,   1.00E+08   ,   1.00E+09   ,   1.00E+10   ,   1.00E+11   ;   %Ak(4)
0   ,   1.00E+07   ,   1.00E+08   ,   1.00E+09   ,   1.00E+10   ,   1.00E+11   ;   %Ak(5)
```

```
0  ,  1.00E+07  ,  1.00E+08  ,  1.00E+09  ,  1.00E+10  ,  1.00E+11  ;  %Ak(6)
0  ,  1.00E+07  ,  1.00E+08  ,  1.00E+09  ,  1.00E+10  ,  1.00E+11  ];  %Ak(7)

%Tested fatigue life corresponding to Aks
Nk=cyc(:,6);%count

%normalized flexural stiffness measured at the number of cycles in cyc
YInorm=[
1.00  ,  0.99  ,  0.98  ,  0.96  ,  0.92  ,  0.89  ;  %Ak(1)
1.00  ,  0.97  ,  0.94  ,  0.90  ,  0.83  ,  0.77  ;  %Ak(2)
1.00  ,  0.96  ,  0.92  ,  0.88  ,  0.72  ,  0.68  ;  %Ak(3)
1.00  ,  0.94  ,  0.87  ,  0.78  ,  0.66  ,  0.58  ;  %Ak(4)
1.00  ,  0.93  ,  0.82  ,  0.73  ,  0.60  ,  0.52  ;  %Ak(5)
1.00  ,  0.90  ,  0.77  ,  0.62  ,  0.40  ,  0.10  ;  %Ak(6)
1.00  ,  0.89  ,  0.74  ,  0.55  ,  0.10  ,  0.10  ];  %Ak(7)

%normalized piezoelectric coeff. measured at the number of cycles in cyc
d31norm=[
1.00  ,  0.99  ,  0.98  ,  0.96  ,  0.94  ,  0.91  ;  %Ak(1)
1.00  ,  0.98  ,  0.96  ,  0.92  ,  0.88  ,  0.85  ;  %Ak(2)
1.00  ,  0.97  ,  0.96  ,  0.90  ,  0.83  ,  0.70  ;  %Ak(3)
1.00  ,  0.97  ,  0.95  ,  0.88  ,  0.78  ,  0.60  ;  %Ak(4)
1.00  ,  0.96  ,  0.95  ,  0.87  ,  0.77  ,  0.55  ;  %Ak(5)
1.00  ,  0.90  ,  0.88  ,  0.82  ,  0.70  ,  0.10  ;  %Ak(6)
1.00  ,  0.80  ,  0.76  ,  0.70  ,  0.55  ,  0.10  ];  %Ak(7)

%normalized capacitence measured at the number of cycles in cyc
Cpnorm=[
1.00  ,  0.99  ,  0.98  ,  0.97  ,  0.93  ,  0.10  ;  %Ak(1)
1.00  ,  0.98  ,  0.97  ,  0.96  ,  0.92  ,  0.10  ;  %Ak(2)
1.00  ,  0.97  ,  0.96  ,  0.95  ,  0.91  ,  0.10  ;  %Ak(3)
1.00  ,  0.96  ,  0.95  ,  0.94  ,  0.90  ,  0.10  ;  %Ak(4)
1.00  ,  0.95  ,  0.94  ,  0.93  ,  0.89  ,  0.10  ;  %Ak(5)
1.00  ,  0.94  ,  0.93  ,  0.92  ,  0.88  ,  0.10  ;  %Ak(6)
1.00  ,  0.93  ,  0.92  ,  0.91  ,  0.87  ,  0.10  ];  %Ak(7)

% %plot the data sets
% figure(2)
% for k=1:1:length(Ak)
%    subplot(3,1,1);semilogx(cyc(k,:),YInorm(k,:),'x-');hold on;grid on;
%    xlabel('Cycles');ylabel('Normalized YI');axis([10^4 10^10 0.5 1]);
%       subplot(3,1,2);semilogx(cyc(k,:),d31norm(k,:),'x-');hold on;grid on;
%    xlabel('Cycles');ylabel('Normalized d31');axis([10^4 10^10 0.5 1]);
%          subplot(3,1,3);semilogx(cyc(k,:),Cpnorm(k,:),'x-');hold on;grid on;
%    xlabel('Cycles');ylabel('Normalized Cp');axis([10^4 10^10 0.5 1]);
% end

%ensure that the test data encompasses the rainflow data
if max(amp)>max(Ak)
display('Error,the maximum amplitude from the rainflow analysis exceeds the maximum amplitude (Ak) used in
testing');
end
for ii=1:1:length(nk_old)
if nk_old(ii)>Nk(ii)
display('Error,the cumulative loading cycles (nk) exceeds the failure cycles (Nk) found from testing');
end
end
%%

%Regroup the rainflow histogram output into the bins defined by the
```

```
%testing data (Ak and nk)

%initialze a counting matrix
g=zeros(length(Ak),length(amp));
for ii=1:1:length(Ak)%loop over all tested amplitudes
for jj=1:1:length(amp)%loop over all amplitudes from rainflow
%if the tested amplitude is less than the rainflow histogram
%amplitude, populate the counting matrix
if Ak(ii)>amp(jj)
g(ii,jj)=1;
end
end
end

%initialze an index matrix
index=zeros(1,length(Ak));
for ii=1:1:length(Ak)%loop over all tested amplitudes
for jj=1:1:length(amp)%loop over all amplitudes from rainflow
%sum the rows of the counting matrix to determine at what
%index A>amp remains valid
index(ii)=index(ii)+g(ii,jj);
end
end

%cummulatively count all of the cycles from the rainflow analysis
%initialize the matrix
cum_count=zeros(1,length(cnt));
cum_count(1)=cnt(1);  %set the first entry
for jj=2:1:length(cnt)%loop over all cycle counts from rainflow
cum_count(jj)=cum_count(jj-1)+cnt(jj);
end

%determine the cycle count (nk_new) in terms of the testing amplitudes (Aks)
nk_new=zeros(1,length(Ak));

%if there are no new cycles less then Ak(1), set the nk_new(1) to zero,
%else, add the cumulative cycles at the index
if index(1)==0
nk_new(1)=0;
else nk_new(1)=cum_count(index(1));%set the first entry
end

%take the difference between cum_count to find new cycles
for ii=2:1:length(Ak)
if index(ii)==0
nk_new(ii)=0;
else if index(ii-1)==0
nk_new(ii)=cum_count(index(ii));
else nk_new(ii)=cum_count(index(ii))-cum_count(index(ii-1));
end
end
end

% %plot the rainflow output with the regrouped Ak/nk's
% %figure(3)
% subplot(2,1,1);stem(amp,cnt);grid on;
% axis([0 Ak(length(Ak)) 0 max(cnt)]);
% xlabel('Amplitude,(m)');ylabel('Cycles');title('Rainflow Output');
% subplot(2,1,2);stem(Ak,nk_new);grid on;
% axis([0 Ak(length(Ak)) 0 max(nk_new)]);
```

```
% xlabel('Amplitude,(m)');ylabel('Cycles');
% title('Rainflow Output Regrouped into Tested Aks');

%%

%Calculate the normalized damage to each variable YI, d31, Cp

%combine the cumulative cycles up to this point with the new cycles just
%calculated
nk_updated=nk_old'+nk_new';

%Find the max and min cycles that bound the current nk
for jj=1:1:length(nk_updated) %loop over all tests
for ii=1:1:length(cyc(1,:))
%Determine lower bound with which to interpolate
if nk_updated(jj)<cyc(jj,ii)
cycle_lower(jj,ii)=0;
else cycle_lower(jj,ii)=1;
end
%Determine upper bound with which to interpolate
if nk_updated(jj)>=cyc(jj,ii)
cycle_upper(jj,ii)=0;
else cycle_upper(jj,ii)=1;
end
end
end

%Left & Right bound of cycles with which to interpolate
for ii=1:1:length(cyc)
cycle_L(ii)=cyc(ii,sum(cycle_lower(ii,:)));
cycle_R(ii)=cyc(ii,length(cyc(1,:))+1-sum(cycle_upper(ii,:)));
end

%--------------YI-----------------------------------------------------
%Left & Right bound of YInorm with which to interpolate
for ii=1:1:length(cyc)
YI_L(ii)=YInorm(ii,sum(cycle_lower(ii,:)));
YI_R(ii)=YInorm(ii,length(cyc(1,:))+1-sum(cycle_upper(ii,:)));
end

%interpolate the current YInorm based on the number of cycles
YInorm_updated=(YI_R-YI_L)./(cycle_R-cycle_L).*(nk_updated'-cycle_L)+YI_L;
%calculate the reduction in YInorm based on the number of cycles
delta_YInorm_damage=YInorm(:,1)-YInorm_updated';
%Calculate the accumulated percent damage
C_YI=sum(delta_YInorm_damage);

%--------------d31----------------------------------------------------
%Left & Right bound of d31norm with which to interpolate
for ii=1:1:length(cyc)
d31_L(ii)=d31norm(ii,sum(cycle_lower(ii,:)));
d31_R(ii)=d31norm(ii,length(cyc(1,:))+1-sum(cycle_upper(ii,:)));
end

%interpolate the current d31norm based on the number of cycles
d31norm_updated=(d31_R-d31_L)./(cycle_R-cycle_L).*(nk_updated'-cycle_L)+d31_L;
%calculate the reduction in d31norm based on the number of cycles
delta_d31norm_damage=d31norm(:,1)-d31norm_updated';
%Calculate the accumulated percent damage
C_d31=sum(delta_d31norm_damage);
```

```
%--------------Cp-----------------------------------------------------
%Left & Right bound of d31norm with which to interpolate
for ii=1:1:length(cyc)
Cp_L(ii)=Cpnorm(ii,sum(cycle_lower(ii,:)));
Cp_R(ii)=Cpnorm(ii,length(cyc(1,:))+1-sum(cycle_upper(ii,:)));
end

%interpolate the current Cpnorm based on the number of cycles
Cpnorm_updated=(Cp_R-Cp_L)./(cycle_R-cycle_L).*(nk_updated'-cycle_L)+Cp_L;
%calculate the reduction in Cpnorm based on the number of cycles
delta_Cpnorm_damage=Cpnorm(:,1)-Cpnorm_updated';
%Calculate the accumulated percent damage
C_Cp=sum(delta_Cpnorm_damage);

%%
%give a warning if the accumulated percent damage exceeds 0.9
if C_YI>0.9
display('Warning, the accumulated damage to the flexural stiffness (C_YI) exceeds 90%');
end
if C_d31>0.9
display('Warning, the accumulated damage to the piezo constant (C_d31) exceeds 90%');
end
if C_Cp>0.9
display('Warning, the accumulated damage to the piezo capacitence (C_Cp) exceeds 90%');
end
```

Piezoelectric Strain Constant

```
function[D31]=UNDAMAGED_PIEZO_CONSTANT_D(Temp_Current,Time_Current)

%Develop a script that takes user time-temperature data for a given
%property and can interpolate the property for a given
%time & temperature

%M_0 represents the magnitude of the property on day 0 at room temperature
%Temp_Current represents the temp (celsius) at which to determine the property
%Time_Current represents the time (yr) at which to determine the property

%%
%Populate the property table as a function of time and temperature

Temp_Increments=[20;120;130;140;150];%degrees celsius
Time_Increments=[0;10]; %years
%User input. Each column corresponds
%to the time increments. Each row corresponds to the temperature
%increments.
M_Table=(-1e-10)*[
1.71    ,   1.71    ;
2.57    ,   2.57    ;
2.57    ,   2.57    ;
2.57    ,   2.57    ;
2.57    ,   2.57    ];%m/V or C/N

% figure(4)
% plot(Temp_Increments,M_Table(:,1)/(-1.71e-10));
% title('Undamaged Piezo Constant=fn(Time,Temperature)');
% xlabel('Temperature(Celsius)');grid on;
% ylabel('Piezo Constant d_3_1 (m/V or C/N)');
% axis([20 100 0 2])
```

```
%%
%Interpolate the expected property at the specified temperature and time

%Find the max and min Temperatures that bound the current temp of interest
for ii=1:1:length(Temp_Increments)
%Determine lower bound of temperature range with which to interpolate
if Temp_Current<Temp_Increments(ii)
Temp_Lower(ii)=0;
else Temp_Lower(ii)=1;
end
%Determine upper bound of temperature range with which to interpolate
if Temp_Current>=Temp_Increments(ii)
Temp_Upper(ii)=0;
else Temp_Upper(ii)=1;
end
end
%Check that Temperature of interest is within range of data
if Temp_Current>=Temp_Increments(length(Temp_Increments))
display('Error [PIEZO_CONSTANT_D], Temperature of interest equals or exceeds the range of values inputted by
the user.');
end
if Temp_Current<Temp_Increments(1)
display('Error [PIEZO_CONSTANT_D], Temperature of interest is less than the range of values inputted by the
user.');
end
%Lower & Upper bound of temperature range with which to interpolate
Temp_Min=Temp_Increments(sum(Temp_Lower));
Temp_Max=Temp_Increments(length(Temp_Increments)+1-sum(Temp_Upper));

%Find the max and min Times that bound the current temp of interest
for ii=1:1:length(Time_Increments)
%Determine lower bound of time range with which to interpolate
if Time_Current<Time_Increments(ii)
Time_Lower(ii)=0;
else Time_Lower(ii)=1;
end
%Determine upper bound of time range with which to interpolate
if Time_Current>=Time_Increments(ii)
Time_Upper(ii)=0;
else Time_Upper(ii)=1;
end
end
%Check that Time of interest is within range of data
if Time_Current>=Time_Increments(length(Time_Increments))
display('Error [PIEZO_CONSTANT_D], Time of interest equals or exceeds the range of values inputted by the
user.');
end
if Time_Current<Time_Increments(1)
display('Error [PIEZO_CONSTANT_D], Time of interest is less than the range of values inputted by the user.');
end
%Lower & Upper bound of time range with which to interpolate
Time_Min=Time_Increments(sum(Time_Lower));
Time_Max=Time_Increments(length(Time_Increments)+1-sum(Time_Upper));

%Find the values of the property at the four points that bound the current
%temperature and time of interest
M_11=M_Table(sum(Temp_Lower),sum(Time_Lower));
M_21=M_Table(sum(length(Temp_Increments)+1-sum(Temp_Upper)),sum(Time_Lower));
M_12=M_Table(sum(Temp_Lower),length(Time_Increments)+1-sum(Time_Upper));
```

```
M_22=M_Table(sum(length(Temp_Increments)+1-sum(Temp_Upper)),length(Time_Increments)+1-
sum(Time_Upper));
%Calculate the coefficients with which to determine the interpolated
%current value of interest
Q=[1, Time_Min, Temp_Min, Time_Min*Temp_Min;
1, Time_Min, Temp_Max, Time_Min*Temp_Max;
1, Time_Max, Temp_Min, Time_Max*Temp_Min;
1, Time_Max, Temp_Max, Time_Max*Temp_Max];
A=[1;Time_Current;Temp_Current;Time_Current*Temp_Current];
B=(Q^-1)'*A;
%Calculate the current value of interest
D31=(B(1,1)*M_11+B(2,1)*M_21+B(3,1)*M_12+B(4,1)*M_22);
```

References

[1] D. Spreemann and Y. Manoli, "Electromagnetic Vibration Energy Harvesting Devices: Architectures, Design, Modeling and Optimization. Volume 35," New York: Springer Science & Business Media, 2012.

[2] T. V. Galchev, J. McCullagh, R. L. Peterson, and K. Najafi, "Harvesting Traffic-Induced Vibrations for Structural Health Monitoring of Bridges," *Journal of Micromechanics and Microengineering*, vol. 21, no. 10, pp. 104005, 2011.

[3] E. Sazonov, H. Li, D. Curry, and P. Pillay, "Self-Powered Sensors for Monitoring of Highway Bridges," *IEEE Sensors Journal*, vol. 9, no. 11, pp. 1422-1429, 2009.

[4] M. Peigney and D. Siegert, "Piezoelectric Energy Harvesting from Traffic-Induced Bridge Vibrations," *Smart Materials and Structures*, vol. 22, no. 9, pp. 095019, 2013.

[5] S.A. Ouellette and M. D. Todd, "Cement Seawater Battery Energy Harvester for Marine Infrastructure Monitoring," *IEEE Sensors Journal*, vol. 14, no. 3, pp. 865-872, 2014.

[6] S. A. Ouellette, D. D. Mascareñas, and M. D. Todd, "Corrosion-Enabled Powering Approach for Structural Health Monitoring Sensor Networks," *SPIE Smart Structures and Materials+ Nondestructive Evaluation and Health Monitoring*, International Society for Optics and Photonics, pp. 728821, 2009.

[7] C. Nagode, M. Ahmadian, and S. Taheri, "Motion-Based Energy Harvesting Devices for Railroad Applications," *2010 Joint Rail Conference*, American Society of Mechanical Engineers, pp. 267-271, 2010.

[8] J. J. Wang, G. P. Penamalli, and L. Zuo, "Electromagnetic Energy Harvesting from Train Induced Railway Track Vibrations," *2012 IEEE/ASME International Conference on Mechatronics and Embedded Systems and Applications (MESA)*, International Society for Optics and Photonics, pp. 29-34, 2012.

[9] C. A. Nelson, S. R. Platt, D. Albrecht, V. Kamarajugadda, and M. Fateh, "Power Harvesting for Railroad Track Health Monitoring Using Piezoelectric and Inductive Devices," *The 15th International Symposium on: Smart Structures and Materials & Nondestructive Evaluation and Health Monitoring*, International Society for Optics and Photonics, pp. 69280R, 2008.

[10] S. R. Anton, A. Erturk, and D. J. Inman, "Multifunctional Unmanned Aerial Vehicle Wing Spar for Low-Power Generation and Storage," *Journal of Aircraft*, vol. 49, no. 1, pp. 292-301, 2012.

[11] N. Baldock and M. R. Mokhtarzadeh-Dehghan, "A Study of Solar-Powered, High-Altitude Unmanned Aerial Vehicles," *Aircraft Engineering and Aerospace Technology*, vol. 78, no. 3, pp. 187-193, 2006.

[12] A. Erturk, S. R. Anton, and D. J. Inman, "Piezoelectric Energy Harvesting from Multifunctional Wing Spars for UAVs: Part 1. Coupled Modeling and Preliminary Analysis," *SPIE Smart Structures and Materials+ Nondestructive Evaluation and Health Monitoring*, International Society for Optics and Photonics, pp. 72880C, 2009.

[13] S. R. Anton, A. Erturk, and D. J. Inman, "Piezoelectric Energy Harvesting from Multifunctional Wing Spars for UAVs: Part 2. Experiments and Storage Applications," *SPIE Smart Structures and Materials+ Nondestructive Evaluation and Health Monitoring*, International Society for Optics and Photonics, pp. 72880D, 2009.

[14] S. W. Arms, C. P. Townsend, D. L. Churchill, S. M. Moon, and N. Phan, "Energy Harvesting Wireless Sensors for Helicopter Damage Tracking," *Annual Forum Proceedings-American Helicopter Society*, vol. 62, no. 2, p. 1336, 2006.

[15] M. Bryant, A. Fang, and E. Garcia, "Self-Powered Smart Blade: Helicopter Blade Energy Harvesting," *SPIE Smart Structures and Materials+ Nondestructive Evaluation and Health Monitoring*. International Society for Optics and Photonics, pp. 764317, 2010.

[16] S. W. Arms, J. H. Galbreath, C. P. Townsend, D. L. Churchill, B. Corneau, R. P. Ketcham, and N. Phan, "Energy Harvesting Wireless Sensors and Networked Timing Synchronization for Aircraft Structural Health Monitoring," *First International Conference on Wireless Communication, Vehicular Technology, Information Theory and Aerospace & Electronic Systems Technology, 2009. Wireless VITAE 2009*, International Society for Optics and Photonics, pp. 16-20, 2009.

[17] G. Park, T. Rosing, M. D. Todd, C. R. Farrar, and W. Hodgkiss, "Energy Harvesting for Structural Health Monitoring Sensor Networks," *Journal of Infrastructure Systems*, vol. 14, no. 1, pp. 64-79, 2008.

[18] A. Dewan, S. U. Ay, M. N. Karim, and H. Beyenal, "Alternative Power Sources for Remote Sensors: A Review," *Journal of Power Sources*, vol. 245, pp. 129-143, 2014.

[19] L. Mateu and F. Moll, "Review of Energy Harvesting Techniques and Applications for Microelectronics (Keynote Address)," *Microtechnologies for the New Millennium 2005*, International Society for Optics and Photonics, pp. 359-373, 2005.

[20] R. J. M. Vullers, R. van Schaijk, I. Doms, C. Van Hoof, and R. Mertens, "Micropower Energy Harvesting," *Solid-State Electronics*, vol. 53, no. 7, pp. 684-693, 2009.

[21] S. Chalasani and J. M. Conrad, "A Survey of Energy Harvesting Sources for Embedded Systems," *IEEE Southeastcon 2008*, International Society for Optics and Photonics, pp. 442-447, 2008.

[22] S. A. Ouellette, "Energy Harvesting Paradigms for Autonomously-Powered Sensor Networks," Dissertation, University of California-San Diego, 2015

[23] M. A. Qidwai, J. P. Thomas, J. C. Kellogg, and J. Baucom, "Energy Harvesting Concepts for Small Electric Unmanned Systems," *Smart Structures and Materials*, International Society for Optics and Photonics, pp. 85, 2004.

[24] S. J. Roundy, "Energy Scavenging for Wireless Sensor Nodes with a Focus on Vibration to Electricity Conversion," University of California-Berkeley, 2003.

[25] N. S. Hudak and G. G. Amatucci, "Small-Scale Energy Harvesting through Thermoelectric, Vibration, and Radiofrequency Power Conversion," *Journal of Applied Physics*, vol. 103, no. 10, pp. 101301, 2008.

[26] D. N. Fry, D. E. Holcomb, J. K. Munro, L. C. Oakes, and M. J. Matson, "Compact Portable Electric Power Sources," Oak Ridge National Laboratory, Tennessee (United States), 1997.

[27] J. A. Paradiso and T. Starner, "Energy Scavenging for Mobile and Wireless Electronics," *IEEE Pervasive Computing*, vol. 4, no. 1, pp. 18–27, 2005.

[28] S. Priya and D. J. Inman, *Energy Harvesting Technologies*, New York: Springer, 2009.

[29] E. Niell, A. Erturk, *Advances in Energy Harvesting Methods*, New York: Springer, 2013.

[30]S. P. Beeby, M. J. Tudor, and N. M. White, "Energy Harvesting Vibration Sources for Microsystems Applications," *Measurement Science and Technology*, vol. 17, no. 12, pp. R175-R195, 2006.

[31] S. Roundy, "On the Effectiveness of Vibration-Based Energy Harvesting," *Journal of Intelligent Material Systems and Structures*, vol. 16, no. 10, pp. 809-823, 2005.

[32] A. H. Meitzler, H. F. Tiersten, A. W. Warner, and D. Berlincourt, "IEEE Standard on Piezoelectricity," New York: Institute of Electrical and Electronics Engineers, 1988.

[33] H. A. Sodano, D. J. Inman and G. Park, "A Review of Power Harvesting from Vibration using Piezoelectric Materials," *Shock and Vibration Digest*, vol. 36, no. 3, pp. 197-206, 2004.

[34] S. Priya, "Advances in Energy Harvesting using Low Profile Piezoelectric Transducers," *Journal of Electroceramics*, vol. 19, no. 1, pp. 167-184, 2007.

[35] S. R. Anton and H. A. Sodano, "A Review of Power Harvesting using Piezoelectric Materials (2003–2006)," *Smart Materials and Structures*, vol. 16, no. 3, pp. R1-R21, 2007.

[36] A. Erturk and D. J. Inman, *Piezoelectric Energy Harvesting*, United Kingdom: John Wiley & Sons, 2011.

[37] D. P. Arnold, "Review of Microscale Magnetic Power Generation," *IEEE Transactions on Magnetics*, vol. 43, no. 11, pp. 3940–3951, 2007.

[38] S. P. Beeby, M. J. Tudor, R. N. Torah, S. Roberts, T. O'Donnell, and S. Roy, "Experimental Comparison of Macro and Micro Scale Electromagnetic Vibration Powered Generators," *Microsystem* Technologies, vol. 13, no. 11-12, pp. 1647-1653, 2007.

[39] S. Roundy, P. K. Wright, and J. Rabaey, "Micro-Electrostatic Vibration-to-Electricity Converters," *Proceedings of the ASME 2002 International Mechanical Engineering Congress and Exposition*, American Society of Mechanical Engineers, pp. 487-496, 2002.

[40] J. O. Mur Miranda, "Electrostatic Vibration-to-Electric Energy Conversion," Dissertation, Massachusetts Institute of Technology, 2004.

[41] S. Meninger, J. O. Mur Miranda, R. Amirtharajah, A. Chandrakasan, and J. H. Lang, "Vibration-to-Electric Energy Conversion," *IEEE Transactions on Very Large Scale Integration (VLSI) Systems*, vol. 9, no. 1, pp. 64-76, 2001.

[42] E. O. Torres and G. A. Rincón-Mora, "Electrostatic Energy-Harvesting and Battery-Charging CMOS System Prototype," *IEEE Transactions on Circuits and Systems I: Regular Papers*, vol. 56, no. 9, pp. 1938-1948, 2009.

[43] P. D. Mitcheson, P. Miao, B. H. Stark, E. M. Yeatman, A. S. Holmes, and T. C. Green, "MEMS Electrostatic Micropower Generator for Low Frequency Operation," *Sensors and Actuators A: Physical*, vol. 115, no. 2, pp.523-529, 2004.

[44] M. E. Staley, "Development of a Prototype Magnetostrictive Energy Harvesting Device," Dissertation, University of Maryland, 2005.

[45] E. W. Lee, "Magnetostriction and Magnetomechanical Effects," *Reports on Progress in Physics*, vol. 18, no. 1, pp. 184-229, 1955.

[46] A. Adly, D. Davino, A. Giustiniani, and C. Visone, "Experimental Tests of a Magnetostrictive Energy Harvesting Device Toward its Modeling," *Journal of Applied Physics*, vol. 107, no. 9, pp. 09A935, 2010.

[47] D. Davino, A. Giustiniani, and C. Visone, "Analysis of a Magnetostrictive Power Harvesting Device with Hysteretic Characteristics," *Journal of Applied Physics*, vol. 105, no. 7, pp. 07A939, 2009.

[48] L. Wang and F. G. Yuan, "Vibration Energy Harvesting by Magnetostrictive Material," *Smart Materials and Structures*, vol. 17, no. 4, pp. 045009, 2008.

[49] A. Lundgren, H. Tiberg, L. Kvarnsjo, A. Bergqvist, and G. Engdahl, "A Magnetostrictive Electric Generator," *IEEE Transactions on Magnetics*, vol. 29, pp. 3150-3152, 1993.

[50] A. Bayrashev, W. P. Robbins, and B. Ziaie, "Low Frequency Wireless Powering of Microsystems using Piezoelectric–Magnetostrictive Laminate Composites," *Sensors and Actuators A: Physical*, vol. 114, no. 2, pp. 244-249, 2004.

[51] T. Lafont, L. Gimeno, J. Delamare, G. A. Lebedev, D. I. Zakharov, B. Viala, O. Cugat, N. Galopin, L. Garbuio, and O. Geoffroy, "Magnetostrictive–Piezoelectric Composite Structures for Energy Harvesting," *Journal of Micromechanics and Microengineering*, vol. 22, no. 9, pp. 094009, 2012.

[52] M. R. Patel, *Wind and Solar Power Systems: Design, Analysis, and Operation*, Boca Raton, Florida: CRC Press, 1999.

[53] T. Ackermann and L. Söder, "Wind Energy Technology and Current Status: A Review," *Renewable and Sustainable Energy Reviews*, vol. 4, no. 4, pp. 315-374, 2000.

[54] T. Ackermann and L. Söder, "An Overview of Wind Energy-Status 2002," *Renewable and Sustainable Energy Reviews*, vol. 6, no. 1, pp. 67-127, 2002.

[55] C. M. Wang, T. Utsunomiya, S. C. Wee, and Y. S. Choo, "Research on Floating Wind Turbines: A Literature Survey," *The IES Journal Part A: Civil & Structural Engineering*, vol. 3, no. 4, pp. 267-277, 2010.

[56] P. L. Fraenkel, "Tidal Current Energy Technologies," *Ibis*, vol. 148, no. s1, pp. 145-151, 2006.

[57] M. J. Khan, G. Bhuyan, M. T. Iqbal, and J. E. Quaicoe, "Hydrokinetic Energy Conversion Systems and Assessment of Horizontal and Vertical Axis Turbines for River and Tidal Applications: A Technology Status Review," *Applied Energy*, vol. 86, no. 10, pp. 1823-1835, 2009.

[58] F. O. Rourke, F. Boyle, and A. Reynolds, "Tidal Energy Update 2009," *Applied Energy*, vol. 87, no. 2, pp. 398-409, 2010.

[59] M. E. McCormick, *Ocean Wave Energy Conversion*, United States: Courier Corporation, 2013.

[60] J. Cruz, *Ocean Wave Energy: Current Status and Future Prespectives*, Berlin: Springer Science & Business Media, 2007.

[61] A, Muetze and J. G. Vining, "Ocean Wave Energy Conversion - A Survey," *Conference Record of the 2006 IEEE Industry Applications Conference*, International Society for Optics and Photonics, pp. 1410-1417, 2006.

[62] B. Drew, A. R. Plummer, and M. Necip Sahinkaya, "A Review of Wave Energy Converter Technology," *Proceedings of the Institution of Mechanical Engineers, Part A: Journal of Power and Energy*, vol. 223, no. 8, pp. 887-902, 2009.

[63] J. Falnes, "A Review of Wave-Energy Extraction," *Marine Structures*, vol. 20, no. 4, pp. 185-201, 2007.

[64] F. D. O. Antonio, "Wave Energy Utilization: A Review of the Technologies," *Renewable and Sustainable Energy Reviews*, vol. 14, no. 3, pp. 899-918, 2010.

[65] J. Sirohi and R. Mahadik, "Piezoelectric Wind Energy Harvester for Low-Power Sensors," *Journal of Intelligent Material Systems and Structures*, pp. 1-14, 2011.

[66] S. Pobering and N. Schwesinger, "A Novel Hydropower Harvesting Device," *2004 International Conference on MEMS, NANO and Smart Systems, ICMENS 2004 Proceedings,* International Society for Optics and Photonics, pp. 480-485, 2004.

[67] H. D. Akaydın, N. Elvin, and Y. Andreopoulos, "Wake of a Cylinder: A Paradigm for Energy Harvesting with Piezoelectric Materials," *Experiments in Fluids*, vol. 49, no. 1, pp. 291-304, 2010.

[68] S. Shi, T. H. New, and Y. Liu, "Flapping Dynamics of a Low Aspect-Ratio Energy-Harvesting Membrane Immersed in a Square Cylinder Wake," *Experimental Thermal and Fluid Science*, vol. 46, pp. 151-161, 2013.

[69] D.A. Wang, C. Y. Chiu, and H. T. Pham, "Electromagnetic Energy Harvesting from Vibrations Induced by Kármán Vortex Street," *Mechatronics*, vol. 22, no. 6, pp. 746-756, 2012.

[70] D. M. Rowe, "Thermoelectrics, an Environmentally-Friendly Source of Electrical Power," *Renewable Energy*, vol. 16, no. 1, pp. 1251-1256, 1999.

[71] S. B. Riffat and X. Ma, "Thermoelectrics: A Review of Present and Potential Applications," *Applied Thermal Engineering*, vol. 23, no. 8, pp. 913-935, 2003.

[72] J. R. Sootsman, D. Y. Chung, and M. G. Kanatzidis, "New and Old Concepts in Thermoelectric Materials," *Angewandte Chemie International Edition*, vol. 48, no. 46, pp. 8616-8639, 2009.

[73] E. E. Lawreence and G. J. Snyder, "A Study of Heat Sink Performance in Air and Soil for Use in a Thermoelectric Energy Harvesting Device," *Proceedings of the 21st International Conference on Thermoelectronics*, pp. 446-449, 2002.

[74] J. Vázquez, M. A. Sanz-Bobi, R. Palacios, and A. Arenas, "State of the Art of Thermoelectric Generators Based on Heat Recovered from the Exhaust Gases of Automobiles," *Proceedings of the 7th European Workshop on Thermoelectrics*, no. 17, 2002.

[75] D. C. Hoang, Y. K. Tan, H. B. Chng, and S. K. Panda, "Thermal Energy Harvesting from Human Warmth for Wireless Body Area Network in Medical Healthcare System," *International Conference on Power Electronics and Drive Systems, PEDS 2009.* International Society for Optics and Photonics, pp. 1277-1282, 2009.

[76] M. Stordeur and I. Stark, “Low Power Thermoelectric Generator – Self-sufficient Energy Supply for Micro Systems,” *Proceedings of International Conference on Thermoelectrics XVI*, International Society for Optics and Photonics, pp. 575–577, 1997.

[77] H. A. Sodano, G. E. Simmers, R. Dereux, and D. J. Inman, “Recharging Batteries using Energy Harvested from Thermal Gradients,” *Journal of Intelligent Material Systems and Structures*, vol. 18, no. 1, pp. 3-10, 2007.

[78] H. S. Han, Y. H. Kim, S. Y. Kim, S. Um, and J. M Hyun, “Performance Measurement and Analysis of a Thermoelectric Power Generator,” *12th IEEE Intersociety Conference on Thermal and Thermomechanical Phenomena in Electronic Systems (ITherm)*, International Society for Optics and Photonics, pp. 1-7, 2010.

[79] B. Parida, S. Iniyan, and R. Goic, “A Review of Solar Photovoltaic Technologies,” *Renewable and Sustainable Energy Reviews*, vol. 15, no. 3, pp. 1625-1636, 2011.

[80] A. S. Joshi, I. Dincer, and B. V. Reddy, “Performance Analysis of Photovoltaic Systems: A Review,” *Renewable and Sustainable Energy Reviews*, vol. 13, no. 8, pp. 1884-1897, 2009.

[81] G. K. Singh, “Solar Power Generation by PV (Photovoltaic) Technology: A Review,” *Energy*, vol. 53, pp. 1-13, 2013.

[82] L. L. Kazmerski, “Photovoltaics: A Review of Cell and Module Technologies,” *Renewable and Sustainable Energy Reviews*, vol. 1, no. 1, pp. 71-170, 1997.

[83] C. S. Solanki, *Solar Photovoltaic Technology and Systems: A Manual for Technicians, Trainers and Engineers*, Delhi: PHI Learning Private Ltd., 2013.

[84] H. S. Rauschenbach, *Solar Cell Array Design Handbook: The Principles and Technology of Photovoltaic Energy Conversion*, New York: Springer Science & Business Media, 2012.

[85] S. R. Anton and D. J. Inman, “Vibration Energy Harvesting for Unmanned Aerial Vehicles." *The 15th International Symposium on: Smart Structures and Materials & Nondestructive Evaluation and Health Monitoring*. International Society for Optics and Photonics, pp. 692824, 2008.

[86] S. G. Bailey and D. J. Flood, “Space Photovoltaics,” *Progress in Photovoltaics: Research and Applications*, vol. 6, no. 1, pp. 1-14, 1998.

[87] V. Raghunathan, A. Kansal, J. Hsu, J. Friedman, and M. Srivastava, “Design Considerations for Solar Energy Harvesting Wireless Embedded Systems,” *Proceedings of the 4th International Symposium on Information Processing in Sensor Networks*, International Society for Optics and Photonics, no. 64, 2005.

[88] D. L. Mascareñas, M. D. Todd, G. Park, and C. R. Farrar, “Development of an Impedance-Based Wireless Sensor Node for Structural Health Monitoring,” *Smart Materials and Structures*, vol. 16, no. 6, pp. 2137-2145, 2007.

[89] M. Piñuela, P. D. Mitcheson, and S. Lucyszyn, “Ambient RF Energy Harvesting in Urban and Semi-Urban Environments,” *IEEE Transactions on Microwave Theory and Techniques*, vol. 61, no. 7, pp. 2715-2726, 2013.

[90] J. A. Hagerty, F. B. Helmbrecht, W. H. McCalpin, R. Zane, and Z. B. Popovic, “Recycling Ambient Microwave Energy with Broad-Band Rectenna Arrays,” *IEEE Transactions on Microwave Theory and Techniques*, vol. 52, no. 3, pp. 1014-1024, 2004.

[91] T. Sogorb, J. V. Llario, J. Pelegri, R. Lajara, and J. Alberola, "Studying the Feasibility of Energy Harvesting from Broadcast RF Station for WSN." *Instrumentation and Measurement Technology Conference Proceedings, 2008,* International Society for Optics and Photonics, pp.1360-1363, 2008.

[92] J. M. Gilbert and F. Balouchi, "Comparison of Energy Harvesting Systems for Wireless Sensor Networks," I*nternational Journal of Automation and Computing*, vol. 5, no. 4, pp. 334-347, 2008.

[93] K. M. Farinholt, N. Miller, W. Sifuentes, J. MacDonald, G. Park, and C. R. Farrar, "Energy Harvesting and Wireless Energy Transmission for Embedded SHM Sensor Nodes," *Structural Health Monitoring,* vol. 9, no. 3, pp269-280, 2010.

[94] K. M. Farinholt, G. Park, and C. R. Farrar, "RF Energy Transmission for a Low-Power Wireless Impedance Sensor Node," *IEEE Sensors Journal,* vol. 9, no. 7, pp. 793-800, 2009.

[95] D. Mascareñas, E. Flynn, M. Todd, G. Park, and C. Farrar, "Wireless Sensor Technologies for Monitoring Civil Structures," *Sound and Vibration,* vol. 42, no. 4, pp. 16-21, 2008.

[96] D. Mascareñas, E. Flynn, C. Farrar, G. Park, and M. Todd, "A Mobile Host Approach for Wireless Powering and Interrogation of Structural Health Monitoring Sensor Networks," *IEEE Sensors Journal,* vol. 9, no. 12, pp. 1719-1726, 2009.

[97] S. G. Taylor, K. M. Farinholt, E. B. Flynn, E. Figueiredo, D. L. Mascareñas, E. A. Moro, G. Park, M. D. Todd, and C. R. Farrar, "A Mobile-Agent-Based Wireless Sensing Network for Structural Monitoring Applications," *Measurement Science and Technology*, vol. 20, no. 4, pp. 045201, 2009.

[98] A. Lal, R. Duggirala, and H. Li, "Pervasive Power: A Radioisotope-Powered Piezoelectric Generator," *IEEE Pervasive Computing*, vol. 4, no. 1, pp. 53-61, 2005.

[99] J. D. Megiatto, A. Antoniuk-Pablant, B. D. Sherman, G. Kodis, M. Gervaldo, T. A. Moore, A. L. Moore, and D. Gust, "Mimicking the Electron Transfer Chain in Photosystem II with a Molecular Triad Thermodynamically Capable of Water Oxidation," *Proceedings of the National Academy of Sciences*, vol. 109, no. 39, pp. 15579-15583, 2012.

[100] Y. Zhao, J. R. Swierk, J. D. Megiatto, B. Sherman, W. J. Youngblod, D. Qin, D. M. Lentz, A. L. Moore, T. A. Moore, D. Gust, and T. E. Mallouk, "Improving the Efficiency of Water Splitting in Dye-Sensitized Solar Cells by Using a Biomimetic Electron Transfer Mediator," *Proceedings of the National Academy of Sciences*, vol. 109, no. 39, pp. 15612-15616, 2012.

[101] Y. Tadesse, S. Zhang, and S. Priya, "Multimodal Energy Harvesting System: Piezoelectric and Electromagnetic," *Journal of Intelligent Material Systems and Structures*, vol. 20, no. 5, pp. 625-632, 2009.

[102] V. R. Challa, M. G. Prasad, and F. T. Fisher, "A Coupled Piezoelectric–Electromagnetic Energy Harvesting Technique for Achieving Increased Power Output Through Damping Matching." *Smart Materials and Structures*, vol. 18, no. 9, pp. 095029, 2009.

[103] C. Pan, W. Guao, L. Dong, G. Zhu, and Z. L. Wang, "Optical Fiber-Based Core–Shell Coaxially Structured Hybrid Cells for Self-Powered Nanosystems," *Advanced Materials*, vol. 24, no. 25, pp. 3356-3361, 2012.

[104] C. Xu, X. Wang, and Z. L. Wang, "Nanowire Structured Hybrid Cell for Concurrently Scavenging Solar and Mechanical Energies," *Journal of the American Chemical Society*, vol. 131, no. 16, pp. 5866-5872, 2009.

[105] Y. Yang, H. Zhang, G. Zhu, S. Lee, Z. H. Lin, and Z. L. Wang, "Flexible Hybrid Energy Cell for Simultaneously Harvesting Thermal, Mechanical, and Solar Energies," *ACS Nano*, vol. 7, no. 1, pp. 785-790, 2012.

[106] T. Starner, "Human-Powered Wearable Computing," *IBM Systems Journal*, vol. 35, no. 3.4, pp. 618-629, 1996.

[107] M. A. Karami and D. J. Inman, "Powering Pacemakers from Heartbeat Vibrations using Linear and Nonlinear Energy Harvesters," *Applied Physics Letters*, vol. 100, no. 4, pp. 042901, 2012.

[108] L. Halámková, J Halámek, V. Bocharova, A. Szczupak, L. Alfonta, and E. Katz, "Implanted Biofuel Cell Operating in a Living Snail," *Journal of the American Chemical Society*, vol. 134, no. 11, pp. 5040-5043, 2012.

[109] A. Zebda, S. Cosnier, J. P. Alcaraz, M. Holzinger, A. Le Goff, C. Gondran, F. Boucher, F. Giroud, K. Gorgy, H. Lamraoui, and P. Cinquin, "Single Glucose Biofuel Cells Implanted in Rats Power Electronic Devices," *Scientific Reports*, vol. 3, no. 1516, pp. 1-5, 2013.

[110] A. Szczupak, J. Halámek, L Halámková, V. Bocharova, L. Alfonta, and E. Katz, "Living Battery–Biofuel Cells Operating In Vivo in Clams," *Energy & Environmental Science*, vol. 5, no. 10, pp. 8891-8895, 2012.

[111] A. J. Bandodkar, W. Jia, and J. Wang, "Tattoo-Based Wearable Electrochemical Devices: A Review." *Electroanalysis*, vol. 27, no. 3, pp. 562-572, 2015.

[112] E. J. Kjolsing and M. D. Todd, "Frequency Response of a Fixed–Fixed Pipe Immersed in Viscous Fluids, Conveying Internal Steady Flow," *Journal of Petroleum Science and Engineering*, vol. 134, pp. 247-256, 2015.

[113] American Petroleum Institute, "Specification 5CT – Specification for Casing and Tubing," Washingtong DC: American Petroleum Institute, 2005.

[114] American Petroleum Institute, "Bulletin 5C3 – API Bulletin on Formulas and Calculations for Casing, Tubing, Drill Pipe, and Line Pipe Properties," Washington DC: American Petroleum Institute, 2008.

[115] J. C. Guerrero, J. A. Pabon, F. M. Auzerais, K. C. Chen, and K. J. Forbes, "Harvesting Energy in Remote Locations," U.S. Patent No. 7,906,861. 15 Mar. 2011.

[116] Z. Murphree, "Method and Device for Harvesting Energy from Fluid Flow," U.S. Patent Application No. 13/463,719. 16 May 2013.

[117] P. Tubel, C. Cantrelle, S. Kruegel, and C. Bergeron, "Methods and Apparatus for In Situ Generation of Power for Devices Deployed in a Tubular," U.S. Patent Application No. 10/896,386. 22 Jul. 2004.

[118] R. L. Schultz, R. K. Michael, C. E. Robison, and P. D. Ringgenberg, "Vibration Based Power Generator," U.S. Patent No. 6,768,214. 27 Jul. 2004.

[119] R. L. Schultz, P. D. Ringgenberg, C. E. Robison, R. K. Michael, and R. I. Bayh III, "Vibration Based Downhole Power Generator," U.S. Patent No. 6,504,258. 7 Jan. 2003.

[120] M. L. Fripp and R. K. Michael, "Vibration Based Power Generator," U.S. Patent No. 7, 199,480. 3 Apr. 2007.

[121 K. C. Chen, J. A. Pabon, P. Ganguly, M. Ocalan, J. C. Guerror, and K. J. Forbes, "Harvesting Energy from Flowing Fluid," U.S. Patent No. 7,560,856. 14 Jul. 2009.

[122] J. A. Pabon and G. Bettin, "Energy Harvesting from Flow-Induced Vibrations," U.S. Patent No. 8,604,634. 10 Dec. 2013.

[123] J. A. Pabon and G. Bettin, "Enhancing the Effectiveness of Energy Harvesting from Flowing Fluid," U.S. Patent No. 8,421,251. 16 Apr. 2013.

[124] R. J. Wetzel, S. Hiron, A. F. Veneruso, D. R. Patel, T. D. MacDougall, and J. Walter, "Harvesting Vibration for Downhole Power Generation," U.S. Patent Application No. 12/400,024. 9 Mar. 2009.

[125] Marlow Industries, "Energy Harvesting TEG Power Strap For Industrial, Chemical, Oil and Gas Applications," Web, 7 Aug. 2013. <http://www.marlow.com/media/marlow/images/support_guide/EverGen_Power_Strap_White_Paper.pdf >

[126] Oscilla Power, "Downhole," Web, 7 Aug. 2013. < http://oscillapower.com/downhole>

[127] Oscilla Power, "iMEC Technology," Web, 7 Aug. 2013. <http://oscillapower.com/imec-technology>

[128] Tubel Technologies, "Downhole Power Generation and Wireless Communications for Intelligent Completion Applications," Web, 7 Aug. 2013. http://www.netl.doe.gov/kmd/cds/disk11/pdfs/NT41601.pdf

[129] Tubel Technologies, "Downhole Power Generation and Wireless Communications for Intelligent Completions Applications," Web, 7 Aug. 2013. <http://www.netl.doe.gov/technologies/oil-gas/publications/EPreports/NT41601_Final.pdf>

[130] S. S. Rao, *Vibration of Continuous Systems*, Hoboken, New Jersey: John Wiley & Sons, 2007

[131] M. T. Wambsganss, S. S. Chen, and J. A. Jendrzejczyk, "Added Mass and Damping of a Vibrating Rod in Confined Viscous Fluids," Springfield, Virginia: National Technical Information Service; U.S. Department of Commerce, 1974.

[132] G. G. Stokes, *Mathematical and Physical Papers Vol.3: On the Effect of the Internal Friction of Fluids on the Motion of Pendulums*, 1851.

[133] L. Rosenhead, *Laminar Boundary Layers*, Oxford: Clarendon Press, 1963.

[134] S. S. Chen, "Fluid Damping for Circular Cylindrical Structures," *Nuclear Engineering and Design*, vol. 63, no.1, pp. 81-100, 1981.

[135] E. O. Tuck, "Calculation of Unsteady Flows due to Small Motions of Cylinders in a Viscous Fluid," *Journal of Engineering Mathematics*, vol. 3, no. 1, pp. 29-44, 1969.

[136] S. S. Chen, M. T. Wambsganss, and J. A. Jendrzejczyk, "Added Mass and Damping of a Vibrating Rod in Confined Viscous Fluids," *Journal of Applied Mechanics*, vol. 43, no. 2, pp. 325-329, 1976.

[137] R. Chilukuri, "Added Mass and Damping for Cylinder Vibrations Within a Confined Fluid Using Deforming Finite Elements," *Journal of Fluids Engineering*, vol. 109, no. 3, pp. 283-288, 1987.

[138] G. A. Cranch, J. E. Lane, G. A. Miller, and J. W. Lou, "Low Frequency Driven Oscillations of Cantilevers in Viscous Fluids at Very Low Reynolds Number," *Journal of Applied Physics*, vol. 113, no. 19, pp. 194904, 2013.

[139] G. A. Cranch, G. A. Miller, and C. K. Kirkendall, "Fiber-Optic, Cantilever-Type Acoustic Motion Velocity Hydrophone," *The Journal of the Acoustical Society of America*, vol. 132, no. 1, pp.103-114, 2012.

[140] V. F. Siniavskii, V. S. Fedotovskii, and A. B. Kukhtin, "Oscillation of a Cylinder in a Viscous Liquid," *Prikladnaia Mekhanika*, vol. 16, pp. 62-67, 1980.

[141] B. Weiss, E. K. Reichel, and B. Jakoby, "Modeling of a Clamped–Clamped Beam Vibrating in a Fluid for Viscosity and Density Sensing Regarding Compressibility," *Sensors and Actuators A: Physical*, vol. 143, no. 2, pp. 293-301, 2008.

[142] S. Basak, A. Raman, and S. V. Garimella, "Hydrodynamic Loading of Microcantilevers Vibrating in Viscous Fluids," *Journal of Applied Physics*, vol. 99, no. 11, pp. 114906, 2006.

[143] J. W. M. Chon, P. Mulvaney, and J. E. Sader, "Experimental Validation of Theoretical Models for the Frequency Response of Atomic Force Microscope Cantilever Beams Immersed in Fluids," *Journal of Applied Physics*, vol. 87, no. 8, pp. 3978-3988, 2000.

[144] C. P. Green and J. E. Sader, "Frequency Response of Cantilever Beams Immersed in Viscous Fluids Near a Solid Surface with Applications to the Atomic Force Microscope," *Journal of Applied Physics*, vol. 98, no. 11, pp. 114913, 2005.

[145] A. Maali, C. Hurth, R. Boisgard, C. Jai, T. Cohen-Bouhacina, and J. P. Aime, "Hydrodynamics of Oscillating Atomic Force Microscopy Cantilevers in Viscous Fluids," *Journal of Applied Physics*, vol. 97, no. 7, pp.074907, 2005.

[146] J.E. Sader, "Frequency Response of Cantilever Beams Immersed in Viscous Fluids with Applications to the Atomic Force Microscope," *Journal of Applied Physics*, vol. 84, no. 1, pp. 64-76, 1998.

[147] B. R. Munson, D. F. Young, and T. H. Okiishi, *Fundamentals of Fluid Mechanics, 5th Edition*, Hoboken, New Jersey: John Wiley & Sons, Inc., 2006.

[148] H. L. Dodds Jr and H. L. Runyan, "Effect of High-Velocity Fluid Flow on the Bending Vibrations and Static Divergence of a Simply Supported Pipe," No. NASA-TN-D-2870. National Aeronautics and Space Administration Hampton VA Langley Research Center, 1965.

[149] G. W. Housner, "Bending Vibrations of a Pipe Line Containing Flowing Fluid," *Journal of Applied Mechanics-Transactions of the ASME*, vol. 19, no. 2, pp. 205-208, 1952.

[150] R. H. Long, "Experimental and Theoretical Study of Transverse Vibration of a Tube Containing Flowing Fluid," *Journal of Applied Mechanics*, vol. 77, no. 1, pp. 65-68, 1955.

[151] S. Naguleswaran and C. J. H. Williams, "Lateral Vibration of a Pipe Conveying a Fluid," *Journal of Mechanical Engineering Science*, vol. 10, no. 3, pp. 228-238, 1968.

[152] R. W. Gregory and M. P. Païdoussis, "Unstable Oscillation of Tubular Cantilevers Conveying Fluid. I. Theory," *Proceedings of the Royal Society of London. Series A. Mathematical and Physical Sciences*, vol. 293, no. 1435, pp. 512-527, 1966.

[153] R. W. Gregory and M. P. Païdoussis, "Unstable Oscillation of Tubular Cantilevers Conveying Fluid. II. Experiments," *Proceedings of the Royal Society of London. Series A. Mathematical and Physical Sciences*, vol. 293, no. 1435, pp. 528-542, 1966.

[154] M. Kheiri, M. P. Païdoussis, G. Costa Del Pozo, and M. Amabili, "Dynamics of a Pipe Conveying Fluid Flexibly Restrained at the Ends," *Journal of Fluids and Structures*, vol. 49, pp. 360-385, 2014.

[155] R. Bao, "Analysis of Fluid-Solid Coupling Characteristics of Oil and Gas Submarine Span Pipelines," *Journal of Pipeline Systems Engineering and Practice*, vol. 6, no. 3, pp. A4014001, 2014.

[156] S. I. Lee and J. Chung, "New Non-Linear Modelling for Vibration Analysis of a Straight Pipe Conveying Fluid," *Journal of Sound and Vibration*, vol. 254, no. 2, pp. 313-325, 2002.

[157] U. Lee, C. H. Pak, and S. C. Hong, "The Dynamics of a Piping System with Internal Unsteady Flow," *Journal of Sound and Vibration*, vol. 180, no. 2, pp. 297-311, 1995.

[158] U. Lee and J. Park, "Spectral Element Modelling and Analysis of a Pipeline Conveying Internal Unsteady Fluid," *Journal of Fluids and Structures*, vol. 22, no. 2, pp. 273-292, 2006.

[159] M. P. Païdoussis and N. T. Issid, "Dynamic Stability of Pipes Conveying Fluid," *Journal of Sound and Vibration*, vol. 33, no. 3, pp. 267-294, 1974.

[160] Y. S. Seo, W. B. Jeong, S. H. Jeong, J. S. Oh, and W. S. Yoo, "Finite Element Analysis of Forced Vibration for a Pipe Conveying Harmonically Pulsating Fluid," *JSME International Journal Series C Mechanical Systems, Machine Elements and Manufacturing*, vol. 48, no. 4, pp. 688-694, 2005.

[161] M. Hosseini, M., M. Sadeghi-Goughari, S. A. Atashipour, and M. Eftekhari, "Vibration Analysis of Single-Walled Carbon Nanotubes Conveying Nanoflow Embedded in a Viscoelastic Medium using Modified Nonlocal Beam Model," *Archives of Mechanics*, vol. 66, no. 4, pp. 217-244, 2014.

[162] I. Lottati and A. Kornecki, "The Effect of an Elastic Foundation and of Dissipative Forces on the Stability of Fluid-Conveying Pipes," *Journal of Sound and Vibration*, vol. 109, no. 2, pp. 327-338, 1986.

[163] P. Soltani, M. M. Taherian, and A. Farshidianfar, "Vibration and Instability of a Viscous-Fluid-Conveying Single-Walled Carbon Nanotube Embedded in a Visco-Elastic Medium," *Journal of Physics D: Applied Physics*, vol. 43, no. 42, pp. 425401, 2010.

[164] T. T. Yeh and S. S. Chen, "The Effect of Fluid Viscosity on Coupled Tube/Fluid Vibrations," *Journal of Sound and Vibration*, vol. 59, no. 3, pp. 453-467, 1978.

[165] M. P. Païdoussis, S. P. Chan, and A. K. Misra, "Dynamics and Stability of Coaxial Cylindrical Shells Containing Flowing Fluid," *Journal of Sound and Vibration*, vol. 97, no. 2, pp. 201-235, 1984.

[166] M. P. Païdoussis, A. K. Misra, and S. P. Chan, "Dynamics and Stability of Coaxial Cylindrical Shells Conveying Viscous Fluid," *Journal of Applied* Mechanics, vol. 52, no. 2, pp. 389-396, 1985.

[167] T. T. Yeh and S. S. Chen, "Dynamics of a Cylindrical Shell System Coupled by Viscous Fluid," *The Journal of the Acoustical Society of America*, vol. 62, no. 2, pp. 262-270, 1977.

[168] M. P. Païdoussis, "Flutter of Conservative Systems of Pipes Conveying Incompressible Fluid," *Journal of Mechanical Engineering Science*, vol. 17, no. 1, pp. 19-25, 1975.

[169] M. P. Païdoussis, *Fluid-Structure Interactions: Slender Structures and Axial Flow, Vol. 1*, Amsterdam: Academic press, 2014.

[170] M. P. Païdoussis and N. T. Issid, "Dynamic Stability of Pipes Conveying Fluid," *Journal of Sound and Vibration*, vol. 33, no. 3, pp. 267-294, 1974.

[171] J. Brill, "Modeling Multiphase Flow in Pipes," *Society of Petroleum Engineers: The Way Ahead*, vol. 6, no. 2, pp. 16-17, 2010.

[172] H. Cholet, *Well Production Practical Handbook*, Editions Technip, 2008.

[173] J. F. Doyle, *Wave Propagation in Structures*, Springer US, 1989.

[174] U. Lee, *Spectral Element Method in Structural Dynamics*, Singapore: John Wiley & Sons, 2009.

[175] U. Lee, I. Jang, and H. Go, "Stability and Dynamic Analysis of Oil Pipelines by Using Spectral Element Method," *Journal of Loss Prevention in the Process Industries*, vol. 22, no. 6, pp. 873-878, 2009.

[176] U. Lee and H. Oh, "The Spectral Element Model for Pipelines Conveying Internal Steady Flow," *Engineering Structures*, vol. 25, no. 8, pp. 1045-1055, 2003.

[177] G. V. Narayanan and D. E. Beskos, "Use of Dynamic Influence Coefficients in Forced Vibration Problems with the Aid of Fast Fourier Transform," *Computers & Structures*, vol. 9, no. 2, pp. 145-150, 1978.

[178] E. Kjolsing and M. Todd, "Shifts in the Fundamental Frequency of a Fluid Conveying Pipe Immersed in a Viscous Fluid for use in the Optimization of an Energy Harvesting System to be Deployed in a Producing Hydrocarbon Well," *SPE Western Regional Meeting*, Society of Petroleum Engineers, 2015.

[179] G.L. Kuiper and A.V. Metrikine, "Experimental Investigation of Dynamic Stability of a Cantilever Pipe Aspirating Fluid," *Journal of Fluids and Structures*, vol. 24, no. 4, pp. 541-558, 2008.

[180] M.P. Païdoussis, C. Semler, and M. Wadham-Gagnon, "A Reappraisal of Why Aspirating Pipes do not Flutter at Infinitesimal Flow," *Journal of Fluids and Structures*, vol. 20, no. 1, pp. 147-156, 2005.

[181] M.P. Païdoussis and G.X. Li, "Pipes Conveying Fluid: a Model Dynamical Problem," *Journal of Fluids and Structures*, vol. 7, no. 2, pp. 137-204, 1993.

[182] V. V. Bolotin, *The Dynamic Stability of Elastic Systems*, Holden-Day, Inc., 1974.

[183] Schlumberger, "Signature Quartz Gauges," Web, 9 Mar. 2015. <http://www.slb.com/services/characterization/testing/drillstem/downhole_test_tools/~/media/Files/testing/product_sheets/pressure/signature_quartz_gauge_ps.ashx>

[184] Schlumberger, "Signature Quartz Gauge Carrier," Web, 9 Mar. 2015. <http://www.slb.com/services/characterization/testing/drillstem/downhole_test_tools/~/media/Files/testing/product_sheets/pressure/signature_quartz_gauge_carrier_ps.ashx>

[185] The Society of Petroleum Engineers – International, "Tubing Selection, Design, and Installation," Web, 9 Mar. 2015. <http://petrowiki.org/PEH%3ATubing_Selection,_Design,_and_Installation>

[186] Schlumberger, "High Pressure, High Temperature," Web, 9 Mar. 2015. <http://www.slb.com/services/technical_challenges/high_pressure_high_temperature.aspx>

[187] The Society of Petroleum Engineers – International, "Strength of Casing and Tubing," Web, 9 Mar. 2015. <http://petrowiki.org/Strength_of_casing_and_tubing>

[188] The Society of Petroleum Engineers – International, "Tubing Design Factors," Web, 9 Mar. 2015. <http://petrowiki.org/Tubing_design_factors>

[189] S. Timoshenko, *Strength of Materials*, New York: R. E. Krieger Publications, 1976.

[190] W. Renpu, *Advanced Well Completion Engineering, 3rd Edition*, Oxford: Gulf Professional Publishing, 2011.

[191] E. Kjolsing and M. Todd, "Gauging the Feasibility of a Downhole Energy Harvesting System Through a Proof-of-Concept Study," *SPIE Smart Structures and Materials+ Nondestructive Evaluation and Health Monitoring*, International Society for Optics and Photonics, pp. 97992K, 2016.

[192] American Petroleum Institute, "Technical Report 1PER15K-1 - Protocol for Verification and Validation of High-pressure High-temperature Equipment, First Edition," Washington DC: American Petroleum Institute, 2013.

[193] J. Chen, B. Young, and B. Uy, "Behavior of High Strength Structural Steel at Elevated Temperatures," *Journal of Strucutural Engineering*, vol. 132, no. 12, pg. 1948-1954, 2006.

[194] J. Outinen and P. Mäkeläinen, "Mechanical Properties of Structural Steel at Elevated Temperatures and After Cooling Down." *Fire and Materials*, vol. 28, no. 2-4, pp. 237-251, 2004.

[195] Eurocode, "Eurocode 3: Design of Steel Structures – Part 1-2: General Rules-Structural Fire Design." Brussels: European Committee for Standardization, 1993.

[196] J. L. Ruddy, J. P. Marlo, S. A. Loanneides, and F. Alfawakhiri, "AISC Design Guide 19: Fire Resistance of Structural Steel Framing," American Institute of Steel Construction, 2003.

[197] A. Lubinski, "Influence of Neutral Axial Stress on Yield and Collapse of Pipe," *Journal of Engineering for Industry*, vol. 97, no. 2, pp. 400-407, 1975.

[198] American Institute of Steel Construction, "AISC Steel Manual, Thirteenth Edition," American Institute of Steel Construction, 2007.

[199] Perpetuum, "Vibration Energy Harvesters," Web, 10 Oct. 2015. < http://www.perpetuum.com/products/vibration-energy-harvester.asp>

[200] C. B. Williams and R. B. Yates, "Analysis of a Micro-Electric Generator for Microsystems," *Sensors and Actuators A*, vol. 52, no. 1, pp. 8-11, 1996.

[201] S. Roundy, P. K. Wright, and J. Rabaey, "A Study of Low Level Vibrations as a Power Source for Wireless Sensor Nodes," *Computer Communications*, vol. 26, no. 11, pp. 1131-1144, 2003.

[202] A. Z. Trimble, "Downhole Vibration Sensing by Vibration Energy Harvesting," Dissertation, Massachusetts Institute of Technology, 2007.

[203] A. Erturk and D. J. Inman, "On Mechanical Modeling of Cantilevered Piezoelectric Vibration Energy Harvesters," *Journal of Intelligent Material Systems and Structures*, vol. 00, pp.1-16, 2008.

[204] S. S. Rao, *Mechanical Vibrations, Vol. 4*, New York: Addison-Wesley, 1995.

[205] A. Erturk, and D. J. Inman, "An Experimentally Validated Bimorph Cantilever Model for Piezoelectric Energy Harvesting from Base Excitations," *Smart Materials and Structures*, vol. 18, no. 2, pp. 025009, 2009.

[206] A. Erturk and D. J. Inman, "A Distributed Parameter Electromechanical Model for Cantilevered Piezoelectric Energy Harvesters," *Journal of Vibration and Acoustics*, vol. 130, no. 4, pp. 041002, 2008.

[207] R. Craig, *Mechanics of Materials, Third Edition*, New York: John Wiley & Sons, 2011

[208] G. K. Ottman, H. F. Hofmann, A. C. Bhatt, and G. A. Lesieutre, "Adaptive Piezoelectric Energy Harvesting Circuit for Wireless Remote Power Supply," *IEEE Transactions on Power Electronics*, vol. 17, no. 5, pp. 669-676, 2002.

[209] J. L. Meriam and L. G. Kraige, *Engineering Mechanics: Dynamics, Vol. 2*, Hoboken, New Jersey: John Wiley & Sons, 2012.

[210] M. W. Hooker, "Properties of PZT-Based Piezoelectric Ceramics Between -150 and 250 C," NASA/CR-1998-208708 National Aeronautics and Space Administration Hampton VA Langley Research Center, 1998.

[211] Y. Ohmachi and N. Uchida, "Temperature Dependence of Elastic, Dielectric, and Piezoelectric Constants in TeO2 Single Crystals," *Journal of Applied Physics*, vol. 41, no. 6, pp. 2307-2311, 1970.

[212] A. D. Nashif, D. I. Jones, and J. P. Henderson, *Vibration Damping*, New York: John Wiley & Sons, 1985.

[213] D. I. Jones, *Handbook of Viscoelastic Vibration Damping*, London: John Wiley & Sons, 2001.

[214] R. G. Sabat, B. K. Mukherjee, W. Ren, and G. Yang, "Temperature Dependence of the Complete Material Coefficients Matrix of Soft and Hard Doped Piezoelectric Lead Zirconate Titanate Ceramics," *Journal of Applied Physics*, vol. 101, no. 6, pp. 064111, 2007.

[215] R. A. Wolf and S. Trolier-McKinstry, "Temperature Dependence of the Piezoelectric Response in Lead Zirconate Titanate Films," *Journal of Applied Physics*, vol. 95, no. 3, pp. 1397-1406, 2004.

[216] Mide, "Products Datasheet," Web, 24 June 2016. < http://info.mide.com/piezo-products/download-piezo-products-datasheets>

[217] B. Boehme and K. J. Wolter, "Study of Temperature Dependent Properties of Organic Substrate Materials," *Microelectronics Reliability*, vol. 48, no. 6, pp. 876-880, 2008.

[218] D. Wang, Y. Fotinich, and G. P. Carman, "Influence of Temperature on the Electromechanical and Fatigue Behavior of Piezoelectric Ceramics," *Journal of Applied Physics*, vol. 83, no. 10, pp. 5342-5350, 1998.

[219] H. Jaffe and D. A. Berlincourt, "Piezoelectric Transducer Materials," *Proceedings of the IEEE*, vol. 53, no. 10, pp. 1372-1386, 1965.

[220] P. Glynne-Jones, S. P. Beeby, and N. M. White, "A Method to Determine the Ageing Rate of Thick-Film PZT Layers," *Measurement Science and Technology*, vol. 12, no. 6, pp. 663-670, 2001.

[221] A. G. Kolbeck, "Aging of Piezoelectricity in Poly (Vinylidene Fluoride)," *Journal of Polymer Science: Polymer Physics Edition*, vol. 20, no. 11, pp. 1987-2001, 1982.

[222] J. F. Shepard Jr, F. Chu, I. Kanno, and S. Trolier-McKinstry, "Characterization and Aging Response of the d31 Piezoelectric Coefficient of Lead Zirconate Titanate Thin Films," *Journal of Applied Physics*, vol. 85, no. 9, pp. 6711-6716, 1999.

[223] Piezo Technologies, "Usage Temperatures of Piezoceramic Materials," Web, 24 June 2016. <http://piezotechnologies.com/knowledge-desk/meggitt-termpature-usage-temperatures>

[224] Piezo Technology, "Piezoelectric Material Data," Web, 24 June 2016. <http://www.piceramic.com/products/piezoelectric-materials.html>

[225] NEC/TOKIN, "Piezoelectric Ceramics," Web, 24 June 2016. <https://www.nec-tokin.com/english/product/pdf_dl/piezoelectricceramics.pdf>

[226] P. Pillatsch, N. Shashoua, A. S. Holmes, E. M. Yeatman, and P. K. Wright, "Degradation of Piezoelectric Materials for Energy Harvesting Applications," *Journal of Physics: Conference Series*, IOP Publishing, vol. 557, no. 1, pp. 012129, 2014.

[227] M. A. Miner, "Cumulative Damage in Fatigue," *Journal of Applied Mechanics*, vol. 12, no. 3, pp. 159-164, 1945.

[228] MathWorks, "Rainflow Counting Algorithm," Web, 10 June 2016. <http://www.mathworks.com/matlabcentral/fileexchange/3026-rainflow-counting-algorithm/content/index.html>

[229] A. Niesony, "Determination of Fragments of Multiaxial Service Loading Strongly Influencing the Fatigue of Machine Components," *Mechanical Systems and Signal Processing*, vol. 23, no. 8, pp. 2712-2721, 2009.

[230] Wolfram, "Fourier Series-Square Wave," Web, 10 June 2016. <http://mathworld.wolfram.com/FourierSeriesSquareWave.html>